

Mechanisms and Machine Science 60

Katia Lucchesi Cavalca  
Hans Ingo Weber *Editors*

# Proceedings of the 10th International Conference on Rotor Dynamics – IFToMM

Vol. 1

 Springer

# Mechanisms and Machine Science

Volume 60

## Series editor

Marco Ceccarelli

LARM: Laboratory of Robotics and Mechatronics

DICeM: University of Cassino and South Latium

Via Di Biasio 43, 03043 Cassino (Fr), Italy

e-mail: ceccarelli@unicas.it

## Editorial Board Members

Alfonso Hernandez

Mechanical Engineering, University of the Basque Country, Bilbao, Vizcaya, Spain

Tian Huang

Department of Mechatronical Engineering, Tianjin University, Tianjin, China

Steven A. Velinsky

Mechanical and Aerospace Engineering, University of California Davis, Davis, California, USA

Yukio Takeda

Mechanical Engineering, Tokyo Institute of Technology, Tokyo, Japan

Burkhard Corves

Institute of Mechanism Theory, Machine D, RWTH Aachen University, Aachen, Nordrhein-Westfalen, Germany

This book series establishes a well defined forum for monographs, edited Books, and proceedings on mechanical engineering with particular emphasis on MMS (Mechanism and Machine Science). The final goal is the publication of research that shows the development of mechanical engineering and particularly MMS in all technical aspects, even in very recent assessments. Published works share an approach by which technical details and formulation are discussed, and discuss modern formalisms with the aim to circulate research and technical achievements for use in professional, research, academic, and teaching activities. This technical approach is an essential characteristic of the series. By discussing technical details and formulations in terms of modern formalisms, the possibility is created not only to show technical developments but also to explain achievements for technical teaching and research activity today and for the future. The book series is intended to collect technical views on developments of the broad field of MMS in a unique frame that can be seen in its totality as an Encyclopaedia of MMS but with the additional purpose of archiving and teaching MMS achievements. Therefore the book series will be of use not only for researchers and teachers in Mechanical Engineering but also for professionals and students for their formation and future work. Indexed in SCOPUS, Ei Compendex, EBSCO Discovery Service, OCLC, ProQuest Summon, Google Scholar and SpringerLink.

More information about this series at <http://www.springer.com/series/8779>

Katia Lucchesi Cavalca · Hans Ingo Weber  
Editors

# Proceedings of the 10th International Conference on Rotor Dynamics – IFToMM

Vol. 1

 Springer

*Editors*

Katia Lucchesi Cavalca  
Faculty of Mechanical Engineering  
University of Campinas  
Campinas, São Paulo  
Brazil

Hans Ingo Weber  
Mechanical Engineering Department  
Pontifical Catholic University of Rio  
de Janeiro  
Rio de Janeiro, Rio de Janeiro  
Brazil

ISSN 2211-0984

ISSN 2211-0992 (electronic)

Mechanisms and Machine Science

ISBN 978-3-319-99261-7

ISBN 978-3-319-99262-4 (eBook)

<https://doi.org/10.1007/978-3-319-99262-4>

Library of Congress Control Number: 2018951101

© Springer Nature Switzerland AG 2019

This work is subject to copyright. All rights are reserved by the Publisher, whether the whole or part of the material is concerned, specifically the rights of translation, reprinting, reuse of illustrations, recitation, broadcasting, reproduction on microfilms or in any other physical way, and transmission or information storage and retrieval, electronic adaptation, computer software, or by similar or dissimilar methodology now known or hereafter developed.

The use of general descriptive names, registered names, trademarks, service marks, etc. in this publication does not imply, even in the absence of a specific statement, that such names are exempt from the relevant protective laws and regulations and therefore free for general use.

The publisher, the authors and the editors are safe to assume that the advice and information in this book are believed to be true and accurate at the date of publication. Neither the publisher nor the authors or the editors give a warranty, express or implied, with respect to the material contained herein or for any errors or omissions that may have been made. The publisher remains neutral with regard to jurisdictional claims in published maps and institutional affiliations.

This Springer imprint is published by the registered company Springer Nature Switzerland AG  
The registered company address is: Gewerbestrasse 11, 6330 Cham, Switzerland

# Preface

Rotordynamics is an area of engineering which congregates a very well-defined community between science and technology. Huge part of power generation uses rotating machines, and engineering had an incredible development since the first steam energy devices. The International Federation for the Promotion of Mechanism and Machine Science (IFTToMM) opened to this community the possibility to present the advances in this area in a quadrennial conference: This resulted in 1982 in the first IFTToMM International Conference on Rotordynamic Problems in Power Plants. The importance of periodically exchanging new ideas and comparing experimental test rigs and field measurements cannot be underestimated. The evolution that took place can easily be followed comparing the papers published in the proceedings since that time. It was obvious to broaden the spectrum and the name became since 1986 IFTToMM International Conference on Rotordynamics. This conference turned out to be a reward for each of the countries and their cities (Tokyo 1986, Lyon 1990, Chicago 1994, Darmstadt 1998, Sydney 2002, Vienna 2006, Seoul 2010, Milano, 2014) for the efforts developing their own research groups on this subject.

Formal academic graduate programs started in Brazil in the late 60s. Only in the 70s, the binomial higher education and research, including hands-on activities in laboratories, started to change the teaching in engineering. UNICAMP, a young university at that time, was a pioneer in graduating engineers able to conceive, design, and construct their ideas. The first crisis of oil prices led to the development of a group handling rotating machines, building flywheels for energy storage, investigating hybrid power systems, and looking for other alternative solutions. In the beginning of the 80s, there was small group of people working in rotordynamics. And there were some recent huge power plants like Ilha Solteira, Jupiá, Itaipú: They needed engineers which could explain the phenomena appearing in a Francis and Kaplan turbines. UNICAMP was eager to put their graduate students to work on open problems in this area. The year was 1982 and the first meeting in Rome was also a good opportunity to start international academic cooperation with several European countries and young researchers on this area as well as engineers had their own cooperation with companies dealing with rotating machines. Several

young scientists then went to Europe to complete their PhD. One highlight in the 2000's was the Alfa II Project, led by Prof. Bachschmidt from Politecnico di Milano on Vibration, Control and Diagnostics (VICONDIA) that put together the Politecnico de Catalunia, DTU, PUC-Rio, UFRJ, University of Uberlândia, ISPJAE from La Habana (Cuba) and University of Concepcion (Chile). But there were several other cooperation programs between Brazilian research groups and, usually, European institutions.

This resulted in a well-developed research area in Brazil. In 1986, the biennial DINAME meeting was started, as a result of a cooperation with Germany, supported by the Alexander von Humboldt Foundation and Volkswagen Foundation investigating the dynamics of a hydraulic Francis turbine. This meeting keeps its tradition and is open to all dynamic problems in mechanical systems. The groups working with rotating machines spread out through the country, and you will find expertise in several applications like turbines, compressors, turbochargers, centrifuges, helicopter blades, dental drills, oil drill strings.

The Brazilian Committee responsible for organizing the present IFToMM Conference felt comfortable to propose Rio de Janeiro in 2018 as the next venue. And this proposal was approved by the IFToMM Rotordynamic Committee at the Milano Conference. The Brazilian Committee is honored to execute this mission. The committee is composed by specialists from several universities throughout the country that shared the burden to organize an important international event. The interaction with industry is the scope of the industry technical committee. The result of the initiative is the selection of 153 papers under 175 submissions, being therefore the second largest IFToMM Rotordynamic conference besides being the first one in Latin America.

The present four volumes printed by Springer Nature with approximately 153 papers reproduce the state of the art of the research throughout the world. These papers were carefully reviewed by two independent reviewers, and its quality as a publication was attested. Volume 1 will focus on bearings and seals, Volume 2 on condition monitoring, fault diagnostics, prognostics as well as dynamic analysis and stability, Volume 3 on active components and vibration control; blades, bladed systems, and impellers; modal testing and identification; nonlinear phenomena in rotordynamics; torsional vibration and geared system dynamics, and Volume 4 on some innovative applications from aero-engines; automotive rotating systems; balancing; electromechanical interactions in rotordynamics; fluid–structure interactions; hydro power plant; parametric and self-excitation; rotordynamics of micro-, nano- and cryogenic machines; turbochargers; uncertainties, reliability, and life predictions of rotating machinery; wind turbines and generators.

As chairwoman and as chairman of the conference, we did not spare efforts in trying to do the best for a successful conference. As we proposed to organize the meeting in 2014, Rio de Janeiro was putting all the effort in the Olympic Games. It was perfectly organized, and everybody was proud of it. It was a climax for the city. In these last two years, there were radical changes some for good like the fight against corruption, some for bad due to the failure in politics and losing control of several important aspects in the everyday life. But Rio is the “marvelous city”

where nature made its best to combine ocean and mountains, and we hope all of the participants will have the opportunity to enjoy it.

Both chairs of the Conference express their gratitude to the TC of Rotordynamics for the thrust and the opportunity given, to the efficient work of the reviewers, to all authors and their students giving reason for the existence of the Conference, to the unbearable support from our colleagues of the local committees. We also appraise the support of the rector of UNICAMP, of its Faculty of Mechanical Engineering and to FUNCAMP foundation for the unconditional support and help with the logistics. We also express our satisfaction for the sponsoring of BorgWarner, MTS Brazil, Siemens, and the funding agencies CNPq—National Council for Scientific and Technological Development and CAPES—Brazilian Federal Agency for Support and Evaluation of Graduate Education.

Katia Cavalca  
Hans I. Weber



# Acknowledgements

To Prof. Hans Weber, who introduced me to research and guided me through the rotordynamic area, for the partnership and thrust by the challenge to organize this meeting, with respect and admiration.

To Prof. Nicolò Bachschmid, my dear doctor degree advisor in the Polytechnic of Milan.

To the colleagues Gregory B. Daniel, Helio F. de Castro, Ricardo U. Mendes, Tiago H. Machado, and Eduardo P. Okabe, for their confidence and friendship, besides the hard work done in finalizing the articles for publishing.

To my dear students to play a so important role and meaning in my professional and personal life.

To my beloved family, my husband Franco and my daughter Bianca, for the unconditional support, affection, and the everyday inspiring presence in my life.

Katia

To Kurt Magnus and the colleagues at the Institute of TU München where I acquired between 1968 and 1971 the fertile soil to let my own initiative in research grow. To some special friends from that time Peter C. Müller, H. H. Müller Slany, Gerhard Schweitzer.

To friends which were relevant in finding my way to rotordynamics, Robert Gasch, Rainer Nordmann, Michel Lalanne.

To my students, the main reward of advising research is the success of the students, our family broad sense. To Franciso Paulo Lepore, my first PhD student and reason of success in the 70s of the group at UNICAMP (we called it GEPROM). To Ilmar Santos, dear student, friend, and colleague. To Katia Cavalca and her incredible capacity of aggregate and leading their students.

To Djenane Pamplona who shares profession and family, for the constant support.

Hans

# Contents

<b>Numerical Identification of Nonlinear Hydrodynamic Forces</b> . . . . .	1
Diogo Stuani Alves and Katia Lucchesi Cavalca	
<b>Thermo-Hydrodynamic Model Influence on First Order Coefficients in Turbocharger Thrust Bearings</b> . . . . .	16
Thales Freitas Peixoto, Gregory Bregion Daniel, and Katia Lucchesi Cavalca	
<b>Study of Stiffness Reduced Order Model Applied to Line and Elliptical Contact Under EHD Lubrication</b> . . . . .	32
Letícia Bizarre, Natália Akemi Hoshikawa Tsuha, and Katia Lucchesi Cavalca	
<b>Stiffness and Damping Reduced Model in EHD Line Contacts</b> . . . . .	43
Natália Akemi Hoshikawa Tsuha, Fábio Nonato, and Katia Lucchesi Cavalca	
<b>Dynamical Characteristic Analysis of Elastic Ring Squeeze Film Damper in Rotor System</b> . . . . .	56
Zhifei Han, Qian Ding, and Wei Zhang	
<b>Unbalance Vibration Compensation Control Using Deep Network for Rotor System with Active Magnetic Bearings</b> . . . . .	72
Xuan Yao, Zhaobo Chen, and Yinghou Jiao	
<b>Unbalance Identification in a Rotor Supported by Active Magnetic Bearing</b> . . . . .	82
Gilberto Machado da Silva and Robson Pederiva	
<b>Numerical Study on the Influence of Gas Foil Thrust Bearings on the Vibrational Behavior</b> . . . . .	97
Tomasz Pronobis, Alexander Ramin, and Robert Liebich	

<b>Magnetic Bearings for Non-static Flywheel Energy Storage Systems (FESS)</b> . . . . .	116
Nikolaj Dagnaes-Hansen and Ilmar F. Santos	
<b>Application of the Controllable Magnetorheological Squeeze Film Dampers for Minimizing Energy Losses and Driving Moment of Rotating Machines</b> . . . . .	132
Jaroslav Zapoměl, Petr Ferfecki, and Jan Kozánek	
<b>Power Loss and Temperature Growth in the Backup Bearing of AMB-Supported High-Speed Electric Motor During a Dropdown</b> . . .	144
Neda Neisi, Eerik Sikanen, Janne E. Heikkinen, Teemu Sillanpää, and Jussi Sopanen	
<b>Simulation of a Test Rig and Identification of Annular Gas Seals Coefficients</b> . . . . .	157
David Maldonado, Diego Godoy, Vinicius Côrtes, Fernando Pinto, and Thiago Ritto	
<b>The Classical Linearization Technique’s Validity for Compliant Bearings</b> . . . . .	177
Sebastian von Osmanski, Jon S. Larsen, and Ilmar F. Santos	
<b>Rotordynamic Force Coefficients of Gas Seals — An Experimental Approach with Active Magnetic Rotor Excitation</b> . . . . .	192
Clemens Griebel	
<b>Analysis of the Rotor Supported by Gas Foil Bearings Considering the Assembly Preload and Hardening Effect</b> . . . . .	208
Grzegorz Żywica, Jan Kiciński, and Małgorzata Bogulicz	
<b>Selection of the Bearing System for a 1 kW ORC Microturbine</b> . . . . .	223
Łukasz Breńkacz, Grzegorz Żywica, and Małgorzata Bogulicz	
<b>Experimental and Theoretical Comparison Between the Ball and Pinned Bearing Working as Backup Bearing for Magnetically Levitated Rotors</b> . . . . .	236
Cesar Augusto Fonseca, Hans Ingo Weber, and Ilmar Ferreira Santos	
<b>Stochastic Analysis of Asymmetric Tilting-Pad Journal Bearings</b> . . . . .	252
Heitor Antonio Pereira da Silva and Rodrigo Nicoletti	
<b>Experimental Structural Analysis of Gas Foil Bearings</b> . . . . .	264
Cédric Kayo and Robert Liebich	
<b>Influence of Manufacturing Errors on the Unbalance Response of Aerodynamic Foil Bearings</b> . . . . .	281
Aurelian Fatu and Mihai Arghir	

**Parametric Sensitivity Analysis of Tilting Pad Bearings to Investigate the Dynamic Behavior of Rotating Machines** . . . . . 292  
 L. R. Ito, D. J. Ramos, Z. de C. Silveira, and G. B. Daniel

**Analysis of Analytical Hydrodynamic Bearing Models on a Reciprocating Compressor** . . . . . 307  
 Eduardo Paiva Okabe, Jaime Hideo Izuka, and Reinhard Resch

**Radial Active Magnetic Bearing Design Optimization** . . . . . 321  
 Javier Betancor, M. Necip Sahinkaya, and Yahya H. Zweiri

**Measurements of Rotordynamic Force Coefficients of Metallic Type Brush Seals** . . . . . 335  
 Pascal Jolly, Olivier Bonneau, Mihai Arghir, Florent Cochain, and Jérôme Dehouve

**Kriging Surrogate Model Dedicated to a Tilting-Pad Journal Bearing** . . . . . 347  
 Arinan De P. Dourado, Jefferson S. Barbosa, Leonardo Sicchieri, Aldemir A. Cavalini Jr., and Valder Steffen Jr.

**Effect of Lubricant Supply Pressure on SFD Performance: Ends Sealed with O-rings and Piston Rings** . . . . . 359  
 Luis San Andrés and Bonjin Koo

**SEMAJIB: A Versatile High Performance Smart Bearing** . . . . . 372  
 Aly El-Shafei

**Measurement Corrections for Active Magnetic Bearing Control** . . . . . 386  
 L. C. A. Almeida, J. M. A. Barbosa, F. C. G. Santos, and P. M. G. del Foyo

**Calculating Rotordynamic Coefficients of Liquid Annular Seals by CFD for Vibration Analysis and Validation at the Test Rig** . . . . . 397  
 Christian Wagner, Stephan Sinzig, Thomas Thümmel, and Daniel Rixen

**Coupled Simulation of Rotor Systems Supported by Journal Bearings** . . . . . 411  
 Nidish Narayanaa Balaji and I. R. Praveen Krishna

**Effect of Texture Region on the Static and Dynamic Characteristic of Partially Textured Journal Bearings** . . . . . 422  
 Hiroo Taura

**Optimized Tribo-Design of Lubricants for Power Loss Reduction in Journal Bearings Used in Process Industry** . . . . . 437  
 Steven Chatterton, Paolo Pennacchi, and Andrea Vania

**Numerical Modeling of Spiral Vibrations Caused by the Presence of Brush Seals** . . . . . 449  
 Paolo Pennacchi, Filippo Cangioli, Andrea Vania, and Steven Chatterton

**Development and Validation of a Bulk-Flow Model for Staggered Labyrinth Seals** ..... 471  
Filippo Cangioli, Giuseppe Vannini, Paolo Pennacchi, Lorenzo Ciuchicchi, Leonardo Nettis, Steven Chatterton, and Andrea Vania

**Effects of Severe Operating Conditions (High Loads/Low Rotational Speeds) on Sleeve Journal Bearings** ..... 491  
Paolo Pennacchi, Steven Chatterton, and Andrea Vania

**Investigation of Cooled Pads for Tilting-Pad Bearings** ..... 505  
Steven Chatterton, Paolo Pennacchi, and Andrea Vania

**Vibration Control of a Gas Turbine-Generator Rotor in a Combined Cycle System by Means of Active Magnetic Bearings** ..... 520  
Rafael Pilotto and Rainer Nordmann



# Numerical Identification of Nonlinear Hydrodynamic Forces

Diogo Stuani Alves<sup>(✉)</sup> and Katia Lucchesi Cavalca

Department of Integrated Systems, Faculty of Mechanical Engineering,  
UNICAMP, Campinas, Brazil  
{dsalves, katia}@fem.unicamp.br

**Abstract.** Bearings are key elements for a detailed dynamical analysis of rotating machines. In this way, a rotating component sustained by flexible supports and transmitting power creates typical problems that are found in several machines, being that small or large turbines, turbo generators, motors, compressors or pumps. Therefore, representative mathematical models, such as the use of bearings nonlinear forces modeling, have been developed in order to simulate specific systems working conditions. The numerical solution of the equation of motion, when considering nonlinear complete solution of finite hydrodynamic bearings, is highly expensive in terms of computational processing time. A solution to overcome this problem without losing the nonlinear characteristics of the component is use a high order Taylor series expansion to characterize the hydrodynamic forces obtained by the Reynolds equation. This procedure accelerates the nominal behavior predictions, facilitating fault models insertion and making feasible actions in control systems design. So, this papers aims to analyze the use of nonlinear coefficients, generated by the high order Taylor series expansion, to simulate the rotor dynamics under strong nonlinear bearing behavior. The results obtained were compared with Reynolds and linear simulations, and demonstrated that the nonlinear coefficients can be successful to represent bearing behavior even in extreme situations.

**Keywords:** Hydrodynamic bearing · Nonlinearities · Force identification  
Nonlinear coefficients · Numerical methods

## 1 Introduction

Rotordynamic study became prominent in the second half of 19<sup>th</sup> century, when the inclusion of rotation speed in the analysis of the dynamic behavior of rotating machines was made necessary. Since then, the search for higher power, lower weight, higher speeds and greater reliability in this kind of machinery has driven the pursuit for solutions that are economically feasible.

However, for a detailed analysis it is necessary take into account several parameters, i.e., besides the rotor dynamics, other system components, as the bearings, must be considered. Although these elements are usually linearly approximated by stiffness and damping coefficients [1, 2] they can have a strong nonlinear behavior. This characteristic is still studied for many researchers [3–6], which emphasize the use of

hydrodynamic bearing model for the real understanding of rotating machines, especially when it presents high vibration amplitudes.

The solution of nonlinear rotor-bearing dynamic problems is highly time consuming, because the Reynolds equations, that gives the nonlinear hydrodynamic forces, must be simultaneously solved with the equation of motion for each time step. Thus, ways to simplify the hydrodynamic forces in order to reduce computational time, with minimum loss of the nonlinear characteristics, are still subject of research until the present time.

Initially, some works [7–9] utilized the analytical short bearing model proposed by Capone [10, 11], since this simplification generates good results for bearings with small  $L/D$  ratio. Nevertheless, due to this limitation new alternatives were evaluated to improve the solution effectiveness for finite length bearings.

Besides analytical solutions, other alternatives were proposed to model the hydrodynamic forces and reduce processing time of the nonlinear dynamic solutions. The Taylor series expansion of the force, trough perturbations in displacement and velocity around the equilibrium position, is one of the most promising. Unlike linear model, the truncation happens for high order terms, generating nonlinear coefficients.

Using least square method and experimental time series for the hydrodynamic forces, Zhao et al. [12] proposed the identification of dynamic coefficients for three different models (24, 28 and 36 coefficients). For all analyzed cases, the nonlinear models were able to represent the bearing force, while the linear model presented discrepancies. In addition, it was observed that the linearized solution presented hydrodynamic force results comparable to the nonlinear model only for excitations lower than 2.5% of the radial clearance.

Asgharifard-Sharabiani and Ahmadian [13] used a subset selection technique to retain the 40 most influent coefficients from a 13<sup>th</sup> order Taylor series expansion, for a rigid rotor supported by tilting-pad bearings. The system degrees of freedom do not consider the angular movement of the pads and the model was valid only for weak nonlinearities. This made possible the use of the same linear coefficients obtained by small perturbation method for the linear part of the new expansion. Therefore, the obtained dynamic results were compared with simulations taking into account the Reynolds model showing good agreement.

The research found in literature for adjustment of nonlinear forces by Taylor series expansion, usually employs simplified rotors for the analysis, not considering basics characteristics found in real situations, as for instance rotor flexibility. Additionally, the analysis were also restricted for situations of weak nonlinearities. Hence, the present work aims to analyze the use of nonlinear force approximation by high order Taylor series expansion, through ridge regression method, in the context of strong nonlinearities. The adjusted forces are obtained from the simulation of a flexible rotor modeled by finite elements and supported by hydrodynamic journal bearings.

## 2 Methodology

Typical elements of rotating systems are rotors, shafts, bearings and foundation, the last one considered rigid for this paper, being a largely employed configuration the Laval/Jeffcott rotor, showed in Fig. 1. Modeling the system through the finite element method [14, 15], with Timoshenko beam, it is possible to represent a continuous system in a finite number of elements, each node having four degrees of freedom, two of translation ( $y$  and  $z$ ) and two of rotation ( $\Theta_y$  and  $\Theta_z$ ). Therefore, using the Lagrange formulation it is possible to find the equation of motion [16]:

$$[M]\{\ddot{q}\} + ([C] + \Omega[G])\{\dot{q}\} + [K]\{q\} = \{F_U\} + \{F_W\} + \{F_H\} \quad (1)$$

where,  $[M]$ ,  $[C]$ ,  $[G]$ ,  $[K]$  are respectively the global mass, damping, gyroscopic and stiffness matrices,  $\Omega$  is the rotor's rotation speed,  $\{q\}$  is the vector with the degrees of freedom,  $\{F_U\}$  is the unbalance force vector,  $\{F_W\}$  is the weight force vector and  $\{F_H\}$  is the hydrodynamic force vector.

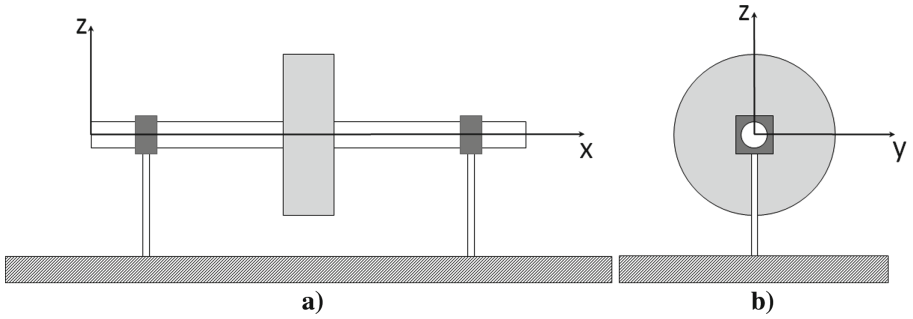


Fig. 1. Typical rotor model: (a) x-z view; (b) y-z view.

The hydrodynamic force is obtained through the pressure distribution generated by the journal motion inside the bearing, which is calculated by the Reynolds equation. This equation derives from the equations of momentum conservation and mass conservation for a viscous fluid, under certain hypothesis. For the bearing scheme seen in Fig. 2, the isoviscous Reynolds equation can be mathematically written as [17]:

$$\frac{\partial}{\partial \theta} \left( h^3 \frac{\partial p}{\partial \theta} \right) + \frac{\partial}{\partial x} \left( h^3 \frac{\partial p}{\partial x} \right) = 6\mu \left( U \frac{\partial h}{\partial \theta} \right) - 12\mu \frac{\partial h}{\partial t} \quad (2)$$

being,  $p$  the pressure,  $\theta$  and  $x$  the circumferential and axial coordinates,  $\mu$  the oil film viscosity,  $U$  the tangential journal velocity,  $t$  the time and  $h$  the lubricant film thickness:

$$h = CR + y \sin \theta - z \cos \theta \quad (3)$$

$CR$  is the bearing radial clearance, and  $y$  and  $z$ , respectively the horizontal and vertical coordinates of the journal center.



With the estimated pressure field, it is possible to evaluate the resultant forces in the oil film. For this, the pressure distribution should be integrated over the bearing area generating the horizontal and vertical force components:

$$\begin{Bmatrix} F_{Hy} \\ F_{Hz} \end{Bmatrix} = \int_{-\frac{L}{2}}^{\frac{L}{2}} \int_{\theta_1}^{\theta_2} p \begin{Bmatrix} \sin \theta \\ -\cos \theta \end{Bmatrix} d\theta dx \tag{4}$$

Thus, the hydrodynamic forces are dependent on the shaft rotational speed as well as position and velocity of the journal center inside the bearing:

$$F_H = F_H(\Omega, y, z, \dot{y}, \dot{z}) \tag{5}$$

So, for displacements around the equilibrium position, a Taylor series expansion [18], depending on the previously described variables, can be performed to create an analytical expression that represents the force generated by the oil film:

$$F_{Hi} = \sum_{j=0}^n \frac{(\{x\} - \{a\})^j}{j!} \left. \frac{\partial^j f(\{x\})}{\partial \{x\}^j} \right|_{\{a\}} \tag{6}$$

in which,  $j$  represents  $y$  or  $z$ ,  $\{x\}$  is the vector with the function variables,  $\{a\}$  is the vector with the bearing equilibrium position for a given rotation and  $n$  is the expansion order.

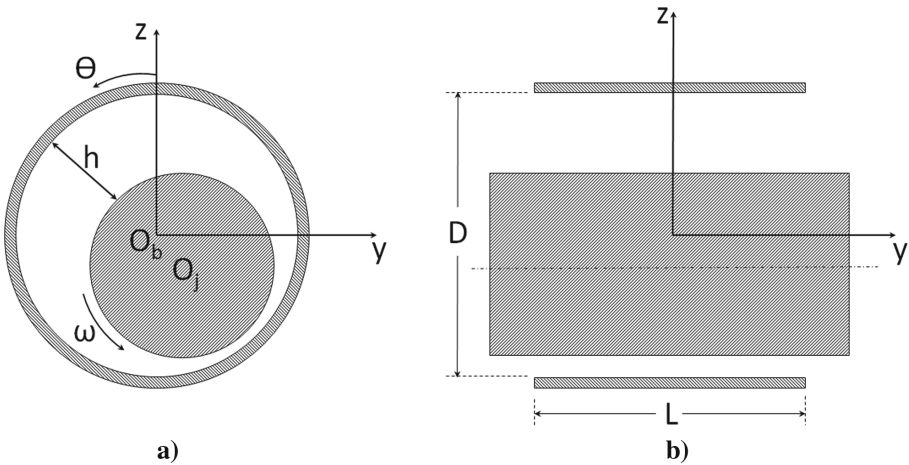


**Fig. 2.** Radial journal bearing scheme: (a) lateral view; (b) axial view

For the first order expansion, one have the classical hydrodynamic force linearization proposed by Lund [1, 2]. In this case, the force is described by eight dynamic coefficients of stiffness ( $K_{mn}$ ) and damping ( $C_{mn}$ ):

$$\begin{aligned} F_y &= F_{y0} + K_{yy} \cdot \Delta y + K_{yz} \cdot \Delta z + C_{yy} \cdot \Delta \dot{y} + C_{yz} \cdot \Delta \dot{z} \\ F_z &= F_{z0} + K_{zy} \cdot \Delta y + K_{zz} \cdot \Delta z + C_{zy} \cdot \Delta \dot{y} + C_{zz} \cdot \Delta \dot{z} \end{aligned} \quad (7)$$

being the coefficients determined by the partial derivative of the force evaluated in the journal equilibrium position:

$$K_{yz} = \left. \frac{\partial F_y}{\partial z} \right|_0; \quad C_{yz} = \left. \frac{\partial F_y}{\partial \dot{z}} \right|_0 \quad (8)$$

However, it is known that the bearing nature can be highly nonlinear and that the linearization is only valid for small vibrations amplitudes. So, for a more accurate analysis of rotating machines, the nonlinear model must be adopted. Nevertheless, the use of nonlinear hydrodynamic forces, by means of simultaneous solution of the Reynolds equation and the equation of motion, is very time consuming. To minimize this problem, it is possible to use an analytical expression based on high order Taylor series expansion as proposed by Zhao et al. [12].

Obtaining  $y(t)$ ,  $z(t)$ ,  $\dot{y}(t)$ ,  $\dot{z}(t)$ ,  $\bar{F}_{Hy}(t)$  and  $\bar{F}_{Hz}(t)$  from a time series analysis, the ridge regression method [19] can be used to minimize the squared difference between the adjusted force ( $F_i(k)$ ) and the force calculated through the Reynolds equation solution ( $\bar{F}_{Hi}(k)$ ). The minimization results in the expansion nonlinear coefficients:

$$\{K\}_i = \arg \min_{K \in \mathbb{R}^N} \sum_{k=1}^M [\bar{F}_{Hi}(k) - F_i(k)]^2 + \lambda \sum_{j=1}^N K_{ij}^2 \quad (9)$$

or in matrix form:

$$\{K\}_i = \arg \min_{K \in \mathbb{R}^N} \left\| \{F_H\}_i - [X]_i \{K\}_i \right\|_2^2 + \lambda \left\| \{K\}_i \right\|_2^2 \quad (10)$$

where,  $\{K\}_i$  is the nonlinear coefficients vector,  $N$  is the coefficient number generated by the Taylor expansion,  $M$  is the number of time steps used to obtain the hydrodynamic forces,  $[X]$  is the predictor matrix and  $\lambda \geq 0$  is the adjustment parameter.

The optimization problem described in Eq. 10 has analytical solution, since it is enough to derive the objective function with respect to the coefficients  $K$ :

$$\{K\}_i = ([X]_i^T [X]_i + \lambda [I])^{-1} [X]_i^T \{F_H\}_i \quad (11)$$

Therefore, for each bearing, and for each direction of the hydrodynamic force, there is a minimization problem, which can generate  $N$  coefficients defined by the order of the Taylor series expansion.

The  $\lambda$  parameter defines the amount of penalization applied to the original least square. When  $\lambda \rightarrow 0$  the same solution generated by the least square method is found. When  $\lambda \rightarrow \infty$  the solution is null. A shrinkage of the coefficients happens for intermediate values, causing a reduction in variance but an increase in bias. Moreover, the penalty introduction improves the conditioning of  $[X]_i^T [X]_i$  matrix. To calculate  $\lambda$  an

one-dimensional minimization process (line search) is used to generate the smallest value for the objective function (Eq. 10).

### 3 Discussion and Results

The rotor used in the simulations was a Laval/Jeffcott rotor, discretized by finite elements as previously mentioned. Ten Timoshenko beam elements and a central rigid disk element, placed at node 6, were used to compose the system. Two identical hydrodynamic bearings are located at nodes 3 and 9. Figure 3 shows the rotor finite element model, Table 1 the detailed discretization, and Table 2 shows the bearing parameters. The excitation force adopted comes from unbalance and was inserted at disk position. The damping matrix  $[C]$  is proportional to the stiffness matrix  $[K]$ , and the proportional coefficient is  $\beta = 1.5 \times 10^{-5}$ . Moreover, shaft and disk are made of steel with elastic modulus of 200 GPa and density of 7850 kg/m<sup>3</sup>.

**Table 1.** Finite elements details.

Element n <sup>o</sup>	Type	Internal diameter (mm)	External diameter (mm)	Length (mm)
1	Beam	0	12	40
2	Beam	0	31	10
3	Beam	0	31	10
4	Beam	0	12	266.5
5	Beam	0	23.5	23.5
6	Beam	0	23.5	23.5
7	Beam	0	12	266.5
8	Beam	0	31	10
9	Beam	0	31	10
10	Beam	0	12	40
11	Rigid disk	23.5	95	47

**Table 2.** Bearings Parameters.

Bearing diameter (D)	31 mm
Bearing length (L)	20 mm
Bearing radial clearance (CR)	90 $\mu$ m
Oil viscosity ( $\mu$ )	50 mPa.s

Because Reynolds equation is a second order differential equation, it does not have a closed solution. Therefore, numerical methods are necessary to find the pressure distribution inside the bearing. The finite volume method, that transform partial differential equations in a set of algebraic equations, was adopted for the simulations [20]. The first critical speed is 22 Hz and, consequently, at 44 Hz the system is subjected to fluid-induced instability.

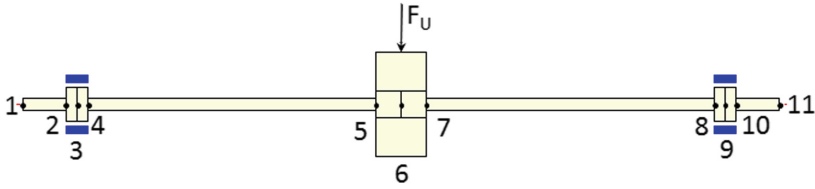


**Fig. 3.** Finite element model

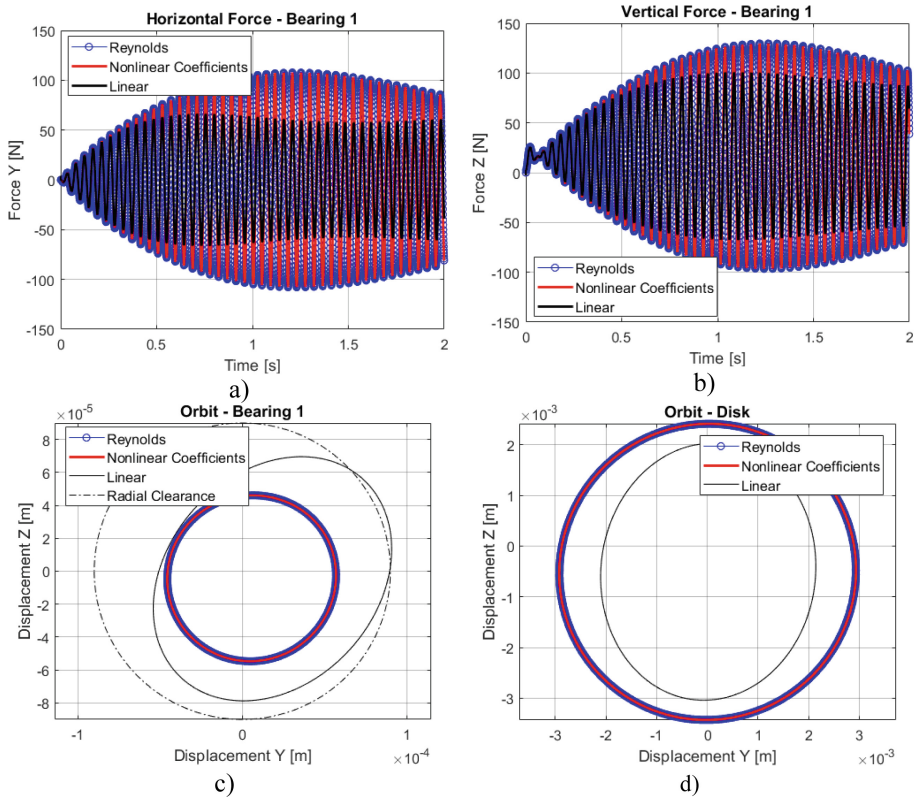


**Fig. 4.** Simulation results for rotational speed equal to 22 Hz: (a) Horizontal hydrodynamic force; (b) Vertical hydrodynamic force; (c) Bearing orbit; (d) Disk orbit.

Furthermore, when considering nonlinearities in a machine simulation, its dynamical behavior is completely changed, and a robust integration method must be employed. So, in this work, the nonlinear implicit iterative Newmark integrator is used. Hence, for each time step, a variable prediction is calculated by Newmark equations and updated by Newton-Raphson method until the equation of motion is satisfied [21].

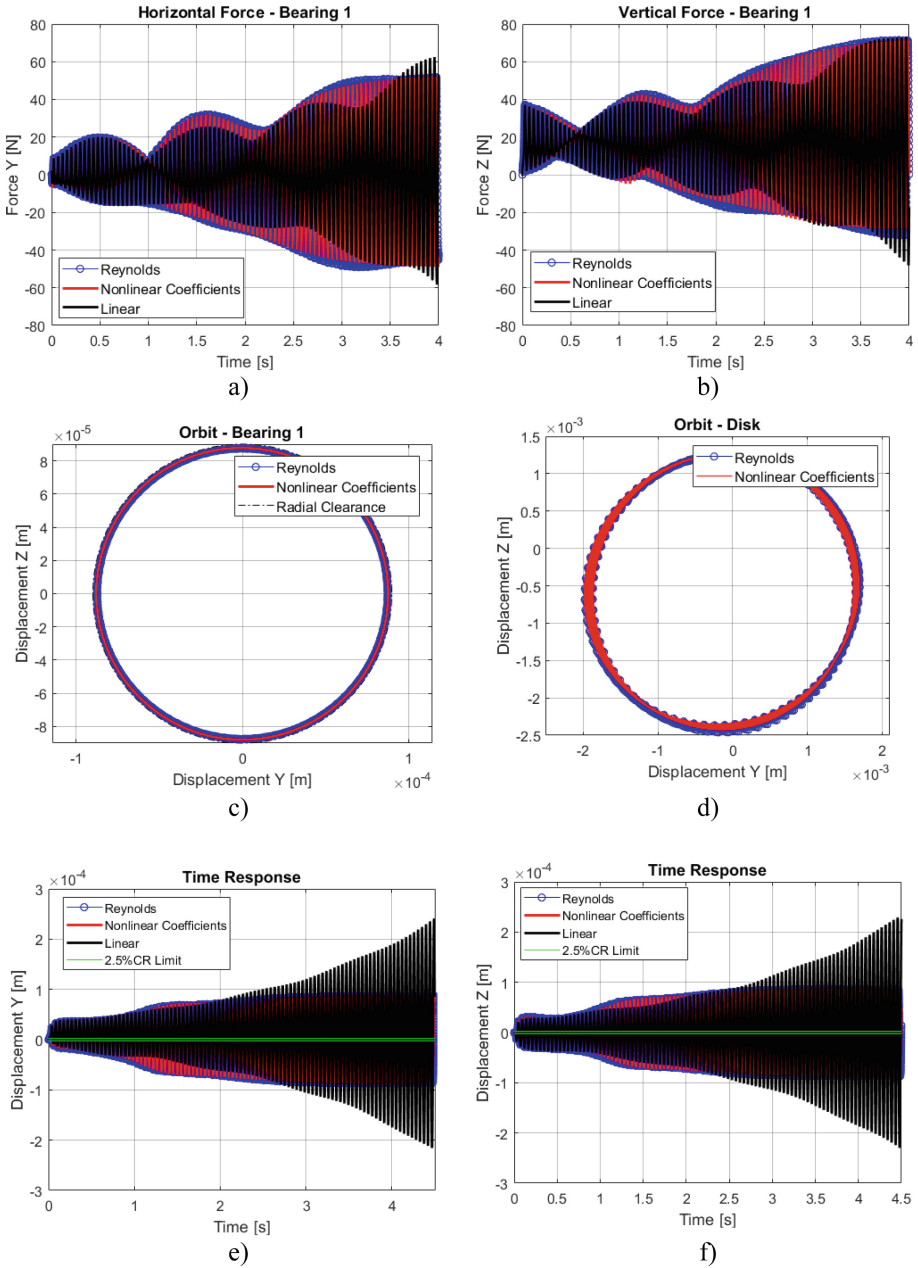


**Fig. 5.** Simulation results for rotational speed equal to 44 Hz: (a) Horizontal hydrodynamic force; (b) Vertical hydrodynamic force; (c) Bearing orbit; (d) Disk orbit; (e) Horizontal bearing displacement; (f) Vertical bearing displacement.

The Reynolds equation should be solved for each bearing and at each iteration of the procedure, resulting in elevated computational time.

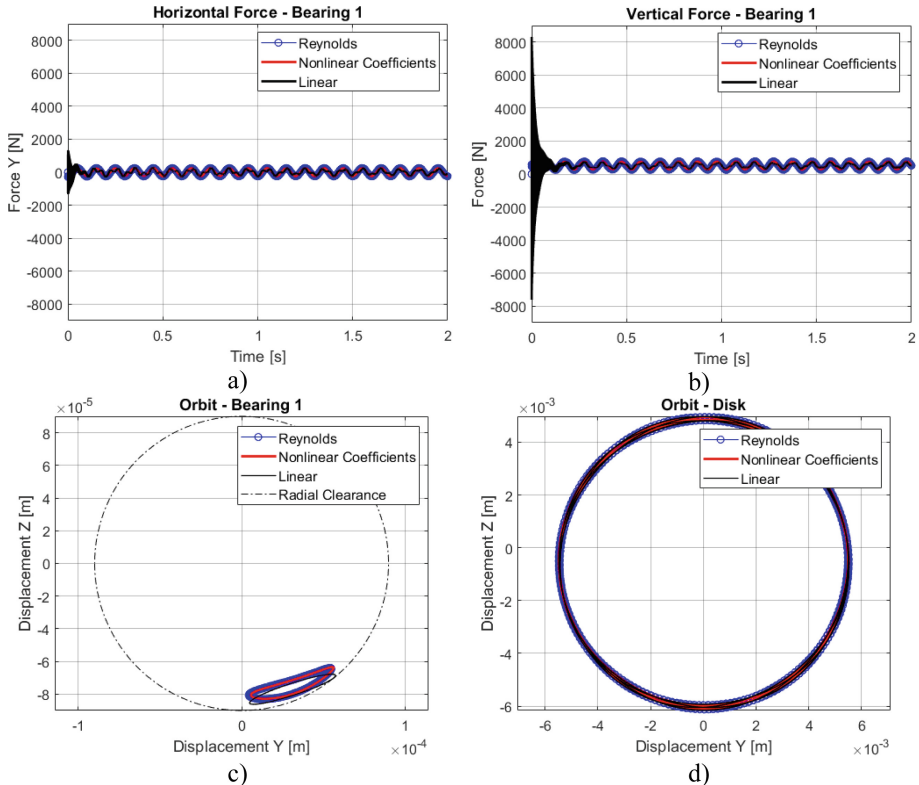


**Fig. 6.** Simulation results for rotational speed equal to 10 Hz and 500 N applied load: (a) Horizontal hydrodynamic force; (b) Vertical hydrodynamic force; (c) Bearing orbit; (d) Disk orbit.

To overcome this problem the hydrodynamic force approximation described in Sect. 2 is utilized. The amount of time needed for a good force adjustment depends on the machine operation condition. However, the transitory part of the movement is of great interest, because it is the path followed by the rotor under this situation and expands the region covered by the adjustment. Despite the initial cost to obtain and adjust the hydrodynamic force given by the Reynolds equation, the simulation time drops from hours to minutes. For this work, it was used a Taylor series expansion up to the fifth order, since this was the lowest order able to fit the case under fluid induced instability.

The simulation cases analyzed take into account situations with strong nonlinear bearing behavior. So, critical rotation speeds, as the first natural frequency (22 Hz) and the fluid induced instability (44 Hz), are selected. Additionally, high unbalance level

contributes to increase nonlinearities, and for the situations previously mentioned a 8.5 g mass placed at 37 mm from the center of the disk is used (Balance Quality Grade G12,8 [22]). Because the rotor is symmetrical, the bearings have the same response. So, only the first bearing is used in the analysis. Notice that results for Reynolds and Nonlinear coefficients are coincident for most of the cases. Those results are shown in Figs. 4 and 5.

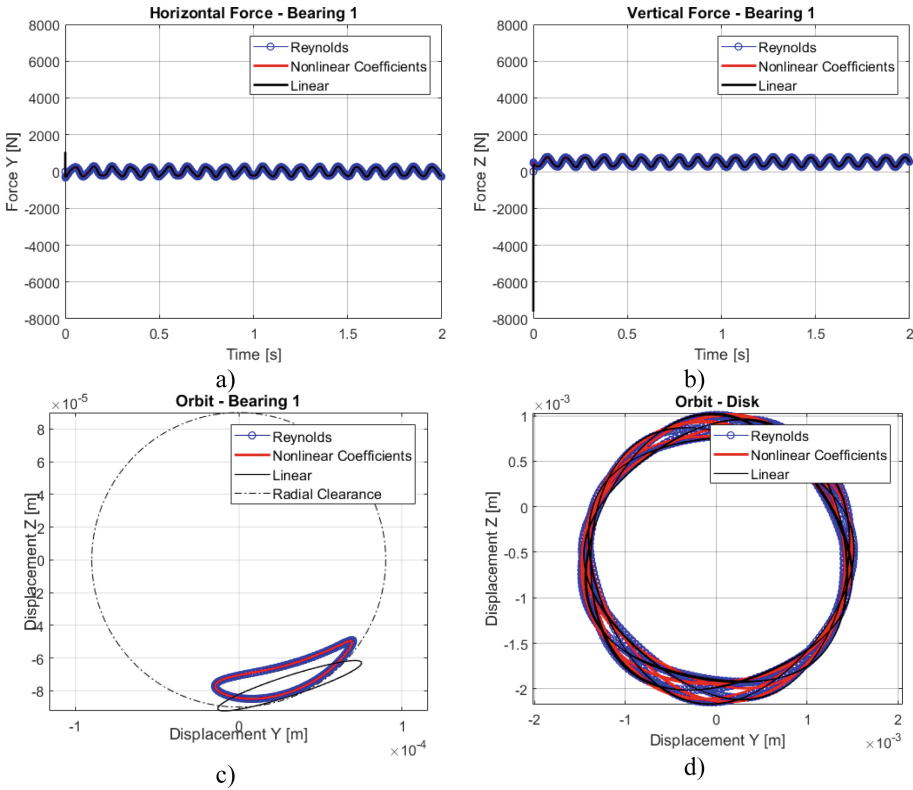


**Fig. 7.** Simulation results for rotational speed equal to 10 Hz, 500 N applied load and unbalance at node 1: (a) Horizontal hydrodynamic force; (b) Vertical hydrodynamic force; (c) Bearing orbit; (d) Disk orbit.

Figure 4a, b show the hydrodynamic forces for horizontal and vertical direction obtained by Reynolds equation, high order Taylor expansion and linear coefficients for 22 Hz. As can be seen, in the beginning of the transitory motion, all hydrodynamic forces are comparable. However, when the displacement amplitude increases, the linear force can no longer represent the original hydrodynamic forces obtained by Reynolds equation. On the other hand, the force calculated by nonlinear coefficients is in good agreement during all period. The same behavior can be seen for the fluid induced instability in Fig. 5a, b, e, f.

Furthermore, observing the orbits presented in Fig. 4c, d, it is clear that the nonlinear coefficients can represent the rotor orbits with higher accuracy while the linear forces violates the bearing clearance and have different shape and size for the disk orbit.

For the fluid induced instability, the nonlinear coefficients can well reproduce the limit circle described by the journal inside the bearing (Fig. 5c) and the whirling movement of the disk (Fig. 5d). Moreover, small discrepancies can be observed in the orbits.

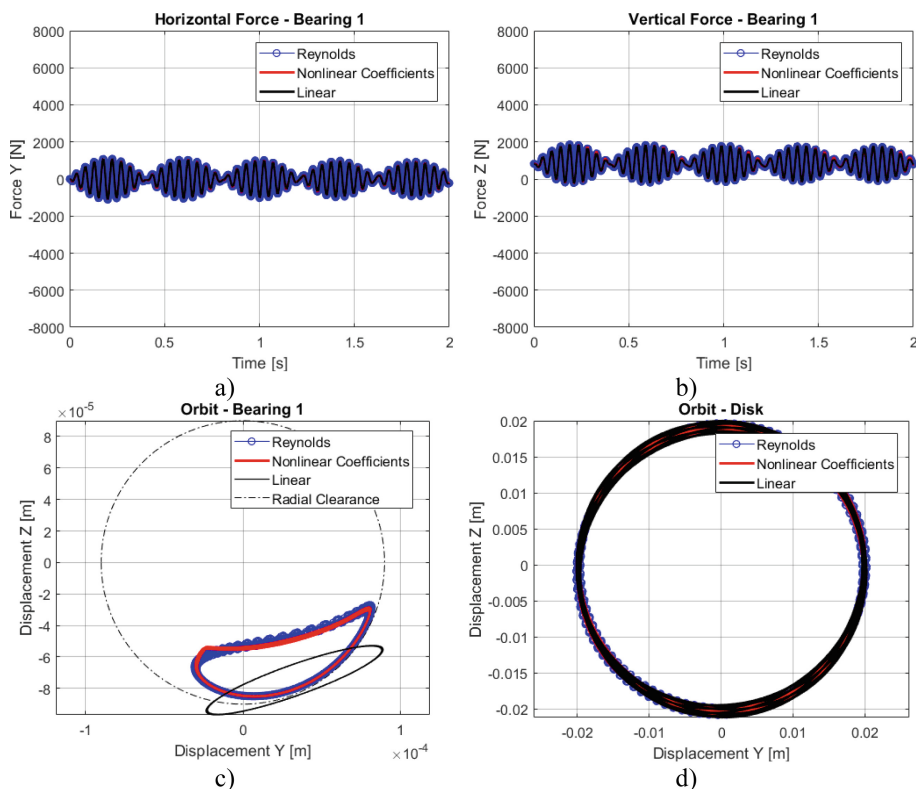


**Fig. 8.** Simulation results for rotational speed equal to 20 Hz and 800 N applied load: (a) Horizontal hydrodynamic force; (b) Vertical hydrodynamic force; (c) Bearing orbit; (d) Disk orbit.

Three special cases, with high eccentricity and extreme unbalance level are also analyzed. Concentrated vertical forces were applied at both bearing nodes in order to keep bearing eccentricity ratio value equal to 0.9. The unbalanced mass was changed to 1.7 kg (Balance Quality Grade G1170). Those hypothetical cases should not occur in reality but are simulated to verify the efficiency of the adjustment under extreme nonlinear situations. For the results in Fig. 6, the concentrated force was set to 500 N and the rotation speed to 10 Hz. In order to make the vibration amplitude of bearing 1



higher, two approaches were followed: (1) the unbalance force was changed from node 6 to node 1 (results in Fig. 7) and (2) preserving unbalance at node 6, at rotational speed of 20 Hz (Balance Quality Grade G2338) (Fig. 8).

Observing Figs. 6, 7 and 8, it is clear that as the bearing vibration amplitude increases higher is the difference between linear and nonlinear models. However, in all cases of linear approximation, the orbits touch or violate the bearing wall, while the nonlinear coefficients model follows the Reynolds orbits.

The most critical case is the one shown in Fig. 8, where high eccentricity is combined with a rotational speed close to the first natural frequency. In this situation, despite a good force adjustment, there are some discrepancies in the journal motion comparing Reynolds and nonlinear coefficients solution. Nevertheless, nonlinear coefficients can perform the overall bearing behavior while linear approximation totally fails.

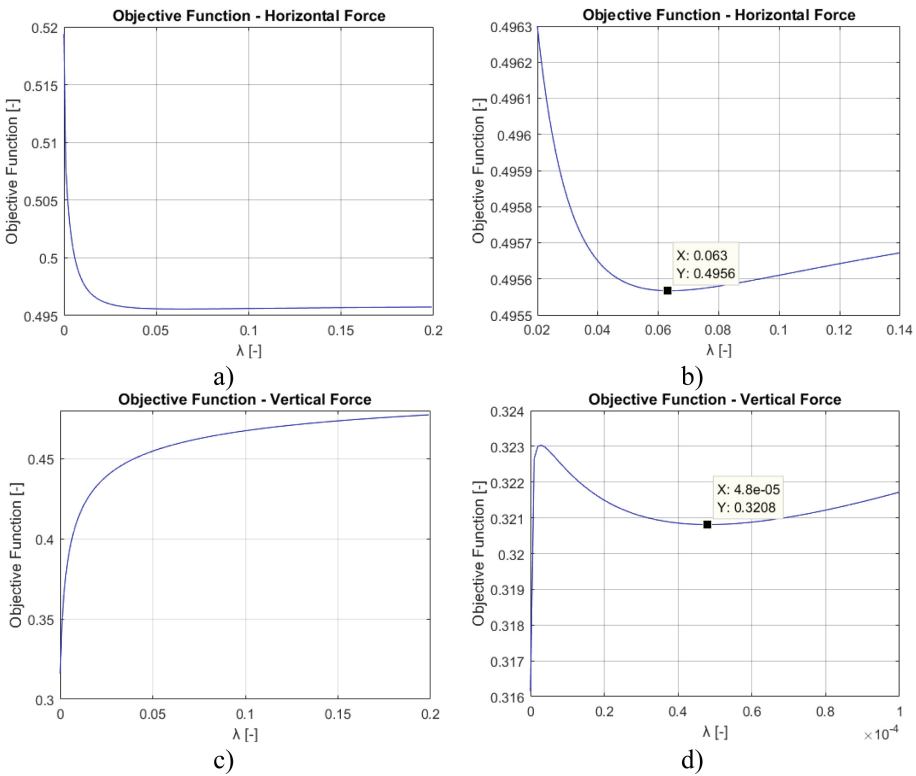


**Fig. 9.** Objective function behavior: (a) For horizontal force adjustment; (b) Zoom in for horizontal force adjustment; (c) For vertical force adjustment; (d) Zoom in for vertical force adjustment.

This difference comes from the amount of penalization used in the adjustment. The desirable value for the penalization parameter is the one that minimizes the objective

function, as can be seen in Fig. 9. However, Fig. 9d shows that all  $\lambda$  values give objective functions higher than the original least square ( $\lambda = 0$ ). In this situations, the tradeoff between variance and bias, that traduces the model accuracy, should be analyzed in order to define a suitable value for  $\lambda$ , since for the original least square method the solution is unbiased but can have high variance. Therefore, for some situations under extremely high nonlinearities, lower variance can be desirable, but this will cause loss in accuracy. Observing Fig. 10 it is possible to obtain  $\lambda$ .

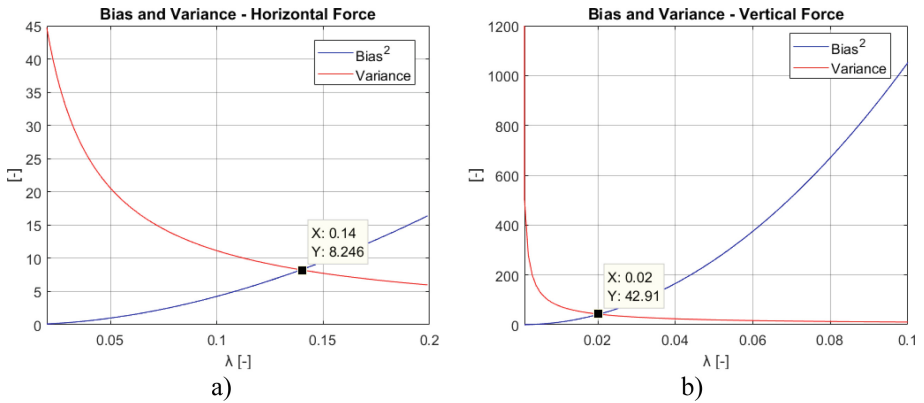


**Fig. 10.** Tradeoff between variance and bias: (a) For the horizontal force adjustment; (b) For the vertical force adjustment.

Nevertheless, for these simulations, it is possible to note that linear and nonlinear hydrodynamic forces are close, but the bearing orbits associated to them are not. In high eccentricities, the wedge term associated to the Reynolds equation is dominant for the pressure generation and consequently for the force calculation. Therefore, shape and behavior of the movement does not affect considerably the force value. However, the linear solution cannot reproduce high order harmonics making linear orbits elliptical, while nonlinear coefficients can satisfactorily reproduce the orbits.

### 4 Conclusions

The paper presented the use of high order Taylor series expansion, by means of nonlinear coefficients, to approximate bearings’ hydrodynamic forces. The simulations were accomplished for rotors submitted to high nonlinear bearing behavior, as critical speeds, fluid induced instability and cases with high eccentricities.

The results showed that nonlinear coefficients model can satisfactorily reproduce hydrodynamic forces and rotor dynamics, greatly reducing the simulation time. Moreover, for situations with extremely high nonlinearities the penalty parameter  $\lambda$  of the ridge regression should promote variance reduction to favor convergence of the dynamic problem. Additionally, when the rotor experiences high eccentricity the linear

and nonlinear hydrodynamic forces have close behavior. However, the response with linear force cannot reproduce high order harmonics changing the bearing orbit shape, what does not happen when nonlinear coefficients are used.

**Acknowledgements.** The authors would like to thank CNPq and grant #2015/20363-6 from the São Paulo Research Foundation (FAPESP) for the financial support to this research.

## References

1. Lund, J.W., Thomsen, K.K.: A calculation method and data for the dynamic coefficients of oil-lubricated journal bearings. In: *Topics in Fluid Bearing and Rotor Bearing System Design and Optimization* ASME, pp. 11–28 (1978)
2. Lund, J.W.: Review of the concept of dynamic coefficients for fluid film journal bearings. *ASME J. Tribol.* **109**, 37–41 (1987)
3. Hattori, H.: Dynamic analysis of a rotor-journal bearing system with large dynamic loads (stiffness and damping coefficients variation in bearing oil films). *JSME Int. J. Ser. C* **36**(2), 251–257 (1993)
4. Khonsari, M.M., Chang, Y.J.: Stability boundary of non-linear orbits within clearance circle of journal bearings. *J. Vib. Acoust.* **115**, 303–307 (1993)
5. Zhao, S.X., Zhou, H., Meng, G., Zhu, J.: Experimental identification of linear oil-film coefficients using least-mean-square method in time domain. *J. Sound Vib.* **287**, 809–825 (2005)
6. Dakel, M., Baguet, S., Dufour, R.: Nonlinear dynamics of a support-excited flexible rotor with hydrodynamic journal bearings. *J. Sound Vib.* **333**, 2774–2799 (2014)
7. Brancati, R., Rocca, E., Russo, M., Russo, R.: Journal orbits and their stability for rigid unbalanced rotors. *J. Tribol.* **117**(4), 709–716 (1995)
8. Castro, H.F., Cavalca, K.L., Nordmann, R.: Whirl and whip instabilities in rotor-bearing system considering a nonlinear force model. *J. Sound Vib.* **317**, 273–293 (2008)
9. Ma, H., Li, H., Niu, H., Song, R., Wen, B.: Nonlinear dynamic analysis of a rotor bearing seal system under two loading conditions. *J. Sound Vib.* **332**, 6128–6154 (2013)
10. Capone, G.: Orbital motions of rigid symmetric rotor supported on journal bearings. *La Mecc. Italiana* **199**, 37–46 (1986)
11. Capone, G.: Analytical description of fluid—dynamic force field in cylindrical journal bearing. *L' Energia Elettrica* **3**, 105–110 (1991)
12. Zhao, S.X., Dai, X.D., Meng, G., Zhu, J.: An experimental study of nonlinear oil-film forces of a journal bearing. *J. Sound Vib.* **287**, 827–843 (2005)
13. Asgharifard-Sharabiani, P., Ahmadian, H.: Nonlinear model identification of oil-lubricated tilting pad bearings. *Tribol. Int.* **92**, 533–543 (2015)
14. Nelson, H.D., McVaugh, J.M.: The dynamics of rotor-bearing systems using finite elements. *ASME J. Eng. Ind.* **98**(2), 593–600 (1976)
15. Nelson, H.D.: A finite rotating shaft element using timoshenko beam theory. *ASME J. Mech. Des.* **102**(4), 793–803 (1980)
16. Genta, G.: *Dynamics of Rotating Systems*, 1st edn. Springer Science + Business Media, New York (2005)
17. Pinkus, O., Sternlicht, S.A.: *Theory of Hydrodynamic Lubrication*. McGraw-Hill, New York (1961)
18. Stewart, J.: *Calculus: Early Transcendentals*, 7th edn. Brooks/Cole Cengage Learning, Belmont (2012)

19. Hastie, T., Tibshirani, R., Friedman, J.H.: The Elements of Statistical Learning: Data Mining, Inference and Prediction, 2nd edn. Springer, Berlin (2009)
20. Patankar, S.V.: Numerical Heat Transfer and Fluid Flow, 1st edn. Hemisphere Publishing Corporation, New York (1980)
21. Bathe, K.: Finite Element Procedures in Engineering Analysis, 1st edn. Prentice-Hall, New Jersey (1982)
22. International Organization for Standardization: Mechanical Vibration – Balance Quality Requirements for Rotors in a Constant (Rigid) State – Part1: Specification and Verification of Balance Tolerances (ISO 1940-1:2003), 2nd edn. ISO Copyright Office, Geneva (2003)



# Thermo-Hydrodynamic Model Influence on First Order Coefficients in Turbocharger Thrust Bearings

Thales Freitas Peixoto<sup>(✉)</sup> , Gregory Bregion Daniel,  
and Katia Lucchesi Cavalca

Laboratory of Rotating Machinery, School of Mechanical Engineering,  
University of Campinas, Campinas, SP, Brazil  
thalesfp@fem.unicamp.br

**Abstract.** High rotation turbochargers, to automotive applications, are continually subjected to axial forces due to gas flows in the turbine and the compressor. These axial forces are supported by lubricated thrust bearings, and their effect is introduced in the dynamic system through its equivalent stiffness and damping coefficients. These coefficients are estimated utilizing a thermo-hydrodynamic model of the bearing, which is composed by the Generalized Reynolds Equation and Energy Equation, to estimate pressure and temperature distribution in the oil film. This work analyzes the influence of geometric and operational parameters of the fixed-geometry thrust bearings in pressure and temperature distributions along the fluid film, solving the governing equations by Finite Volume Method. Along with the pressure distribution, the supported axial load is evaluated and, after that, the equivalent coefficients are estimated. In this work, the Energy equation is solved utilizing 3D model and 2D model (neglecting the radial heat exchange), to check the difference in these results in a computationally less expensive model, and other simplifications, disregarding the conduction heat exchange in the circumferential direction and the convection heat exchange in the axial direction. The load capacity and the equivalent coefficients are compared with a purely hydrodynamic model, disregarding the viscosity variation through the oil film. In lower rotational speeds, the heat generated by fluid shear is small, so a HD model can be utilized considering a constant mean temperature of the oil film. This last approach can reduce the cost to solve the pressure distribution that govern the oil flow in the bearing clearance.

**Keywords:** Thrust bearing · Thermo-hydrodynamic lubrication  
Generalized reynolds equation · Dynamic coefficients

## 1 Introduction

When Lord Reynolds [1] firstly introduced the partial differential equation that governs pressure distribution on thin viscous fluid films, he used a simplified form of Navier-Stokes equations along with the continuity equation to obtain an equation for the pressure distribution in the converging gap between bearing surfaces. The Reynolds

equation, however, considers a constant viscosity and is useful only when the temperature does not change significantly throughout the film. To take into account the fluid properties variation with the temperature, Dowson [2] introduced the generalized Reynolds equation, an equation derived with a minimum of restrictive assumptions, from the fundamental equations of fluid dynamics and, in 1966, Dowson and March [3] developed a thermo-hydrodynamic analysis, considering both the generalized Reynolds Equation and the Energy Equation, along with the heat conduction equation, applied to the fluid and the solids (both the bearing and the shaft), to better design procedures for journal bearings. The thermo-hydrodynamic analysis has been increasingly important, mainly due to the high rotational speeds of rotating machines.

Particularly to automotive applications, turbochargers have been used to increase the internal combustion engine performance since 1905, when Alfred Büchi successfully develop the first modern turbocharger, driven by the engine exhausting gases [4]. Nowadays, turbochargers work at high rotational speeds, ranging from 150,000 to 350,000 rpm [5]. These high speeds directly affect the temperature rise in the bearings lubricant, due to fluid shear, which generates high viscous dissipation, changing the viscosity of oil film circulating in the bearings, affecting the pressure distribution and, consequently, the load capacity of the bearing and its dynamic behavior.

Many authors have been studying the thermal effects when calculating the fluid pressure distribution in bearings. Along with the generalized Reynolds equation and the Energy equation in the oil film, authors considered other phenomena. For instance, for journal bearings, Khonsari and Beaman [6] considered cavitation effects and mixing of recirculating oil and supply oil at the inlet; Ott and Paradissiadis [7] considered cavitation and reverse flow at the oil inlet; Han and Paranjpe [8], who did a rigorous THD analysis on journal bearings, including reverse and recirculating flow, cavitation and considering a full 3D energy equation, without further simplifications; Gupta et al. [9], who did a simplified THD analysis to industrial application; and Paranjpe and Han [10] did a transient THD analysis on dynamically loaded journal bearings.

Specifically for thrust bearings, Huebner [11] considered also heat exchange with the surfaces; Ettles [12], the elasticity and thermal distortion on the surfaces; Kim et al. [13], the three-dimensional variation of lubricant viscosity and density; Colynuck and Medley [14], situations with backflow, comparing different numerical methods; and Brockett et al. [15], a fully 3D model, with heat transfer and elastic and thermal deformations in the pads. In the beginning of the 21st century, Almqvist et al. [16] compared numerical and experimental results in thrust bearings; Glavatskih et al. [17] empirically observed the influence of the lubricant in thrust bearings; Yuan et al. [18] did a thermo-elasto-hydrodynamic analysis on pivoted pad thrust bearings; Dobrica and Fillon [19] compared the results obtained by the Reynolds equation with the Navier-Stokes equations; and Dadouche et al. [20] empirically observed the operational parameters influence on thrust bearing performances. More recently, Jiang et al. [21] did a thermo-elasto-hydrodynamic analysis on tilting pad thrust bearings; Vieira et al. [22] analyzed the influence of the viscosity variation on the behavior of fixed-geometry thrust bearings; Chatzisavvas et al. [23] investigated the influence of thrust bearings on lateral rotor oscillations; Daniel et al. [24] did a sensitivity analysis on a turbocharger thrust bearing model, comparing simulated and experimental results; and Remy et al.

[25] introduced a transient model of the Reynolds equation to represent multigrade engine oils.

In this work, fixed-geometry thrust bearings in turbochargers are studied. The pressure and temperature field are estimated for different rotational speeds, solving simultaneously the generalized Reynolds equation and the Energy equation, by the Finite Volume Method. The numerical solution to the Reynolds equation gives the pressure distribution throughout the oil film, dependent on the temperature distribution due to the viscosity-temperature relation. The numerical solution of the Energy Equation gives the temperature distribution and this equation can be simplified, in some cases, to reduce the computational cost on solving these partial differential equations. The influence of these simplifications compared with the complete model are analyzed in a wide range of rotational speed, concerning the modeling performance, being this one of the major contributions of the work. It is also estimated the equivalent stiffness and damping coefficients of the thrust bearing, to account for the bearing dynamic behavior in the turbocharger axial vibration. Just the first order coefficients are estimated, by perturbation methods (i.e., a perturbation of displacement or velocity around the static equilibrium position of the system).

## 2 Methodology

This section presents the governing equations utilized in this work, along with the fixed geometry thrust bearings considered, the boundary conditions and the numerical methods developed. The assumptions admitted on this work are laminar flow in thermo-hydrodynamic steady state operation, with no cavitation and no slip at fluid-solid interfaces; the inertia and body forces are negligible compared to viscous and pressure terms in the momentum equations; the lubricant is a Newtonian fluid, with constant density, thermal conductivity and specific heat and its viscosity is a function only of temperature; the thermal and elastic distortions are neglected (the surface pads and runner are rigid); and the velocity gradients across the film are much more important than all other velocity gradients, because of the film thin thickness.

### 2.1 Bearing Geometry

The geometry of the bearing considered in the simulations is schematically shown in Fig. 1. The oil film shape may be specified a priori, since no thermal and elastic deformations are considered in the model. The film thickness for the pad is shown in Eq. 1.

$$h(r, \theta) = \begin{cases} h_0 + s_h \left(1 - \frac{\theta}{\theta_{ramp}}\right), & \theta \leq \theta_{ramp} \\ h_0, & \theta > \theta_{ramp} \end{cases} \quad (1)$$

wherein  $h_0$  is the minimum film thickness,  $s_h$  is the shoulder height and  $\theta_{ramp}$  is the angular length of the converging gap, schematically shown.

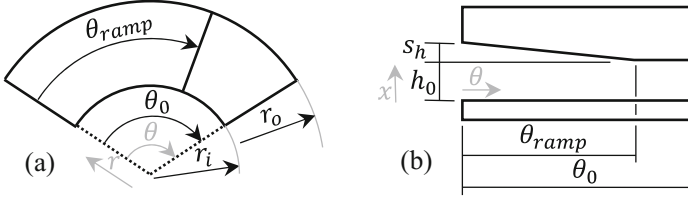


**Fig. 1.** Thrust bearing (a) variables and (b) oil film thickness profile

## 2.2 Generalized Reynolds Equation

To study the thrust bearings, it is more convenient to write the governing equations in cylindrical coordinates. It is common practice to neglect the pressure variation along the film thickness, so the pressure  $p$  is only function of the radial and circumferential coordinates, i.e.,  $p = p(r, \theta)$ . The generalized Reynolds equation takes into account three-dimensional viscosity variation in the film and is written as [2, 15]:

$$\frac{1}{r} \frac{\partial}{\partial \theta} \left( F_2 \frac{\partial p}{\partial \theta} \right) + \frac{1}{r} \frac{\partial}{\partial r} \left( r F_2 \frac{\partial p}{\partial r} \right) = \Omega \frac{\partial}{\partial \theta} \left( F_1 \right) + \frac{\partial h}{\partial t} \quad (2)$$

in which  $\Omega$  is the rotational speed of the collar,  $\theta$  and  $r$  are the cylindrical coordinates,  $p$  is the pressure along the film and the functions  $F_0$ ,  $F_1$  and  $F_2$  depends on the viscosity variation through the film thickness  $h$ , from the collar to the bearing, defined as:

$$F_0 = \int_0^h \frac{1}{\mu} dx, \quad F_1 = \int_0^h \frac{x}{\mu} dx, \quad F_2 = \int_0^h \frac{x^2}{\mu} dx - \frac{F_1^2}{F_0} \quad (3)$$

The boundary conditions for this equation are atmospheric pressure at all boundaries (the oil is either entering or leaving the bearing pad at atmospheric pressure).

## 2.3 Energy Equation

The viscosity changes with the temperature and the temperature distribution can be estimated solving the Energy equation [2, 15]:

$$\rho c_p \left( u \frac{\partial T}{\partial x} + \frac{v_\theta}{r} \frac{\partial T}{\partial \theta} + v_r \frac{\partial T}{\partial r} \right) = k \left( \frac{\partial^2 T}{\partial x^2} + \frac{1}{r} \frac{\partial}{\partial r} \left( r \frac{\partial T}{\partial r} \right) + \frac{1}{r^2} \frac{\partial^2 T}{\partial \theta^2} \right) + \mu \left( \left( \frac{\partial v_r}{\partial x} \right)^2 + \left( \frac{\partial v_\theta}{\partial x} \right)^2 \right) \quad (4)$$

in which  $u$ ,  $v_\theta$  and  $v_r$  are the axial, circumferential and radial velocities, respectively,  $\rho$ ,  $c_p$  and  $k$  are the density, specific heat and thermal conductivity, the lubricant properties,  $\mu$  is the viscosity and  $T$ , the temperature. It is assumed a fully 3D Energy equation, i.e., the temperature is a function of all coordinates  $T = T(r, \theta, x)$  and heat transfer may occur by convection and conduction on the three directions.

The boundary conditions are still a big uncertainty in thermo-hydrodynamic models and a lot of research and experimental investigation have been done to find appropriate



boundary conditions on thermal analysis in lubrication on bearings. Some authors [11, 16, 18, 19, 26] employed a solution considering heat transfer in the surfaces and heat exchange between the lubricant film and those surfaces. They observed the heat exchange in the rigid surfaces can usually be neglected and adiabatic boundary condition is good enough to model most of hydrodynamic bearings. On the outlets of the converging gap between the bearing surfaces, boundary conditions are also adiabatic, as has been previously noticed by [23]. The inlet temperature of the oil film still has some debate over it, as many authors [11, 16, 18, 19, 21, 23] consider a constant temperature through the entire inlet surface. However, works such as [22, 25], consider a model of mixing the recirculating oil and supply oil at the inlet. This is the approach in this work. The boundary conditions, then, can be explicit written as:

$$T(r, \theta, x)|_{\theta=0} = \frac{T_{rep}Q_{rep} + T(r, \theta_0, x)Q(r, \theta_0, x)}{Q_{rep} + Q(r, \theta_0, x)} \quad (5)$$

$$T(r, \theta, x)|_{x=0} = T_{shaft} \quad (6)$$

$$\left. \frac{\partial T}{\partial x} \right|_{x=h} = \left. \frac{\partial T}{\partial r} \right|_{r=r_i} = \left. \frac{\partial T}{\partial r} \right|_{r=r_o} = \left. \frac{\partial T}{\partial \theta} \right|_{\theta=\theta_0} = 0 \quad (7)$$

Equation 5 states that the temperature of the oil entering a volume control at the bearing inlet is considered as an ideal mixture of the replacement oil and the hot oil carried over from the previous pad [15, 22, 25]. It is calculated as a weighted arithmetic mean of the temperatures of the replacement oil and the hot oil carried over. The replacement oil temperature is  $T_{rep}$  and its volumetric flow is  $Q_{rep}$ , calculated as:

$$Q_{rep} = \frac{A_{VC}}{A_{inlet}} Q_{lat} \quad (8)$$

wherein  $A_{VC}$  is the inlet area of the control volume at the bearing inlet, given as  $A_{out} = \Delta r \Delta x|_{\theta=\theta_0}$  in the FVM discretization,  $A_{inlet}$  is the total entrance area of the bearing inlet, and  $Q_{lat}$  is the volumetric flow of the recirculating oil, given as  $Q_{lat} = Q_{r_i} + Q_{r_o} = \int_A v_r dA|_{r=r_i} + \int_A v_r dA|_{r=r_o}$ . The hot oil carried over from the previous segment has temperature  $T(r, \theta_0, x)$  and its volumetric flow is  $Q(r, \theta_0, x) = \int_A v_{\theta} dA|_{\theta=\theta_0}$ .

Equation 6 considers the bearing runner as an isothermal component, whose temperature is pretty close to the supply oil temperature [11, 17, 26],  $T_{shaft} = T_{rep}$ . Equation 7 considers adiabatic boundary conditions on the bearing pad, the inner and outer radii and at the trailing edge [15, 23].

## 2.4 Simplifications in the Energy Equation

For very high velocities, as is the case for the circumferential linear velocity, heat transfer may be modeled only by convection. On the other hand, for very low

velocities, as is the case for the velocity across the fluid film thickness, heat transfer may be modeled only by diffusion. This analysis has been done by several authors and they tend to neglect one or more terms in the Energy equation. For instance, while works [8, 10, 15, 16, 22, 24] consider heat transfer in all directions, others [3, 6, 7, 14, 19] neglect heat transfer in the radial direction. Also, [6, 19] neglect conduction in the circumferential direction. Huebner [11] also neglects this term, while several authors [13, 17, 18, 20, 25] neglect conduction in both the circumferential and radial directions. Chatzisavvas et al. [23] neglect the circumferential conduction and the axial convection. Other authors [12, 21] neglect heat transfer in the axial direction. Finally, Gupta et al. [9] consider only convection in the circumferential direction and conduction in the axial direction.

This leads to the simplifications in the Energy equation shown in Table 1. Case 1 considers heat transfer in all directions in the Energy equation, while case 2 neglects heat transfer in the radial direction, it then becomes a 2D Energy equation, and case 3 neglects radial heat exchange, the axial convection and the circumferential conduction, it is the simplest model for the Energy equation. When radial heat transfer is neglected, the fluid shear proportional to the radial velocity gradient is also neglected.

**Table 1.** Simplifications on the energy equation

Case	Acronym	Terms neglected
1	THD 3D	None
2	THD 2D	$v_r \frac{\partial T}{\partial r}, \frac{1}{r} \frac{\partial}{\partial r} (r \frac{\partial T}{\partial r}), \mu \left( \frac{\partial v_r}{\partial x} \right)^2$
3	THD Simpl.	$v_r \frac{\partial T}{\partial r}, \frac{1}{r} \frac{\partial}{\partial r} (r \frac{\partial T}{\partial r}), u \frac{\partial T}{\partial x}, \frac{1}{r^2} \frac{\partial^2 T}{\partial \theta^2}, \mu \left( \frac{\partial v_r}{\partial x} \right)^2$

## 2.5 Velocity Field

The circumferential and radial velocities are calculated from the pressure distribution, similar to Dowson's Equations [2], given by [11]:

$$v_\theta = \frac{\partial p}{\partial \theta} \left( I_1 - \frac{F_1}{F_0} I_0 \right) + r \Omega \left( 1 - \frac{I_0}{F_0} \right) \quad (9)$$

$$v_r = \frac{\partial p}{\partial r} \left( I_1 - \frac{F_1}{F_0} I_0 \right) \quad (10)$$

in which the integrals  $I_0$  and  $I_1$  resembles the  $F_0$  and  $F_1$ , but with the limits of integration changed from  $(0, h)$  to  $(0, x)$ :

$$I_0 = \int_0^x \frac{1}{\mu} dx, \quad I_1 = \int_0^x \frac{x}{\mu} dx, \quad (11)$$

The axial velocity is calculated from the continuity equation, Eq. 12, integrated in a volume control, considering no slip condition at the runner,  $u|_{x=0} = 0$ , and integrating it for every control volume, from bottom to top.

$$\frac{1}{r} \frac{\partial(rv_r)}{\partial r} + \frac{1}{r} \frac{\partial v_\theta}{\partial \theta} + \frac{\partial u}{\partial x} = 0 \quad (12)$$

## 2.6 Solution of Pressure and Temperature Equations by the FVM

The generalized Reynolds equation and Energy equation are partial differential equations that must be solved simultaneously to obtain pressure and temperature distributions on the oil film. To solve it, the Finite Volume Method (FVM) is employed. The solution domain is divided on orthogonal hexahedral control volumes, changing the  $x$  coordinate to non-dimensional form  $\bar{x} = x/h(r, \theta)$ , and discretized finite difference equations are obtained for each control volume. Variables at each control volume boundary are interpolated between adjacent control volume centers and the pressure equation for an interior control volume can be written as

$$a_P P_P = a_E P_E + a_W P_W + a_N P_N + a_S P_S + S_u \quad (13)$$

whose coefficients are

$$\begin{aligned} a_E &= \frac{F_{2e} h_e \Delta r}{r_e \Delta \theta} & a_N &= \frac{F_{2n} h_n r_n \Delta \theta}{\Delta r} \\ a_W &= \frac{F_{2w} h_w \Delta r}{r_w \Delta \theta} & a_S &= \frac{F_{2s} h_s r_s \Delta \theta}{\Delta r} \\ S_u &= - \left( \Omega \frac{\partial}{\partial \theta} \left( \frac{F_1}{F_0} \right) + \frac{\partial h}{\partial t} \right)_P & a_P &= a_E + a_W + a_N + a_S \end{aligned} \quad (14)$$

The temperature equation is analogously discretized, but, since this is a 3D equation, the temperature equation for a control volume reads

$$\begin{aligned} a_P T_P &= a_E T_E + a_W T_W + a_N T_N + a_S T_S + a_T T_T + a_B T_B + S_u \\ a_P &= \sum_{nb} a_{nb} - S_P \end{aligned} \quad (15)$$

Just as before, the central coefficient  $a_P$  is the sum of the neighbor coefficients with a  $-S_P$  term to account for boundary conditions. The equations for the neighbor coefficients are obtained using the Weighted-Upstream Differencing Scheme (WUDS), proposed by Raithby and Torrance [27], written as:

$$a_E = \beta_e D_e - F_e \left( \frac{1}{2} - \alpha_e \right) \quad a_W = \beta_w D_w + F_w \left( \frac{1}{2} + \alpha_w \right) \quad (16)$$

Analogous expressions for the other faces are written in the same manner. The coefficients  $\alpha$  and  $\beta$ , Eq. 17, are written as a function of the Peclet cell number, defined for a face  $f$ , as the ratio of the convective flux by the diffusion coefficient,  $Pe_f = F_f/D_f$ .

$$\alpha = \frac{Pe|Pe|}{10+2Pe^2} \quad \beta = \frac{1+0.005Pe^2}{1+0.05Pe^2} \quad (17)$$

The convective flux ( $F$ ) and the diffusion coefficients ( $D$ ) are defined as:

$$\begin{aligned}
F_e &= v_{\theta_e} h_e \Delta r \Delta \bar{x} & F_w &= v_{\theta_e} h_e \Delta r \Delta \bar{x} & F_n &= v_{r_n} r_n h_n \Delta \theta \Delta \bar{x} & F_s &= v_{r_s} r_s h_s \Delta \theta \Delta \bar{x} \\
F_t &= u_r r_t \Delta r \Delta \theta & F_b &= u_b r_b \Delta r \Delta \theta & D_e &= \frac{k}{\rho c_p} \frac{h_e \Delta r \Delta \bar{x}}{\Delta \theta} & D_w &= \frac{k}{\rho c_p} \frac{h_w \Delta r \Delta \bar{x}}{\Delta \theta} \\
D_n &= \frac{k}{\rho c_p} \frac{r_n h_n \Delta \theta \Delta \bar{x}}{\Delta r} & D_s &= \frac{k}{\rho c_p} \frac{r_s h_s \Delta \theta \Delta \bar{x}}{\Delta r} & D_t &= \frac{k}{\rho c_p} \frac{r_t \Delta r \Delta \theta}{h_t \Delta \bar{x}} & D_b &= \frac{k}{\rho c_p} \frac{r_b \Delta r \Delta \theta}{h_b \Delta \bar{x}}
\end{aligned} \quad (18)$$

Equations 13 and 15 are discretized equations of the pressure and temperature equation and form a linear system, solved by the Gauss-Seidel method until global convergence is obtained.

## 2.7 Equivalent Coefficients

To study the dynamic behavior of the bearing, equivalent stiffness and damping coefficients are estimated. These estimates are approximated calculating the supported load rate with respect to the oil film thickness and the squeeze velocity [28], i.e.,

$$K_{xx} = -\frac{\partial W}{\partial h} \approx -\frac{\Delta W}{\Delta h} \quad C_{xx} = -\frac{\partial W}{\partial \dot{h}} = -\frac{\Delta W}{\Delta \dot{h}} \quad (19)$$

The derivatives are estimated by a finite difference. After global convergence is obtained, the load supported by the pad is calculated integrating the pressure distribution:

$$W_{pad} = \int_A p r dr d\theta \cong \sum p r \Delta r \Delta \theta \quad (20)$$

The pressure distribution is then recalculated, with a perturbation around the equilibrium position,  $h_0|_{new} = h_0 + \Delta h$  or with a normal squeeze velocity  $\partial h / \partial t = \dot{\Delta h}$  and the load supported for each case is also recalculated. With these values, the thrust bearing equivalent coefficients is estimated.

## 2.8 Axial Thrust in Turbochargers

Peixoto [29] presented a simple model of the axial force in a turbocharger, in steady state, due to the turbine thrust, as a function of the rotational speed:

$$F = \frac{\rho A_2 r_2 r_3}{\tan \alpha_2 \tan \beta_3} \Omega^2 \quad (21)$$

wherein  $\rho$  is the density of the gas entering the turbine and the other parameters are turbine geometric parameters in the turbocharger.  $A_2$  is the inlet area,  $r_2$  and  $r_3$  are, respectively, the inlet and outlet blade radius and  $\alpha_2$  and  $\beta_3$ , the velocity triangles inlet angle and outlet angle.

### 3 Results

#### 3.1 Temperature Distribution in the Oil Film

The numerical analyses are performed for a thrust bearing, whose dimensions are shown in Table 2. This first analysis investigates the temperature distribution in a thrust bearing. The bearing described in Table 2 is simulated considering the shaft temperature equal to the replacement oil temperature.

**Table 2.** Thrust bearing dimensions and operational parameters

$r_o$ [mm]	$r_i$ [mm]	$\theta_0$ [°]	$\theta_{ramp}$ [°]	$h_0$ [ $\mu$ m]	$s_h$ [ $\mu$ m]	$T_{replacement}$ [°C]
15.0	8.5	100	75	50	30	25

It is considered a constant rotational speed, equal to 10,000 rpm and a minimum oil film thickness of 50  $\mu$ m. The calculations are performed considering the full 3D Energy equation, Eq. 3. The pressure distribution is shown in Fig. 2, for both the HD model and the THD model. The temperature distribution is shown in Fig. 3 for the inner, medium and outer radius and at the bearing surface.

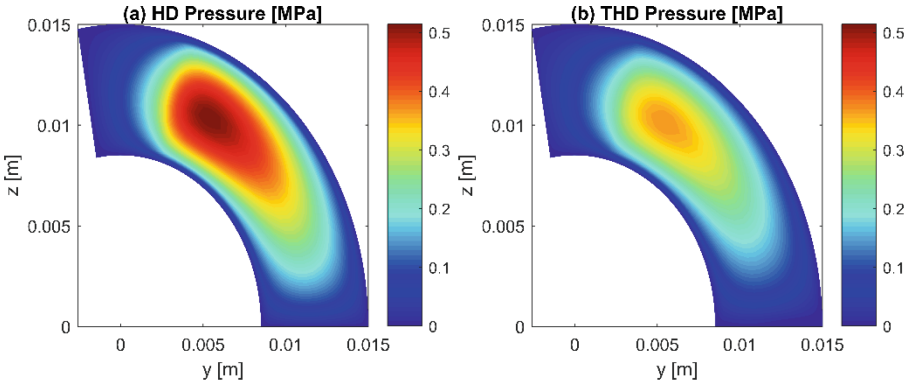


**Fig. 2.** Pressure distribution, 10,000 rpm: (a) HD model, (b) THD model

The pressure distribution shown in Fig. 2 uses the same scale to analyze the difference in the pressure distribution of both models. As expected, the THD model predicts a lower maximum pressure, since the temperature rise lowers the fluid viscosity. The maximum pressure for the THD model is about 0.369 MPa, while for the HD model, it is about 0.517 MPa. The pressure distribution, however, does not change significantly.

It can be observed from the temperature distributions shown in Fig. 3a to c that the greater the radius, the greater the temperature. The position of the maximum temperature of 38.9 °C is located at the outer radius, in the minimum oil film thickness, as expected, since the linear speed of the runner is higher at the outer radius and, therefore, the fluid shear is greater at this position. Figure 3d shows the temperature

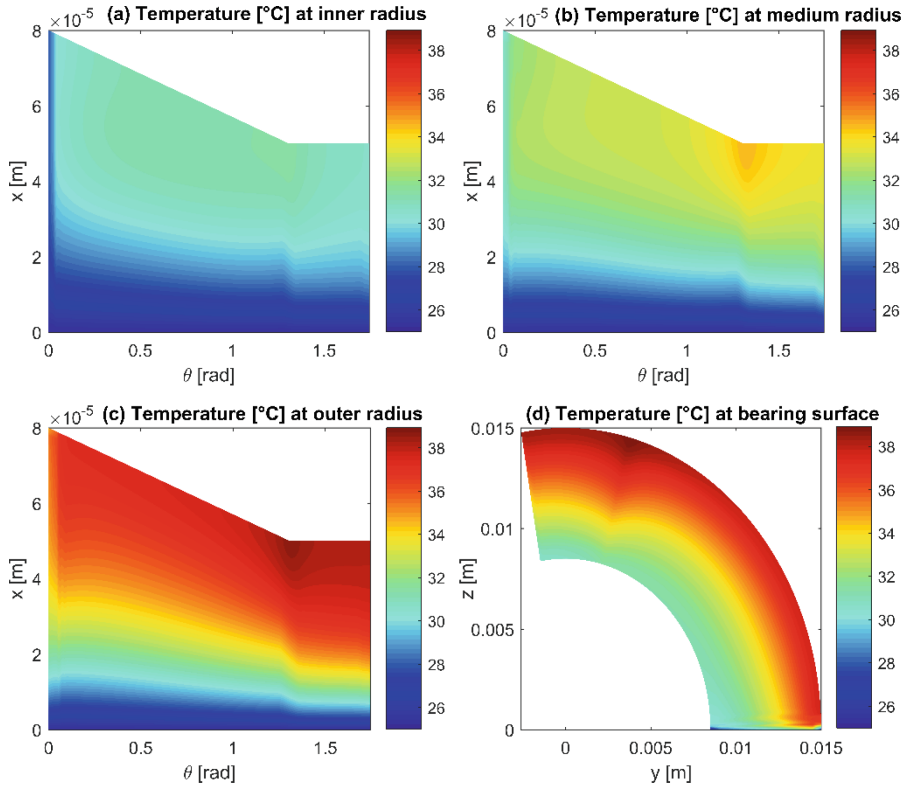


**Fig. 3.** Temperature distribution, 10,000 rpm, at (a) Inner radius, (b) Medium radius, (c) Outer Radius, (d) Bearing surface

distribution at the bearing surface, considered as adiabatic. Again, it can be observed that the maximum temperature occurs at the outer radius position.

It is also observed in Fig. 3a to c sudden changes of temperature near the leading edge (around  $\theta = 0$ rad). These high sudden temperature gradients are due to the numerical approximations of the modeling. The equations for the volumes on the leading edge are different than those on the interior of the domain. The discretized equations for these volume controls are different to account for the boundary conditions leading to some discrepancies.

**Table 3.** Maximum and mean pressure and temperature, for different rotational speeds

$\Omega$ [rpm]	$P_{\text{mean}}$ HD [MPa]	$P_{\text{max}}$ HD [MPa]	$P_{\text{mean}}$ THD [MPa]	$P_{\text{max}}$ THD [MPa]	$T_{\text{mean}}$ [°C]	$T_{\text{max}}$ [°C]
5,000	0.105	0.259	0.105	0.258	25.0	25.0
10,000	0.210	0.517	0.155	0.369	31.8	38.9
25,000	0.524	1.293	0.250	0.829	43.9	74.3
50,000	1.048	2.59	0.368	0.951	48.4	130.7

This same analysis is performed for different rotational speeds and the results for supported load, maximum and mean pressure and temperature are summarized in Table 3. Table 3 presents the pressure for the HD model and the THD, considering the full 3D Energy equation. It is seen that for low rotational speed (5,000 rpm), no difference is observed from the HD and THD model. However, for higher rotational speeds, the difference in the models are not negligible. It can be seen that the temperature rise lowers the viscosity and, consequently, the pressure in the oil film. An important observation, for high rotational speeds, is the necessity in the design to account for the proper cooling of the lubricant, so operation is not compromised. It is assumed in the simulations a constant temperature of 25 °C for the replacement oil, which assumes proper cooling of the oil leaving the bearings.

### 3.2 Simplifications in Energy Equation

Table 4 summarizes the results for each case shown in Table 1. Case 1 is the result obtained for the fully 3D equation, called THD 3D. Case 2 neglects radial heat transfer and is called THD 2D and Case 3 is the simplest model, neglecting radial heat transfer, axial convection and circumferential conduction, called THD Simpl. The  $\Delta$  symbol denotes the percentage difference of the simpler models in comparison with the full 3D equation and it is also calculated the supported load,  $F_{pad}$ , of the bearing pad. The results are shown for the same rotational speeds shown in Table 3.

It is seen from Table 4 that the simplest model can be used for low rotational speeds. For rotational speeds up to 5,000 rpm, the HD model can be utilized, and for rotational speeds from 5,000 to 25,000 rpm, the THD 2D model, neglecting radial heat transfer, can be used, since differences smaller than 1% are observed for the supported load. The biggest difference is in the maximum temperature, in which the 2D model overestimates it in about 6%. For the rotational speed of 50,000 rpm, differences of about 10% are observed in the supported load, and this model may be inadequate for high rotational speeds.

The simplest model, THD Simpl, neglecting radial heat transfer, axial convection and circumferential conduction, is adequate only for low rotational speeds. Differences of about 12% are observed, for the rotational speed of 10,000 rpm. To 25,000 rpm, the supported load is underestimate in about 40% and, in 50,000 rpm, it underestimates it in about 52%. The mean temperature of the oil film is also overestimated in about 48%.

In general, since the simpler models of the Energy equation neglect some terms in the Energy equation, it is expected a higher temperature, which was observed. This compromises the pressure distribution in the pad, which lowers the supported load. The oil film temperature is overestimate in high rotational speeds, so care must be taken on the assumptions admitted for the lubrication analysis of a thrust bearing. This considerations are important because the computational cost can be reduced if the simpler models are utilized, but these models are valid only for low rotational speeds.

**Table 4.** Supported load, maximum and mean pressure and temperature percentual difference, for different simplifications of the energy equation

	5,000 rpm					10,000 rpm				
	THD 3D	THD 2D	$\Delta$	THD Simpl	$\Delta$	THD 3D	THD 2D	$\Delta$	THD Simpl	$\Delta$
$F_{\text{pad}}$ [N]	13.9	13.9	0.00%	13.9	-0.00%	20.5	20.5	-0.09%	17.9	12.9%
$P_{\text{mean}}$ [MPa]	0.105	0.105	0.00%	0.105	0.00%	0.155	0.156	-0.15%	0.136	12.7%
$P_{\text{max}}$ [MPa]	0.258	0.258	0.00%	0.258	0.00%	0.369	0.371	-0.29%	0.326	11.6%
$T_{\text{mean}}$ [°C]	25.0	25.0	0.00%	25.0	0.00%	31.8	31.8	-0.10%	34.1	-7.46%
$T_{\text{max}}$ [°C]	25.0	25.0	0.00%	25.0	0.00%	38.9	39.1	-0.40%	43.7	-12.1%
	25,000 rpm					50,000 rpm				
	THD 3D	THD 2D	$\Delta$	THD Simpl	$\Delta$	THD 3D	THD 2D	$\Delta$	THD Simpl	$\Delta$
$F_{\text{pad}}$ [N]	33.1	33.0	-0.04%	20.0	-39.6%	48.4	44.0	-9.03%	23.2	-52.1%
$P_{\text{mean}}$ [MPa]	0.250	0.251	0.17%	0.152	-39.1%	0.368	0.336	-8.71%	0.179	-51.2%
$P_{\text{max}}$ [MPa]	0.829	0.836	0.85%	0.366	-55.8%	0.951	0.914	-3.91%	0.457	-51.9%
$T_{\text{mean}}$ [°C]	43.9	43.7	-0.40%	57.8	31.7%	48.4	50.0	3.39%	71.5	47.8%
$T_{\text{max}}$ [°C]	74.3	79.0	6.38%	91.0	22.6%	130.7	136	4.41%	105.7	-19.1%

### 3.3 Equivalent Coefficients

This section presents the influence of thermal effects on the dynamic behavior of the thrust bearing in a turbocharger. Equation 21 is first utilized to obtain the axial force in the thrust bearing, i.e., the supported load of the pad, shown in Fig. 4a, as a function of the rotational speed. The minimum oil film thickness,  $h_0$ , is then estimated for each speed, to find the static equilibrium position of the thrust bearing that supports the load, shown in Fig. 4b, and small perturbations of displacement and velocity are applied to estimate the equivalent coefficients.

As previously noticed, the THD model predicts a rise in the film temperature, which lowers the pressure and, consequently, the supported load. Therefore, the estimated minimum oil film thickness is smaller for the THD models than the HD model. It is also observed that the simpler models, that overestimate the film temperature, underestimates the minimum oil film thickness. The calculations for the simpler models were performed for a limited range of the rotational speeds, since the overestimated temperature was too high for high rotational speeds, as shown in Fig. 5.

The equivalent stiffness and damping coefficients were calculated and are shown in Fig. 6, for rotational speeds up to 50,000 rpm, to compare the different THD models presented in Table 1, and in Fig. 7, to compare the HD and THD models for rotational speed up to 150,000 rpm. It is observed THD model predicts a stiffer equivalent coefficient, since the thinner the film, the stiffer the system becomes.



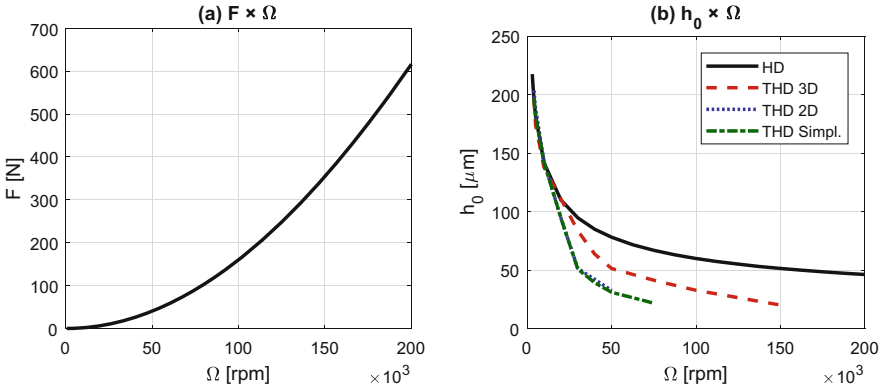


Fig. 4. (a) Axial thrust in the turbocharger and (b) Minimum oil film thickness

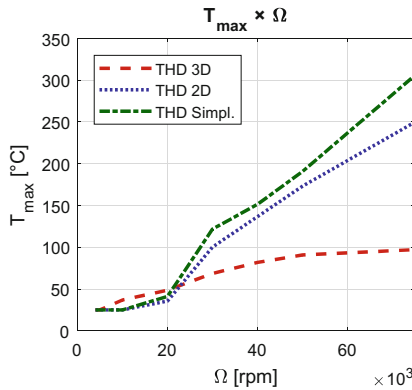
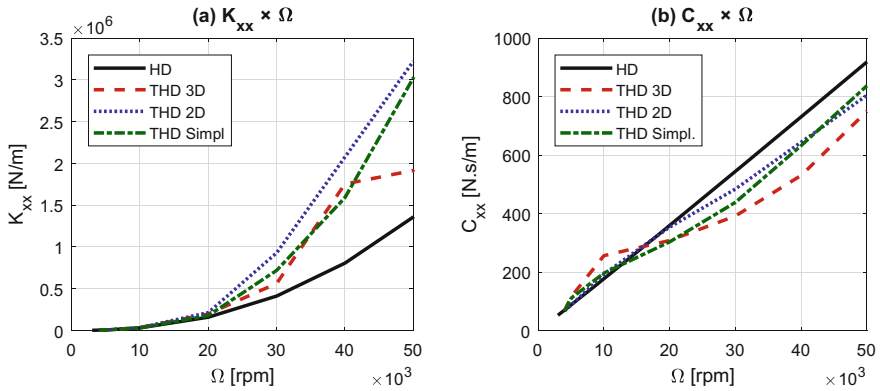


Fig. 5. Predicted maximum temperature of the THD models

It is seen from Fig. 6 that for rotational speeds up to about 10,000 rpm, the three THD models predicts equivalent stiffness and damping coefficients almost equal, with differences of the simpler models to the full 3D Energy equation smaller than 10%. The differences are bigger for higher rotational speeds and, as noticed before, the models are inadequate to represent thrust bearings in turbochargers in high rotational speeds.

It can be observed from Fig. 7 the difference between the HD and THD models, for rotational speeds up to 150,000 rpm. It is noticed the behavior of the stiffness coefficient is the same as the force, quadratic with the rotational speed, while the damping coefficient grows linearly with the speed. This tendency is observed for both models. However THD model predicts a stiffer equivalent coefficient and a lower damping coefficient. Nevertheless, the coefficients remain in the same order of magnitude.



**Fig. 6.** Comparison of THD models: equivalent (a) stiffness and (b) damping coefficients

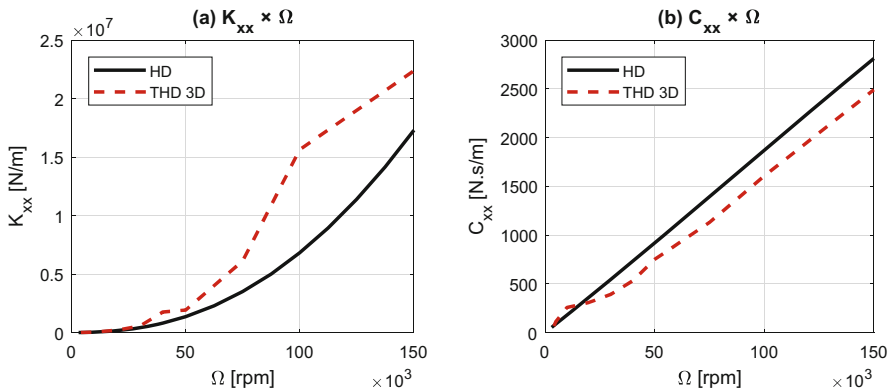


**Fig. 7.** HD and THD models comparison: equivalent (a) stiffness and (b) damping coefficients

## 4 Conclusions

This paper studied the pressure and temperature distribution of a turbocharger thrust bearing operating in thermo-hydrodynamic regime and the influence of geometric and operational parameters in these results. The influence of neglecting some terms in the Energy equation, to ease the computations, was investigated. A 2D model of the Energy equation, neglecting radial heat transfer, and a simpler model, neglecting also axial convection and circumferential conduction, were considered. Up to 20,000 rpm, the 2D model may be employed, with results obtained with a difference no more than 10%. The simplest model may be employed only for low rotational speeds. This is advantageous for faster simulations, but have a limited range of application.

It was also investigated the HD and THD differences in the bearing dynamic behavior. The THD model predicts a stiffer coefficient, since the temperature rise

lowers the pressure and the supported load of a bearing pad, and consequently, a thinner oil film is necessary to support the axial load. The damping coefficient of the THD model was a little smaller than the HD model, but both coefficients remain in the same order of magnitude.

**Acknowledgments.** The authors would like to thank BorgWarner Brasil Ltda., CAPES and CNPq for supporting this research.

## References

1. Reynolds, O.: On the theory of lubrication and its application to Mr. Beauchamp tower's experiments, including an experimental determination of the viscosity of olive oil. *Philos. Trans. R. Soc. Lond.* **177**, 157–234 (1886). <https://doi.org/10.1098/rstl.1886.0005>
2. Dowson, D.: A generalized reynolds equation for fluid-film lubrication. *Int. J. Mech. Sci.* **4**, 159–170 (1962). [https://doi.org/10.1016/S0020-7403\(62\)80038-1](https://doi.org/10.1016/S0020-7403(62)80038-1)
3. Dowson, D., March, C.N.: Paper 6: a thermohydrodynamic analysis of journal bearings. *Proc. Inst. Mech. Eng. Conf. Proc.* **181**, 117–126 (1966). [https://doi.org/10.1243/PIME\\_CONF\\_1966\\_181\\_306\\_02](https://doi.org/10.1243/PIME_CONF_1966_181_306_02)
4. Siuru (Jr.), W.D.: Automotive superchargers and turbochargers. In: *Handbook of Turbo-machinery*, pp. 813–860 (2003)
5. Nguyen-Schäfer, H.: *Rotordynamics of Automotive Turbochargers* (2015)
6. Khonsari, M.M., Beaman, J.J.: Thermohydrodynamic analysis of laminar incompressible journal bearings. *ASLE Trans.* **29**, 141–150 (1986). <https://doi.org/10.1080/05698198608981671>
7. Ott, H.H., Paradissiadis, G.: Thermohydrodynamic analysis of journal bearings considering cavitation and reverse flow. *J. Tribol.* **110**, 439–447 (1988)
8. Han, T., Paranjpe, R.S.: A finite volume analysis of the thermohydrodynamic performance of finite journal bearings. *J. Tribol.* **112**(3), 557–565 (1990)
9. Gupta, G., Hammond, C.R., Szeri, A.Z.: An approximate THD theory for journal bearings. *ASME J. Tribol.* **112**, 224–229 (1990)
10. Paranjpe, R.S., Han, T.: A transient thermohydrodynamic analysis including mass conserving cavitation for dynamically loaded journal bearings. *J. Tribol.* **117**(3), 369–378 (1995)
11. Huebner, K.H.: A three-dimensional thermohydrodynamic analysis of sector thrust bearings. *ASLE Trans.* **17**, 62–73 (1974). <https://doi.org/10.1080/05698197408981439>
12. Ettles, C.: The development of a generalized computer analysis for sector shaped tilting pad thrust bearings. *ASLE Trans.* **19**, 153–163 (1976). <https://doi.org/10.1080/05698197608982789>
13. Kim, K.W., Tanaka, M., Hori, Y.: A three-dimensional analysis of thermohydrodynamic performance thrust bearings. *J. Tribol.* **105**, 1–7 (1983)
14. Colnuck, A.J., Medley, J.B.: Comparison of two finite difference methods for the numerical analysis of thermohydrodynamic lubrication. *Tribol. Trans.* **32**, 346–356 (1989). <https://doi.org/10.1080/10402008908981899>
15. Brockett, T.S., Barrett, L.E., Allaire, P.E.: Thermoelastohydrodynamic analysis of fixed geometry thrust bearings including runner deformation. *Tribol. Trans.* **39**, 555–562 (1996). <https://doi.org/10.1080/10402009608983566>

16. Almqvist, T., Glavatskih, S.B., Larsson, R.: THD analysis of tilting pad thrust bearings - comparison between theory and experiments. *J. Tribol.* **122**, 412–417 (2000). <https://doi.org/10.1115/1.555377>
17. Glavatskih, S.B., Fillon, M., Larsson, R.: The significance of oil thermal properties on the performance of a tilting-pad thrust bearing. *J. Tribol.* **124**, 377 (2002). <https://doi.org/10.1115/1.1405129>
18. Yuan, X., Zhu, J., Chen, Z., Wang, H., Zhang, C.: A three-dimensional TEHD model and an optimum surface profile design of pivoted pad thrust bearings with large dimensions. *Tribol. Trans.* **46**, 153–160 (2003). <https://doi.org/10.1080/10402000308982611>
19. Dobrica, M., Fillon, M.: Reynolds' model suitability in simulating rayleigh step bearing thermohydrodynamic problems. *Tribol. Trans.* **48**, 522–530 (2005). <https://doi.org/10.1080/05698190500385088>
20. Dadouche, A., Fillon, M., Dmochowski, W.: Performance of a hydrodynamic fixed geometry thrust bearing: comparison between experimental data and numerical results. *Tribol. Trans.* **49**, 419–426 (2006). <https://doi.org/10.1080/10402000600781457>
21. Jiang, X., Wang, J., Fang, J.: Thermal elasto-hydrodynamic lubrication analysis of tilting pad thrust bearings. *Proc. Inst. Mech. Eng. Part J: J. Eng. Tribol.* **225**, 51–57 (2011). <https://doi.org/10.1177/2041305X10394408>
22. Vieira, L.C., Watanabe, P.N., Cavalca, K.L.: Analysis of the influence of fluid temperature variation on the behavior of turbocharger lubricated thrust bearings. In: Pennacchi, P. (ed.) *Proceedings of the 9th IFToMM International Conference on Rotor Dynamics*. MMS, vol. 21, pp. 1091–1101. Springer, Cham (2015). [https://doi.org/10.1007/978-3-319-06590-8\\_89](https://doi.org/10.1007/978-3-319-06590-8_89)
23. Chatzisavvas, I., Boyaci, A., Lehn, A., Mahner, M., Schweizer, B., Koutsovasilis, P.: On the influence of thrust bearings on the nonlinear rotor vibrations of turbochargers. In: *Proceedings ASME Turbo Expo 2016: Turbomachinery Technical Conference and Exposition*, pp. 1–10 (2016). <https://doi.org/10.1115/gt2016-58168>
24. Daniel, G.B., Vieira, L.C., Cavalca, K.L.: Sensitivity analysis of the dynamic characteristics of thrust bearings. In: *Proceedings of the 3rd International Symposium on Uncertainty Quantification and Stochastic Modeling*, Rio de Janeiro, Brazil, pp. 1–10. ABCM Brazilian Society of Mechanical Sciences and Engineering (2016)
25. Remy, B., Bou-Saïd, B., Lamquin, T.: Fluid inertia and energy dissipation in turbocharger thrust bearings. *Tribol. Int.* **95**, 139–146 (2016). <https://doi.org/10.1016/j.triboint.2015.11.014>
26. Hori, Y.: *Hydrodynamic lubrication*. Springer, Tokyo (2006)
27. Raithby, G.D., Torrance, K.E.: Upstream-weighted differencing schemes and their application to elliptic problems involving fluid flow. *Comput. Fluids* **2**, 191–206 (1974)
28. Lund, J.W.: Review of the concept of dynamic coefficients for fluid film journal bearings. *J. Tribol.* **109**, 37 (1987). <https://doi.org/10.1115/1.3261324>
29. Peixoto, T.F.: *Analysis of rotors supported by thrust bearings*, Master thesis (2016). <http://www.repositorio.unicamp.br/handle/REPOSIP/305451>



# Study of Stiffness Reduced Order Model Applied to Line and Elliptical Contact Under EHD Lubrication

Leticia Bizarre<sup>(✉)</sup>, Natália Akemi Hoshikawa Tsuha,  
and Katia Lucchesi Cavalca

Faculty of Mechanical Engineering, UNICAMP, R. Mendeleyev, 200,  
Postal Box 6122, Campinas, SP 13083-970, Brazil  
{leticia.bizarre, natalia.akemi, katia}@fem.unicamp.br

**Abstract.** Nonconforming contact study is fundamental to model the behavior of mechanical equipment such as bearings and gears. In order to predict lifetime of rolling element bearings, film thickness and pressure distribution can describe the lubrication condition, allowing the analysis of the contact response to load, rotation speed, oil parameters and geometry. The EHD elliptical contact can be approximate to an equivalent line contact when taken the central line at the major ellipsis axis, since the maximum Hertzian pressure, lubrication oil, rotation speed and radius of curvature are identical. A comparison between the stiffness reduced order model of elliptical contact and an equivalent line contact, based on an explicit load-distribution relation, is accomplished. Moes load and lubrication dimensionless parameters describe the contacts along with the elliptical contact ellipticity. The influence of speed and ellipticity were verified on the oil film and pressure in a range of load conditions, as well as EHD stiffness reduced order model parameters. The ellipticity range evaluates the similarity between both kinds of contact and verifies its equivalence.

The present work analyses the contact reduced order model and its main parameter influence, the EHD stiffness. As the contact properties, film thickness and pressure distribution, directly affect the lifetime estimation of rolling element bearings, the study can bring useful insights during project stage. Moreover, an improved EHD nominal model can promisingly be applied in fault identification in rotating systems and other mechanisms.

**Keywords:** Line contact · Elliptical contact · EHD lubrication  
Stiffness reduced order model

## 1 Introduction

Expansion of industry sectors and development of new systems and products demand a continuous improvement of their elements characteristics and performance. Components like rolling bearings and gears are widely applied in this scenery and they are an example of a particular type of contact between its parts, the nonconforming contact. The study of the contact and its properties is indispensable to predict the influence of

the lubrication in the whole system, for example, some researchers applied the contact properties studies on the modeling of bearings and cams [1–4].

Therefore, the analysis of lubrication condition is applied to verify the contact response to load variations, speed rotation, oil parameters and contact geometry. This analysis observes the pressure profile, oil film thickness and, in the present work, the variation of the nonlinear force parameters, like the stiffness on contact. Herein, an equivalent line contact was calculated from the elliptical contact and the main equivalence characteristic is a range of similar Hertzian pressure, allowing to observe the behavior of the force parameters on contact reduced order model, for these two different types of contact geometry. The evaluation of equivalence between the contacts allows to apply simulations of a line contact, that is simplified with pressure gradient in only one direction, to predict the behavior of oil film thickness and pressure profile of the elliptical contact that demands higher computational cost. For example, studies of fatigue failure and dynamic models of bearings, gears and other components can improve their results using the contact model [5]. An equivalent line contact can be used as first approximation for elliptical contact cases leading to reduce time consumption of simulations, and helping with the convergence.

The present study investigates the influence of the contact geometry in the nonlinear force contact parameters, the best approach for line and elliptical geometries and the range of best approximation between both contacts models.

## 2 Methodology

The methodology is divided into three main parts: EHD lubrication contact theory, equations of equivalent line contact from an elliptical contact, and the nonlinear force reduced order model on the contact.

### 2.1 EHD Lubrication Contact Theory

Considering non-conforming contacts, between surfaces with a different radius of curvature, the EHD lubrication theory refers to the study of extreme conditions of a very thin lubricant film with high shear rates and high pressure. Thus, for this type of lubrication regime, the elastic deformation is considered as well as the variation of density and viscosity with pressure.

The pressure equation (Eq. 1) derived by Reynolds [6], as presented in Venner [7], is applied for elliptical contact in this work. It is possible to note the fluid film thickness  $h(x, y)$  dependency and also the density  $\rho$  and viscosity  $\eta$ . The term  $u_m$  is the mean relative velocity between the surfaces.

$$\frac{\partial}{\partial x} \left( \frac{\rho \cdot h^3}{12 \cdot \eta} \frac{\partial p}{\partial x} \right) + \frac{\partial}{\partial y} \left( \frac{\rho \cdot h^3}{12 \cdot \eta} \frac{\partial p}{\partial y} \right) - u_m \frac{\partial(\rho h)}{\partial x} - \frac{\partial(\rho h)}{\partial t} = 0 \quad (1)$$

The viscosity/pressure relation (Eq. 2) was empirically proposed by Roelands [8], where  $\eta_0$  is the atmospheric viscosity,  $z$  is the pressure viscosity index and

$p_0 = 1.96 \cdot 10^8$  Pa. For the density/pressure, the Dowson and Higginson [9] relation (Eq. 3) was applied, where  $\rho_0$  is the density at atmospheric pressure.

$$\eta(p) = \eta_0 \cdot \exp\left(\left(\ln(\eta_0) + 9.67\right) \cdot \left(-1 + \left(1 + \frac{p}{p_0}\right)^z\right)\right) \quad (2)$$

$$\rho(p) = \rho_0 \frac{5.9 \cdot 10^8 + 1.34p}{5.9 \cdot 10^8 + p} \quad (3)$$

In addition, Venner [7] presents the fluid film thickness (Eq. 4), where  $E'$  is the reduced modulus of elasticity,  $R_x$  and  $R_y$  are the reduced radius of curvature and  $h_0$  is the mutual approach of the bodies. Figure 1 represents the film thickness  $h(x, y)$ , the bodies approach  $h_0$  and the global deformation of both bodies in contact.

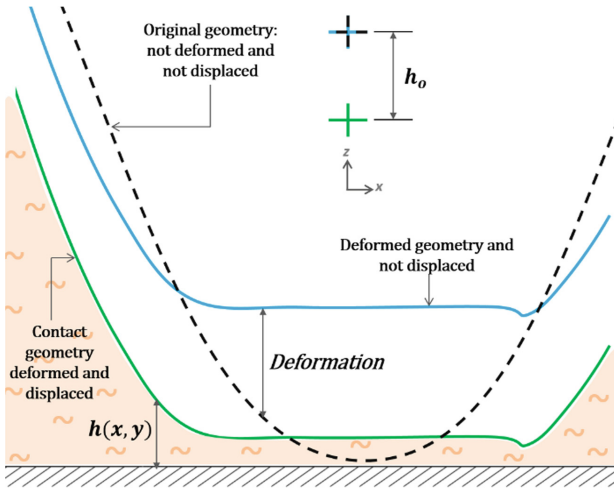


**Fig. 1.** Representation of fluid film thickness and deformations (Tsuha et al. [3])

$$h(x, y) = h_0 + \frac{x^2}{2 \cdot R_x} + \frac{y^2}{2 \cdot R_y} + \frac{2}{\pi \cdot E'} \iint_{\Gamma} \frac{p(x', y') dx'}{\sqrt{(x - x')^2 + (y - y')^2}} dx' dy' \quad (4)$$

Equation 5 gives the forces, which come from the integral of pressure over the film area (contact force) to be balanced by the external load applied normally to the contact area.

$$w = \int_{-\infty}^{+\infty} \int_{-\infty}^{+\infty} p(x', y') dx' dy' \quad (5)$$

In order to reduce the number of variables and, consequently, simplify the numerical solution, the equating was made dimensionless using the Hertzian dry contact parameters and the viscosity/density at ambient pressure. Equation 6 contains all dimensionless variables as presented in Venner [7]. The variables  $a$  and  $b$  are the minor and major axis of the ellipse, respectively, and  $E$  and  $K$  are the first and second elliptic integral.

$$X = \frac{x}{a}; Y = \frac{y}{b}; P = \frac{p}{p_h}; H = \frac{h}{\frac{a^2}{2R} \cdot K \cdot E}; \bar{\eta} = \frac{\eta}{\eta_0}; \bar{\rho} = \frac{\rho}{\rho_0} \quad (6)$$

The final step is to characterize each contact applying the Moes parameters derived in Moes [10], describing the contact in function of load and lubrication characteristics. Equation 7 contains the Moes load parameter ( $M$ ) and lubrication parameter ( $L$ ).

$$M = \frac{f}{E' \cdot R_x^2} \left( \frac{\eta_0 \cdot u_m}{E' \cdot R_x} \right)^{-\frac{3}{4}}; L = \alpha \cdot E' \left( \frac{\eta_0 \cdot u_m}{E' \cdot R_x} \right)^{\frac{1}{4}} \quad (7)$$

## 2.2 Equivalent Line Contact Using an Elliptical Contact

From the description of the elliptical contact proposed in the previous section, and based on the work of Canzi et al. [11] and Nijenbanning et al. [12], a line contact can be approached in a condition of equal Hertz's pressure and when half-width  $l = b_e$  (Fig. 2) and  $R_l = R_x$ . The Reynolds Equation for the line contact is similar to Eq. 1. However, it can be simplified in y direction, since this direction is reasonably larger than the x direction. The term  $a_e$  is a minor half-width Hertzian contact and  $R_x$  is the reduced radius of curvature in x direction for elliptical contact. Therefore, the dimensionless Moes Parameters ( $L_l$  and  $M_l$ ) are calculated for the line contact [12] applying the  $L_e$  and elliptical contact parameters:

$$L_l = L_e \quad (8)$$

$$M_l = \frac{w}{E' \cdot R_l} \left( \frac{E' \cdot R_l}{\eta_0 \cdot u_m} \right) \quad (9)$$

$$w = \frac{3 \cdot F_e}{4 \cdot b_e}, k = \frac{a_e}{b_e} \quad (10)$$

where  $L_e$  is the Lubricant Moes Parameter,  $w$  is an equivalent load that uses the load on contact  $F_e$ . All these parameters are from the reference elliptical contact.

Figure 2 contains a scheme of elliptical and line contacts due to the contact of the bearing/raceway and the sphere or roller element. The contact ellipticity ( $k$ ) is obtained from the relation presented in Eq. 10 and allows to characterize each elliptical contact along with the Moes parameters.



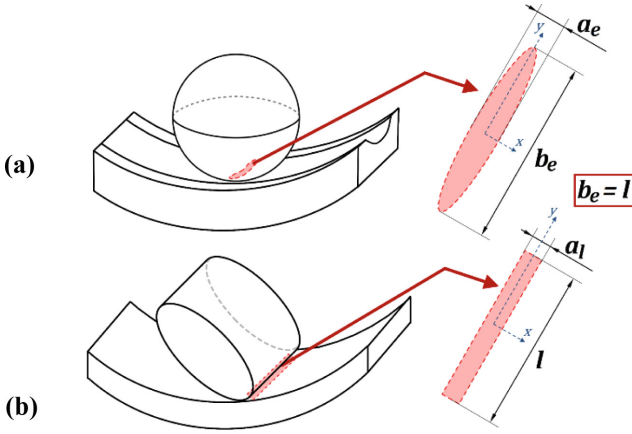


**Fig. 2.** Example of elliptical (a) and linear (b) contact with the respective area of contact and their dimensions.

### 2.3 Nonlinear Force Contact Reduced Order Model

Nonato and Cavalca [13, 14] developed a reduced order model of contact force that relates forces ( $F$ ) and displacements ( $\delta$ ) on the elastohydrodynamic elliptic contact. Equation 11 presents the nonlinear relation proposed:  $K$  is the stiffness;  $d$  is an exponent that assumes the value of unity for the line contact and varies for the elliptical contact, and  $\Delta F$  is an offset force. For the elliptical contact, the exponent  $d$  assumes higher values in all lubrication conditions when compared to the line contact, and the maximum value achieved in Hertzian condition, 1.5. In lubricated line contact, the exponent  $d$  tends to the unity [3], differently from Hertzian contact, where it is approximated to 10/9.

$$F = K \cdot \delta^d + \Delta F \quad (11)$$

In the present study, applying data of  $M$ ,  $L$  and the ellipticity  $k$ , the system of equations for the EHD lubricated contact was solved by a multi-level algorithm. The results of force and displacement for a static simulation on the contact were utilized in an optimization based on the Levenberg-Marquardt Method [15] to calculate the nonlinear parameters  $K$ ,  $d$  and  $\Delta F$ , as presented in Bizarre et al. [16, 17]. This process of solution was applied for both type of contacts. The variation of parameter  $d$  ranges from 1 to 1.5 for elliptical contacts. However, according to Tsuchi et al. [3], for line contacts, the parameter  $d$  of Eq. 11 assumes the value of unity.

## 3 Results and Discussion

Section 2 provides the basis for the numerical results of this study. Table 1 contains the data of Ellipticity ( $k$ ), Moes parameter of load ( $M$ ) and of lubricant ( $L$ ) for the reference elliptical contact. These contacts were calculated using a 7006 ball bearing geometry.

Five velocities were evaluated in order to analyze the behavior of force contact reduced order model parameters in function of different work conditions, leading to different lubricant Moes parameter  $L$ . Moreover, since ellipticity is an important parameter in approximation between line and elliptical contacts, according to Nijenbanning et al. [12] and Canzi et al. [11],  $k$  was also evaluated to be studied and it ranges from 0.0863 (original 7006 ball bearing ellipticity) to 0.5. For each ellipticity  $k$ , all  $L$  (velocities) was tested with all load range  $f$  ( $M$ ).

Figure 3 presents the process of data simulation: for each value of ellipticity was fixed a velocity and simulated all loads  $f$ , as shown by the arrows in the figure. The process is repeated for all ellipticity.

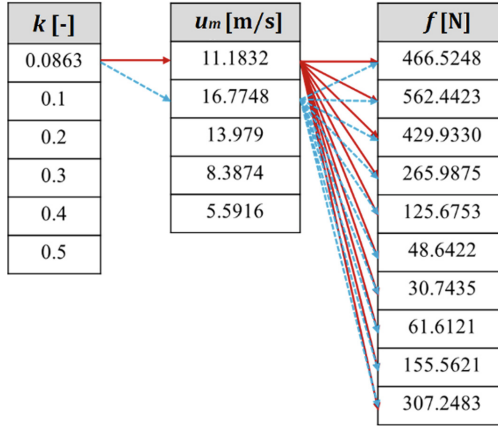


**Fig. 3.** Ellipticity data, Moes parameters of lubricant ( $L$ ) and load ( $M$ ) for the reference elliptical contact used to calculate the equivalent line contact.

Applying Eqs. 7 to 10 and the data present in Table 1, the equivalent line contact can be calculated. Then, the nonlinear parameters were optimized for both cases, line and elliptical contacts, and the results are shown in Fig. 4.

As expected, for line contact, the results did not show significant sensitivity with different values of ellipticity for the elliptical contact. However, for elliptical contact, the ellipticity presented a great influence on the results of all three parameters (Fig. 4). The EHD reduced stiffness ( $K$ ) and force offset ( $\Delta F$ ) show similar behavior tendency for both types of contact with respect to relative velocity (Fig. 4(a), (b), (d) and (e)). With increasing of velocity, both contacts tend to decrease the EHD stiffness and to increase the  $\Delta F$  (Fig. 4(a), (c), (d) and (f)). The difference for elliptical contact is the exponent  $d$  decreasing with velocity increasing and, as expected,  $d$  also decreases when ellipticity decreases, which, in this case, tends to the line contact (Fig. 4(b) and (e)). In case of stiffness, the elliptical contact shows to be more rigid than the line one, while for the  $\Delta F$  parameter, the equivalent line case resulted in higher values of offset force, agreeing with the lower values of stiffness (Fig. 4(a), (b), (d) and (e)). The range of EHD stiffness in line contact is less sensitive in comparison with the elliptical contact.

Nevertheless, the offset force  $\Delta F$  is less affected by velocity in elliptical than in line contact due to its stiffer character.

In elliptical geometry, the EHD stiffness and the force offset  $\Delta F$  increase with the decreasing of ellipticity  $k$  (Fig. 4(a), (b), (d) and (e)). For line contact, the  $d$  parameter is assumed unitary during the optimization (Fig. 4(f)).

Therefore, the nonlinear parameters results presented a coherent behavior with the variation of velocity and ellipticity (the variation of ellipticity for the elliptical contact, which gives different equivalent line contacts) for both contacts.

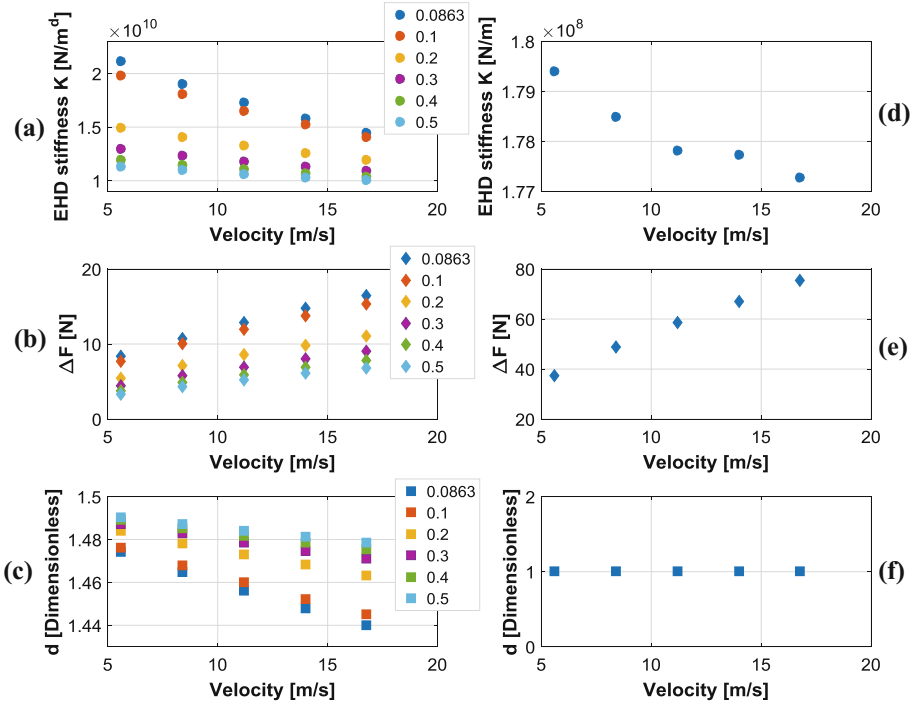


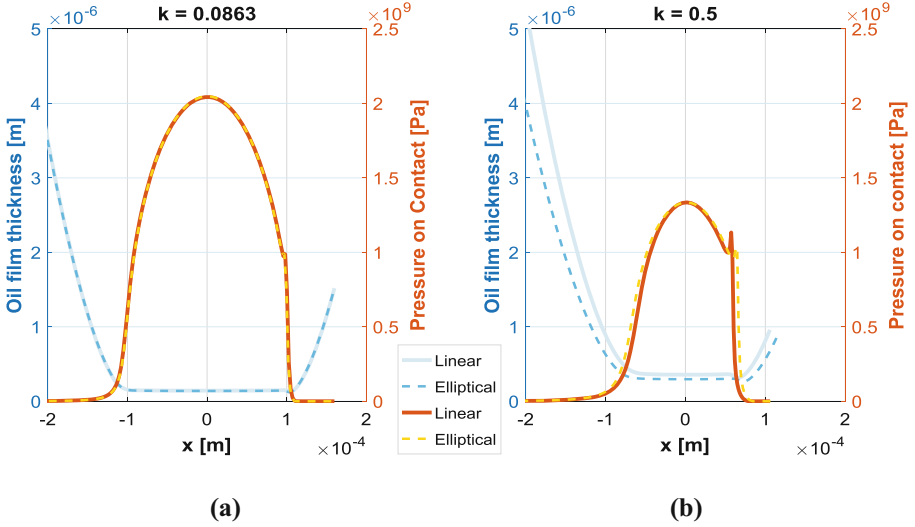
**Fig. 4.** Nonlinear parameters results of  $K$ ,  $d$  and  $\Delta F$  for elliptical contact ((a), (b), (c)) and line contact ((d), (e) and (f)) varying with the velocity ( $U_s$ ) and the ellipticity ( $k$ ).

From Fig. 4, two main cases can be highlighted in Table 1, representing the extreme conditions: low speed and high load (1) and high speed and low load (2).

Figure 5 contains the results of fluid film thickness and contact pressure for these two conditions described in Table 1, comparing the equivalence applied between line and elliptical contacts.

**Table 1.** Ellipticity data and Moes parameters for the two extreme cases.

	$k$ [-]	$L$ [-]	$M$ [-]
Case 1	0.0863	11.759	3949.421
Case 2	0.5	15.476	214.469

**Fig. 5.** Fluid film Thickness and Pressure distribution profile for Case 1 (a) and Case 2 (b) for the elliptical contact and its equivalent line contact.

The approximation of line and elliptical contact proved valid at low velocities and high load with low ellipticity. Figure 5 shows great similarity between pressure and thickness for  $k = 0.0863$ . Through  $k = 0.5$  (case 2), although the curves are still close, small discrepancies can be observed in the oil film thickness.

The difference between the extreme cases is also noted in the approximation of the contact area width, while for Case 1 the difference between the terms  $a_k$  and  $l$  is 0.4391%, for Case 2 this difference is 8.1633%, which reflects on pressure and oil film thickness, as shown in Fig. 5. The same behavior presented in Nijenbanning et al. [12] was found for pressure and oil film thickness, and using these results, forces and displacements on contact were analyzed.

**Table 2.** Values of width for elliptical ( $a_e$ ) and line contact ( $b_l$ ) for cases in Table 1.

	$k = 0.0863$	$k = 0.5$
Line	$b_l = 1.0656E-04$	$b_l = 7.0498E-05$
Elliptical	$a_e = 1.0609E-04$	$a_e = 7.6764E-05$
Relative percentage error	0.4391%	8.1633%

The displacements and forces on contact used to optimize the nonlinear parameters ( $K$ ,  $d$  and  $\Delta F$ ) are given in Fig. 6, for line and elliptical contact, with an ellipticity of 0.0863, 0.2 and 0.5. The results for line contact did not presented a relevant sensitivity regarding ellipticity, being located on the same curve, whereas the elliptical contacts present significant influence of ellipticities.

Another observation from Fig. 6 is the difference of load level between line and elliptical contact. Although the displacements for both models tested have the same order of magnitude, the forces are much higher in line contact. This behavior indicates that, although film thickness and pressure distribution are close in both models (Fig. 5), the same tendency was not observed for displacements and forces (Fig. 6). The same force magnitude implies in different and higher displacement for elliptical contact and this difference increases with the ellipticity. Therefore, under lubrication point of view, the ellipticity that better approaches the line contact is  $k = 0.0863$ . The equivalence of line and elliptical contacts presents a good agreement for the oil film thickness and the pressure profile on the contact central line in cases of low ellipticity. This similarity, however, cannot guarantee that the whole profiles of oil film thickness and pressure outside this central line are similar for both contact geometries, contributing for differences on the contact forces and displacements. The EHD lubrication model and the Hertz contact model can assume similar results for forces and displacements in high level of loads, indicating the equivalence of both models can be reasonably assumed in extreme conditions of load and ellipticity.

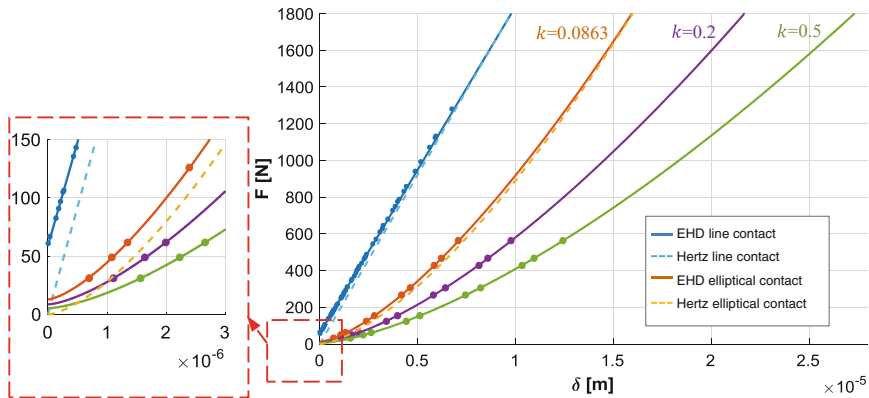


**Fig. 6.** Comparison of force versus displacement curves for ellipticities of: 0.0863, 0.2 and 0.5, simulated for line and elliptical contact. Full line is related to EHD lubrication in  $u_m = 11.1832$  m/s and dashed line to Hertz contact with  $k = 0.0863$ .

## 4 Conclusions

This work contains a discussion about the equivalence between elliptical and line contact models based on the hypothesis that both contacts have the same Hertz's pressure and the contact area widths can be approximately equal. Taken the ellipticity

data and Moes parameters (Ball bearing 7006), the EHD lubrication regime is numerically simulated (Multilevel) and the nonlinear parameters are optimized (Levenberg-Marquardt).

Comparing the results of nonlinear parameters ( $K$ ,  $d$  and  $\Delta F$ ) for both contacts type, it is possible to notice that, for the two types of contact, elastohydrodynamic reduced stiffness and force offset present the same tendency with the variation of velocity and that the elliptical contact is stiffer than the line equivalent. The increase of velocity leads to a decreasing of EHD stiffness and an increasing in  $\Delta F$  for both contacts and decreases index  $d$  in elliptical case. Furthermore, the elliptical contact has influence of the ellipticity and the same does not occur with the line contact. Ellipticity increasing tends to decrease EHD reduced stiffness and  $\Delta F$  and to increase exponent  $d$ .

As presented in Nijenbanning et al. [12] and Canzi et al. [11] the oil film thickness and pressure profile presented a good approximation in cases of high load, low rotation and low ellipticity, because this configuration tends to a Hertzian line contact. Since the outline of equivalence between both types of contact geometries is based on Hertzian contact theory, the elliptic contact area approaches the line contact area due to the load and speed conditions that tend to a behavior of a dry contact. Thus, although these two contact properties present a good agreement, the results of nonlinear contact force parameters show discrepancies, revealing that the behavior of the forces and deformations in the contact are different. Consequently, the equivalence can only be used for restrict conditions in order to avoid misleading in design parameters (for example, lifetime).

Therefore, when applied in a project phase, the equivalence between line and elliptical contact must respect the parameters of comparison that follows the same tendency, as oil film thickness and pressure distribution. The differences observed for forces and displacements of the models tested lead to variations that can affect the surface fatigue process, an important factor in the estimation of bearing lifetime.

## References

1. Wijnant, Y.H.: Contact dynamics in the field of elastohydrodynamic lubrication. Ph.D. thesis, University of Twente (1998)
2. Wensing, J.A.: On the dynamics of ball bearings. Ph.D. thesis, University of Twente (1998)
3. Tsuha, N.A.H., Nonato, F., Cavalca, K.L.: Formulation of a reduced order model for the stiffness on elastohydrodynamic line contacts applied to cam-follower mechanism. *Mech. Mach. Theory* **113**, 22–39 (2017)
4. Bizarre, L., Nonato, F., Cavalca, K.L.: Formulation of five degrees of freedom ball bearing model accounting for the nonlinear stiffness and damping of elastohydrodynamic point contacts. *Mech. Mach. Theory* **124**, 179–196 (2018)
5. Liu, J., Shao, Y.: An improved analytical model for a lubricated roller bearing including a localized defect with different edge shapes. *J. Vib. Control* 1–14 (2017)
6. Reynolds, O.: On the theory of lubrication and its application to M. Beauchamps tower's experiments, including an experimental determination of the viscosity of olive oil. *Phil. Trans. Roy. Soc.* **177**, 157–234 (1886)
7. Venner, C.H., Lubrecht, A.A.: *Multilevel Methods in Lubrication*, vol. 37, 400 p. Elsevier, Amsterdam (2001)

8. Roelands, C.J.A.: Correlational aspects of the viscosity-temperature-pressure relationship of lubricating oils. Ph.D. Thesis, Technical University Delft (1966)
9. Dowson, D., Higginson, G.R.: *Elasto-Hydrodynamic Lubrication – SI Edition*, 1st edn. Pergamon Press, Great Britain (1977)
10. Moes, H.: Optimum similarity analysis with applications to elasto-hydrodynamic lubrication. *Wear* **159**, 56–66 (1992)
11. Canzi, A., Venner, C.H., Lubrecht, A.A.: Film thickness prediction in elasto-hydrodynamically lubricated elliptical contacts. *Proc. Inst. Mech. Eng. Part J: J. Eng. Tribol.* **224**, 917–923 (2010)
12. Nijebanning, G., Venner, C.H., Moes, H.: Film thickness in elasto-hydrodynamically lubricated elliptic contacts. *Wear* **176**, 217–229 (1994)
13. Nonato, F., Cavalca, K.L.: On the non-linear dynamic behavior of elasto-hydrodynamic lubricated point contact. *J. Sound Vib.* **329**, 4656–4671 (2010)
14. Nonato, F., Cavalca, K.L.: An approach for including the stiffness and damping of elasto-hydrodynamic point contacts in deep groove ball bearing equilibrium models. *J. Sound Vib.* **333**, 6960–6978 (2014)
15. Marquardt, D.W.: An algorithm for least-squares estimation of nonlinear parameters. *J. Soc. Ind. Appl. Math.* **11**, 431–441 (1963)
16. Bizarre, L., Nonato, F., Cavalca, K.L.: EHD modeling of angular contact ball element bearings. In: 9th IFToMM International Conference on Rotor Dynamics, Milan, vol. 1, pp. 1–10 (2014)
17. Bizarre, L., Nonato, F., Cavalca, K.L.: Investigation on the convergence of EHD lubrication in angular contact ball bearing. In: 11th International Conference on Vibrations in Rotating Machinery, Proceedings of the Institution of Mechanical Engineers, London (2016)



# Stiffness and Damping Reduced Model in EHD Line Contacts

Natália Akemi Hoshikawa Tsuha<sup>(✉)</sup>, Fábio Nonato,  
and Katia Lucchesi Cavalca

Faculty of Mechanical Engineering, UNICAMP,  
Postal Box 6122, Campinas, SP 13083-970, Brazil  
{natalia.akemi, katia}@fem.unicamp.br,  
fabio.nonato@ge.com

**Abstract.** The increasing of operation speed and demand for precision in machinery make lubrication conditions a crucial aspect in order to maximize lifetime of rotor dynamic components. The elastohydrodynamic (EHD) regime more frequently occurs in nonconforming lubricated contacts with local elastic deformation due to high pressure in small contact area. The objective of this work is to analyze the EHD force reduced model applied to line contact based on restitutive and dissipative terms. In restitutive force term, an EHD stiffness approach is evaluated considering an explicit force-displacement relation with two independent parameters - stiffness and a constant surface separation force. Steady-state EHD contact numerical results allow estimating the restitutive parameters. The dissipative force term is composed by linear viscous damping. The damping is characterized by numerical simulation using the principle of energy conservation in transient elastohydrodynamic lubricated system. The influence of load and speed variations in damping fluctuations are investigated.

The EHD reduced force model characterizes the lubricated contact in just three parameters (oil film stiffness, EHD constant surface separation force and viscous damping), simplifying the lubrication problem in comparison of solving EHD system of equations at each work condition and time step. This model can be applied to any nonconforming EHD line contact as cams, gears, needle element rolling bearings and cylindrical roller bearings in dynamic analysis and project stage development. Furthermore, an accurate contact model increases machine reliability, being promising to be used in model-based fault identification.

**Keywords:** EHD stiffness · EHD damping · Line contact  
Elastohydrodynamic lubrication · Principle of energy conservation

## 1 Introduction

In the past, contribution of oil film from elastohydrodynamic (EHD) lubrication was neglected in studies of dynamics of machine elements and other nonconforming mechanisms as rolling bearings, gears and cams. However, regarding rolling bearings, the contact between rolling element and raceway significantly impacts its dynamic equilibrium and, consequently, the rotor response. Recently, the need for more accurate



modeling of rotating components has been demanded due to its invaluable contribution in vibration level and dynamic behavior prediction of the whole mechanical system.

Few studies have been done in order to understand and characterize the dynamic behavior of EHD lubricated contact for both elliptic and line geometries. Wijnant et al. [1] studied the influence of EHD elliptic contact on ball bearings and proposed an implicit dimensionless expression for EHD stiffness and viscous damping. Nonato and Cavalca [2] suggested an explicit polynomial approximation to dimensionless contact force for EHD point contacts using a least square method. Afterwards, Nonato and Cavalca [3] proposed an explicit dimensional load-displacement relation based on a nonlinear spring and viscous damping, making possible to characterize the deep groove ball bearing. Bizarre et al. [4] applied the model developed by [3] in angular contact ball element bearings. Further, Tsuha et al. [5, 6] extended the approach of [3] in order to propose a stiffness reduced model with an explicit load-displacement relation to EHD line contacts.

Wiegert et al. [7] proposed a simplified model of EHD line contact combining hydrodynamic and Hertzian models in order to replicate an EHD oscillatory vibration response. Qin et al. [8] suggested a load-dependent EHD stiffness calculation and applied the model to cam-follower contacts. Ankouni et al. [9] proposed a dimensionless linear viscous damper expression calculating hysteresis loop from numerical simulations of harmonic load excitation based on Moes parameters [10]. Zhang et al. [11] investigated oil film stiffness and damping under EHD lubrication contact-vibration. Damping was formulated using the principle of energy conservation and oil stiffness was estimated in function of applied load.

The objective of this work is to analyze the EHD force reduced model in line contacts based on restitutive and dissipative terms. In restitutive force term, an EHD stiffness approach is evaluated considering an explicit force-displacement relation proposed in [6]. The dissipative force term is composed by linear viscous damping, characterized by numerical simulation using the principle of energy conservation [11] in transient EHD lubricated system [12].

## 2 Transient EHD Lubrication

In infinite line contact, where  $y$ -direction is reasonable larger than the  $x$ -direction (Fig. 1), a uniform approach of oil film thickness and pressure gradient distribution in  $y$ -direction can give a good approximation to the problem. In this case, isothermal Reynolds Equation is simplified in  $y$ -direction:

$$\frac{\partial}{\partial x} \left( \frac{\rho h^3}{6\eta} \frac{\partial p}{\partial x} \right) - \frac{\partial(u_s \rho h)}{\partial x} - \frac{\partial(\rho h)}{\partial t} = 0 \quad (1)$$

where  $h$  is the full lubricant film thickness,  $p$  is the pressure,  $u_s$  is the sum of velocities between both contact surfaces  $u_s = u_1 + u_2$ ,  $\rho$  is the fluid film density,  $\eta$  is the oil absolute viscosity and  $t$  is the time reference.

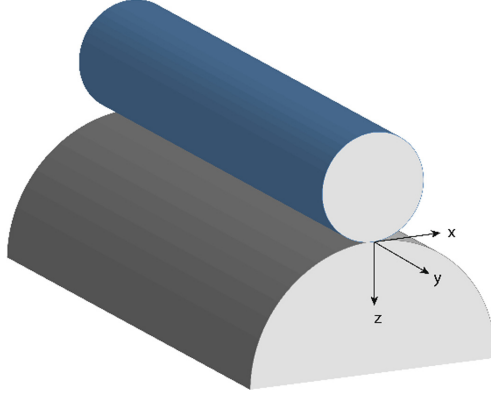


**Fig. 1.** Infinite line contact.

Pressure magnitude in EHD lubricated contacts is high in comparison with hydrodynamic lubrication. In this case, the fluid properties changes with pressure should be taken into account. In this study, the viscosity-pressure relation given by Roelands [13], in function of viscosity  $\eta_0$  at atmospheric pressure  $p_0$ , and density-pressure relation by Dowson and Higginson [14] are assumed. Moreover, due to high pressure in small contact area, the elasto-hydrodynamic regime occurs more frequently in nonconforming lubricated contacts with local elastic deformation. So, the film thickness equation, taking into account the elastic deformation term in line contact is [15]:

$$h(x, t) = -\delta(t) + \frac{x^2}{2R} - \frac{4}{\pi E'} \int_{-\infty}^{\infty} p(x', t) \ln \left| \frac{(x - x')}{x_0} \right| dx' \quad (2)$$

where  $\delta$  is the approximation between the contact bodies, the second term is related to contact geometry and the third term is the integral which represents the elastic deformation.  $E'$  is the reduced modulus of elasticity  $E' = \frac{2}{(1-\nu_1^2)/E_1 + (1-\nu_2^2)/E_2}$ ,  $R$  is the reduced radius of curvature  $R^{-1} = R_1^{-1} + R_2^{-1}$  and subscript numbers relate to the contact bodies.

The main difference between transient and steady-state EHD problem is the equation of motion given by Eq. (3):

$$m_e \ddot{\delta}(t) + l \int_{-\infty}^{+\infty} p(x, t) dx = f(t) \quad (3)$$

where  $\ddot{\delta}(t)$  is the acceleration between contact bodies,  $m_e = \pi R^2 l \rho_c$  is the modal mass of reduced contact,  $l$  is the effective length of contact surface,  $\rho_c$  is the density of contact bodies and  $f(t)$  is the contact force.

When the regime is in steady state,  $\ddot{\delta}(t)$  tends to zero and the equation of motion reduces to force balance equation. When a harmonic excitation of amplitude  $A$  and excitation frequency  $\omega_e$  is applied,  $f(t) = f_0(1 + A \sin(\omega_e t))$  [12]. However, in

free-vibration problems,  $f(t) = f_0$  where  $f_0$  is the force applied on the contact. To obtain the complete EHD dynamic response for a line contact, dimensionless parameters, based on Hertzian contact, are applied (Table 1). In Table 1,  $p_h$  is the maximum dry contact pressure,  $b$  is the half width of contact area,  $X$  is the dimensionless  $x$  direction,  $P$  is the dimensionless pressure,  $H$  is the dimensionless film thickness and  $\bar{\Delta}$  is the dimensionless displacement  $\delta$ .  $F, T, \bar{\rho}, \bar{\eta}$  and  $M_e$  are respectively the dimensionless force, time, density, viscosity and modal mass.  $\zeta$  and  $\lambda$  are dimensionless parameters of Reynold's Eq. (4).

**Table 1.** Dimensionless parameters based on dry contact Hertzian model.

Dimensionless parameters			
$X = x/b$	$P = p/p_h$	$H = hR/b^2$	$\bar{\Delta} = \delta R/b^2$
$b = \sqrt{\frac{8f_0 R}{\pi E' l}}$	$p_h = \frac{2f_0}{\pi b l}$		$\lambda = \frac{6\eta_0 u_s R^2}{b^3 p_h}$
$M_e = \frac{m u_s^2}{4R f_0}$	$\zeta = \frac{\bar{\rho} H^3}{\bar{\eta} \lambda}$		$F = \frac{f}{f_0}$
$\bar{\rho} = \rho/\rho_0$	$\bar{\eta} = \eta/\eta_0$		$T = t u_s / 2b$

The dimensional Reynolds Equation, film thickness equation and contact's motion equation are given by Eqs. (1), (2) and (3). Their dimensionless versions, Eqs. (4), (5) and (6), are respectively.

$$\frac{\partial}{\partial X} \left( \zeta \frac{\partial P}{\partial X} \right) - \frac{\partial(\bar{\rho}H)}{\partial X} - \frac{\partial(\bar{\rho}H)}{\partial T} = 0 \quad (4)$$

$$H(X, T) = -\bar{\Delta}(T) + \frac{X^2}{2} - \frac{1}{\pi} \int_{-\infty}^{+\infty} P(X', T) \ln|X - X'| dX' \quad (5)$$

$$M_e \ddot{\bar{\Delta}}(T) + \frac{2}{\pi} \int_{-\infty}^{+\infty} P(X, T) dX = F(T) \quad (6)$$

Regarding the numerical solution of EHD system of equations, two multilevel techniques were evaluated [16]. Finite-difference discretization of Reynolds Equation is numerically solved by Multigrid, and Multilevel Multi-Integration (MLMI) is applied to integrate deformation in film thickness equation. In order to solve the system in time domain of each contact of rolling element, a Newmark- $\beta$  integrator is used to obtain the transient response of contact's motion equation. Newmark's scheme has the advantage of solving directly the second order differential equations without using state-space representation, so this method was adopted over others ODE solvers.

### 3 Reduced Contact Force Model

EHD oil film equivalent system must take in consideration a restitutive and a dissipative term to describe the complete dynamic response. On the point of view of contact dynamics, an equivalent single degree of freedom EHD reduced model can be

represented by an EHD set of stiffness and viscous damping (see Fig. 2) and Eq. (7) is the contact's motion equation when the total contact force  $f(t)$  is a combination of inertial  $f_I(t)$ , dissipative  $f_C(t)$  and restitutive  $f_K(t)$  terms. Tangential forces in the contact due to sliding motion are not considered here.

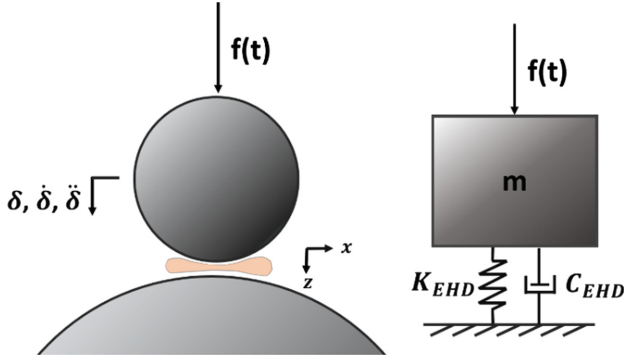


**Fig. 2.** Local representation of mutual approach  $\delta$ , velocity  $\dot{\delta}$  and acceleration  $\ddot{\delta}$  in a generic EHD contact and an equivalent single degree of freedom EHD model represented by a reduced stiffness and viscous damping (adapted from [6]).

$$f(t) = f_I(t) + f_C(t) + f_K(t) \quad (7)$$

Extended from elliptic model by Nonato and Cavalca [3], a restitutive reduced force model for EHD line contact was previously suggested by Tsuchi et al. [6]:

$$f_0 = K_{EHD}\delta_0 + \Delta F \quad (8)$$

where  $K_{EHD}$  is the EHD stiffness,  $\Delta F$  is an EHD constant surface separation force and  $\delta_0$  is the steady state equilibrium position for external static load  $f_0$ .

EHD restitutive force approximation is evaluated considering an explicit dimensional load-displacement relation with two independent parameters – stiffness  $K_{EHD}$  and an EHD constant surface separation force  $\Delta F$ . The restitutive force parameters can be obtained by curve fitting the mutual approach  $\delta_0$  at equilibrium to different external load levels. Levenberg-Marquardt method [17] was used to adjust the reduced order model given in Eq. (8) to the points generated by numerical simulations of EHD lubricated problem. After  $K_{EHD}$  and  $\Delta F$  are evaluated, these parameters can be applied in the transient analysis (Eq. 9).

$$f_K(t) = K_{EHD}\delta(t) + \Delta F \quad (9)$$

The dissipative force term is composed by linear viscous damping ( $C_{EHD}$ ) equivalence from oil film. Thus, the contact equation of motion for free vibration condition can be presented as:

$$m_e \ddot{\delta}(t) + c_{EHD} \dot{\delta}(t) + K_{EHD} \delta(t) + \Delta F = f_0 \quad (10)$$

Making the same assumption as Zhang et al. [11],  $\Delta\delta = (\delta - \delta_0)$ ,  $\Delta\dot{\delta} = (\dot{\delta} - \dot{\delta}_0) = \dot{\delta}$ ,  $\Delta\ddot{\delta} = (\ddot{\delta} - \ddot{\delta}_0) = \ddot{\delta}$ , Eq. (10) can be rewritten as:

$$m_e \Delta\ddot{\delta}(t) + c_{EHD} \Delta\dot{\delta}(t) + K_{EHD} \Delta\delta(t) = 0 \quad (11)$$

And energy of for inertial, dissipative and restitutive forces, given by Zhang et al. [11], are respectively  $E_I$ ,  $E_C$ ,  $E_K$ :

$$E_I(t) = \int_{\Delta\delta(0)}^{\Delta\delta(t)} m_e \Delta\ddot{\delta} d\Delta\delta = \int_0^t m_e \Delta\ddot{\delta} \Delta\dot{\delta} dt \quad (12)$$

$$E_C(t) = \int_{\Delta\delta(0)}^{\Delta\delta(t)} c_{EHD} \Delta\dot{\delta} d\Delta\delta = \int_0^t c_{EHD} (\Delta\dot{\delta})^2 dt \quad (13)$$

$$E_K(t) = \int_{\Delta\delta(0)}^{\Delta\delta(t)} K_{EHD} \Delta\delta d\Delta\delta = \int_0^t K_{EHD} \Delta\delta \Delta\dot{\delta} dt \quad (14)$$

At a first moment, there is only restitutive energy in free-vibration resulted from initial displacement input ( $\Delta\delta(0) \neq 0$ ). As time goes on in damped systems, dissipative energy is non-null at steady-state. Applying the principle of energy conservation in transient free-vibration EHD lubricated system:

$$\frac{1}{2} K_{EHD} [\Delta\delta(0)]^2 = \int_0^{t \rightarrow \infty} c_{EHD} (\Delta\dot{\delta})^2 dt \quad (15)$$

And viscous damping can be calculated as:

$$c_{EHD} = \frac{\frac{1}{2} K_{EHD} [\Delta\delta(0)]^2}{\int_0^{t \rightarrow \infty} (\Delta\dot{\delta})^2 dt} \quad (16)$$

The expression in Eq. (16) for viscous damping is the same presented in Zhang et al. [11]. However, as the EHD reduced stiffness is proposed to be calculated differently,  $K_{EHD}$  being a load-independent parameter, viscous damping also distinguishes from [11].

## 4 Results and Discussion

To better understand the behavior of both restitutive and dissipative parameters –  $K_{EHD}$ ,  $\Delta F$  and  $c_{EHD}$ , the line contact reduced model was applied to needle element bearing contacts with external radial load. Table 2 shows the geometric data of the bearing.

**Table 2.** NA4908 needle rolling element bearing geometric data.

Pitch diameter [m]	0.053
Rolling element diameter [m]	0.005
Clearance [m]	0.00
Effective contact length [m]	0.122
Number of elements	22

Initially, the system of equations containing equilibrium of forces in each rolling element and force balance in whole bearing was evaluated for rotational speed of 5000 rpm in dry contact case [18]. Two levels of pure radial load were applied: 30 kN and 50 kN. The load distribution for inner and outer raceways for each roller element, in function of azimuth angle, is presented in Fig. 3. The element located at azimuth angle equal to zero is the most loaded one. Outer race contact forces are higher than inner race contact forces, because of centrifugal forces of the rolling elements included in the model. However, these loading differences between inner and outer raceways due to inertial forces have a minor contribution here regarding the external loads magnitude.

Figure 4 shows free-vibration response of EHD lubricated contact for the most loaded element with 30 kN of radial force. Displacement  $\delta$  oscillates around the steady-state equilibrium position  $\delta_0$  while relative displacement  $\Delta\delta$ , velocity  $\Delta\dot{\delta}$  and acceleration  $\Delta\ddot{\delta}$  oscillate around zero and finally reaches zero in steady-state. Minimum film thickness  $h_m$  also oscillates while the equivalent system did not already reach the steady-state. Similar behavior of displacement, velocity, acceleration and film thickness can be observed in a lower load contact (Fig. 5). However, comparing the dynamic response between both elements, the damping effect is clearly more evident in the lower load roller. In both cases, the initial condition for displacement disturbance in free-vibration contact is 20% of the static equilibrium position.

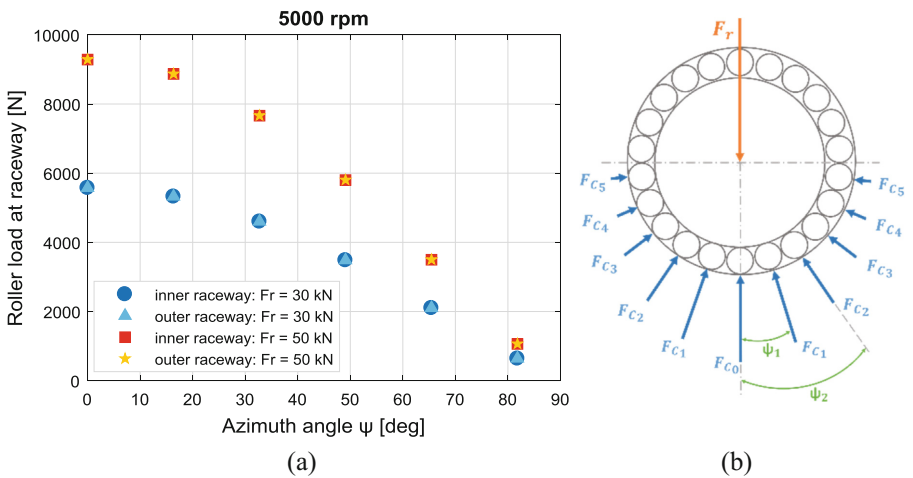


**Fig. 3.** (a) Element load at inner and outer raceways in function of azimuth angle for radial load of 30 kN and 50 kN and rotational speed of 5000 rpm. (b) Scheme of force distribution in rolling element bearing.

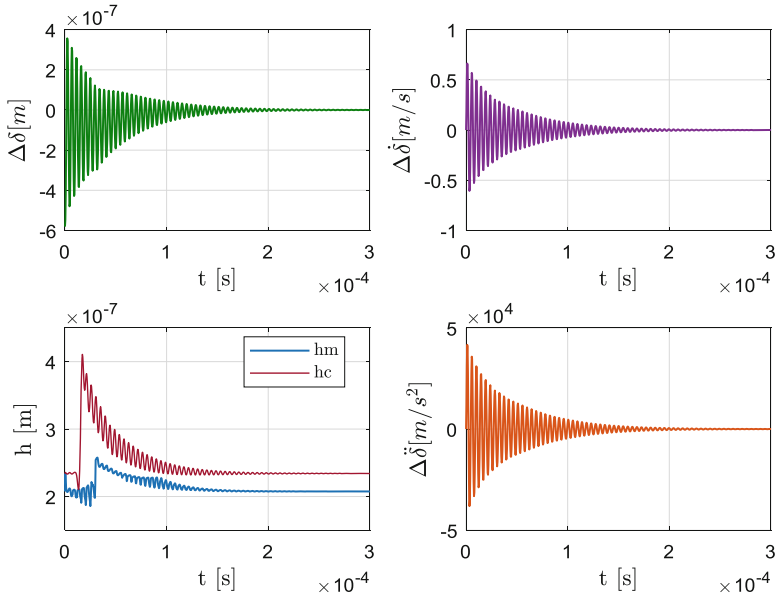


**Fig. 4.** Relative displacement  $\Delta\delta$ , velocity  $\Delta\dot{\delta}$ , acceleration  $\Delta\ddot{\delta}$ , central and minimum film thickness,  $h_c$  and  $h_m$ , for the EHD contact between roller and inner raceway located at azimuth degree  $0^\circ$ . Radial force of 30 kN and rotational speed of 5000 rpm.

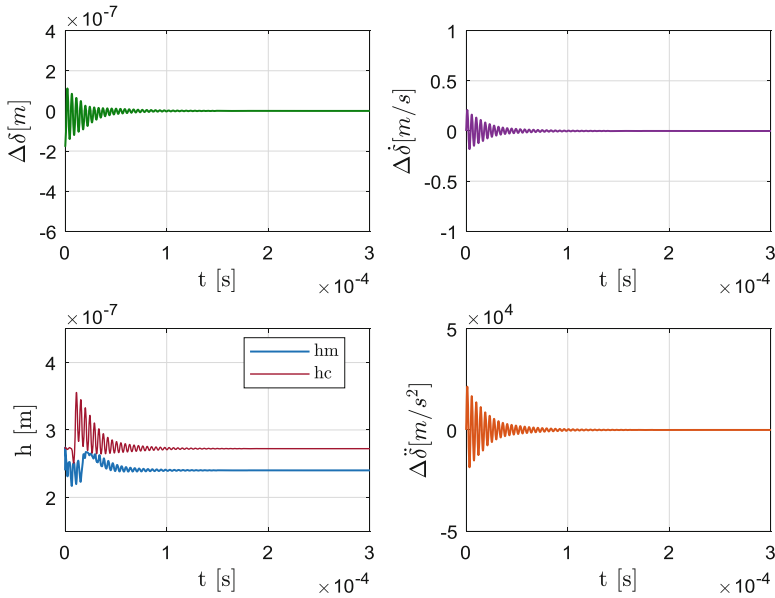


**Fig. 5.** Relative displacement  $\Delta\delta$ , velocity  $\Delta\dot{\delta}$ , acceleration  $\Delta\ddot{\delta}$ , central and minimum film thickness,  $h_c$  and  $h_m$ , for the EHD contact between roller and inner raceway located at azimuth degree  $65.45^\circ$ . Radial force of 30 kN and rotational speed of 5000 rpm.

All loaded elements from dynamic analysis of needle rolling bearing were subjected to EHD transient lubrication simulation. However, for lightly loaded elements,  $\delta$  can be predicted negative, which indicates that the lubrication characteristic contact is more hydrodynamic than elastohydrodynamic, according to Nonato and Cavalca [3]. The contacts whose displacement  $\delta$  are positive can be seen in Fig. 6 for radial load of 30 kN and 50 kN. Curve fitting was accomplished using Levenberg-Marquardt method [17]. The EHD stiffness obtained for inner raceway was  $1.7346 \cdot 10^9$  N/m and the EHD constant surface separation force  $\Delta F$  was 541.80 N, while reduced stiffness and  $\Delta F$  of outer raceway were  $K_{EHD} = 1.7326 \cdot 10^9$  N/m and  $\Delta F = 586.98$  N. As the geometry and radius of curvature are different between both raceways, the contact parameters must be too. Inner raceway has a smaller radius of curvature, namely, a smaller contact area, which means a stiffer contact. The larger radius of curvature of outer raceway allows more oil film and, consequently, higher EHD constant surface separation force ( $\Delta F$ ).

Unlike EHD stiffness, damping shows a load-dependent behavior. Along increasing of load, the model shows a tendency of decreasing viscous damping, Fig. 7, as expected based on EHD transient responses in Figs. 4 and 5. Further, the damping behavior in each raceway seems to have similar tendency regardless of externally applied load. It is noticed the geometric influence of contact in EHD damping. Since inner raceway has a smaller radius of curvature, film thickness decreases and reduces viscous damping.

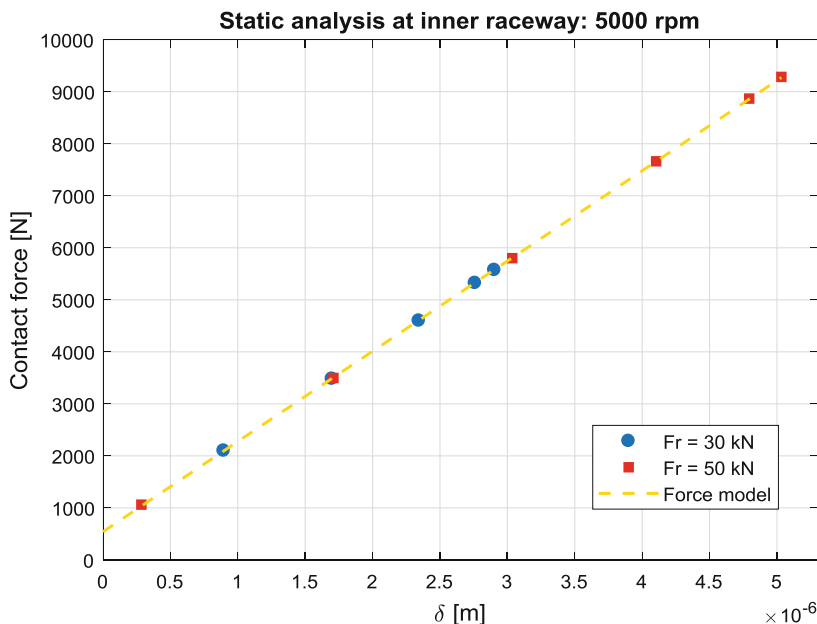


**Fig. 6.** Restitutive reduced force model for the contacts between roller and inner raceway at 5000 rpm. Blue circles are the points of each rolling element under EHD lubrication in the condition of radial load of 30 kN and red squares are related to radial load of 50 kN.



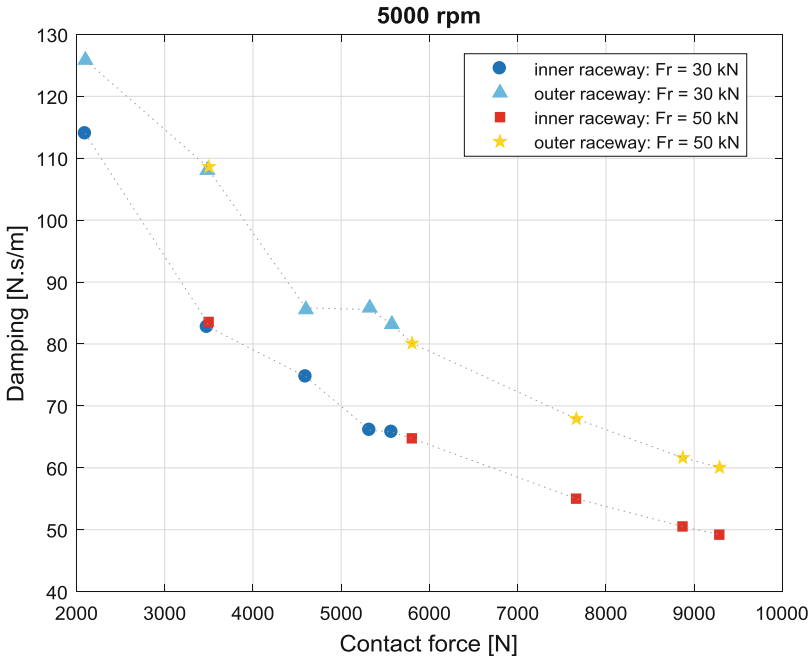


**Fig. 7.** Viscous damping of EHD contact of a rolling bearing at 5000 rpm and two different load level conditions: 30 kN and 50 kN.

In order to analyze the influence of rotation speed on the contact force, the previously studied needle rolling bearing under load of 50 kN was analyzed at 6000 rpm. Increasing of velocity causes an increment in film thickness. As consequence, the contact stiffness reduces in both raceways (Table 3).

**Table 3.** Restitutive EHD parameters of contacts at inner and outer raceways in condition of a radial load of 50 kN and 5000 rpm and 6000 rpm.

Inner raceway	$K_{EHD}$ [N/m]	5000 rpm	$1.7346 \cdot 10^9$
		6000 rpm	$1.7320 \cdot 10^9$
	$\Delta F$ [N]	5000 rpm	541.80
		6000 rpm	612.33
Outer raceway	$K_{EHD}$ [N/m]	5000 rpm	$1.7326 \cdot 10^9$
		6000 rpm	$1.7298 \cdot 10^9$
	$\Delta F$ [N]	5000 rpm	586.98
		6000 rpm	662.87

On the other hand, there is an increasing of surface separation component  $\Delta F$  that can be observed in curve fitting of restitutive force in Fig. 8. This increasing of rotation speed, however, reduces damping (see Fig. 9). Similar behavior of viscous damping in EHD line contact was predicted by Ankouni et al. [9] and Zhang et al. [11]. In hydrodynamic lubrication, an increment in speed stiffens fluid film and, as consequence, reduces viscous damping, being a similar physical phenomena observed here.

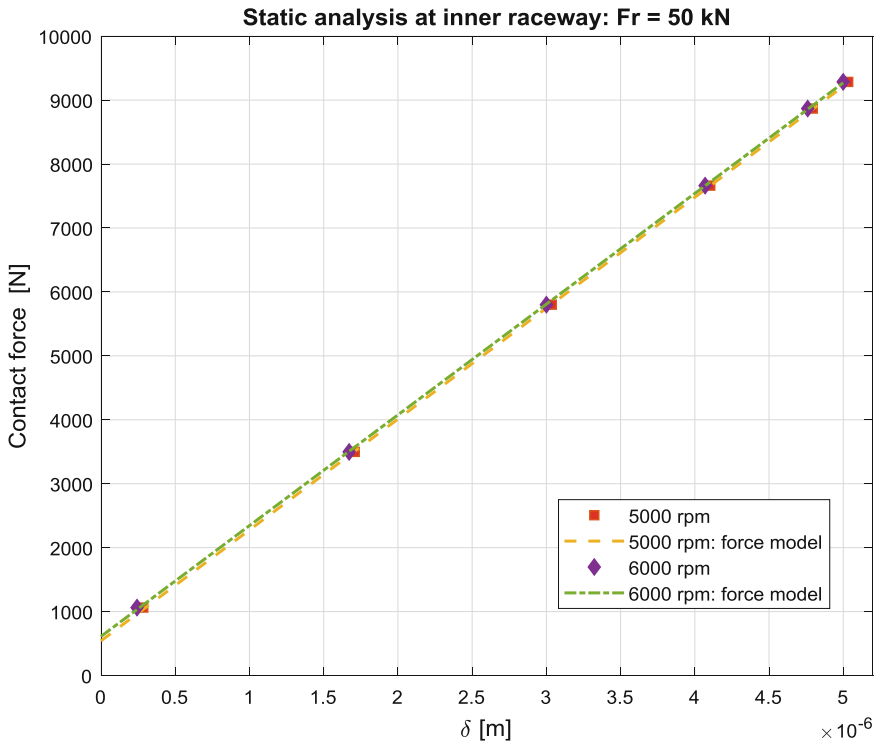


**Fig. 8.** Restitutive reduced force model for the contacts between roller and inner raceway with pure radial load of 50 kN. Red squares are the points of each rolling element under EHD lubrication in work condition of 5000 rpm and purple diamonds are related to rotational speed of 6000 rpm.

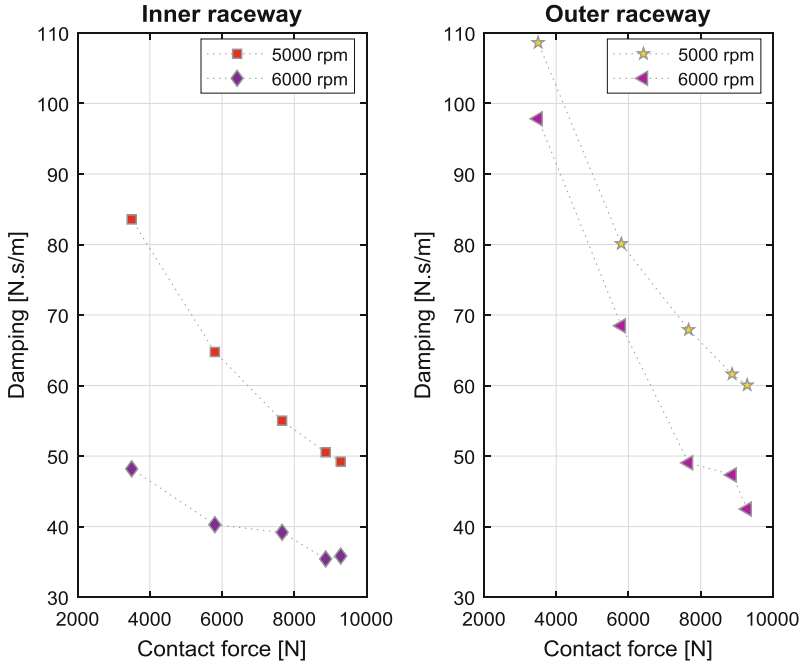


**Fig. 9.** Comparison between viscous damping of EHD contact of rolling bearing at 5000 rpm and 6000 rpm under 50 kN.

## 5 Conclusions

The aim of this study is the analysis of EHD contact reduced model in function of a set of stiffness and viscous damping parameters, that can be calculated from an equivalent contact under EHD transient lubrication. In order to fulfill the objective, the reduced force model is applied to a real needle rolling element bearing in different work conditions.

The EHD reduced stiffness and the constant surface separation force  $\Delta F$  are independents of external load. Though, viscous damping presented is inversely proportional to load in the cases studied here. Regardless geometry, inner raceway contacts present higher  $K_{EHD}$ , lower  $\Delta F$  and lower  $C_{EHD}$  than outer raceway. Moreover, an increasing in velocity leads to decreasing of contact stiffness and increment in  $\Delta F$ , as expected based on results of [6]. The viscous damping, on the other way, decreases with gain in velocity, agreeing with theoretical studies of [9, 11].

Thus, this model can be promisingly applied to nonconforming EHD line contacts. Once the force parameters of the contact are obtained, a more realistic response of bearing dynamics can be evaluated and, consequently, a better lifetime estimation. Furthermore, a more accurate contact model increases machine reliability and also can be used in control technique and model-based fault identification.

**Acknowledgments.** The authors would like to thank CAPES and CNPq for funding support to this research.

## References

1. Wijnant, Y.H., Wensing, J.A., Nijen, G.C.: The influence of lubrication on the dynamic behavior of ball bearings. *J. Sound Vib.* **222**, 579–596 (1999)
2. Nonato, F., Cavalca, K.L.: On the non-linear dynamic behavior of elastohydrodynamic lubricated point contact. *J. Sound Vib.* **329**, 4656–4671 (2010)
3. Nonato, F., Cavalca, K.L.: An approach for including the stiffness and damping of elastohydrodynamic point contacts in deep groove ball bearing equilibrium models. *J. Sound Vib.* **333**, 6960–6978 (2014)
4. Bizarre, L., Nonato, F., Cavalca, K.L.: EHD modeling of angular contact ball element bearings. In: 9th IFToMM International Conference on Rotor Dynamics, Milan, pp. 1–10 (2014)
5. Tsuha, N.A.H., Nonato, F., Cavalca, K.L.: An approach for the equivalent stiffness of elastohydrodynamic line contact. In: Proceedings of IMechE 2016 - VIRM11 – 11th Conference on Vibrations in Rotating Machinery, Manchester, pp. 355–365 (2016)
6. Tsuha, N.A.H., Nonato, F., Cavalca, K.L.: Formulation of a reduced order model for the stiffness on elastohydrodynamic line contacts applied to cam-follower mechanism. *Mech. Mach. Theory* **113**, 22–39 (2017)
7. Wiegert, B., Hetzler, H., Seemann, W.: A simplified elastohydrodynamic contact model capturing the nonlinear vibration behavior. *Tribol. Int.* **59**, 79–89 (2013)
8. Qin, W., Chao, J., Duan, L.: Study on stiffness of elastohydrodynamic line contact. *Mech. Mach. Theory* **86**, 36–47 (2015)
9. Ankouni, M., Lubrecht, A.A., Velex, P.: Modelling of damping in lubricated line contacts – applications to spur gear dynamic simulation. *Proc. Inst. Mech. Eng. Part C: J. Mech. Eng. Sci.* **230**, 1222–1232 (2016)
10. Moes, H.: Optimum similarity analysis with applications to elastohydrodynamic lubrication. *Wear* **159**, 57–66 (1992)
11. Zhang, Y., Huaiju, L., Zhu, C., Liu, M., Song, C.: Oil film stiffness and damping in an elastohydrodynamic lubrication line contact-vibration. *J. Mech. Sci. Technol.* **30**, 3031–3039 (2016)
12. Wijnant, Y.H.: Contact dynamics in the field of elastohydrodynamic lubrication. Ph.D. thesis, University of Twente (1998)
13. Roelands, C.J.A.: Correlational aspects of the viscosity-temperature-pressure relationship of lubricating oils. Ph.D. thesis, Technical University of Delft (1966)
14. Dowson, D., Higginson, G.R.: *Elasto-Hydrodynamic Lubrication – SI Edition*. Pergamon Press, Oxford (1977)
15. Venner, C.H.: Multilevel solution of the EHL line and point contact problems. Ph.D. thesis, University of Twente (1991)
16. Venner, C.H., Lubrecht, A.A.: *Multilevel Methods in Lubrication*. Tribology Series, Technology and Engineering, vol. 37, Elsevier, Amsterdam (2000)
17. Marquardt, D.W.: An algorithm for least-squares estimation of nonlinear parameters. *J. Soc. Ind. Appl. Math.* **11**, 431–441 (1963)
18. Harris, T.A.: *Rolling Bearing Analysis*. Wiley, New York (1991)



# Dynamical Characteristic Analysis of Elastic Ring Squeeze Film Damper in Rotor System

Zhifei Han, Qian Ding<sup>(✉)</sup>, and Wei Zhang

Department of Mechanics, Tianjin University, Tianjin 300350, China  
qding@tju.edu.cn

**Abstract.** By placing an elastic ring inside the oil chamber, elastic ring squeeze film damper (ERSFD) has better performance than classic squeeze film damper (SFD) in suppressing nonlinear characteristic and good application potential in aircraft engines and gas turbines. However, it is not easy to combine the deformation analysis on the elastic ring with the oil film analysis based on Reynolds equations and dynamic analysis of the ERSFD-supported rotor accurately. In this paper, based on the Kirchhoff assumption, the finite element method (FEM) is employed to investigate the deformation of elastic ring. First, the oil film pressure and force are analyzed by solving the Reynolds equations. Then the deformation of elastic ring, oil film force and rotor motion are determined simultaneously to analyze the oil film coefficients of ERSFD and the response of rotor system. Using the proposed procedure of calculation, dynamic characteristic of the ERSFD is investigated and we found that the ERSFD is better than the SFD in preventing bi-stable vibration of rotor by lightening the nonlinearity level of the oil film. Then influences of the ERSFD parameters, number of elastic ring boss, ring thickness and oil film thickness respectively, on the oil film characteristics are discussed. The study reveals that three effects of elastic ring make better dynamical performance of ERSFD than SFD.

**Keywords:** Elastic ring squeeze film damper · Rotor system  
Dynamical characteristic

## 1 Introduction

Squeeze film dampers (SFD) are widely used in aero-engines to control the stability and vibration of rotor systems [1]. However, the SFD has high nonlinear characteristic, which brings bi-stable and non-synchronous responses with large amplitude for the rotors [2]. The large-amplitude response can result in rotor/state rubs and fatigue [3]. In ref [4], nonlinear responses such as jump phenomenon, sub-harmonic and quasi-periodic vibrations are predicted for a range of bearing and mass unbalance parameters by Zhao [5]. Bonello [6] believes that the SFD-rotor system is prone to a periodic motion with sub-synchronous frequency components under highly eccentric around the first critical speed. Bi-stable response of a flexible rotor supported on SFD with centralizing springs are studied in [7] by synchronous circular centered-orbit motion solution, numerical integration method and slow acceleration method respectively. Influences of bearing parameters and mass ratio on bifurcation of

response of a flexible SFD-rotor are investigated by Inayat-Hussain [8]. Bifurcation of an unsymmetrical SFD-rotor system is analyzed in [9] by using singularity methods, to provide suggestions to avoid harmful phenomenon. The dynamical characteristics of SFD and dual clearance squeeze film damper (DCSFD) are experimentally investigated in ref. [10–12]

Placing an elastic ring inside the oil chamber results elastic ring SFD or ERSFD, as shown in Fig. 1(a). ERSFD not only retains the advantages of SFD, but also has better performance in suppressing nonlinear characteristic. Generally, a number of bosses are designed uniformly locating on the inside and outside surfaces of the elastic ring, which contact with the outer race of ball bearing and the housing, respectively. Lubricating oil film inside the chamber between the ring and outer race of bearing is defined as the inner oil film, and that between the ring and housing is defined as the outer oil film. The inner and outer oil chambers are connected with each other through the oil hole on elastic ring. The ERSFD, used in fanjet successfully, integrates the functions of damping and frequency modulation as revealed in ref. [13] by analyzing Reynolds equations of the inner/outer oil films. Hong [14] finds that ERSFD can automatically adjust the oil film thickness by taking advantage of the transverse deformation of the elastic ring, which reduces nonlinear characteristics of oil film markedly. In ref. [15], dynamical response of an ERSFD-rotor under influences of axial force, oil supply, structural parameters and unbalance are experimentally investigated. Based on Hirs bulk flow theory and Moody friction factor equation, Kang analyzes oil characteristics of ERSFD by considering the shearing effect of the outer squeeze film [16]. Zhang [17] analyzes the oil film characteristics and the bearing capacity with different pedestal contact status during a whirl period.

Deformation of the elastic ring plays an important role in determining the dynamic characteristic of the ERSFD. Finite element softwares, such as ANSYS, are often used to analyze the elastic ring deformation, in which the elastic ring can be modeled by solid elements [14, 15, 17]. But the computation is time-consuming, especially for a large amount of elements. To simplify the deformation estimation, the elastic ring can also be supposed to be composed of several thin plates or beams with simply supports [18]. Though computation is easier, accuracy of the deformation calculation is not high enough because the boundary conditions adopted are rather rough. In addition, the deformation analyses by the both computation procedure are not easy being combined with the hydrodynamic lubrication analysis of the ERSFD oil film, based on Reynolds equations, and dynamic analysis of the ERSFD-rotor.

In this paper, based on the Kirchhoff assumption of FEM, the flat shell element is employed to establish the model of the elastic ring to investigate the deformation of elastic ring. The coupled Reynolds equations of inner and outer oil film are established respectively to calculate oil coefficients and pressure. Eccentricity and offset angle are investigated by rotor equations. Then the equivalent restoring force of ERSFD is estimated by Reynolds equations. Runge-Kutta and finite difference method (FDM) are used to solve the above equations, sixteen oil film dynamic coefficients of ERSFD and the response of rotor system.

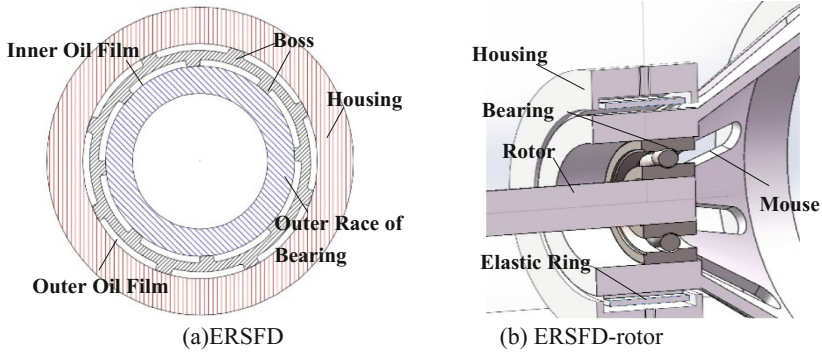


Fig. 1. Schematic model

## 2 Basic Principle and Method

### 2.1 Elastic Ring Model

Because the size of thickness is much smaller than that of length and width, elastic ring can be taken as a thin shell structure. According to the theory of plate and shell [19], four-node rectangular flat shell elements, composed of plane stress elements and Kirchhoff plane bending elements, can be used to analyze the deformation of elastic ring fast and accurately in case the grids are dense enough. The parameters of elastic are listed in Table 1.

Table 1. Parameters of the ERSFD

Parameters	Value
Elastic ring width (mm)	10
Elastic ring poisson ration	0.3
Oil density (kg/m <sup>3</sup> )	785
Elasticity modulus of elastic ring (Mpa)	1.96
Fluid viscosity (cp)	18.82
Length of damper (mm)	10
Inner radius of damper (mm)	32.5
Elastic ring boss width (mm)	4

Based on the two type elements mentioned above, stiffness matrix of a flat shell element is expressed as

$$K_{ij} = \begin{bmatrix} K_{ij}^{(p)} & 0 & 0 & 0 & 0 \\ & 0 & 0 & 0 & 0 \\ 0 & 0 & & & \\ 0 & 0 & K_{ij}^{(b)} & & \\ 0 & 0 & 0 & 0 & 0 \end{bmatrix} \quad (1)$$

where  $K_{ij}^{(p)}$  and  $K_{ij}^{(b)}$  are stiffness coefficients of the plane stress element and Kirchhoff plane bending element respectively. Displacements of nodes in local coordinates are determined by Eq. (2). Because the rotation of  $z$  axis doesn't exist in the assumption of Kirchhoff, the relevant position is set to be 0.

$$a_i = [u_i, v_i, w_i, \theta_{xi}, \theta_{yi}, 0]^T \quad (2)$$

where  $u_i$ ,  $v_i$  and  $w_i$  are displacements along  $x$ ,  $y$  and  $z$  directions, respectively.  $\theta_{xi}$  and  $\theta_{yi}$  are rotating angles around  $x$  and  $y$  axes. According to the Fig. 2, displacements in local coordinate can be transformed to the integral coordinate as

$$a'_i = [u'_i, v'_i, w'_i, \theta'_{xi}, \theta'_{yi}, 0]^T \quad (3)$$

The transformation relations between the local and integral coordinates are

$$a'_i = H a_i, a_i = H^T a'_i \quad (4)$$

where the  $H$  is transfer matrix given in [19].

Dividing the elastic ring into 48 elements circumferentially and 9 elements axially, the model of elastic ring consists of 432 flat shell elements. The boundary condition of model is that the tangential, radial and axial displacements of all bosses are restrained.

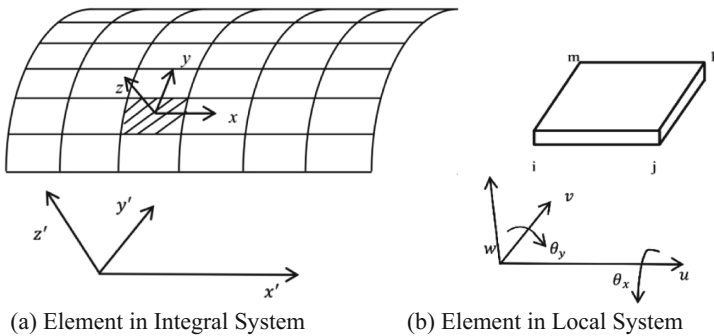


**Fig. 2.** Flat shell elements



2.2 Oil Film Pressure

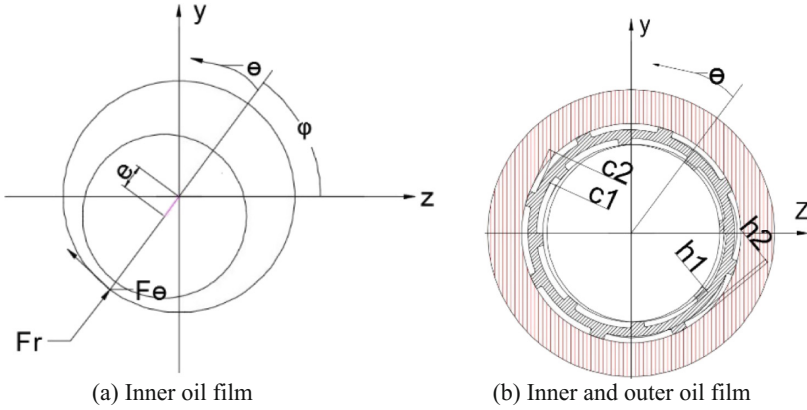


Fig. 3. Movements of ERSFD

Based on the short  $\pi$ -film assumption, transient Reynolds equations of the inner and outer oil films of the ERSFD are given by [13]

$$\frac{1}{R^2} \frac{\partial}{\partial \theta} \left( h_1^3 \frac{\partial p_1}{\partial \theta} \right) + \frac{\partial}{\partial x} \left( h_1^3 \frac{\partial p_1}{\partial x} \right) = -12\mu\Omega \left( \frac{\partial h_1}{\partial \theta} - \frac{\partial r}{\partial \theta} \right) + 12\mu \frac{\partial h_1}{\partial t} + \rho h^2 \frac{\partial^2 h}{\partial t^2} \quad (5)$$

and

$$\frac{1}{R^2} \frac{\partial}{\partial \theta} \left( h_2^3 \frac{\partial p_2}{\partial \theta} \right) + \frac{\partial}{\partial x} \left( h_2^3 \frac{\partial p_2}{\partial x} \right) = 12\eta \frac{\partial r}{\partial t} \quad (6)$$

respectively.  $\mu$  is the fluid viscosity,  $\rho$  the lubricating oil density,  $R$  the radius and  $\Omega$  the whirling velocity. As shown in Figs. 2(a) and 3(a),  $\theta$  and  $x$  are the circumferential and the axial coordinates.  $p_1$  and  $p_2$  represent the inner and outer oil film pressures to be solved.  $h_1$  and  $h_2$  are the inner and outer oil film thicknesses, while  $c_1$  and  $c_2$  are initial inner and outer oil chamber clearances, as shown in Fig. 7(b).

$$\begin{cases} h_1 = c_1 + r(\theta) + e \cos \theta \\ \frac{\partial h_1}{\partial \theta} = \frac{\partial r}{\partial \theta} - e \sin \theta \\ \frac{\partial h_1}{\partial t} = \dot{r} + \dot{e} \cos \theta \end{cases} \quad \text{and} \quad \begin{cases} h_2 = c_2 - r(\theta) \\ \frac{\partial h_2}{\partial \theta} = -\frac{\partial r}{\partial \theta} \\ \frac{\partial h_2}{\partial t} = -\dot{r} \end{cases} \quad (7)$$

where  $r$  and  $e = \sqrt{z^2 + y^2}$  are deformation of the elastic ring and whirling eccentricity of the journal respectively.  $\dot{r}$  and  $\dot{e}$  are the first derivatives of  $r$  and  $e$ .  $\varepsilon = e/c_1$  is defined as the eccentricity ratio.

To obtain the inner and outer oil film pressures, the finite difference method is used to solve the Reynolds equations [17].

### 2.3 Oil Film Force

Integrating the oil film pressure from  $\theta_1$  to  $\theta_2$ , the lower and upper boundary angles of the squeezing oil film, results oil film forces in radial and circumferential directions as

$$\begin{bmatrix} F_r \\ F_\theta \end{bmatrix} = - \int_{\theta_1}^{\theta_2} \left( \int_{-\frac{l}{2}}^{\frac{l}{2}} P dx \right) \begin{bmatrix} -\cos\theta \\ \sin\theta \end{bmatrix} R d\theta \quad (8)$$

which can be transformed to  $x$  and  $y$  directions

$$\begin{bmatrix} F_z \\ F_y \end{bmatrix} = \begin{bmatrix} F_r \cdot \cos\varphi - F_\theta \cdot \sin\varphi \\ F_r \cdot \sin\varphi + F_\theta \cdot \cos\varphi \end{bmatrix} \quad (9)$$

where  $\theta$  is the circumferential coordinate and  $\varphi$  is the offset angle of the journal, as shown in Fig. 3(a).

### 2.4 Equation of Motion

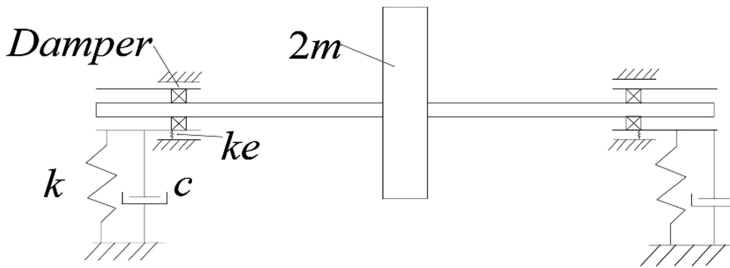


Fig. 4. Model of a rigid rotor supported on two ERSFDs

Supposing the elastic ring always contacts with the housing and outer race of bearing during the whole period of operation, as shown in Fig. 3(b). The dynamical equations of motion of a ERSFD supported rigid Jeffcott rotor, shown in Fig. 4, are deduced as

$$\begin{cases} m\ddot{z} + (k + k_e)z + c\dot{z} = m\omega^2 e_u \cos(\omega t) + F_z \\ m\ddot{y} + (k + k_e)y + c\dot{y} = m\omega^2 e_u \sin(\omega t) + F_y - G \end{cases} \quad (10)$$

where  $k$  is stiffness of the mouse cage of bearing (see Fig. 1(b)),  $k_e$  equivalent stiffness of the elastic ring,  $c$  damping of the system, and  $m$  half mass of the disk with unbalance distance  $e_u$ , respectively. The fourth-order Runge-Kutta method is used to solve Eq. (10). Speed ratio is defined by

$$\lambda = \frac{\omega}{p_n} \quad (11)$$

where  $p_n = \sqrt{(k + k_e)/m}$  is natural frequency of the shaft/disk system.

### 2.5 Solution Procedure

The solution procedure is shown in Fig. 5. First, dynamic responses are obtained by solving Eq. (10) and the oil film thickness is calculated under the obtained whirling eccentricity condition, as well the deformation of elastic ring. Then the oil film pressure and force are calculated by finite difference method (FDM) for oil film thickness distribution and deformation of elastic ring is determined by FEM under the obtained inner and outer oil film pressures. Then the inner oil film force is adopted to calculate the new dynamic response. The simulation procedure will be carried out until steady-state response is obtained.

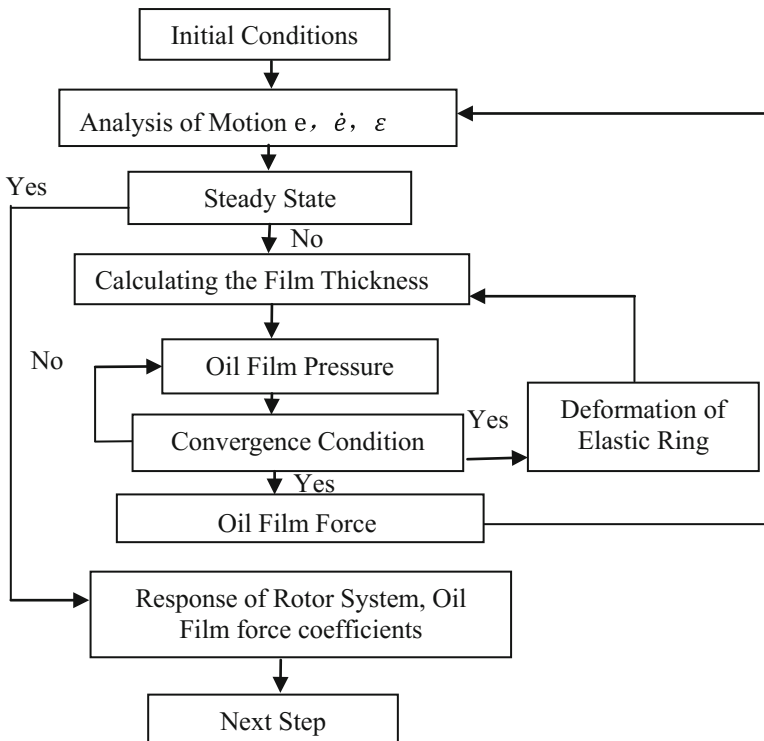


Fig. 5. Procedure of calculation

### 3 Pressure and Thickness of the Inner Oil Film

For comparison, the inner pressure and oil film thickness of both the ERSFD and SFD with oil film thickness  $c_s=0.2$  mm are presented in Fig. 6. One finds that the peak pressure value of ERSFD is less than that of SFD, and the pressure distribution of SFD is circumferentially asymmetrical due to the journal whirl. Figure 6(c) presents the influence of deformation/elasticity of the ring on the inner oil film pressure. The

red/black lines represent the film thickness of the rigid/elastic ring. The corresponding inner pressures of the ERSFD are  $P_r$  and  $P_e$ . One finds that the oil film thickness increases with the deformation of the elastic ring at the squeezing area. Correspondingly, the oil film pressures are reduced. Contrasting  $P_r$  and  $P_e$ , the asymmetrical distribution of pressure is lessened by the elastic ring deformation.

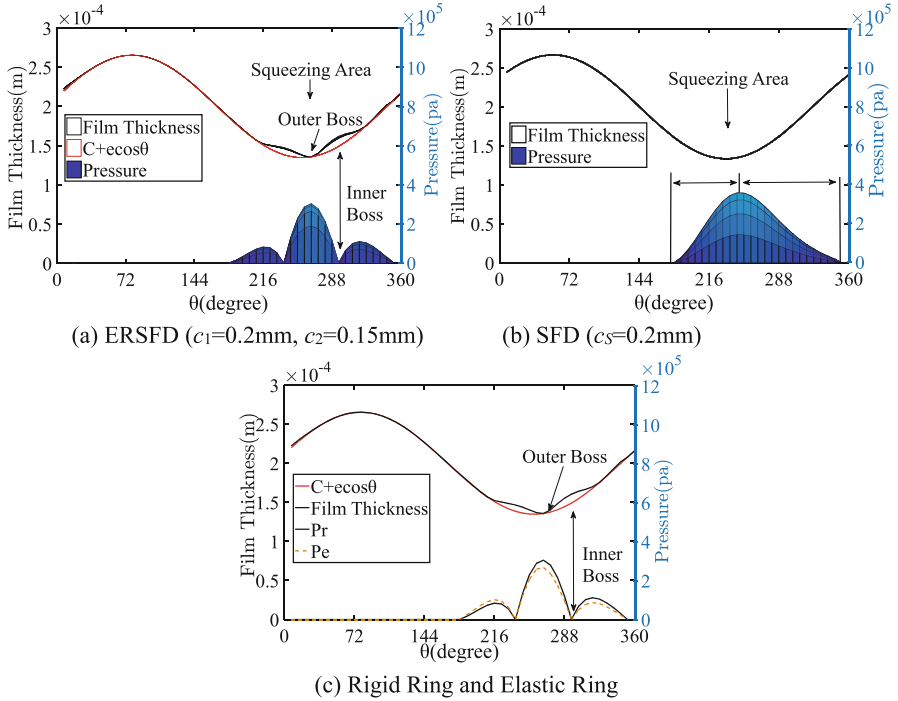


Fig. 6. Inner pressure and oil film thickness

## 4 Dynamical Coefficients

The oil film damping and inertia force coefficients are defined by Center Circular Orbit (CCO) method [20, 21]. Noted that there is no direct interaction between the journal and the outer oil film, thus the outer oil film dynamic coefficients are quite small. When the static eccentricity ratio  $\varepsilon < 0.51$  and the amplitude of vibration  $D_{\max}/c_1 < 0.51$ , oil film stiffness has been ignored. Thus the equations of motion of ERSFD are

$$\begin{bmatrix} M_{zz} & M_{yz} \\ M_{zy} & M_{yy} \end{bmatrix} \begin{bmatrix} \ddot{z} \\ \ddot{y} \end{bmatrix} + \begin{bmatrix} C_{zz} & C_{yz} \\ C_{zy} & C_{yy} \end{bmatrix} \begin{bmatrix} \dot{z} \\ \dot{y} \end{bmatrix} = \begin{bmatrix} F_z \\ F_y \end{bmatrix} \quad (12)$$

The direct flourier transform (DFT) is applied as

$$\begin{bmatrix} z \\ y \end{bmatrix} = \begin{bmatrix} \bar{z} \\ \bar{y} \end{bmatrix} e^{i\omega t}, \begin{bmatrix} F_z \\ F_y \end{bmatrix} = \begin{bmatrix} \bar{F}_z \\ \bar{F}_y \end{bmatrix} e^{i\omega t} \quad (13)$$

After some algebraic operation, following equations are obtained

$$\begin{aligned} -\omega^2 M_{zz} + \omega C_{zy} + i(\omega^2 M_{zy} + \omega C_{zz}) &= \frac{\bar{F}_z}{z} \\ -\omega^2 M_{yy} + \omega C_{yz} + i(\omega C_{yy} - \omega^2 M_{yz}) &= \frac{\bar{F}_y}{y} \end{aligned} \quad (14)$$

The cross coefficients are negligible as detailed in ref [22], the direct oil film coefficients are obtained

$$\begin{aligned} M_{zz} &= -\frac{1}{\omega^2} Re\left(\frac{\bar{F}_z}{z}\right) & C_{zz} &= \frac{1}{\omega} Im\left(\frac{\bar{F}_z}{z}\right) \\ M_{yy} &= -\frac{1}{\omega^2} Re\left(\frac{\bar{F}_y}{y}\right) & C_{yy} &= \frac{1}{\omega} Im\left(\frac{\bar{F}_y}{y}\right) \end{aligned} \quad (15)$$

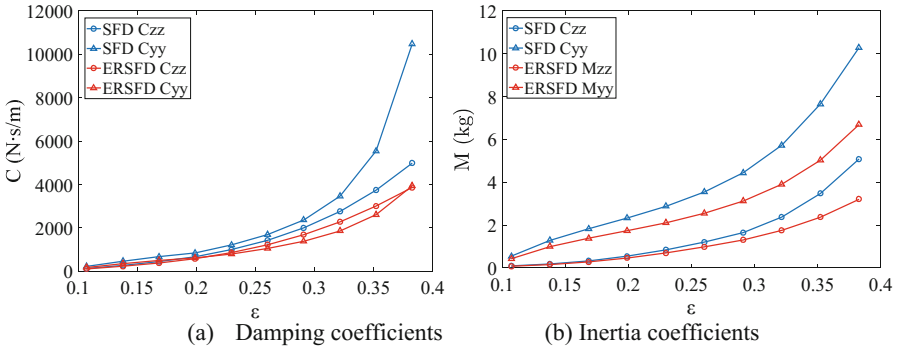


Fig. 7. Oil film characteristics of ERSFD and SFD

### 4.1 Basic Oil Film Characteristics

The original clearances of the inner and outer chambers of ERSFD are chosen as  $c_1 = 0.4$  mm and  $c_2 = 0.15$  mm, and the boss number is 4.

From Fig. 7, we find that the nonlinear degree of the coefficients of SFD is higher than that of ERSFD as the eccentricity increases further. The results mean that the nonlinearity can be suppressed by using of the elastic ring inside SFD. For example, oil film damping and inertia of SFD are almost twice larger than that of ERSFD when  $\epsilon = 0.38$ .

### 4.2 Influences of Structure Parameters on Oil Film Dynamic Coefficients

Influences of the boss amount, film thickness and ring thickness on oil film inertia and damping coefficients of ERSFD are analyzed in this section. From Fig. 8, one finds that oil film coefficients of ERSFD, with elastic ring thickness 0.95 mm and boss amount 4, 6 and 8 respectively, increase nonlinearly with the eccentricity ratio. Besides, increase of the elastic ring boss amount can also reduce the level of nonlinearity of ERSFD. The reason is that the un-symmetrical distribution of pressure is decreased by the divided oil chamber/film and deformation of the elastic ring.

Oil film dynamic coefficients of ERSFD with different oil film thickness and different elastic ring thickness are showed in Figs. 9 and 10 respectively. We find that both the increase of oil film thickness and decrease of elastic ring thickness can result in increase of the ability to restrain the nonlinear characteristics for ERSFD.

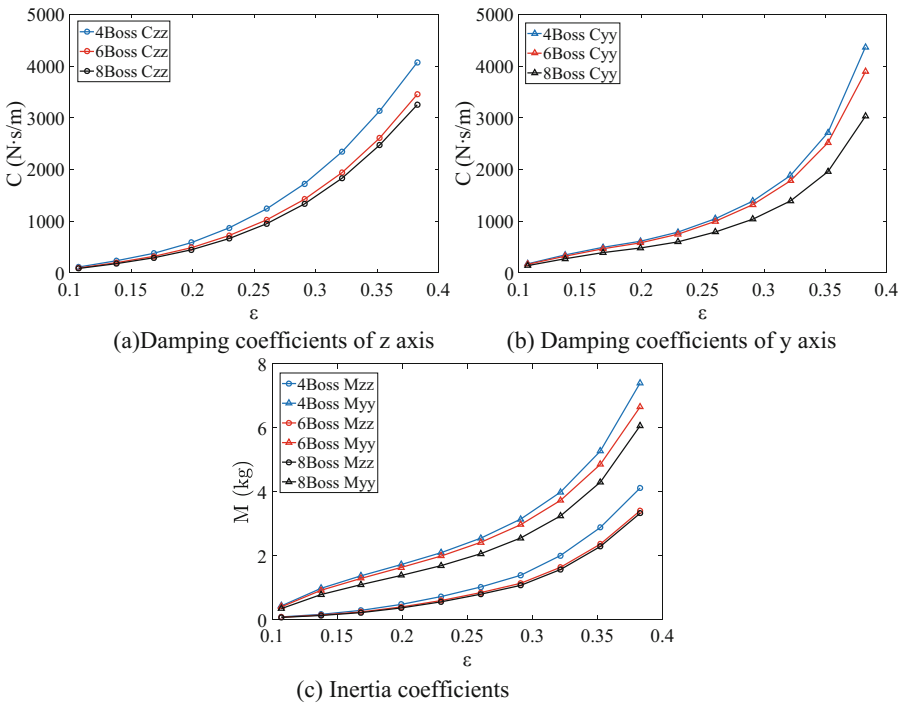


**Fig. 8.** Influence of boss number on dynamic characteristics of the ERSFD with 0.95 mm elastic ring thickness

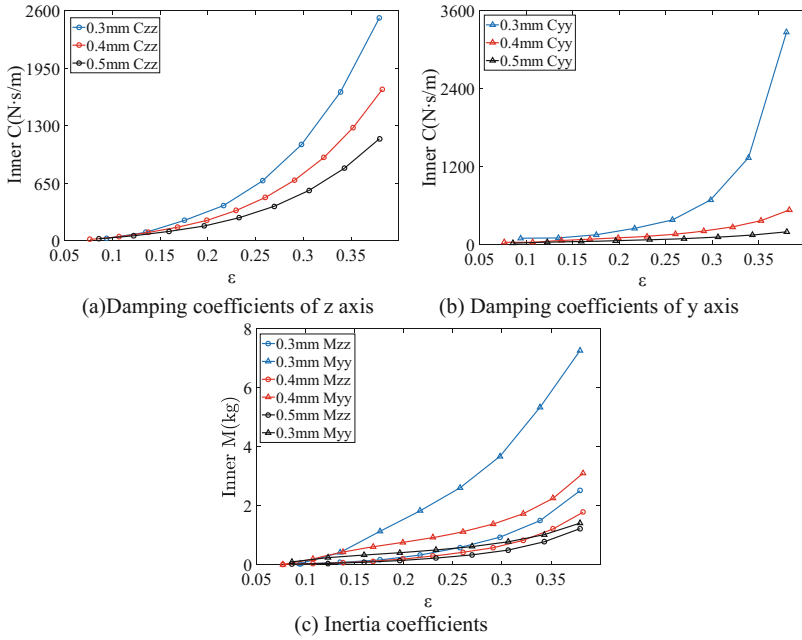


**Fig. 9.** Influence of oil film thickness on dynamic characteristics of the ERSFD with 8-boss elastic ring

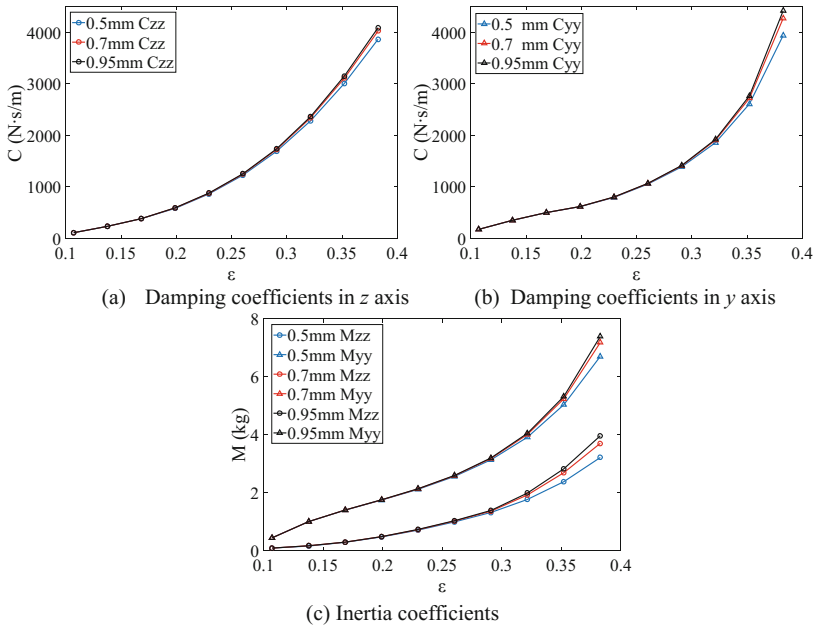


**Fig. 10.** Influence of elastic ring thickness on dynamic characteristics of the ERSFD with 8-boss elastic ring

## 5 Dynamical Response of ERSFD-Rotor System

Select the system parameter values to be

$$k = 8 \times 10^6 \text{N/m}, c = 80 \text{N} \cdot \text{m/s}, \mu = 18.82 \text{cp}, m = 10 \text{kg},$$

$$e_u = 1 \times 10^{-6} \text{m}, c_1 = c_s = 0.4 \text{mm}, c_2 = 0.15 \text{mm}$$

The displacement of the disk from its static equilibrium position is determined by

$$D = \sqrt{x^2 + \left(y - \frac{mg}{k + k_e}\right)^2} \quad (16)$$

Denoting the maximum of  $D$  by  $D_{\max}$ , which is also known as amplitude of vibration of rotor, the amplitude-frequency responses of the rotor systems with different dampers, operating through the critical speeds, are numerical simulated and presented in Fig. 11. In the small picture, the resonant amplitudes of the three systems are also illustrated near the speed ratio  $\lambda = 1$ . One finds that both the ERSFD and SFD can suppress vibration of rotor.

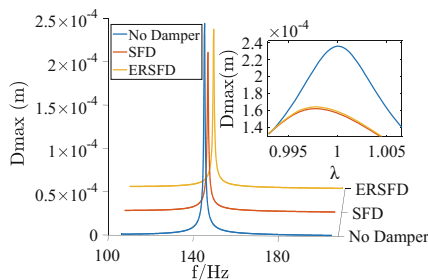


**Fig. 11.** Dynamical responses of the SFD-rotor systems, with/without damper and with ERSFD (with 4 boss and elastic ring thickness 0.5 mm)

### 5.1 Influences of ERSFD Parameters on the System Dynamics

Dynamic response of the ERSFD-rotor systems with 8 bosses, 0.5 mm elastic ring thickness and oil film thickness 0.3, 0.4 and 0.6 mm respectively, are shown in the Fig. 12(a). It can be found that  $D_{\max}$  decreases with the decrease of oil film thickness, while the critical speed is hardly affected by the change of oil film thickness. By contrasting Figs. 9 and 12(a), influence of oil film thickness on reducing vibration and nonlinearity is different, thus oil film thickness should be chosen according to the actual demand of the vibration reduction and nonlinearity suppression.

Response of ERSFD-rotor systems with 4 bosses,  $c_1 = 0.4$  mm and  $c_2 = 0.15$  mm and different values of elastic ring thickness, 0.5 mm, 0.7 mm and 0.95 mm respectively, are presented in Fig. 12(b). We can find that  $D_{\max}$  of the system with elastic



ring thickness 0.5 mm and 0.7 mm are almost same but smaller than the case the elastic ring thickness is 0.95 mm.

Figure 12(c) is amplitude-frequency curves of the ERSFD-rotor system with elastic ring thickness 0.5 mm and 4, 6 and 8 bosses respectively. One finds that  $D_{max}$  increases with the increase of amount of elastic ring boss. Moreover, the increase of support inertia with the increase of boss amount results in the increase of critical speed. By comparing with Fig. 8, increase of boss number will increase the ability of the ERSFD to suppress the nonlinearity of oil film but decrease the ability to reduce vibration. Thus the boss amount should be chosen according to the actual demand of the vibration reduction and the nonlinearity suppression.

Noted that the difference of vibration amplitudes of different system are mainly influence by their oil film rather than different elastic ring stiffness which can change system damping ratio.

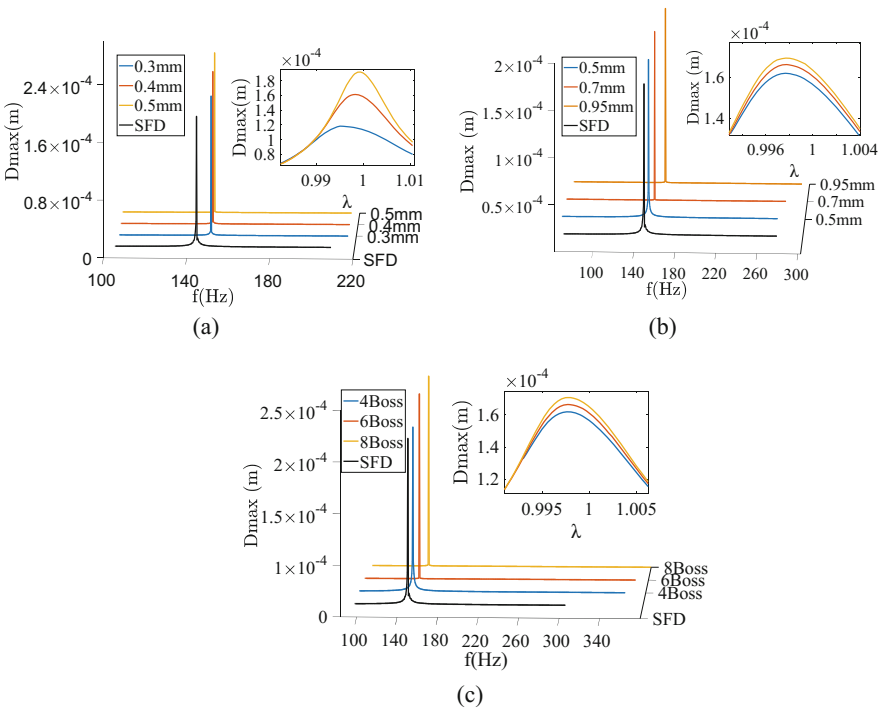


**Fig. 12.** Dynamical responses of ERSFD-rotor system, (a) inner oil film thickness is 0.3, 0.4 and 0.6 mm (8 bosses and 0.5 mm thickness of elastic ring); (b) elastic ring thickness is 0.5 mm, 0.7 mm and 0.95 mm (4 bosses,  $c_1 = 0.4$  mm and  $c_2 = 0.15$  mm); (c) elastic ring with 4, 6 and 8 bosses (0.5 mm thickness,  $c_1 = 0.4$  mm and  $c_2 = 0.15$  mm).

## 5.2 Bi-stable Response

Amplitude-frequency responses of ERSFD-rotor with 4 boss and 0.5 mm elastic ring thickness and SFD-rotor with the centering spring are shown in Fig. 13. There is obvious jump phenomenon for the SFD-system as the frequency swipes up and down across the resonant frequency of the system. The jump is a typical vibration behavior for nonlinear systems and can bring harmful impacts to the system. Whereas such a nonlinear phenomenon doesn't appear in ERSFD-system. That is the elastic ring can light nonlinearity of SFD. We also find that the resonant curve of SFD system behaves softening stiffness characteristic.

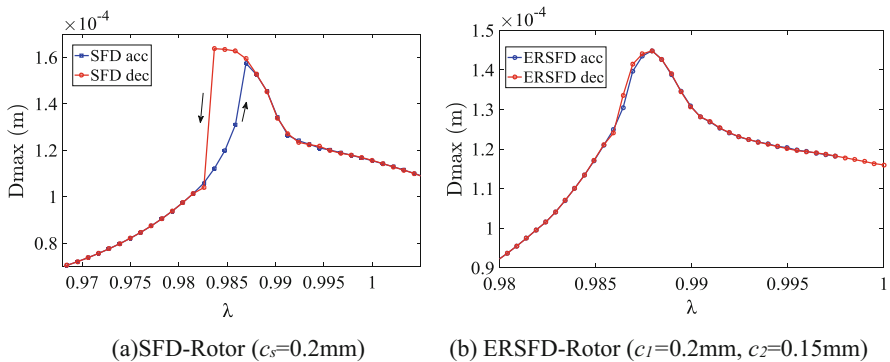


**Fig. 13.** Bi-stable resonance of the SFD-rotor is suppressed by ERSFD ( $k = 1 \times 10^6 \text{ N/m}$ ,  $c = 20 \text{ N} \cdot \text{m/s}$ ,  $\mu = 1 \text{ cp}$ ,  $m = 3 \text{ kg}$ ,  $e_u = 2.7 \times 10^{-6} \text{ m}$ )

## 6 Conclusion

In this paper, the flat shell element based on the Kirchhoff assumption is adopted to establish the elastic ring model. The deformation of the elastic ring, oil film force and rotor motion were determined simultaneously to analyze the oil film coefficients of the ERSFD and response of the rotors. Results are summarized in follows.

- (1) ERSFD performance better in preventing bi-stable or jump vibration of rotor by decreasing the nonlinear effects of the oil film.
- (2) Elastic ring brings three effects to ERSFD. First, deformation of the elastic ring adjusts oil film thickness. Second, the bosses of the elastic ring divide the oil chamber into several sections. As a result, unbalanced distribution of oil film thickness is lightened and the nonlinear degree of the oil film is decreased. Third, the elastic ring can modulate the natural frequency of the rotor system by changing the support stiffness.
- (3) Increase of boss number and oil film thickness inside ERSFD can suppress the nonlinearity of oil film but not vibration of rotor. So the structural parameters of an ERSFD-rotor system should be carefully selected to acquire a good vibration

reduction performance. However, thin elastic ring thickness is always good for reducing vibration and suppressing oil film nonlinearity.

**Funding.** This research is supported by the National Natural Science of China under Grant No. 51575378.

## References

1. Siew, C.C., Hill, M., Holmes, R.: Evaluation of various fluid-film models for use in the analysis of squeeze film dampers with a central groove. *Tribol. Int.* **35**(8), 533–547 (2002)
2. Zhao, J.Y., Hahn, E.J.: Eccentric operation and blade-loss simulation of a rigid rotor supported by an improved squeeze film damper. *J. Tribol.* **177**(3), 490–497 (1995)
3. Rezvani, M.A., Hahn, E.J.: Floating ring squeeze film damper: theoretical analysis. *Tribol. Int.* **33**(3), 249–258 (2000)
4. Zhao, J.Y., Linnett, I.W., Mclean, L.J.: Stability and bifurcation of unbalanced response of a squeeze film damped flexible rotor. *J. Tribol.* **116**(2), 361–368 (1994)
5. Zhao, M., Ren, P., Li, J.: Double static analysis of multi-rotor system with squeeze film damper. *J. Propul. Technol.* **25**(1), 66–70 (2004)
6. Bonello, P., Brennan, M.J., Holmes, R.: Non-linear modelling of rotor dynamic systems with squeeze film dampers—an efficient integrated approach. *J. Sound Vib.* **249**(4), 743–773 (2002)
7. Zhu, C., Robb, D., Ewins, D.: Analysis of the multiple-solution response of a flexible rotor supported on non-linear squeeze film dampers. *J. Sound Vib.* **252**(3), 389–408 (2002)
8. Inayat-Hussain, J.I.: Bifurcations of a flexible rotor response in squeeze-film dampers without centering springs. *Chaos Solitons Fractals* **24**(2), 583–596 (2005)
9. Chen, H., Hou, L., Chen, Y.: Bifurcation analysis of a rigid-rotor squeeze film damper system with unsymmetrical stiffness supports. *Arch. Appl. Mech.* **87**, 1347–1364 (2017)
10. San Andrés, L.: Force coefficients for a large clearance open ends squeeze film damper with a central feed groove: experiments and predictions. *Tribol. Int.* **71**, 17–25 (2014)
11. Jeung, S.H.: Performance of an open ends squeeze film damper operating with large amplitude orbital motions: experimental analysis and assessment of the accuracy of the linearized force coefficients model. Texas A&M Univ: College Station (2013)
12. Moraru, L., et al.: Dynamic modeling of a dual clearance squeeze film damper—part I: test rig and dynamic model with one damper. *Tribol. Trans.* **46**, 170–178 (2003)
13. Zhou, M., Li, Q.H., Yan, L.T.: Experimental investigation and application of an elastic ring squeeze film damper. *J. Aerosp. Power* **13**(4), 408–412 (1998)
14. Hong, J., Deng, Y.W., Zang, D.Y.: Dynamic design method of elastic ring squeeze film damper. *J. Beijing Univ. Aeronaut. Astronaut.* **32**(6), 649–653 (2006)
15. Cao, L., Gao, D.P., Jiang, H.P.: Investigation on critical speed characteristics of elastic ring SFD-rotor system. *J. Propul. Technol.* **29**(2), 235–239 (2008)
16. Kang, Z.H., Ren, X.M., Wang, Z.: New dynamic model of the 3D squeeze film system with a floating ring. *J. Mech. Strength* **31**(06), 892–895 (2009)
17. Zhang, W., Ding, Q.: Elastic ring deformation and pedestal contact status analysis of elastic ring squeeze film damper. *J. Sound Vib.* **346**, 314–327 (2015)
18. Dai, X.J., Wang, G.M.: Analysis on stiffness of corrugated ring in a rotor-bearing support. *J. Harbin Inst. Technol.* **26**(5), 40–43 (1994)

19. Neto, M.A., et al.: *Engineering Computation of Structures: The Finite Element Method*, 1st edn. Springer, Cham (2015)
20. San Andrés, L., Delgado, A.: Identification of force coefficients in a squeeze film damper with a mechanical end seal—centered circular orbit tests. *Trans. ASME* **126**, 660–668 (2007)
21. Wang, Z., Xu, N., Yu, X.: The dynamic characteristic analysis of elastic ring squeeze film damper by fluid-structure interaction approach. In: *Proceedings of ASME Turbo Expo 2017: Turbomachinery Technical Conference and Exposition*, Charlotte, NC, USA (2017)
22. San Andrés, L.: Squeeze film dampers: operation, models and technical issues. *Modern Lubrication Theory*, Notes 13, Texas A&M University Digital Libraries (2010). <https://repository.tamu.edu/handle/1969.1/93197>. Accessed 02 May 2011



# Unbalance Vibration Compensation Control Using Deep Network for Rotor System with Active Magnetic Bearings

Xuan Yao, Zhaobo Chen<sup>(✉)</sup>, and Yinghou Jiao

School of Mechatronics Engineering, Harbin Institute of Technology,  
Harbin 150001, China  
chenzb@hit.edu.cn

**Abstract.** Unbalance vibration directly affects the operational precision, stability and life of rotary machinery. Profiting from the active control speciality of active magnetic bearing (AMB), unbalance vibration of rotor system with AMBs can be compensated and controlled automatically. This paper considers unbalance vibration minimum for rotor system with AMBs. Deep learning theory is utilized to design a compensation controller, which is added to the PID feedback control. The structure of the compensation controller is established by a deep neural network with 2 hidden layers, and its operation algorithms are designed. Model of a 4-DOF rigid rotor with AMBs is established for controller parameter setting and simulation. The unbalance vibration control of different controllers at fixed rotational speed is simulated, and the control effects of the proposed controller are demonstrated via unbalance vibration analysis and control current analysis. This research provides a new adaptive control approach for AMB control of unbalance minimum compensation, and it can also be applied in other multi-dimension vibration control.

**Keywords:** Active magnetic bearing · Unbalance vibration  
Compensation controller design · Deep neural network

## 1 Introduction

The unwanted vibration caused by mass unbalance and asymmetry, is inevitable in real system. Unbalance vibration, which directly affects the operational precision, stability and life of the system, is a common problem in rotor machinery. Active magnetic bearings (AMBs) have got increasing applications in rotor machinery because of their several advantages over conventional mechanical bearings such as no-lubrication and no-wear [1]. Moreover, AMBs have the possibility to change the mechanical properties of rotor system by active control, meaning that the unbalance vibration can be minimized specifically by real-time compensation control of AMBs.

As automatic balancing control [2], unbalance vibration control is one main kind of unbalance control of AMB. The control target is to minimize the radial displacement of rotor caused by unbalance vibration. However, it is not easy to provide suitable control current for unbalance vibration from the complex rotor dynamics as well as the non-linear electromagnetic characteristics. Various control methods have been applied in

this area. Lei et al. did a lot work on AMBs of a high temperature gas-cooled reactor. They proposed an adaptive unbalance vibration control method based on notch filters to achieve the “displacement nulling” control or “current nulling” control [3]. They also designed a frequency-domain iterative learning control (ILC) algorithm and reduced the vibration significantly [4]. Tung et al. added a model-based unbalance compensator using fuzzy gain tuning mechanism to PID controller and testified its effect in accuracy via simulation and experiment [5]. Kuseyri designed an  $H_\infty$  controller based on system model with uncertainties to deal with the unbalance and to keep the robust stability of the whole system [6]. Fang et al. proposed a feedforward controller, with a general notch filter for unbalance vibration identification and a gain phase modifier (GPM) for precise control current, to realize the minimum vibration force and torque with smaller vibration displacement [7]. Okubo et al. studied the unbalance vibration control for five-axes active magnetic bearing systems and successfully applied the method of automatic balancing system (ABS) and peak-of-gain control (PGC) [8]. Heindel et al. derived a model-free controller of Jeffcott rotor with AMBs for unbalance and resonance elimination [9]. Qiao and Hu proposed an optimal influence coefficient control method using unbalanced vibration of all nodes on the rotor as the control objective function for multinode unbalanced vibration of flexible rotor [10]. Saito and wakui designed an unbalance vibration compensator using a tracking filter for the axial direction of AMBs [11]. Cui et al. proposed a method based on phase-shift notch filter to control unbalance vibration within the whole frequency range. The phase shift in the band-pass filter can be adaptive adjusted with respect to rotor speed [12]. Jiang et al. proposed an unbalance compensation method by recursive seeking the real-time position of unbalance mass. Their method has good effectiveness with low computational cost [13].

Neural network is also an attractive approach for compensation control because of its excellent fitting capability. Paul et al. used a MLP-network to compensate remaining unbalances at magnetic bearings [14]. With the development of processor performance, deep learning method and deep network, which dominate image identification [15], have been employed for identification and compensation of mechanical system [16].

In a word, feature extraction of unbalance vibration from the complex and coupled rotor dynamic signals is a key for unbalance vibration control. Thus, the identification ability of algorithm directly affect the control precision. In this study, an unbalance vibration compensation control method based on deep learning theory is proposed for AMB-rotor system to enhance operational precision. The model of a 4-DOF AMB-rotor system is established containing a rigid rotor model and a nonlinear AMB model. PID feedback controller is adopted to guarantee the stability of the close-loop system. An adaptive unbalance compensator is designed using a dual-layer neural network based on deep learning theory. The rotor dynamics at a fixed frequency are simulated. Vibration and control current of different controllers are analyzed to indicate the effect of the proposed method.

## 2 Model of Rotor with AMBs

The schematic of a horizontal rotor system suspended by 2 AMBs is shown in Fig. 1.  $O_c$  is the center of rotor with the coordinates  $\mathbf{x}_c = [x_c, x_\theta, y_c, y_\theta]^T$ .  $\mathbf{x} = [x_a, x_b, y_a, y_b]^T$  is rotor displacement at AMB position detected by sensors. The rotor is assumed to be rigid and symmetrical, and both static unbalance and dynamic unbalance are considered. So the dynamic model of this 4-DOF AMB-rotor system is

$$\begin{cases} m\ddot{x}_c = F_{xa} + F_{xb} + e_r m \omega^2 \cos(\omega t) \\ m\ddot{y}_c = F_{ya} + F_{yb} + e_r m \omega^2 \sin(\omega t) - mg \\ I\ddot{x}_\theta + I_z \omega \dot{y}_\theta = -l_a F_{ya} + l_b F_{yb} + e_\varepsilon I \omega^2 \sin(\omega t) \\ I\ddot{y}_\theta - I_z \omega \dot{x}_\theta = l_a F_{xa} - l_b F_{xb} + e_\varepsilon I \omega^2 \cos(\omega t) \end{cases} \quad (1)$$

$$\mathbf{x} = \begin{bmatrix} 1 & 0 & 0 & l_a \\ 1 & 0 & 0 & -l_b \\ 0 & -l_a & 1 & 0 \\ 0 & l_b & 1 & 0 \end{bmatrix} \cdot \mathbf{x}_c \quad (2)$$

where  $m$  is the mass of rotor,  $I$  and  $I_z$  are rotary inertia of axis x/y and axis z respectively,  $\omega$  is the angular speed of rotation around axis z,  $l_a/l_b$  is the distance between AMB a/b and rotor center,  $e_r/e_\varepsilon$  is radial/axial eccentric error, and  $\mathbf{F}_{AMB} = [F_{xa}, F_{xb}, F_{ya}, F_{yb}]^T$  is active control force of AMBs.

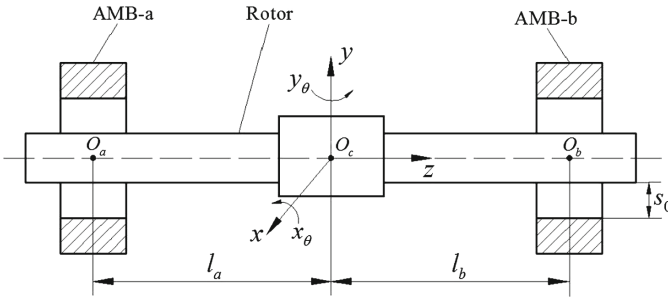


Fig. 1. Schematic of a rotor system with AMBs.

Commonly the AMBs are differential driven, so the magnetic force on each DOF is described as [1]:

$$F_{AMB} = k \cos \alpha \left[ \left( \frac{i_0 - i_c}{s_0 - x} \right)^2 - \left( \frac{i_0 + i_c}{s_0 + x} \right)^2 \right] \quad (3)$$

where  $k$  is the electromagnetic coefficient,  $\alpha$  is the angle of pole,  $i_0$  is the bias current,  $i_c$  is the control current,  $x$  is the rotor displacement at AMB position, and  $s_0$  is the rated air gap.

To set parameters of linear controller like PID and robust control, Eq. (3) can be linearized as

$$F_{AMB} = k \cos \alpha \left( \frac{4i_0^2}{s_0^3} x - \frac{4i_0}{s_0^2} i_c \right) = k_s x - k_i i_c \quad (4)$$

The model of power amplifier and sensor are simplified and regarded as one-order inertial link with pure hysteresis respectively.

### 3 Design of Compensation Controller

#### 3.1 Structure of the Proposed Controller

The block diagram of the AMB-rotor system is shown in Fig. 2. A PID controller is used as the main controller, like the most common cases [17]. The compensation controller based on deep network approach is added parallel to the main controller to deal with unbalance vibration specifically.  $Re$  is the expected position of rotor. The error of rotor position  $e$  is inputted in the main controller and compensation controller to produce the control signal respectively. The control current  $i_c$  is obtained by adding the output of the 2 controllers, and is transformed to magnetic force  $F_{AMB}$  acting on the rotor via the power amplifier. Finally, the rotor displacement at AMB position  $x$  is detected by sensor and used as feedback signal.

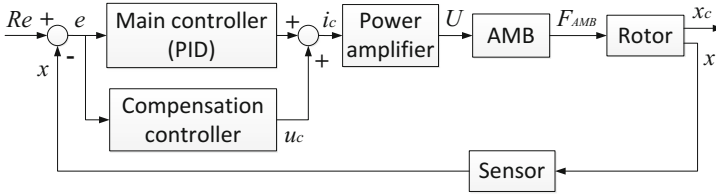


Fig. 2. Block diagram of AMB-rotor system.

The compensation controller is proposed based on deep learning theory. This controller is established by a deep neural network (DNN) with 2 hidden layers. The structure of the controller is shown in Fig. 3. The input of the network is the position error  $e$ . In the input layer, a matrix  $[e]$  consisting of the last 5 data of  $e$  is obtained via down sampling and memory operation. In the 2 hidden layers, the input of the layer is processed by function  $f$ . Finally in the output layer, the output of the controller  $u_c$  is calculated by function  $f_o$ . At the same time,  $e$  and its derivative are used in back-propagation algorithm to update the parameters of function  $f$  and  $f_o$  on line.



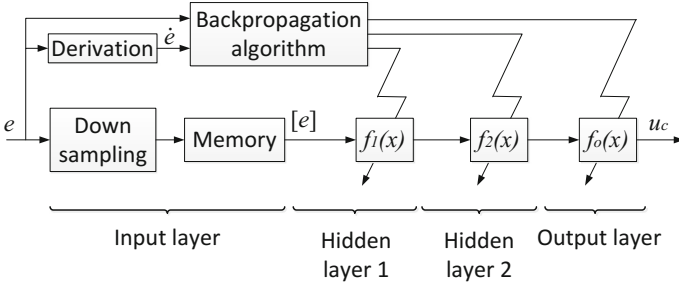


Fig. 3. Structure of the compensation controller.

### 3.2 Algorithm of the Compensation Controller

The function  $f$  in the hidden layer is

$$f(x) = \varphi(\omega x + b) \tag{5}$$

where  $\varphi$  is the activation function,  $\omega$  and  $b$  are the weights and biases of neurons respectively. For each DOF,  $\omega$  is a matrix of size  $5 \times 5$  and  $b$  is a vector of size  $1 \times 5$ .  $\omega$  and  $b$  are independent for each DOF and each layer.

The activation function  $f$  has many common forms. For real time control, the computational complexity should be considered, so a simple function called ReLU (Rectified Linear Unit) [18] is used in this study

$$\varphi(x) = \max(x, 0) \tag{6}$$

$$\frac{\partial \varphi}{\partial x} = \text{sign}(\varphi(x)) \tag{7}$$

The function  $f_o$  in the output layer is a linear function

$$f_o(x) = \omega_o x + b_o \tag{8}$$

where  $\omega_o$  and  $b_o$  are the weights and bias of the output layer respectively.

The loss function  $E$  is set via a factor  $\eta$  imitating the sliding mode control [19]:

$$\eta = e_c + \dot{e}_c = T(e + \dot{e}) \tag{9}$$

$$E = \eta^T \cdot \dot{\eta} \tag{10}$$

where  $T$  is the transformation matrix from  $x$  to  $x_c$ .

We can calculate that

$$\frac{\partial E}{\partial u_c} = -k_i T(e + \dot{e}) \tag{11}$$

Then the weights and biases can be updated by backpropagation algorithm [20] based on the gradient descent method with a constant-value learning rate  $\gamma$ .

## 4 Analysis of Simulation Results

### 4.1 Parameters of Simulation

The dynamics of system are simulated with 10 kHz sample frequency in the *MATLAB-Simulink* environment. The disturbance forces are considered as gaussian white noise. The parameters of the AMB-rotor system are given in Table 1 and the parameters of controller are given in Table 2.

**Table 1.** Parameters of the AMB-rotor system.

Name of parameter	Symbol	Value
Mass of rotor	$m$	2 kg
Rotor diameter	$D$	40 mm
Rotational speed	$n$	6000 r/min
Distance between bearing a and rotor bgeometric center	$l_a$	100 mm
Distance between bearing a and rotor bgeometric center	$l_b$	100 mm
Rotary inertia of axis x/y	$I$	0.02 kg·m <sup>2</sup>
Rotary inertia of axis z	$I_z$	0.001 kg·m <sup>2</sup>
Eccentric error	$e_r$	$5 \times 10^{-6}$ m
Eccentric angle	$e_\varepsilon$	$2 \times 10^{-3}$ rad
Rated air gap	$s_0$	0.8 mm
Available air gap	$s_a$	0.4 mm
Constant of magnetic force	$k$	$3.14 \times 10^{-6}$
Angle of pole	$\alpha$	$\pi/8$ rad
Bias current	$i_0$	2 A
Cutoff frequency of Power amplifier	$f_a$	500 Hz
Cutoff frequency of sensor	$f_s$	3000 Hz

**Table 2.** Parameters of controller.

Name of parameter	Symbol	Value
Proportional coefficient	$K_P$	$1.5 \times 10^4$
Integral coefficient	$K_I$	$1 \times 10^5$
Differential coefficient	$K_D$	25
Displacement coefficient	$k_s$	$9.82 \times 10^4$
Current coefficient	$k_i$	39.3
Number of weights in each hidden layer	$N_{oh}$	$5 \times 5 \times 4$
Number of biases in each hidden layer	$N_{bh}$	$5 \times 4$
Number of weights in output layer	$N_{oo}$	$5 \times 4$
Number of biases in output layer	$N_{bo}$	4
Learning rate	$\gamma$	$1 \times 10^{-6}$

### 4.2 Unbalance Vibration Analysis

The motion orbit of the rotor center without and with the compensation controller is shown in Fig. 4. It is obvious that the displacement of the rotor is reduced remarkably by the compensation controller from about 13  $\mu\text{m}$  to within 3  $\mu\text{m}$ . The radial vibration at direction x in frequency domain by FFT is shown in Fig. 5. The vibration synchronous with the rotational speed (100 Hz) is compensated and well restrained by the compensation controller.

The effect of the proposed compensation controller is also compared with a common RBF (Radial Basic Function) network compensation controller. The total vibration comparison is presented in Table 3. From the table, the proposed compensation controller by DNN has better compensation effects than that by RBF network in unbalance vibration control of AMB system.

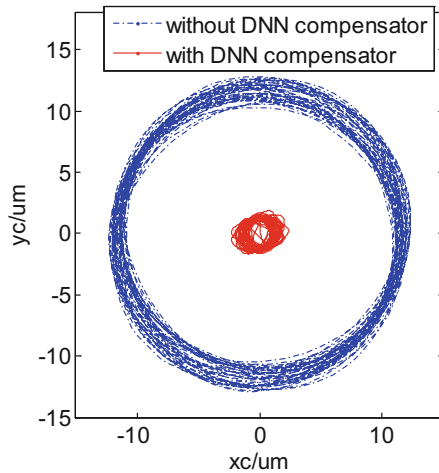


Fig. 4. Motion orbit of the rotor center.

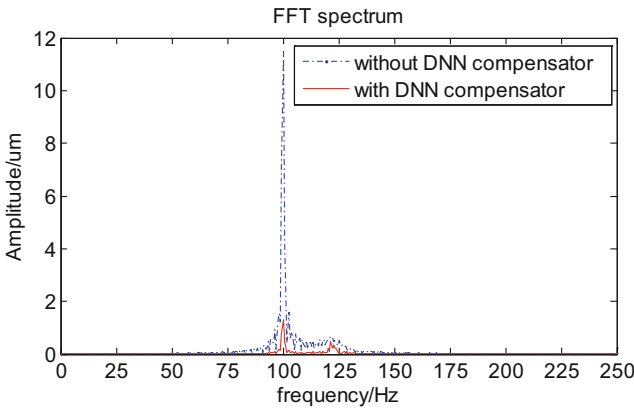


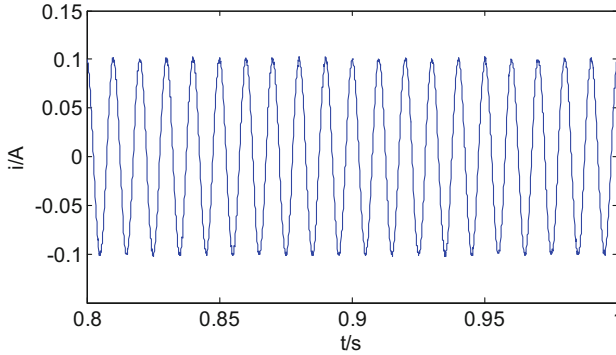
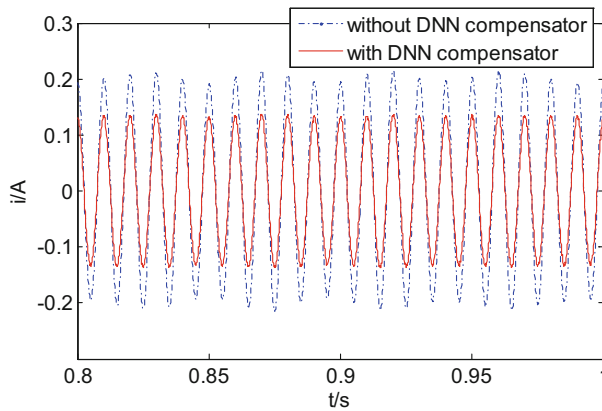
Fig. 5. Radial vibration at direction x in frequency domain.

**Table 3.** Vibration comparison of 3 controllers.

Controller	Maximum radial vibration
PID	12.5 $\mu\text{m}$
PID with RBFNN	2.94 $\mu\text{m}$
PID with DNN	2.37 $\mu\text{m}$

### 4.3 Control Current Analysis

Figures 6, 7 and 8 respectively represent the output of the compensation controller, the total control current without and with the compensation controller, and their FFT forms in frequency domain. All the current results are of AMB a at direction x. The waveform and frequency of the output of the compensation controller are approximate to these of the unbalance vibration, indicating that the the compensation controller recognizes and compensates the unbalance vibration well.

**Fig. 6.** Output of compensation controller.**Fig. 7.** Control current.

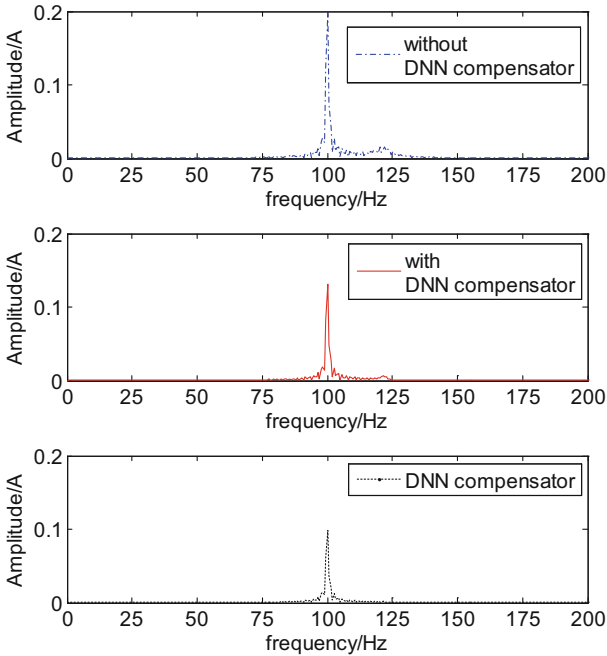


**Fig. 8.** Control current comparison in frequency domain.

It can also be observed that though the synchronous compensation is enhanced by adding the compensation controller, the total control current decreases from about 0.2 A to about 0.13 A. Since the unbalance vibration is well controlled, the displacement of rotor decreases dramatically. So much less output of main controller is needed, leading to a less total control current.

## 5 Conclusion

In this study, a compensation controller using deep learning theory is proposed for unbalance vibration of rotor system with AMBs. The compensation controller is established by a deep network with 2 hidden layers and the operation algorithms are designed. The compensation controller is joint with a PID controller to implement the integrated control scheme. The control effect is evaluated via simulation on a 4-DOF AMB-rotor system. From the simulation results, the proposed compensation controller implements well compensation and reduces vibration significantly. Moreover, the total control current reduces on account of the large decrease of rotor vibration. In conclusion, the proposed compensation controller is effective in unbalance vibration control and in improving the operational precision of the rotor system.

**Acknowledgements.** This work is supported by the National Natural Science Foundation of China (Grant No. 11772103).

## References

1. Schweitzer, G., Maslen, E.H.: *Magnetic Bearings: Theory, Design, and Application to Rotating Machinery*. Springer, Berlin (2009)
2. Chen, Q., Liu, G., Han, B.: Unbalance vibration suppression for AMBs system using adaptive notch filter. *Mech. Syst. Signal Process.* **93**, 136–150 (2017)
3. Hui, C., Shi, L., Wang, J., Yu, S.: Adaptive unbalance vibration control of active magnetic bearing systems for the HTR-10GT. In: *International Conference on Nuclear Engineering*, pp. 793–801. ASME, Xi'an (2010)
4. He, Y., Shi, L., Shi, Z., Sun, Z.: Unbalance compensation of a full scale test rig designed for HTR-10GT: a frequency-domain approach based on iterative learning control. *Science and Technology and Nuclear Installations*, pp. 1–15 (2017)
5. Tung, P.C., Tsai, M.T., Chen, K.Y., Fan, Y.H., Chou, F.C.: Design of model-based unbalance compensator with fuzzy gain tuning mechanism for an active magnetic bearing system. *Expert Syst. Appl.* **38**(10), 12861–12868 (2011)
6. Kuseyri, İ.S.: Robust control and unbalance compensation of rotor/active magnetic bearing systems. *J. Vib. Control* **18**(6), 817–832 (2012)
7. Fang, J., Xu, X., Xie, J.: Active vibration control of rotor imbalance in active magnetic bearing systems. *J. Vib. Control* **21**(4), 684–700 (2013)
8. Okubo, S., Nakamura, Y., Wakui, S.: Unbalance vibration control for active magnetic bearing using automatic balancing system and peak-of-gain control. In: *IEEE International Conference on Mechatronics*, vol. 307, pp. 105–110. IEEE, Vicenza (2013)
9. Heindel, S., Becker, F., Rinderknecht, S.: Unbalance and resonance elimination with active bearings on a Jeffcott rotor. *Mech. Syst. Signal Process.* **85**, 339–353 (2017)
10. Qiao, X., Hu, G.: Active control for multinode unbalanced vibration of flexible spindle rotor system with active magnetic bearing. *Shock Vib.* **12**, 1–9 (2017)
11. Saito, D., Waku, S.: Trial of applying unbalance vibration compensator to axial position of the rotor with active magnetic bearings. *J. Jpn. Soc. Precis. Eng.* **84**(2), 210–208 (2018)
12. Cui, P.L., Zhao, G.Z., Fang, J.C., Li, H.T.: Adaptive control of unbalance vibration for magnetic bearings based on phase-shift notch filter within the whole frequency range. *J. Vib. Shock* **34**(20), 16–20 (2015)
13. Jiang, K., Zhu, C., Chen, L.: Unbalance compensation by recursive seeking unbalance mass position in active magnetic bearing-rotor system. *IEEE Trans. Ind. Electron.* **62**(9), 5655–5664 (2015)
14. Paul, M., Hofmann, W., Steffani, H.F.: Compensation for unbalances with aid of neural networks. In: *Proceedings of the Sixth International Symposium on Magnetic Bearings*, pp. 693–701. Massachusetts Institute of Technology (MIT), Cambridge MA (1998)
15. Lecun, Y., Bengio, Y., Hinton, G.: Deep learning. *Nature* **521**(7553), 436–444 (2015)
16. Punjani, A., Abbeel, P.: Deep learning helicopter dynamics models. In: *IEEE International Conference on Robotics and Automation*, pp. 3223–3230. IEEE, Seattle (2015)
17. Hung, J.Y.: Magnetic bearing control using fuzzy logic. *IEEE Trans. Ind. Appl.* **31**(6), 1492–1497 (1995)
18. Dahl, G.E., Sainath, T.N., Hinton, G.E.: Improving deep neural networks for LVCSR using rectified linear units and dropout. In: *IEEE International Conference on Acoustics, Speech and Signal Processing*, vol. 26, pp. 8609–8613. IEEE, Vancouver (2013)
19. Sun, T., Pei, H., Pan, Y., Zhou, H., Zhang, C.: Neural network-based sliding mode adaptive control for robot manipulators. *Neurocomputing* **74**(14–15), 2377–2384 (2011)
20. Lecun, Y., Bengio, Y., Hinton, G.: Deep learning. *Nature* **521**(7553), 436–444 (2015)



# Unbalance Identification in a Rotor Supported by Active Magnetic Bearing

Gilberto Machado da Silva<sup>1</sup>  and Robson Pederiva<sup>2</sup> 

<sup>1</sup> Technology College - Arthur Azevedo and Herminio Ometto University Center, Araras, Brazil

[gilberto.silva@fatecmm.edu.br](mailto:gilberto.silva@fatecmm.edu.br)

<sup>2</sup> Faculty of Mechanical Engineering, University of Campinas, Campinas, Brazil  
[robson@fem.unicamp.br](mailto:robson@fem.unicamp.br)

**Abstract.** This paper presents a formulation for unbalance fault detection in flexible rotors supported by active magnetic bearings, AMB. The model-based procedure makes use of the correlation equations, through the matrix formulation of Ljapunov for stationary linear systems along with artificial neural networks. This procedure only uses measured state variables. Through the correlation of the output variables, a group of relations involving the physical parameters of the system together with the matrices of correlations of the measured variables is generated. Unbalance changes are detected through the monitoring of variation of physical parameters related to unbalance and comparison of theoretical and estimated correlation functions. Artificial neural networks are used to map correlations involving states that are not measured. The proposed method is applied in a flexible rotor model composed of four rigid disks, a pair of active four pole magnetic bearings with feedback control. The unbalance change is applied in individual planes and in several planes simultaneously.

**Keywords:** Magnetic bearings · Fault diagnosis · Unbalance

## 1 Introduction

Modern Rotary machines have become increasingly complex and sophisticated. The development of materials, whether it is new alloys or composite materials, lighter and more resistant, allow to work at higher and higher rotations, supercritical rotations, high operating loads and high reliability.

Active magnetic bearings have a number of advantages over conventional bearings because they work without mechanical contact and do not require lubrication system. This greatly increases the life of the equipment, reducing wear, energy consumption, besides enabling active vibration control, ease of maintenance and monitoring. They are applicable in a series of equipment such as: ultracentrifuges, turbomachinery, vacuum pumps, sealed pumps, machine tools, flywheels and compressors [1].

A rotating machine whether supported by magnetic bearing, or conventional bearings, may be subject to electrical failures such as control failures, sensor or actuators [2, 3] or subjected to mechanical failures, which are associated with the rotor.

Mechanical failures are characterized by defects that may arise in the rotor of a machine during its life in operation. These defects may be due to process, maintenance, design or assembly errors. They can cause localized defects: transverse cracks [4, 5], shaft bow [6], misalignments [7], bearing faults [8, 9] and unbalance failures. Among the localized defects, unbalance failure has become the most common fault. Changing the imbalance is the most common cause of vibration in rotating machines that can raise vibration levels of the equipment and consequently generate excessive forces in the bearings resulting in loss of efficiency and shortening the life of the system [10]. Sudhakar et al. [11], presents two approaches to identify unbalance failures. It proposes a method by minimizing equivalent loads and another by minimizing vibrations. In order to identify the fault, it uses the measurement of transverse vibrations in only one point of the system and concludes that the vibration minimization method is more effective because it presents minor errors. Sanches et al. [6] studies the simultaneous identification of faults by imbalance and shaft bow of the rotor, as the measured response number is lower than the total degree of freedom of the rotor, uses an auxiliary system (filter) and techniques of order reduction of the adjusted model. Chatzisavvas et al. [12], proposes a robust procedure for the identification of misalignment using the equivalent load method based on sparse vibration measurements. The procedure is based on the Least Angle Regression (LAR) technique for fault detection. Castro et al. [13], proposed the use of optimization techniques based on metaheuristic search methods (genetic algorithms and simulated annealing) to identify the amplitude and phase of unbalance present in a hydrodynamic bearing rotor. Aenis et al. [14], apply an algorithm for fault detection in a centrifugal pump with magnetic bearings based on transfer functions and measured magnetic forces. Tiwari et al. [15] apply an algorithm to identify the dynamic parameters, stiffness and damping, and the unbalance in previously defined planes of a flexible rotor supported by active magnetic bearings. The algorithm is based simultaneously on the current measurements of the control and in response to unbalance and concludes that under some conditions the experimental results differ from the theoretical ones. Eduardo et al. [16], through the matrix equation of Ljapunov, developed a set of correlation equations related to the physical parameters of the system together with artificial neural networks to detect mechanical failures in a rotor and concludes that under some conditions the experimental results differ from the theoretical ones. Vyas et al. [17] presents the design of artificial neural networks to identify five mechanical failures in rotary machines among them unbalance faults. A learning algorithm was applied in backpropagation of a non-linear multilayer network. The static moments of the signals acquired through sensors fixed in the housing of the bearings that are used to train the neural networks. Li et al. [18] developed an unbalance failure detection system on rotating machines based on neural networks in back propagation (BPN). It uses acoustic signals such as input from neural networks and normalized power spectra. The method is sensitive to rotational changes and has limitations for detecting faults near natural frequencies.

The problem of failure detection applied to rotational system with magnetic bearing has a special difficulty because the mechanical system equations are associated to the system control structure. The measurement of all state variables normally is not possible in real systems and the knowledge of stiffness and damping values are also difficult to be identified. In order to avoid this practical characteristic we propose a



methodology that works with the structure of the model and generate compatibility equations involving correlations between a reduced numbers of state variables. These relations are obtained by the matrix equation of Ljapunov.

The use of correlation equations was already studied by Silva et al. [9, 19, 20], but it was investigated failures associated to physical parameters related to stiffness and electrical failures of the magnetic bearing control system. The effect of unbalance faults cannot be detected by simple measurement of vibration amplitudes because the magnetic bearing control actuates in order to compensate any increase of vibration caused by the fault.

In this work the same formulation is applied to identify unbalance faults. We study a rotating system composed by four discs and by different combinations of unbalance distribution we can test the efficiency of the proposed method. The failure detection method is based on knowledge of the mathematical model structure developed for the mechanical and control system, along with the force laws of the bearings. The system is excited by unbalance and white noise forces. By the analysis of the matrix equation of Ljapunov it was chosen a set of equations that describe the behavior of the system involving the physical parameters, along with the equations of correlation between the measured states. The terms of the correlation equations related to states that cannot be measured are mapped through Artificial Neural Networks, ANN. A neural network was generated for each equation of interest. At the end, the difference between the measured correlations (with failure) and the expected correlations (without failure) is calculated. Observing these differences and the equation where they are manifested, we arrive at the conclusion of the location of the unbalance fault.

## 2 System Model and State Space Equation

The system under study consists of a rotor composed of flexible shaft on which are mounted four disks. In the external disks, there is a pair of active magnetic bearings, on the inner disks the motor and the rotation sensor, shown in Fig. 1.

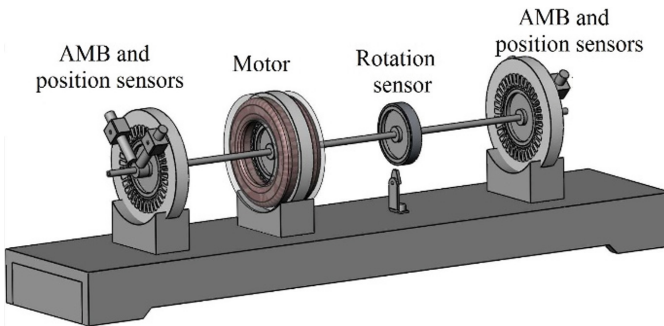


**Fig. 1.** System configuration.

### 2.1 Rotor Model

For the mathematical rotor model the finite element standard formulation (FEM) was used. In Fig. 2 the rotor model consists of four nodes, four disks ( $d_1, d_2, d_3$  and  $d_4$ ) and three length shaft segments ( $L_1, L_2$  and  $L_3$ ). The fixed coordinate system ( $X, Y$  and  $Z$ ) is considered and the system rotates with an angular velocity  $\omega$ . Minor axial displacements are not considered. The transverse section of the shaft and the disks have their movements described by the translations  $y(t)$  and  $z(t)$  and by the rotations  $\theta(t)$  and  $\varphi(t)$  respectively around the  $Y$  and  $Z$  axes and the four nodes.

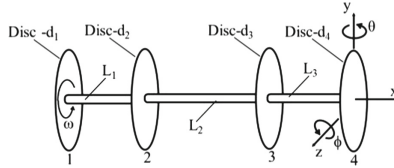


Fig. 2. The rotor system model for the numerical simulation.

The rotor model can be represented by the following differential equation:

$$M \ddot{\xi} + G \dot{\xi} + K \xi = f(t) \tag{1}$$

In Eq. (1):  $M$  is the mass and inertia matrix of the disk and shaft elements,  $G$  is the gyroscopic effect matrix of the disks and the shaft elements,  $K$  is the stiffness matrix of the shaft and  $f(t)$  is the vector of external forces that includes magnetic force  $f_m(t)$ , unbalance forces  $f_u(t)$  and white noise  $H(t)$ , where:

$$\xi(t) = [y_1 \ y_2 \ y_3 \ y_4 \ \phi_1 \ \phi_2 \ \phi_2 \ \phi_4 \ z_1 \ z_2 \ z_3 \ z_4 \ \theta_1 \ \theta_2 \ \theta_3 \ \theta_4]^T \tag{2}$$

The vector  $\xi(t)$  represents displacements ( $y$  and  $z$ ) and rotations ( $\varphi$  and  $\Theta$ ) of the system.

### 2.2 Unbalance Force

In rotary systems, the imbalance can be caused by eccentric masses located in different planes and angular positions of the disks. Since the unbalance mass is smaller than the mass of the disk, the vector of unbalance forces is given by:

$$\begin{Bmatrix} f_y \\ f_z \end{Bmatrix} = m_u r_u \omega^2 \begin{Bmatrix} \cos(\omega t + \beta) \\ \sin(\omega t + \beta) \end{Bmatrix} \tag{3}$$

In Eq. (3):  $m_u$  represents the unbalance mass,  $r_u$  is the unbalance radius,  $\omega$  is the rotor rotation and  $\beta$  stands for the phase angle. The complete vector of unbalance forces is given by:

$$f_u(t) = [f_{y1} \ f_{z1} \ f_{y3} \ f_{y4} \ 0 \ 0 \ 0 \ 0 \ f_{z1} \ f_{z2} \ f_{z3} \ f_{z4} \ 0 \ 0 \ 0 \ 0]^T \quad (4)$$

### 2.3 AMB and Controller Model

The configuration of a 4-pole magnetic bearing is shown in Fig. 3. The electromagnetic force is inversely proportional to the distance, and when applying an electromagnetic force to the rotor the tendency is to be attracted to the minimum possible distance between its surface and the electromagnet.

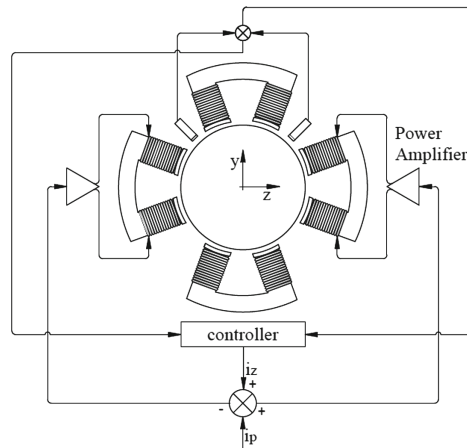


Fig. 3. Schematic representation of a radial AMB.

In order to have magnetic force in both directions, two diametrically opposed coils are used for each actuation direction (y and z) considering two half-axes, one positive and one negative. The currents  $i_+$  and  $i_-$  are the currents in the coils of the z-axis (positive) and z (negative) respectively, with the same value for the y-axis. The total actuation current for each axis is rectified in such a way that only the positive portion (positive half-cycle) is sent to the positive half-axis and analogously only the negative part (negative half-cycle) is sent to the negative half-axis. For the set of coils acting in the same direction, regardless of the current signal, it will exert a pulling force. In all the bearings, a DC current of polarization  $i_p$  is introduced so that there is rigidity around the point of operation. Therefore, a continuous current is added with the current signal going to the positive half-axis and subtracting the same direct current that goes to the negative half-axis. In closed loop, the system operates by reading the sensor that determines the position of the rotor. In this case as the sensor is not positioned in the direction of actuation, the sensor reading is added through an equivalent gain that passes to the controllers reading of the displacements of each direction (y and z). The controller process the information and send to the power amplifier a signal that is converted in a proportional signal of current. This signal is sent to the bearing actuator coil and transformed into magnetic force through the actuator gains, working in closed

loop. The force applied to the rotor in a pair of coils can be expressed by the following expression for the two half-axes [1]:

$$f_m(i,z) = -km \left( \frac{i_b}{z} \right)^2 \quad (5)$$

In Eq. (5):  $z$  is the distance between the rotor and the stator of the bearing,  $i_b$  is the bias current and  $km$  is the bearing constant depending on the air permeability, number of coils and the cross sectional area in the gap, [21]. For a semi-axis linearizing the magnetic force around the point of operation, we have:

$$f(i,z) = km_z z(t) - km_i i_c(t) \quad (6)$$

Where:

$$km_z = \frac{4 km i_b^2}{g^3} \text{ and } km_i = \frac{4 km i_b}{g^2} \quad (7)$$

The first term of Eq. (6)  $km_z$  represents the displacement force term. Since it depends only on the displacement and is directly incorporated into the mechanical stiffness matrix, its positive value will be added as a negative-spring. The second term  $km_i$  correspond to the gain of the magnetic actuator and the power stage is modelled as a gain  $k_p$  for each actuation direction. The controller is a sixth-order SISO (single in – single out) that has sufficient dynamic characteristics for the system control's need. For each control direction according to Fig. 3, the dynamic of the control modelled in the state space is given by:

$$\dot{x}_c(t) = A_c x_c(t) + B_c y_c(t) \text{ and } f_m = C_c x_c(t) \quad (8)$$

In Eq. (8):  $A_c$  is the dynamic matrix of the controllers,  $B_c$  is the input matrix of the controller,  $y_c$  is the input vector of the mechanical system with the  $k_s$  gain of the sensor,  $C_c$  is the output matrix of the control and  $x_c$  is the vector of control states with the  $k_m$  gain of the magnetic actuator and  $k_p$  power stage gain. Since the controller is of the sixth order, there are six control states for each actuation axis.

## 2.4 The Complete State Space Equation of the Closed Loop System

The equation in the state space of the mechanical system is given by:

$$\dot{x}_m(t) = A_m x_m(t) + B_m f_e(t) \text{ and } y_m(t) = C_m x_m(t) \quad (9)$$

Where:

$$A_m = \begin{bmatrix} Z & I \\ -M^{-1}K & -M^{-1}G \end{bmatrix} \text{ and } B_m = \begin{bmatrix} Z \\ -M^{-1} \end{bmatrix} \quad (10)$$

$$C_m = [I \quad Z] \text{ and } x_m(t) = \begin{bmatrix} \xi(t) \\ \dot{\xi}(t) \end{bmatrix} \quad (11)$$

In Eq. (9):  $A_m$  is the dynamic matrix,  $B_m$  is the input matrix,  $C_m$  is the output matrix,  $y_m$  is the mechanical state vector that can be measured and  $x_m(t)$  is the state vector of the mechanical system.  $Z$  is matrix of zeros,  $I$  represents the identity matrix and the points indicate the differentiation with respect to time. From Eqs. (8) and (9) the final equation in the state space composed by the mechanical and control models is given by:

$$\dot{x}_f(t) = A_f x_f(t) + B_f f(t) \quad (12)$$

where:

$$A_f = \begin{bmatrix} A_m & B_m C_c \\ B_c C_m & A_c \end{bmatrix}, B_f = \begin{bmatrix} B_m \\ 0 \end{bmatrix} \text{ and } x_f = \begin{bmatrix} x_m \\ x_c \end{bmatrix} \quad (13)$$

In Eq. (12):  $A_f$  refers to the dynamic matrix of the complete system,  $B_f$  represents the input matrix, with  $f(t)$  being the vector of external forces unbalance, magnetic force and white noise,  $x_f$  is the complete vector in state space in closed loop, composed of the measured mechanical and control states and  $f(t)$  represent the magnetic forces, unbalance forces and white noise. The closed-loop matrices will be used in the expansion of the Matrix Equation of Ljapunov, which is the basis of the proposed method.

### 3 Correlation Functions and Artificial Neural Networks

The invariant system with stationary inputs is considered. Under these conditions the correlation functions assume values constant in time and depend only on the time interval [16], given by:

$$R_{x_f}(\tau_i) = \varepsilon \{ x_f(t) \cdot x_f^T(t + \tau_i) \} \quad (14)$$

Where:  $\varepsilon$  is the mathematical expectation.

Replacing the solution of Eq. (12) in Eq. (14), we have:

$$A_f R_{x_f} + R_{x_f} A_f^T + B_f R_{x_u} B_f^T + R_{x_f x_u} B_f^T = 0 \quad (15)$$

Equation (15) is called the Ljapunov matrix equation for stationary linear systems, being the basis for the development of the fault diagnosis method proposed in this work, where:

$$R_{x_f} = \begin{bmatrix} R_{x_m x_m} & R_{x_m x_c} \\ R_{x_c x_m} & R_{x_c x_c} \end{bmatrix} \quad (16)$$

$$R_{x_u x_f} = [R_{x_u x_m} \quad R_{x_u x_c}] \quad (17)$$

$$R_{x_f x_u} = \begin{bmatrix} R_{x_m x_u} \\ R_{x_c x_u} \end{bmatrix} \quad (18)$$

In Eq. (16)  $R_{x_m x_m}$  is the matrix that shows the autocorrelations of the mechanical states,  $R_{x_m x_c}$  the correlations between the mechanical and control states,  $R_{x_c x_m}$  the correlations between the control and mechanical states,  $R_{x_c x_c}$  the autocorrelations of the control states. In Eq. (17)  $R_{x_u x_m}$  correlations between the unbalances and mechanical states,  $R_{x_u x_c}$  the correlations between the unbalances and control states. In Eq. (18)  $R_{x_m x_u}$  the correlations between the mechanical states and unbalances, and  $R_{x_c x_u}$  the correlations between the control and unbalance states. From the result of the expansion of Eq. (15) we have selected the equations that contain the correlations with the proposed failures. In order to select the equations that correlate with mechanical fault parameters, a three-steps method was used: (a) find, within the dynamic state matrix Eq. (12), the element that relates to the fault; (b) select the matrix column that relates to measurable states Eqs. (16), (17) and (18); (c) with help of the search command of the software, locate the desired equations. The equations selected for the proposed failures are given by Eqs. (19) to (22):

- Parameters and correlations related to disk  $d_1$  in direction  $z_1$ :

$$\begin{aligned} k_{11}Rz_1z_1 + k_{12}Rz_2z_1 + k_{16}R\theta_2z_1 + R\dot{z}_1\dot{z}_1 + b_1Rz_{1u}z_1 + b_1c_{z11}Rz_{11c}z_1 + b_1c_{z12}Rz_{12c}z_1 \\ + b_1c_{z13}Rz_{13c}z_1 + b_1c_{z14}Rz_{14c}z_1 + b_1c_{z15}Rz_{15c}z_1 + b_1c_{z16}Rz_{16c}z_1 + c_{11}R\dot{z}_1z_1 = 0 \end{aligned} \quad (19)$$

- Parameters and correlations related to disk  $d_2$  in direction  $z_2$ :

$$k_{21}Rz_1z_2 + k_{22}Rz_2z_2 + k_{23}Rz_3z_2 + k_{27}R\phi_3z_2 + k_{25}R\phi_1z_1 + R\dot{z}_2\dot{z}_2 + b_2Rz_{2u}z_2 + c_{22}R\dot{z}_2z_2 = 0 \quad (20)$$

- Parameters and correlations related to disk  $d_3$  in direction  $z_3$ :

$$k_{23}Rz_2z_3 + k_{33}Rz_3z_3 + k_{34}Rz_4z_3 + k_{36}R\phi_2z_3 + k_{37}R\phi_3z_3 + R\dot{z}_3\dot{z}_3 + b_3Rz_{3u}z_3 + c_{33}R\dot{z}_3z_3 = 0 \quad (21)$$

- Parameters and correlations related to disk  $d_4$  in direction  $z_4$ :

$$\begin{aligned} k_{44}Rz_4z_4 + k_{43}Rz_3z_4 + k_{46}R\theta_3z_4 + R\dot{z}_4\dot{z}_4 + b_4Rz_{4u}z_4 + b_4c_{z44}Rz_{41c}z_4 + b_4c_{z42}Rz_{42c}z_4 \\ + b_4c_{z43}Rz_{43c}z_4 + b_4c_{z44}Rz_{44c}z_4 + b_4c_{z45}Rz_{45c}z_4 + b_4c_{z46}Rz_{46c}z_4 + c_{44}R\dot{z}_4z_4 = 0 \end{aligned} \quad (22)$$

The states measured are the linear displacements and velocities of the 4 disks in the horizontal direction and the first five control states in the same direction. It is interesting to note among the selected correlation equations, there are different relationships with

the physical parameters of the system, whether they are electrical or mechanical. Any change in given parameter that is related to the equation will cause changes in the equality of the respective equation. This change is an indication that the equation is sensitive to the change of this parameter. In Eqs. (19) to (22) there are relations with the stiffness parameters of the axis elements  $k_{ij}$ . As nodes 1 and 4 are the actuators of the bearing, one can also observe the presence of terms of the output matrix of the electrical system, the parameters  $cz_{ij}$ , which are directly related to the parameters of the magnetic bearing. Terms  $b_1, b_2, b_3$  and  $b_4$  are terms of the input matrix of the mechanical system and are related to the input forces: unbalance force and white noise. For the method used, it is enough to know to which correlations are associated each parameter, not being necessary to know the numerical values of these parameters. The variation of the relation between the correlations will indicate that there was variation in the associated parameters, depending on which equation this will occur indicative of failure or not, and its location in the system. The terms of the compatibility equations, Eqs. (19) to (22), that correlate unmeasurable variables will be mapped by neural networks. The autocorrelation  $Rz_1z_1$  was isolated from the right side of Eq. (19),  $Rz_2z_2$ , from Eq. (20),  $Rz_3z_3$  from Eq. (21) and  $Rz_4z_4$  from Eq. (22). In all cases the other parameters were divided by the parameter related to each isolated auto correlation. Terms difficult to measure were excluded and possible measurement correlations were entered as neural network inputs. The terms isolated at the output of each neural network corresponding to each selected compatibility equation, are shown in Table 1.

**Table 1.** Parameters of the Neural Networks

Eq.	State	Node	Inputs	Output	ANN
(19)	$z_1$	1	$Rz_2z_1, R\dot{z}_1z_1, R\dot{z}_1\dot{z}_1, Rz_{11c}z_4, Rz_{12c}z_4, Rz_{13c}z_4, Rz_{14c}z_4$	$Rz_1z_1$	$A_1$
(20)	$z_2$	2	$Rz_1z_2, Rz_3z_2, R\dot{z}_2\dot{z}_2, R\dot{z}_2z_2$	$Rz_2z_2$	$A_2$
(21)	$z_3$	3	$Rz_2z_3, Rz_4z_3, R\dot{z}_3\dot{z}_3, R\dot{z}_3z_3$	$Rz_3z_3$	$A_3$
(22)	$z_4$	4	$Rz_3z_4, R\dot{z}_4z_4, R\dot{z}_4\dot{z}_4, Rz_{41c}z_4, Rz_{42c}z_4, Rz_{43c}z_4, Rz_{44c}z_4$	$Rz_4z_4$	$A_4$

Artificial neural networks are structured by interconnected elements called neurons, arranged in layers, and each neuron is responsible for the mapping of input and output data, determined by the activation function. A neuron receives as input a signal multiplied by a synaptic weight; these inputs are summed and handled by an activation function, producing an output signal. Figure 4 shows the network configurations for mapping Eqs. (19) to (22).

The neural networks used have 1 input layer, 1 intermediate layer with 10 neurons each, using a sigmoidal activation function and an output. For the training of the networks the Levenberg Marquart algorithm was used. The output autocorrelations of the  $A_1, A_2, A_3$  and  $A_4$  architectures were trained to the system without failure.

The comparison between the faultless and faulted output is done by calculating the mean square deviation (MSD), given by:

$$\text{MSD} = \left( \frac{1}{N} \sum_{i=1}^N (\text{Rx}_f - \bar{\text{R}}\text{x}_f)^2 \right)^{\frac{1}{2}} \quad (23)$$

In Eq. (23):  $\text{Rx}_f$  is the self-correlation of the network output (faulty),  $\bar{\text{R}}\text{x}_f$  is the expected network output autocorrelation (no fault) and  $N$  is the number of training data.

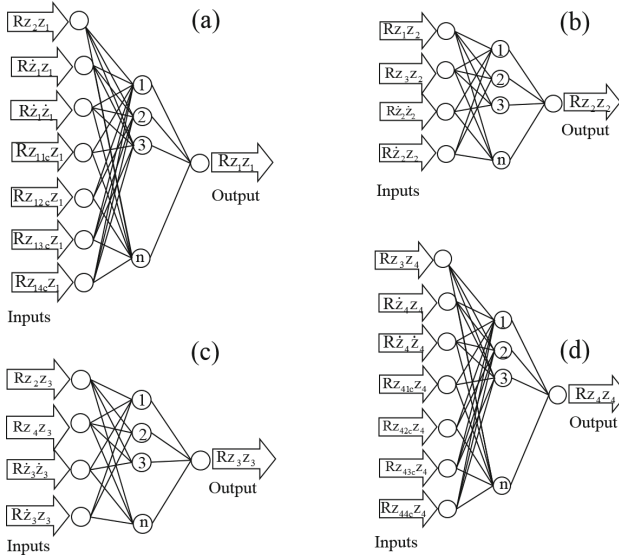


**Fig. 4.** Artificial Neural Networks: (a) Network  $A_1$ , (b) Network  $A_2$ , (c) Network  $A_3$ , (d) Network  $A_4$ .

## 4 Results

The time domain response of the system was obtained through MatLab - Simulink software. The Simulink model is essentially made of a block consisting of space of mechanical states equations, Eq. (9), whose output are the displacements  $y_1$ ,  $z_1$ ,  $y_4$  and  $z_4$  that pass through the gains of the sensors and feed the four blocks composed by the equations of Eq. (8); their outputs pass through the bearing gains and power stage that feedback with the magnetic force in each direction of actuation of the magnetic bearing. The system is excited by external unbalance force and white noise. The mechanical states  $y_1$ ,  $y_2$ ,  $y_3$ ,  $y_4$ ,  $z_1$ ,  $z_2$ ,  $z_3$  and  $z_4$  are obtained simultaneously and the six control states in the direction  $Z_{1c}$  and in the direction  $Z_{4c}$  in fixed rotation of 3000 RPM. The failure-free system parameters are listed in Table 2.

The system was initially considered to have a residual unbalance of 0.1 g at zero degrees in the unbalance radius of 25 mm on all disks. Correlation functions were calculated and these results were used to train the neural networks, using the input and output correlations shown in Fig. 4. The Levenberg Marquart algorithm was used for



**Table 2.** Physical properties of the rotor and AMB's.

	Parameter	Value	Unit
<i>Disks</i>			
Mass	$m_d$	$8.80 \cdot 10^{-2}$	kg
Moment inertia	$I_d$	$3.10 \cdot 10^{-5}$	$\text{kg}\cdot\text{m}^2$
Polar moment of inertia	$I_p$	$6.02 \cdot 10^{-5}$	$\text{kg}\cdot\text{m}^2$
<i>Shaft</i>			
Length	$L_1, L_2, L_3$	0.150	m
Cross section	$A_{\text{shaft}}$	$1.57 \cdot 10^{-5}$	$\text{m}^2$
Moment of inertia of area	$I_e$	$5.10 \cdot 10^{-11}$	$\text{m}^4$
<i>AMB's</i>			
Gain of the sensor	$k_s$	1900	V/m
Gain of the power amplifier	$k_p$	-0.25	A/V
Gain of the bearing	$k_m$	8	N/A
Negative spring	$k_z$	-2450	N/m
Bias current	$i_b$	0.307	A
Air gap	$g$	$10^{-3}$	m

training the networks, adjusted for the following characteristics: sigmoidal activation function, admissible global error  $10^{-6}$  and learning rate  $10^{-4}$ . For the training of the networks the noise-free system was considered, the correlations were calculated by the expansion of Eq. (15) and the inputs and outputs for the neural networks shown in Fig. 4 were obtained. Several magnitudes of white noise were added to the system in order to test the ability to map the networks in the presence of noise.

The white noise magnitude was added based on the percentage of the RMS value of the unbalance force ( $f_u$ ). The mean square error MSD, Eq. (23) which relates the outputs of the fault and faultless networks was used to compare the different levels of white noise, the results of which are shown in Table 3.

**Table 3.** Mean square deviation without fault and with white noise

White noise level (%)	MSD [%]			
	$A_1$	$A_2$	$A_3$	$A_4$
10	0.222	0.059	0.017	0.002
20	0.282	0.072	0.032	0.021
30	0.213	0.061	0.067	0.051

Looking at the results shown in Table 3, we note that through the correct choice of the equations, avoiding terms involving correlations between excitation forces and responses, the results are very good.

Even training the neural networks with only unbalance as excitation force, with addition of white noise forces in different levels, the MSD parameter did not changes significantly.

With the configuration of networks defined and in the presence of 30% white noise, the condition of rotation variation of the system was analyzed. Starting from an initial rotation of 600 RPM to the nominal rotation of 3000 RPM in 600 RPM intervals, the results are presented in Table 4.

**Table 4.** Mean square deviation with variation of the rotation, without fault and with white noise

	Rotation [RPM]	600	1200	1800	2400	3000
MSD [%]	A1	0.273	1.172	0.725	0.663	0.213
	A2	0.102	2.613	0.301	0.148	0.061
	A3	0.391	2.559	0.208	0.074	0.067
	A4	0.122	0.139	0.062	0.095	0.051

It is interesting to point out that the neural networks were robust and maintained their mapping capacity in the presence of white noise and rotation variation. Networks did not take these variations as potential flaws.

Figure 5 shows the excitation by unbalance (5a) and by white noise (5b). In this case, the RMS value of the white noise represents 30% of the RMS value of the unbalance. Figure (5c, d) show some responses in time domain and (5e) and (5f) some correlation functions.

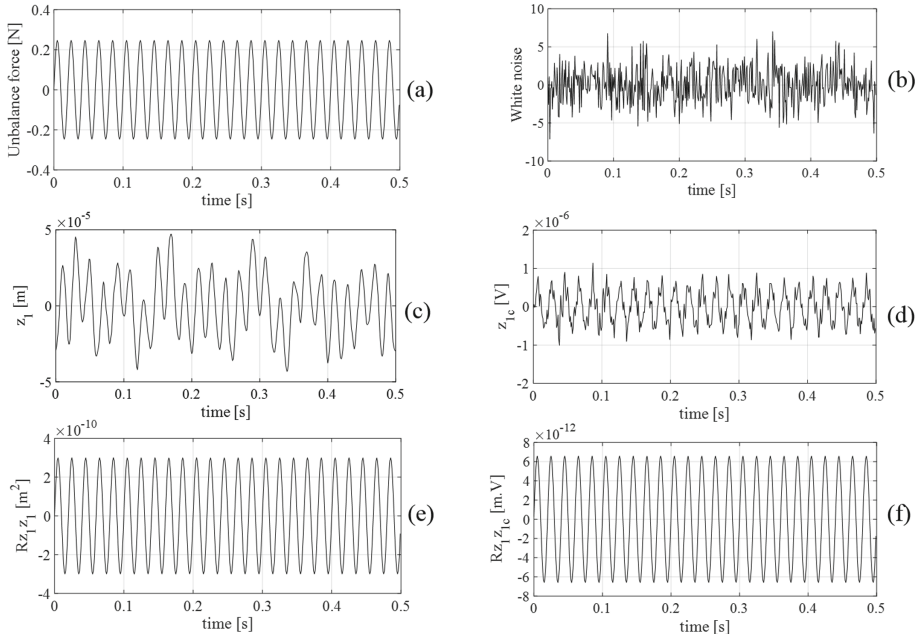


**Fig. 5.** (a) Unbalance force, (b) White noise, (c) displacement  $z_1$ , (d) first state of controller  $z_{1c}$ , (e) Autocorrelation  $Rz_1z_1$  and (f) Correlation  $Rz_1z_{1c}$ .

The unbalance faults imposed on the system were divided into 10 cases with masses always being placed in an unbalance radius of 25 mm, that is, only the mass value and the phase where they were placed were changed. The simulated cases are listed below:

- Case # 1 - 1 g was placed on disk  $d_1$  only in  $0^\circ$  phase.
- Case # 2 - 1 g was placed on disk  $d_2$  only in phase  $0^\circ$ .
- Case # 3 - was placed 1 g only on disk  $d_3$  in phase  $0^\circ$ .
- Case # 4 - only 1 g was placed on the  $d_4$  disk in the  $0^\circ$  phase.
- Case # 5 - 1 g was placed at  $0^\circ$  on the disks  $d_1, d_2, d_3$  and  $d_4$  simultaneously.
- Case # 6 - 1 g was placed on disk  $d_1$  in the  $0^\circ$  phase, 1 g on disk  $d_2$  in the  $90^\circ$  phase, 1 g on disk  $d_3$  in the  $0^\circ$  phase and 1 g on disk  $d_4$  in the  $0^\circ$  phase, simultaneously.
- Case # 7 - 1 g was placed on disk  $d_3$  in the  $90^\circ$  phase and 1 g on disk  $d_4$  in the  $0^\circ$  phase, simultaneously.
- Case # 8 - 1 g was placed on disk  $d_2$  in the  $0^\circ$  phase and 1 g on disk  $d_3$  in the  $90^\circ$  phase, simultaneously.
- Case # 9 - 1 g was placed on disk  $d_3$  in the  $180^\circ$  phase and 1 g on disk  $d_4$  in the  $0^\circ$  phase, simultaneously.
- Case # 10 - 1 g was placed on the disk  $d_2$  in the  $0^\circ$  phase and 1 g on the disk  $d_3$  in the  $180^\circ$  phase, simultaneously.

For the ten simulated cases, the outputs of the respective neural networks were taken and the mean square error (MSD) for all networks was calculated in relation to the case with white noise and without failure, the results are show in Table 5.

**Table 5.** Fault unbalance configurations and MSD [%]

Case	Unbalance mass [g]/phase [degree]				MSD [%]			
	Disk- $d_1$	Disk- $d_2$	Disk- $d_3$	Disk- $d_4$	$A_1$	$A_2$	$A_3$	$A_4$
Training	0.1 g/ $0^\circ$	0.1 g/ $0^\circ$	0.1 g/ $0^\circ$	0.1 g/ $0^\circ$	-	-	-	-
Case #1	1.0 g/ $0^\circ$	-	-	-	27.22	3.15	3.41	2.88
Case #2	-	1.0 g/ $0^\circ$	-	-	3.88	37.53	1.42	1.32
Case #3	-	-	1.0 g/ $0^\circ$	-	2.56	2.03	37.09	3.60
Case #4	-	-	-	1.0 g/ $0^\circ$	1.58	3.47	3.31	26.75
Case #5	1.0 g/ $0^\circ$	1.0 g/ $0^\circ$	1.0 g/ $0^\circ$	1.0 g/ $0^\circ$	25.55	33.70	33.80	24.97
Case #6	1.0 g/ $0^\circ$	1.0 g/ $90^\circ$	1.0 g/ $0^\circ$	1.0 g/ $90^\circ$	27.49	20.75	39.86	19.71
Case #7			1.0 g/ $0^\circ$	1.0 g/ $90^\circ$	2.31	3.71	22.57	28.66
Case #8		1.0 g/ $90^\circ$	1.0 g/ $0^\circ$	-	4.31	28.50	56.95	6.74
Case #9			1.0 g/ $180^\circ$	1.0 g/ $0^\circ$	4.44	8.45	56.93	25.02
Case #10		1.0 g/ $0^\circ$	1.0 g/ $180^\circ$		8.64	37.40	20.97	7.41

Considering the results show in Table 5, in the training process the white noise-free system was considered and for the cases with failure, the level was 30%. We did not change this level considering the results shown in Table 3 that states the low sensitivity of the neural networks architectures related to this parameter.

The numerical simulations were made considering rotation of 3000 RPM.

In the cases where the failures were imposed, the errors (MSD) appeared in the neural networks corresponding to the discs of the imposed fault. Although it presented a small increase in the error of the other networks, the values do not compromise the detection of the imposed failure.

When they were imposed only on disks d1 - case # 1, d2 - case # 2, d<sub>3</sub> - case # 3 or d4 - case # 4, the errors appeared only in the neural networks corresponding to those disks.

When the fault was imposed on 4 disks, the error appeared for the 4 neural networks, case # 5.

When the fault was imposed on two disks simultaneously the errors appeared only in the neural networks corresponding to those disks.

It is also interesting to note that even changing the phase angle between the disks, the neural networks were able to map the errors - cases # 6 to case # 10, showing the efficiency of the proposed method for the studied cases.

It is important to note that even taking small number of measurements, in order to detect the disc plane of the fault we need at least one displacement measurement per disc.

## 5 Conclusion

In this work the fault detection method based on the Ljapunov matrix equation and artificial neural networks in a flexible rotor with active magnetic bearings was presented. Through the method it was possible to detect unbalance faults. For application of the proposed method it is not necessary to know whether the values of the parameters of the model are electric or mechanical, only its structure in the model. Considering that several states are not possible to be measured, they are mapped by the neural networks. The method is insensitive to the addition of white noise at the entrance, not taking this factor as possible fault. It is emphasized the need for at least one displacement sensor in the planes where it is desired to detect the fault. The test bench is been constructed in order to apply this methodology to a real system.

**Acknowledgement.** The authors would like to thank CAPES, CNPq and grant # 2015/20363-6 from the São Paulo Research Foundation (FAPESP) for the financial support to this research.

## References

1. Schweitzer, G., Maslen, E.H.: *Magnetic Bearings: Theory, Design, and Application to Rotating Machinery*. Springer, Berlin (2009)
2. Tsai, C., King, Y.H., Lee, R.M.: Fault diagnosis for magnetic bearing. *Mech. Syst. Signal Process.* **23**(4), 1339–1351 (2009)
3. Zhang, Y.Z., Zhang, L.Z., Luo, X.Y., Guan, X.P.: Sensor/actuator faults detection for networked control systems via predictive control. *Int. J. Autom. Comput.* **10**(3), 173–180 (2013)

4. Cavalini Jr., A.A., Sanches, L., Bachschmid, N., Steffen Jr., V.: Crack identification for rotating machines based on a nonlinear approach. *Mech. Syst. Signal Process.* **79**, 72–85 (2016)
5. Sampaio, D.L., Nicoletti, R.: Detection of cracks in shafts with the approximated entropy algorithm. *Mech. Syst. Signal Process.* **72–73**, 286–302 (2016)
6. Sanches, F.D., Pederiva, R.: Theoretical and experimental identification of the simultaneous occurrence of unbalance and shaft bow in a Laval rotor. *Mech. Mach. Theory* **101**, 209–221 (2016)
7. Reddy, M.C.S., Sekhar, A.S.: Detection and monitoring of coupling misalignment in rotors using torque measurements. *Measurement* **61**, 111–122 (2015)
8. Samanta, B., Al-Balushi, K.R.: Artificial neural network based fault diagnostics of rolling element bearings using time-domain features. *Mech. Syst. Signal Process.* **17(2)**, 317–328 (2003)
9. Silva, G.M., Pederiva, R.: Diagnosis in a rotor supported by active magnetic bearings. In: *Proceedings of the 7th IFToMM International Conference on Rotor Dynamics, International Federation for the Promotion of Mechanism and Machine Science, 2006 Vienna, Austria*
10. Mogal, S.P., Lalwani, D.I.: A brief review on fault diagnosis of rotating machineries. *Appl. Mech. Mater.* **541–542**, 635–640 (2014)
11. Sudhakar, G.N.D.S., Sekhar, A.S.: Identification of unbalance in a rotor bearing system. *J. Sound Vib.* **330**, 2299–2313 (2011)
12. Chatzisavvas, I., Dohnal, F.: Unbalance identification using the least angle regression technique. *Mech. Syst. Signal Process.* **50–51**, 706–717 (2015)
13. Castro, H.F., Cavalca, K.L., Camargo, L.W.F., Bachschmid, N.: Identification of unbalance forces by metaheuristic search algorithms. *Mech. Syst. Signal Process.* **24**, 1785–1798 (2010)
14. Aenis, M., Nordamann, R.: Active magnetic bearing for the identification and fault diagnosis in turbomachinery. *Mechatronics* **12(8)**, 1011–1021 (2002)
15. Tiwari, R., Chougale, A.: Identification of bearing dynamic parameters and unbalance states in a flexible rotor system fully levitated on active magnetic bearings. *Mechatronics* **24**, 274–286 (2014)
16. Eduardo, A.C., Pederiva, R.: Parameter monitoring of a rotor system excited by stochastic forces. In: *Proceedings of the 6th IFToMM International Conference on Rotor Dynamics, International Federation for the Promotion of Mechanism and Machine Science, 2002 Sidney, Australia*
17. Vyas, N.S., Satishkumar, D.: Artificial neural network design for fault identification in a rotor-bearing system. *Mech. Mach. Theory* **36**, 157–175 (2001)
18. Li, W., Tsai, Y.P., Chiu, C.L.: The experimental study of the expert system for diagnosing unbalances by ANN and acoustic signals. *J. Sound Vib.* **272**, 69–83 (2004)
19. Silva, G.M., Pederiva, R.: Mechanical fault diagnosis in a flexible rotor through correlations functions and artificial neural network. In: *Proceedings of the XII DINAME - International Symposium on Dynamic Problems of Mechanics, 2007, Ilhabela, Brazil*
20. Silva, G.M., Pederiva, R.: Fault diagnosis in a flexible rotor supported by active magnetic bearings. In: *Proceedings of the 1th Brazilian Workshop on Magnetic Bearings, 2013, Rio de Janeiro, Brazil*
21. Mendes, R.U., Cavalca, K.L., Ferreira, L.O.S.: Analysis of a complete model of rotating machinery excited by magnetic actuator system. *Proc. Inst. Mech. Eng. Part C: J. Mech. Eng. Sci.* **227**, 48–64 (2012)



# Numerical Study on the Influence of Gas Foil Thrust Bearings on the Vibrational Behavior

Tomasz Pronobis<sup>(✉)</sup>, Alexander Ramin, and Robert Liebich

Engineering Design and Product Reliability, Technical University Berlin,  
10623 Berlin, Germany

tomasz.pronobis@tu-berlin.de

<http://www.kup.tu-berlin.de>

**Abstract.** Gas Foil Bearings (GFBs) have a promising future in high-speed turbomachinery such as air cycle machines and turbochargers. To achieve complete oil-free operation of the rotor support structure Gas Foil Thrust Bearings (GFTBs) can be used in combination with Gas Foil Journal Bearings (GFJBs). The present study numerically investigates the influence of GFTBs on the rotordynamic behaviour. In a first step the perturbation method is used to calculate linearized stiffness and damping coefficients. The perturbation approach used in this study is widely used in GFJBs resulting in uncoupled first-order equations to calculate the stiffness and damping parameters. Previously published approaches for GFTBs were relying either on coupled first order equations or were independent of excitation frequency. The calculated bearing parameters are validated against numerically calculated data published in the available literature. Linear stability analysis for a rigid rotor supported by GFTBs is performed and later extended for a rotor supported by both GFTBs and GFJBs.

**Keywords:** Foil bearings · Hydrodynamic lubrication  
Static and dynamic characteristics

## 1 Introduction

The higher reliability of Gas foil bearings (GFBs) compared to rolling element bearings lead to their first industrial application in air cycle machines starting in the 1970s [1]. Since then the development of GFBs lead to major improvements in load capacity [2,3], temperature durability [4,5] and number of start stop cycles [4]. The successful use of GFBs was demonstrated in several applications like oil-free turbochargers [6–8], cryogenic turboexpanders [9], turbojet engines [5] and gas turbines [10]. However the difficulty to accurately predict dynamic performance is still one of the main obstacles in larger scale GFB operation and therefore a current research topic. Compared to Gas Foil Journal Bearings (GFJBs) the dynamic performance of their Thrust Bearing counterparts

(GFTBs) has been investigated to a lesser extent. Yet the advantages of GFBS can only be exploited if the rotor is supported by GFBS in both directions. Thus the motivation of this work is given.

GFTBs as schematically depicted in Fig. 1 consist of a backing plate to which two metal foils are attached. The corrugated bump foil is flexible and allows the bearing wall to deform while the upper top foil serves as a smooth surface to capture the air and generate the pressure. Because of the rotation of the runner, air is sucked between top foil and runner and compressed in the converging ramp geometry build by top and bump foil Fig. 1. The foils deform due to the generated pressure.

In one of the first numerical investigations of GFTBs Heshmat et al. [11] conducted parametric studies to obtain optimal geometry for a bearing with constant and uniformly distributed stiffness. In 1999 Iordanoff et al. [12] developed a simplified method to calculate GFTB geometric parameters to fit desired load capacity and speed requirements. In the mentioned study Coulomb friction was considered when calculating the constant (in time) stiffness of the bump foil and that stiffness was linearly distributed from free to fixed end. This assumption was based on a previous study [13]. The influence of the elasticity of the supporting structure was analyzed in a work by Heshmat et al. [14], who used Finite Element Methods (FEM) to calculate the deformation of the foils and Finite Difference Methods (FDM) to discretize the gas film. A similar approach was followed by Park et al. [15] who used coupled FEM/FDM to obtain static equilibrium conditions. This equilibrium was then perturbed by small amplitude motions, which allowed to linearize the Reynolds equation and therefore to calculate linear first order stiffness and damping parameters. The tilting condition of the thrust pad was analyzed and a modified Reynolds equation was used to account for small Knudsen numbers.

A slightly different perturbation approach than applied by Park et al. was used by Gad and Kaneko [16] to examine the dynamic parameters of a Generation II GFTB. In so called Generation II GFTBs the stiffness of the foil structure is adjustable in one direction. The bearing studied had a slotted bump foil with varying amount of bumps in radial direction resulting in a radial stiffness distribution. The structural model used was developed in a previous work [17] and takes into account bump interaction, friction, the possibility of foil separation of the flat segment between bumps and a more realistic boundary condition at the top foil trailing edge (which is modelled as a cantilever beam instead of a rigid support). In their work Gad and Kaneko were the first to consider the centrifugal forces due to the inertia of the gas film showing that they have a negligible effect on the load capacity.

Feng et al. [18] made a similar perturbation approach like Park et al. [15] and were the first to calculate excitation frequency dependent stiffness and damping parameters of GFTBs, however these parameters were only calculated in axial direction. The structural link-spring model used was developed in a previous work [19] accounting for bump interaction, friction and top foil deformation, which were calculated using a FEM shell model.

The presented study also focuses on dynamic stiffness and damping parameters of GFTBs but using a slightly different perturbation approach which is widely used in GFJBs e.g. [20, 21, 21]. The advantage of this approach compared to the previously published methods for GFTBs is that by assuming harmonic perturbation no additional assumptions regarding the time derivatives of the perturbations have to be made. The resulting linearized equations are uncoupled (which was not the case in the works of Feng and Park [15, 18]) and allow to calculate excitation frequency dependent stiffness and damping parameters (which was not the case in the work of Gad and Kaneko [16]). To the author's knowledge excitation frequency dependent tilting stiffness and damping of GFTBs will be presented for the first time in openly accessible literature. This allows to couple the radial and axial degrees of freedom. The dynamic behavior of a system supported by both GFJBs and GFTBs can therefore be analyzed. A stability analysis of a fully GFB supported rotor bearing system is performed in this work. This is a novelty in gas foil bearing research.

## 2 Theoretical Model

The relation between pressure  $p$  distribution and the thickness of the air film  $h$  is described by the isothermal Reynolds equation for a compressible ideal gas:

$$\frac{\partial}{\partial r} \left( r p h^3 \frac{\partial p}{\partial r} \right) + \frac{1}{r} \frac{\partial}{\partial \theta} \left( p h^3 \frac{\partial p}{\partial \theta} \right) = 6 \mu_a \Omega r \frac{\partial}{\partial \theta} (p h) + 12 \mu_a r \frac{\partial}{\partial t} (p h). \quad (1)$$

$r$  and  $\theta$  are the radial and the angular coordinates,  $\mu_a$  is the ambient viscosity and  $\Omega$  the rotation velocity. By substituting the following equations:

$$p = \bar{p} p_a, \quad h = \bar{h} c, \quad r = \bar{r} r_o, \quad t = \bar{t} \omega \quad (2)$$

$$\gamma = \frac{\omega}{\Omega}, \quad \Lambda = \frac{6 \mu_a \Omega}{p_a} \left( \frac{r_o}{c} \right)^2 \quad (3)$$

into the dimensional Reynolds equation (1) the nondimensional form can be obtained. The nominal film thickness  $c$  is the distance between the runner and the undeformed top foil schematically displayed in Fig. 1.  $\omega$  is the excitation frequency all other variables in the above equations are explained in Table 1 which is given in the appendix.

$$\frac{\partial}{\partial \bar{r}} \left( \bar{r} \bar{p} \bar{h}^3 \frac{\partial \bar{p}}{\partial \bar{r}} \right) + \frac{1}{\bar{r}} \frac{\partial}{\partial \theta} \left( \bar{p} \bar{h}^3 \frac{\partial \bar{p}}{\partial \theta} \right) = \Lambda \bar{r} \frac{\partial}{\partial \theta} (\bar{p} \bar{h}) + 2 \Lambda \gamma \bar{r} \frac{\partial}{\partial \bar{t}} (\bar{p} \bar{h}). \quad (4)$$

The dimensionless film thickness is given by:

$$\bar{h}(\bar{r}, \theta) = \begin{cases} 1 + H \left( 1 - \frac{1}{b\beta} \theta \right), & 0 \leq \theta < b\beta \\ 1 + \bar{\delta}(\bar{r}, \theta), & b\beta \leq \theta \leq \beta \end{cases} \quad (5)$$

where  $H = \frac{h_{ramp}}{c}$  is the nondimensional ramp height and  $\bar{\delta}(\bar{r}, \theta) = \frac{\delta(r, \theta)}{c}$  is the nondimensional foil deformation. The pad angle  $\beta$  and the ramp angle  $b \cdot \beta$



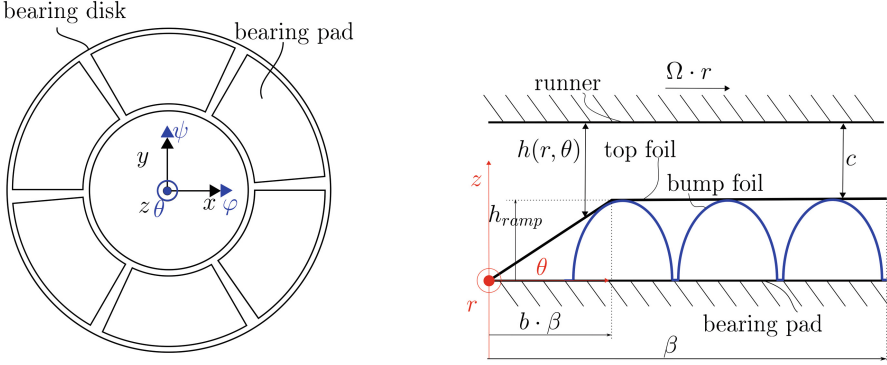


**Fig. 1.** GFB structure: left: schematic GFTB model, right: film thickness and foil configuration

shown in Fig. 1. In this work the foil deformation is calculated by the simple elastic foundation model (SEFM):

$$\bar{\delta}(\bar{r}, \theta) = S(\bar{p} - 1) \quad (6)$$

where  $S$  is the nondimensional bump compliance given by Jordanoff [12]. For GFJBs this method has proven as a quick and in many cases sufficiently accurate method of calculating foil deformation e.g. [20, 21, 21]. In a recent study [22] time integration with SEFM and a more elaborate model are compared to experimental data showing better agreement for SEFM. The conclusion of von Osmanski et al. is that the role of friction might be overestimated because sticking seems to be the prevailing state. In the validation Sect. 3 it is going to be shown that the stiffness and damping parameters calculated using this method are in good agreement with those obtained by Gad and Kaneko who used a more elaborate structural model.

## 2.1 Perturbation Method

The perturbation method applied in this work was used by Lund in 1968 [23] to calculate stiffness and damping parameters as well as stability borders for rigid gas journal bearings. On the basis of this work similar approaches were published for GFJBs e.g. [20, 21, 24, 25]). The rotor experiences small harmonic motions  $\Delta$  with excitation frequency  $\omega$  around its static equilibrium position:

$$\Delta_z = \hat{\Delta}_z e^{i\omega t}, \quad \dot{\Delta}_z = i\omega \hat{\Delta}_z e^{i\omega t} \quad (7)$$

$$\Delta_\varphi = \hat{\Delta}_\varphi e^{i\omega t}, \quad \dot{\Delta}_\varphi = i\omega \hat{\Delta}_\varphi e^{i\omega t} \quad (8)$$

$$\Delta_\psi = \hat{\Delta}_\psi e^{i\omega t}, \quad \dot{\Delta}_\psi = i\omega \hat{\Delta}_\psi e^{i\omega t} \quad (9)$$

By assuming harmonic perturbations their time derivatives can be easily expressed. The previously published perturbation approaches for GFTBs [15, 16,

18] did not make the restriction of harmonic motions but had to make additional assumptions when setting up the time derivatives. On the other hand harmonic perturbations are a reasonable assumption if the frequency dependency of the resulting stiffness and damping parameters is of interest.

$$h = h_0 + \Delta_z + \Delta_\varphi r \sin(\theta) + \Delta_\psi r \cos(\theta) + \Delta\delta \quad (10)$$

$$\begin{aligned} p &= p_0 + \Delta_z \frac{\partial p}{\partial z} + \Delta_\varphi \frac{\partial p}{\partial \varphi} + \Delta_\psi \frac{\partial p}{\partial \psi} + \mathcal{O}(\Delta^2) \\ &= p_0 + \hat{\Delta}_z p_z e^{i\omega t} + \hat{\Delta}_\varphi p_\varphi e^{i\omega t} + \hat{\Delta}_\psi p_\psi e^{i\omega t} \end{aligned} \quad (11)$$

$$\Delta\delta = K_f(p_0 - p_a + \Delta_z p_z + \Delta_\varphi p_\varphi + \Delta_\psi p_\psi) \quad (12)$$

In the notation above the index  $( )_0$  labels the static equilibrium position of the associated variable. The reaction of the pressure to the small perturbation can be expressed through a Taylor series where orders higher than one are neglected.

The nondimensional, perturbed Reynolds equations (13, 14, 24, 25) can be obtained by inserting the perturbed variables (10-12) into the dimensional Reynolds equation (1), normalizing by using equations (2, 3, 5, 15) and neglecting all terms with higher perturbation order than  $\Delta^1$ . When inserting pressure  $p$  and film thickness  $h$  Eq. (11, 10) into the Reynolds equation (1) their time derivatives can be performed because the time dependency around static equilibrium  $p_0$  and  $h_0$  is given by assuming harmonic perturbations Eq. (7-9).

Equation of order  $\Delta^0$ :

$$\frac{\partial}{\partial \bar{r}} \left( \bar{r} \bar{p}_0 \bar{h}_0^{-3} \frac{\partial \bar{p}_0}{\partial \bar{r}} \right) + \frac{1}{\bar{r}} \frac{\partial}{\partial \theta} \left( \bar{p}_0 \bar{h}_0^{-3} \frac{\partial \bar{p}_0}{\partial \theta} \right) = \Lambda \bar{r} \frac{\partial}{\partial \theta} (\bar{p}_0 \bar{h}_0). \quad (13)$$

Equation of order  $\Delta_z^{-1}$ :

$$\begin{aligned} &\frac{\partial}{\partial \bar{r}} \left( \bar{r} \bar{p}_z \bar{h}_0^{-3} \frac{\partial \bar{p}_0}{\partial \bar{r}} + 3 \bar{r} \bar{p}_0 \bar{h}_0^{-2} (1 + S \bar{p}_z) \frac{\partial \bar{p}_0}{\partial \bar{r}} + \bar{r} \bar{p}_0 \bar{h}_0^{-3} \frac{\partial \bar{p}_z}{\partial \bar{r}} \right) \\ &+ \frac{1}{\bar{r}} \frac{\partial}{\partial \theta} \left( \bar{p}_z \bar{h}_0^{-3} \frac{\partial \bar{p}_0}{\partial \theta} + 3 \bar{p}_0 \bar{h}_0^{-2} (1 + S \bar{p}_z) \frac{\partial \bar{p}_0}{\partial \theta} + \bar{p}_0 \bar{h}_0^{-3} \frac{\partial \bar{p}_z}{\partial \theta} \right) \\ &= \Lambda \bar{r} \frac{\partial}{\partial \theta} (\bar{h}_0 \bar{p}_z + \bar{p}_0 (1 + S \bar{p}_z)) + i 2 \gamma \Lambda \bar{r} (\bar{h}_0 \bar{p}_z + \bar{p}_0 (1 + S \bar{p}_z)). \end{aligned} \quad (14)$$

With the following normalizations:

$$\bar{p}_z = \frac{p_z c}{p_a}, \quad \bar{p}_\varphi = \frac{p_\varphi}{p_a}, \quad \bar{p}_\psi = \frac{p_\psi}{p_a}, \quad \bar{\Delta}_z = \frac{\Delta_z}{c}. \quad (15)$$

The boundary conditions at  $r = r_o$ ,  $r = r_i$ ,  $\theta = 0$ ,  $\theta = \beta$  are as follows:

$$\bar{p}_0 = 1 \quad (16)$$

$$\bar{p}_z = \bar{p}_\varphi = \bar{p}_\psi = 0. \quad (17)$$

The first equation (13) is a nonlinear differential equation of zeroth order in perturbation  $\Delta$  and gives the stationary equilibrium solution of pressure and

film thickness  $p_0$ ,  $h_0$ . This equation is discretized by applying Finite Differences (FD) and solved iteratively by using Newton-Raphson method. The solution has to be inserted into the first order differential equation of perturbation  $\Delta_z$  (14). For brevity the perturbed equations for  $\Delta_\varphi$  Eq. (24) and  $\Delta_\psi$  Eq. (25) are only given in the appendix. The first order equations are linear and can therefore be solved by using MATLAB's *mldivide* algorithm. The resulting perturbed values  $\overline{p}_z$ ,  $\overline{p}_\varphi$ ,  $\overline{p}_\psi$  are complex. They are dependent of running speed  $\Omega$ , excitation frequency  $\omega$  and external load  $W$  which is implicitly given by specifying the nominal film thickness  $c$ . Integrating the perturbed values  $\overline{p}_z$ ,  $\overline{p}_\varphi$ ,  $\overline{p}_\psi$  multiplied with the associated perturbations over the pad area  $A_{pad}$  results in forces and moments which are linearly dependent of perturbations (because higher orders were neglected). This forces and moments can therefore be expressed through linear stiffness and damping coefficients:

$$\begin{aligned} & \begin{bmatrix} K_{zz} & K_{z\varphi} & K_{z\psi} \\ K_{\varphi z} & K_{\varphi\varphi} & K_{\varphi\psi} \\ K_{\psi z} & K_{\psi\varphi} & K_{\psi\psi} \end{bmatrix} + i\gamma\omega \begin{bmatrix} C_{zz} & C_{z\varphi} & C_{z\psi} \\ C_{\varphi z} & C_{\varphi\varphi} & C_{\varphi\psi} \\ C_{\psi z} & C_{\psi\varphi} & C_{\psi\psi} \end{bmatrix} \\ & = \frac{p_a r_o^2}{c} \iint_{A_{pad}} \begin{bmatrix} \overline{p}_z & c\overline{p}_\varphi & c\overline{p}_\psi \\ \overline{p}_z r_o \overline{r} \sin(\theta) & c\overline{p}_\varphi r_o \overline{r} \sin(\theta) & c\overline{p}_\psi r_o \overline{r} \sin(\theta) \\ \overline{p}_z r_o \overline{r} \cos(\theta) & c\overline{p}_\varphi r_o \overline{r} \cos(\theta) & c\overline{p}_\psi r_o \overline{r} \cos(\theta) \end{bmatrix} \overline{r} d\overline{r} d\theta. \quad (18) \end{aligned}$$

The first index of stiffness  $K_{\alpha\beta}$  or damping  $C_{\alpha\beta}$  gives the direction of the associated force or moment while the second index gives the direction of the perturbation. Therefore the different parameters  $K_{\alpha\beta}$ ,  $C_{\alpha\beta}$  also have different units.

### 3 Validation

To validate the developed numerical routine, calculated results of bearing stiffness and damping parameters are compared to published results by Gad and Kaneko [16]. This work was chosen because the used perturbation approach is the closest compared to the approach used in this paper. Additionally the first order equations (14, 24, 25) can easily be modified to match those of Gad and Kaneko. The parameters of the investigated bearing are given in [16]. The mentioned bearing is a second generation GFTB with 5 bump foil strips. The bump foil strips have 3, 4, 5, 6 and 5 bumps starting from the radially innermost to the outermost strip. Although SEFM is used, the varying number of bumps is accounted for by specifying a different stiffness coefficient for each strip.

To validate the results of the zeroth order equation (13) the obtained results of load and torque are compared to those published by Gad and Kaneko. As can be seen in Fig. 2 generally a good agreement is achieved. The largest relative deviation of load of  $\approx 10.5\%$  occurs at the maximum simulated running speed of 80 krpm. It can be explained by the different structural models used.

In order to verify the results of the first order equations a comparison of the resulting linearized bearing coefficients is shown in Fig. 3. Note that the bearing

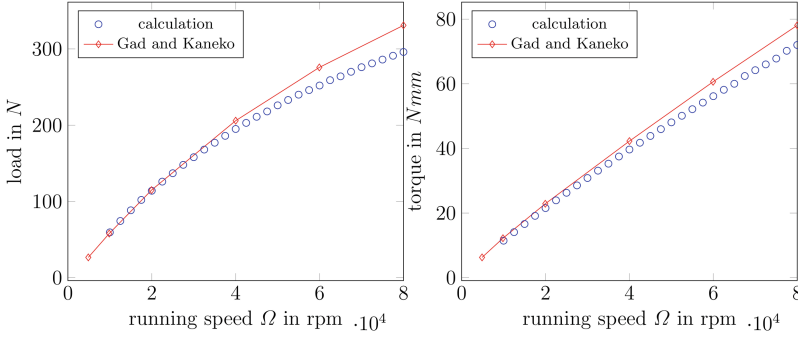


**Fig. 2.** Load and torque over running speed: calculation and values of Gad and Kaneko [16]

parameters were calculated with the ratio  $\gamma$  of excitation frequency to running speed set to  $\gamma = 1$  while the bearing parameters calculated by Gad and Kaneko are independent of  $\gamma$ . The excitation frequency ratio of  $\gamma = 1$  was chosen as an arbitrary but representative value. The stiffness and damping values show significant discrepancies. The reason for the discrepancy lies in the different perturbation methods.

To confirm that the cause of this discrepancies lies in the different perturbation approaches the derived first order equations (14, 24, 25) are modified to match those of Gad and Kaneko. A comparison of the first order equations from both works reveals that the obtained stiffness values should be identical when excitation frequency  $\gamma = 0$  and foil compliance  $S = 0$  are set to zero in the first order Eq. (14, 24, 25) (but not in the zeroth order Eq. 13). The first order equations also have to be adjusted to match those of Gad and Kaneko. The terms responsible for damping should be identical when  $S = 0$  and the terms  $i2\gamma\Delta\bar{r}h_0\bar{p}_{z/\varphi/\psi}$  in (14, 24, 25) are neglected. After neglecting the mentioned terms,  $\gamma$  still appears in the first order equations but has no influence on the damping parameters because it cancels out while normalizing. It is important to note that foil compliance  $S$  is set to zero only in the first order equations. When calculating equilibrium pressure by solving the zero order Eq. (13) the foil compliance  $S$  still needs to be considered and cannot be set to zero.

The results obtained with these modifications are shown in Fig. 4. An acceptable accordance with the values published by Gad and Kaneko is achieved by modifying the first order equations. Although the modifications lead to identical first order equations there remains a significant discrepancy between the calculated and the published main stiffness values ( $K_{zz}$ ,  $K_{\varphi\varphi}$ ,  $K_{\psi\psi}$ ). The maximum relative deviation is approximately 18%. This deviation is explained by the different results obtained for the equilibrium pressure due to different structural models. It is the cause of the discrepancy shown in Fig. 2 which has the same shape as the discrepancy observed for ( $K_{zz}$ ,  $K_{\varphi\varphi}$ ,  $K_{\psi\psi}$ ). Therefore it is

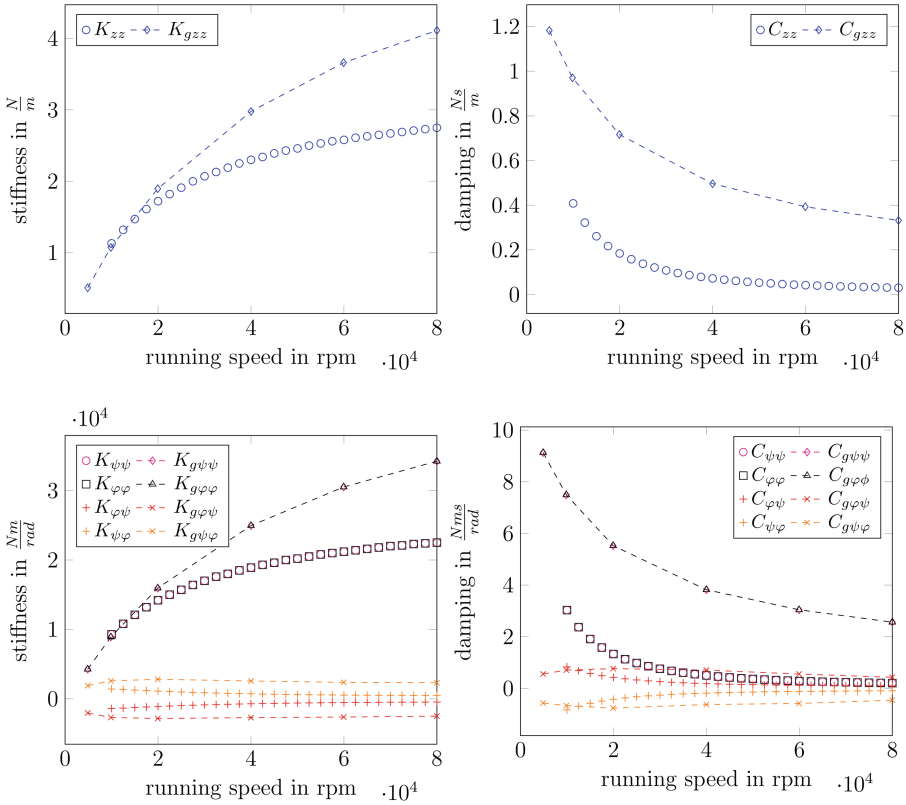


**Fig. 3.** Linearized stiffness and damping parameters  $K_{\alpha\beta}$ ,  $C_{\alpha\beta}$  calculated in this work with  $\gamma = 1$  and calculated by Gad and Kaneko [16]  $K_{g\alpha\beta}$ ,  $C_{g\alpha\beta}$  (dashed lines)

concluded that the implemented algorithm to calculate the linearized bearing parameters delivers valid results.

On the other hand it becomes evident when comparing Figs.4 and 3 that excitation frequency  $\gamma$  and foil compliance  $S$  do have a relevant influence on the bearing parameters. Stiffness values of Gad and Kaneko are valid for constant perturbation ( $\gamma = 0$ ) and stiff foil structures ( $S = 0$  when the influence of pressure perturbation on foil deformation is negligible). Note that  $K_{z\varphi}$ ,  $K_{z\psi}$ ,  $K_{\varphi z}$ ,  $K_{\psi z}$  and  $C_{z\varphi}$ ,  $C_{z\psi}$ ,  $C_{\varphi z}$ ,  $C_{\psi z}$  are negligible (in both works) and therefore not depicted. Conclusively perturbations in  $\psi$  and  $\varphi$  direction do not cause a force in  $z$  direction. Also perturbations in  $z$  direction do not lead to moments in  $\psi$  or  $\varphi$  direction.

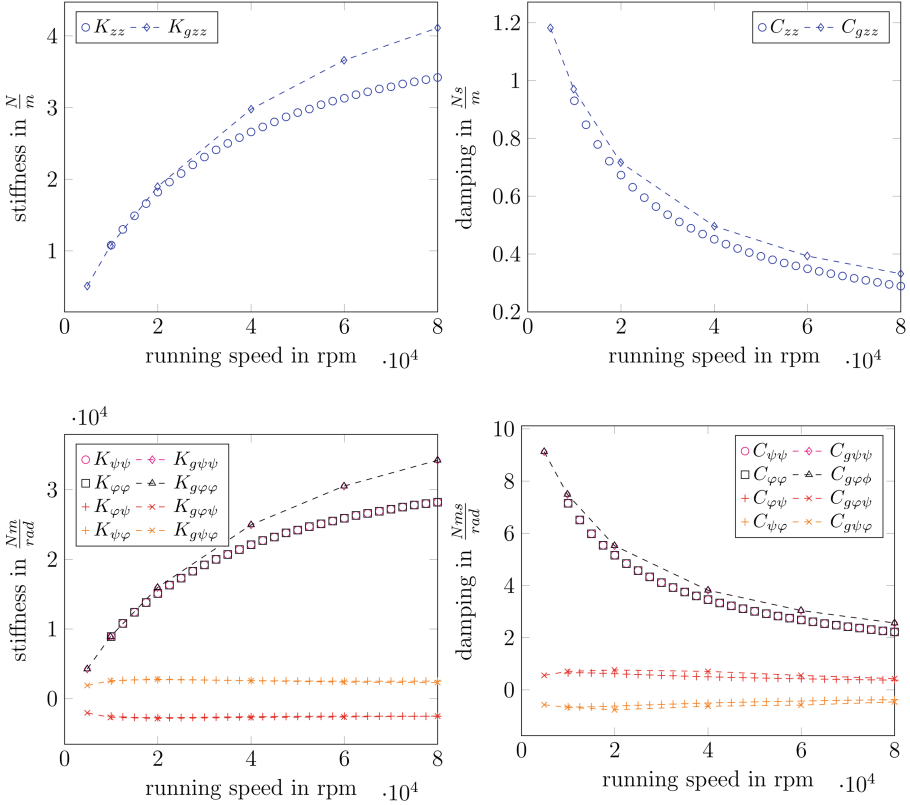


**Fig. 4.** Linearized stiffness and damping parameters  $K_{\alpha\beta}$ ,  $C_{\alpha\beta}$  calculated in this work with  $\gamma = 0$ ,  $S = 0$  and modified first order equations versus calculation by Gad and Kaneko [16]  $K_{g\alpha\beta}$ ,  $C_{g\alpha\beta}$  (dashed lines)

## 4 Numerical Results

### 4.1 Bearing Parameters

In this subsection parametric studies on the linearized bearing parameters introduced in Eq. (18) are conducted. The input data used for the investigated bearing are given in Table 1 in the appendix. This data is used unless other parameters are explicitly given in the text. The given bearing geometry was chosen to match currently manufactured GFTBs at the department of Engineering Design and Product Reliability at the Technical University Berlin. It is planned to experimentally investigate those bearings in the future. In a first study the excitation frequency ratio  $\gamma$  is varied from 0.1 to 2, meaning that the excitation frequency  $\omega$  varies from 0.1 to 2 times the running speed  $\Omega$ . Bump height ratio  $H = \frac{h_{ramp}}{c}$  is set to 5 for this calculation.

The results of this parametric study are shown in Fig. 5. Again the negligible parameters  $K_{z\varphi}$ ,  $K_{z\psi}$ ,  $K_{\varphi z}$ ,  $K_{\psi z}$  and  $C_{z\varphi}$ ,  $C_{z\psi}$ ,  $C_{\varphi z}$ ,  $C_{\psi z}$  are not displayed. The

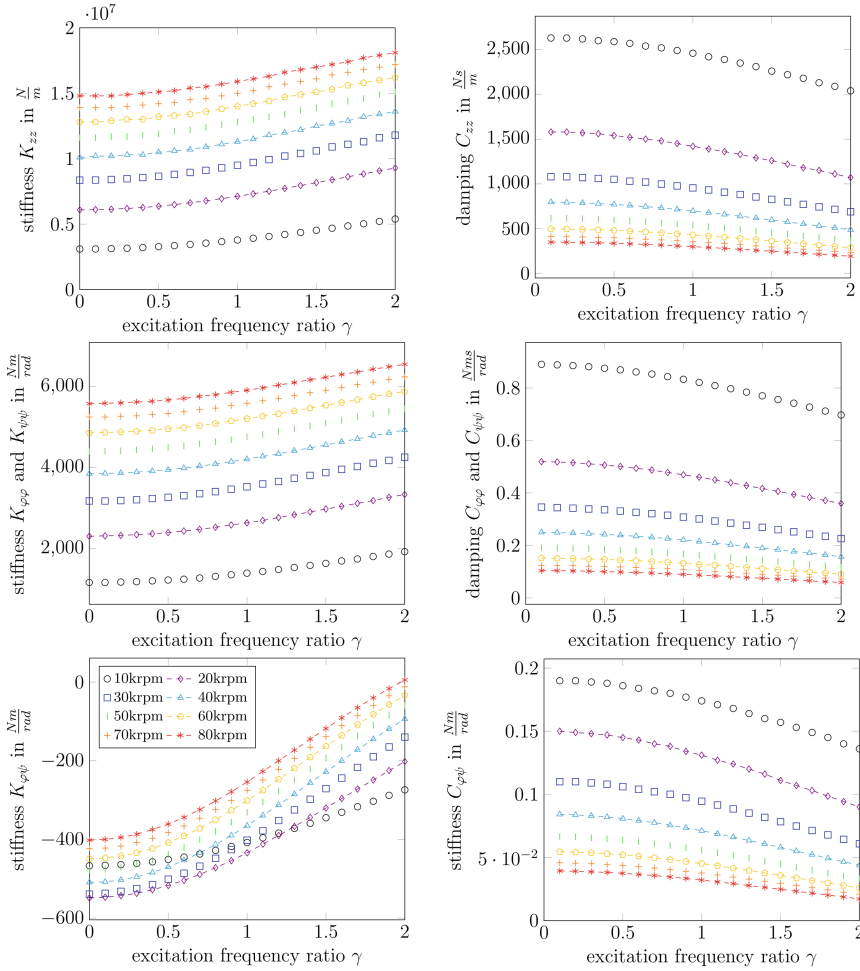


**Fig. 5.** Linearized stiffness and damping parameters in dependence of running speed and excitation frequency for the bearing specified in Table 1 in the appendix and  $H = 5$ . The legend for all plots is shown in the left bottom subfigure.

differently colored and marked lines in each plot indicate the running speed of the rotor. The plot reveals that the main stiffness parameters  $K_{zz}$ ,  $K_{\varphi\varphi}$  and  $K_{\psi\psi}$  increase with higher excitation frequency ratio  $\gamma$ . This results are in qualitative agreement with Feng [18] who calculated the same tendencies for  $K_{zz}$  and  $C_{zz}$  while all the other parameters are published for the first time in dependency of excitation frequency.

For small values of  $\Omega$  the relative influence of excitation frequency is the highest. For example:  $K_{zz}$  at  $\Omega = 10$  krpm rises about 74% from  $\gamma = 0$  to  $\gamma = 2$  while at 80 krpm the rise is only 22%. The main angle stiffness  $K_{\varphi\varphi}$  and  $K_{\psi\psi}$  exhibit the same qualitative behavior. The cross coupled angle stiffness  $K_{\varphi\psi}$

has the same value but opposite sign as  $K_{\psi\varphi}$  making the stiffness matrix skew symmetric. This means that a positive perturbation in  $\psi$  direction leads to a negative moment in  $\varphi$  direction and vice versa. For brevity reasons the display of  $K_{\psi\varphi}$  is omitted in Fig. 5. The absolute values of these cross coupled stiffness are an order of magnitude smaller than the main angle stiffness. Interestingly the absolute values of these cross coupled stiffness show the opposite behavior than all other stiffness parameters: they decline at higher values of  $\gamma$  and  $\Omega$ . The main stiffness parameters  $K_{zz}$ ,  $K_{\varphi\varphi}$  and  $K_{\psi\psi}$  all increase with  $\Omega$ , while the absolute values of the cross coupled stiffness parameters decrease.

In the investigated  $\gamma$ - and  $\Omega$ -range the running speed is the dominating parameter leading to an approximate 320% rise of  $K_{zz}$  from 10 to 80 krpm at  $\gamma = 1$ . However the influence of excitation frequency cannot be neglected. The cross coupled stiffness for example has a greater dependency of  $\gamma$  than of  $\Omega$  in the investigated parameter range. The magnitude of increase or decrease is larger at small  $\Omega$  and continuously gets smaller for higher  $\Omega$ . At high rotation speeds the main stiffness values seem to converge to a maximum value while the cross coupled values approach zero. A skew symmetric stiffness matrix is generally considered as negative for the stability behavior [26] indicating that the bearing stability might benefit from the calculated characteristic of  $K_{\varphi\psi}$  and  $K_{\psi\varphi}$  at high running speed and excitation frequency.

Unfortunately the damping parameters show the opposite characteristic and have the smallest values at high  $\Omega$  and  $\gamma$  therefore enlarging the risk of instability in this operational range. Which of these effects will prevail will be analyzed in the following Subsect. (4.2). The decrease of damping is relatively more pronounced than the increase of their stiffness counterparts:  $C_{zz}$  falls to 12% from 10 to 80 krpm running speed at  $\gamma = 1$ . The relative influence of  $\gamma$  on damping is the highest for high values of  $\Omega$ : at 80 krpm  $C_{zz}$  decreases to 55% at  $\gamma = 0.1$  compared to its value  $\gamma = 2$ , at 10 krpm  $C_{zz}$  only decreases to 78%. The damping matrix is also skew symmetric  $C_{\varphi\psi} = -C_{\psi\varphi}$  thus only  $C_{\varphi\psi}$  is presented in Fig. 5.

## 4.2 Stability Analysis

To analyze the influence of GFTBs on the vibrational behavior the previously calculated stiffness and damping parameters are used for an eigenvalue analysis. The rotor geometry is aimed to mimic a planned test rig and specified in Table 2 shown in the appendix. To emphasize the impact of GFTBs on the stability a rigid rotor with only one ideally rigid radial bearing is investigated. Only one radial bearing is used so that the rotor is allowed to tilt in  $\varphi$  and  $\psi$  direction. In practice it is desirable to contain axial forces in both directions therefore 2 GFTBs are necessary. It is assumed in this study that both bearings have the same stiffness and damping coefficients. For this to be the case the bearings need the same nominal clearance and the rotor is not subjected to any external axial force. Still both bearings transmit a force to the rotor of the same magnitude  $F_0$  but opposite sign. If an external axial force is now applied to the rotor the rotor will move in the direction of the force causing an increase of one bearing



force of the magnitude  $\Delta F_I = K_{zz}\Delta z$  while the bearing force in the opposite direction decreases with the same magnitude. Thus the resulting reaction force of both bearings combined is:  $\Delta F = 2K_{zz}\Delta z$ . This bearing combination can be modeled like preloaded springs and the following equation of motion around the equilibrium position results:

$$\begin{aligned} \begin{bmatrix} m & 0 & 0 \\ 0 & J_x & 0 \\ 0 & 0 & J_y \end{bmatrix} \begin{Bmatrix} \ddot{\Delta z} \\ \ddot{\Delta\varphi} \\ \ddot{\Delta\psi} \end{Bmatrix} + 2 \begin{bmatrix} C_{zz} & 0 & 0 \\ 0 & C_{\varphi\varphi} & C_{\varphi\psi} \\ 0 & C_{\psi\varphi} & C_{\psi\psi} \end{bmatrix} \begin{Bmatrix} \dot{\Delta z} \\ \dot{\Delta\varphi} \\ \dot{\Delta\psi} \end{Bmatrix} + 2 \begin{bmatrix} K_{zz} & 0 & 0 \\ 0 & K_{\varphi\varphi} & K_{\varphi\psi} \\ 0 & K_{\psi\varphi} & K_{\psi\psi} \end{bmatrix} \begin{Bmatrix} \Delta z \\ \Delta\varphi \\ \Delta\psi \end{Bmatrix} \\ = \begin{Bmatrix} F_z \\ M_\varphi \\ M_\psi \end{Bmatrix}. \end{aligned} \tag{19}$$

This Eq. (19) uses the findings of the bearing parameter Sect. 4.1:  $K_{z\varphi} = K_{z\psi} = K_{\varphi z} = K_{\psi z} = C_{z\varphi} = C_{z\psi} = C_{\varphi z} = C_{\psi z} = 0$ . The Eq. (19) could be further simplified because in the previous section it was shown that:  $K_{\varphi\psi} = -K_{\psi\varphi}$ ,  $C_{\varphi\psi} = -C_{\psi\varphi}$ . To perform a linear stability analysis only the homogenous part of the above equation is used and it is transformed so that a generalized eigenvalue problem will result.

$$\begin{aligned} \underline{\underline{M}}\ddot{q} + \underline{\underline{C}}(\Omega, \omega)\dot{q} + \underline{\underline{K}}(\Omega, \omega)q &= \underline{\underline{0}} \\ \begin{bmatrix} 0 & \underline{\underline{I}} \\ -\underline{\underline{M}}^{-1}\underline{\underline{K}} & -\underline{\underline{M}}^{-1}\underline{\underline{C}} \end{bmatrix} \begin{Bmatrix} q \\ \dot{q} \end{Bmatrix} &= \frac{d}{dt} \begin{Bmatrix} q \\ \dot{q} \end{Bmatrix} \text{ with } q = \hat{q}e^{\lambda t} \\ \begin{bmatrix} 0 & \underline{\underline{I}} \\ -\underline{\underline{M}}^{-1}\underline{\underline{K}} & -\underline{\underline{M}}^{-1}\underline{\underline{C}} \end{bmatrix} \begin{Bmatrix} q \\ \dot{q} \end{Bmatrix} &= \lambda \begin{Bmatrix} q \\ \dot{q} \end{Bmatrix} \end{aligned} \tag{20}$$

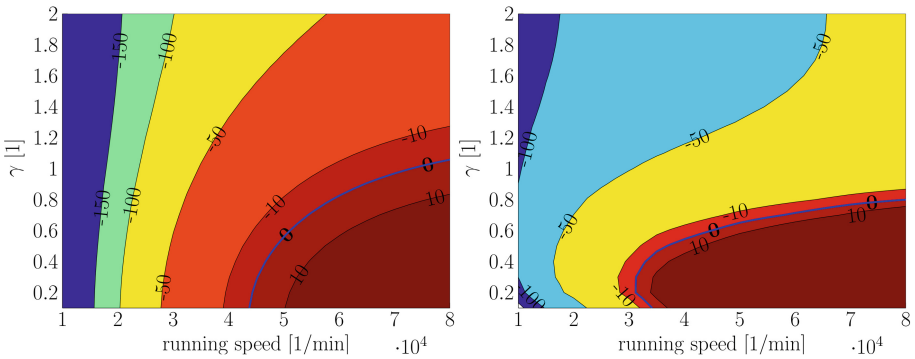


**Fig. 6.** Stability Maps, left: rigid rotor and rigid radial bearing, right: rigid rotor and rigid axial support

$\underline{\underline{I}}$  is the unit matrix. This eigenvalue problem is solved and instability occurs when the maximum of the real parts of the eigenvalues is greater than zero

$max(real(\lambda_i)) > 0$ . Therefore Eq. (20) is solved for each calculated parameter set  $(\Omega, \omega)$ . Where running speed  $\Omega$  is increased in steps of 2.5 krpm and  $\gamma$  in steps of 0.1. This maximum real value of the eigenvalues  $\lambda_i$  is shown in the left top contourplot of Fig. 6. The numbers on the line show the maximum real part of the eigenvalues. Therefore the line with the zero-label, marked with a blue line, is the linear stability border for the investigated configuration. It has to be emphasized that linear instability does not necessarily lead to unlimited growth of amplitudes and therefore results in possible contact between rotor and stator. Instead the growth of amplitudes occurring at linear stability border leads to a change of bearing stiffness and damping. In this case the calculated stiffness and damping parameters are no longer valid because the assumption of small perturbation amplitudes no longer holds. This change of stiffness and damping may lead to a stable limit cycle operation of the bearing which was documented for GFJBs e.g. [27, 28].

The simulated rotor-bearing system has a linear stability border, which starts at approximately 44 krpm and stretches in the shape of a quarter circle to the maximum simulated running speed of 80 krpm and  $\gamma$  values slightly above 1. This means when excitation frequency equals running speed, which is very likely, at running speeds close to 80 krpm a growth of amplitudes should occur. It can be said that the instability range appears for small values of excitation frequency ratio  $\gamma$  and large values of  $\omega$ . In this parameter range the cross coupled stiffness still have a significant magnitude (see Fig. 5) while damping values are low. Skew symmetric cross coupled stiffness parameters in addition with small damping values could therefore be the cause of this instability.

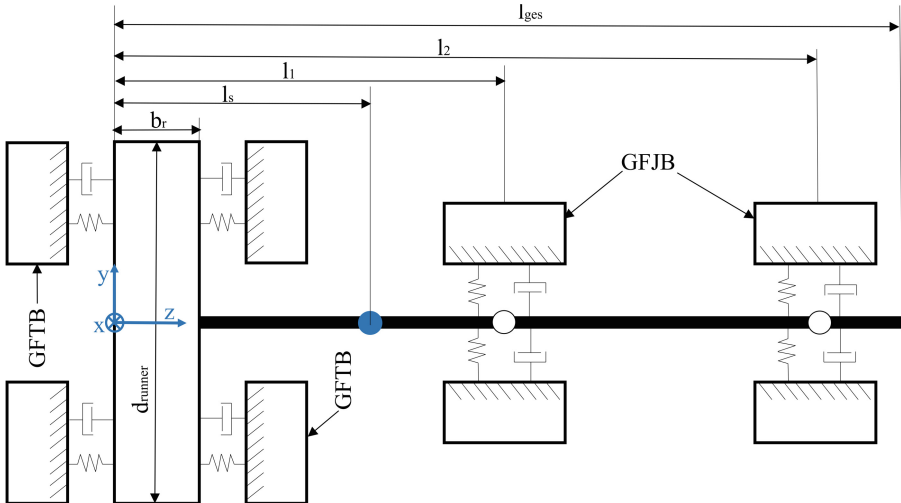


Fig. 7. Schematic visualization of the investigated rotor bearing system

To simulate a realistic rotor bearing system two identical GFJBs were added to the system at length  $l_1$  and  $l_2$ , see Fig. 7. Their linearized stiffness and damping coefficients were calculated using the perturbation method described in this work. The degrees of freedom of the perturbation for these bearing are the  $x$  and  $y$ -direction shown in Fig. 7. To isolate the influence of these radial bearings the stability map of the investigated rigid rotor is calculated for rigid axial support. The equation of motion for the rotor supported by 2 GFJBs and a rigid axial bearing is as follows:

$$\begin{bmatrix} m & 0 \\ 0 & m \end{bmatrix} \begin{Bmatrix} \dot{\Delta x} \\ \dot{\Delta y} \end{Bmatrix} + 2 \begin{bmatrix} C_{xx} & C_{xy} \\ C_{yx} & C_{yy} \end{bmatrix} \begin{Bmatrix} \Delta x \\ \Delta y \end{Bmatrix} + 2 \begin{bmatrix} K_{xx} & K_{xy} \\ K_{yx} & K_{yy} \end{bmatrix} \begin{Bmatrix} \Delta x \\ \Delta y \end{Bmatrix} = \begin{Bmatrix} F_x \\ F_y \end{Bmatrix}. \quad (21)$$

The stiffness and damping parameters of the GFJBs were calculated for a bearing with radius  $r_{rad} = 13$  mm, length  $l_{rad} = 20$  mm, load per bearing  $W_{rad} = 4$  N, nominal clearance  $c_{rad} = 60\mu\text{m}$  and nondimensional foil compliance  $S = 0.29$ . The eigenvalue problem Eq. (20) is solved and again the largest real part of the eigenvalue is critical for the stability behaviour. The result is visualized in the right diagram of Fig. 6. For this bearing configuration linear stability border occurs at 35 krpm at  $\gamma = 0.1$ . Then for slightly larger values of  $\gamma \approx 0.3$  the stability border already starts at 32 krpm. From there on linear instability occurs up to 80 krpm and  $\gamma$  values of about 0.75.

To analyze the influence of both bearing types acting together on a rigid rotor first the equation of motion has to be derived by applying force and momentum equilibrium in the center of mass. It is obvious that adding GFJBs will also influence the tilting motion of the rotor and therefore its tilting stiffness and damping. Additionally a tilting with  $\psi$  or  $\varphi$  of the rotor will lead to a displacement of the rotor inside the GFJBs:  $x_1 = x + \sin(\psi)l_{1s} \approx x + \psi l_{1s}$  and  $y_1 \approx x - \varphi l_{1s}$  with  $l_{1s} = l_1 - l_s$  (analogously for the GFJB 2), where  $l_s$  denotes the distance to the center of mass. Therefore the resulting stiffness matrix will have a coupling between tilting and radial motion. Stiffness, mass matrix and state vector are given in Eq. (22, 23). The damping matrix has the same structure as the stiffness matrix and is therefore not displayed.

$$\underline{\underline{M}} = \begin{bmatrix} m & 0 & 0 & 0 & 0 \\ 0 & m & 0 & 0 & 0 \\ 0 & 0 & m & 0 & 0 \\ 0 & 0 & 0 & J & 0 \\ 0 & 0 & 0 & 0 & J \end{bmatrix}, \quad \underline{\underline{q}} = \begin{Bmatrix} \Delta z \\ \Delta y \\ \Delta x \\ \Delta \varphi \\ \Delta \psi \end{Bmatrix} \quad (22)$$

$$\underline{\underline{K}} = \begin{bmatrix} 2K_{zz} & 0 & 0 & 0 & 0 \\ 0 & 2K_{yy} & 2K_{yx} & -K_{yy}(l_{1s} + l_{2s}) & +K_{yx}(l_{1s} + l_{2s}) \\ 0 & 2K_{xy} & 2K_{xx} & -K_{xy}(l_{1s} + l_{2s}) & +K_{xx}(l_{1s} + l_{2s}) \\ 0 & -K_{yy}(l_{1s} + l_{2s}) & -K_{yx}(l_{1s} + l_{2s}) & 2K_{\varphi\varphi} + K_{yy}(l_{1s}^2 + l_{2s}^2) & 2K_{\varphi\psi} - K_{yx}(l_{1s}^2 + l_{2s}^2) \\ 0 & K_{xy}(l_{1s} + l_{2s}) & K_{xx}(l_{1s} + l_{2s}) & 2K_{\psi\varphi} - K_{xy}(l_{1s}^2 + l_{2s}^2) & 2K_{\psi\psi} + K_{xx}(l_{1s}^2 + l_{2s}^2) \end{bmatrix} \quad (23)$$

The stability map of this system is not displayed because it is almost identical to the stability map of the rotor with rigid axial support and two GFJBs shown

on the right of Fig. 6. Actually the eigenvalues of the system are not identical but relatively close to each other so that it is hard to distinguish between the stability maps with the current resolution of  $\Delta\Omega = 2.5$  krpm and  $\Delta\gamma = 0.1$ . The instability region of the GFTBs is not present anymore in the full system. It can therefore be concluded that the instability region on the left stability map of Fig. 6 was caused by a tilting movement of the rotor which is now prevented due to additional tilting stiffness provided by the GFJBs. The GFJBs influence the tilting stiffness of the rotor but have no effect on the axial stiffness. This means that in the investigated parameter region no axial instability exists. It is even probable that an ideal GFTB will have no axial instability at all because since:  $K_{z\varphi} = K_{z\psi} = C_{z\varphi} = C_{z\psi} = 0$  this degree of freedom is completely decoupled and therefore behaves similar to an one mass oscillator which is always stable as long as stiffness and damping are positive. However if a thrust bearing has varying pad stiffness, for example due to manufacturing imperfections this will lead to  $K_{z\varphi} \neq 0$   $K_{z\psi} \neq 0$  and therefore might induce axial instability.

Although the tilting  $\Delta\varphi$ ,  $\Delta\psi$  has an influence on the  $\Delta y$ ,  $\Delta x$  degrees of freedom this effect seems to be negligible at least for the investigated rotor bearing configuration. The presence of GFTBs has little influence on the stability behavior. This may change when the radial foil bearings are relatively soft compared to the thrust bearings. Also the influence of the coupling of both bearing types might be more pronounced if tilting stiffness and damping parameters are calculated for the journal bearings.

## 5 Conclusion

In this work a novel perturbation approach in the field of GFTBs and the resulting linearized bearing parameters are presented. This approach delivers excitation frequency dependent bearing parameters. The novel tilting stiffness and damping parameters of the GFTBs calculated with the introduced approach allow for the first time to examine the influence of coupling GFJBs and GFTBs on the dynamic behavior. The impact of perturbations on foil deformation is taken into account. The presented parameters are used for a stability analysis of a rigid rotor supported by both journal and thrust foil bearings. The obtained numerical results lead to the following conclusions:

1. Stiffness and damping matrices of GFTBs are skew symmetric
2. Main stiffness values increase with excitation frequency while main damping values decrease. The absolute values of the cross coupled, skew symmetric stiffness and damping parameters falls with larger excitation frequency
3. The coupling parameters between tilting and axial motion  $K_{z\varphi}$ ,  $K_{z\psi}$ ,  $C_{z\varphi}$ ,  $C_{z\psi}$  are negligible
4. GFTBs are susceptible to tilting instability at large running speeds and small excitation frequencies.

5. However in most cases this instability will be circumvented by radial support. The overall stability behavior is dominated by the GFJBs at least for the investigated rotor configuration.
6. Axial instability is not detected and might not occur for the case of a "perfect" GFTB, because the coupling bearing parameters are close to zero (see 3.). Therefore the axial degree of freedom is decoupled and behaves similar to an one mass oscillator.

To further investigate the coupling between journal and thrust foil bearings more rotor bearing configurations have to be simulated. The influence of the elasticity of the rotor including gyroscopic effects has to be studied. The quality of the results of the linearized stability can be validated numerically by conducting transient calculations and experimentally. A test rig supported by GFJBs and GFTBs is currently in planning at the department of Engineering Design and Product Reliability at the Technical University Berlin to research the effects of coupling both bearing types on dynamic behavior.

## A Appendix

### First order equations

Equation of order  $\Delta_\varphi^1$  :

$$\begin{aligned}
& \frac{\partial}{\partial \bar{r}} \left( \bar{r} \bar{p}_\varphi \bar{h}_0^3 \frac{\partial \bar{p}_0}{\partial \bar{r}} + 3 \bar{r} \frac{r}{c} \sin(\theta) \bar{p}_0 \bar{h}_0^2 (1 + S \bar{p}_\varphi) \frac{\partial \bar{p}_0}{\partial \bar{r}} + \bar{r} \bar{p}_0 \bar{h}_0^3 \frac{\partial \bar{p}_\varphi}{\partial \bar{r}} \right) \\
& + \frac{1}{\bar{r}} \frac{\partial}{\partial \theta} \left( \bar{p}_\varphi \bar{h}_0^3 \frac{\partial \bar{p}_0}{\partial \theta} + 3 \frac{r}{c} \sin(\theta) \bar{p}_0 \bar{h}_0^2 (1 + S \bar{p}_\varphi) \frac{\partial \bar{p}_0}{\partial \theta} + \bar{p}_0 \bar{h}_0^3 \frac{\partial \bar{p}_\varphi}{\partial \theta} \right) \\
& = \Lambda \bar{r} \frac{\partial}{\partial \theta} \left( \bar{h}_0 \bar{p}_\varphi + \bar{p}_0 \frac{r}{c} \sin(\theta) (1 + S \bar{p}_\varphi) \right) + i 2 \gamma \Lambda \bar{r} \left( \bar{h}_0 \bar{p}_\varphi + \bar{p}_0 \frac{r}{c} \sin(\theta) (1 + S \bar{p}_\varphi) \right)
\end{aligned} \tag{24}$$

Equation of order  $\Delta_\psi^1$  :

$$\begin{aligned}
& \frac{\partial}{\partial \bar{r}} \left( \bar{r} \bar{p}_\psi \bar{h}_0^3 \frac{\partial \bar{p}_0}{\partial \bar{r}} + 3 \bar{r} \frac{r}{c} \cos(\theta) \bar{p}_0 \bar{h}_0^2 (1 + S \bar{p}_\psi) \frac{\partial \bar{p}_0}{\partial \bar{r}} + \bar{r} \bar{p}_0 \bar{h}_0^3 \frac{\partial \bar{p}_\psi}{\partial \bar{r}} \right) \\
& + \frac{1}{\bar{r}} \frac{\partial}{\partial \theta} \left( \bar{p}_\psi \bar{h}_0^3 \frac{\partial \bar{p}_0}{\partial \theta} + 3 \frac{r}{c} \cos(\theta) \bar{p}_0 \bar{h}_0^2 (1 + S \bar{p}_\psi) \frac{\partial \bar{p}_0}{\partial \theta} + \bar{p}_0 \bar{h}_0^3 \frac{\partial \bar{p}_\psi}{\partial \theta} \right) \\
& = \Lambda \bar{r} \frac{\partial}{\partial \theta} \left( \bar{h}_0 \bar{p}_\psi + \bar{p}_0 \frac{r}{c} \cos(\theta) (1 + S \bar{p}_\psi) \right) + i 2 \gamma \Lambda \bar{r} \left( \bar{h}_0 \bar{p}_\psi + \bar{p}_0 \frac{r}{c} \cos(\theta) (1 + S \bar{p}_\psi) \right)
\end{aligned} \tag{25}$$

**Table 1.** Parameters of the investigated bearing

Parameter	Variable	Value	Unit
Inner radius	$r_i$	15	mm
Outer radius	$r_o$	35	mm
Pad angle	$\beta$	51	°
Ramp angle	$b \cdot \beta$	22.5	°
Pad number	$N_{pad}$	6	-
Viscosity	$\mu_a$	$1.95 \cdot 10^{-5}$	$\frac{Ns}{m^2}$
Ambient pressure	$p_a$	101325	$\frac{N}{m^2}$
Young's Modulus	$E$	$2.14 \cdot 10^{11}$	$\frac{N}{m^2}$
Foil compliance	$S$	0.242	-
Nominal film thickness	$c$	10	$\mu m$

**Table 2.** Shaft parameters

Parameter	Variable	Value	Unit
Shaft length	$l_{ges}$	130	mm
Runner width	$b_r$	7	mm
Shaft diameter	$d_w$	26	mm
Runner diameter	$d_{runner}$	84	mm
Length to GFJB 1	$l_1$	48	mm
Length to GFJB 2	$l_2$	89	mm
Length to center of mass	$l_s$	44.3	mm
Young's modulus shaft	$E$	$2.10 \cdot 10^{11}$	$\frac{N}{m^2}$
Poisson ratio	$\nu$	0.3	-
Moment of inertia y,z	$J_{x,y}$	$308.8 \cdot 10^{-4}$	kg·mm <sup>2</sup>
Rotor mass	$m_r$	276	g

## References

1. Agrawal, G.L.: Foil air/gas bearing technology - an overview. ASME paper, 97 (1997)
2. Heshmat, H.: Advancements in the performance of aerodynamic foil journal bearings: high speed and load capability. ASME J. Tribol. **116**(2), 287–295 (1994)
3. DellaCorte, C., Valco, M.J.: Load capacity estimation of foil air journal bearings for oil-free turbomachinery applications. Tribol. Trans. **43**(4), 795–801 (2000)
4. DellaCorte, C., Lukaszewicz, V., Valco, M.J., Radil, K.C., Heshmat, H.: Performance and durability of high temperature foil air bearings for oil-free turbomachinery. Tribol. Trans. **43**(4), 774–780 (2000)
5. Heshmat, H., Walton II, J.F., Tomaszewski, M.J.: Demonstration of a turbojet engine using an air foil bearing. Gas **1**, 1–2 (2005)

6. Heshmat, H., Walton, J.F., DellaCorte, C., Valco, M.J.: Oil-free turbocharger demonstration paves way to gas turbine engine applications. ASME paper 2000-GT-0620 (2000)
7. Lee, Y.-B., Kwon, S.B., Kim, T.H., Sim, K.: Feasibility study of an oil-free turbocharger supported on gas foil bearings via on-road tests of a two-liter class diesel vehicle. *J. Eng. Gas Turbines Power* **135**(5), 052701 (2013)
8. Sim, K., Lee, Y.-B., Kim, T.H.: Rotordynamic analysis of an oil-free turbocharger supported on lobed gas foil bearings—predictions versus test data. *Tribol. Trans.* **57**(6), 1086–1095 (2014)
9. Xiong, L.-Y., Wu, G., Hou, Y., Liu, L.-Q., Ling, M.-F., Chen, C.-Z.: Development of aerodynamic foil journal bearings for a high speed cryogenic turboexpander. *Cryogenics* **37**(4), 221–230 (1997)
10. Kim, D., Lee, A.S., Choi, B.S.: Evaluation of foil bearing performance and nonlinear rotordynamics of 120 kw oil-free gas turbine generator. *J. Eng. Gas Turbines Power* **136**(3), 032504 (2014)
11. Heshmat, H., Walowitz, J.A., Pinkus, O.: Analysis of gas lubricated compliant thrust bearings. *ASME J. Lubr. Technol.* **105**(4), 638–646 (1983)
12. Iordanoff, I.: Analysis of an aerodynamic compliant foil thrust bearing: method for a rapid design. *J. Tribol.* **121**(4), 816–822 (1999)
13. Ku, C.-P.R., Heshmat, H.: Compliant foil bearing structural stiffness analysis: part—theoretical model including strip and variable bump foil geometry. *J. Tribol.* **114**(2), 394–400 (1992)
14. Heshmat, C.A.D.S., Xu, D.S., Heshmat, H.: Analysis of gas lubricated foil thrust bearings using coupled finite element and finite difference methods. *J. Tribol. (Trans. ASME) (USA)* **122**(1), 199–210 (2000)
15. Park, D.-J., Kim, C.-H., Jang, G.-H., Lee, Y.-B.: Theoretical considerations of static and dynamic characteristics of air foil thrust bearing with tilt and slip flow. *Tribol. Int.* **41**(4), 282–295 (2008)
16. Gad, A.M., Kaneko, S.: Performance characteristics of gas-lubricated bump-type foil thrust bearing. *Proc. Inst. Mech. Eng. Part J: J. Eng. Tribol.* **229**(6), 746–762 (2015)
17. Gad, A.M., Kaneko, S.: A new structural stiffness model for bump-type foil bearings: application to generation ii gas lubricated foil thrust bearing. *J. Tribol.* **136**(4), 041701 (2014)
18. Feng, K., Liu, L.-J., Guo, Z.-Y., Zhao, X.-Y.: Parametric study on static and dynamic characteristics of bump-type gas foil thrust bearing for oil-free turbomachinery. *Proc. Inst. Mech. Eng. Part J: J. Eng. Tribol.* **229**(10), 1247–1263 (2015)
19. Feng, K., Kaneko, S.: Analytical model of bump-type foil bearings using a link-spring structure and a finite-element shell model. *J. Tribol.* **132**(2), 021706 (2010)
20. Larsen, J.S., Santos, I.: Compliant foil journal bearings—investigation of dynamic properties. In: *SIRM 2013* (2013)
21. Kim, T.H., San Andrés, L.: Heavily loaded gas foil bearings: a model anchored to test data. *J. Eng. Gas Turbines Power* **130**(1), 012504 (2008)
22. von Osmanski, S., Larsen, J.S., Santos, I.F.: On the incorporation of friction into a simultaneously coupled time domain model of a rigid rotor supported by air foil bearings. *Technische Mechanik* **37**(2–5), 291–302 (2017)
23. Lund, J.W.: Calculation of stiffness and damping properties of gas bearings. *J. Lubr. Technol.* **90**(4), 793–803 (1968)
24. Kim, T.H.: Heavily loaded gas foil bearings: a model anchored to test data. *J. Tribol.* **129**(2), 354–364 (2007)

25. Carpino, M., Talmage, G.: Prediction of rotor dynamic coefficients in gas lubricated foil journal bearings with corrugated sub-foils. *Tribol. Trans.* **49**(3), 400–409 (2006)
26. Gasch, R., Nordmann, R., Pfützner, H.: *Rotordynamik*. Springer, Heidelberg (2006)
27. Heshmat, H.: Operation of foil bearings beyond the bending critical mode. *J. Tribol. (Trans. ASME)(USA)* **122**(1), 192–198 (2000)
28. San Andres, L., Kim, T.H.: Forced nonlinear response of gas foil bearing supported rotors. *Tribol. Int.* **41**(8), 704–715 (2008)





# Magnetic Bearings for Non-static Flywheel Energy Storage Systems (FESS)

Nikolaj Dagnaes-Hansen and Ilmar F. Santos<sup>(✉)</sup>

Technical University of Denmark, Kongens Lyngby, Denmark  
ifs@mek.dtu.dk

**Abstract.** Proper dimensioning of magnetic bearings for non-static gimballed FESS is currently hindered by the lack of models that can predict the maximum forces in the bearings. If FESS is to compete with conventional electro-chemical batteries in terms of energy density, the magnetic bearings must be dimensioned optimally for weight and size. Magnetically suspended FESS has been experimentally investigated; however, the methods for theoretically predicting magnetic bearing loads are still limited. This paper presents how to determine such magnetic bearing loads in a gimballed FESS subject to a moving foundation. The predicted forces are compared with measurements from an experimental test bench with good agreement. Furthermore, the maximum forces in a gimballed FESS are compared with maximum forces in a non-gimballed FESS. It was found that the gyroscopic forces in the non-gimballed case quickly become critical making the gimbal mount essential for reducing magnetic bearing loads.

**Keywords:** Active magnetic bearings · Permanent magnet bearings  
Flywheel energy storage system

## 1 Introduction

Energy storage currently poses a bottleneck in the transition towards a more efficient and greener energy sector as energy storage improvements are needed to more effectively buffer a fluctuating energy supply and demand. The same applies in the transport sector where electric energy still suffers disadvantages over fossil fuels due to energy density, price, lifetime, chemical and fire hazards, among others. Modern high-speed FESS can potentially overcome these disadvantages if certain engineering challenges regarding FESS design are solved. One is flywheel suspension, usually comprising magnetic bearings for low-friction vacuum operation. Before FESS can be utilized in non-static transport applications such as cars and ships, the magnetic bearings must be designed specifically for the accelerations, movements, and gyroscopic couplings of a high inertia flywheel rotor subject to severe outer perturbations. Rotational movements of the FESS-powered vehicle cause large gyroscopic forces which motivates the use of a passive gimbal mount to decouple flywheel rotations from vehicle rotations.

However, such a mount introduces new dynamics which interacts with the magnetic suspension. To avoid this, one can use an active gimbal where the gimbal movements are controlled. This however, is at the expense of increased system complexity. In summary, three different ways of dealing with gyroscopic forces can be used: an active gimbal mount, a passive gimbal mount, or simply letting the bearings deal with the gyroscopic forces (no gimbal mount). The last option – no gimbal – has been used for non-static application from the gyrobus [2] in the 1950's to today's successful application in the motor sports industry for kinetic energy recovery systems (KERS) such as in the winning car of the 2012 Le Mans Prototype [3]. Due to the large forces however, active magnetic bearings (AMBs) are not used, except in some particular spacecraft attitude control systems [4]. They are on the other hand used in active two-axis gimballed systems such as [5] where test bench results of a system subject to base rotations are shown to successfully attenuate gyroscopic forces using gain-scheduled control of gimbal motors based on rotational speed. In [6] a FESS is used to power a golf cart. The active gimbal mount is controlled using feed-forward input shaping and the active magnetic homopolar bearings are operated without any bias. In between the complex system of an active gimballed FESS and the simple non-gimballed FESS, we have the passive gimbal mount which has been investigated by researchers at the Center of Electromechanics, University of Texas. In [7], they identify the main sources of FESS bearing loads in roadway vehicle application. They classify the sources of bearings loads into four: shock, vibration, manoeuvring, and rotor imbalance. Furthermore, they identify an important sub-classification of manoeuvring which is gyrodynamics. It is found that vehicle shock and gyrodynamics are the most significant sources that give grounds for installing the flywheel axis vertical and in a two-axis gimbal mount. In [8], they present a prototype which they use for experimental testing. The AMBs are successfully maintaining the rotor levitated during vibration and shock motions corresponding to 150% of expected motions of a transit bus. Their passive gimbal mount is found to reduce bearings loads by about 65%, and they use shock isolators to reduce transmitted axial shock by 65%. While the passive gimbal mount is experimentally demonstrating its use, a mathematical model of the interacting dynamics of gimbal, flywheel, housing and bearings is needed to further optimise the design. Such a multi-body model is presented in [9]. The motions of the gimbal, housing, and rotor can be determined based on model parameters and the input to the model: the base frame accelerations. Active magnetic bearing (AMB) and permanent magnet bearing (PMB) forces are incorporated in the model. In addition to the four classifications from [7], the model can also be used to determine bearing loads coming from gyrocompass effects. A case study is carried out, where optimal design parameters in regard to minimum displacements and minimum bearing forces are determined. A test bench of the same system is found in [10]. The test bench design is presented and the bench is used to validate the mathematical model by comparing simulated and experimentally obtained motions of rotor and housing. The next step is to utilise the model and the test bench for the assessment of reactions forces, especially the AMB bearing loads.

In this framework, the original contribution of this work consists of demonstrating how to determine the maximum AMB forces in a magnetically suspended flywheel with and without gimbal when the foundation (the vehicle) is moving. Given the input vehicle accelerations, the AMB forces will be determined numerically using the model and experimentally using the test bench.

The article is organised as follows: First, a mathematical multi-body model of the gimbal, housing, and rotor is presented. Second, an experimentally test bench of a gimbaled FESS on a moving foundation is presented. Finally, the test bench is used to experimentally investigate the AMB forces when subject to the critical perturbations. The experimental results are compared with results obtained using the mathematical model.

## 2 Mathematical Modelling

A thorough description of the mathematical model is given in [9] and the model will only briefly be presented here. Its overall framework is a multi-body model. Global and body-attached frames are defined in Figs. 1 and 2. The rotation of the earth is included in the model while all other celestial motions are neglected. All bodies, that is housing, gimbal, and rotor, are assumed rigid. Using the Newton-Euler method, we find the force and moment equilibria of the three bodies. Reaction forces  $\mathbf{f}_1, \mathbf{f}_2, \dots, \mathbf{f}_7$  are defined in Fig. 2. The mass of each body is denoted  $m_g, m_h,$  and  $m_r$  respectively. Correspondingly, the weight of each body is denoted  $\mathbf{w}_h, \mathbf{w}_g,$  and  $\mathbf{w}_r$  and mass moment of inertia  $\mathbf{I}_g, \mathbf{I}_h,$  and  $\mathbf{I}_r$ . The force and moment equilibrium equations of gimbal, housing, and rotor become:

$$B_4 \mathbf{f}_1 + B_4 \mathbf{f}_2 + B_4 \mathbf{f}_3 + B_4 \mathbf{f}_4 - B_4 \mathbf{w}_g = m_g B_4 \mathbf{a}_4 \quad (1)$$

$$B_4 \mathbf{l}_{g1} \times B_4 \mathbf{f}_1 + B_4 \mathbf{l}_{g2} \times B_4 \mathbf{f}_2 + B_4 \mathbf{l}_{h1} \times B_4 \mathbf{f}_1 + B_4 \mathbf{l}_{h2} \times B_4 \mathbf{f}_2 + B_4 \boldsymbol{\tau}_1 + B_4 \boldsymbol{\tau}_3 \\ = B_4 \mathbf{I}_g B_4 \dot{\boldsymbol{\omega}}_4 + B_4 \boldsymbol{\omega}_4 \times (B_4 \mathbf{I}_g B_4 \boldsymbol{\omega}_4) \quad (2)$$

$$-B_5 \mathbf{f}_3 - B_5 \mathbf{f}_4 + B_5 \mathbf{f}_5 - B_5 \mathbf{f}_6 - B_5 \mathbf{f}_7 - B_5 \mathbf{w}_h = m_h B_5 \mathbf{a}_5 \quad (3)$$

$$-B_5 \mathbf{l}_{h1} \times B_5 \mathbf{f}_3 - B_5 \mathbf{l}_{h2} \times B_5 \mathbf{f}_4 - (B_5 \mathbf{r}_{4-5} + B_5 \mathbf{r}_{5-7} + B_5 \mathbf{r}_a) \times B_5 \mathbf{f}_5 \\ - (B_5 \mathbf{r}_{4-5} + B_5 \mathbf{r}_{5-7} + B_5 \mathbf{r}_b) \times B_5 \mathbf{f}_6 - B_7 \mathbf{r}_e \times B_7 \mathbf{f}_7 \\ - B_5 \mathbf{r}_{4-5} \times B_5 \mathbf{w}_h - B_5 \boldsymbol{\tau}_3 \\ = B_5 \mathbf{I}_h B_5 \dot{\boldsymbol{\omega}}_5 + B_5 \boldsymbol{\omega}_5 \times (B_5 \mathbf{I}_h B_5 \boldsymbol{\omega}_5) + m_h B_5 \mathbf{r}_{4-5} \times B_5 \mathbf{a}_4. \quad (4)$$

$$I \mathbf{f}_5 + I \mathbf{f}_6 + I \mathbf{f}_7 - I \mathbf{w}_r + I \mathbf{f}_u = m_r I \mathbf{a}_7. \quad (5)$$

$$B_7 \boldsymbol{\tau}_7 + B_7 \mathbf{r}_a \times B_7 \mathbf{f}_5 + B_7 \mathbf{r}_b \times B_7 \mathbf{f}_6 + B_7 \mathbf{r}_e \times B_7 \mathbf{f}_7 + B_7 \mathbf{r}_u \times B_7 \mathbf{f}_u \\ = B_7 \mathbf{I}_r B_7 \dot{\boldsymbol{\omega}}_8 + B_7 \boldsymbol{\omega}_7 \times (B_7 \mathbf{I}_r B_7 \boldsymbol{\omega}_8) \quad (6)$$

where the left subscript ( $I, B_1, B_2, \dots, B_7$ ) denotes the reference frame in which the vector is represented. Absolute accelerations of gimbal, housing, and rotor are  $\mathbf{a}_4, \mathbf{a}_5,$  and  $\mathbf{a}_7$  respectively, while absolute angular velocities are  $\boldsymbol{\omega}_4, \boldsymbol{\omega}_5,$  and  $\boldsymbol{\omega}_8$ . Furthermore, rotor absolute angular velocity excluding spinning velocity  $\boldsymbol{\Omega}$ , is denoted  $\boldsymbol{\omega}_7$ . We assume the rotor to be axisymmetric in order to be able to evaluate the equilibrium in reference frame  $B_7$ . The moment arms  $B_4 \mathbf{l}_{h1} = \{0 \ -h \ 0\}^T$ ,



**Fig. 1.** Sketch of a FESS (illustrated as a cylinder) located at the surface of the earth.

$B_4 \mathbf{l}_{h_2} = \{0 \ h \ 0\}^T$ ,  $B_4 \mathbf{l}_{g_1} = \{0 \ -G \ 0\}^T$ , and  $B_4 \mathbf{l}_{g_2} = \{0 \ G \ 0\}^T$  are lengths from gimbal center of mass (CM) to the point of attack of each force. The gimbal CM is assumed to be located on the gimbal pivot axes. The vector from the gimbal CM to the housing's CM is denoted  $B_5 \mathbf{r}_{4-5} = \{0 \ 0 \ -l\}^T$ , while the relative position of the rotor's CM to the housing's CM is  $B_5 \mathbf{r}_{5-7} = \{x(t) \ y(t) \ z(t)\}^T$ . The vectors from the rotor's CM to the point of attack of magnetic forces of top AMB, bottom AMB, and PMB are  $B_7 \mathbf{r}_a = \{0 \ 0 \ (a - z)\}^T$ ,  $B_7 \mathbf{r}_b = \{0 \ 0 \ -(b + z)\}^T$ , and  $B_7 \mathbf{r}_c = \{0 \ 0 \ -(e + z)\}^T$  respectively. Here, it is assumed that the angles  $\eta$ , and  $\zeta$  are small. Similarly, the vectors from the rotor's CM to the sensors are  $B_7 \mathbf{r}_c = \{0 \ 0 \ c - z\}^T$  and  $B_7 \mathbf{r}_d = \{0 \ 0 \ -d - z\}^T$ .

The joints connecting the gimbal to the housing and to the base frame are assumed ideal rotational joints. The friction torques in the joints,  $B_4 \boldsymbol{\tau}_1 = \{0 \ \tau_{y_1} \ 0\}^T$  and  $B_4 \boldsymbol{\tau}_3 = \{\tau_{x_3} \ 0 \ 0\}^T$ , are found empirically to be:

$$\begin{aligned}
 \tau_{y_1} &= -\mu_{y_1} \dot{\alpha} - \nu_{y_1} \left( |\alpha|^{p_{y_1}} \text{sign}(\dot{\alpha}) |\dot{\alpha}|^{0.2} - \text{sign}(\alpha) |\dot{\alpha}|^{0.2} \right) \\
 \tau_{x_3} &= \mu_{x_3} \dot{\beta} + \nu_{x_3} \left( |\beta|^{p_{x_3}} \text{sign}(\dot{\beta}) |\dot{\beta}|^{0.2} - \text{sign}(\beta) |\dot{\beta}|^{0.2} \right)
 \end{aligned} \tag{7}$$

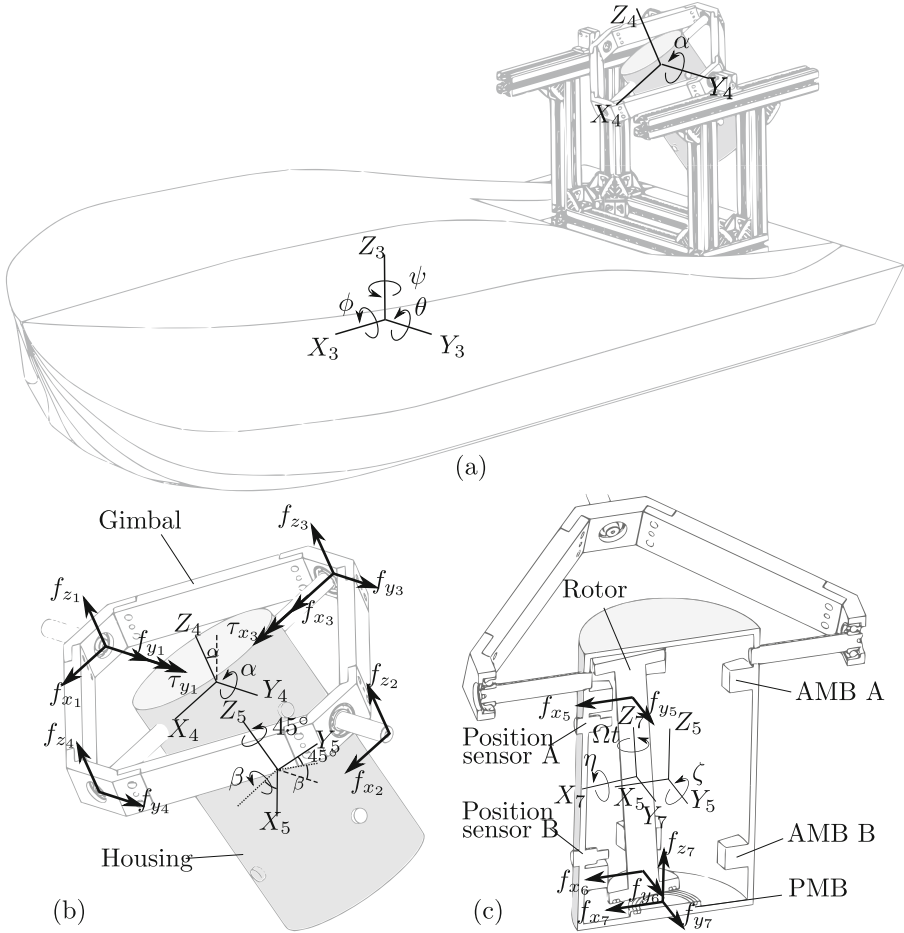


**Fig. 2.** (a): The moving foundation represented as a boat. (b): Gimbal and housing. (c): Cross-sectional view of housing and rotor.

where  $\mu_{y_1}$ ,  $\nu_{y_1}$ ,  $p_{y_1}$ ,  $\mu_{x_3}$ ,  $\nu_{x_3}$ , and  $p_{x_3}$  are empirical constants.

The rotor imbalance force coming from the unbalance  $u$  is

$$B_7 \mathbf{f}_u = u \Omega^2 \{ \cos(\Omega t) \quad \sin(\Omega t) \quad 0 \}^T. \quad (8)$$

The forces in the AMBs,  $B_5 \mathbf{f}_5 = \{ f_{x_5} \quad f_{y_5} \quad 0 \}^T$  and  $B_6 \mathbf{f}_6 = \{ f_{x_6} \quad f_{y_6} \quad 0 \}^T$ , are derived from Ampère’s circuital law, Ohm’s law, and Faraday’s law assuming no leakage, no fringing, magnetostatic behaviour, insignificant magnetic reluctance of the steel, and constant flux density. E.g., for  $f_{x_5}$  this yields:

$$f_{x_5} = \cos(\pi/8) (k_i i_{x_A} + k_s x_{b_A}) \quad (9)$$

where  $x_{b_A}$  is the rotor radial displacement at the bearings,  $k_i$  is the force-current factor and  $k_s$  is force-displacement factor [9]:

$$k_i = \mu_0 n^2 A \frac{i_0}{x_0^2}, \quad k_s = k_i \frac{i_0}{x_0} \quad (10)$$

where  $\mu_0$  is the permeability in vacuum,  $i_0$  is bias current,  $x_0$  is nominal air gap,  $A$  is the cross-sectional area of each magnet pole, and  $n$  is the number of coil windings around that pole. The AMB coil current  $i_{x_A}$  is governed by:

$$R\dot{i}_{x_A} + L\ddot{i}_{x_A} + k_u\dot{x}_{b_A} = -K_c \left( K_p \left( T_d\dot{x}_{se_A} + x_{se_A} + K_i e_{x_{se_A}} \right) + i_{x_A} \right) \quad (11)$$

where  $R$  is coil resistance,  $L$  is inductance, and  $k_u$  is the motion induced voltage coefficient. The constants  $K_c$ ,  $K_p$ ,  $T_d$ , and  $K_i$  dictate the dynamics of the Proportional-Integral-Derivative (PID) control algorithm. The radial displacement at the sensor is  $x_{se_A}$  while  $e_{x_{se_A}}$  is the integrated displacement:

$$\dot{e}_{x_{se}} = x_{se}. \quad (12)$$

The force of the PMB  ${}_{B_7}\mathbf{f}_7 = \{f_{x_7} \ f_{y_7} \ f_{z_7}\}^T$  is found using the Biot-Savart law [11] by approximating the magnetization as electric currents flowing on the axial surfaces of the magnet rings that the bearing consists of. The magnetic flux density coming from a specific current conductor on the stator part of the PMB is found as:

$${}_{B_5}\mathbf{B}' = \frac{\mu_0}{4\pi} i \int \frac{{}_{B_5}d\mathbf{l}' \times {}_{B_5}\hat{\mathbf{z}}}{r^2} \quad (13)$$

where the current conductor is split into infinitesimal vector elements  $d\mathbf{l}'$ . The vector from  $d\mathbf{l}'$  to the point where  $B'$  is evaluated is denoted  $\mathbf{r}$  and has direction  $\hat{\mathbf{z}}$  (unit vector) and length  $r$ . The electric current is found as

$$i = M \frac{w}{n_z} \quad (14)$$

where  $w$  is the height of the magnet ring,  $n_z$  is the number of current conductors on each surface, and  $M$  is the magnetic moment. The total magnetic field density coming from the stator is then

$${}_{B_5}\mathbf{B} = \sum_{n_r} \sum_{n_z} {}_{B_5}\mathbf{B}'. \quad (15)$$

where  $n_r$  is the number of axial surfaces on the stator. We find the force acting on each current conductor on the rotor part of the PMB using the Lorentz force law:

$${}_{B_7}\mathbf{f}' = i \int ({}_{B_7}d\mathbf{l}' \times {}_{B_7}\mathbf{B}) \quad (16)$$

and the total force on the rotor as

$${}_{B_7}\mathbf{f}_7 = \sum_{n_r} \sum_{n_z} {}_{B_7}\mathbf{f}'. \quad (17)$$

Finally,  $\mathbf{B}_7 \mathbf{f}_7$  is implemented in the multi-body model by first evaluating Eq. (17) for many different rotor positions and based on this, approximating the force with the linear relationship:

$$\mathbf{B}_7 \mathbf{f}_7 = \{k_r(x - \eta e) \quad k_r(y + \eta e) \quad k_z(z - z_0)\}^T \quad (18)$$

where  $k_r$  and  $k_z$  are constants and  $z_0$  is the axial equilibrium position of the rotor.

The force and moment equations, Eqs. (1)–(6), the four coil current equations (Eq. (11)), and the four constraints for the displacement integral (Eq. (12)) are set up in a system of equations

$$\mathbf{A} \mathbf{x} = \mathbf{b} \quad (19)$$

and solved in time for the unknowns

$$\mathbf{x} = \{\ddot{x} \quad \ddot{y} \quad \ddot{z} \quad \ddot{\eta} \quad \dot{\Omega} \quad \dot{i}_{x_A} \quad \dot{i}_{y_A} \quad \dot{i}_{x_B} \quad \dot{i}_{y_B} \quad \dot{e}_{x_{se_A}} \quad \dot{e}_{y_{se_A}} \quad \dot{e}_{x_{se_B}} \quad \dot{e}_{y_{se_B}} \quad f_{x_1} \quad f_{y_1} \quad f_{z_1} \quad f_{x_2} \quad f_{z_2} \quad f_{x_3} \quad f_{y_3} \quad f_{z_3} \quad f_{y_4} \quad f_{z_4} \quad \ddot{\alpha} \quad \ddot{\beta}\}^T. \quad (20)$$

### 3 Experimental Investigation

The experimental test bench can be seen in Fig. 3. Using the pneumatic actuators ⑧ ⑨, the frame is rotated and translated causing the gimbal, housing, and rotor to move. The acceleration of the frame is measured using an accelerometer ⑩ and is then used as input to the simulations. The accelerations of housing and rotor are measured using the accelerometer ④ and the position sensors ⑫. The coil currents are measured using hall effect sensors. The AMB forces are then calculated from the measured rotor position and coil current using Eq. (9) and compared to simulated results.

Figure 4 gives two examples of the dynamical behaviour of rotor displacements and AMB forces, when the frame is tilted. The left column shows the dynamical behaviour when the housing is gimbal-mounted and the right column shows the response without gimbal mounting, or in other words, when the housing is tilting with the frame. Figures 4a–d show the rotor displacements while Figs. 4e–h show the AMB forces in each direction. With gimbal (left column), the tilting frame perturbs the housing due to friction in the gimbal joints. The housing then starts to swing which causes the rotor to be displaced as well. This results in a measured maximum rotor displacement of 42  $\mu\text{m}$  (in  $X_5$ -direction) and simulated maximum rotor displacement of 43  $\mu\text{m}$  i.e. 2% deviation. The largest absolute force is also occurring in the  $X_5$ -direction and is experimentally measured to be 21 N while the simulation results yield 22 N, leading to a 5% deviation. For the non-gimballed case, the frame and the housing tilt, forcing the rotor to tilt as well. This creates a gyroscopic effect – the last term in Eq. 6 – causing the rotor to rotate perpendicular to the rotation of the frame. This can be seen in Fig. 4b and c as displacements both in  $X_5$  and  $Y_5$  directions. Consequently, the maximum absolute force is 28 N both for the experimental and numerical case. It can be concluded that the mathematical model predicts the

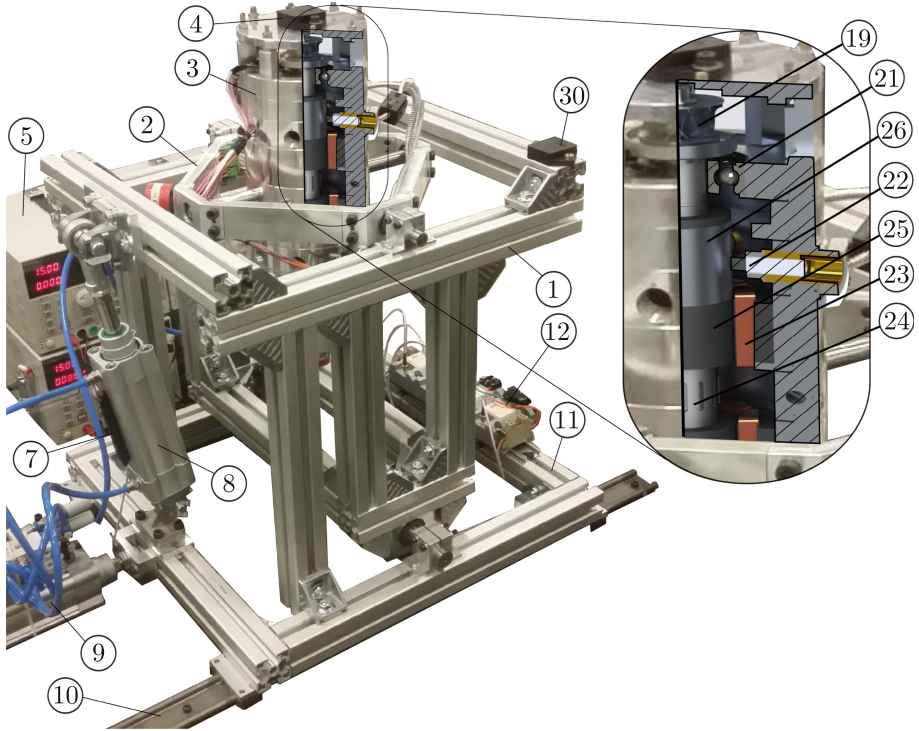


**Fig. 3.** Test bench with rotating frame ① , gimbal ② , housing ③ , housing accelerometer ④ , AMB amplifiers ⑤ , pneumatic actuator position sensor ⑦ , pneumatic actuator for rotation ⑧ , pneumatic actuator for translation ⑨ , rail ⑩ , translating frame ⑪ , proximity probe conditioners ⑫ , compressor wheel ⑲ , backup bearing ⑳ , proximity probe ㉒ , AMB stator ㉓ , rotor steel shaft ㉔ , magnetic steel sheet hub ㉕ , aluminium hub ㉖ , and frame accelerometer ㉟ .

maximum displacements and forces accurately, and that the forces are of equal magnitude for the non-gimballed and gimballed FESS in this particular case. However, if the gyroscopic moment is to be increased by either increasing rotor speed  $\Omega$ , frame rotation velocity  $\dot{\theta}$ , or rotor polar mass moment of inertia  $I_{rp}$ , the forces will not be of equal magnitude for the non-gimballed and gimballed FESS. This can be seen in Fig. 5 where the maximum force (the circled locations in Fig. 4e and f) is plotted for a gimballed and non-gimballed FESS for varying rotor rotational speed  $\Omega$ . As seen, the experimental and numerical results are in good agreement. For the gimballed case, the forces are increasing to 21 N at 31 kRPM. Here, the force is peaking due to a resonance of the swinging housing. Afterwards, the force is decreasing due to a decrease in housing swing amplitudes. For the non-gimballed case, the force continues to increase dictated by the last term in Eq. 6. It should be noted that the polar mass moment of inertia



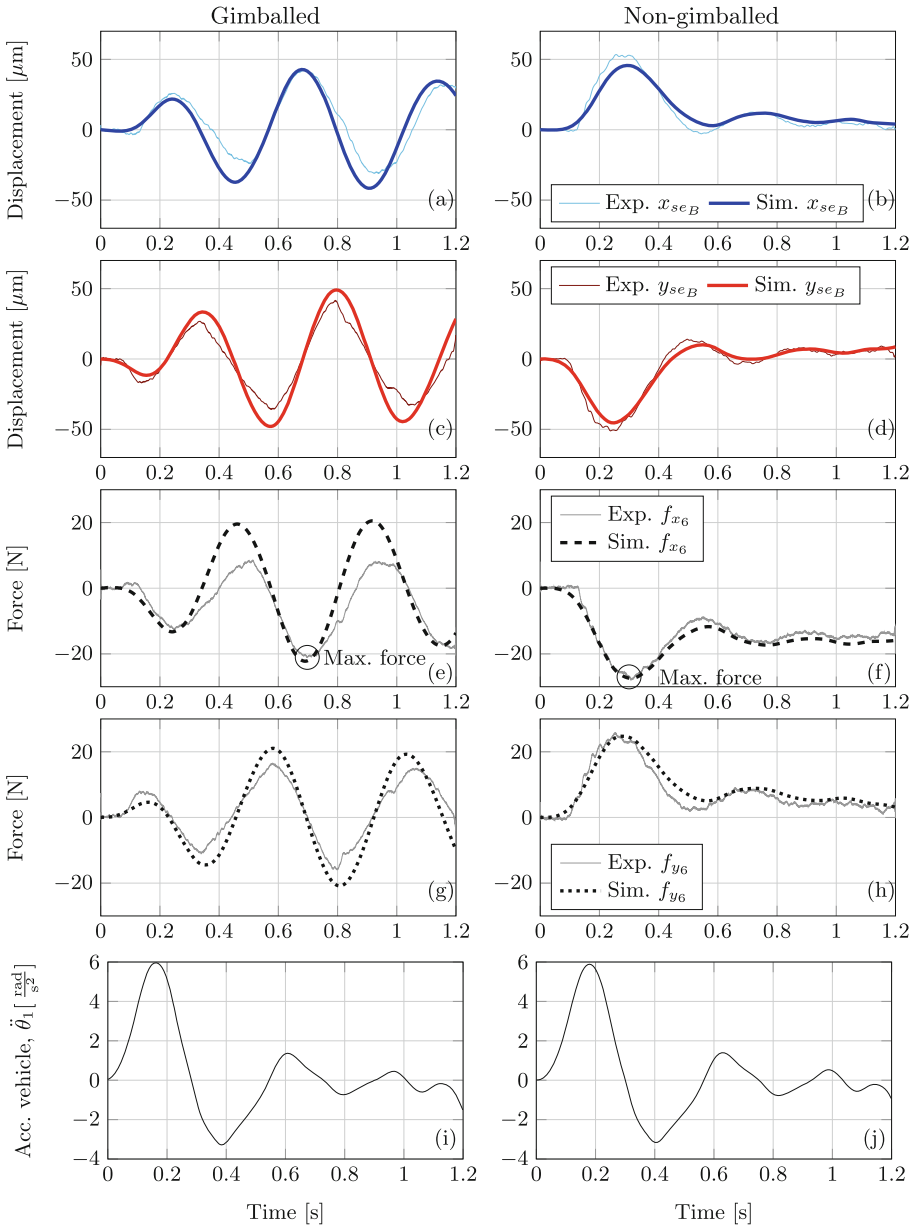


**Fig. 4.** Foundation is pitching at an angular acceleration of  $\ddot{\theta}_1$  and rotor is spinning at 31kRPM. The figures in the left column show the responses for a gimbaled system while the figures in the right column show the responses for a non-gimbaled system. Figures (a), (b), (c), and (d) show the rotor displacement at bottom sensors in  $X_5$  and  $Y_5$ -direction. Figures (e), (f), (g), and (h) show AMB forces at bottom bearing in  $X_5$  and  $Y_5$ -direction. Figures (i) and (j) show the angular accelerations of the frame which have been measured experimentally and used for simulating the two systems (left: gimbaled and right: non-gimbaled).

of the test bench rotor is much smaller than the mass moment of inertia for a real FESS flywheel.

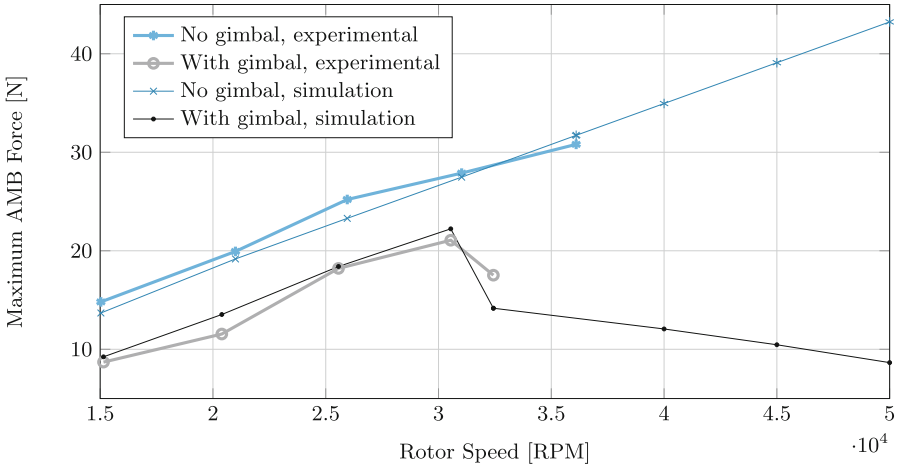


**Fig. 5.** Forces as function of RPM when foundation is rolling.

Other than the gyroscopic force, Murphy et al. [7] also find that the impact force can cause critical scenarios for some vehicle FESS applications. In Fig. 6, two examples of impact testing are seen. In both cases, the frame is translationally accelerating (surging) and the housing is gimbal-mounted. In the left column case, the translational acceleration is small (peak of  $-0.88 \text{ m/s}^2$ ) while the right column shows a case with higher translational acceleration (peak of  $-3.7 \text{ m/s}^2$ ). The gray area spans the time in which the frame is surging. The red area spans the time in which impact is happening. The overall behaviour of the movements of both rotor and housing as well as the AMB forces are captured accurately. However, the magnitude of the vibrations obtained from simulation seem to have some deviation from the experimentally measured. Especially during impact, the mathematical model has difficulties capturing the maximum rotor displacements and AMB forces. This is due to higher frequency dynamics which excite non-modelled flexible modes of frame, gimbal, housing, and gimbal joints. Although the dynamics during impact are not captured well by the model, the ensuing free response is in good agreement, thus the model can be used to predict the forces of the free response after impact.

The final type of bearing load that we will investigate is the one occurring from the rotation of the earth. When the FESS is mounted in a gimbal mount, it resembles a gyrocompass too much to ignore the gyroscopic interaction of flywheel and earth. In the mathematical model, one can choose to include the rotation of the earth. However, the dynamics of this gyrocompass effect take place on a time scale much slower than the other dynamics present in the mathematical model. Therefore, one can also choose to look at the gyrocompass effect

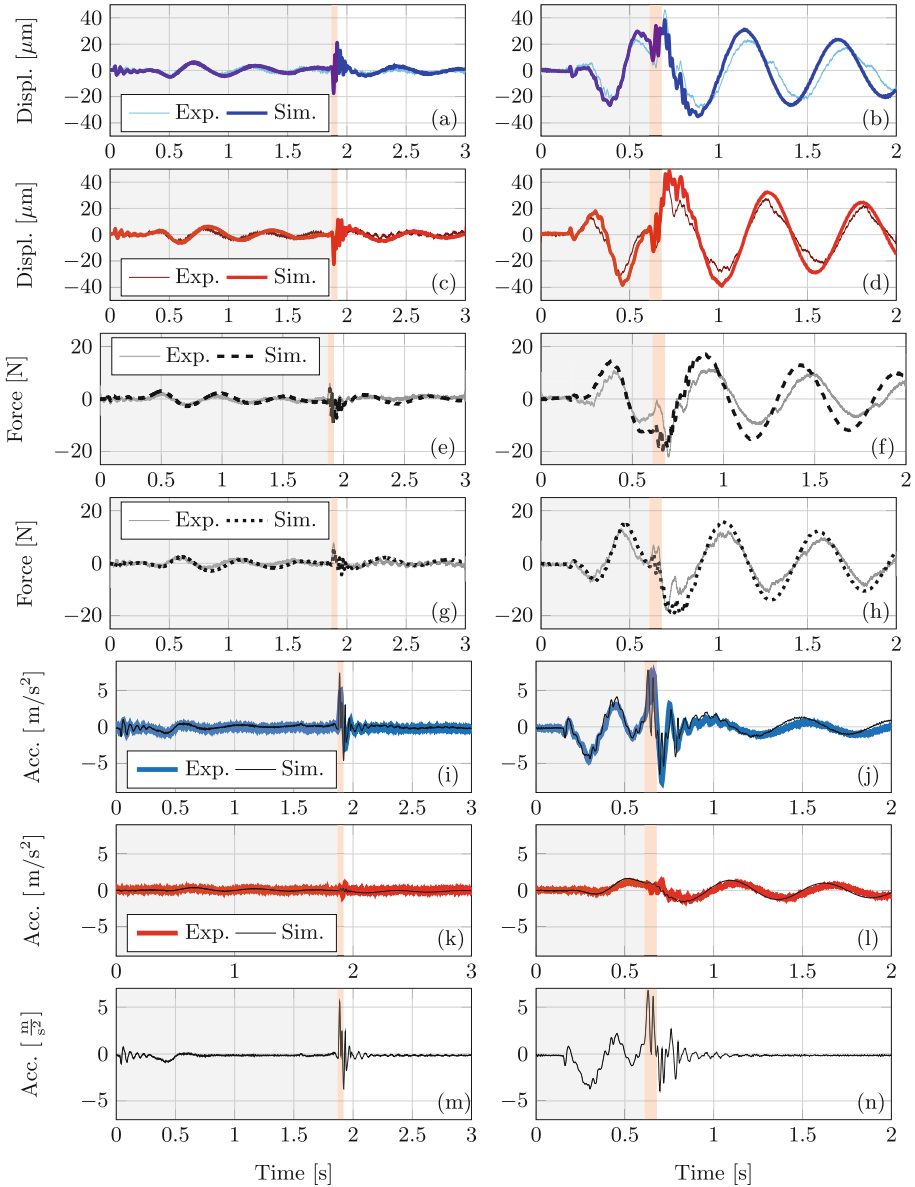


**Fig. 6.** Foundation is surging and rotor is spinning at 26 kRPM. The figures in the left column show the responses for one case (small frame acceleration) and the right column show another case (high frame acceleration). In both cases, the housing is gimbal-mounted. Figures (a), (b), (c), and (d) show the rotor displacement at bottom sensors in  $X_5$  and  $Y_5$ -direction. Figures (e), (f), (g), and (h) show AMB forces at bottom bearing in  $X_5$  and  $Y_5$ -direction. Figures (i), (j), (k), and (l) show the accelerations at the location of the accelerometer ④ in  $X_5$  and  $Y_5$ -direction. Figures (m) and (n) show the angular accelerations of the frame which have been measured experimentally and used for simulating the two cases. The gray area spans the time in which the frame is surging, while the red area spans the time in which impact is occurring.

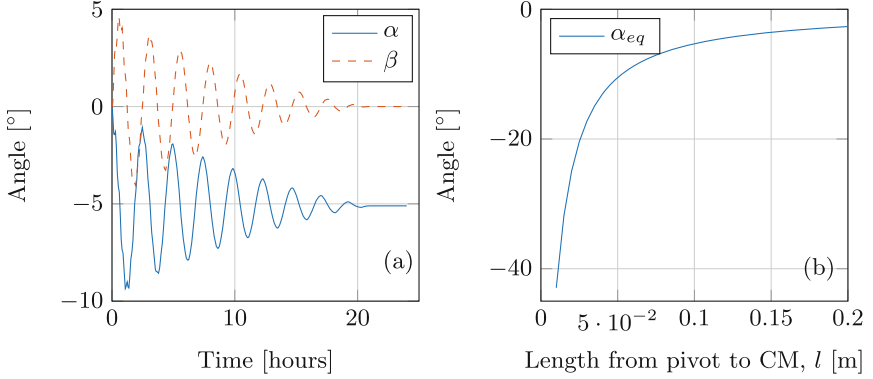


**Fig. 7.** The dynamics and static equilibrium of housing and rotor when taking into account the rotation of the earth. Flywheel specifications: Rotor mass  $m = 50$  kg, rotor polar mass moment of inertia  $I_{r_p} = 6 \text{ m}^2\text{kg}$ , location: equator  $\delta = \pi/2$ , rotor speed  $\Omega = 100$  kRPM. (a): The response of housing/rotor in time when the distance between pivot point and rotor CM is  $l = 0.1$  m. (b): The angle at which  $\alpha$  is in equilibrium for varying distance,  $l$ , between pivot point and rotor CM.

alone in a more simple model. In the following, we will only look at the reference frames  $\mathbf{B}_0$ ,  $\mathbf{B}_{0'}$ ,  $\mathbf{B}_4$ , and  $\mathbf{B}_5$ . We will consider gimbal and housing to be massless such that only inertia of the rotor is present. Furthermore we will neither look at rotor displacements relative to housing nor movements of the foundation but only the pitch and roll of the housing/rotor ( $\alpha$  and  $\beta$ ). In Fig. 7a, the 24-h response for a large FESS initially positioned in its desired vertically aligned position is shown. The FESS has a mass of  $m = 50$  kg and a polar mass moment of inertia of  $I_{r_p} = 6 \text{ m}^2\text{kg}$ . It is located at equator,  $\delta = \pi/2$  and spinning at 100 kRPM. The rotor center of mass is displaced from the pivot point with  $l = 0.1$  m which introduces a pendulum spring force giving the FESS a natural home position of vertical – had it not been for the rotation of the earth. As seen in Fig. 7a, the gyroscopic moment is forcing the rotor away from the vertical position. This causes, together with the pendulum spring, the roll and pitch angles,  $\alpha$  and  $\beta$ , to oscillate until the friction in the joints has dampened out all dynamics and the equilibrium has occurred. The angle of  $\alpha_{eq}$  at which equilibrium occurs, can be approximated from the moment equilibrium equation of the rotor:

$$\alpha_{eq} = \tan^{-1} \left( \frac{m l g}{\Omega \Omega_{earth} I_{r_p} \sin(\delta)} \right), \quad (21)$$

where higher order terms are neglected and it is assumed that  $\alpha$  and  $\beta$  are small. From this formula, one can also explain why the gyrocompass effect has not been experimentally validated in this work: Using the values for the test bench, we find that (for test bench located at DTU, Kgs. Lyngby, Denmark,  $\delta = 34$ ):

$$\alpha_{eq} = \tan^{-1} \left( \frac{3 \cdot 0.018 \cdot 9.82}{(40000/60 \cdot 2\pi) \cdot 7.27 \cdot 10^{-5} \cdot 0.00075 \sin(\frac{34}{180}\pi)} \right) = 0.014^\circ, \quad (22)$$

which would be hard to detect. Therefore, we go back to the case of the larger 50 kg FESS. In Fig. 7b, the equilibrium angle  $\alpha_{eq}$  is plotted for varying displacement of the rotor center of mass  $l$ . We see clearly that an undesirably large  $\alpha_{eq}$  will occur for low  $l$ . For example, if the distance between pivot point and rotor CM is  $l = 0.01$  m, the rotor will position itself with an angle of more than  $40^\circ$ . This will result in a static load on the AMBs, from the weight of the rotor, which is in no way desirable. From the previous examples where the foundation/vehicle was rolling and surging, we saw how the gimballed housing was swinging due to the distance  $l$  between pivot point and rotor CM. This motivates letting  $l$  be small in order to decrease the swinging pendulum motions caused by a moving foundation. In this section we saw how a small  $l$  causes large housing/rotor rotations due to the rotations of earth. This motivates letting  $l$  be large in order to decrease  $\alpha_{eq}$ . Therefore, it is important when designing the FESS, that  $l$  is chosen correctly so neither  $\alpha_{eq}$  nor the swinging motions due to a moving foundation become too large.

## 4 Conclusion

A numerical and experimental investigation of the AMB loads in a FESS with and without gimbal mount has been carried out. The focus has been on three different kinds of sources of bearings loads: gyrodynamic from a rotating frame, shock from when the moving frame experiences impact, and gyrocompass effects from the interaction of the flywheel spin and the rotation of the earth. When the frame is rotating, it is seen how the gimballed flywheel starts to swing like a pendulum. It is found that the maximum AMB forces are predicted accurately, e.g. for a rotor spinning at 31 kRPM, the deviations between the mathematical model and the experiments in the gimballed case are 2% for displacement and 5% for AMB force. For the non-gimballed case, the maximum force predicted by the mathematical model is coinciding with the measured value when the rotor is spinning at 31 kRPM. When looking at the maximum AMB forces for increasing rotor speed, it is demonstrated how the AMB forces keep on increasing for the non-gimballed case. In the gimballed case, a peak in AMB force of 21 N occurs at 31 kRPM. Afterwards, the AMB force decreases with increasing rotor speed.

When exposing the FESS to a shock, it is found that the rotor displacements and AMB forces are not accurately predicted during impact. However, the ensuing free response of the rotor can be predicted by the model.

Finally, when investigating the effect of the rotation of the earth, it was found that for a low distance between rotor center of mass and gimbal pivot point, the rotation of the earth does significantly affect the FESS equilibrium. This means that the home position of the rotor will not be vertical but instead will be at an angle with respect to vertical. This results in a non-intentional static load on the AMBs from the weight of the rotor. Therefore, it is concluded that the distance between rotor center of mass and gimbal pivot point must be chosen correctly in order to be large enough for mitigating the effect of the rotation of the earth while at the same time not be so large that the swinging pendulum motions

become critical when the foundation is moving. This distance, from rotor center of mass to gimbal pivot point, is a good example of a system design parameter that can be profitably chosen by the help of the mathematical model because different scenarios then can be simulated.

## Appendix

Input parameters for the mathematical model:

	Unit	Description	Value
$z_0$	[m]	Rotor axial equilibrium	0.0109
$z_{3-4}$	[m]	Distance from vehicle CM to gimbal CM	0.413
$l$	[m]	Distance from gimbal pivot point to housing CM	0.0177
$l_{acc}$	[m]	Distance from pivot point to accelerometer <sup>④</sup>	0.1802
$a$	[m]	Length from rotor CM to AMB A	0.0412
$b$	[m]	Length from rotor CM to AMB B	0.0348
$c$	[m]	Length from rotor CM to sensor A	0.0852
$d$	[m]	Length from rotor CM to sensor B	0.0748
$e$	[m]	Length from rotor CM to PMB	0.1384
$G$	[m]	Gimbal outer diameter	0.158
$h$	[m]	Gimbal inner diameter	0.158
$\mu_{y_1}$	[m <sup>2</sup> N/s]	Friction coefficient	0.112
$\mu_{x_3}$	[m <sup>2</sup> N/s]	Friction coefficient	0.056
$\nu_{y_1}$	[ ]	Friction coefficient	0.042
$\nu_{x_3}$	[ ]	Friction coefficient	0.028
$p_{y_1}$	[-]	Friction parameter	0.02
$p_{x_3}$	[-]	Friction parameter	0.02
$m_r$	[kg]	Rotor mass	3
$m_h$	[kg]	Housing mass	14.8
$m_g$	[kg]	Gimbal mass	1.634
$I_{r_p}$	[m <sup>2</sup> g]	Rotor polar mass moment of inertia	0.75
$I_{h_p}$	[m <sup>2</sup> g]	Housing polar mass moment of inertia	46
$I_{g_p}$	[m <sup>2</sup> g]	Gimbal polar mass moment of inertia	34
$I_{r_t}$	[m <sup>2</sup> g]	Rotor transversal mass moment of inertia	24.5
$I_{h_t}$	[m <sup>2</sup> kg]	Housing transversal mass moment of inertia	167
$I_{g_t}$	[m <sup>2</sup> kg]	Gimbal transversal mass moment of inertia	15.7
$g$	[m/s <sup>2</sup> ]	Acceleration of gravity	9.82
$M$	[kA/m]	Magnetic moment	955

(continued)

(continued)

	Unit	Description	Value
$w$	[mm]	Magnet ring height and width	3
$n_z$	[-]	Number of current conductors axially	10
$n_r$	[-]	Number of current conductors radially	3
$r$	[mm]	Radius of current conductors	21.3, 24.3, 27.3
$k_r$	[kN/m]	PMB radial stiffness	-17
$k_z$	[kN/m]	PMB axial stiffness	40
$h_0$	[mm]	PMB air gap	2.3
$\mu_0$	[H/m]	Permeability in free space	$4\pi \cdot 10^{-7}$
$K_c$	[V/A]	Current control proportional parameter	150
$K_p$	[A/m]	Position control proportional parameter	3000
$T_d$	[ms]	Position control derivative parameter	1.2
$K_i$	[1/s]	Position control integral parameter	3.33
$k_i$	[N/A]	Force/current factor	$k_{i_{x_A}} = 152$ $k_{i_{x_B}} = 177$ $k_{i_{y_A}} = 187$ $k_{i_{y_B}} = 166$
$k_s$	[N/mm]	Force/displacement factor	$k_{s_{x_A}} = 182$ $k_{s_{x_B}} = 226$ $k_{s_{y_A}} = 240$ $k_{s_{y_B}} = 216$
$k_u$	V/(m/s <sup>2</sup> )	Motion induced voltage coefficient	$1.17k_i$
$L$	H	Inductance	$0.00042k_i$
$\omega_c$	[Hz]	Low-pass filter cut-off frequency	920
$\zeta$	[-]	Low-pass filter damping ratio	1
$R$	[ $\Omega$ ]	Coil resistance	4.5

## References

1. Flynn, M.M., Zierer, J.J., Thompson, R.C.: Performance testing of a vehicular flywheel energy system. SAE Technical Papers, pp. 1–10. SAE International (2005). <https://doi.org/10.4271/2005-01-0809>
2. Genta, G.: Kinetic Energy Storage. Butterworth-Heinemann, Oxford (1985)
3. Williams Hybrid Power (2013). [http://www.ukintpress-conferences.com/uploads/SPKPMW13R/d1\\_s1.p2\\_ian\\_foley.pdf](http://www.ukintpress-conferences.com/uploads/SPKPMW13R/d1_s1.p2_ian_foley.pdf). Accessed 6 Feb 2018
4. Dever, T.: Development of a high specific energy flywheel module, and studies to quantify its mission applications and benefits (2013). <http://ntrs.nasa.gov/archive/nasa/casi.ntrs.nasa.gov/20150009522.pdf>. Accessed 6 Feb 2018
5. Nakai, H., Matsuda, A., Suzuki, M.: Development and testing of the suspension for a flywheel battery. Control Eng. Pract. **9**(10), 1039–1046 (2001)
6. Rachmanto, B., Nonami, K.: A study on AMB-flywheel powered electric vehicle. J. Syst. Design Dyn. **3**, 659–670 (2009)

7. Murphy, B.T., Bresie, D.A., Beno, J.H.: Bearing loads in a vehicular flywheel battery. SAE Technical Paper 970213 (1997). <https://doi.org/10.4271/979213>
8. Hawkins, L., Murphy, B., Zierer, J., Hayes, R.: Shock and vibration testing of an AMB supported energy storage flywheel. *JSME Int. J. Ser. C-Mech. Syst. Mach. Elem. Manuf.* **46**(2), 429–435 (2003)
9. Dagnaes-Hansen, N., Santos, I.F.: Magnetically suspended flywheel in gimbal mount - nonlinear modelling and simulation. *J. Sound Vib.* **432**, 327–350 (2018)
10. Dagnaes-Hansen, N., Santos, I.F.: Magnetically suspended ywheel in gimbal mount - test bench design and experimental validation (submitted)
11. Griffiths, D.J.: *Introduction to Electrodynamics*. Prentice-Hall, Englewood (1981)





# Application of the Controllable Magnetorheological Squeeze Film Dampers for Minimizing Energy Losses and Driving Moment of Rotating Machines

Jaroslav Zapoměl<sup>1,2</sup>(✉), Petr Ferfecki<sup>2</sup>, and Jan Kozánek<sup>1</sup>

<sup>1</sup> The Institute of Thermomechanics,  
Dolejškova 5, 18200 Prague, Czech Republic  
{zapomel, kozanek}@it.cas.cz

<sup>2</sup> VŠB-Technical University of Ostrava,  
17. listopadu 15, 70833 Ostrava, Czech Republic  
{jaroslav.zapomel, petr.ferfecki}@vsb.cz

**Abstract.** The energy losses generated in rolling element bearings rise with increasing magnitude of the force transmitted between the rotor and the stationary part. A frequently used technological solution, which makes it possible to minimize the transmitted force, consists in adding damping devices to the rotor supports. To achieve their optimum performance in a wide range of operating speeds, their damping effect must be adaptable to the current angular velocity. This is offered by magnetorheological squeeze film dampers. Their main parts are two concentric rings separated by a layer of magnetorheological oil. Its squeezing produces the damping force. As magnetorheological fluids are sensitive to magnetic induction, the change of magnetic flux passing through the lubricating film changes the damping force. The goal of the carried out investigations was to study the influence of controllable damping in rotor supports on energy losses and driving moment of the motor in different velocity ranges. The investigations were performed by computational simulations. The rotor was rigid, supported by magnetorheological squeeze film dampers, and excited by its unbalance. The results show that appropriate adaptation of the magnitude of the damping force to the current operating speed arrives at minimizing the energy losses generated in the rotor supports. The performed analysis shows a new possibility of magnetorheological squeeze film dampers, which leads to improvement of performance of rotating machines and points out at a new field of their prospective application.

**Keywords:** Rolling resistances in bearings · Energy losses reduction  
Driving moment minimization · Controllable damping  
Magnetorheological squeeze film dampers · Mathematical modelling

## 1 Introduction

The rotor weight, unbalance, ground excitation, and technological loading induce the forces transmitted between the rotating and the stationary part of rotating machines. Except the wear of the support elements, they cause resistances against the rotor

turning, which arrives at a variation of the driving moment, heating of the bearings and bearing housings, and consequently, at energy losses.

Because of high stiffness and low resistance against rotation the rotors are frequently mounted in rolling element bearings. To reduce the force transmitted to the rotor stationary part the damping devices are added to the support elements. In the field of rotor dynamics, the squeeze film dampers working on the principle of squeezing a thin layer of lubricating film between two concentric rings are often used. A simple dynamical analysis of a rigid rotor excited by the unbalance [1] shows that the magnitude of the transmitted force depends on the speed of the rotor rotation and amount of damping in the rotor support elements (Fig. 1).

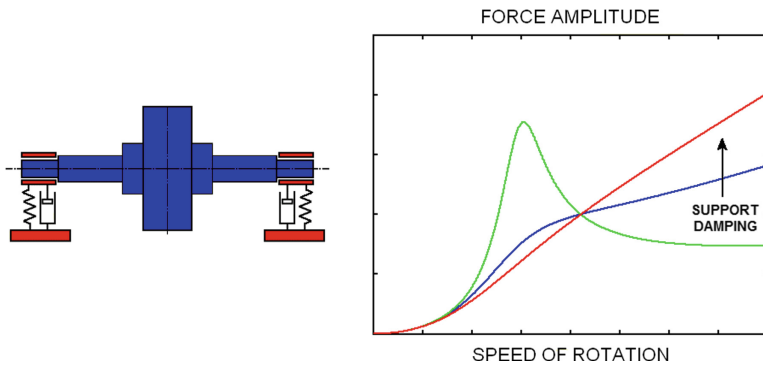


**Fig. 1.** Dependence of the transmitted force on speed and support damping.

As evident from Fig. 1, to minimize the force transmitted between the rotor and its stationary part in a wide range of operating speeds, the damping effect of the damping devices placed in the rotor supports must be controllable and adaptable to the current operating conditions.

Several design strategies based on mechanical, hydraulic, or electromagnetic principles have been developed to control the damping force. New and efficient possibilities consist in utilizing smart and advanced lubricating materials, the physical properties of which are reversibly changed by the action of an electric or magnetic field.

The operation of electrorheological squeeze film dampers requires high voltage to be used between the damper rings. Their application in the field of rotordynamics and the development of their mathematical models are discussed in [2, 3].

The magnetorheological dampers are, by contrast, supplied with low voltage and the electric current of units of amperes. The details on their design, work, and experimental investigations are reported in many journal articles and conference papers, e.g. in [4, 5]. The mathematical model of a short squeeze film magnetorheological damper developed for analysis of both the steady state and transient vibrations of rotors by Zapomel et al. can be found in [6]. Its application for investigation of minimizing the energy losses in supports of simple rotor systems is reported in [7]. The optimum current control in a wide range of operating speeds is presented in [8].

This paper deals with rigid rotors supported by magnetorheological squeeze film dampers. The attention is focused on the energy dissipation due to the damping process, on the energy losses caused by resistances against the rotor rotation in the rotor supports, and on the effect of these factors on the variation of the moment driving the rotor. The study is aimed at the possibilities of minimizing the energy losses and variation of the driving moment by means of control of the magnitude of the magnetorheological damping force in different speed ranges. The results of the carried out computational simulations show that appropriate adaptation of the damping force to the operating speed makes it possible to minimize the energy losses and variation of the moment maintaining a rigid rotor in turning at a constant angular velocity.

## 2 Modelling of the Magnetorheological Squeeze Film Damper

The principal parts of magnetorheological squeeze film dampers (Fig. 2) are two concentric rings. The gap between them is filled with a thin layer of magnetorheological oil. The inner ring is coupled with the shaft by a rolling element bearing and with the damper housing by flexible elements (often by a cage spring). The outer ring is fixed to the damper body. Squeezing the lubricating layer due to the rotor lateral vibration produces the damping force. The electric current generates magnetic flux in electric coils embedded in the damper body. The flux passes through the lubricant and because of the sensitivity of magnetorheological oils to magnetic induction (magnetic flux density) the change of the current can be used to control the damping force.

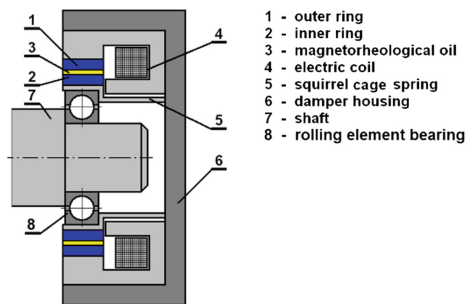


**Fig. 2.** A magnetorheological squeeze film damper.

The developed mathematical model of the magnetorheological squeeze film damper is based on assumptions of the classical theory of lubrication, except that for the lubricant. The magnetorheological oil is represented by bilinear material, the yielding shear stress of which is a function of magnetic induction.

Then the pressure distribution in the full oil film is described by the Reynolds equation adapted to bilinear material. Its derivation of which can be found in [6]

$$\frac{\partial}{\partial Z} \left( \frac{1}{\eta_C} h^3 p' \right) = 12\dot{h} \quad \text{for } 0 \leq Z \leq Z_C, \quad (1)$$

$$\frac{\partial}{\partial Z} \left[ \frac{1}{\eta} \left( h^3 p' + 3h^2 \tau_y + 8 \frac{\tau_C^3}{p'^2} - 12 \frac{\tau_y \tau_C^2}{p'^2} \right) - \frac{8}{\eta_C} \frac{\tau_C^3}{p'^2} \right] = 12\dot{h} \quad \text{for } \dot{h} < 0, Z > Z_C, \quad (2)$$

$$Z_C = -\frac{\tau_C h^2}{6\eta_C \dot{h}}, \quad (3)$$

$$p'_C = -\frac{2\tau_C}{h}. \quad (4)$$

$p$  is the pressure,  $p'$  stands for the pressure gradient in the axial direction,  $Z$  is the axial coordinate defining the position in the oil film,  $h$  is the film thickness,  $\tau_y$  is the yielding shear stress,  $\tau_C$  is the shear stress at the core border (the core is the region in the oil layer where the flow velocity rate is low and the oil behaves almost as solid matter [9, 10]),  $\eta_C$  is the oil dynamic viscosity in the core area,  $\eta$  is the oil dynamic viscosity outside the core area,  $Z_C$  defines the axial coordinate of the location where the core touches the rings surfaces, denotes the pressure gradient in the axial direction at location  $Z_C$ , and  $(\cdot)$  denotes the first derivative with respect to time.

At locations where the thickness of the oil layer rises with time ( $\dot{h} > 0$ ), a cavitation is assumed. Based on the results of measurements, it is supposed that pressure of the medium in cavitation areas remains constant and equal to the pressure in the ambient space [11].

The  $y$  and  $z$  components of the hydraulic damping force ( $F_{mry}$ ,  $F_{mrz}$ , respectively) are calculated by integration of the pressure distribution  $p_d$  around the circumference and along the length  $L_D$  of the damper taking into account different pressure profiles in noncavitated and cavitated regions

$$F_{mry} = -2R_D \int_0^{\frac{L_D}{2}} \int_0^{2\pi} p_d \cos \varphi \, d\varphi \, dZ, \quad (5)$$

$$F_{mrz} = -2R_D \int_0^{\frac{L_D}{2}} \int_0^{2\pi} p_d \sin \varphi \, d\varphi \, dZ. \quad (6)$$

$R_D$  is the mean radius of the damper clearance and  $\varphi$  is the circumferential coordinate of the position in the oil film.

As evident from (2), the yielding shear stress determines the pressure distribution in the damper gap and consequently, components of the damping force. Its dependence on magnetic induction is approximated by a power function

$$\tau_y = k_y B^{n_y}. \quad (7)$$

$B$  is the magnetic induction, and  $k_y$  and  $n_y$  are the proportional and exponential material constants of the magnetorheological oil.

The damper body is assumed to be composed of a set of meridian segments and each segment as a divided core of an electromagnet. This idea enables magnetic induction to be expressed in the damper gap

$$B = k_B \mu_0 \mu_{MR} \frac{I}{h}. \quad (8)$$

$\mu_0$  is the vacuum permeability,  $\mu_{MR}$  is the relative permeability of the magnetorheological oil,  $I$  is the applied current, and  $k_B$  is the damper design parameter [12].

### 3 Energy Losses in the Support Elements

The rotor is coupled with the stationary part through rolling element bearings mounted in the inner damper rings, which are connected with the damper housing by a cage spring. Material damping, friction due to the slip of the rolling elements in the contact areas, and hydraulic resistance produced by the lubricant are the main causes of dissipation of mechanical energy in rolling element bearings.

The rolling resistance moment  $M_B$  acting on the rotor journal in the direction opposite to its rotation is proportional to the equivalent force  $F_{BE}$  transmitted through the bearing [13]

$$M_B = F_{BE} f_B \frac{d_H}{2}. \quad (9)$$

$d_H$  is the diameter of the bearing hole (diameter of the shaft journal) and  $f_B$  is the rolling resistance coefficient of the bearing, the magnitude of which depends on the bearing type.

The equivalent force is defined

$$F_B = X F_R + Y F_A. \quad (10)$$

$F_R, F_A$  are the radial and axial components of the force transmitted through the bearing and  $X, Y$  are the radial and axial loading coefficients [13].

Consequently, the loss power  $P_B$  is given by a product of the rolling resistance moment  $M_B$  and angular speed of the rotor rotation  $\omega$

$$P_B = M_B \omega. \quad (11)$$

## 4 The Investigated Rotor System

The investigated rotor (Fig. 3) is rigid. It consists of a shaft and one disc attached to it. The rotor is coupled with the rigid stationary part by two magnetorheological squeeze film dampers at both its ends. The rotor is loaded by its weight and by the disc unbalance. The cage springs are prestressed to eliminate their deflection caused by the rotor weight. The whole system can be considered as symmetric with respect to the disc middle plane. The rotor is coupled with the motor by a teeth coupling. The whole system turns at constant angular speed.

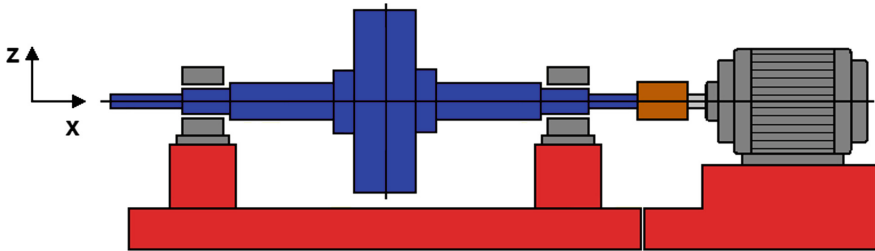


Fig. 3. The investigated rotor system.

In the computational model, the rotor is considered as absolutely rigid, and the magnetorheological dampers are represented by springs and force couplings. The equations of motion were set up by employing the Lagrange equations of the second kind. After performing the manipulations, they take the form

$$m_R \ddot{y} = -b_P \dot{y} - 2k_D y + m_R e_T \dot{\vartheta}^2 \cos \vartheta + 2F_{mry} \quad (12)$$

$$m_R \ddot{z} = -b_P \dot{z} - 2k_D z + m_R e_T \dot{\vartheta}^2 \sin \vartheta - m_R g + 2F_{mrz} + 2F_{PS} \quad (13)$$

$$M_M = -m_R e_T \ddot{y} \sin \vartheta + m_R e_T \ddot{z} \cos \vartheta + m_R e_T g \cos \vartheta + 2M_B \quad (14)$$

$m_R$  is the rotor mass,  $k_D$  is the stiffness of one squirrel cage spring,  $b_P$  is the rotor damping coefficient (environment),  $e_T$  is eccentricity of the rotor centre of gravity,  $g$  is the gravity acceleration,  $t$  is the time,  $y$ ,  $z$  are displacements of the rotor centre in the horizontal and vertical directions,  $F_{PS}$  is the force prestressing the squirrel cage spring,  $\vartheta$  is the rotor angular position, and  $(\cdot)$  denotes the second derivative with respect to time.

As rotation of the motor is assumed to be constant, Eqs. (12) and (13) are decoupled from Eq. (14). The latter is used to determine the time history of the driving moment  $M_M$ , which ensures constant angular velocity of the rotor.

The steady state solution of the motion Eqs. (12) and (13) was obtained by application of the trigonometric collocation method.

## 5 Results of the Simulations

The technological parameters of the analysed rotor system are: the rotor mass 430 kg, the coefficient of the rotor linear damping caused by the environment 100 Ns/m, the stiffness of one cage spring 3.0 MN/m, the eccentricity of the rotor centre of gravity 50  $\mu\text{m}$ , the magnetorheological squeeze film damper length/diameter 50/150 mm, the width of the damper gap 0.8 mm, the oil dynamic viscosity outside the core area 0.2 Pas, the oil dynamic viscosity in the core area 300 Pas, the magnetorheological oil proportional and exponential constants 20000, 1.1, respectively, the oil relative permeability 6, the damper design parameter 60, the shaft journal diameter 110 mm, the bearing rolling resistance coefficient 0.0015, and the bearing radial and axial loading coefficients 1.0, 0.0, respectively.

The task was to analyse the behaviour of the studied system for two magnitudes of the operating speed: 130, 500 rad/s.

A simple dynamical analysis provides the approximate value of the critical speed 118 rad/s. It implies the investigated velocities are close to and higher than the critical one.

The steady state orbits of the rotor centre for angular velocities 130 and 500 rad/s are drawn in Fig. 4. It is evident that rising damping leads to substantial reduction of the orbit size for the velocity close to the critical one. On the other hand, increasing damping has almost no influence on the vibration if the rotor turns at speed sufficiently higher than the critical one.

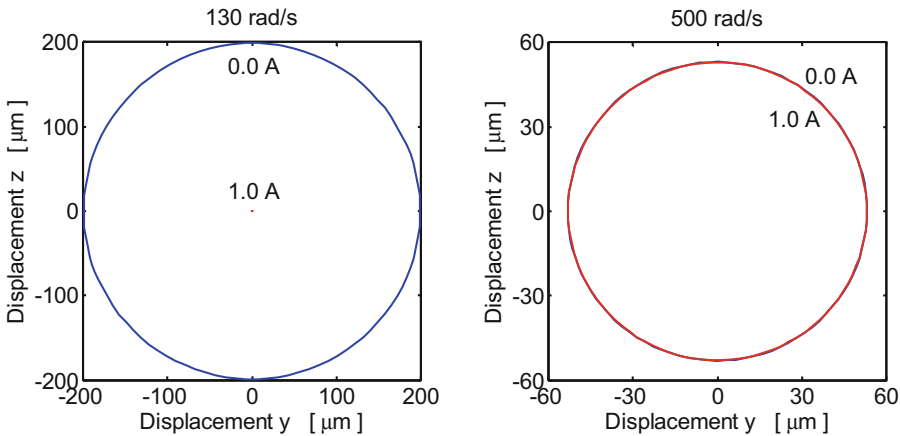
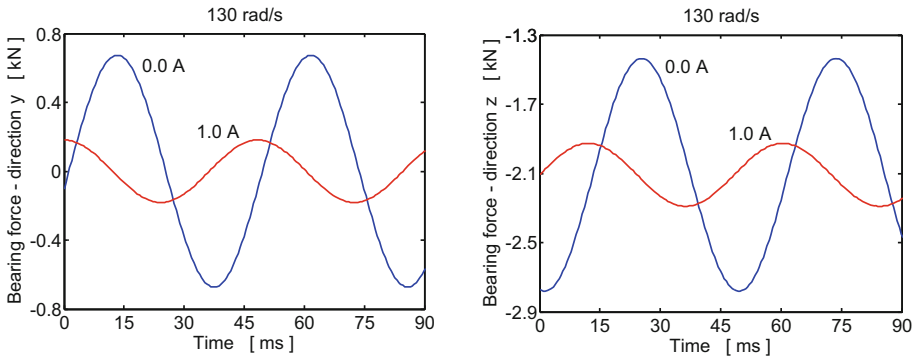


Fig. 4. Steady state orbits of the rotor centre.

The time history of the force transmitted through one bearing in the horizontal ( $y$ ) and vertical ( $z$ ) directions is depicted in Fig. 5. The results are related to the case when the rotor turns at speed of 130 rad/s. The mean value of the vertical component is not zero because of the transmission of the rotor weight.

The time histories of the equivalent force, which determines energy losses in rolling element bearings, are drawn for two velocities of 130 and 500 rad/s and for two magnitudes of the applied current (0.0, 1.0 A) in Figs. 6 and 7. The results show that

the rising damping (rising magnitude of the applied current) reduces the maximum value of the equivalent force and its variation for the velocity close to the critical one (130 rad/s), while for higher angular speed (500 rad/s) it leads to increase in its magnitude and variation.



**Fig. 5.** Time history of the y and z components of the force transmitted to the stationary part.

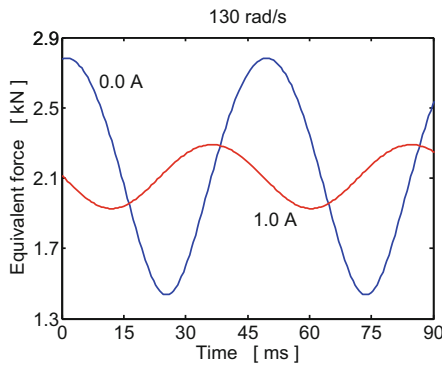


**Fig. 6.** Time history of the equivalent force (130 rad/s).

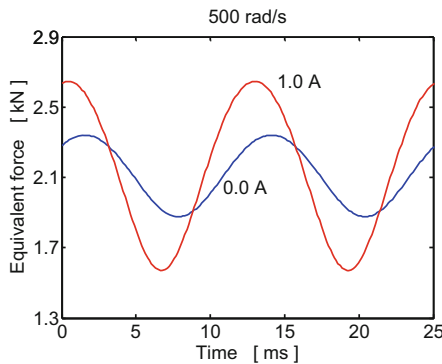


**Fig. 7.** Time history of the equivalent force (500 rad/s).



As evident from Fig. 8, the same holds for the loss power caused by the rolling resistance in the rotor bearings and fully corresponds to the dependence of the loss power on the applied current as drawn in Fig. 9. For the velocity close to the critical speed (130 rad/s), rising current reduces the loss power. When the current reaches magnitude of about 0.7 A, the vibration of the rotor is almost suppressed and the loss power takes a constant value. On the other hand, for the velocity sufficiently higher than the critical one, rising current (damping effect) increases the energy losses generated in the bearings.

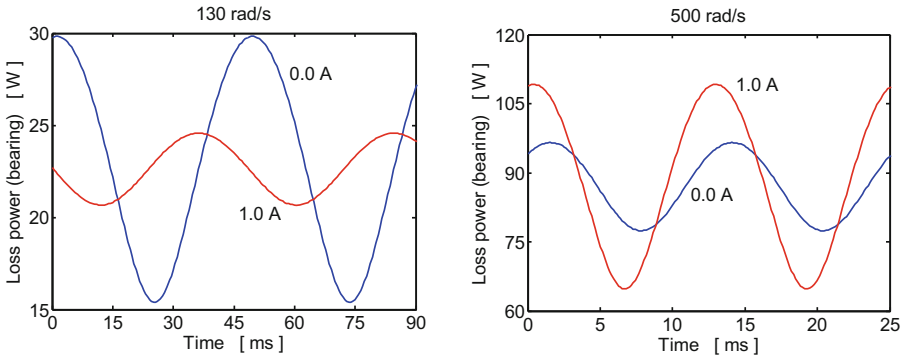


**Fig. 8.** Time history of the loss power caused by the rolling resistances.

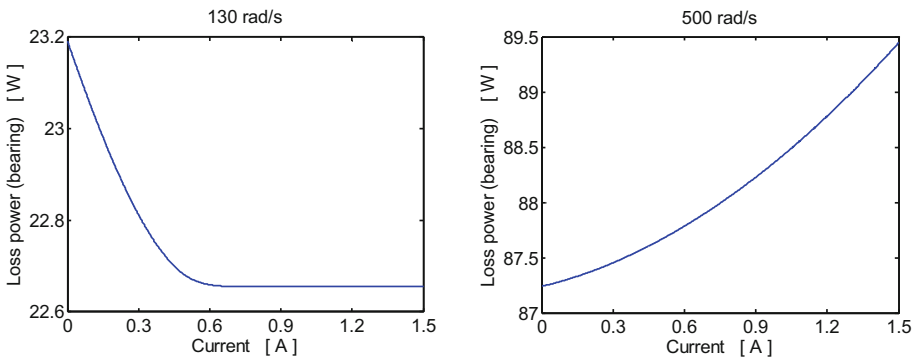


**Fig. 9.** Dependence of the loss power in the bearing on the applied current (damping effect).

Another source of the energy losses is the oil film, the squeezing of which arrives at the energy dissipation and thus at the vibration attenuation. For the angular speed of 130 rad/s rising current increases the damping effect, reduces the vibration amplitude (Fig. 4), and the energy dissipation in oil film (Fig. 10). For angular velocity sufficiently higher than the critical one rising current increases the loss power while attenuation of the vibration amplitude remains almost unchanged (Fig. 4).

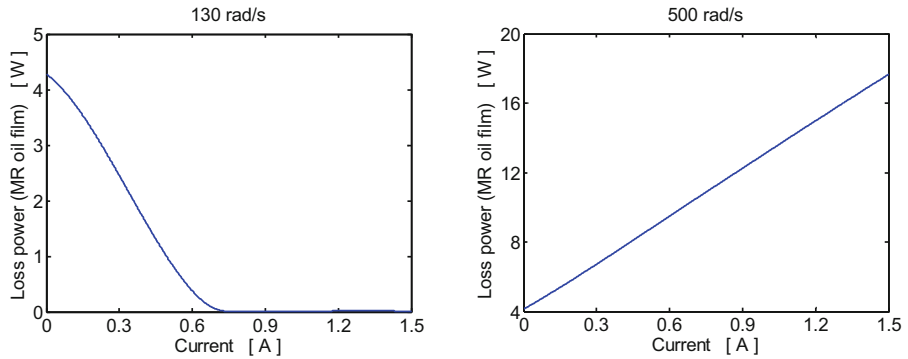


**Fig. 10.** Dependence of the loss power in the oil film on the applied current (damping effect).

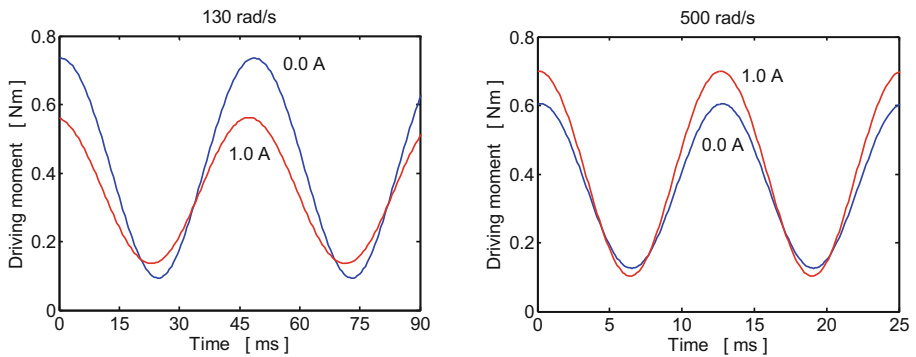


**Fig. 11.** Time history of the driving moment of the motor.

The time histories of the driving moment (the moment of the motor) for operating speeds of 130 and 500 rad/s and for two magnitudes of the applied current (0.0, 1.0 A) are depicted in Fig. 11. The driving moment depends on the rolling resistance moment in the bearings, the energy dissipated in the lubricating layer, and on the rotor unbalance. All these factors are time variable, which implies that to achieve a constant speed of the rotor rotation, the magnitude of the driving moment must be a periodic function of time.

The dependence of the power of the driving motor on the current feeding the magnetorheological dampers is evident from Fig. 12. It shows that rising damping (rising current) leads to reducing the power of the motor for the speed of rotation close to the resonance one while for higher angular speed rising damping rises the power. Taking into account the results drawn in Fig. 4 related to higher angular speed, decrease of damping reduces the energy losses but has almost no influence on the rotor vibration amplitude. These results clearly demonstrate the efficiency of controlling the damping effect with the aim of minimizing the energy losses during the operation of rotating machines.

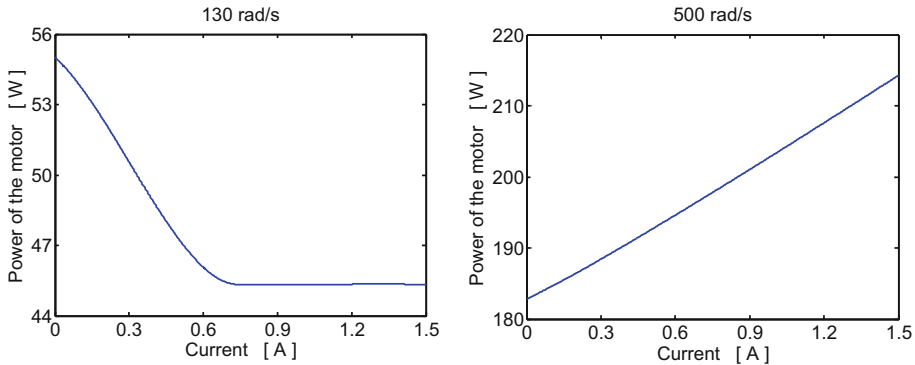


**Fig. 12.** Dependence of the power of the motor on the applied current (damping effect).

## 6 Conclusions

The investigation of the influence of the damping effect on energy losses in rolling element bearings and on the moment and loss power of the driving motor operating in different speed ranges was the subject of the accomplished research. The damping effect is controlled by the change of magnetic flux passing through the thin layer of lubricating oil of magnetorheological squeeze film dampers. The results of the performed computational simulations confirm that appropriate adaptation of the damping force to the speed of the rotor rotation makes it possible to reduce the energy losses and the driving moment of the motor. The development of the new mathematical model of a short magnetorheological squeeze film damper, its implementation in the computational procedures for investigation of energy losses and driving moment of rigid rotors, and learning more on the influence of the controllable squeeze film dampers on the behaviour of rotor systems are the principle contributions of the carried out research work. The possibility of employing the magnetorheological squeeze film dampers to improve the technological parameters of rotating machines represents new potential of their application in the field of rotordynamics.

**Acknowledgements.** The research work reported in this article was made possible by the National Programme of Sustainability (project LQ1602 - IT4Innovations excellence in science) and by the Czech Academy of Sciences (project Strategy AV21 - Efficient Energy Transformation and Storage). The support is highly acknowledged.


## References

1. Zapoměl, J., Ferfecki, P., Kozánek, J.: Determination of the transient vibrations of a rigid rotor attenuated by a semiactive magnetorheological damping device by means of computational modelling. *Appl. Comput. Mech.* **7**, 223–234 (2013)
2. Morishita, S., Mitsui, J.: Controllable squeeze film damper (An application of electro-rheological fluid). *ASME J. Vib. Acoust.* **114**, 354–357 (1992)

3. Jung, S.Y., Choi, S.B.: Analysis of a short squeeze-film damper operating with electrorheological fluids. *Tribol. Trans.* **38**, 857–862 (1995)
4. Wang, J., Meng, G.: Magnetorheological fluid devices: principles, characteristics and applications in mechanical engineering. In: *Proceedings of the Institution of Mechanical Engineers. Part L: Journal of Materials: Design and Applications*, vol. 215, pp. 165–174 (2001)
5. Gong, X., Ruan, X., Xuan, S., Yan, Q., Deng, H.: Magnetorheological damper working in squeeze model. *Adv. Mech. Eng.* **6**, 410158 (2014)
6. Zapoměl, J., Ferfecki, P., Forte, P.: A new mathematical model of a short magnetorheological squeeze film damper for rotordynamic applications based on a bilinear oil representation - derivation of the governing equations. *Appl. Math. Model.* **52**, 558–575 (2017)
7. Zapoměl, J., Ferfecki, P.: Application of the magnetorheological squeeze film dampers for reducing energy losses in supports of rotors of rotating machines. In: *Proceedings of the ASME 2017 International Design Engineering Technical Conferences and Computers and Information in Engineering Conference IDETC/CIE 2017, DETC2017-67433*, Cleveland, OH, USA (2017)
8. Zapoměl, J., Ferfecki, P.: Vibration attenuation of rotating machines by application of magnetorheological dampers to minimize energy losses in the rotor supports. *J. Phys: Conf. Ser.* **744**, 012154 (2016)
9. Çeşmeci, Ş., Engin, T.: Modeling and testing of a field-controllable magnetorheological fluid damper. *Int. J. Mech. Sci.* **52**, 1036–1046 (2010)
10. Gertzos, K.P., Nikolakopoulos, P.G., Papadopoulos, C.A.: CFD analysis of journal bearing hydrodynamic lubrication by Bingham lubricant. *Tribol. Int.* **41**, 1190–1204 (2008)
11. Zeidan, F.Y., Vance, J.M.: Cavitation leading to a two phase fluid in a squeeze film damper. *Tribol. Trans.* **32**, 100–104 (1989)
12. Ferfecki, P., Zapoměl, J., Kozánek, J.: Analysis of the vibration attenuation of rotors supported by magnetorheological squeeze film dampers as a multiphysical finite element problem. *Adv. Eng. Softw.* **104**, 1–11 (2017)
13. Bolek A., Kochman J.: *Machine Parts*, vol. 1 (in Czech), 5th ed. SNTL, Prague (1989)



# Power Loss and Temperature Growth in the Backup Bearing of AMB-Supported High-Speed Electric Motor During a Dropdown

Neda Neisi<sup>(✉)</sup> , Eerik Sikanen, Janne E. Heikkinen,  
Teemu Sillanpää, and Jussi Sopanen

Lappeenranta University of Technology, Skinnarilankatu 34,  
53850 Lappeenranta, Finland  
neda.neisi@lut.fi

**Abstract.** This paper presents a simulation model for the dropdown of a high-speed electric motor utilizing the active magnetic bearings (AMB). In the circumstance that there is not a sufficient electromagnetic field or the system experiences excessive load, the rotor drops instantly on the backup bearings. The dropdown is accompanied by a considerable friction between the surfaces of the rotor and backup bearings. This study evaluates the heat generation and thermal behavior of backup bearing that are essential for the design of AMB systems. The model enables to calculate the power loss resulted from the friction between the rotor and backup bearing. The simulation includes the FE-model of the rotor and the backup bearing model. The one-dimensional thermal network has been applied to the thermal model of the bearing. The study concentrates on evaluating the friction heat generated and thermal growth of the deep groove ball bearing type in the non-drive end of the motor.

**Keywords:** Backup bearing · Rotor · Dropdown · Friction · Thermal analysis

## 1 Introduction

Applying the active magnetic bearings (AMB) enables to attain high-speed electric motors. In case of deficiency of electromagnetic field or overload, the rotor drops at once and there is a noticeable friction and possible rub between the rotor and backup bearings. The simulation of a dropdown event of the AMB supported rotor presented in the study of Kärkkäinen et al. [1] and Ecker [2] demonstrates the contact forces and the friction force in the dropdown. The presence of the electromagnetic force, specifically in the beginning of dropdown, can be a reason for the difference between the numerical simulation results and the recorded data of dropdown [3]. In previous studies the backup bearing is also known as touchdown bearing. The contact of the rotor and touchdown bearing, transient temperature as well as various controlling systems for AMB supported rotors have been discussed in the paper presented by Keogh [4, 5].

The friction heat generated in the dropdown can increase the temperature of the backup bearing which can lead to the thermally induced failure of the bearings. The thermally induced failure has been outlined as a source of failure in the conventional rotor-bearings [6, 7]. The thermal growth in the backup bearing can be analyzed by applying the equivalent electric circuit which has been demonstrated in the previous researches on AMB supported rotors [8–10]. By increasing the number of nodes used in the thermal model, the results are reported to be closer to the measurement results [11]. Jin et al. [9] provided a model for the single and double-decker catcher bearing (SDCB, DDCB). Their study indicated that applying the DDCB results in lower temperature rise in the bearing. In addition to high speed rotating machines, the thermo-mechanical analysis of bearing in the high-speed machine tools has been studied in recent years [12, 13]. Apart from this, the effect of the direction of the oil injection point on the heat generation [14] and the roller bearing with grease [15] are other aspects that have been studied in the field of thermal modeling of the bearings.

Current study presents the heat generation, temperature rise and thermal growth of the backup bearing of an AMB supported rotor. The system under investigation is an electric motor with the operational speed of 15000 rpm and 350 kW rated power. The case study comprises a flexible electric motor and two backup bearings, the combined FE-model of the rotor and the dynamic and thermal model of the backup bearing are demonstrated. Furthermore, the frictional heat from the contact of the rotor and backup bearing and the internal friction in the bearings are calculated.

## 2 Rotor Model

Current study applies the Timoshenko beam element for the FE-model of the case study shown in Fig. 1. The slitted rotor is made out of steel alloy and includes copper end rings. During the regular operation of the system, the electric rotor is levitated in the electromagnetic field produced by AMBs. In case of failure or shortage in the electromagnetic field, rotor drops on the backup bearings that protect the system for further damages. In Fig. 1 the locations of the backup bearings are shown by dashed line. Equation (1) presents the general equation of motion for rotating systems [16]:

$$\mathbf{M}\ddot{\mathbf{X}} + (\mathbf{C} + \omega\mathbf{G})\dot{\mathbf{X}} + \mathbf{K}\mathbf{X} = \omega^2\mathbf{F}_1 + \mathbf{F}_2 \quad (1)$$

where  $\mathbf{M}$ ,  $\mathbf{C}$ ,  $\mathbf{K}$ , and  $\mathbf{G}$  present the mass, damping, stiffness and gyroscopic matrix, respectively.  $\mathbf{X}$  represents the vector of the generalized coordinate. The vector  $\mathbf{F}_1$  and  $\mathbf{F}_2$  are the vector of nodal unbalance, and the vector of externally applied forces, respectively. The angular speed of the rotor is denoted as  $\omega$ .

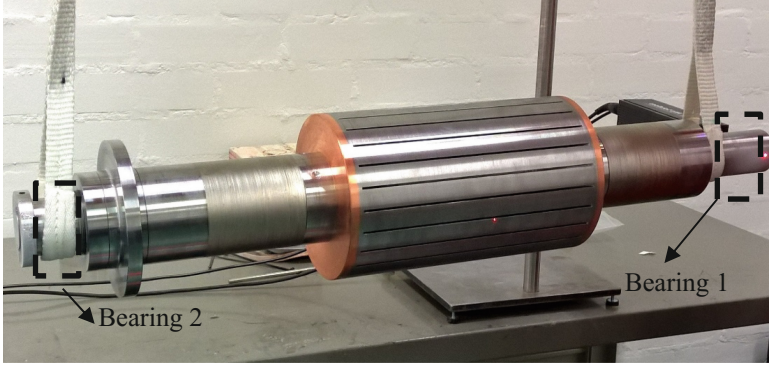


Fig. 1. System under investigation [17]

### 3 Backup Bearing Model

In the dropdown, the rotor is supported by two different types of backup bearings, a deep groove ball bearing in one end supporting radial direction only and a pair of angular contact bearings providing also a hard stop in the axial direction. This study concentrates on studying the friction heat generated and thermal model of the deep groove ball bearing (Bearing 1, Fig. 1). The backup bearing is modeled according to the model presented in a paper by Sopenan and Mikkola [18]. Equation (2) expresses the relative displacement between races (Fig. 2):

$$\begin{aligned} e_j^r &= e_x \cos \beta_j + e_y \sin \beta_j \\ e_j^t &= e_z - (\psi_x \sin \beta_j + \psi_y \cos \beta_j)(R_{in} + \varepsilon_{in} + r_{in}) \end{aligned} \quad (2)$$

where  $e_x$ ,  $e_y$  and  $e_z$  are the relative displacements of the bearing races along the main direction. The tilting of the inner race in  $x$ ,  $y$ -directions are shown by  $\psi_x$  and  $\psi_y$ . Angle  $\beta_j$  is the attitude angle of  $j^{\text{th}}$  ball. The following equation gives the distance between the races:

$$D_j = r_{out} + r_{in} - \frac{(R_{in} + \varepsilon_{in}) + r_{in} + e_j^r - (R_{out} + \varepsilon_{out}) + r_{out}}{\cos \varphi_j} \quad (3)$$

where the contact angle is denoted as  $\varphi_j$ :

$$\varphi_j = \tan^{-1} \left( \frac{e_j^t}{R_{in} + \varepsilon_{in} + r_{in} + e_j^r - R_{out} - \varepsilon_{out} + r_{out}} \right) \quad (4)$$

The inner race radius ( $R_{in}$ ) and inner race groove radius ( $r_{in}$ ) are shown in Fig. 2. In above equation, the thermal expansion of the inner race and outer race are denoted as  $\varepsilon_{in}$  and  $\varepsilon_{out}$ , correspondingly.

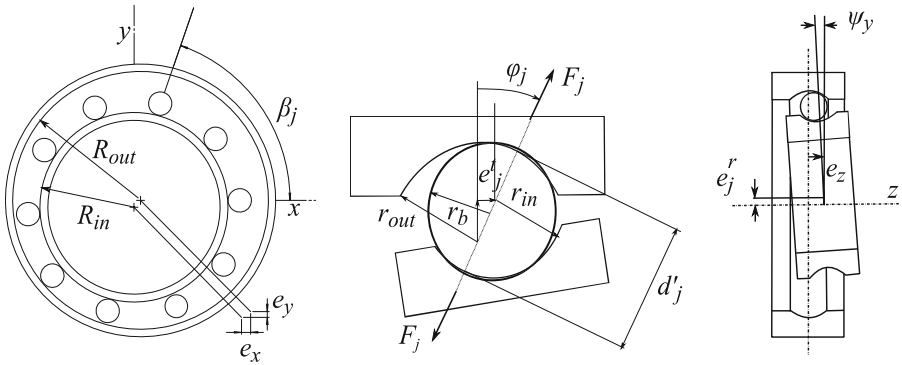


**Fig. 2.** Ball bearing model

Thus, the total elastic deformation of the inner ring can be found to be:

$$\delta_j^{tot} = d_j + \varepsilon_b - D_j \tag{5}$$

where  $\varepsilon_b$  represents the thermal expansion of balls. Then, the Hertzian contact theory can be used to calculate the contact force between the ball  $j^{th}$  and the inner race:

$$F_j = K_c^{tot} \left( \delta_j^{tot} \right)^{3/2} \tag{6}$$

where  $K_c^{tot}$  is total contact stiffness.

### 3.1 Contact

The modified Hertzian contact model is used for calculation of the contact force between the rotor and backup bearing [1]:

$$F_r = \begin{cases} K \delta^{10/9} \left( 1 + (3/2) \lambda \delta \right) & ; e_r > c_r \text{ and } F_r > 0 \\ 0 & ; e_r \leq c_r \text{ and } F_r \leq 0 \end{cases} \tag{7}$$

where  $F_r$  is the contact force between the rotor and inner race, the contact stiffness between the rotor and inner race is denoted as  $K$  and  $\lambda$ , is a contact parameter. The penetration of the rotor in the backup bearing is given by:

$$\delta = e_r - c_r + \varepsilon_{in} \tag{8}$$

where the calculation of the radius of the air gap between the rotor and backup bearing ( $c_r$ ), the radial displacement of the rotor ( $e_r$ ) have been demonstrated in the study of Kärkkäinen et al. [1]. The friction force ( $F_\mu$ ) between the rotor and inner race is as follows [1]:



$$F_{\mu} = \mu F_r \tag{9}$$

In the simulation, the coordinate transformation has been used to map the coordinate system in the FE-model of rotor and bearing model.

### 3.2 Thermal Model

In the thermal model of a bearing, the heat sources are the friction between the rotor and the inner race and the friction inside of the bearing. A schematic of the equivalent electrical circuit of the thermal model of the bearing is depicted in Fig. 3. The details of the calculation of the thermal resistance can be found in [10].

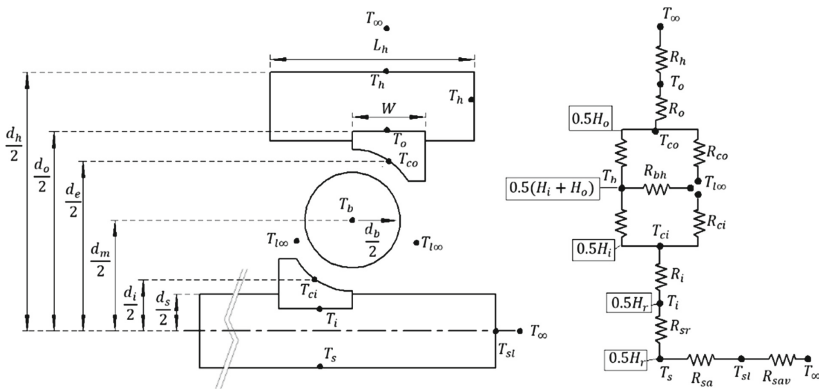


Fig. 3. Thermal resistance model of the bearing

Each node of the heat transfer model should satisfy the heat transfer equilibrium.

$$H_i - H_o = M_{brg} C \frac{dT}{dt} \tag{10}$$

where  $H_i$  and  $H_o$  are input and outflow power loss, respectively. The lumped mass of element and the specific heat are denoted as  $M_{brg}$  and  $C$ , respectively and  $dT/dt$  represents the temperature gradient.

### 3.3 Power Loss

The power loss due to the interaction of the rotor and inner race is given by [10]:

$$H_r = F_{\mu} V_{rel} \tag{11}$$

where the relative velocity between the rotor and inner race is denoted as  $V_{rel}$  and  $F_{\mu}$  represents the friction force. The friction torque in the bearing is also known as global friction torque [9]:

$$M = M_L + M_V \quad (12)$$

The first term is the load dependent friction torque [10]:

$$M_L = f_1 P d_m \quad (13)$$

The second term of Eq. (12) represents the velocity dependent friction torque [10]

$$\begin{cases} M_V = 10^{-7} f_2 (vN)^{2/3} d_m^3 & vN > 2000 \\ M_V = 160 \times 10^{-7} f_2 d_m^3 & vN \leq 2000 \end{cases} \quad (14)$$

where, the coefficients  $f_1$  and  $f_2$  are depended on the bearing design and bearing load,  $P$  represents the equivalent load,  $v$  is kinematic viscosity and the speed of inner race is denoted as  $N$  and the pitch diameter is shown by  $d_m$ . The spinning torque due to the spinning of the ball around its own axis is follows [10]

$$M_{si} = \frac{3\mu F_j a \bar{\zeta}}{8} \quad (15)$$

where  $\mu$  is friction coefficient,  $F_j$  is contact force and  $\bar{\zeta}$  is the elliptical integral of second type. The heat generation at inner the race and outer is given by [10]:

$$\begin{aligned} H_i &= \sum_j H_{ij} = \sum_j (\omega_b M_{ij} + \omega_{si} M_{si}) \\ H_o &= \sum_j H_{oj} = \sum_j (\omega_b M_{oj} + \omega_{so} M_{so}) \end{aligned} \quad (16)$$

where,  $M_{ij}$  and  $M_{oj}$  show the friction torque in inner race and outer race, respectively. The angular velocity of the ball is denoted as  $\omega_b$ . The spinning velocity of the ball in inner ring and out race are  $\omega_{si}$  and  $\omega_{so}$ , correspondingly.

### 3.4 Thermal Expansion

The thermal expansion of the bearing components has been accounted for updating the bearing force. The thermal expansion of the bearing components can be calculated as follows:

$$\varepsilon_{in} = \frac{\alpha_i (1 + \nu_i) r_s}{3 r_i + r_s} [\Delta T_i (2r_s + r_i) + \Delta T_{ci} (2r_i + r_s)] \quad (17)$$

$$\varepsilon_{out} = \frac{\alpha_o (1 + \nu_o) r_{out}}{3 r_{out} + r_h} [\Delta T_{out} (2r_{out} + r_h) + \Delta T_h (2r_h + r_{out})] \quad (18)$$

$$\varepsilon_b = \alpha_b r_b T_b \quad (19)$$

where  $r$  is the radius,  $\alpha$  and  $\nu$  are the thermal expansion coefficient and poisson ratio, respectively. The difference between the temperature of the bearing with the ambient temperature is denoted as  $\Delta T$ . The subscripts *in*, *out*, *b*, *s*, *h* and *ci* show the inner race, outer race, ball, shaft, housing and the contact of ball/inner race, respectively.

## 4 Case Studies and Results

The parameters required to analyze the case study of a rotor is shown in Table 1. The main dimensions of the rotor are depicted in Fig. 4. The backup bearing under investigation is the deep groove ball bearing 6014 (Bearing 1).

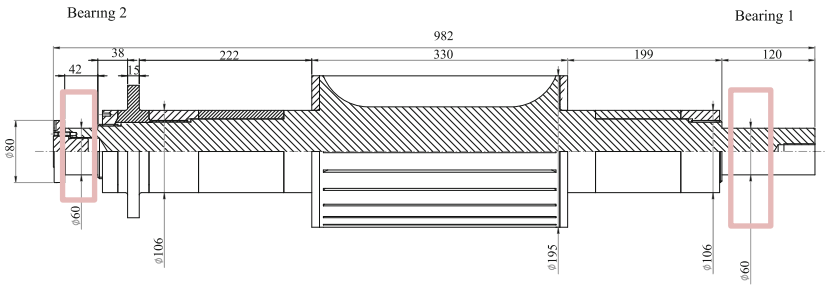


**Fig. 4.** The main dimensions of the rotor

**Table 1.** The main data for the simulation of the rotor dropdown.

Initial rotation speed of the rotor	15000 rpm
Modulus of elasticity	$2.0 \cdot 10^{11}$ Pa
Material density	$7801 \text{ kg/m}^3$
Mass of rotor	109.7 kg
Poisson's ratio	0.3
Effective mass of support, NDE	50 kg
Support stiffness of NDE ( $K_y$ , $K_z$ )	$(1.5, 1.1) \cdot 10^9 \text{ N/m}$
Supports damping ratio	5%
Effective mass of support, DE	85 kg
Support stiffness of DE ( $K_y$ , $K_z$ )	$(2.7, 1.5) \cdot 10^9 \text{ N/m}$
Contact stiffness between rotor and inner race (bearing 1)_Brg1	$1.144 \cdot 10^9 \text{ N/m}^{1.11}$
Contact stiffness between rotor and inner race (bearing 2)_Brg2	$1.73 \cdot 10^9 \text{ N/m}^{1.11}$
Air gap (radial)	250 $\mu\text{m}$
Polar moment of inertia of rotor	$0.39 \text{ kgm}^2$
Diametric moment of inertia of rotor	$4.5535 \text{ kgm}^2$
Unbalance mass at AMB disk	$1.07 \cdot 10^{-6} \text{ kg} \cdot \text{m}$ @ $180^\circ$
Unbalance mass rotor windings part	$2.78 \cdot 10^{-6} \text{ kg} \cdot \text{m}$ @ $180^\circ$
Static contact friction coefficient between rotor and inner race	0.05
Dynamic contact friction coefficient between rotor and inner race	0.1

#### 4.1 Orbital Motion of Rotor

As can be seen in Fig. 5, when the rotor drops and contacts the backup bearing, the vertical displacement of the rotor is more than the air gap indicating deformations in the structure. After the initial hit, rotor bounces back, up to the height more than half of the air gap clearance. Then, the rotor falls for the second time and bounces back. This behavior is repeated as long as the rotor settles on the bearing lower bottom. In addition, the vertical displacement of the rotor in the contact with the backup bearing 1 and 2 found to be different. This difference can be attributed to the following reasons. Firstly, due to the unsymmetrical structure of the supports and housings, the stiffness of the supports are different in both ends. Secondly, the backup bearings on both ends of the machine have different types and configurations.

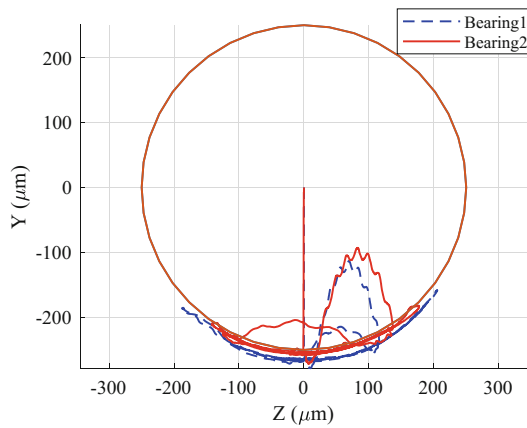
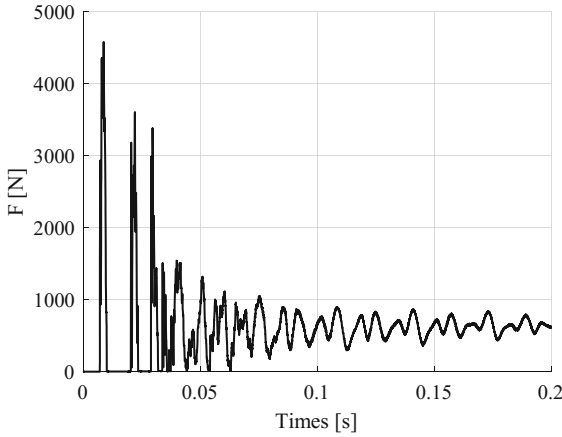


Fig. 5. The orbital motion of rotor at the location of backup bearings

#### 4.2 Contact Force

In the model, the contact force between the individual ball and bearing race is obtained. Then, by considering the attitude angle of the balls, the total contact force in the bearing is calculated. Figure 6 shows the magnitude of the contact force in the bearing. In the first hit of the rotor and bearing, the bearing experiences high contact force about 4500 N. Then, the contact force decreases rapidly and for a couple of milliseconds, the contact force becomes zero. Afterward, the bearing undergoes another high contact load. After this peak, the contact force becomes zero for the second time. Then, the several rise and fall in the magnitude of the contact force are observed until the force stabilizes. The highest contact force in the bearing is due to the high kinetic energy of the rotor at the start of the dropdown. When the rotor bounces back the contact force is zero. The reduction in the magnitude of the contact force in the bearing can be attributed to the dissipation of the kinetic energy in the form of heat. From 0.03 s until the end of the simulation, the rotor has a continues contact with the bearing and the contact force tends to stabilize.



**Fig. 6.** Contact force in the bearing

### 4.3 Friction Loss

Figure 7 depicts the velocity dependent, load dependent, and global friction torque in the backup bearing. In the dropdown, the velocity dependent friction torque increases up to 0.5 Nm. Then, the friction torque heads to the uniform level. The load dependent friction torque is considerably lower than the velocity dependent on torque. Just after the dropdown, it has the highest peak of 0.1 Nm and then decreases until it reaches the uniform level. The velocity dependent friction torque is depended on the angular velocity of the inner ring. As the inner ring accelerates, this term increases and when the rotor and inner ring rotates with the same angular velocity, it becomes uniform. The load dependent friction torque is influenced by the equivalent load carried by the bearing and the highest friction torque occurs in the first contact of rotor and bearing. It

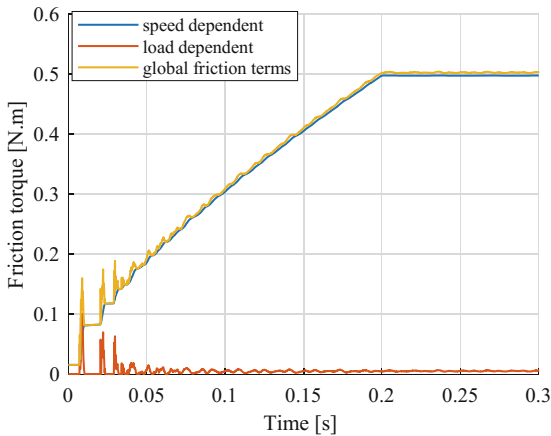
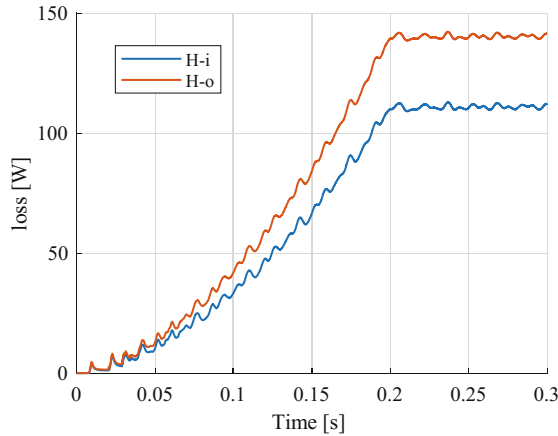


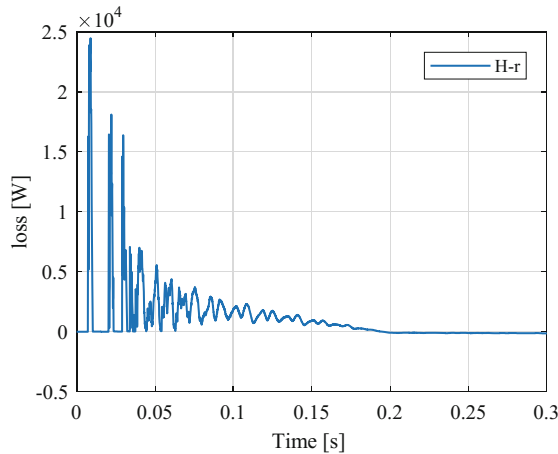
**Fig. 7.** Friction torque in the backup bearing

is clear from the figure that because of the high rotation speed of the rotor, the global friction torque is mainly affected by the velocity dependent friction torque.

The heat generated in the contact of the ball and inner ring and the contact of the rotor and inner ring are depicted in Fig. 8. As a result of the high contact force between the rotor and backup bearing as well as high relative velocity between the rotor and inner ring, the heat generated between the rotor and the inner ring is noticeably higher than the heat generated between the contact of the ball and inner ring.



a)



b)

**Fig. 8.** Internal heat generation in the backup bearing (a) heat generation between the ball and bearing races, (b) heat generation between rotor and inner ring

#### 4.4 Temperature Rise

The temperature rise in the backup bearing is mainly affected by the material property, geometry, and the friction heat generation. Figure 9 shows the temperature of the contact of the ball and inner ring. The temperature in the contact between inner and ball is increased from the ambient temperature to almost 296 K and then for a long time tends to be uniform. As shown in Fig. 8, when the inner ring accelerates the heat generation in the inner ring increases (H-i), and when the inner ring rotates with the same speed as rotor the heat generation in the inner ring tends to be uniform. This shows that the temperature rise in the inner ring is highly affected by the acceleration of the inner ring and the heat generation in the inner ring.

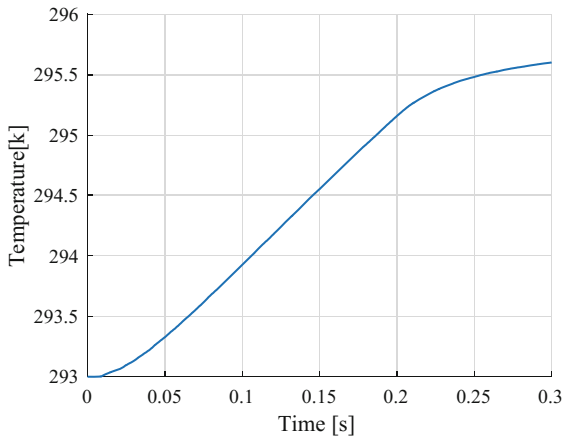


**Fig. 9.** Temperature increase of inner ring

## 5 Conclusion

Current study presented a simulation model for the dropdown of an electric motor supported by active magnetic bearing. The simulation is obtained on the base of the FE-model of the rotor and the dynamic model of the backup bearing. The friction heat generated in the dropdown and the thermal growth of the bearing component was taken into account. The rotor orbit, contact force, in the backup bearing, as well as the friction heat generated in the bearing were presented. The results indicated that in the early stages of the dropdown, the backup bearing suffers from the high contact force and then the contact forces either between rotor and backup bearing or the bearing force are decreased. The simulation results revealed that the acceleration of the inner ring and the friction force between the rotor and inner ring has a significant effect on the friction heat generated between the rotor and inner race. In order to develop a more accurate model for dropdown simulation, it is essential to identify the difference between the simulation of the rotor drop and a sudden drop of the rotor on the backup bearing. In addition, because of the complicated geometry of bearing housing assembly, some

simplification might be required for developing the thermal model of the backup bearing. This might result in the difference between the numerical solution and measurements. It should be noted that in this simulation, at the beginning of the dropdown, the rotor is located in the center. However, in the dropdown of the rotor in AMB due to electromagnetic field, the initial position of the rotor can be different from the center. In future development, the influence of the AMB force in the initial condition of the rotor should be considered.

## References

1. Kärkkäinen, A., Sopanen, J., Mikkola, A.: Dynamic simulation of a flexible rotor during drop on retainer bearings. *J. Sound Vib.* **306**, 601–617 (2007)
2. Ecker, H.: Nonlinear stability analysis of a single mass rotor contacting a rigid backup bearing. In: *Proceedings of the Euromech Colloquium*, pp. 79–88, Loughborough, UK (1998)
3. Schmied, J., Pradetto, J.C.: Behaviour of a one ton compressor rotor being dropped into the auxiliary bearings. In: *Proceeding of the Third International Symposium on Magnetic Bearings*, Alexandria, pp. 145–156 (1992)
4. Keogh, P.S.: Contact dynamic phenomena in rotating machines: active/passive considerations. *Mech. Syst. Signal Process.* **29**, 19–33 (2012)
5. Keogh, P.S., Yong, W.Y.: Thermal assessment of dynamic rotor/auxiliary bearing contact events. *ASME J. Tribol.* **129**, 143–152 (2007)
6. Burton, R.A., Staph, H.E.: Thermally activated seizure of angular contact bearings. *Tribol. Trans.* **10**, 408–417 (1967)
7. Takabi, J., Khonsari, M.M.: On the thermally-induced failure of rolling element bearings. *Tribol. Int.* **94**, 661–674 (2016)
8. Sun, G.: Rotor drop and following thermal growth simulations using detailed auxiliary bearing and damper models. *J. Sound Vib.* **289**, 334–359 (2006)
9. Jin, C., Zhu, Y., Xu, L., Xu, Y., Zheng, Y.: The thermodynamic properties of a new type catcher bearing used in active magnetic bearings system. *Appl. Therm. Eng.* **82**, 253–263 (2015)
10. Zhao, Y., Yang, G., Shi, Z., Zhao, L.: Thermal analysis and simulation of auxiliary bearings and its application in the high temperature reactor-10. *J. Tribol.* **138**, (2016)
11. Zheng, D., Chen, W.: Thermal performances on angular contact ball bearing of high-speed spindle considering structural constraints under oil-air lubrication. *Tribol. Int.* **109**, 593–601 (2017)
12. Jin, C., Wu, B., Hu, Y.: Heat generation modeling of ball bearing based on internal load distribution. *Tribol. Int.* **45**, 8–15 (2012)
13. Zahedi, A., Movahhedy, M.R.: Thermo-mechanical modeling of high speed spindles. *Scientia Iranica* **19**, 282–293 (2012)
14. Flouros, M.: Correlations for heat generation and outer ring temperature of high speed and highly loaded ball bearings in an aero-engine. *Aerosp. Sci. Technol.* **10**, 611–617 (2006)
15. Ma, F., Li, Z., Qiu, S., Wu, B., An, Q.: Transient thermal analysis of grease-lubricated spherical roller bearings. *Tribol. Int.* **93**, 115–123 (2016)



16. Kärkkäinen, A.: Dynamic simulations of rotors during drop on retainer bearings. Ph.D. thesis, Lappeenranta University of Technology, Finland (2007)
17. Halminen, O.: Multibody models for examination of touchdown bearing systems. Ph.D. thesis, Lappeenranta University of Technology, Finland (2016)
18. Sopanen, J., Mikkola, A.: Dynamic model of a deep-groove ball bearing including localized and distributed defects. Part 1: Theory. In: Proceedings of the Institution of Mechanical Engineers Part, K Journal of Multi-body Dynamics, vol. 217, pp. 201–211(2003)



# Simulation of a Test Rig and Identification of Annular Gas Seals Coefficients

David Maldonado<sup>(✉)</sup>, Diego Godoy<sup>(✉)</sup>, Vinicius Côrtes<sup>(✉)</sup>, Fernando Pinto<sup>(✉)</sup>,  
and Thiago Ritto<sup>(✉)</sup>

Department of Mechanical Engineering, Centro de Tecnologia,  
Federal University of Rio de Janeiro, Ilha do Fundão, Rio de Janeiro 21945-970, Brazil  
{david.julian,dgodoy,fcpinto}@ufrj.br,  
viniciuscortes@poli.ufrj.br, tritto@mecanica.ufrj.br

**Abstract.** This paper shows some preliminary results of an ongoing test rig for coefficients identification of annular gas seals. The test rig is being built in the Laboratory of Vibrations and Acoustics (LAVI) at the Federal University of Rio de Janeiro. The main objective of the rig is to determine both the damping and stiffness created by annular gas seals (honeycomb, labyrinth, hole-pattern, etc.) to a flexible rotor. The paper is divided in three parts. First, the characteristics and components of the rig are shown. Then, a rotordynamic model is proposed based on the finite element method, in which the rotor is divided into smaller elements and the seals are represented as punctual stiffness and damping. Some simulated results of this model is shown and analyzed. Finally, preliminary experimental results are shown and discussed.

**Keywords:** Annular gas seals · Rotordynamical flexible model  
Inverse problem · Impedance matrix · Seal test rig  
Uncertainty quantification

## 1 Introduction

Annular gas seals are one of the main parts of centrifugal compressors and other rotating machines. Their main function is to reduce the return of high pressure gas back to lower pressure stages. As well as bearings, their dynamic characteristics must be known in order to prevent and predict the machine's behavior. As shown by Smith [11], and Cochrane [4], the fluid forces induce by the fluid may take the system to an unstable state. If an appropriate linear analysis is carried out, that fact can be explained by idealizing the seal as a stiffness-damping system. The system stability depends on the values those coefficients take.

Different theoretical models have been proposed to determine the seals coefficients. The main variables that are taken into account are pressure drop, fluid velocity, seal geometry and gas composition. One of the first approaches proposed was the single-control-volume, by Iwatsubo [6] and Childs and Scharrer [3]. Then, Wyssman [14] presented a modified version, or a two-control volume

approach, for labyrinth seals. Dietzen and Nordamnn [5] applied a finite difference method to solve the Navier-Stokes equations with some assumptions. More recently, the problem is been investigated using computational fluid dynamics (CFD), in which more complex problems are addressed, such as seals coefficients of impellers.

Relevant experimental results have been shown only by few authors [2, 12, 13]. They are obtained using similar test rigs, but different identification methods. Childs [2] used a rig composed of a rigid rotor, two hydrostatic bearings and two labyrinth seals in a back-to-back configuration. A transverse force is applied to the stator by two shakers, and measurements of position, acceleration and force are used to determine an impedance matrix, whose entries are related to the seals coefficients. Vannini et al. [12] determined the coefficients of labyrinth seals using a rig from General Electrics. The rig is similar to the Childs rig, but instead of hydrostatic bearings, active magnetic bearings where used both for support and excitation. Harmonic motions are imposed to the rotor and a linear model is used to obtain the coefficients. Wagner et al. [13], using a rig from SIEMENS (similar to the rig from GR), determined the coefficients by measuring tangential and radial forces, which are directly related to the coefficients. The above mentioned papers used similar procedures to obtain the parameters. The rotor is set to a fixed rotational speed and is excited over a frequency band. Also, the pressure drop and fluid tangential velocity are measured and held constant.

This paper aims to show the preliminary results of an ongoing test rig designed to determine annular gas seals coefficients acting on a flexible rotor. The test rig is being built in the Laboratory of Acoustics and Vibrations (LAVI) at the Federal University of Rio de Janeiro. The rig is composed of a flexible rotor, two labyrinth seals in a back-to-back configuration, two rolling bearings and two electromagnetic actuators. Despite the rig is not fully operational, some relevant analysis, simulations and preliminary results are shown here.

The present paper also has the intention of proposing a computational model and an identification strategy. The model is based on the finite element method, in which the rotor is divided into smaller regions and considered 8-dof Euler-Bernoulli beams. For simplicity, bearings, seals and electromagnetic forces are considered acting on a single node, respectively. The identification procedure, based on the paper of San Andrés [9], is tested computationally. First, harmonic forces are applied at the actuators location and the displacements values at the sensors location are obtained. With this measurements, a impedance matrix is determined, and consequently, the seals coefficients. Moreover, the impact of uncertainties is addressed by adding noise to the displacement and current values.

This article is organized as follows. In Sect. 2, the main characteristics of the test rig, the instrumentation scheme and the electromagnetic actuators model are presented. In Sect. 3, the rotordynamical model is shown. The identification methodology is described in in Sect. 4. In Sect. 5, some numerical results are presented. In Sect. 6, some experimental results are discussed. Finally, in Sect. 7, the work conclusions are stated.

## 2 Test Rig Characteristics

The main purpose of the test rig is to investigate the characteristics of annular gas seals. Specifically, to identify their dynamic coefficients: stiffness and damping. As few literature on similar rigs were found, this work is relevant to the field. Nevertheless, the rig is still under development and some final adjustments are being done. Currently, the rig is able to rotate over a speed range and to excite the rotor to the desired at a single frequency, but the pressure drop has not been controlled yet. The following subsections will describe the mechanical characteristics, the instrumentation scheme and the actuators model.

### 2.1 Mechanical Characteristics

The rig is divided in three parts. The high pressure chamber, where the inlet high pressure is connected. The low pressure chamber, where the gas exits to the atmosphere. And the test section, between the high and low pressure chambers, where the seals are located. The cross section and the main parts of the rig are shown in Fig. 1 and Tables 1 and 2.

The inlet pressure is connected to the high pressure chamber and an inlet ring (red part) distributes the pressure radially. Then, the gas passes through a pre-swirl ring (yellow part) to set a certain circumferential speed. The clearance between the seals (orange parts) and rotor forces the gas to leak to the low pressure chamber, through a regulator valve. The effects of the pressure and velocity fields, created in the clearance, are considered to be stiffness and damping forces. The coefficients associated to those forces are obtained by applying radial forces using 2 magnetic actuators (part 9). Due to the small seal-to-rotor clearance, two touchdowns are located near the seals to avoid contact. The clearance is measured by two set of displacement sensors (part 5). Unbalance disks (blue parts) are located on the rotor to apply synchronous forces. Finally, a brushless DC motor is used to drive the rotor (part 12).

**Table 1.** Main characteristics of the test rig.

Characteristic	Value
Maximum test pressure	40 bar
Maximum counter-pressure	25 bar
Maximum rotor speed	8000 RPM
Rotor length	800 mm
Test section diameter	40 mm
Test section length	120 mm
Seal radial gap	0.4 mm
Safety touchdown radial gap	0.25 mm
Approximate test rig weight	65 kg

**Table 2.** Main parts of the test rig.

Number	Description	Qty.
1	Rotor	1
2	Bearing flange	2
3	Balancing disk	2
4	Center assembly	1
5	Sensor bushing	4
6	Low pressure chamber	2
7	Cover	2
8	O-ring	6
9	Electromagnetic actuator stator	2
10	Electromagnetic actuator rotor	2
11	Bearing	2
12	Motor	1

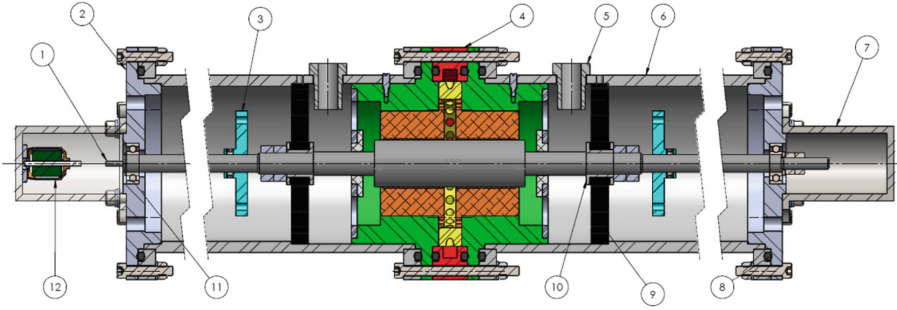


**Fig. 1.** Test rig cross section; see Table 2.

*Materials.* Most parts are made of carbon steel, including the rotor. The two touchdown systems in place are low friction Teflon stators, as it is easier to assemble and less prone to damage the rotor when compared to rigid bearings. The seals are aluminum, because it is softer than the steel and will take the damage if the touchdown comes to fail.

*Pressure.* The initial input was a test pressure of 40 bar. The pressure target was partially achieved, because the maximum pressure for the high pressure chamber is 40 bar, but a pressure of 40 bar in the low pressure chamber would lead to an overly heavy and bulky rig, so it was limited to 25 bar to stay below the allowable stress.

*Operation speed.* The target rotation speed was 20000 RPM. In order to avoid noise and complexity a direct drive was mandatory, but finding an electric motor powerful enough at a compatible size and rated for this speed proved to be a hard task. The solution was to use small brushless motors, which limited the speed to 8000 RPM for the most common models. As will be shown further, the nominal motor speed lays between the first and second natural frequencies.

*Rotor Flexibility.* The usual configuration layout for this type of test rig is a rigid rotor supported by active electromagnetic bearings. This type of bearing can simultaneously levitate and excite the rotor, without the need of an additional actuator. When the rig project started, the laboratory staff was still acquiring experience with active electromagnetic bearings. Therefore, it was decided to use regular ball bearings to support the rotor and electromagnetic actuators to excite the flexible rotor. This fact implied two challenges: the modeling of the rotor deflections and the adequate rigidity of the rotor. The modeling of flexible rotors was obtained by the rotordynamic software LAVIRot, developed by the laboratory staff. The rigidity had to be enough so that the rotor would not touch the touchdown safety system just by the influence of gravity, but also flexible enough to respond to the seal forces in the rig test pressure and the electromagnetic actuator.

*Seal and Swirl Generator.* The first seal fabricated is a labyrinth seal, mainly due to its simple geometry, but also due to the wider availability of bibliography describing their geometry and behavior. The swirl generator imposes tangential

speed to the gas and it is a closer approach to the operation of typical turbomachinery. Tests with and without swirl generator can be carried out to analyze the behavior of gas tangential speed.

*Balancing.* Besides the electromagnetic actuators, the rig has two symmetrically positioned disks that can be used to add an unbalanced mass to the rotor. This was dimensioned in a way that the maximum unbalance allowed would not make the rotor touch the seal.

## 2.2 Instrumentation

The rig is set up with sensors, actuators, power systems and processing units to apply forces and acquire signals. The gas is supplied by a 10-bar air compressor and regulated by a valve. The pressure is measured by two manometers, for inlet and output, respectively. The rotor speed is measured by an encoder. Two electromagnetic actuators are located symmetrically along the rotor and are used to apply transverse excitations. A set of current sensors are used to measure the current from each of actuators coils. The rotor-to-seal displacements are measured by two sets of inductive proximity sensors, located near the seal in an orthogonal configuration. The actuator forces are determined indirectly by the current and displacement measurements, according to a linearized equation. The excitation signal is created in a computer running Labview and is amplified by a set of power devices connected to the coils. The rig and some of its components are shown in Fig. 2.

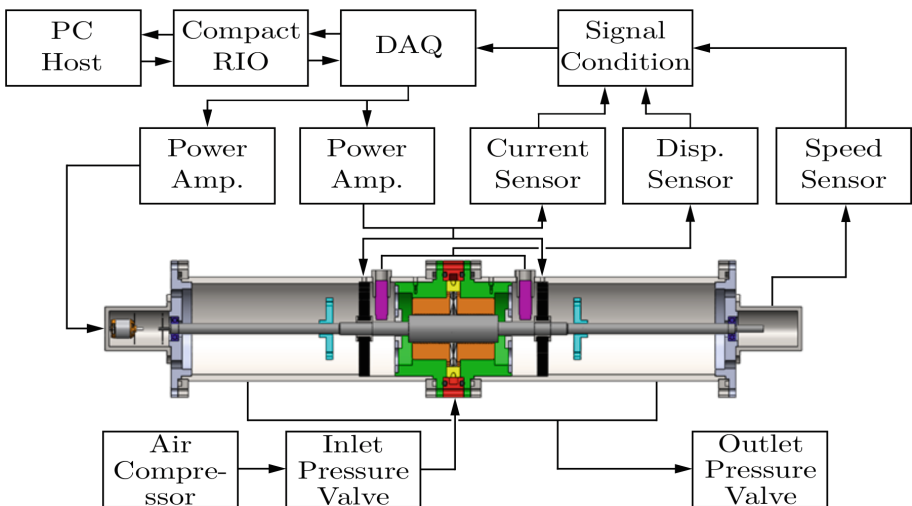


Fig. 2. Test rig instrumentation and control scheme.

### 2.3 Electromagnetic Actuators Model

For identification purposes, literature presents several types of excitation as impulsive excitation, using instrumented hammers, or pseudorandom excitation, performed by hydraulic actuators. A detailed background of those methods are described by Nordmann [8] and Lee [7]. In the last 25 years, excitation using electromagnetic devices became an interesting area of research and development due to frictionless operation. Practically, any input signal can be used as excitation on this kind of devices. A typical electromagnet configuration used in many test rigs is the horseshoe differential, since its control can be easily implemented (e.g. decoupled PID) [10]. One modification of the latter is the 8-pole circular stator magnet, shown in Fig. 4a, which can be set as a horizontal and a vertical



**Fig. 3.** Test-rig

differential configuration separately, if one assume that the magnetic flux coupling between those axes is negligible. If the rotor displacements are small with respect to the air gap, a linearized current model can be proposed by establishing a base current operation  $i_0$ . In this way, the current in the pole pair of each side depends both on the base current  $i_0$  and the excitation current  $i_x$ , as shown in Fig. 4b. Since the test rig is equipped with ball bearings, no control current is necessary to maintain the concentricity between rotor and stator.

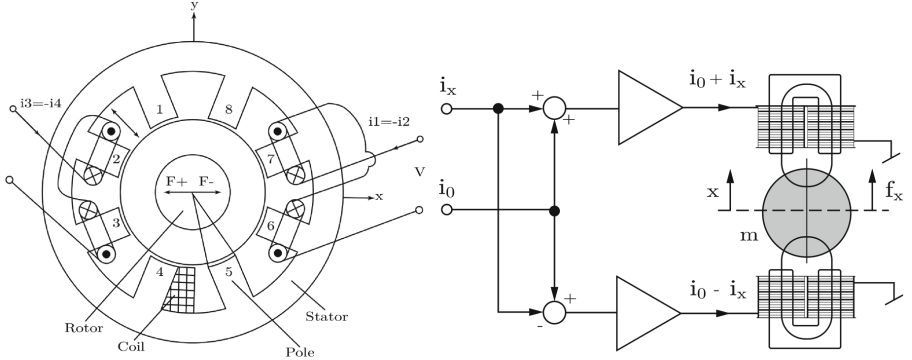


**Fig. 4.** (a) Eight poles circular electromagnet with horseshoe configuration (modified [1]). (b) Electromagnet with horseshoe differential configuration (modified [10]).

According to Chiba [1], the net force, along the vertical or horizontal axis, applied to the rotor is directly proportional to the square of the current in the coil, and inversely proportional to the square of the distance between each pole and the rotor surface. Mathematically, it can be expressed as follows (Disregarding the losses due to temperature, hysteresis and Eddy currents):

$$f_k = \frac{\xi_k \beta \mu_o N^2 A_g}{2} \left( \frac{(i_0 + i_k)^2}{(g_0 - k)^2} - \frac{(i_0 - i_k)^2}{(g_0 + k)^2} \right), \quad k = \{x, y\} \quad (1)$$

where  $A_g$ ,  $g_0$  and  $\mu_o$  are the pole cross section area, the nominal air gap and the permeability of free space respectively.  $\beta$  is the configuration factor (in this case  $\beta = 0.9232$ ),  $\xi_k$  is an experimental calibration factor and  $N$  is the number of turns in the coil. As the operation ranges of the rotor are smaller than the nominal air gap, a linearization of Eq. 1 is possible and the electromagnetic forces are described by:

$$f_k = \frac{\xi_k \beta \mu_o N^2 A_g}{2} \left( \frac{i_0}{g_0^2} i_k + \frac{i_0^2}{g_0^3} k \right) = c_i i_k + c_s k, \quad k = \{x, y\} \quad (2)$$

### 3 Rotordynamic Model

The rig is represented as a flexible rotor with two ball bearings, 2 seals in the middle, two sensors and two actuators. For simplicity, a finite-element representation



is used, and the rotor is divided into smaller regions. Each region is considered as a 8-dof Euler-Bernoulli beam with two displacements  $x$ ,  $y$  and two rotations  $\phi$ ,  $\theta$ . The system matrices are obtained using the software LAVIRot, developed in LAVI. The bearings and seals parameters are modeled as stiffness and damping acting on a single node. Similarly, the actuators forces and sensors readings are modeled as forces and variables acting or measuring a single node. The final system equations are defined as follows (Fig. 5):

$$\mathbf{M}\ddot{\mathbf{u}}(t) + (\mathbf{C} + \mathbf{G})\dot{\mathbf{u}}(t) + \mathbf{K}\mathbf{u}(t) = \mathbf{f}_m(t) + \mathbf{f}_u(t) \quad (3a)$$

$$\text{Electromagnetic forces: } \mathbf{f}_m(t) = c_i i \mathbf{K}_i + c_s \mathbf{K}_s \begin{bmatrix} x_{a1} \\ y_{a1} \\ x_{a2} \\ y_{a2} \end{bmatrix} \quad (3b)$$

$$\text{Unbalance forces: } \mathbf{f}_u(t) = m_d r_u \Omega^2 \mathbf{K}_u \begin{bmatrix} \cos(\Omega t) \\ \sin(\Omega t) \end{bmatrix} \quad (3c)$$

where  $\Omega$  is the nominal rotational speed of the machine,  $\omega$  is the actuators force frequency,  $\mathbf{M}$  is the mass matrix,  $\mathbf{G}(\Omega)$  is the gyroscopic matrix and  $\mathbf{u}(t)$  is the generalized displacement vector (rotations and displacements). The stiffness and damping matrices,  $\mathbf{K}(\omega, \Omega)$  and  $\mathbf{C}(\omega, \Omega)$ , depend on  $\omega$  and  $\Omega$  because the seal coefficients vary with the rotor speed and actuator force frequency. The external force vector is comprised of the actuators electromagnetic force, which depends on the actuators position  $[x_{a1}, y_{a1}, x_{a2}, y_{a2}]^T$ , and the residual unbalance force. Matrices  $\mathbf{K}_i$ ,  $\mathbf{K}_s$  and  $\mathbf{K}_u$  are transformations from local to global coordinates. Note that matrices  $\mathbf{M}$ ,  $\mathbf{C}$ ,  $\mathbf{G}$ , and  $\mathbf{K}$  have dimension  $n \times n$ , while  $\mathbf{K}_i$  is  $n \times 1$ ,  $\mathbf{K}_s$  is  $n \times 4$ , and  $\mathbf{K}_u$  is  $n \times 2$ .

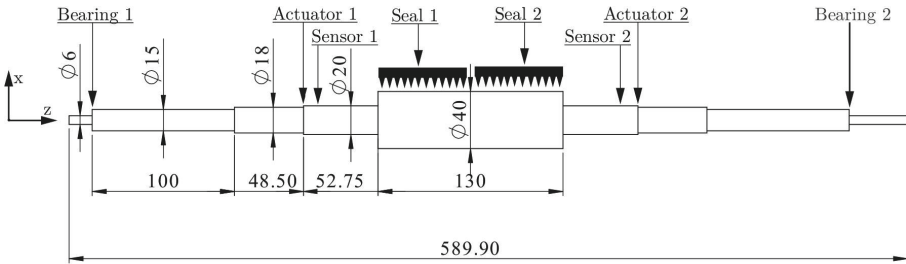


Fig. 5. Representation of the test-rig

The bearings behavior are modeled as constant stiffness and damping, i.e., they are frequency-independent and not sensible to other variables. As the rotor-to-seal displacements are small ( $\leq 100$  microns), the following seal linear model is adopted:

$$\begin{bmatrix} -f_{xs} \\ -f_{ys} \end{bmatrix} = \begin{bmatrix} K(\omega) & k(\omega) \\ -k(\omega) & K(\omega) \end{bmatrix} \begin{bmatrix} u_{xs} \\ u_{ys} \end{bmatrix} + \begin{bmatrix} C(\omega) & c(\omega) \\ -c(\omega) & C(\omega) \end{bmatrix} \begin{bmatrix} \dot{u}_{xs} \\ \dot{u}_{ys} \end{bmatrix} \quad (4)$$

where,  $K$ ,  $C$  are the direct stiffness and damping, and  $k$ ,  $c$  are the cross-coupled stiffness and damping. These parameters depend on the seal geometry, gas properties, and operational parameters such as rotor speed and actuators excitation frequency. This model considers a concentric configuration and the effects of non-concentric configurations are out of the scope of this article.

## 4 Identification Methodology

Seals parameters can be obtained by exciting the rotor, measuring the displacements of some points and then applying an identification method, as shown in the block diagram of Fig. 6. The excitation signals  $\mathbf{v}$  are set from a computer or signal generator and taken to a magnetic actuator system, which creates the excitation forces  $\mathbf{f}_a$ . These forces are applied to the rig and measurements  $\hat{\mathbf{u}}_s$  are taken close to the seals location using displacement sensors. Also, current sensors are used to obtain the electromagnetic actuator coils currents  $\hat{\mathbf{i}}_a$ . Those measurements are the inputs for the identification method, which outputs the estimated parameter vector  $\hat{\mathbf{p}} = [K, k, C, c]$ .

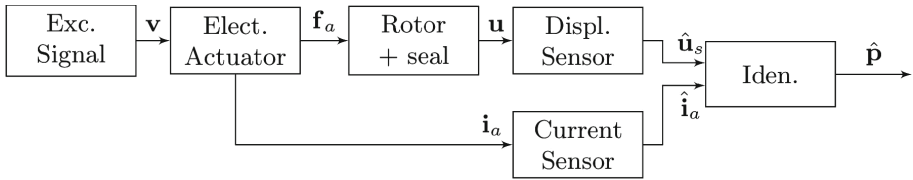


**Fig. 6.** Block diagram of system excitation and parameters identification.

Seals forces are contained in the measurements as a response to the excitation. Those forces are considered as a linear decomposition in the seals displacements-velocity space, as shown in Eq. 4. The identification strategy applied in the present work uses impedance matrices [2]. The procedure is similar to the one proposed by San Andrés and De Santiago [9], in the context of bearing coefficients identification.

### 4.1 Identification Method

The method is based on the previous hypothesis of linearity described by Eq. 3a. If periodic forces are applied to the system, the frequency behavior for both the forces and displacement can be determined using the Fourier Transform:

$$\mathbf{u}(t) \xrightarrow{\mathcal{F}} \mathbf{U}(\omega) \quad (5a)$$

$$\mathbf{f}(t) \xrightarrow{\mathcal{F}} \mathbf{F}(\omega) \quad (5b)$$

Using Eq. 5a and 5b in Eq. 3a yields the frequency-dependent system of Eq. 6, which takes into account the rotor, bearings and seals model.

$$(-\omega^2 \mathbf{M} + i\omega (\mathbf{C}(\omega) + \mathbf{G}(\Omega)) + \mathbf{K}(\omega)) \mathbf{U}(\omega) = \mathbf{F}(\omega) \quad (6a)$$

$$\mathbf{Z}(\omega) \mathbf{u}(\omega) = \mathbf{F}(\omega) \quad (6b)$$

This equation is expanded to separate the rotor-bearing forces from the seals forces, as shown in Eq. 7, where the overbar stands for a reordered matrix or vector,  $\bar{\mathbf{Z}}_R$  is the rotor-bearing impedance,  $\mathbf{u}_{s1}$  and  $\mathbf{u}_{s2}$  are the seals measurements,  $\mathbf{u}_R$  are the rotor-bearing displacements,  $\mathbf{Z}_1$  and  $\mathbf{Z}_2$  are the seals impedance and  $\mathbf{f}$  are the external forces.

$$\bar{\mathbf{Z}}\bar{\mathbf{U}} = \bar{\mathbf{Z}}_R \begin{bmatrix} \mathbf{U}_{s1} \\ \mathbf{U}_{s2} \\ \mathbf{U}_R \end{bmatrix} + \begin{bmatrix} \mathbf{Z}_{s1} & \mathbf{0} & \mathbf{0} \\ \mathbf{0} & \mathbf{Z}_{s2} & \mathbf{0} \\ \mathbf{0} & \mathbf{0} & \mathbf{0} \end{bmatrix} \begin{bmatrix} \mathbf{U}_{s1} \\ \mathbf{U}_{s2} \\ \mathbf{U}_R \end{bmatrix} = \begin{bmatrix} \mathbf{0} \\ \mathbf{0} \\ \mathbf{F} \end{bmatrix} \quad (7)$$

From Eq. 7, it is possible to obtain the rotor-bearings  $\mathbf{u}_R$  displacements and seals forces  $\mathbf{f}_{s1}$  and  $\mathbf{f}_{s2}$  as shown in Eqs. 8 and 9.

$$\mathbf{U}_R = \mathbf{Z}_{R33}^{-1} \{ \mathbf{F} - \mathbf{Z}_{R31} \mathbf{U}_{s1} - \mathbf{Z}_{R32} \mathbf{U}_{s2} \} \quad (8)$$

$$\mathbf{f}_{s1} = \mathbf{Z}_{s1} \mathbf{U}_{s1} = -(\mathbf{Z}_{R11} \mathbf{U}_{s1} + \mathbf{Z}_{R12} \mathbf{U}_{s2} + \mathbf{Z}_{R13} \mathbf{U}_R) \quad (9)$$

$$\mathbf{f}_{s2} = \mathbf{Z}_{s2} \mathbf{U}_{s2} = -(\mathbf{Z}_{R21} \mathbf{U}_{s1} + \mathbf{Z}_{R22} \mathbf{U}_{s2} + \mathbf{Z}_{R23} \mathbf{U}_R)$$

As Eq. 9 has more unknowns parameters than algebraic equations, two independent excitations are applied as follows:

$$\begin{bmatrix} \mathbf{Z}_{s1} \\ \mathbf{Z}_{s2} \end{bmatrix} \begin{bmatrix} \mathbf{U}_{s11} & \mathbf{U}_{s12} \\ \mathbf{U}_{s21} & \mathbf{U}_{s22} \end{bmatrix} = \begin{bmatrix} \mathbf{F}_{s11} & \mathbf{F}_{s12} \\ \mathbf{F}_{s21} & \mathbf{F}_{s22} \end{bmatrix} \quad (10)$$

Thus, the coefficients of each seal are readily obtained by taking the real and imaginary part of  $\mathbf{Z}_{sk}$  matrices of Eq. 11.

$$\mathbf{Z}_{sk} = \begin{bmatrix} \mathbf{F}_{k1} & \mathbf{F}_{k2} \end{bmatrix} \begin{bmatrix} \mathbf{U}_{k1} & \mathbf{U}_{k2} \end{bmatrix}^{-1} = \begin{bmatrix} K_{sk} + i\omega C_{sk} & k_{sk} + i\omega c_{sk} \\ -k_{sk} + i\omega c_{sk} & K_{sk} + i\omega C_{sk} \end{bmatrix} \quad k = 1, 2 \quad (11)$$

The process of exciting and measuring determines the seal response along with other undesired responses, such as imbalance force and bearing forces. A way to isolate the seal response is to obtain a measurements baseline with no inlet pressure which determines the undesired forces responses. Then, the rig is pressurized and a new set of measurements is acquired. Finally, the seals coefficients are obtained using Eq. 12.

$$\mathbf{Z}_s = \mathbf{Z}_{exp} - \mathbf{Z}_{base} \quad (12)$$

Thus, the identification of parameters from other components, such as bearings or rotor unbalance, are not necessary.

## 5 Numerical Results

### 5.1 Campbell Diagram

Considering the system with no seals, the rotor resonance frequencies can be analyzed by using a Campbell Diagram, which shows the frequency of the mode shapes at different rotor speed. First, the following no forcing state-space representation is used:

$$\begin{bmatrix} \dot{\mathbf{u}} \\ \ddot{\mathbf{u}} \end{bmatrix} = \begin{bmatrix} \mathbf{0} & \mathbf{I} \\ -\mathbf{M}^{-1}\mathbf{K} & -\mathbf{M}^{-1}(\mathbf{C} + \mathbf{G}) \end{bmatrix} \begin{bmatrix} \mathbf{u} \\ \dot{\mathbf{u}} \end{bmatrix} \quad (13)$$

Equation 13 yields the following eigenvalue problem:

$$\mathbf{A}\boldsymbol{\nu}_k = \omega_k\boldsymbol{\nu}_k \quad (14)$$

where  $\omega_k$  is the natural frequency corresponding to the  $k$ -th mode shape. The results of a Campbell Diagram simulation is shown in Fig. 7. This diagram shows the frequency of each mode shape ( $\omega$ ) as the speed of rotation ( $\Omega$ ) increases from 0 to 50000 RPM. At  $\Omega = 0$ , the three first natural frequencies can be seen in the vertical axis. When increasing  $\Omega$ , each frequency splits into 2 lines: the forward and backward whirl. The dotted line shows the line  $\omega = \Omega$ , which intercept with the whirls correspond to the critical speeds. As the rotor is not provided of inertia disks, the effect of inertia cross-coupling does not considerably changes the mode shapes.

### 5.2 Frequency Response Function

The effect of the excitation frequency on the rotor behavior can be assessed by plotting the Frequency Response Function of the rotor, defined as follows:

$$\mathbf{H} = (-\mathbf{M}\omega^2 + (\mathbf{C} + \mathbf{G})j\omega + \mathbf{K})^{-1} \quad (15)$$

In Fig. 8 is shown a simulation of a FRF calculated at the seal location (middle of the rotor). It shows the amplitude of the oscillations as actuators frequency increase. Each peak correspond to the natural frequencies, and they are the same as shown in the Campbell diagram.

### 5.3 Mode Shapes

The mode shapes are useful to visualize the rotor behavior at different resonance frequencies. For small damping systems, the mode shapes can be obtained by taking the imaginary part of the FRF at each resonance frequency. The first two modes of the rotor are shown in Fig. 9.

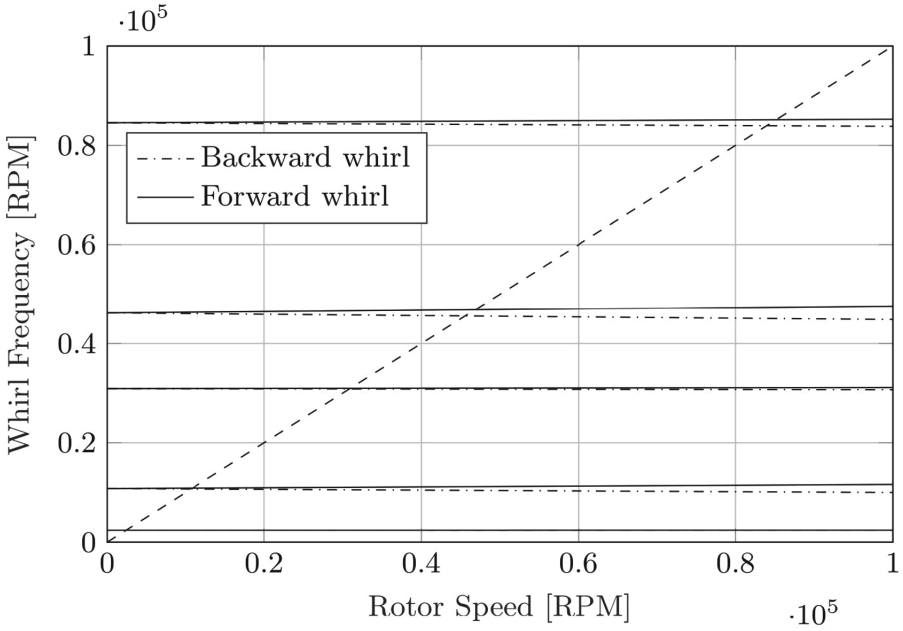


Fig. 7. Campbell diagram of the rotor with the first 5 natural frequencies.

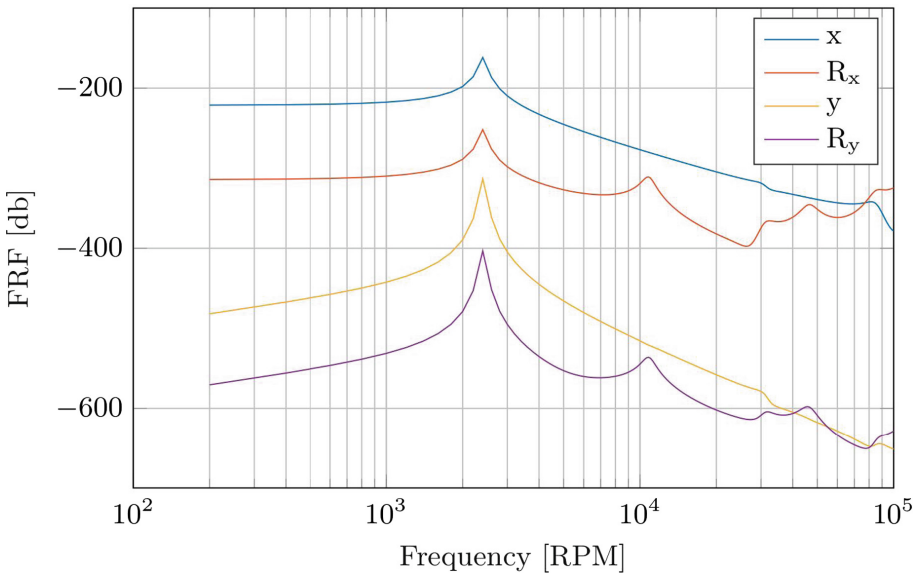
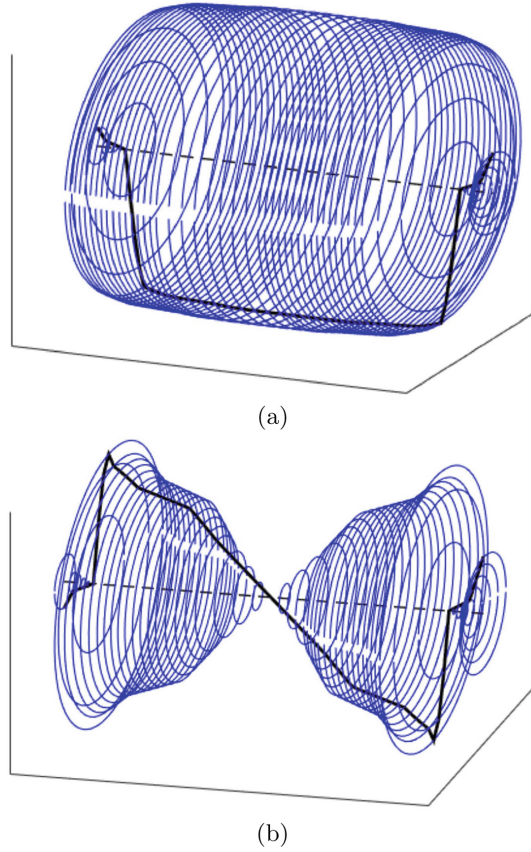


Fig. 8. Frequency Response Functions.  $x$  and  $y$  are the displacements FRF.  $R_x$  and  $R_y$  are the rotations FRF.



**Fig. 9.** Mode shapes of the rotor: (a) rotor first mode at 2322 RPM and (b) rotor second mode at 10400 RPM

#### 5.4 Orbits

Figure 10 shows the Orbits from left sensors (left chart) and right sensors (right chart) for an excitation of 100 Hz. It is noted that the orbits are not symmetric.

#### 5.5 Identification Method

Since the constructed test rig is still not fully operational, the identification method is tested in a computer simulation with the synthetic experimental data of Eq. 16. Variables  $\hat{\mathbf{u}}_s$  and  $\hat{i}$  are the seal displacement and coil current sensor measurements,  $\mathbf{u}$  and  $i$  are the exact seal displacement and coils current values, and  $n_u$  and  $n_i$  are independent and identically distributed (iid) noises with zero mean and standard deviation  $\sigma_u$  and  $\sigma_i$ . For simulation purposes, an arbitrary representative noise values are used. The exact values of variables are obtained by solving Eq. 3a and considering a single-frequency harmonic signals at 100 Hz

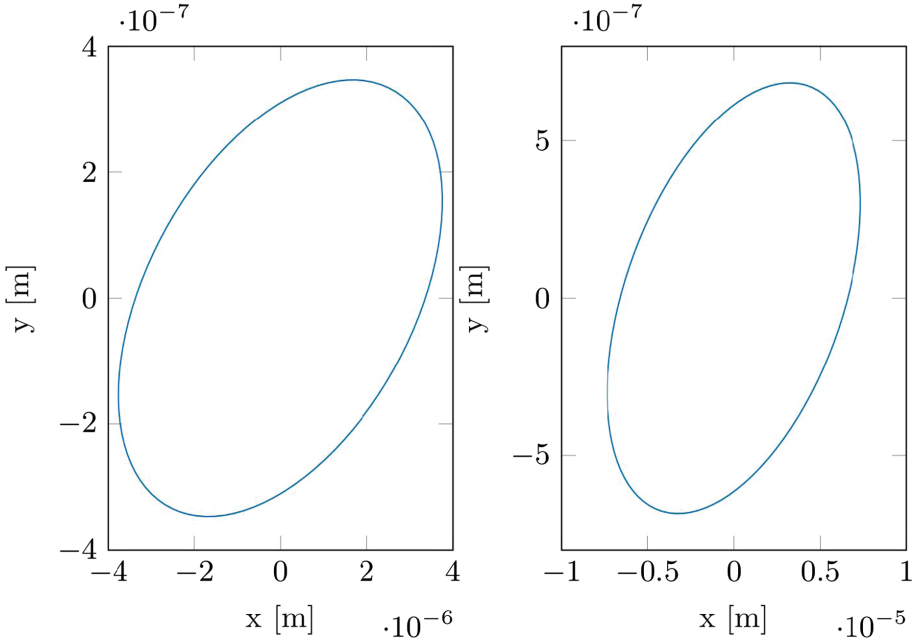


**Fig. 10.** Orbits from left sensors (Left figure) and right sensors (Right figure) for an excitation of 100 Hz.

**Table 3.** Parameters of numerical simulations.

Parameter	Value	Units
<u>Rotor</u>		
Bearings Stiffness	$10^8$	N/m <sup>2</sup>
Rotor damping	0.08	-
Rotor FEA elements	41	-
Rotor speed	80	RPM
<u>Actuators</u>		
$\xi$	1	-
$\beta$	0.924	-
$\mu_0$	$4\pi \times 10^{-7}$	H/m
$N$	180	-
$A_0$	235	mm <sup>2</sup>
$i_0$	2	A
$g_0$	1	mm
$L$	$10^{-3}$	H
$R$	1	$\Omega$
$m_u$	1	g
$r_u$	1	mm

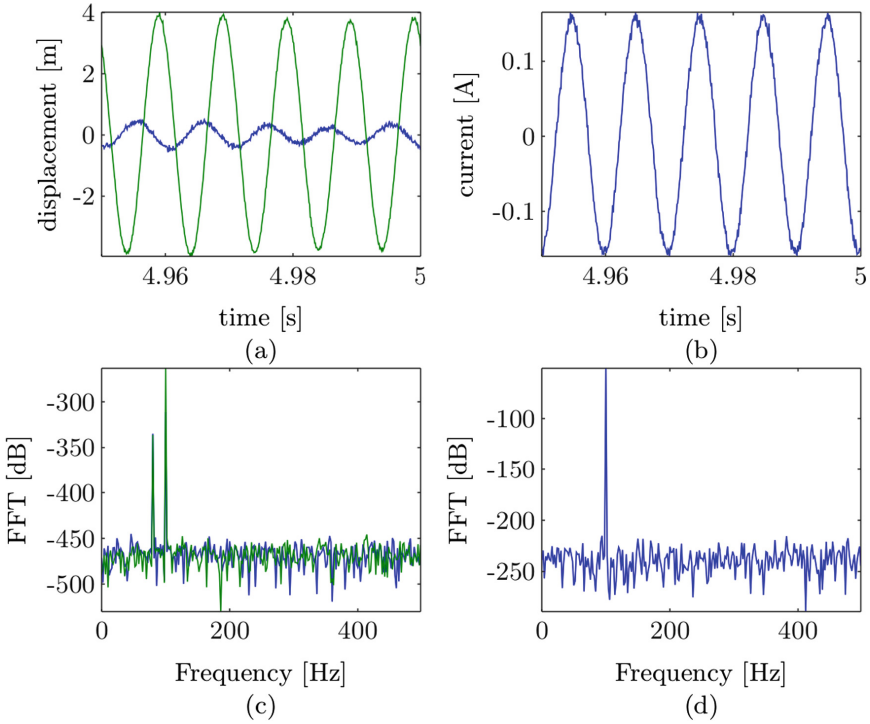
  

Parameter	Value	Units
<u>Noise</u>		
Disp. sensor noise	$\sigma_u = 5 \times 10^{-8}$	m
Current sensor noise	$\sigma_i = 5 \times 10^{-2}$	A
<u>FFT</u>		
Simulation time	5	s
Sampling freq.	1	KHz
FFT window	Hanning	-
<u>Excitation</u>		
Excitation frequency 1	100	Hz
Excitation frequency 2	200	Hz
Seal parameters@100 Hz	$K = 5 \times 10^4$	N/m <sup>2</sup>
	$k = 2 \times 10^3$	N/m <sup>2</sup>
	$C = 5 \times 10^2$	Ns/m <sup>2</sup>
	$c = 1 \times 10^2$	Ns/m <sup>2</sup>
Seal parameters@200 Hz	$K = 7 \times 10^5$	N/m <sup>2</sup>
	$k = 4 \times 10^4$	N/m <sup>2</sup>
	$C = 9 \times 10^2$	Ns/m <sup>2</sup>
	$c = 4 \times 10^2$	Ns/m <sup>2</sup>

and 200 Hz, with the parameters shown in Table 3. First, the system response is obtained for a set of seal parameters, simulating the rig behavior at 100 Hz. Then, the seal parameters are changed to simulate the rig behavior at 200 Hz. Each excitation signal is applied to two orthogonal directions, as detailed in Sect. 4. The simulations are carried out considering a single rotor speed of 80 RPM because its effect on the parameters will not be discussed.

$$\begin{aligned}\hat{\mathbf{u}}_s &= \mathbf{u}_s + \mathbf{n}_u, & \mathbf{n}_u &\sim N(E\{\mathbf{n}_u\} = \mathbf{0}, \text{var}\{\mathbf{n}_u\} = \boldsymbol{\sigma}_u^2) \\ \hat{i}_a &= i + n_i, & n_i &\sim N(E\{n_i\} = 0, \text{var}\{n_i\} = \sigma_i^2)\end{aligned}\quad (16)$$

Figure 11 shows the numerical results for an excitation in the  $x$ -direction. Figures 11a and b show the current and seal displacements measurements in the  $x$  (green signal) and  $y$  (blue signal) directions. Figures 11c and d show their respective frequency-domain response. Despite the excitation was applied in a single direction, the cross-coupled terms acts in an orthogonal direction to the excitation. The noise applied to the system creates a distortion both in time and frequency domain. In the latter, the system behavior is better analyzed. The system responds with a harmonic content of 100 Hz and a white noise equally distributed over a frequency band. The rotation speed does not appear in the displacement FFT since a very low unbalance force is applied.



**Fig. 11.** Simulated results for an excitation in the  $x$ -direction at 100 Hz. The displacements correspond to the actuator 1. The green curve is the displacement in the  $x$ -direction and the blue curve is the displacement in the  $y$ -direction. The current correspond to the excitation current of actuator 1.

The stochastic model of measurements causes an uncertain output of the identification method, which means that every time the method is run it will



**Table 4.** Statistics of the identification method output for 2 cases.

Exc. freq.	Coef.	Mean	Std. Dev.	CV	Error (%)
100 Hz	$K$ [N/m <sup>2</sup> ]	$5.0 \times 10^4$	$5.5 \times 10^3$	$1.1 \times 10^{-1}$	$1.4 \times 10^{-1}$
	$k$ [N/m <sup>2</sup> ]	$2.0 \times 10^3$	$4.9 \times 10^2$	$2.5 \times 10^{-1}$	1.1
	$C$ [Ns/m <sup>2</sup> ]	$5.0 \times 10^2$	7.8	$1.6 \times 10^{-2}$	$5.2 \times 10^{-2}$
	$c$ [Ns/m <sup>2</sup> ]	$9.9 \times 10^1$	$9.1 \times 10^{-1}$	$9.1 \times 10^{-3}$	$1.9 \times 10^{-2}$
200 Hz	$K$ [N/m <sup>2</sup> ]	$7.0 \times 10^5$	$7.6 \times 10^4$	$1.1 \times 10^{-1}$	$5.0 \times 10^{-1}$
	$k$ [N/m <sup>2</sup> ]	$4.1 \times 10^4$	$1.6 \times 10^4$	$4.1 \times 10^{-1}$	1.4
	$C$ [Ns/m <sup>2</sup> ]	$8.9 \times 10^2$	$5.8 \times 10^1$	$6.4 \times 10^{-2}$	$2.5 \times 10^{-2}$
	$c$ [Ns/m <sup>2</sup> ]	$3.99 \times 10^2$	$1.3 \times 10^1$	$3.3 \times 10^{-2}$	$2.7 \times 10^{-1}$

produce different set of parameters. In order to assess the identification method estimates, a Matlab code is implemented to run the method 100 times and statistics about the parameters are computed. In both cases, the method estimated the parameters' value within an error of less that 5.0% (except for  $K$  with an error of 32.07% at 200 Hz), with a coefficient of variation of less than 0.82, as shown in Table 4.

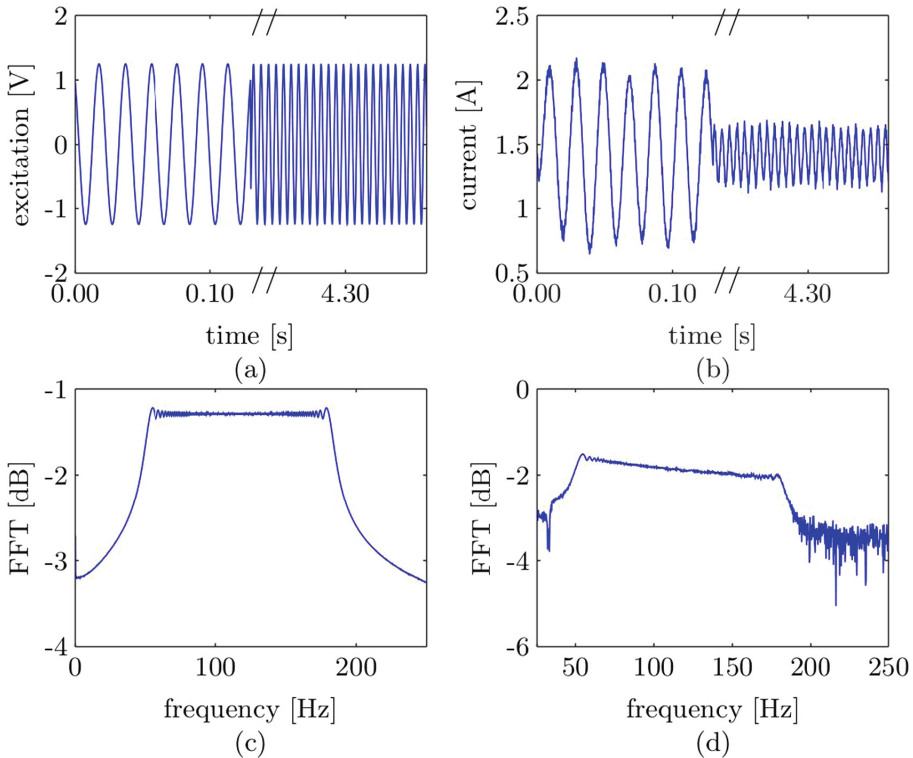


**Fig. 12.** Experimental results of the sweep excitation in the x-direction. The excitation signal is the output voltage from the NI boards. The current is measured in the top coil of actuator 1.

## 6 Preliminary Experimental Results

As of today, the test rig can operate with no pressure drop, i.e., only the baseline is fully operational. Also, variables such as pre-swirl or flow rate are not yet available. Those variables and the results for different pressure drops, rotor speed and excitation frequency will be presented in future works.

In the previous section, a pure harmonic signal was considered. For the experimental results, a sweep signal was used to excite the system from 50 Hz to 200 Hz. This was done to reduce the experiments duration. Also, the experiment was done with no rotor speed.

The experiment results are shown in Figs. 12, 13 and 14. They show the results of the baseline excitation in the x-direction. For better visualization purpose, only the initial and final parts of the time-domain data are shown. Figure 12a shows the displacement of actuator 1 in the x-direction. Its frequency-domain representation is shown in Fig. 12c, where the flat amplitude represents an equally distributed signal over the excitation band. Figure 13a shows the force in time-domain of actuator 1 in the x-direction. Its frequency-domain representa-

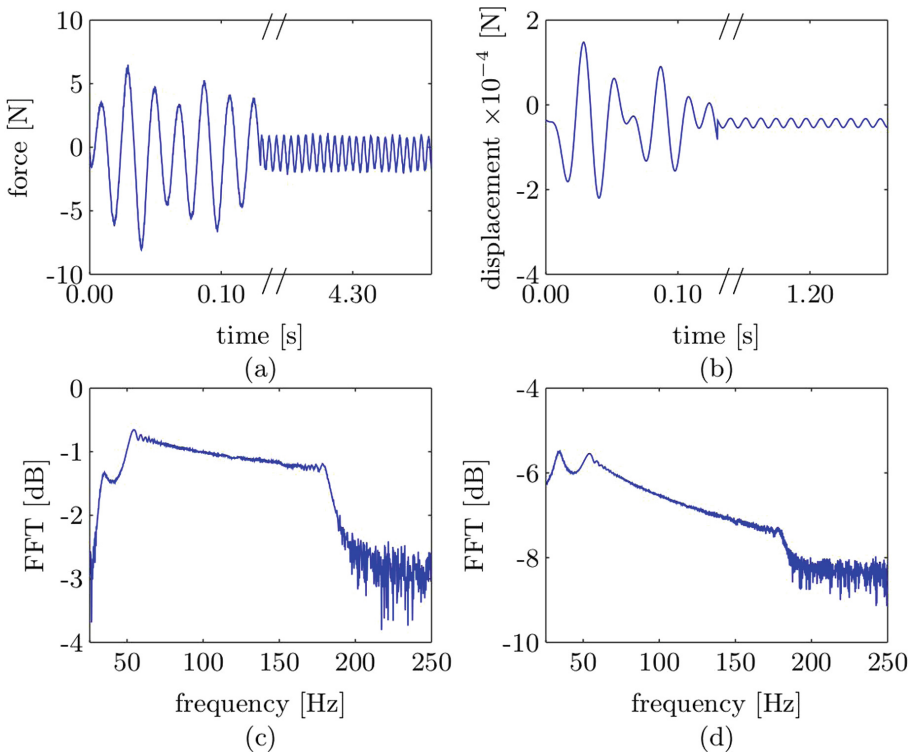


**Fig. 13.** Experimental results of the sweep excitation in the x-direction. The force is measured at the actuator 1 in the x-direction. The seal displacement is the mean displacement between actuator 1 and 2.

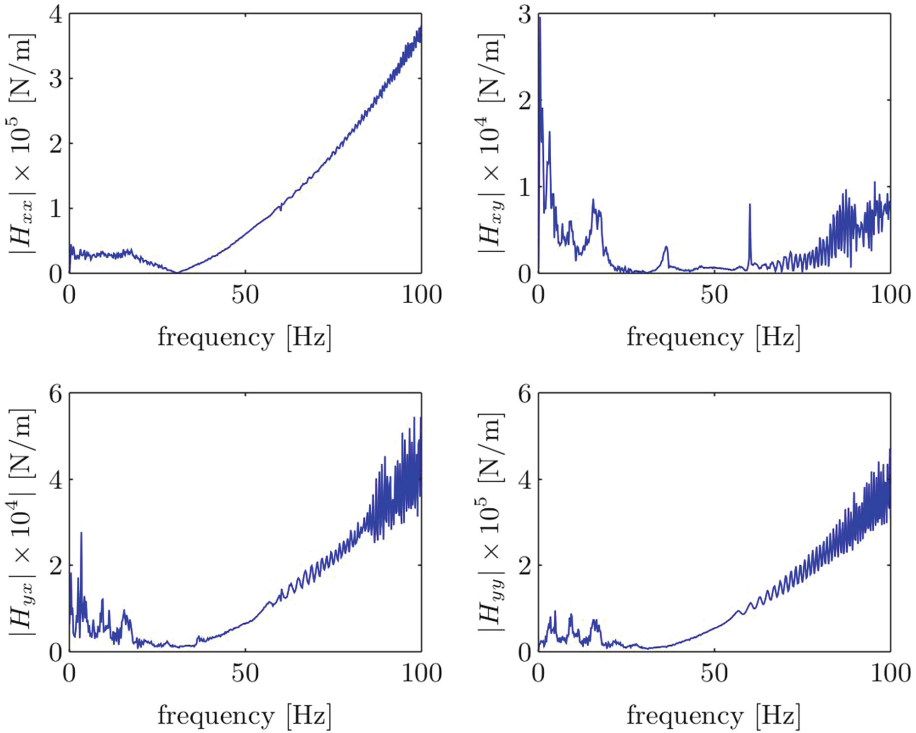


**Fig. 14.** Direct and crfigoss-coupled impedance for the rotor during the baseline operation.

tion is shown in Fig. 13c. The force does not show a constant amplitude because of the actuator and rotor dynamics over the excitation band. The actuator force decreases over the frequency for a constant excitation. The baseline impedances are shown in Fig. 14. Figures 14a and d show the direct impedances in the x and y directions. Figures 14b and c show the cross-couple impedances.

The results for high frequencies are affected considerably by the measurement noise. This occurred because the force and displacement amplitudes decrease with the frequency, which decreases the signal-to-noise value. Thus, only the impedances from 50 Hz to 100 Hz are shown. In order to overcome the problem, an estimator (such as  $H_1$ ,  $H_2$ ,  $H_3$ , etc.) can be used to reduce the effect of the noise on the results. Also, an excitation signal can be designed to increase its amplitude with the frequency. Nevertheless, as the seal-to-rotor clearance is small, rubbing phenomenon may occur.

## 7 Conclusions

The construction of a test rig for annular gas seals brings important benefits to the area of oil & gas as they use rotating machines in several processes.

Centrifugal compressors are one of those machines, and their correct operation depends on different components. This paper focused on the annular gas seals, which can destabilize rotating machines during operation. In order to estimate the seals parameters, the design of a test rig was shown. Two labyrinth seals are placed inside the rig and they are excited using two electromagnetic actuators.

An identification methodology to estimate annular gas seals was proposed. As the rotor is flexible, two ball bearings were placed on both ends, and two electromagnetic actuators were placed symmetrically closed to the seals. The identification method is based on computing a impedance matrix by exciting the rotor in two orthogonal directions.

Numerical results were shown to test the identification method before using experimental data. The deterministic model of the rotor was created using a finite-element model with Euler-Bernoulli beams. The response was computed considering a small unbalance force and electromagnetic forces. The seal displacement measurements were computed using the exact solution with an additive gaussian noise. That data was used in the identification method to estimate the direct and crossed-couple stiffness, and the direct and cross-couple damping of the seal. As the measurement were considered as random variables, the method was tested using 100 samples for two different excitation frequencies. Finally, statistics for each parameters were computed, showing that the variance and error between the mean value and the exact value are small.

Preliminary results of the identification method were shown. Experimental force, current, displacement and voltage signals were shown to explain the behavior of the machine during the baseline operation. The sweep signal excitation reduced the experiments time by varying the frequency of a harmonic wave between a frequency band. Finally, the impedances of the rotor were computed to show the behavior for different excitation frequencies. Because of the rotor and actuator dynamics, the excitation amplitude near 200 Hz is too slow compared to the noise, and thus, the impedances are not reliable. As a future work, the impedances will be computed using different estimators as  $H_1$ ,  $H_2$  or  $H_3$ , in order to enhance the results on noisy measurements. Also, the impedances will be computed with different rotor speed, excitation frequencies and pressure drops.

**Acknowledgements.** The authors would like to thank the support of the Brazilian agencies CNPq, CAPES and FAPERJ.

## References

1. Chiba, A., Fukao, T., Ichikawa, O., Oshima, M., Takemoto, M., Dorrell, D.G.: Magnetic Bearings and Bearingless Drives. Elsevier, New York City (2005)
2. Childs, D., Hale, K.: A test apparatus and facility to identify the rotordynamic coefficients of high-speed hydrostatic bearings. *J. Tribol.* **116**(2), 337–343 (1994)
3. Childs, D.W., Scharrer, J.K.: An Iwatsubo-based solution for labyrinth seals: comparison to experimental results. *J. Eng. Gas Turbines Power* **108**(2), 325 (1986)
4. Cochrane, W.W.: New-generation compressors injecting gas at Ekofisk, pp. 63–70

5. Dietzen, F.J., Nordmann, R.: Calculating rotordynamic coefficients of seals by finite-difference techniques. *J. Tribol.* **109**(3), 388–394 (1987)
6. Iwatsubo, T., Takahara, K., Kawai, R.: A new model of labyrinth seal for prediction of the dynamic force. In: *Rotordynamic Instability Problems in High-Performance Turbomachinery*, College Station, TX, May, pp. 28–30 (1984)
7. Lee, C.W.: *Mechatronics in Rotating Machinery*. Vienna, Austria (2006)
8. Nordmann, R.: Identification techniques in rotordynamics. *Diagnostics of Rotating Machines in Power Plants*. International Centre for Mechanical Sciences, vol. 352, pp. 1–24. Springer, Vienna (1994)
9. San Andrés, L., De Santiago, O.C.: Identification of bearing force coefficients from measurements of imbalance response of a flexible rotor. In: *ASME Turbo Expo 2004: Power for Land, Sea, and Air*, pp. 843–850. American Society of Mechanical Engineers (2004). <http://proceedings.asmedigitalcollection.asme.org/proceeding.aspx?articleid=1637661>
10. Schweitzer, G., Maslen, E.H.: *Magnetic Bearings: Theory, Design, and Application to Rotating Machinery*. Springer, Heidelberg (2009)
11. Smith, K.: An operational history of fractional frequency whirl. In: *Proceedings, 4th Turbomachinery Symposium*, pp. 115–125 (1974)
12. Vannini, G., Cioncolini, S., Calicchio, V., Tedone, F.: Development of a high pressure rotordynamic test rig for centrifugal compressors internal seals characterization. In: *Proceedings of the Fortieth Turbomachinery Symposium*, Houston, TX, September, pp. 12–15 (2011)
13. Wagner, N.G., Steff, K., Gausmann, R., Schmidt, M.: Investigations on the dynamic coefficients of impeller eye labyrinth seals. In: *Proceedings of the Thirty-Eighth Turbomachinery Symposium*, Houston, TX, September, pp. 14–17 (2009)
14. Wyssmann, H.R., Pham, T.C., Jenny, R.J.: Prediction of stiffness and damping coefficients for centrifugal compressor labyrinth seals. *J. Eng. Gas Turbines Power* **106**(4), 920 (1984)



# The Classical Linearization Technique's Validity for Compliant Bearings

Sebastian von Osmanski<sup>1</sup>, Jon S. Larsen<sup>2</sup>, and Ilmar F. Santos<sup>1</sup>(✉)

<sup>1</sup> Technical University of Denmark, Kongens Lyngby, Denmark  
ifs@mek.dtu.dk

<sup>2</sup> GEA Process Engineering A/S, Søborg, Denmark

**Abstract.** The Gas Foil Bearing (GFB) is a promising and environmentally friendly technology allowing support of high-speed rotating machinery with low power loss and without oil or electronics. Unfortunately, GFBs provide limited damping, making an accurate prediction of the Onset Speed of Instability (OSI) critical. This has traditionally been assessed using linearised coefficients derived from the perturbed Reynolds Equation with compliance included implicitly. Recent work has, however, revealed significant discrepancies between OSIs predicted using these techniques and those observed from nonlinear analysis. In the present work, the perturbation method's underlying assumption on the pressure field is investigated by including the hitherto neglected pressure-compliance dependency directly. This leads to an extended perturbation akin to that commonly applied to tilting pad bearings and is shown to predict OSIs with much better agreement to time integration results. The extended perturbation method is cumbersome, but serves to highlight the error introduced when applying the classical perturbation method—as developed for rigid bearings by J. W. Lund—to GFBs.

**Keywords:** Gas Foil Bearings · Perturbation · Stability

## 1 Introduction

Due to the limited damping provided by GFBs, an accurate prediction of the Onset Speed of Instability (OSI) remains critical to their application. In order to predict the lateral vibration response of GFB-supported rotors, and hence their stability, it is possible to apply linear [6, 8–11, 13, 16, 19, 24] as well as nonlinear [1–3, 7, 12, 20] approaches. In the linear approach, the gas film forces are fundamentally represented by equivalent springs and dampers with coefficients derived from a linearisation of the Reynolds Equation (RE) around one or several states of equilibrium. The calculation of such gas film coefficients can be achieved by a numerical perturbation or analytically as proposed by Lund [17]. Peng and Carpino [19] were among the first to apply Lund's perturbation technique to GFBs and such analyses have since been performed by numerous authors [6, 10, 24]. Some of these have furthermore compared their results to

nonlinear analyses showing varying levels of agreement. In recent work by the authors [14], this has been investigated by comparing the OSI of an industrial GFB-supported rotor predicted from the classical frequency domain technique to the stability limits observed from nonlinear time integration. Here, using equivalent numerical implementations for the two approaches, a significant discrepancy was demonstrated and shown to be increasing with the level of compliance.

A possible root cause of the observed disagreement can be found in a primary assumption of the classical perturbation approach, namely that the pressure field depends exclusively on the rotor position and velocity. Assuming subsequently the rotor to perform small harmonic oscillations, a Taylor series expansion can be inserted into RE to solve for the eight bearing stiffness and damping coefficients.

In the present work, the importance of the—thus far neglected—pressure–compliance dependency is investigated. The pressure field is thus assumed to depend not only on the rotor position and velocity, but also on the degrees of freedom (DOFs) representing the foil deflection. This additionally requires the solution of a dynamic pressure field for each of the foil DOFs and hence provides a coefficient matrix with contributions from each of these, analogous to the coefficient matrices often used for tilting pad journal bearings. Using a simple and widely studied GFB configuration [21] supporting a point mass as starting point, OSI predictions from the extended perturbation method are compared to results from both a classical perturbation method and a simultaneous nonlinear time integration. These two reference models are identical to those previously presented by the authors [11, 12, 14] and have been experimentally validated. It should be emphasized that the vibrations occurring at the investigated OSI stems from a self-excited instability and thus are related exclusively to the homogeneous part of the equation system. This should not be confused with the onset of forced subsynchronous vibrations caused by the unbalance excitation in conjunction with the nonlinear GFB characteristics. The appearance of the latter is influenced by the level of unbalance, while the former is not.

The additional terms included in the extended perturbation multiplies the effort needed to attain the bearing coefficients and complicates their subsequent interpretation, but the extension is demonstrated to provide results in much better agreement to those obtainable from nonlinear time integration. The challenges of the extension are discussed and the significance of the foil–compliance terms is treated to illuminate the error introduced when neglecting them. In this sense, the novel contribution of the present work is to identify the limits of validity for the classical perturbation method with respect to compliance.

## 2 The Extended Perturbation Method

In addition to the eccentricities, the pressure field  $p$  is assumed to depend on  $N$  DOFs. These dependencies can be collected in the vector  $\mathbf{q}$  as

$$\mathbf{q} = \{e_x \ e_y \ w_1 \ \cdots \ w_N\}^T \in \mathbb{R}^{2+N}, \quad (1)$$

where  $e_x$  and  $e_y$  are the rotor eccentricity components and  $w_j$  denotes the  $j$ -th foil compliance DOF. Using Eq. (1), a first order Taylor series expansion of the pressure field around a state  $(\mathbf{q}_0, \dot{\mathbf{q}}_0)$  can be written as

$$p = p(\mathbf{q}, \dot{\mathbf{q}}) \approx p(\mathbf{q}_0, \dot{\mathbf{q}}_0) + \left. \frac{\partial p}{\partial \mathbf{q}} \right|_{\mathbf{q}_0, \dot{\mathbf{q}}_0} (\mathbf{q} - \mathbf{q}_0) + \left. \frac{\partial p}{\partial \dot{\mathbf{q}}} \right|_{\mathbf{q}_0, \dot{\mathbf{q}}_0} (\dot{\mathbf{q}} - \dot{\mathbf{q}}_0). \quad (2)$$

Defining  $\mathbf{q}_0$  as the stationary point where  $\dot{\mathbf{q}} = 0$ , and assuming all DOFs to exhibit small harmonic oscillations around this point with frequency  $\omega_s$  as

$$e_\gamma = e_{\gamma 0} + \Delta e_\gamma e^{i\omega_s t}, \quad \gamma = x, y \quad \text{and} \quad w_j = w_{j0} + \Delta w_j e^{i\omega_s t}, \quad j = 1, \dots, N, \quad (3)$$

the pressure field expansion from Eq. (2) becomes

$$p = p_0 + p_x \Lambda_x + p_y \Lambda_y + \sum_{j=1}^N p_{w_j} \Lambda_j, \quad (4)$$

where

$$p_0 = p(\mathbf{q}_0), \quad (5)$$

$$p_\gamma = \left( \left. \frac{\partial p}{\partial e_\gamma} \right|_{\mathbf{q}_0} + i\omega_s \left. \frac{\partial p}{\partial \dot{e}_\gamma} \right|_{\mathbf{q}_0} \right), \quad \gamma = x, y, \quad (6)$$

$$p_{w_j} = \left( \left. \frac{\partial p}{\partial w_j} \right|_{\mathbf{q}_0} + i\omega_s \left. \frac{\partial p}{\partial \dot{w}_j} \right|_{\mathbf{q}_0} \right), \quad j = 1, \dots, N, \quad (7)$$

$$\Lambda_\gamma = \Delta e_\gamma e^{i\omega_s t}, \quad \gamma = x, y, \quad (8)$$

$$\Lambda_j = \Delta w_j e^{i\omega_s t}, \quad j = 1, \dots, N, \quad (9)$$

so that  $p_0 \in \mathbb{R}$  and  $p_\gamma, p_{w_j}, \Lambda_\gamma, \Lambda_j \in \mathbb{C}$ .

## 2.1 The Film Height Function

For the present purpose of investigating the pressure–compliance dependency, the rotor is assumed to be perfectly aligned and the foil is assumed to deform uniformly in the axial direction. Axial film height variations are hence neglected and the film height function becomes one-dimensional. This has previously been shown to be reasonable [23], but the proposed perturbation method is not restricted to such assumptions.

Referring to Fig. 1b, the film height is composed of a rigid contribution,

$$h_r = C + e_x \cos \theta + e_y \sin \theta, \quad (10)$$

and a compliant contribution  $h_c$  stemming from the deformation of the foil structure. It is hence necessary to establish a relation between the foil DOFs  $w_j$  and the deformed shape of the top foil. The foil DOFs could be representing Fourier series amplitudes or polynomial coefficients, but for now they will represent discrete point deformations directly such that  $w_j = h_c(\theta_j)$ . To simplify the



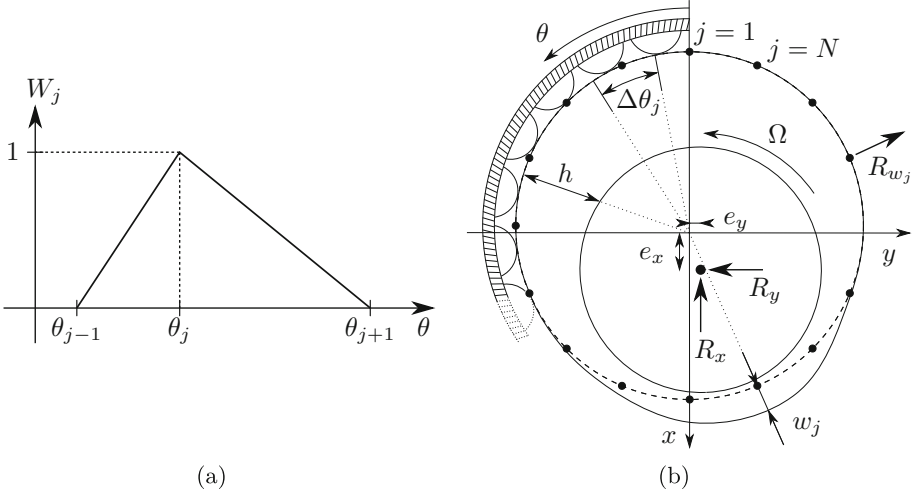


**Fig. 1.** (a) Weight function associated with the  $j$ -th foil compliance DOF; (b) Schematics of the GFB and illustration of the perturbed DOFs.

numerical implementation, the points  $\theta_j$  are furthermore chosen to be coincident with the circumferential discretization of the fluid film.

In order to evaluate the deformed shape between the discrete points, a simple linear interpolation is applied that is consistent with the linear shape functions applied for the finite element (FE) discretization of RE. A weight function is hence defined for each foil DOF as illustrated in Fig. 1a and given as

$$W_j(\theta) = \begin{cases} \frac{\theta - \theta_{j-1}}{\theta_j - \theta_{j-1}} & \text{if } \theta_{j-1} < \theta < \theta_j \\ \frac{\theta_{j+1} - \theta}{\theta_{j+1} - \theta_j} & \text{if } \theta_j \leq \theta < \theta_{j+1} \\ 0 & \text{otherwise,} \end{cases} \quad (11)$$

such that the continuous compliant film height contribution can be written as

$$h_c = \sum_{j=1}^N w_j W_j(\theta). \quad (12)$$

This finally allows, when introducing the perturbations from Eq. (3), the perturbed film height to be written as

$$h = h_r + h_c = h_0 + \Lambda_x \cos \theta + \Lambda_y \sin \theta + \sum_{j=1}^N \Lambda_j W_j(\theta) \quad (13)$$

where the static film height  $h_0$  is given from

$$h_0 = C + e_{x0} \cos \theta + e_{y0} \sin \theta + \sum_{j=1}^N w_{j0} W_j(\theta). \quad (14)$$

## 2.2 Perturbation of Reynolds Equation

Defining the circumferential and axial coordinates  $\Theta = \theta R$  and  $z$  in a bearing with radius  $R$ , the isothermal, compressible and transient RE can be written as

$$\frac{\partial}{\partial \Theta} \left( \frac{ph^3}{12\mu} \frac{\partial p}{\partial \Theta} \right) + \frac{\partial}{\partial z} \left( \frac{ph^3}{12\mu} \frac{\partial p}{\partial z} \right) = \frac{\partial}{\partial \Theta} (phU) + \frac{\partial}{\partial t} (ph), \quad (15)$$

where  $\mu$  is the gas viscosity and  $U = R\Omega/2$  is the circumferential gas film velocity. Substituting Eqs. (4) and (13) into Eq. (15) while neglecting higher order terms, the zeroth and first order equations can be separated. The zeroth order equation obtains the familiar form

$$\frac{\partial}{\partial \Theta} \left( \frac{p_0 h_0^3}{12\mu} \frac{\partial p_0}{\partial \Theta} \right) + \frac{\partial}{\partial z} \left( \frac{p_0 h_0^3}{12\mu} \frac{\partial p_0}{\partial z} \right) = \frac{\partial}{\partial \Theta} (p_0 h_0 U), \quad (16)$$

while the two first order equations for  $p_x$  and  $p_y$  can be written as

$$\begin{aligned} & \frac{\partial}{\partial \Theta} \left( \frac{p_0 h_0^3}{12\mu} \frac{\partial p_\gamma}{\partial \Theta} \right) + \frac{\partial}{\partial z} \left( \frac{p_0 h_0^3}{12\mu} \frac{\partial p_\gamma}{\partial z} \right) + \frac{\partial}{\partial \Theta} \left( \frac{p_\gamma h_0^3}{12\mu} \frac{\partial p_0}{\partial \Theta} \right) + \\ & \frac{\partial}{\partial z} \left( \frac{p_\gamma h_0^3}{12\mu} \frac{\partial p_0}{\partial z} \right) - \frac{\partial}{\partial \Theta} (p_\gamma h_0 U) - i\omega_s p_\gamma h_0 = -\frac{\partial}{\partial \Theta} \left( \frac{p_0 h_0^2 f_\gamma}{4\mu} \frac{\partial p_0}{\partial \Theta} \right) \\ & - \frac{\partial}{\partial z} \left( \frac{p_0 h_0^2 f_\gamma}{4\mu} \frac{\partial p_0}{\partial z} \right) + \frac{\partial}{\partial \Theta} (p_0 U f_\gamma) + i\omega_s p_0 f_\gamma, \quad \gamma = x, y, \end{aligned} \quad (17)$$

where  $f_x = \cos \theta$  and  $f_y = \sin \theta$ , and, finally, the  $N$  first order equations for  $p_{w_j}$  related to the foil DOFs become

$$\begin{aligned} & \frac{\partial}{\partial \Theta} \left( \frac{p_0 h_0^3}{12\mu} \frac{\partial p_{w_j}}{\partial \Theta} \right) + \frac{\partial}{\partial z} \left( \frac{p_0 h_0^3}{12\mu} \frac{\partial p_{w_j}}{\partial z} \right) + \frac{\partial}{\partial \Theta} \left( \frac{p_{w_j} h_0^3}{12\mu} \frac{\partial p_0}{\partial \Theta} \right) + \\ & \frac{\partial}{\partial z} \left( \frac{p_{w_j} h_0^3}{12\mu} \frac{\partial p_0}{\partial z} \right) - \frac{\partial}{\partial \Theta} (p_{w_j} h_0 U) - i\omega_s p_{w_j} h_0 = -\frac{\partial}{\partial \Theta} \left( \frac{p_0 h_0^2 W_j}{4\mu} \frac{\partial p_0}{\partial \Theta} \right) \\ & - \frac{\partial}{\partial z} \left( \frac{p_0 h_0^2 W_j}{4\mu} \frac{\partial p_0}{\partial z} \right) + \frac{\partial}{\partial \Theta} (p_0 U W_j) + i\omega_s p_0 W_j, \quad j = 1, \dots, N. \end{aligned} \quad (18)$$

## 2.3 The Coefficient Matrix

Having obtained  $p_0$ ,  $p_\gamma$  and  $p_{w_j}$  by a suitable numerical solution scheme, these can be integrated to obtain the fluid film forces  $\mathbf{f}$ . Using Eq. (4), these can be written as

$$\mathbf{f} = \left\{ \begin{array}{l} \int_0^L \int_0^{2\pi} (p - p_a) \begin{Bmatrix} \cos \theta \\ \sin \theta \end{Bmatrix} R d\theta dz \\ \int_0^L \int_{\theta_1 - \frac{1}{2}\Delta\theta_1}^{\theta_1 + \frac{1}{2}\Delta\theta_1} (p - p_a) R d\theta dz \\ \vdots \\ \int_0^L \int_{\theta_N - \frac{1}{2}\Delta\theta_N}^{\theta_N + \frac{1}{2}\Delta\theta_N} (p - p_a) R d\theta dz \end{array} \right\} = \mathbf{f}_0 + \begin{bmatrix} \mathbf{Z}_{ee} & \mathbf{Z}_{ew} \\ \mathbf{Z}_{we} & \mathbf{Z}_{ww} \end{bmatrix} \tilde{\mathbf{q}} e^{i\omega_s t}, \quad (19)$$

where the static force is given as the vector

$$\mathbf{f}_0 = \begin{Bmatrix} \int_0^L \int_0^{2\pi} (p_0 - p_a) \begin{Bmatrix} \cos \theta \\ \sin \theta \end{Bmatrix} R d\theta dz \\ \int_0^L \int_{\theta_1 - \frac{1}{2}\Delta\theta_1}^{\theta_1 + \frac{1}{2}\Delta\theta_1} (p_0 - p_a) R d\theta dz \\ \vdots \\ \int_0^L \int_{\theta_N - \frac{1}{2}\Delta\theta_N}^{\theta_N + \frac{1}{2}\Delta\theta_N} (p_0 - p_a) R d\theta dz \end{Bmatrix} \in \mathbb{R}^{2+N}, \quad (20)$$

and the dynamic forces are expressed in terms of the perturbation vector

$$\tilde{\mathbf{q}} = \{\Delta e_x \ \Delta e_y \ \Delta w_1 \ \cdots \ \Delta w_N\}^T \in \mathbb{R}^{2+N}, \quad (21)$$

along with the matrix  $\mathbf{Z}$  with blocks given as

$$\mathbf{Z}_{ee} = \int_0^L \int_0^{2\pi} \begin{bmatrix} p_x \cos \theta & p_y \cos \theta \\ p_x \sin \theta & p_y \sin \theta \end{bmatrix} R d\theta dz \in \mathbb{C}^{2 \times 2}, \quad (22)$$

$$\mathbf{Z}_{ew} = \int_0^L \int_0^{2\pi} \begin{bmatrix} p_{w_1} \cos \theta \ \cdots \ p_{w_N} \cos \theta \\ p_{w_1} \sin \theta \ \cdots \ p_{w_N} \sin \theta \end{bmatrix} R d\theta dz \in \mathbb{C}^{2 \times N}, \quad (23)$$

$$\mathbf{Z}_{we} = \begin{bmatrix} \int_0^L \int_{\theta_1 - \frac{1}{2}\Delta\theta_1}^{\theta_1 + \frac{1}{2}\Delta\theta_1} [p_x \ p_y] R d\theta dz \\ \vdots \\ \int_0^L \int_{\theta_N - \frac{1}{2}\Delta\theta_N}^{\theta_N + \frac{1}{2}\Delta\theta_N} [p_x \ p_y] R d\theta dz \end{bmatrix} \in \mathbb{C}^{N \times 2}, \quad (24)$$

$$\mathbf{Z}_{ww} = \begin{bmatrix} \int_0^L \int_{\theta_1 - \frac{1}{2}\Delta\theta_1}^{\theta_1 + \frac{1}{2}\Delta\theta_1} [p_{w_1} \ \cdots \ p_{w_N}] R d\theta dz \\ \vdots \\ \int_0^L \int_{\theta_N - \frac{1}{2}\Delta\theta_N}^{\theta_N + \frac{1}{2}\Delta\theta_N} [p_{w_1} \ \cdots \ p_{w_N}] R d\theta dz \end{bmatrix} \in \mathbb{C}^{N \times N}. \quad (25)$$

Finally,  $\mathbf{Z}$  is related to the dynamic stiffness and damping coefficients as

$$\mathbf{K}_{\text{fluid}} = \text{Re}(\mathbf{Z}) = \begin{bmatrix} k_{xx} & k_{xy} & k_{xw_1} & \cdots & k_{xw_N} \\ k_{yx} & k_{yy} & k_{yw_1} & \cdots & k_{yw_N} \\ k_{w_1x} & k_{w_1y} & k_{w_1w_1} & \cdots & k_{w_1w_N} \\ \vdots & \vdots & \vdots & \ddots & \vdots \\ k_{w_Nx} & k_{w_Ny} & k_{w_Nw_1} & \cdots & k_{w_Nw_N} \end{bmatrix} \in \mathbb{R}^{(2+N) \times (2+N)}, \quad (26)$$

$$\mathbf{D}_{\text{fluid}} = \frac{1}{\omega_s} \text{Im}(\mathbf{Z}) = \begin{bmatrix} d_{xx} & d_{xy} & d_{xw_1} & \cdots & d_{xw_N} \\ d_{yx} & d_{yy} & d_{yw_1} & \cdots & d_{yw_N} \\ d_{w_1x} & d_{w_1y} & d_{w_1w_1} & \cdots & d_{w_1w_N} \\ \vdots & \vdots & \vdots & \ddots & \vdots \\ d_{w_Nx} & d_{w_Ny} & d_{w_Nw_1} & \cdots & d_{w_Nw_N} \end{bmatrix} \in \mathbb{R}^{(2+N) \times (2+N)}. \quad (27)$$

## 2.4 Including the Foil Stiffness and Damping

The bearing coefficients in Eqs. (26) and (27) are derived from the dynamic pressure fields and thus contain merely the contributions from the fluid film.

When evaluating the displacement of the  $j$ -th foil DOF from its equilibrium  $w_{j0}$ , the stiffness and damping of the foil itself should furthermore be considered.

Various elaborate foil structure models are available in the literature [4, 15, 18, 22], but the added complexity of these would not benefit the present comparison. Instead, the Simple Elastic Foundation Model (SEFM), as introduced by Heshmat et al. [5], is employed with a uniform baseline stiffness derived from the widely applied expression by Walowit and Anno [25]

$$k = \frac{E_b}{2S_b} \left( \frac{t_b}{l_0} \right)^3 (1 - \nu_b^2)^{-1}, \quad (28)$$

where  $E_b$ ,  $S_b$ ,  $t_b$ ,  $l_0$  and  $\nu_b$  are the bump foil's Young's modulus, pitch, thickness, half bump length and Poisson's ratio, respectively. The damping is assumed viscous and expressed simply as  $d = k\eta/\omega_s$  where  $\eta$  is a loss factor. A fundamental assumption of the SEFM is that all points in the foil behave independently, meaning that the foil structure is assumed not to contribute any cross couplings. Furthermore, the foil is not directly affecting the  $e_x, e_y$  DOFs, meaning that the stiffness and damping matrices stemming from the bump foil can be written as

$$\begin{aligned} \mathbf{K}_{\text{foil}} &= LRk \text{diag} [0 \ 0 \ \Delta\theta_1 \ \cdots \ \Delta\theta_N] \in \mathbb{R}^{(2+N) \times (2+N)}, \\ \mathbf{D}_{\text{foil}} &= \eta\omega_s^{-1} \mathbf{K}_{\text{foil}} \in \mathbb{R}^{(2+N) \times (2+N)}, \end{aligned} \quad (29)$$

where  $L$  is the axial length of the bearing and  $\Delta\theta_j$  is the angular segment ascribed to the  $j$ -th foil DOF as illustrated in Fig. 1b.

## 2.5 The Mass Matrix

The rotor is modelled as a point mass, implying that neither polar nor transverse inertia is considered. Combining the rotor mass with a rough estimate of the foil mass ascribed to each foil DOF, the system mass matrix is constructed as

$$\mathbf{M} = \text{diag} [m_x \ m_y \ m'_{\text{foil}} R\Delta\theta_1 \ \cdots \ m'_{\text{foil}} R\Delta\theta_N] \in \mathbb{R}^{(2+N) \times (2+N)}, \quad (30)$$

where  $m_x = m_y$  is the rotor mass and  $m'_{\text{foil}}$  is the average mass of the foil structure per unit circumferential length.

## 2.6 System Assembly

Combining Eqs. (26), (27), (29) and (30), the linearised  $2 + N$  equations of motion for the rotor-bearing system can be written as

$$\mathbf{M}\ddot{\tilde{\mathbf{q}}} + \underbrace{(\mathbf{D}_{\text{foil}} + \mathbf{D}_{\text{fluid}})}_{\equiv \mathbf{D}(\omega_s, \Omega)} \dot{\tilde{\mathbf{q}}} + \underbrace{(\mathbf{K}_{\text{foil}} + \mathbf{K}_{\text{fluid}})}_{\equiv \mathbf{K}(\omega_s, \Omega)} \tilde{\mathbf{q}} = \mathbf{0}, \quad (31)$$

which can be recast into first order form using the state vector  $\mathbf{z} = \{\tilde{\mathbf{q}} \ \dot{\tilde{\mathbf{q}}}\}^T$  as

$$\dot{\mathbf{z}} = \underbrace{\begin{bmatrix} \mathbf{0} & \mathbf{I} \\ \mathbf{M}^{-1}\mathbf{K}(\omega_s, \Omega) & \mathbf{M}^{-1}\mathbf{D}(\omega_s, \Omega) \end{bmatrix}}_{\equiv \mathbf{A}(\omega_s, \Omega)} \mathbf{z}, \quad (32)$$

where  $\mathbf{0}$  and  $\mathbf{I}$  denote  $(2 + N) \times (2 + N)$  zero and identity matrices, respectively.

### 3 Review of the Classical Two-DOF Perturbation

To emphasize the novel aspects of the proposed extended perturbation, a brief review of the traditional two-DOF approach employed with variations by e.g. [6, 8–11, 13, 16, 19, 24] is included. As originally introduced in the appendix of [17], a fundamental assumption is for the pressure field to be given as a function of rotor position and velocity only. This means that a Taylor expansion leads to a perturbed pressure field given as

$$p = p_0 + p_x \Lambda_x + p_y \Lambda_y, \quad (33)$$

which should be compared to Eq. (4) of the extended perturbation. The foil compliance is then introduced implicitly through the film height function as

$$h = C + e_x \cos \theta + e_y \sin \theta + f_{h_c}(p), \quad (34)$$

where  $f_{h_c}(p)$  is some function supplying the compliant film height as a function of pressure. For the SEFM incorporating a loss factor, this would be

$$f_{h_c}(p) = k_c^{-1}(p - p_a) \quad \text{where } k_c = k(1 + i\eta). \quad (35)$$

Inserting the film height Eq. (34) and perturbed pressure Eq. (33) into RE from Eq. (15), equations for  $p_0$  and  $p_\gamma$  can be separated. The zeroth order equation is identical to the one obtained for the extended perturbation in Eq. (16), while the first order equations for  $p_\gamma$  become

$$\begin{aligned} \frac{\partial}{\partial \Theta} \left( \frac{p_0 h_0^3}{12\mu} \frac{\partial p_\gamma}{\partial \Theta} \right) + \frac{\partial}{\partial z} \left( \frac{p_0 h_0^3}{12\mu} \frac{\partial p_\gamma}{\partial z} \right) + \frac{\partial}{\partial \Theta} \left( \frac{p_\gamma h_0^2 (h_0 + [3p_0 k_c^{-1}])}{12\mu} \frac{\partial p_0}{\partial \Theta} \right) \\ + \frac{\partial}{\partial z} \left( \frac{p_\gamma h_0^2 (h_0 + [3p_0 k_c^{-1}])}{12\mu} \frac{\partial p_0}{\partial z} \right) - \frac{\partial}{\partial \Theta} (p_\gamma (h_0 + [p_0 k_c^{-1}])) U \\ - i\omega_s p_\gamma (h_0 + [p_0 k_c^{-1}]) = - \frac{\partial}{\partial \Theta} \left( \frac{p_0 h_0^2 f_\gamma}{4\mu} \frac{\partial p_0}{\partial \Theta} \right) \\ - \frac{\partial}{\partial z} \left( \frac{p_0 h_0^2 f_\gamma}{4\mu} \frac{\partial p_0}{\partial z} \right) + \frac{\partial}{\partial \Theta} (p_0 U f_\gamma) + i\omega_s p_0 f_\gamma, \quad \gamma = x, y \end{aligned} \quad (36)$$

where

$$h_0 = C + e_{x0} \cos \theta + e_{y0} \sin \theta + k_c^{-1}(p_0 - p_a). \quad (37)$$

which should be compared to Eq. (17) of the extended perturbation (the differences are framed in square brackets). The classical technique hence requires the solution of a nonlinear equation for  $p_0$  and two linear complex equations for  $p_\gamma$  from which the bearing coefficients can be extracted as

$$\begin{bmatrix} k_{xx} & k_{xy} \\ k_{yx} & k_{yy} \end{bmatrix} + i\omega_s \begin{bmatrix} d_{xx} & d_{xy} \\ d_{yx} & d_{yy} \end{bmatrix} = \int_0^L \int_0^{2\pi} \begin{bmatrix} p_x \cos \theta & p_y \cos \theta \\ p_x \sin \theta & p_y \sin \theta \end{bmatrix} R d\theta dz \in \mathbb{C}^{2 \times 2}, \quad (38)$$

involving only the two rotor DOFs (per bearing).

## 4 Solution Strategy

The zeroth order Eq. (16) is a nonlinear real equation in  $p_0$  where  $h_0$  is given from Eq. (14). The assumption of an axially uniform deformation combined with the SEFM means that when solving for  $p_0$ , the discrete foil compliance  $w_j$  is calculated in each iteration from the local mean axial static pressure as

$$w_j = \frac{1}{k} \left( \frac{1}{L} \int_0^L p_0(\theta_j) dz - p_a \right). \quad (39)$$

The zeroth order equation is identical to that presented by the authors in [11] and the same solution strategy based on an FE discretization and Newton-Raphson iteration is employed. Notice that sub-ambient pressures are discarded when integrating the pressure fields (the Gumbel condition). As described in [11], this is meant to represent the effect of the top foil separation from the bump foil [5].

The  $2 + N$  first order Eqs. (17) and (18) for  $p_\gamma$  and  $p_{w_j}$  are linear complex equations which are solved using the FE discretization documented in [11]. Notice that while [11] treats the solution to the  $p_\gamma$  equations produced by an implicit treatment of the foil compliance as in Eq. (36), this collapses into Eq. (17) for  $k_c^{-1} = 0$  and the same solution method can be applied.

A converged mesh of 17 axial (over half the bearing length, as symmetry is exploited) and 114 circumferential elements is used giving 2070 nodes. The number of circumferential locations, and hence the number of  $p_{w_j}$  equation systems to be solved, is thus  $N = 115$ .

## 5 Results and Discussion

The proposed method is evaluated by predicting the OSI for the simplest possible case of a point mass supported by a single-pad GFB in the widely studied configuration [21] listed in Table 1. The OSI is calculated using: (a) a simultaneous nonlinear time integration; (b) a classical two-DOF perturbation; and (c) the proposed extended perturbation. For the present bearing, Eq. (28) predicts a foil stiffness of 4.6417 GN/m<sup>3</sup> (case 2) which is evaluated along with a practically rigid (case 1: 4641.7 GN/m<sup>3</sup>) and a more flexible (case 3: 2.3209 GN/m<sup>3</sup>) variant. To put these stiffness levels into perspective, the maximum static foil deflection in the three cases at 20 kRPM are 0.00, 0.21 and 0.40 times  $C$  respectively.

### 5.1 Stability Analysis: Frequency Domain

To assess the linear stability limit of the rotor system described by Eq. (32), a solution on the standard form  $\tilde{\mathbf{z}} = \tilde{\mathbf{z}}_0 e^{\lambda t}$  is substituted to produce the standard eigenvalue problem  $\mathbf{A}(\omega_s, \Omega) \tilde{\mathbf{z}} = \lambda \tilde{\mathbf{z}}$ . Having solved this, an eigenvalue  $\lambda_i$  with positive real part then indicates the corresponding eigenmode  $\tilde{\mathbf{z}}_i$  to be unstable.

Applying the classical two-DOF perturbation to a single bearing with coefficients given from Eq. (38), four eigenvalues in complex conjugated pairs are

**Table 1.** Properties of the GFB configuration, mainly from [21].

<b>Journal</b>			
Load, $W_x = m_x g$	30 N	Mass, $m = m_x = m_y$	3.059 kg
<b>Bearing configuration</b>			
Bearing radius, $R$	19.05 mm	Pad leading edge, $\theta_l$	0°
Bearing length, $L$	38.10 mm	Pad trailing edge, $\theta_t$	360°
Radial clearance, $C$	31.80 $\mu\text{m}$		
<b>Fluid properties</b>			
Ambient pressure, $p_a$	101.3 kPa	Viscosity, $\mu$	$1.950 \times 10^5 \text{ Pa s}$
<b>Foil structure properties</b>			
Foil thickness, $t_b$	0.1016 mm	Bump pitch, $S_b$	4.572 mm
Bump half length, $l_0$	1.778 mm	Bump height, $h_b$	0.5080 mm
Young's modulus $E_b$	207.0 GPa	Poisson's ratio, $\nu_b$	0.3
Density, $\rho_b$	8280 $\text{kg/m}^3$	Loss factor, $\eta$	0.2

obtained. By contrast, the extended perturbation in its current implementation and with the applied mesh results in  $2(2 + 115) = 234$  eigenvalues. As the eigenvalues of both methods depend on the oscillation frequency and the angular velocity, the stability limit, i.e. the OSI, is characterised by the condition

$$\text{Re}(\lambda_i(\omega_s, \Omega = \Omega_{\text{OSI}})) = 0 \quad \wedge \quad \text{Im}(\lambda_i(\omega_s, \Omega = \Omega_{\text{OSI}})) = \omega_s, \quad (40)$$

requiring the eigenvalue problem to be solved over a range of excitation frequencies and angular velocities. Here it should be highlighted that one should keep track of the eigenvalue order in between the  $(\omega_s, \Omega)$  evaluation points. This is a trivial task for the two complex conjugated pairs arising from the two-DOF approach, but becomes a significant challenge for the 117 pairs obtained from the extended perturbation. At present, this has been handled by comparing the structure of the corresponding eigenvectors.

The result is shown in Fig. 2, where the contours of the logarithmic decrement (LD)  $\delta = -2\pi \text{Re}(\lambda) / \text{Im}(\lambda)$  is plotted along with a single contour showing the concurrence of the excitation frequency  $\omega_s$  and the damped natural frequency  $\omega_d = \text{Im}(\lambda)$ . The crossing of the  $\delta = 0$  contour is exactly where Eq. (40) is fulfilled and thus marks the OSI. The shown plot is for one of the two eigenmodes dominated by the rotor and is the one first becoming unstable. The mass of the foil from Eq. (30) used in the eigenvalue solution is a rough estimate, but it has been verified that this has a vanishing influence on the OSI.

A similar plot is shown in Fig. 3, but obtained using the traditional two-DOF perturbation method. The maps are similar, but the OSI is shifted more than 4kRPM and it is worth emphasizing the difference in computational cost. While both stability maps are based on solutions to 2805 eigenvalue problems, the extended perturbation requires solving 117  $2070 \times 2070$  complex linear equation systems to obtain the coefficients forming each of the  $234 \times 234$  eigenvalue prob-

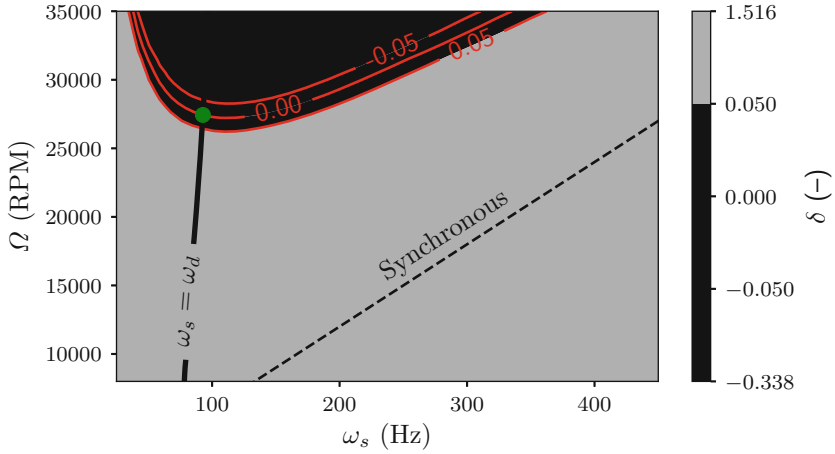


**Fig. 2.** Case 3 stability map based on the extended perturbation and eigenvalue solutions over a  $51 \times 55$  ( $\omega_s, \Omega$ ) grid. The OSI is marked at (92.8 Hz, 27 424 RPM).

lems to be solved. In the traditional perturbation, each eigenvalue problem is merely  $4 \times 4$  and the coefficients can be extracted from just two complex linear equation system solutions. The effort related to solving the zeroth order equation for each value of  $\Omega$  is, however, the same for both methods. For the current implementation, the two-DOF perturbation calculations for Fig. 3 take around 45 s while the extended perturbation calculations for Fig. 2 take 10 times longer.

### 5.2 Stability Analysis: Time Domain

In the nonlinear sense, the stability limit is characterised by a breakdown of structural stability due to a small change in the angular velocity. At this point, the system Jacobian evaluated at the singular point representing the static equilibrium obtains an eigenvalue with zero real part. After this point, the behaviour will be governed by the system’s nonlinear characteristics and should not be compared to the linear solutions.

To assess the stability limit, Eq. (15) is FE discretized and simultaneously integrated in time with zero unbalance as described in [14]. The implementation has been carefully aligned to that used when solving the perturbed equations. A time integration can hence be started from the static equilibrium found from Eq. (16) and the development of the oscillation amplitude can be observed. Such analysis is, however, subject to several challenges. First, even for an asymptotically stable state, the vibration amplitude of a numerical integration will never reach zero. Instead, it converges towards a noise floor specific to the numerical implementation. Initiating a time integration from a static equilibrium will hence always imply some oscillation. Second, even before the true structural stability limit is reached at  $\Omega = \Omega_{OSL}$ , the static equilibrium state’s basin of attraction



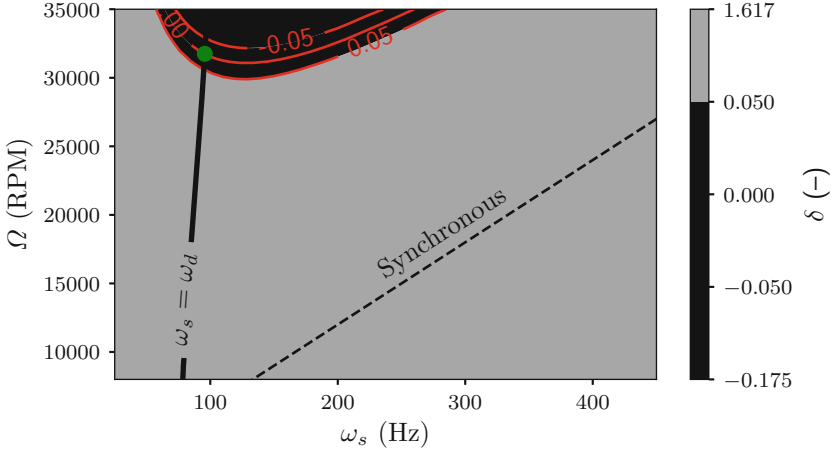


**Fig. 3.** Case 3 stability map based on the two-DOF perturbation and eigenvalue solutions over a  $51 \times 55$  ( $\omega_s, \Omega$ ) grid. The OSI is marked at (95.7 Hz, 31 769 RPM).

will gradually narrow, increasing the possibility that an incidental numerical perturbation will push the system away from the stable equilibrium.

To demonstrate the uncertainty related to the OSI using time integration, 1 s simulations have been initialized from their static equilibria for every 10 RPM in the range 23–25 kRPM. For each response it is easy to judge whether the oscillation remains within the numerical noise level or grows exponentially. In Fig. 4a, it is shown that some responses grow exponentially from around 23 kRPM, but that this is not persistent until 25.5 kRPM. This is, however, highly dependent on the tolerances applied in both the steady state solver and the subsequent time integration. More consistent results were found to be achievable when perturbing the static eccentricity just enough to leave the numerical noise floor. An initial perturbation of  $10^{-10}$  on the eccentricity ratio ( $= 31.8 \times 10^{-16}$  m) thus results in tiny, but very clean oscillations from which the decay or growth can be identified. Plotting the LD obtained from curve fitting to each time series shows a monotonically decreasing curve with a distinct zero-crossing as shown in Fig. 4b. The OSI identified using this method is denoted  $\tilde{\Omega}_{\text{OSI}}$  to distinguish it from the more firmly defined OSI resulting from the frequency domain analysis.

### 5.3 Comparison of OSIs

The OSIs obtained using the perturbation methods and time integration are listed in Table 2 for all three cases of foil stiffness. The excitation frequencies at the OSI are likewise listed for comparison. For the time integration, the latter has been extracted from frequency spectra based on 5 s simulations at angular frequencies slightly above  $\tilde{\Omega}_{\text{OSI}}$ . The relative OSI discrepancies are plotted in Fig. 5 as a function of foil flexibility, and the extended perturbation is seen to provide results better in agreement with the nonlinear time integration results.

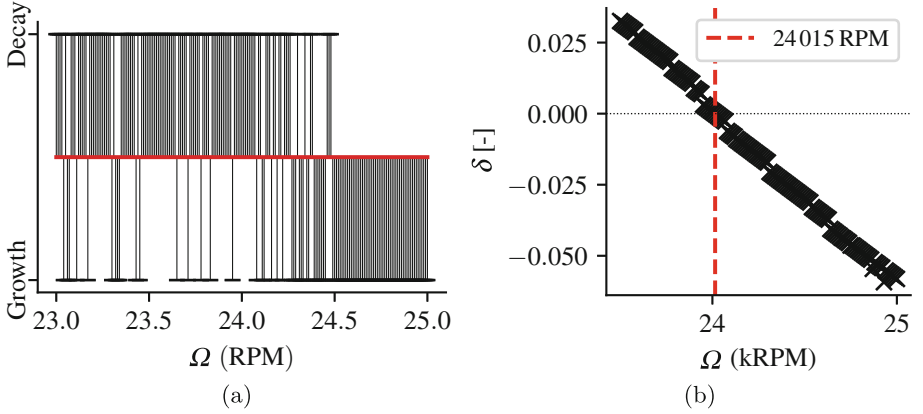


**Fig. 4.** (a) Stability of static equilibria judged from 1 s simulations for every 10 RPM (case 2); (b) LDs obtained by curve fitting to 0.25 s simulation after a rotor perturbation of  $C \times 10^{-10} = 31.8 \times 10^{-16}$  m for every 10 RPM (case 2).

**Table 2.** Comparison of obtained OSIs

Case	Foil stiffness	Time integration		Two-DOF perturb.		Extended perturb.	
	$k$ (GN/m <sup>3</sup> )	$\tilde{\Omega}_{OSI}$ (RPM)	$\tilde{\omega}_s$ (Hz)	$\Omega_{OSI}$ (RPM)	$\omega_s$ (Hz)	$\Omega_{OSI}$ (RPM)	$\omega_s$ (Hz)
1	4641.7	20 868	112.8	21 731	107.5	21 731	107.5
2	4.6417	24 015	101.8	27 868	103.4	24 987	101.0
3	2.3209	25 118	91.7	31 769	95.6	27 424	92.8

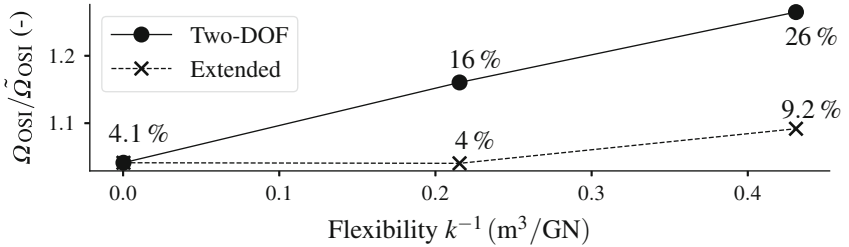


**Fig. 5.** Foil structure flexibility versus the discrepancy in the predicted OSI relative to the time integration result for both perturbation methods.

## 6 Conclusion

Discrepancies in OSI between the traditional perturbation approach and time integration results were pointed out in [14], and this was postulated to be caused by a deficiency in the pressure expansion. This has been investigated in the present work by carrying through the perturbation method while including the additional pressure-compliance terms in the Taylor expansion. In the presented

form, these terms are treated straightforwardly using a high number of discrete foil deflections leading to a rather comprehensive model. This approach is debatable, as are the concrete choices of GFB properties and numerical schemes. The extended perturbation method has, however, been demonstrated to predict OSIs in much better agreement to time integration results, indicating the pressure–compliance terms to be significant.

Irrespective of the physical interpretation of the foil DOFs and their subsequent implementation, the fluid film coefficients affecting each foil DOF are eventually added to the contribution from the foil structure itself. The significance of the pressure–compliance terms will hence decrease for an increasingly stiff foil structure, matching the expectation for the two–DOF perturbation to be adequate for rigid bearings. This has also been demonstrated to be the case using the present implementation, as the methods converge for a very stiff foil.

When lowering the foil stiffness, the significance increases as the discrepancy of the two-DOF method grows and the two perturbation methods diverge. The baseline discrepancy of around 4% is ascribed to the determination of the time integration OSI, while the increased inconsistency of 9.2% for case 3 should be further investigated. The agreement is, however, still significantly better than the 26% discrepancy of the classical two-DOF method.

In conclusion, caution should be exercised if the classical perturbation method is applied to compliant bearings and the OSI of these should rather be assessed using either nonlinear methods or an extended perturbation as presented here.

## References

1. Baum, C., Hetzler, H., Seemann, W.: On the stability of balanced rigid rotors in air foil bearings. In: Proceedings of 11th Internationale Tagung Schwingungen in Rotierenden Maschinen (SIRM 2015), Magdeburg, Germany, pp. 23–25 (2015)
2. Bonello, P., Pham, H.M.: The efficient computation of the nonlinear dynamic response of a foil-air bearing rotor system. *J. Sound Vib.* **333**(15), 3459–3478 (2014). <https://doi.org/10.1016/j.jsv.2014.03.001>
3. Bonello, P., Pham, H.M.: Nonlinear dynamic analysis of high speed oil-free turbomachinery with focus on stability and self-excited vibration. *J. Tribol.* **136**(4), 041705 (2014). <https://doi.org/10.1115/1.4027859>
4. Feng, K., Kaneko, S.: Analytical model of bump-type foil bearings using a link-spring structure and a finite-element shell model. *J. Tribol.* **132**(2), 021706 (2010). <https://doi.org/10.1115/1.4001169>
5. Heshmat, H., Walowit, J.A., Pinkus, O.: Analysis of gas-lubricated foil journal bearings. *J. Tribol. Technol.* **105**(4), 647–655 (1983). <https://doi.org/10.1115/1.3254697>
6. Hoffmann, R., Pronobis, T., Liebich, R.: The impact of modified corrugated bump structures on the rotor dynamic performance of gas foil bearings. In: Turbo Expo, ASME, p. V07BT32A012 (2014). <https://doi.org/10.1115/GT2014-25636>
7. Hoffmann, R., Pronobis, T., Liebich, R.: Non-linear stability analysis of a modified gas foil bearing structure. In: Proceedings of the 9th IFToMM International Conference on Rotor Dynamics, pp. 1259–1276 (2015). [https://doi.org/10.1007/978-3-319-06590-8\\_103](https://doi.org/10.1007/978-3-319-06590-8_103)

8. Kim, T.H., Andres, L.S.: Heavily loaded gas foil bearings: a model anchored to test data. *J. Eng. Gas Turbine Power* **130**(1), 012504 (2008). <https://doi.org/10.1115/1.2770494>
9. Kim, T.H., San Andrés, L.: Limits for high-speed operation of gas foil bearings. *J. Tribol.* **128**(3), 670–673 (2006). <https://doi.org/10.1115/1.2197851>
10. Kim, T.H., San Andrés, L.: Analysis of advanced gas foil bearings with piecewise linear elastic supports. *Tribol. Int.* **40**(8), 1239–1245 (2007). <https://doi.org/10.1016/j.triboint.2007.01.022>
11. Larsen, J.S., Santos, I.F.: Efficient solution of the non-linear reynolds equation for compressible fluid using the finite element method. *J. Braz. Soc. Mech. Sci. Eng.* **37**(3), 945–957 (2014). <https://doi.org/10.1007/s40430-014-0220-5>
12. Larsen, J.S., Santos, I.F.: On the nonlinear steady-state response of rigid rotors supported by air foil bearings—theory and experiments. *J. Sound Vib.* **346**, 284–297 (2015). <https://doi.org/10.1016/j.jsv.2015.02.017>
13. Larsen, J.S., Hansen, A.J., Santos, I.F.: Experimental and theoretical analysis of a rigid rotor supported by air foil bearings. *Mech. Ind.* **16**(1), 106 (2015). <https://doi.org/10.1051/meca/2014066>
14. Larsen, J.S., Santos, I.F., von Osmanski, S.: Stability of rigid rotors supported by air foil bearings: comparison of two fundamental approaches. *J. Sound Vib.* **381**, 179–191 (2016). <https://doi.org/10.1016/j.jsv.2016.06.022>
15. Le Lez, S., Arghir, M., Frene, J.: Nonlinear numerical prediction of gas foil bearing stability and unbalanced response. *J. Eng. Gas Turbine Power* **131**(1), 012503 (2009). <https://doi.org/10.1115/1.2967481>
16. Lee, Y.B., Kim, T.H., Kim, C.H., Lee, N.S., Choi, D.H.: Unbalance response of a super-critical rotor supported by foil bearings—comparison with test results. *Tribol. Trans.* **47**(1), 54–60 (2004). <https://doi.org/10.1080/05698190490279038>
17. Lund, J.W.: Calculation of stiffness and damping properties of gas bearings. *J. Tribol. Technol.* **90**(4), 793–803 (1968). <https://doi.org/10.1115/1.3601723>
18. von Osmanski, S., Larsen, J.S., Santos, I.F.: A fully coupled air foil bearing model considering friction - theory & experiment. *J. Sound Vib.* **400**, 660–679 (2017). <https://doi.org/10.1016/j.jsv.2017.04.008>
19. Peng, J.P., Carpino, M.: Calculation of stiffness and damping coefficients for elastically supported gas foil bearings. *J. Tribol.* **115**(1), 20–27 (1993). <https://doi.org/10.1115/1.2920982>
20. Pham, H.M., Bonello, P.: Efficient techniques for the computation of the nonlinear dynamics of a foil-air bearing rotor system. In: *Turbo Expo, ASME, Texas, USA* (2013) <https://doi.org/10.1115/GT2013-94389>
21. Ruscitto, D., Mc Cormick, J., Gray, S.: Hydrodynamic air lubricated compliant surface bearing for an automotive gas turbine engine I – journal bearing performance. Technical report CR-135368, NASA, Cleveland, Ohio (1978)
22. San Andrés, L., Kim, T.H.: Improvements to the analysis of gas foil bearings: integration of top foil 1D and 2D structural models. In: *Turbo Expo, ASME, Montreal, Canada, vol. 5*, pp. 779–789 (2007). <https://doi.org/10.1115/GT2007-27249>
23. San Andrés, L., Kim, T.H.: Analysis of gas foil bearings integrating FE top foil models. *Tribol. Int.* **42**(1), 111–120 (2009). <https://doi.org/10.1016/j.triboint.2008.05.003>
24. Vleugels, P., Waumans, T., Peirs, J., Al-Bender, F., Reynaerts, D.: High-speed bearings for micro gas turbines: stability analysis of foil bearings. *J. Micromech. Microeng.* **16**(9), 282–289 (2006). <https://doi.org/10.1088/0960-1317/16/9/S16>
25. Walowit, J.A., Anno, J.N.: *Modern Developments in Lubrication Mechanics*. Applied Science Publishers, London (1975)



# Rotordynamic Force Coefficients of Gas Seals — An Experimental Approach with Active Magnetic Rotor Excitation

Clemens Griebel<sup>(✉)</sup>

Chair of Energy Systems, Technical University of Munich, 85748 Garching, Germany  
clemens.griebel@tum.de  
<http://www.es.mw.tum.de>

**Abstract.** Gas seals are important components in turbomachines to guarantee high internal efficiency by restricting undesired leakage flows. Moreover, it is important to identify their rotordynamic force coefficients for the use in rotordynamic analyses of turbomachinery. Experimental methods to determine the full set of rotordynamic coefficients require a relative motion between rotor and stator, e.g. using Active Magnetic Bearing (AMB) technology. A unique approach is used in the present test rig, where a single AMB is used as an exciter on a flexible rotor supported by two fluid film bearings. Following an AMB upgrade, a new measurement principle was introduced based on the mechanical impedance method. The present paper describes the upgrade measures on the test rig, the measurement procedure and the parameter identification method along with a calculation scheme for the combined measurement uncertainty. First measurements on a fully partitioned pocket damper seal are performed to validate the new hardware and parameter identification procedure.

**Keywords:** Gas seals · Rotordynamic force coefficients  
Active magnetic bearing

## 1 Introduction

Gas seals are important components in various types of turbomachines to restrict undesired leakage flows between adjacent regions of different pressures while accommodating high relative surface speeds. This guarantees high internal efficiency by a more effective use of working fluid and the suppression of secondary flows. However, turbomachinery seals can significantly influence the vibration of a rotordynamic system due to the aerodynamic forces arising from the gas flow within the sealing cavities and gaps.

Aerodynamic seal forces might be small compared to the forces in bearings, but their circumferential components can have a pronounced destabilizing effect. The impact of seals on rotordynamics is supported by the fact that they are possibly close to the maximum amplitude spot of different rotordynamic

mode shapes. The potential for self-excited vibrations provoked by conventional labyrinth seals were discovered decades ago [1–3]. Since then many experimental and theoretical works were performed to analyze the effect of seals on system stability.

The consideration of seal forces in rotordynamic analyses of turbomachines is made possible when knowing the rotordynamic force coefficients of the respective seal configuration. These have to be determined on component level by theoretical analysis and experiments.

### 1.1 Rotordynamic Force Coefficients of Gas Seals

Just as in oil bearings and liquid seals, the rotordynamic behavior of gas seals depends on its inertial, stiffness and damping characteristics. These are quantified by introducing rotordynamic coefficients after linearizing aerodynamic reaction forces which arise due to the gas flow in the seal cavities:

$$-\underbrace{\begin{bmatrix} M_{xx} & M_{xy} \\ M_{yx} & M_{yy} \end{bmatrix}}_{\underline{\underline{M}}} \begin{bmatrix} \ddot{x} \\ \ddot{y} \end{bmatrix} (t) - \underbrace{\begin{bmatrix} C_{xx} & C_{xy} \\ C_{yx} & C_{yy} \end{bmatrix}}_{\underline{\underline{C}}} \begin{bmatrix} \dot{x} \\ \dot{y} \end{bmatrix} (t) - \underbrace{\begin{bmatrix} K_{xx} & K_{xy} \\ K_{yx} & K_{yy} \end{bmatrix}}_{\underline{\underline{K}}} \begin{bmatrix} x \\ y \end{bmatrix} (t) = \begin{bmatrix} f_x \\ f_y \end{bmatrix} (t) \quad (1)$$

with the rotor position  $x$  and  $y$ , the seal reaction force vector  $f$  and the rotordynamic coefficient matrices  $\underline{\underline{M}}$ ,  $\underline{\underline{C}}$  and  $\underline{\underline{K}}$  for added mass, damping and stiffness.

The rotordynamic coefficients in Eq. (1) are first-order derivatives of aerodynamic reaction components with respect to position, velocity, and acceleration of the shaft center:

$$K_{mn} = \left. \frac{\partial f_m}{\partial n} \right|_0; \quad C_{mn} = \left. \frac{\partial f_m}{\partial \dot{n}} \right|_0; \quad M_{mn} = \left. \frac{\partial f_m}{\partial \ddot{n}} \right|_0; \quad m, n = x, y. \quad (2)$$

The inertial (added-mass) coefficient matrix  $\underline{\underline{M}}$  might play an important role in rotordynamic analysis, especially for liquid seals. For gas seals, the added-mass coefficients are very small and are therefore usually neglected.

The cross-coupled damping  $C_{xy}$  is often not taken into account during the dynamic analysis due to its small levels in annular gas seals and negligible effect on the system's rotordynamics.

For a direction-independent presentation of coefficients averaged values are used:

$$\begin{aligned} K_{avg} &= \frac{(K_{xx} + K_{yy})}{2} & C_{avg} &= \frac{(C_{xx} + C_{yy})}{2} \\ k_{avg} &= \frac{(K_{xy} - K_{yx})}{2} & c_{avg} &= \frac{(C_{xy} - C_{yx})}{2} \end{aligned} \quad (3)$$

### 1.2 Impedance Method

Due to the harmonic relative motion of rotor and stator it is convenient to identify the rotordynamic coefficients in the frequency domain by determining

the transfer function of seal reaction forces and displacements. This approach is often denominated as impedance method and will be described in the following.

For the experimental identification of rotordynamic force coefficients using the impedance method, the seal forces and rotor displacements measured in the time domain are Fourier transformed:

$$\begin{aligned} x(t) &\text{---} \circ D_x(\omega) & \dot{x}(t) &\text{---} \circ i\omega \cdot D_x(\omega) & f_x(t) &\text{---} \circ F_x(\omega) \\ y(t) &\text{---} \circ D_y(\omega) & \dot{y}(t) &\text{---} \circ i\omega \cdot D_y(\omega) & f_y(t) &\text{---} \circ F_y(\omega) \end{aligned} \quad (4)$$

This way the equation of motion (Eq. 1) is transferred into the frequency domain:

$$-i\omega \begin{bmatrix} C_{xx} & C_{xy} \\ C_{yx} & C_{yy} \end{bmatrix} \begin{bmatrix} D_x \\ D_y \end{bmatrix}(\omega) - \begin{bmatrix} K_{xx} & K_{xy} \\ K_{yx} & K_{yy} \end{bmatrix} \begin{bmatrix} D_x \\ D_y \end{bmatrix}(\omega) = \begin{bmatrix} F_x \\ F_y \end{bmatrix}(\omega) \in \mathbb{C}^{(2 \times 2)} \quad (5)$$

with the rotordynamic stiffness  $K_{mn}$  and damping  $C_{mn}$  coefficients introduced above. As outlined above for the application in gas seals the mass terms are neglected. This equation can be rearranged to yield the impedance matrix  $\underline{\underline{H}}(\omega)$ :

$$\underbrace{[i\omega \underline{\underline{C}} + \underline{\underline{K}}]}_{\underline{\underline{H}}(\omega)} \cdot \underline{\underline{D}}(\omega) = -\underline{\underline{F}}(\omega) \quad (6)$$

As there are only two equations for four unknowns in  $\underline{\underline{H}}(\omega) \in \mathbb{C}^{(2 \times 2)}$ , two linear independent solutions are needed to solve Eq. (6). The resulting four equations are rearranged such that all components of  $\underline{\underline{H}}(\omega)$  can be directly calculated from two sets (1)/(2) of displacement and force data:

$$\begin{aligned} H_{xx} &= \frac{F_x^{(2)} D_y^{(1)} - F_x^{(1)} D_y^{(2)}}{D_x^{(1)} D_y^{(2)} - D_x^{(2)} D_y^{(1)}} & H_{xy} &= \frac{F_x^{(1)} D_x^{(2)} - F_x^{(2)} D_x^{(1)}}{D_y^{(2)} D_x^{(1)} - D_y^{(1)} D_x^{(2)}} \\ H_{yx} &= \frac{F_y^{(2)} D_y^{(1)} - F_y^{(1)} D_y^{(2)}}{D_y^{(2)} D_x^{(1)} - D_y^{(1)} D_x^{(2)}} & H_{yy} &= \frac{F_y^{(1)} D_x^{(2)} - F_y^{(2)} D_x^{(1)}}{D_y^{(2)} D_x^{(1)} - D_x^{(2)} D_y^{(1)}} \end{aligned} \quad (7)$$

Knowing all four impedances  $H_{mn}$  the rotordynamic force coefficients  $K_{mn}$ ,  $C_{mn}$  can be evaluated as their real and imaginary parts, respectively:

$$\begin{bmatrix} K_{xx} & K_{xy} \\ K_{yx} & K_{yy} \end{bmatrix} = \Re\{\underline{\underline{H}}(\omega)\} \quad \begin{bmatrix} C_{xx} & C_{xy} \\ C_{yx} & C_{yy} \end{bmatrix} = \frac{1}{\omega} \Im\{\underline{\underline{H}}(\omega)\} \quad (8)$$

### 1.3 Experimental Methods

Different experimental approaches and parameter calculation methods for the experimental determination of force coefficients in gas seals are documented in the literature. The identification of both the stiffness and damping coefficients in Eq. (1) requires a dynamic experiment with a relative motion between rotor and stator, i.e. the seal. This can be reached by either exciting the rotor or the stator to a harmonic motion.

**Stator Excitation.** Few experimental approaches based on stator excitation are reported for the investigation of gas seals.

Ransom et al. use piezoelectric load guns to excite the test seal housing in two orthogonal directions. The test seal is located at the free end of a vertical shaft supported by ball bearings. An iterative parameter identification method in the frequency domain is used to calculate the direct stiffness and damping coefficients [4].

Dawson, Childs et al. presented a test rig where a rigid rotor supported by hydrodynamic bearings is surrounded by a housing containing two test seals in a back-to-back arrangement. Two hydraulic shakers allow the excitation of the test stator in two orthogonal directions. The reaction forces are measured with load cells and combined with displacement and acceleration data to obtain the impedance matrix [5].

The same test rig was also used for the identification of force coefficients using pressure transducers which were directly integrated in the seal cavities. One advantage of this method is that due to the direct identification of seal reaction forces there is no need for a separate baseline test to correct for the stator's inertial forces [6].

**Mechanical Rotor Excitation.** Experimental methods which rely on rotor excitation provide a closer modeling of the real application case and are described in the following.

Decades ago, Wright reported on an approach based on measuring dynamic rotor displacement. A vertical rotor is supported by ball bearings in a way that it allows a whirl motion of its top disc adjacent to the test labyrinth seal. The whirl motion is controlled by tuning springs, adjustable dampers and pneumatic bellows to initiate forward or backward whirl motions. Vibration frequency and logarithmic decrement is observed to quantify radial stiffness and direct damping [7].

Childs et al. presented a test rig where the test rotor allows a horizontal translational motion using a single hydraulic shaker. The seal coefficients are evaluated in the time domain applying a dedicated synchronous sampling routine. The whole set of eight coefficients is identified using two data sets both with x-excitation but with initial eccentricity either in x- or y-direction [8].

Millsaps and Sanchez used a test rig with a vertical shaft in shaft arrangement to create a circular rotor whirl motion. The dynamic cavity pressure is measured by means of differential pressure transducers in the seal land and evaluated in the time domain to obtain the tangential seal reaction force. This way, direct damping is calculated [9].

A relatively reduced approach was presented by Laos et al. using a single electromagnetic shaker to excite a vertical shaft in a non-rotating test assembly. The test seal journal force and acceleration data is processed in the frequency domain to identify direct damping [10].



**AMB Rotor Excitation.** An attractive way to create a relative rotor-stator-motion is using Active Magnetic Bearing (AMB) technology. Primarily developed for the stabilization of rotor systems, it offers great flexibility in an test rig environment by its ability to impose different motion patterns to a shaft when used as an exciter mechanism.

To the author's knowledge the first test rig deploying AMB technology in the context of experimental investigation of gas seals was presented by Wagner and Pietruszka. The rigid test rotor is supported by two magnetic bearings within a high pressure containment while two test seals are mounted in the rotor center forming a back-to-back arrangement. AMB forces are calculated using a linear relationship from coil currents and rotor position [11]. First experimental results on labyrinth seals were presented by Wagner and Steff. They calculated seal coefficients for different excitation frequencies by applying linear regression over whirl frequency in the frequency domain [12]. After an upgrade with new magnetic bearings for an increased operational parameter range, seal parameters are calculated from the measured impedance matrix. Improvements in AMB force calculation are included like subtraction of gas forces in the AMB air gap identified from baseline tests [13].

Vannini et al. presented a test rig where the test cell with two magnetic bearings similar to Wagner et al.'s setup is integrated in a full-scale high pressure turbocompressor housing. AMB forces are calculated from coil currents and rotor-stator air gaps. The seal reaction forces are identified in the frequency domain by including a force mismatch identified from baseline tests into the rotor equation of motion [14].

Zutavern's experimental approach also deploys two magnetic bearings at each end of a test rotor with two test seals in the center but it is different from the previous concepts in two ways. Firstly, AMB forces are measured at the magnet coils with fibre-optic strain gauges. Secondly, the rotor is not assumed as rigid and has two discs to provide gyroscopic coupling. The seal coefficients are identified in the frequency domain and result from an error minimization routine compared to a theoretical transfer function predicted by a FEM model [15].

A completely different approach had been developed by Kwanka for the test rig which sets the basis for this paper. A single magnetic bearing is used as a contactless exciter mechanism for a very flexible rotor system supported by two hydrodynamic journal bearings. The test seals are located in the rotor center and pressurized by preswirled air flow (see Fig. 1). AMB forces act in the form of calibrated direct and cross-coupled stiffnesses and are adjusted such that the rotor system is excited to its stability limit at the first natural frequency of approximately 30 Hz. When pressurizing the test seal, any direct and cross-coupled forces generated by the flow through the seal have to be compensated by adjusting the AMB radial and tangential stiffnesses. Hence, the seal parameters are identified from the difference in AMB parameters for repeated unpressurized and pressurized tests. This eliminates any other influence of the test rotor system, e.g. the journal bearings. A force conversion routine was developed and validated

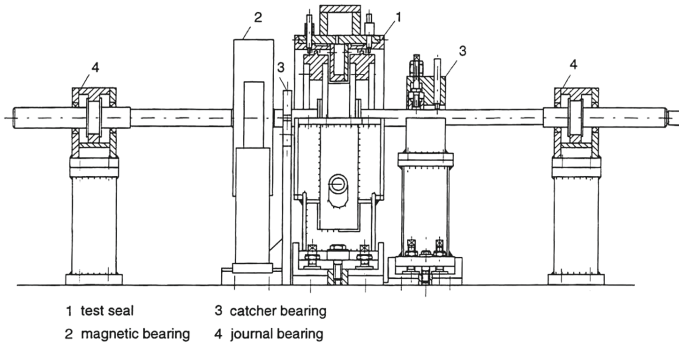


**Fig. 1.** Side view of main components in test rig developed by Kwanka [16]

to account for the different axial positions of AMB and seal force. By performing tests for forward and backward whirl the four stiffness and damping coefficients were obtained under the symmetry assumption. The variation of journal bearing distance allowed the variation of test frequency in a small range (approx.  $\pm 5$  Hz) [16].

That test rig has been used for the experimental determination of force coefficients for many labyrinth and brush seal configurations [17–20]. However, the existing magnetic exciter proved to have insufficient force capabilities especially when testing contacting seals such as brush seals. Moreover, the tests could be performed in a small frequency range only. Therefore, it was decided to upgrade the magnetic exciter system and introduce the impedance method as a new measurement principle.

## 2 Test Rig

The following section describes the test rig located at TUM Institute for Energy Systems and recent upgrade measures.

### 2.1 General Setup and Upgrade

The upgraded dynamic test rig is shown in Fig. 2. Key feature is a flexible rotor system provided by a slender central shaft of 25 mm diameter. This shaft is supported by oil-lubricated journal bearings with an adjustable span distance in the range 770...860 mm. A 6 mm diameter torsional damper shaft couples the frequency-controlled electric motor with a maximum rotational speed of 1500 rpm to the rotor system.

The aluminum rotor of 179.64 mm diameter is located in the middle of the bearing distance and mounted on the shaft by two collets. Steel linings adjacent to the test seals provide increased abrasion resistance when testing contacting seals. On both sides of the test rotor adjustable safety bearings allow for a limitation of rotor whirl amplitudes in the event of unstable test rig operation.

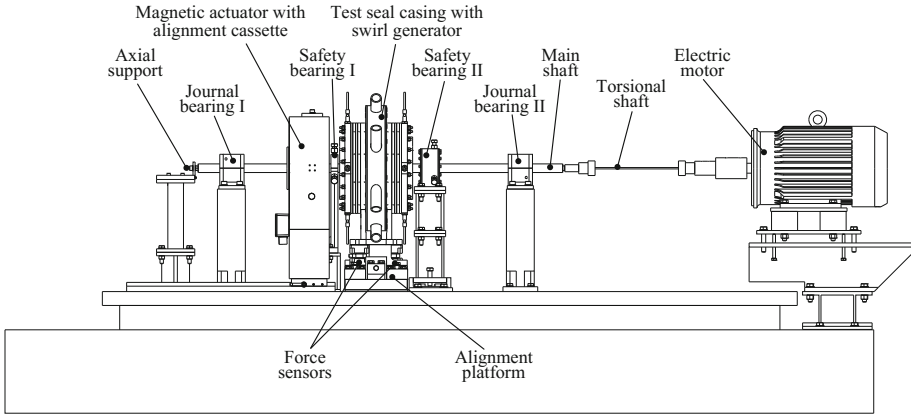


**Fig. 2.** Side view of the test rig with motor, journal bearings, test seal casing and magnetic exciter

The test seals are mounted on the test seal casing in a back-to-back arrangement, compensating for axial forces caused by the pressure drop over the seals and facilitating force measurement due to the duplication of seal forces. Main features of the seal casing are the inflow chamber with swirl generator rings discharging to the seal inlets plus a central bypass chamber allowing for a variable adjustment of preswirl velocity independently from pressure level and leakage mass flow. Air at ambient temperature is the working medium provided by the facility compressed air grid and a 130 kW screw compressor serving as a recirculation device. The seal leakage mass flow discharges to the atmosphere and is measured by a Coriolis mass flow meter. The leakage flow measurement accuracy was determined as  $\pm 0.05\%$  FSO by an in-situ calibration for the relevant measurement range using a critical nozzle. The operating conditions of the air supply system can be found in Table 1.

**Table 1.** Operational range of air supply system

Prechamber pressure	0...1300 kPa
Preswirl velocity	80...200 m/s
Mass flow	0...0.8 kg/s

The newly upgraded magnetic exciter system is located in closest possible distance to the test seal casing. Key components replaced are the commercial AMB system and a custom mounting bracket for test rig integration. The actuator is a radial magnetic bearing with 8 poles and a nominal air gap of  $450\ \mu\text{m}$ . The magnetic forces are exerted on a laminated rotor sleeve of 144.1 mm diameter which is mounted on the shaft by a clamping bush. The maximum design

force is 3.2 kN but maximum forces up to 4 kN at coil currents of approximately 12.5 A were observed using force sensors attached to the test rig shaft. The force was targeted to enable rotor excitation at orbits of 100  $\mu\text{m}$  amplitude up to frequencies of 200 Hz. A sensor ring comprising two capacitive proximity sensors is mounted adjacent to the AMB stator and provides rotor position data for the controller. The actuator is driven by a commercial magnetic bearing control unit with 300 VDC bus voltage which is accessible via a MATLAB interface.

Core component of the mounting solution is a cassette accommodating the AMB stator by means of an interference fit. The sensor ring has a tight clearance fit and was machined within close concentricity tolerance compared to the stator. The complete AMB cassette sits within a mounting bracket in a way that allows precise horizontal and vertical position adjustment. The final centering of the test rig shaft was reached using two precisely machined centering discs. Prior to fabrication, the whole assembly was analyzed by means of FEM simulation. In static structural analyses the maximum deformation was predicted to be 6  $\mu\text{m}$  for a 4.2 kN static force in horizontal direction while the peak von Mises stresses were much lower than the material's tensile strength. A modal analysis computed the first eigenfrequency at 346 Hz which represents a considerable safety margin to the targeted excitation frequencies.

Following the significantly increased load capability of the new actor system, the journal bearing pedestals were replaced by a stiffer design based on FEM calculations.

All components are placed on a planar steel table which is bolted to a massive cast iron and concrete machine bed.

## 2.2 Sensors and Data Acquisition

Precise and coherent measurement of the dynamic rotor motion within the stator, in this case the gas seal, and the resulting reactive forces is key for the experimental investigation of rotordynamic force coefficients.

In the present test rig, the rotor position is measured at both test seals by four eddy current sensors each. Their resolution is 1  $\mu\text{m}$  and the sensitivity curve was determined in situ using high-precision mechanical gauges.

For force measurement, an attempt was made to evaluate the AMB force from the coil currents and rotor position but did not yield the desired force measurement accuracy. Therefore, it was decided to measure forces directly at the seals by integrating force sensors in the test seal casing support structure. Due to their high mechanical stiffness, piezoelectric force sensors were selected for force measurement. Two 3-axis force sensors are used based on available models and for design reasons. The calculated resonance frequency of the test seal casing supported by the force sensors is approximately 900 Hz. Three single channel charge amplifiers are used for data acquisition. Due to their purely analog circuit, no time delays have to be expected. When using piezoelectric force sensors, the charge amplifiers' time constant has to be considered. In this case, the "Long" setting guarantees that charge drift will not affect measurement for the needed

acquisition times of a few seconds. The measurement accuracy of a force measurement chain is composed of different contributions from the force sensors and the charge amplifiers. Therefore, the force measurement accuracy was checked for the complete measurement chain using specified weights which were determined using a laboratory scale with 0.5 g resolution. Measurements were taken including both increasing and decreasing load, thus including hysteresis error and repeated ten times for x- and y-axis each. Considering absolute values of measured relative deviations, the average deviation was 0.9% while the maximum deviation found in each measurement was 1.93% in average. As the check was done separately for the two directions corresponding to the test rig's x- and y-direction and no combined calibration load was applied, cross-talk was taken into account based on the manufacturer's calibration certificate (see Table 2). By summing up all contributions (worst-case scenario) the total measurement uncertainty of the force measurement can be specified as  $\pm 1.5\%$  of reading.

**Table 2.** Measurement uncertainty of force measurement (all values defined as of reading)

Source	Relative uncertainty
Sensors & DAQ (Avg.)	$\pm 0.9\%$
Cross talk $F_x \rightarrow F_y$	$\pm 0.2\%$
Cross talk $F_y \rightarrow F_x$	$\pm 0.4\%$
Total force measurement uncertainty	$\pm 1.5\%$

All data channels are acquired in parallel at 10 kHz sampling rate via one multi-channel data acquisition module, thus guaranteeing data coherence. A Queue Structure available in LabVIEW for data transfer within the data acquisition program excludes data loss even in case of software lags by means of its buffering functionality. All data is stored to a `txt`-file for further data processing and parameter evaluation.

### 3 Parameter Identification

As outlined in the introduction, the established impedance method was introduced as a new measurement principle along with the test rig upgrade. To the author's knowledge it was not applied in the context of gas seals combining AMB rotor excitation and force measurement at the stator so far. Its implementation is presented in the following along with a concept to capture corresponding measurement uncertainty.

#### 3.1 Data Processing

The basis for the identification of seal force coefficients are the equations described in Sect. 1.2.

Due to the two-flow design of the test rig, the measured force data  $f_{x/y, M}$  is divided by two in the time domain and the sign is inverted to relate the measured stator forces to the rotor:

$$\underbrace{\begin{bmatrix} f_x(t) \\ f_y(t) \end{bmatrix}}_{\text{Single seal}} = -\frac{1}{2} \cdot \underbrace{\begin{bmatrix} f_{x, M}(t) \\ f_{y, M}(t) \end{bmatrix}}_{\text{Measured}} \quad (9)$$

Despite the stiff design of the test rig's base plate, there is a force reading at the stator when performing rotor excitation. Considering the force sensor stiffnesses, the corresponding displacement of the seal housing is smaller than 1  $\mu\text{m}$ , thus having negligible effect on the measurement of rotor displacement. However, force measurement is adjusted by performing a baseline test with unpressurized test seals and subtracting baseline from the measurements with pressurized seal following the force superposition assumption. Due to the linearity of the Fourier transform, the adjustment is performed in the frequency domain at the respective whirl frequency  $\omega$  used in that measurement:

$$\underbrace{\begin{bmatrix} F_x(\omega) \\ F_y(\omega) \end{bmatrix}}_{\text{Seal}} = \underbrace{\begin{bmatrix} F_{x, T}(\omega) \\ F_{y, T}(\omega) \end{bmatrix}}_{\text{Total}} - \underbrace{\begin{bmatrix} F_{x, B}(\omega) \\ F_{y, B}(\omega) \end{bmatrix}}_{\text{Baseline}} \in \mathbb{C} \quad (10)$$

To guarantee coherence of the two data sets with and without pressurization, each data set is phase shift prior to subtraction assuming the displacement data in x-direction as a reference. The latter is phase shift such that its phase is 0° and the same shift is applied to all other data within the same data set, i.e. y-displacement and forces in x- and y-direction.

### 3.2 Measurement Uncertainties

The identification of rotordynamic force coefficients using the impedance method requires several repeated measurements which are all affected by the measurement uncertainty of the sensors involved. Therefore, the combined measurement uncertainty  $u(y)$  has to be determined applying error propagation [21]:

$$u(y) = \sqrt{\sum_{i=1}^m \left( \frac{\partial f}{\partial x_i} \right)^2 u^2(x_i)} \quad (11)$$

where  $f$  is the functional relation between the wanted parameter  $y$  and the measurements  $x_i$  with their corresponding uncertainties  $u(x_i)$ .

For the present application, the functional relation between measurement and seal coefficients is given by Eqs. (7), (10) and (8). The error propagation is calculated in the frequency domain which is valid due to the linearity of the Fourier transform. The input parameters for these equations  $x_i$  are summarized in Table 4 and their uncertainties  $u(x_i)$  can be found in Table 3.

**Table 3.** Summary of measurement uncertainties  $u(x_i)$

Source	Uncertainty
Force sensors $u_{rel}(F)$	$\pm 1.5\%$
Position sensors $u(D)$	$\pm 1 \mu m$

When applied to Eq. (7) combined with the force difference in Eq. (10), the error propagation consists of the following contributions as shown for the impedance  $H_{xx}$  as an example:

$$u(H_{xx}) = \sqrt{\left(\frac{\partial H_{xx}}{\partial F_{x,B}^{(1)}}\right)^2 \cdot (F_{x,B}^{(1)} \cdot u_{rel}(F))^2 + \left(\frac{\partial H_{xx}}{\partial F_{x,T}^{(1)}}\right)^2 \cdot (F_{x,T}^{(1)} \cdot u_{rel}(F))^2 + \left(\frac{\partial H_{xx}}{\partial F_{x,B}^{(2)}}\right)^2 \cdot (F_{x,B}^{(2)} \cdot u_{rel}(F))^2 + \left(\frac{\partial H_{xx}}{\partial F_{x,T}^{(2)}}\right)^2 \cdot (F_{x,T}^{(2)} \cdot u_{rel}(F))^2 + \left(\frac{\partial H_{xx}}{\partial D_x^{(1)}}\right)^2 \cdot u(D)^2 + \left(\frac{\partial H_{xx}}{\partial D_x^{(2)}}\right)^2 \cdot u(D)^2 + \left(\frac{\partial H_{xx}}{\partial D_y^{(1)}}\right)^2 \cdot u(D)^2 + \left(\frac{\partial H_{xx}}{\partial D_y^{(2)}}\right)^2 \cdot u(D)^2} \quad (12)$$

All partial derivatives in Eq. 12 can be calculated analytically from the respective impedance equation in Eq. 7.

Finally the complete result for the rotordynamic force coefficients together with their corresponding measurement uncertainty can be given as follows:

$$\begin{aligned} K_{mn} &= \Re\{H_{mn}\} \pm \Re\{u(H_{mn})\} \quad ; \quad m, n = x, y \\ C_{mn} &= \frac{\Im\{H_{mn}\}}{\omega} \pm \frac{\Im\{u(H_{mn})\}}{\omega} \end{aligned} \quad (13)$$

**Table 4.** Summary of measurements  $x_i$  required for parameter identification

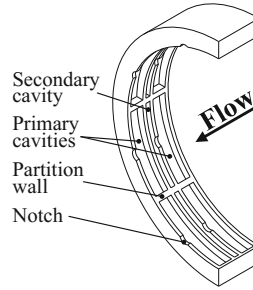
	Baseline		Pressurized	
	Excitation (1)	Excitation (2)	Excitation (1)	Excitation (2)
Forces	$F_{x,B}^{(1)}, F_{y,B}^{(1)}$	$F_{x,B}^{(2)}, F_{y,B}^{(2)}$	$F_{x,T}^{(1)}, F_{y,T}^{(1)}$	$F_{x,T}^{(2)}, F_{y,T}^{(2)}$
Displacements			$D_x^{(1)}, D_y^{(1)}$	$D_x^{(2)}, D_y^{(2)}$

## 4 Validation

To prove the function of the new approach and validate its results, first test measurements on a damper seal are performed.

**Table 5.** FPDS design parameters

Parameter	Value
Number of blades	4
Number of pockets	8
Seal length [mm]	40
Clearance [mm]	0.38
Clearance ratio [-]	1:1.4

**Fig. 3.** Inner view of FPDS design

#### 4.1 Test Measurements

The seal design used for test measurements is a fully partitioned pocket damper seal with four blades and eight partition walls (see Fig. 3 and Table 5). Notches in the outlet blade of each primary cavity create a diverging clearance. Its specialty is that it is a very short design with a length to diameter ratio as low as 0.22 which facilitate an application at blade shrouds and as an interstage seal.

For the experiments, the following procedure was followed for each measurement:

1. Start pressurization (not applicable for baseline)
2. Reset force measurement
3. Start excitation
4. Start data logging for 2–3 s.

Two excitation patterns were tested to obtain the two data sets needed for the evaluation of all eight force coefficients. The first was forward/backward excitation, i.e. an excitation with circular rotor orbits in same (forward) and opposed (backward) direction of rotor rotation. The second scheme was linear excitation in two orthogonal directions, i.e. along the x- and y-axes of the magnetic actuator which are rotated by  $45^\circ$  compared to the test rig's global coordinate system. The test results for both excitation patterns showed good agreement, however, the calculated measurement uncertainties resulted in lower levels for excitation in x- and y-direction. Moreover, test rig operation was more stable when using linear excitation, which is why this excitation pattern was used for all following measurements. All tests were performed with  $100 \text{ m/s}$  preswirl velocity at the seal inlet. The span distance between the journal bearings was 830 mm for tests without rotor rotation and 800 mm for the rotating tests (Fig. 4). In conformity with previous operation of the test rig before the upgrade, the rotor speed was set to 720 rpm [20].

#### 4.2 Results

The test results for 2 and 4 bar inlet pressure are shown in Figs. (5) and (6). While all eight coefficients along with their respective measurement uncertainties were



evaluated as described above, the stiffness and damping coefficients are presented in the form of direction-independent (average) coefficients according to Eq. (3).

Direct stiffness is moderately positive for 2 bar inlet pressure and shows a slightly decreasing trend for increasing whirl frequency while rotor rotation has negligible effect. At 4 bar, direct stiffness is negative showing an increasing (less negative) trend over whirl frequency with a maximum at 60 Hz excitation frequency. Negative direct stiffness with increasing trend was also observed in a previous CFD study at similar operating conditions [22].

Cross-coupled (CC) stiffness is positive throughout the parameter range and more than doubles its magnitude when increasing inlet pressure from 2 bar to 4 bar. At 2 bar the influence of rotor rotation is very small, however, at 4 bar an increase in cross-coupled stiffness can be observed when adding rotor rotation. The value at 60 Hz shows a pronounced deviation towards lower CC stiffness which is even lower than in the case without rotor rotation.

Direct damping is significantly positive, confirming functioning of the damper seal. At low pressure (2 bar) both the frequency dependence and the influence of rotor rotation is negligible. At 4 bar, direct damping is significantly higher and a moderately decreasing trend can be observed for higher excitation frequencies while at 60 Hz there is a global minimum. Similar to CC stiffness, rotor rotation causes an increase in direct damping and intensifies the deviation at 60 Hz whirl frequency. This deviation was repeatable in all tests with varying excitation amplitudes and excitation patterns and might be explained by e.g. a resonance like effect in the dynamic pressure distribution within the pockets of the tested seal at this excitation frequency, possibly also arising from the specific test rig

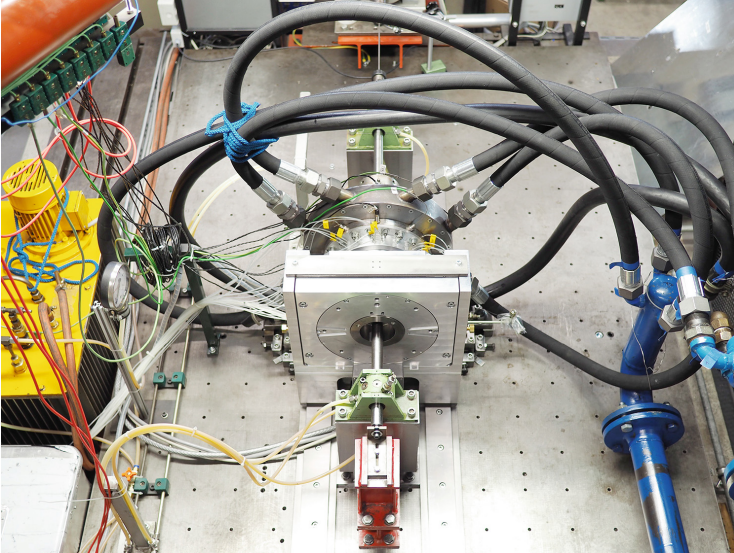


**Fig. 4.** Test rig setup for test measurements

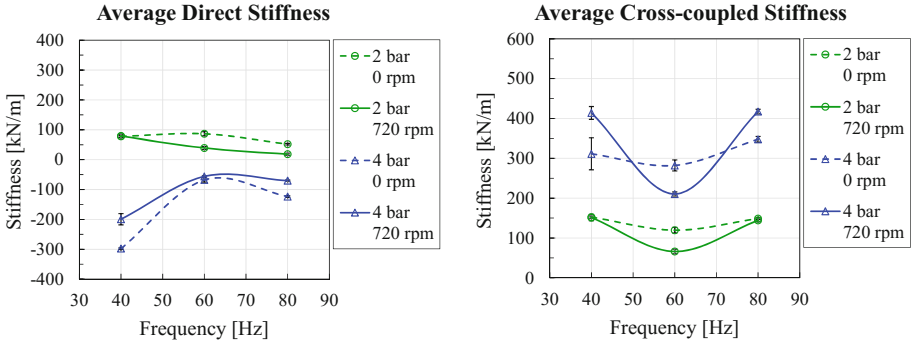


**Fig. 5.** Results of FPDS test measurements: direct and cross-coupled stiffness.

arrangement with double flow. This assumption is supported by the fact that the phenomenon is more visible with rotor rotation whose fifth harmonic coincides with the whirl frequency at 60 Hz. It confirms the importance of the dynamic pocket pressure distribution, often denominated as pressure modulation, for the rotordynamic performance of pocket damper seals [10].

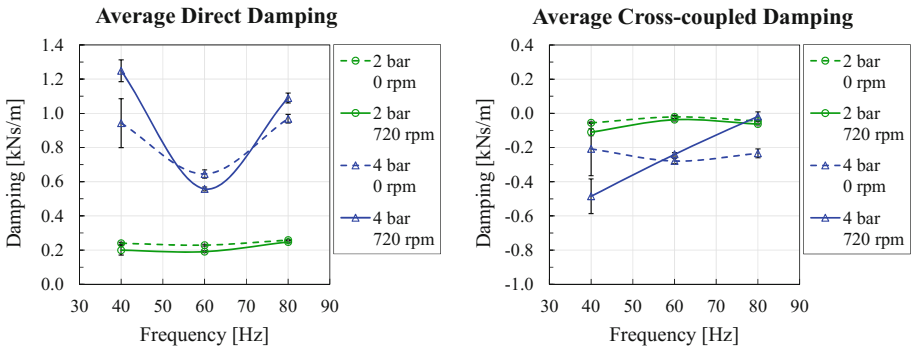


**Fig. 6.** Results of FPDS test measurements: direct and cross-coupled damping.

Cross-coupled damping is at low negative levels and independent from whirl frequency except at 4 bar with rotor rotation where CC damping is increasing (less negative) for higher excitation frequency.

## 5 Conclusions

The present paper describes the upgrade, calibration and commissioning of an existing dynamic rotor test rig with a more powerful AMB system. The configuration of the test rig is unique in that it only uses a single AMB as an exciter mechanism in a very flexible rotor system. Along with the upgrade, a

new measurement principle was introduced based on the established impedance method.

First test measurements on a damper seal for different excitation frequencies and inlet pressures with and without rotor rotation prove the operability of the upgraded test rig. Measurement results for the tested short fully partitioned pocket damper seal reveal negative direct stiffness except at low pressure and positive cross-coupled stiffness as well as positive direct damping throughout the parameter range. Both signs and magnitudes of the presented coefficients are in line with a previous CFD study at similar operating conditions. The calculation scheme proposed to derive the combined measurement uncertainty resulting from all four measurements required for the identification of rotordynamic force coefficients yields reasonable uncertainty levels.

**Acknowledgement.** The work has been funded by the German Federal Ministry for Economic Affairs and Energy, and GE Power within the project “COOREFLEX-Turbo: 3.2.6”.


## References

1. Thomas, H.J.: Instabile eigenschwingungen von turbinenläufern, angefacht durch die spaltströmungen in stopfbuchsen und beschauflungen. Technical report, AEG (1956)
2. Lomakin, A.: Calculation of critical number of revolutions and the conditions necessary for dynamic stability of rotors in high-pressure hydraulic machine when taking into account forces originating in sealings. *Energomashinostroenie* **4**(4), 1–5 (1958). (in Russian)
3. Alford, J.: Protecting turbomachinery from self-excited rotor whirl. *ASME J. Eng. Power* **87**, 333–344 (1965)
4. Ransom, D., Li, J., San Andres, L., Vance, J.M.: Experimental force coefficients for a two-bladed labyrinth seal and a four-pocket damper seal. *J. Tribol.* **121**, 370–376 (1999)
5. Dawson, M.P., Childs, D.W., Holt, C.G., Phillips, S.G.: Measurements versus predictions for the dynamic impedance of annular gas seals-part 1: test facility and apparatus. *J. Eng. Gas Turbines Power* **124**, 958–962 (2002)
6. Ertas, B.H., Gamal, A., Vance, J.M.: Rotordynamic force coefficients of pocket damper seals. *J. Turbomach.* **128**, 725–737 (2006)
7. Wright, D.V.: Air model tests of labyrinth seal forces on a whirling rotor. *J. Eng. Power* **100**, 533–543 (1978)
8. Childs, D.W., Nelson, C.E., Nicks, C., Scharrer, J., Elrod, D., Hale, K.: Theory versus experiment for the rotordynamic coefficients of annular gas seals: Part 1-test facility and apparatus. *J. Eng. Gas Turbines Power* **108**, 426–432 (1986)
9. Millsaps, K., Martinez-Sanchez, M.: Dynamic forces from single gland labyrinth seals: part 1-ideal and viscous decomposition. *J. Turbomach.* **116**, 686–693 (1994)
10. Laos, H., Vance, J.M., Buchanan, S.: Hybrid brush pocket damper seals for turbomachinery. *J. Eng. Gas Turbines Power* **122**, 330–336 (2000)
11. Wagner, N.G., Pietruszka, W.D.: Identification of rotordynamic parameters on a test stand with active magnetic bearings. In: *Symposium on Magnetic Bearings*, pp. 289–299 (1988)

12. Wagner, N.G., Steff, K.: Dynamic labyrinth coefficients from a high-pressure full-scale test rig using magnetic bearings. In: *Rotordynamic Instability Problems in High-Performance Turbomachinery*, pp. 95–111 (1996)
13. Wagner, N.G., Steff, K., Gausmann, R., Schmidt, M.: Investigation on the dynamic coefficients of impeller eye labyrinth seals. In: *38th Turbomachinery Symposium*, pp. 53–69 (2009)
14. Vannini, G., Cioncolini, S., Calicchio, V., Tedone, F.: Development of a high pressure rotordynamic test rig for centrifugal compressors internal seals characterization. In: *40th Turbomachinery Symposium* (2011)
15. Zutavern, Z.: Identification of rotordynamic forces in a flexible rotor system using magnetic bearings. Ph.D. thesis (2006)
16. Kwanka, K.: Variation of fluid flow forces in seals with rotor bending. In: Cudney, H.H. (ed.) *15th Biennial Conference on Mechanical Vibration and Noise* (1995)
17. Kwanka, K., Nagel, M.: Experimental rotordynamic coefficients of short labyrinth gas seals. In: *Rotordynamic Instability Problems in High-Performance Turbomachinery*, pp. 135–144. Texas A&M University (1996)
18. Kwanka, K.: Rotordynamic coefficients of short labyrinth gas seals—general dependency on geometric and physical parameters. *Tribol. Trans.* **50**(4), 558–563 (2007)
19. Pugachev, A.O., Deckner, M.: Analysis of the experimental and CFD-based theoretical methods for studying rotordynamic characteristics of labyrinth gas seals: Gt2010-22058. In: *ASME Turbo Expo* (2010)
20. Gaszner, M., Pugachev, A.O., Georgakis, C., Cooper, P.: Leakage and rotordynamic coefficients of brush seals with zero cold clearance used in an arrangement with labyrinth fins. *J. Eng. Gas Turbines Power* **135**(12), 122506-1–122506-11 (2013)
21. DIN - German Institute for Standardization: *Din 1319 fundamentals of metrology - part 3: evaluation of measurements of a single measurand, measurement uncertainty* (1995)
22. Griebel, C.: Impact analysis of pocket damper seal geometry variations on leakage performance and rotordynamic force coefficients using CFD: Gt2018-76864. In: *ASME Turbo Expo* (2018)



# Analysis of the Rotor Supported by Gas Foil Bearings Considering the Assembly Preload and Hardening Effect

Grzegorz Żywica<sup>(✉)</sup> , Jan Kiciński, and Małgorzata Bogulicz

Institute of Fluid Flow Machinery, Polish Academy of Sciences,  
Fiszera 14, 80-231 Gdansk, Poland  
gzywica@imp.gda.pl

**Abstract.** This article discusses a new method for modelling elastic deformations of a foil bearing's structure, taking into account key phenomena influencing its characteristics. Special attention was paid to the assembly preload, which has an impact on the stiffness of the supporting system and thus also on the static and dynamic properties of the rotor. There has been proposed the method which allows for the inclusion of a selected preload into the bearing model. A new FEM model of the foil bearing's structure has been described. This model was coupled with an in-house developed flow model of the bearing and the entire rotating system. Computations were made for several assembly preload values, taking into account changes in the bearing structure stiffness as the load increases. The changes in stiffness associated with the load changes were due to the nonlinear geometry of the foils, and also due to the contact phenomena, including friction between components. The applied calculation algorithm allowed to take into account all these phenomena. The results obtained using the developed model confirm the very high influence of the foil bearing's pre-clamp and the progressive stiffness on the properties of the rotating system. Numerical models of this type can pave the way for a further development of foil bearings and for their wider use in modern high-speed fluid-flow machines.

**Keywords:** Foil bearings · High-speed bearings · Assembly preload

## 1 Introduction

Gas foil bearings are the next generation of aerodynamic bearings in which special elastic-damping elements are introduced between the journal and the bush in order to improve their dynamic properties and reduce wear during start-ups. In practice, these elements usually take the form of thin metal foils of suitable shapes and sizes [1], and their surfaces are covered with appropriately selected functional materials [2]. Gas foil bearings are usually designed to withstand extreme operating conditions covering very high rotational speeds (over 100,000 rpm) and high temperatures (above 200°C). Such bearings have many advantages that make them a preferred option for high-speed machines such as gas and vapor microturbines, compressors or turbo-expanders [1, 3]. Because foil bearings do not require an oil lubricating system, they are good candidates as components of oil-free fluid-flow machinery [4, 5].

Over recent years a great deal of attention has been paid to modelling phenomena occurring in foil bearings [6–8], and yet there is a lack of universal models that would enable a reliable assessment of their properties over the wide speed and load range. Such models are very useful in order to make design process of a new foil bearing shorter and reduce the experimental studies required to the preliminary assessment of bearing properties and carrying out the structure optimization analyses [9, 10]. By prediction of static and dynamic characteristics of the bearing, such models allow engineers to assess the operation of a rotating system under certain conditions [6]. The operation of a foil bearing is characterized by a number of physical phenomena, a theoretical description of which is in fact very complex. This implies that in order to characterize the bearing operation efficiently, one must apply advanced numerical models. The most important phenomena which should be included in the model are the following: interactions between the flow layer and the structural layer, contact phenomena and nonlinear behavior of the flexible foil assembly. At low rotational speeds, the dry or mixed friction between the bearing journal and the top foil is observed. A theoretical approach to analyze the way a foil bearing operates under conditions in which the gaseous lubricating film starts to form itself is very challenging. The increase in speed causes that a desirable fluid friction appears. Only such conditions ensure a stable operation of the rotor and low friction losses at the bearing node. Modelling problems are also caused by a preliminary clamp, which almost always occurs in foil bearings. This is due to the assembly preload which is necessary to obtain proper properties at high rotational speeds and operational loads.

Many research and development centers from all over the world are involved in the progress of the foil bearing technology. The works cover both theoretical and experimental issues [1, 2]. A lot of attention is devoted to the optimization of bearing construction and its tribological properties, including a selection of appropriate construction and functional materials. Depending on operating conditions, sliding coatings are made of selected materials, i.e. metals, metal-ceramic composites or plastics [2, 11]. When a foil bearing operates at low temperatures (i.e. up to 200 °C), the best durability and friction properties are achieved by using soft sliding coatings made of plastics. At high temperatures, metal-ceramic composites are rather preferred [12]. A fabrication of foil bearings is also challenging due to the dependence on sheet metal forming to produce the compliant structure [13]. Due to elastic deformations of thin foils, achieving high accuracy is difficult. It also complicates getting a precise radial clearance or preload in such bearings.

In terms of its construction, a foil bearing is a very complex system, the theoretical description of which is extremely difficult. It is necessary to consider several physical phenomena that occur simultaneously, and in addition, they interact with one another [9, 14]. Therefore, in that case, too much simplified numerical models have a very limited application—they may be applied only at a very preliminary design stage. Computing performances of today's computer workstations are not a barrier to performing numerical analyses of complex mechanical systems such as foil bearings. Numerical models can consist of up to several millions of degrees of freedom. In the latest publications, you can find examples of advanced numerical models of such bearings that allow predicting not only the properties of the bearings but also of the rotors that they support [14–18]. But the available literature is missing examples of

numerical analyses in which the assembly preload was directly considered. The results of experimental tests have shown that the bearing clearance and its preliminary preload are decisive for the properties of the foil bearing [19–21], therefore, if they occur, they should be taken into account.

In the authors' opinion, there is insufficient attention paid to the impact of the preliminary preload on the characteristics of a foil bearing. It is obvious that this is a very important issue for it has a crucial impact on the rotor dynamics, the starting torque as well as wear and durability of the bearing. The further part of the article describes the research aimed at the development of a numerical model of the foil bearing, which would allow simulations of the assembly preload and other specific properties of such a mechanical system.

## 2 Numerical Model

Computer programs for analyzing bearings and rotating systems have been developing by the authors of this article at the Institute of Fluid Flow Machinery of the Polish Academy of Sciences (IMP PAN) for many years now. So far, models of both hydrodynamic and aerodynamic foil bearings have been developed, which take into account phenomena occurring both in the structural and flow support layer. Structural analyses are conducted using the ABAQUS commercial software, and flow analyses concerning bearings are carried out using in-house programs from the MESWIR series [22]. In last years a new software package called MESLOF [14], which is based on the MESWIR software, has been elaborated by the authors. The gas bearing model is based on the Reynolds equation for compressible fluids. This is an isothermal model, which means that it does not take into account the impact of temperature on the gas viscosity. As part of the static analysis, the model allows determining the pressure distribution and reaction of the gaseous lubrication film due to rotational motion of the journal. The dynamic analysis enables determining stiffness and damping coefficients at the actually considered moment of a gas bearing's operation, considering the rotational speed, bearing load and irregular geometry of the lubrication gap. More details on the gas bearing model used can be found in monograph [4]. Currently, through the combination of the in-house computer programs and the all-purpose FEM software ABAQUS, it is possible to conduct analyses that take into account the complex geometry of foils and contact phenomena occurring in foil bearings. The developed algorithm also includes the fluid-structure interactions that occur in such a bearing as well as changes in its geometry during analysis. The created numerical model takes into account the assembly preload, what is discussed in detail in this chapter.

### 2.1 FEM Model of the Supporting Structure

#### Previously Used Method for Determining Deformations

So far, during analyzing foil bearings, elastic deformations of the structural support layer used to be determined in a simplified manner—bypassing the assembly clamp of the top foil. Such a bearing model (thanks to its capability of analyzing contact

phenomena and considering interactions between the flow and structure) was still a very advanced tool. Its main drawback was the sensitivity to large deformations due to the irregular shape of the lubrication gap, resulting from hydrodynamic or aerodynamic pressure. These deformations have hitherto been determined without taking into account a preload of the compliant foils assembly, which meant that with respect to the radial clearance of the bearing, they were relatively large. It is due to the fact that the dominating component of the displacement of individual FEM mesh nodes was the displacements resulting from the clearance—the initial distances between bearing elements. The previously used method for determining foil assembly deformations consisted of the following stages:

- determination of hydrodynamic/aerodynamic pressure in the bearing's lubrication gap – without deformations (MESWIR),
- loading the bearing's top foil by forces corresponding to determined hydrodynamic/aerodynamic pressure (ABAQUS),
- determination of elastic deformations of the foil assembly, i.e. displacements of the top foil nodes (ABAQUS),
- modification of the lubrication gap's geometry based on the determined deformations of the top foil (MESWIR),
- determination of a new hydrodynamic/aerodynamic pressure distribution for the modified geometry of the lubrication gap (MESWIR).

The calculation cycle described above was run iteratively until the desired convergence criteria in subsequent iterations were achieved. The achievement of convergence depended on the percentage difference of displacements in subsequent iterations. The calculation process was considered terminated once changes in the lubrication gap's geometry were small enough in subsequent iterations.

### **New Method for Determining Deformations**

In the proposed new method for determining deformations of the compliant foil assembly, an additional step of analysis was introduced, consisting of preloading the foils, which is realized in a real bearing using a preliminary clamp—the nominal diameter of the journal is larger than the inner diameter of the foils assembly mounted inside the bush. During numerical analyses, the clamp is taken into account in the additional calculation step (performed first) by increasing the journal diameter of to the desired value. In the numerical model this is accomplished by dividing the journal into 4 equal parts – quadrants (Fig. 1) and then moving them apart in appropriate directions by the assumed displacement value. In order to accurately map the geometry of the journal with the target diameter, the radius of the quadrants being moved apart has to correspond to this diameter. The subsequent stages of the analysis, carried out according to the new method, are as follows:

- obtaining an initial clamp in the bearing by loading the foils assembly with the journal of the assumed diameter (ABAQUS),
- determination of the hydrodynamic pressure distribution on the cylindrical bearing's lubrication gap – without deformations (MESWIR),
- loading the top foil (already pre-loaded by the journal) with forces corresponding to the pressure determined in the lubrication gap (ABAQUS),



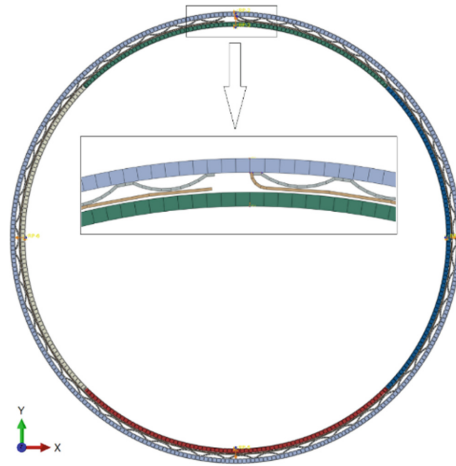


**Fig. 1.** FEM model of the foil bearing’s structure used in deformation analyses (division of the journal into 4 parts is indicated by colors).

- determination of elastic deformations of the pre-clamped foil assembly, i.e. displacements of the top foil nodes (ABAQUS),
- modification of the lubrication gap based on the deformations of the top foil, bypassing the deformations caused by pre-clamping the journal (MESWIR),
- determination of a new hydrodynamic pressure distribution for the modified geometry of the lubrication gap (MESWIR).

The above calculation process is repeated until the assumed convergence conditions are met. Graphic illustrations that bring us closer to the used method are shown in Figs. 2 and 3. In this method, the displacement of a part of the journal to the right position causes initial loading of the foils assembly, as it takes place during assembly of the actual bearing. In this way, foil bearings with a pre-clamp can be modeled.

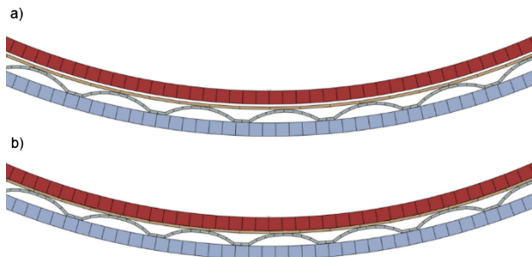


**Fig. 2.** Fragment of the FEM model of the foil bearing structure before (a) and after (b) increasing the journal diameter.

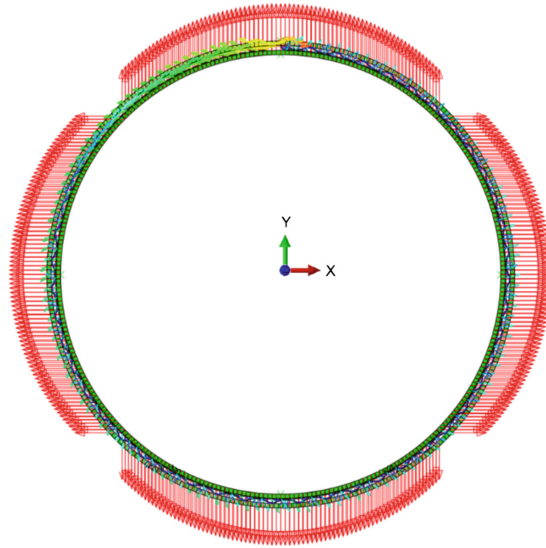


**Fig. 3.** Displacements of the foils and the journal parts in the foil bearing model, presented using displacement vectors of individual nodes.

## 2.2 Implementation of the Proposed Method in the Calculation Program

In order to be able to start using the new method for analyzing deformations of the foils assembly, it was necessary to introduce some changes to the computational algorithms used so far. Therefore, the MESLOF program code has been modified. This program automatically collects selected results obtained from various applications and transfers them between the MESWIR and ABAQUS software (Fig. 4). The algorithm implemented in the MESLOF program is presented in Fig. 5. According to the new concept of modelling a foil bearing, deformations of its foils are obtained in two calculation steps. In the first step, displacements of the FEM mesh nodes resulting from the pre-clamp of the journal between the foils are determined. In the second step, displacements of the nodes caused by the pressure acting in the lubrication gap are additionally determined. The obtained shape of the lubrication gap is subsequently used to determine the characteristics of each bearing, and then, of the entire rotor.

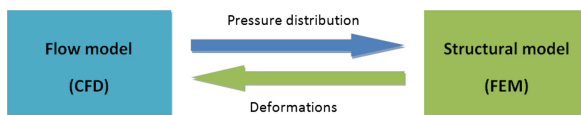


**Fig. 4.** General scheme for data exchange between CFD (MESWIR) and FEM (ABAQUS) models in the numerical analysis of foil bearings.

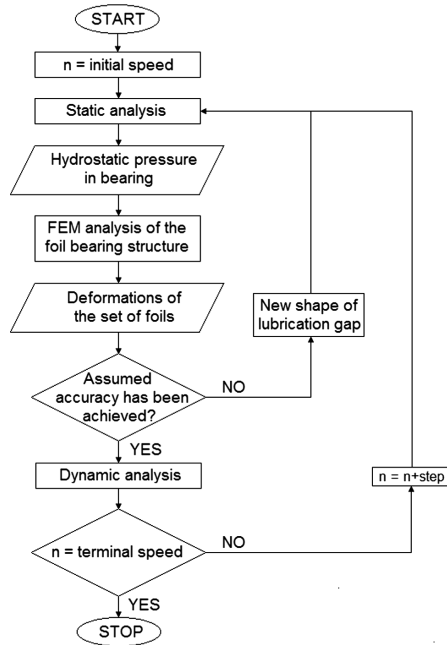


**Fig. 5.** Block diagram of the algorithm for analyzing rotors supported by foil bearings.

In the modified MESLOF program, computations are carried out as follows:

1. A set of data files is prepared for the MESWIR program, and also for the FEM model created in the ABAQUS software. The FEM model implemented in ABAQUS considers the foils' geometry and has a defined set of nodes at which forces acting on the top foil's surface are defined—corresponding to acting pressure. The bearing model in the MESWIR program was prepared in such a way that it is possible to fit the FEM mesh of the top foil to it.
2. The MESWIR program performs static analysis of the rotating system and yields pressure distributions in lubrication gaps corresponding to the static positions of bearing journals.
3. In the MESLOF program, forces—corresponding to the determined pressure distribution—are computed at individual nodes.
4. Data files, containing forces assigned to nodes and acting on the inner surface of the top foil, are created for the ABAQUS model.
5. The ABAQUS program computes a distribution of the displacements of the top foil's nodes in two calculation steps: (1) as a result of the pre-clamp and (2) as a result of pressure acting in the lubrication wedge.
6. Taking into account the difference between displacements obtained in the first and second calculation step, the MESLOF program creates a data file for the MESWIR program, into which it saves new shapes of both lubrication gaps.

7. The MESWIR program performs calculations of pressure distributions for modified shapes of lubrication gaps.

Steps 2–7 are repeated until the convergence conditions are met.

8. The MESWIR program conducts a dynamic analysis of the rotating system by adopting stiffness and damping coefficients of the lubricating film that were computed for modified shapes of the lubrication gaps (i.e. the ones obtained in the last step of the iterative algorithm).

The stiffness and damping coefficients of gas bearings are determined iteratively, separately for each analysed rotational speed of the rotor. Because various loads act on each of bearings, each bearing has to be analyzed separately. That is why stiffness and damping coefficients of both bearings can take different values. This obviously has an effect on dynamic characteristics of the rotor.

### 3 Verification of Results

#### 3.1 Characteristics of the Analyzed System

The tested rotor consists of a steel shaft with two disks and is supported on two first-generation foil bearings (Fig. 6). The nominal diameter of the shaft and of the bearings is 50.8 mm. The length of the rotor, together with discs mounted on its both ends, is 364 mm. The weight of the entire rotating system is 6.9 kg. The model also includes residual unbalance, which is 4.2 g·mm ( $46^\circ$ ) and 7.5 g·mm ( $87^\circ$ ) for the first and second disk, respectively. The rotor model was developed on the basis of data provided in publication [23].

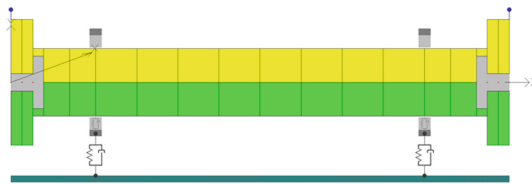


Fig. 6. FEM model of the analyzed rotor.

The FEM model of the rotor comprises 18 Timoshenko-type beam elements, with six degrees of freedom in each node. The rotor has a symmetrical arrangement of disks—meaning that they are situated at both ends of the hollow shaft, and, what is more, are geometrically uniform and of the same mass. The bearings are situated symmetrically as well. In all simulations, each bearing carried a static load of 33.8 N plus an additional dynamic load originating from the residual unbalance. Analyses were carried out for aerodynamic bearings, with air (having a dynamic viscosity of  $1.85 \cdot 10^{-5}$  Pa·s) as a lubricant. Dimensions of the bearings are equal to those specified in article [23], and are as follows: bearing width 40.6 mm, journal diameter 50.8 mm,  $L/D \approx 0.8$ . The

nominal radial clearance, whose value was necessary to start the flow analysis of the bearings, was 20  $\mu\text{m}$ . This is the optimal value that allows analyzing bearings operation over a wide range of rotational speeds. This value was only used during analyzes of bearings carried out in the MESWIR program and had nothing to do with the initial clamp values being inserted into the ABAQUS model—thus the ones needed to determine the shape of the lubrication gap.

The foil bearing's structure and the shape of the lubrication gap were mapped using a two-dimensional FEM model, which, as mentioned before, was developed in the ABAQUS software. The geometry of the top and bump foils is depicted in Fig. 1. The model consists of 2,898 finite elements (of the CPE4RH type), with 10,824 degrees of freedom. In finding a solution, the developed model takes into account, among other things, the following issues: contact phenomena between the mating bearing components (i.e. between the top and bump foils as well as between the journal and the bush), friction between these components (coefficient of friction was 0.2), load due to the aerodynamic pressure.

### 3.2 Analysis of the Foil Bearings with Assembly Preloads

The research described herein cover several computational series. All computations were made for the same rotor model, and changes were introduced only to the bearing model itself and they consisted in altering the journal diameter and thereby altering the assembly preload. All computation variants are listed in Table 1. In addition to assembly preload values, the structural stiffness of the bearing structure (both in the vertical and horizontal direction) is given, the value of which was computationally determined taking into account the initial assembly preload. Since in all the analyzed cases the stiffness in the horizontal direction was almost twice lower than the stiffness in the vertical direction, the obtained values have been rounded. For each bearing variant analyzed, the assumed initial value of the damping coefficient of the foils assembly in both directions was equal to 1,000 N·s/m.

**Table 1.** Basic parameters of the analyzed variants of foil bearings.

No.	Assembly preload [ $\mu\text{m}$ ]	Structural stiffness in vertical direction [N/m]	Structural stiffness in horizontal direction [N/m]
1	0	$10.6 \cdot 10^6$	$5.3 \cdot 10^6$
2	5	$52.4 \cdot 10^6$	$26.2 \cdot 10^6$
3	7.5	$700 \cdot 10^6$	$350 \cdot 10^6$
4	10	$1,020 \cdot 10^6$	$510 \cdot 10^6$
5	15	$1,160 \cdot 10^6$	$580 \cdot 10^6$
6	30	$1,430 \cdot 10^6$	$715 \cdot 10^6$

Already the results obtained during several first computational series showed that the assumed value of clearance/clamp in the bearing has a decisive influence on local and global deformations of the foils assembly. With a low clearance or a very small assembly preload (0.5  $\mu\text{m}$ ) one could observe very large deformations of the foils

assembly caused by the pressure of the lubricating wedge. In some places, displacements of the nodes situated on the top foil's surface were greater than the nominal radial clearance necessary for the formation of a lubricating wedge. Thus, very irregular deformations occurred at the perimeter of the bush, hindering the formation of a stable lubricating film that could have provided a sufficient bearing capacity. After applying the assembly preload values from the range of 7.5–30  $\mu\text{m}$  (which caused the top foil to be pressed against each bulge of the bump foil), completely different characteristics of the bearing structure began to appear. The top foil became very stiff around the entire circumference, and the maximum displacement of the nodes did not exceed several micrometers.

Due to the above-mentioned abrupt change in the properties of the foils assembly, the full results from the analysis of the bearings and of the rotor are presented only for three selected computation variants: 5, 7.5 and 10  $\mu\text{m}$ . The results for the “no assembly preload” case were very similar to the ones from the variant with an assembly preload of 5  $\mu\text{m}$ . The variants with an assembly preload of 15  $\mu\text{m}$  and 30  $\mu\text{m}$  yielded almost identical results as in the 10  $\mu\text{m}$  variant. A sudden change in the characteristics of the foils assembly can also be seen based on the stiffness values given in Table 1.

### Assembly preload 5 $\mu\text{m}$

For the case of the rotor with bearings in which the assembly preload was only 5  $\mu\text{m}$ , it was possible to achieve convergence only for several rotational speeds from the range of 10,000–14,000 rpm. After analyzing the results, it turned out that an assembly preload of 5  $\mu\text{m}$  was too small to allow the journal to press the top foil against the bump foil. In addition, the mesh used in the model had a negative effect on the reduction of the actual value of the assembly preload and prevented a precise mapping of the circular geometry (due to the distance between nodes and linear shape functions used). As a result of the low stiffness of the underloaded foils assembly, and under the influence of pressure, significant deformations occurred that caused an irregular shape of the lubrication gap (Fig. 7). Such a shape of the lubrication gap did not allow to achieve convergence of the iterative process in a wider range of rotational speeds.

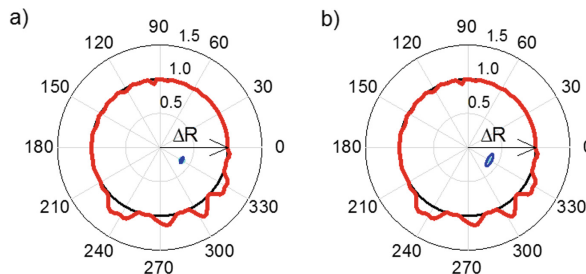


**Fig. 7.** Bush deformations and vibration trajectories of the journals of two foil bearings with an assembly preload of 5  $\mu\text{m}$  at a speed of 10,000 rpm, presented in relation to the radial clearance (a—bearing No. 1, b—bearing No. 2).

The obtained results showed that vibration trajectories of the rotor increased as rotational speeds increased. Due to convergence problems, no solutions could be obtained for speeds higher than 14,000 rpm. This indicated that there were no good conditions for the formation of a stable gaseous lubricating wedge.

### Assembly preload 7.5 $\mu\text{m}$

Increasing the initial assembly preload to 7.5  $\mu\text{m}$  caused the top foil to be pressed against the bump foil and, consequently, the stiffness of the foils assembly rose. Under these conditions, the bearing operated stably over a wide range of speeds. A stable operation of the system and very small deformations of the lubrication gap can be seen in Fig. 8. The vibration amplitudes (in two directions) of one bearing journal are shown in Fig. 9, as a function of the rotational speed. Only vibrations of bearing No. 2 are presented in this article. Due to the greater unbalance on one side of the rotor, vibration amplitudes of the journal No. 2 are higher than amplitudes of the journal No. 1. The presented graph shows that there is no clear resonance in the range of speeds up to 40,000 rpm. The vibration amplitudes gradually increased to a speed of approximately 35,000 rpm, but even in this range, the maximum vibration amplitude of both bearings did not exceed several micrometers. This is due to the fact that, having regard to a very high stiffness of the foils assembly, the stiffness of the gaseous lubrication film and of the shaft was of great importance. Since the stiffness of the thin lubrication film is high, there were quite low vibration amplitudes over the entire rotational speed range.

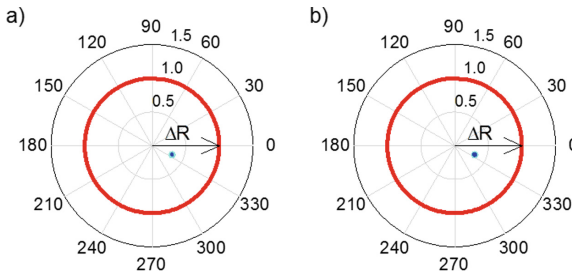


**Fig. 8.** Bush deformations and vibration trajectories of the journals of two foil bearings with an assembly preload of 7.5  $\mu\text{m}$  at a speed of 10,000 rpm, presented in relation to the radial clearance (a—bearing No. 1, b—bearing No. 2).

### Assembly preload 10 $\mu\text{m}$

After re-increasing the assembly preload, this time up to 10  $\mu\text{m}$ , the rotating system had very similar static and dynamic properties to the system with an assembly preload of 7.5  $\mu\text{m}$ . After a series of calculations, it turned out that the obtained vibration trajectories of the journals (Fig. 10) and vibration amplitude curves (Fig. 11) are almost identical to the results described in the previous case (Figs. 8 and 9). The vibration amplitude curves from two cases are not very different from each other—both the horizontal and vertical curves. As previously, the aerodynamic pressure in the bearings did not cause large deformations of the foils assembly. The foils were tightly compressed between the journal and the bush.

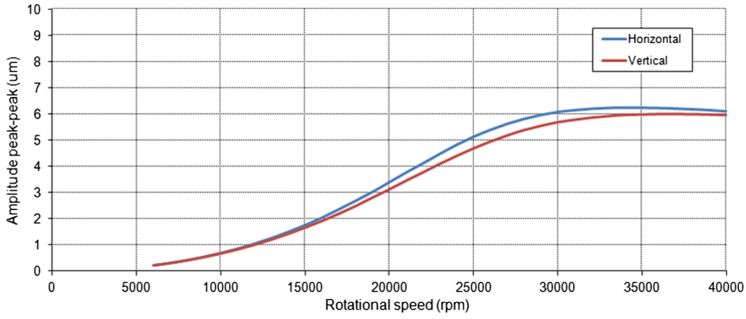


**Fig. 9.** Vibration amplitudes of the journal of bearing No. 2 vs. rotational speed. (assembly preload is  $7.5 \mu\text{m}$ ).

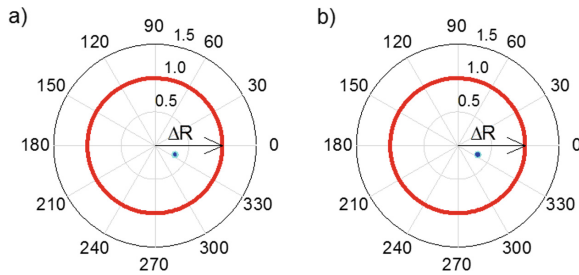


**Fig. 10.** Bush deformations and vibration trajectories of the journals of two foil bearings with an assembly preload of  $10 \mu\text{m}$  at a speed of 10,000 rpm, presented in relation to the radial clearance (a—bearing No. 1, b—bearing No. 2).

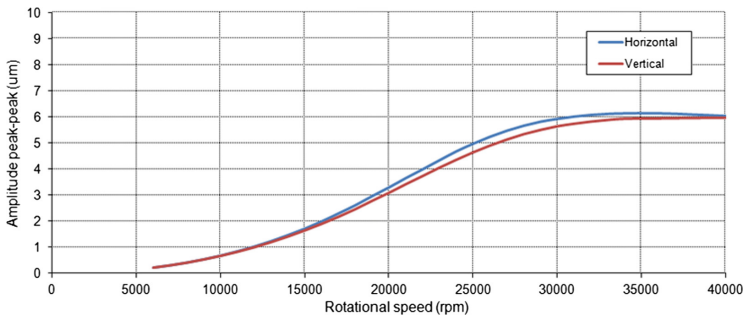


**Fig. 11.** Vibration amplitudes of the journal of bearing No. 2 vs. rotational speed. (assembly preload is  $10 \mu\text{m}$ ).

What is more, the vibration trajectories of the rotor itself and its shape bear evidence of the stable operation of the entire rotating system. Figure 12 shows the zoomed in vibration trajectories of the rotor at the highest speed analyzed. Even at such a high rotational speed, only a slight deflection of the shaft was observed, and vibration



amplitudes did not exceed several micrometers. Probably the analyzed rotor could operate properly also at higher speeds.

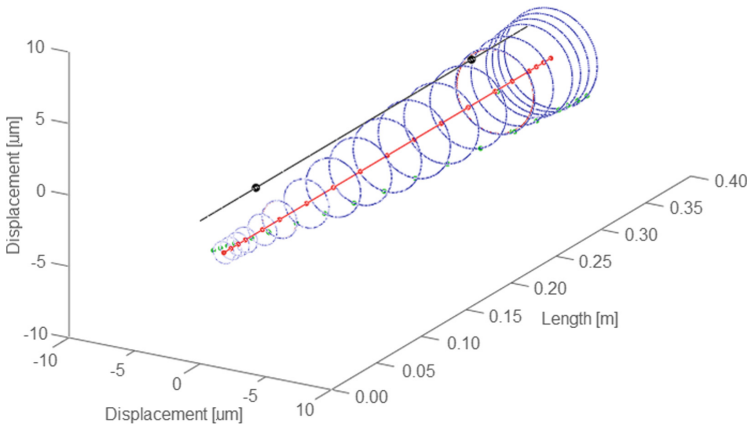


**Fig. 12.** Shape of the rotating shaft supported by two foil bearings with an assembly preload of  $10\ \mu\text{m}$ , at a speed of 40,000 rpm.

## 4 Conclusions

The article describes a new method for modeling elastic deformations of a compliant foils assembly in foil bearings. The method allows taking into account the assembly preload in a bearing. The foil bearing model and the calculation algorithm were discussed. After this, there is a presentation of results of the analysis, the aim of which was to check the proposed method in practice, using a selected example of a rotating system. The conducted calculations made it possible to assess the impact of the assembly preload in foil bearings on dynamic properties of the entire rotating system. Based on the simulations conducted so far, the following conclusions can be drawn:

- As the assembly preload increased, some operational characteristics of the foil bearing changed dramatically. This was related to a clamping of the top foil between the journal and the bump foil. Pressing the top foil against bulges of the bump foil around its entire circumference caused that the assembly of two interacting foils became more and more rigid. However, further increase of the assembly preload no longer caused any significant changes in the stiffness characteristics of the system.
- In the analyzed system, very small assembly preloads (e.g.  $5\ \mu\text{m}$ ) did not cause the journal to be pressed against the top foil. It resulted from the method of modeling a circular surface using finite elements with edges defined by straight lines (i.e. first-order curves). Elements of this type are significantly better in solving contact problems than elements whose edges are defined by higher-order curves. Compacting the mesh, in turn, increased the number of degrees of freedom and made the

computation time longer. It should, therefore, be borne in mind that low assembly preload values in the model could be equated with the clearance in a bearing.

- The conducted analyzes show that after considering the assembly preload in the model, the geometry and thickness of the foils started to play a less important role in the bearing's operation. The stiffness of the foils assembly pressed by the journal is relatively high, so altering the geometry of these foils in such a bearing would have very little or no impact on bearing characteristics. The situation was different in previous research when at that time it was assumed that there had been too big radial clearance in tested bearings.
- It should be emphasized that the results described herein were obtained using computer simulations, and they have not yet been verified experimentally. During the production of foil bearings, a high level of accuracy in the manufacture of thin metal foils is hard to achieve due to elastic deformation effect. Given the above fact, it is difficult to obtain a uniform pressing of the foils around the whole perimeter of the journal. It is also difficult to obtain an appropriate nominal radial clearance or assembly preload with an accuracy of a few micrometers. That is why some discrepancies can be expected between the results of the computer simulation described in this article and an experiment that is still to be conducted.

The results obtained using the developed model confirm a strong influence of the pre-clamp on the foil bearing's stiffness and thus on the operating properties of the rotating system. The numerical research carried out initially proved the proper operation of the developed model and its usefulness. After an experimental verification, it could be used for a trustworthy assessment (and an optimization) of the properties of rotors supported by gas foil bearings. In the authors' opinion, the developed method is able to reflect processes occurring in foil bearings, in which there is usually an assembly preload. Models of this type can pave the way for a further development of foil bearings and for their wider use in modern high-speed turbomachinery.

**Acknowledgements.** The work presented in this article was supported by the scientific project No. 2016/21/D/ST8/01711, financed by the National Science Centre (NCN) in Poland.

## References

1. DellaCorte, C.: Oil-free shaft support system rotordynamics: past, present and future challenges and opportunities. *Mech. Syst. Signal Process.* **29**, 67–76 (2012)
2. Żywica, G., Bagiński, P., Banaszek, S.: Experimental studies on foil bearing with a sliding coating made of synthetic material. *J. Tribol. Trans. ASME* **138**(1), 011301 (2016)
3. Bruckner, R.J.: An assessment of gas foil bearing scalability and the potential benefits to civilian turbofan engines. In: *Proceedings of ASME Turbo Expo 2010, Glasgow (UK)*, GT2010–22118 (2010)
4. Kiciński, J., Żywica, G.: *Steam Microturbines in Distributed Cogeneration*. Springer, Cham (2014)
5. Tkacz, E., Kozanecka, D., Kozanecki, Z., Łagodziński, J.: Oil-free bearing development for high-speed turbomachinery in distributed energy systems—dynamic and environmental evaluation. *Open Eng.* **3**, 343–348 (2015)

6. Żywica, G., Kiciński, J., Bagiński, P.: The static and dynamic numerical analysis of the foil bearing structure. *J. Vib. Eng. Technol.* **4**(3), 213–220 (2016)
7. Osmanski, S., Larsen, J.S., Santos, I.F.: A fully coupled air foil bearing model considering friction—Theory & experiment. *J. Sound Vib.* **400**, 660–679 (2017)
8. Akson, S., Aksit, M.F.: A fully coupled 3D thermo-elastohydrodynamics model for a bump-type compliant foil journal bearing. *Tribol. Int.* **82**, 110–122 (2015)
9. Miąskowski, W., Pietkiewicz, P., Żywica, G.: Modeling foil bearings. *Tech. Sci.* **12**, 241–248 (2009)
10. Tkacz, E., Kozanecki, Z., Kozanecka, D.: Numerical methods for theoretical analysis of foil bearing dynamics. *Mech. Res. Commun.* **82**, 9–13 (2017)
11. Heshmat, H., Hryniwicz, P., Walton II, J.F., Willis, J.P., Jahanmir, S., DellaCorte, C.: Low-friction wear-resistant coatings for high-temperature foil bearings. *Tribol. Int.* **38**, 1059–1075 (2005)
12. Jahanmir, S., Heshmat, H., Heshmat, C.: Assessment of tribological coatings for foil bearing applications. *Tribol. Trans.* **52**(2), 231–242 (2009)
13. Shalash, K., Shiffmann, J.: On the manufacturing of compliant foil bearings. *J. Manuf. Process.* **25**, 357–368 (2017)
14. Żywica, G., Bogulicz, M., Bagiński, P.: Modelling and analysis of the rotating systems with gas foil bearings under transient operating conditions. *Tribologia* **2**, 167–173 (2017)
15. Larsen, J.S., Hansen, A.J.T., Santos, I.F.: Experimental and theoretical analysis of a rigid rotor supported by air foil bearings. *Mech. Ind.* **16**, 106–119 (2015)
16. Larsen, J.S., Santos, I.F.: On the nonlinear steady-state response of rigid rotors supported by air foil bearings—theory and experiments. *J. Sound Vib.* **346**, 284–297 (2015)
17. Gu, Y., Ma, Y., Ren, G.: Stability and vibration characteristics of a rotor-gas foil bearings system with high-static-low-dynamic-stiffness supports. *J. Sound Vib.* **397**, 152–170 (2017)
18. Bonello, P., Bin Hassan, M.F.: An experimental and theoretical analysis of a foil-air bearing rotor system. *J. Sound Vib.* **413**, 395–420 (2018)
19. Rubio, D., San Andres, L.: Bump-type foil bearing structural stiffness: experiments and predictions. *J. Eng. Gas Turbines Power* **128**, 653–660 (2006)
20. Hou, Y., Ma, B., Yang, S., et al.: Experimental study on bump-foil gas bearing with different diametric clearance configurations. *J. Mech. Sci. Technol.* **29**(5), 2089–2095 (2015)
21. Hoffmann, R., Liebich, R.: Experimental and numerical analysis of the dynamic behaviour of a foil bearing structure affected by metal shims. *Tribol. Int.* **115**, 378–388 (2017)
22. Kiciński, J.: *Rotor Dynamics*. IMP PAN Publishers, Gdansk (2006)
23. Howard, S.A., San Andres, L.: A new analysis tool assessment for rotordynamic modeling of gas foil bearings. *NASA/TM-2010-216354* (2010)



# Selection of the Bearing System for a 1 kW ORC Microturbine

Łukasz Breńkacz<sup>(✉)</sup> , Grzegorz Żywica ,  
and Małgorzata Bogulicz

Institute of Fluid Flow Machinery, Polish Academy of Sciences,  
80-283 Gdansk, Poland  
lbrenkacz@imp.gda.pl

**Abstract.** The article describes an analysis of various bearing systems for the rotor of an ORC turbine with an electric power of 1 kW. The nominal rotational speed of the newly designed single-stage axial-flow turbine is 100,000 rpm. The turbine is supplied with a low-boiling medium's vapor and this medium is not compatible with all typical materials used for constructing power turbines. Additionally, the turbine must be an oil-free machine. In one of the design variants, the turbine rotor disk is to be made of plastic and the temperature of the working medium directed to the vanes will be approx. 150°C (at a pressure of 10 bar). Three different bearing systems were considered: 1. bearings lubricated with a low-boiling medium's liquid; 2. gas bearings lubricated with a low-boiling medium's vapor; 3. rolling bearings. After initial analysis, it was found that hydrodynamic bearings lubricated with a low-boiling medium did not work properly in this case and it was decided to conduct a detailed analysis of the second and third type of bearings. The two bearing systems are associated with changes in the geometry of the rotor, which in turn strongly affect the dynamic performance of the entire rotating system. The dynamic analysis of the rotor is the subject of the conducted research and constitutes part of the bearing selection process. This article presents the process of selecting and optimizing the bearing system for the rotor of a 1 kW turbine.

**Keywords:** High-speed bearings · Microturbine · ORC system

## 1 Introduction

Over recent years, systems based on renewable energy sources have played an increasingly important role in international markets [1]. ORC (Organic Rankine Cycle) systems—combined with, for example, a biomass boiler—can be used in single-family houses, thus allowing independence from a national energy grid [2]. The use of such energy systems contributes to the consumption of smaller quantities of fossil fuels and smaller emissions of harmful greenhouse gases into the atmosphere, and what is more, it increases energy security and the comfort of residents [3].

Scientific literature is rich in publications regarding microturbines. Paper [4] shows an example of one of the smallest microturbines. This microturbine, whose rotor diameter is 10 mm, is capable of generating maximally 28 watts of mechanical power

at a rotational speed of approximately 100,000 rpm. The rotor is supported by rolling bearings. New types of microturbines often require the use of new materials [5].

An example of a microturbine with floating ring journal bearings is presented in article [6]. The prototype system ran safely at speeds up to 100,000 rpm under no-load. An experimental characterization of a gas microturbine converted to full humid air operation is presented in paper [7].

In the process of designing micro-power energy turbines (with an electric power of a few kilowatts), it is necessary to ensure stable operating conditions with the maximum reduction of noise and vibration levels [8].

In addition, the key aspect is to design an appropriate bearing system. The optimization process of the bearing system for a 700 kW turbine, operating in an ORC system, is discussed in article [9].

This article presents results of the analysis conducted for the bearing system of an ORC turbine with an electric power of 1 kW. Other operating conditions (such as rotational speed, shaft mass, and temperature) result in the need to apply another bearing system, and thus the use of new tools for its analysis. The properties of bearings can be analyzed using experimental methods (if prototypes are available [10, 11]) or numerical computations. For the purposes of the research described in this article, computer programs for analyzing complex rotating systems, developed at the IMP PAN [12], were used. The article discusses the works related to the selection of the bearing system for the rotor of a 1 kW turbogenerator. The turbogenerator's rotor will operate under unusual conditions that result from a very high nominal rotational speed, elevated temperatures and the presence of a low-boiling medium. Only after flow computations of the turbine, it turned out that the nominal rotational speed is 100,000 rpm. However, given this fact, it is necessary to ensure failure-free operation of the rotor at speeds up to 120,000 rpm. The ambient temperature of the bearings is expected to be approx. 120 °C. It is also to be expected that due to the turbogenerator's structure, a low-boiling medium in the form of a two-phase mixture will be present in the places where the bearings are to be mounted.

## 2 Structural Analysis of the Turbogenerator's Rotor

The initial design of the rotor has been developed based on the computation results to date and the IMP PAN team's experience gained when designing turbine expanders used in micro-power ORC cogeneration systems. Only after the preliminary computations of the thermodynamic cycle were carried out and the external dimensions of the rotor's disk were estimated, a structural design of the rotor was developed. An electric generator was selected as well. Two diagrams of the turbogenerator's rotor with aerodynamic (upper diagram) and super-precise rolling (lower diagram) bearings are presented in Fig. 1.

It was assumed that the turbogenerator has to be of the oil-free type. This means that during operation neither bearings nor its other parts will require oil lubrication. It is a very modern solution with many advantages. The most important of them are the following: there will be no contamination of the ORC system's working medium with a bearing lubricant, a hermetically-sealed casing of the microturbine, no need to use

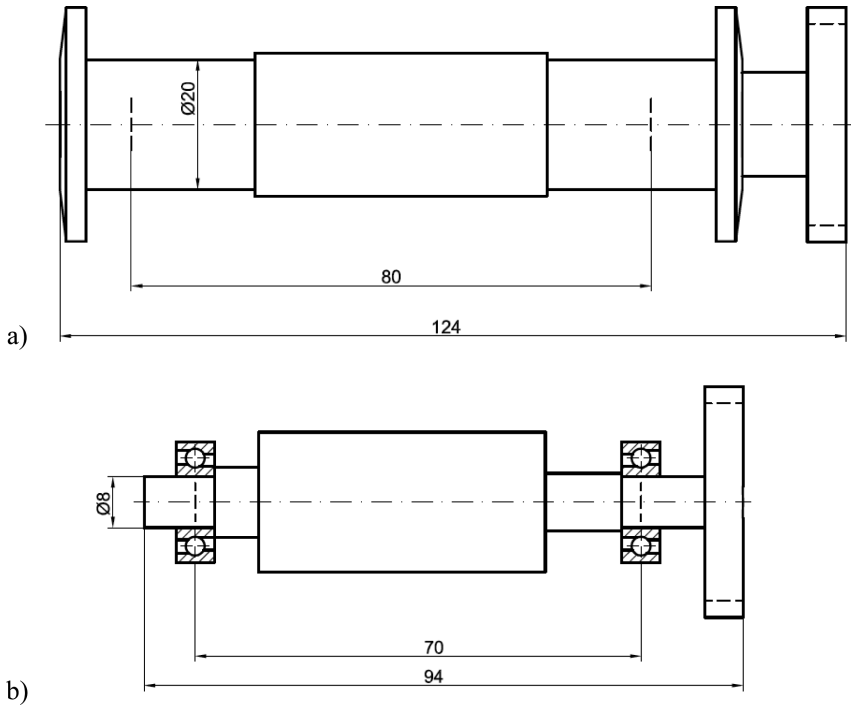


**Fig. 1.** Diagram of the 1 kW ORC turbogenerator's rotor supported by: (a) aerodynamic bearings, (b) rolling bearings.

hermetic seals within the casing (between the turbine and bearing parts), no external power supply system for the bearings. All these features are very important in systems with working mediums of the low-boiling type—which tend to have a high penetrability. Such a solution also has some drawbacks. Rolling bearings designed for very high speeds work better with oil lubrication. Grease lubrication in rolling bearings does not allow very high rotational speeds to be achieved. There are specialized designs of rolling bearings lubricated with grease that enable stable operation with high speeds, but these are solutions “on the verge of technical possibilities”. It follows that there is an absolute necessity to thoroughly investigate each and every newly designed bearing system.

The first tested ORC turbogenerator is equipped with rolling bearings with a diameter of 8 mm. The second turbogenerator's rotor is supported by aerodynamic bearings that have a diameter of 20 mm (after optimization). Thanks to small dimensions of the generator and of the rotor disk, the developed rotor is characterized by very small external dimensions. The following parts of the article discuss results of the analyzes carried out for two bearing systems with gas bearings and high-speed rolling bearings. It was initially estimated that each of these bearing systems can be used in the target solution. Testing of the systems was aimed at determining the key parameters of the bearings and checking them for correct operation.

### 3 Gas Bearings

Gas bearings are one of the two bearing variants considered. The research covered aerodynamic bearings with different diameters. Only after the optimization process was completed, the bearings with diameters  $D_1 = D_2 = 20$  mm and the width respectively  $L_1 = 16$  mm and  $L_2 = 18$  mm were selected for further analysis. The bearing No. 1 is situated on the left-hand side of Fig. 2 (in other words, further away from the rotor disk than bearing No. 2).

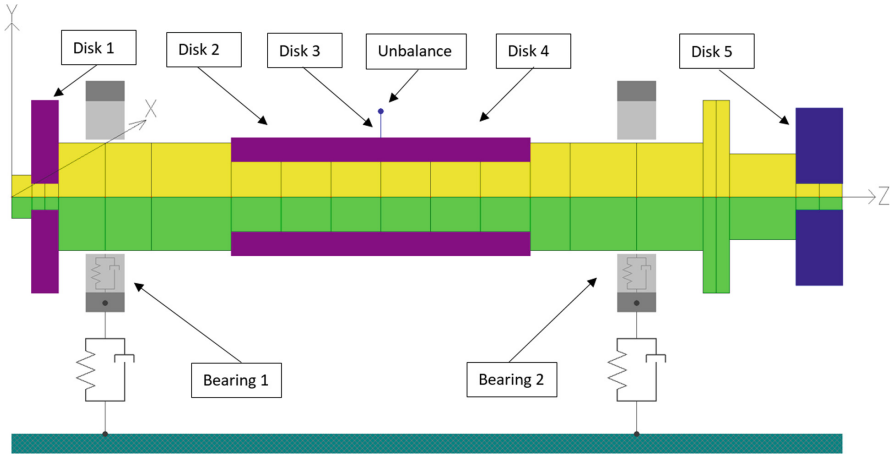


Fig. 2. FEM model of the 1 kW turbogenerator's rotor with aerodynamic bearings.

#### 3.1 Analysis of the Rotor with Gas Bearings

There was conducted a kinetostatic and dynamic analysis of the turbogenerator's rotor supported by aerodynamic bearings. For this purpose, computations were performed using the KINWIR-G and LDW-G computer programs, which belong to the MESWIR environment used for carrying out simulations on rotor – bearings systems. The FEM (Finit- Element Method) model of the rotor, used in those simulations, is presented in Fig. 2.

This model comprises 20 Timoshenko-type beam elements, with six degrees of freedom in each node. The keep plate is modeled as a disk placed at shaft node No. 3, and the generator as three disks situated at shaft nodes with numbers 8, 10 and 12. The rotor disk is modeled as a disk located at shaft node No. 20. The rotor is supported by two aerodynamic bearings, the shaft nodes of which have numbers 5 and 15.

Stiffness and damping coefficients of the lubricating film were computed using the MESWIR environment. In the subsequent stages of the analysis, the static equilibrium point was determined, and afterward, a series of calculations for neighboring points were made (altering the position of the journal). At each position of the journal, the Reynolds equation was solved using the Alternating Direction Implicit (ADI) method [13]. On this basis, values of pressure and forces acting on the bearing journal were

found, what in turn was the starting point for estimating the values of stiffness and damping coefficients. These coefficients changed with the rotational speed change and their values at the nominal speed are listed in Table 1.

**Table 1.** Stiffness and damping coefficients of aerodynamic bearings for the nominal speed (100,000 rpm).

Parameter	Stiffness [N/m]	Damping [Ns/m]
Bearing 1 xx	$3.14 \cdot 10^6$	471
Bearing 1 yy	$1.66 \cdot 10^6$	249
Bearing 2 xx	$3.55 \cdot 10^6$	533
Bearing 2 yy	$2.94 \cdot 10^6$	441

The dimensions of the bearings are as follows: diameter –  $D_1 = D_2 = 20$  mm, width— $L_1 = 16$  mm and  $L_2 = 18$  mm, absolute radial clearance— $15 \mu\text{m}$ . It was assumed that the rotor and the first four disks (counting from the left) are made of steel with a density of  $7,860 \text{ kg/m}^3$ , and the disk that models the keep plate is made of aluminum with a density of  $2,700 \text{ kg/m}^3$ . The total mass of the rotor is 0.361 kg. The kinetostatic load is 1.5071 N and 2.0316 N, respectively for the first and second bearing. The residual unbalance was 0.361 gmm, according to the requirements of ISO 1940-1 standard [14]. The dynamic viscosity of the working medium was  $0.101 \times 10^{-4} \text{ Ns/m}^2$  at a temperature of  $130 \text{ }^\circ\text{C}$ . Computations were carried out for the speed range of 5,000–150,000 rpm.

Figure 3 shows the relative vibrations of the nodes corresponding to the bearing journals and the vibrations of the nodes in which the disks were modeled. Lubricating wedges, enabling the correct operation of aerodynamic bearings, formed themselves already at a speed of 7,000 rpm. The highest vibration amplitudes of the journals occurred at a rotational speed of 70,000 rpm, and were, respectively, approx.  $1.8 \mu\text{m}$  and approx.  $1.1 \mu\text{m}$  for the first and second bearing. The maximum amplitude of vibration of disk No. 1 was about  $1.95 \mu\text{m}$  and was registered at a speed of 85,000 rpm. Vibrations of disks No. 2, 3 and 4 increased up to a speed of approx. 65,000 rpm and their maximum vibration amplitudes were respectively about  $1.62 \mu\text{m}$ ,  $1.52 \mu\text{m}$  and  $1.37 \mu\text{m}$ . Then, vibration levels of these three discs decreased slightly, and in the speed range of 90,000 rpm–100,000 rpm began to increase again, reaching the highest vibration amplitudes at the end of the analysed speed range ( $1.64 \mu\text{m}$ ,  $1.87 \mu\text{m}$  and  $1.66 \mu\text{m}$ , for the first, second and third disk, respectively). The vibration level of the fifth disk rose across the whole analyzed speed range, reaching the maximum vibration amplitude of  $1.48 \mu\text{m}$ .

Vibration trajectories of the shaft nodes are shown in Fig. 4, for the following rotational speeds: 10,000 rpm (i.e. immediately after the lubricating wedge has formed itself), 70,000 rpm (at highest displacements of bearing journals), 85,000 rpm (that is the speed at which the highest vibration amplitude of disk No. 1 occurred), 120,000 rpm (i.e. at the highest tested speed). Figure 5 presents vibration trajectories of the bearing journals obtained at the same four rotational speeds.



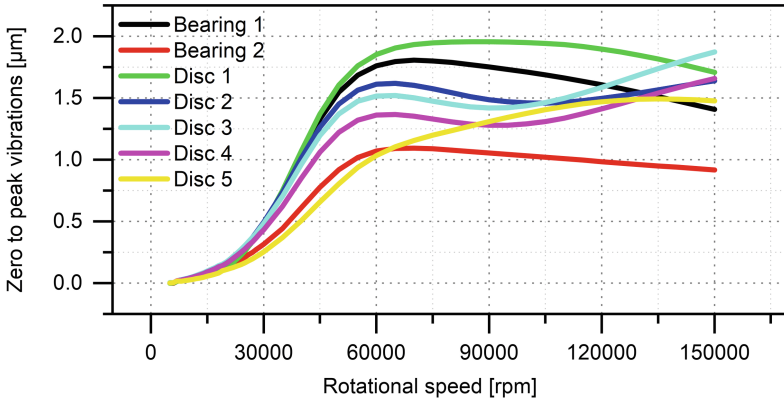


**Fig. 3.** Vibration amplitudes of the gas bearings' journals vs. rotational speed.

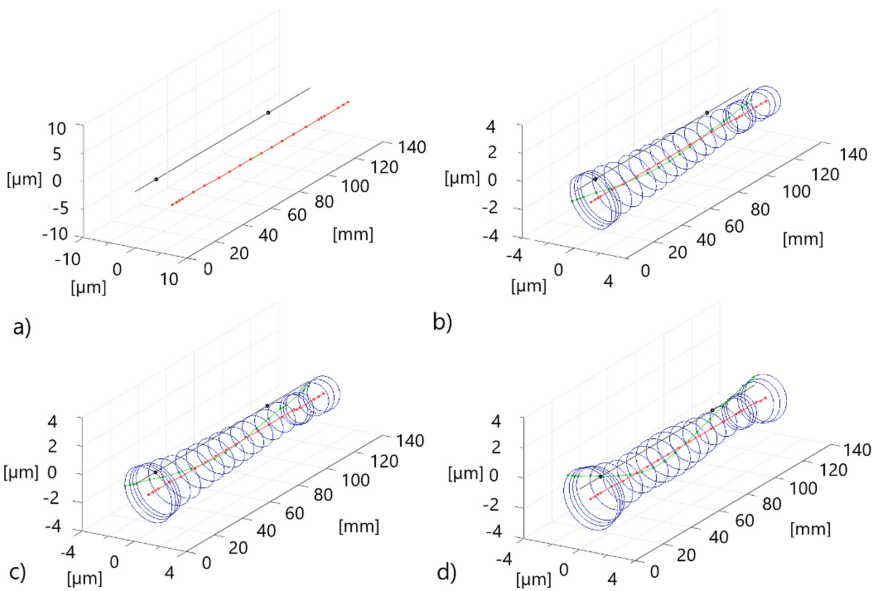


**Fig. 4.** Vibration trajectories of the rotor's shaft nodes of the 1 kW ORC microturbine with aerodynamic bearings at four rotational speeds: (a) 10,000 rpm, (b) 70,000 rpm, (c) 85,000 rpm, (d) 120,000 rpm.

The results of analyzes conducted for the rotor of the 1 kW ORC microturbine, supported on aerodynamic bearings show that the vibration amplitudes of the rotating system are small and did not exceed 2 μm in the entire tested speed range of 5,000–150,000 rpm. Both bearings started to operate properly already at a speed of 7,000 rpm.

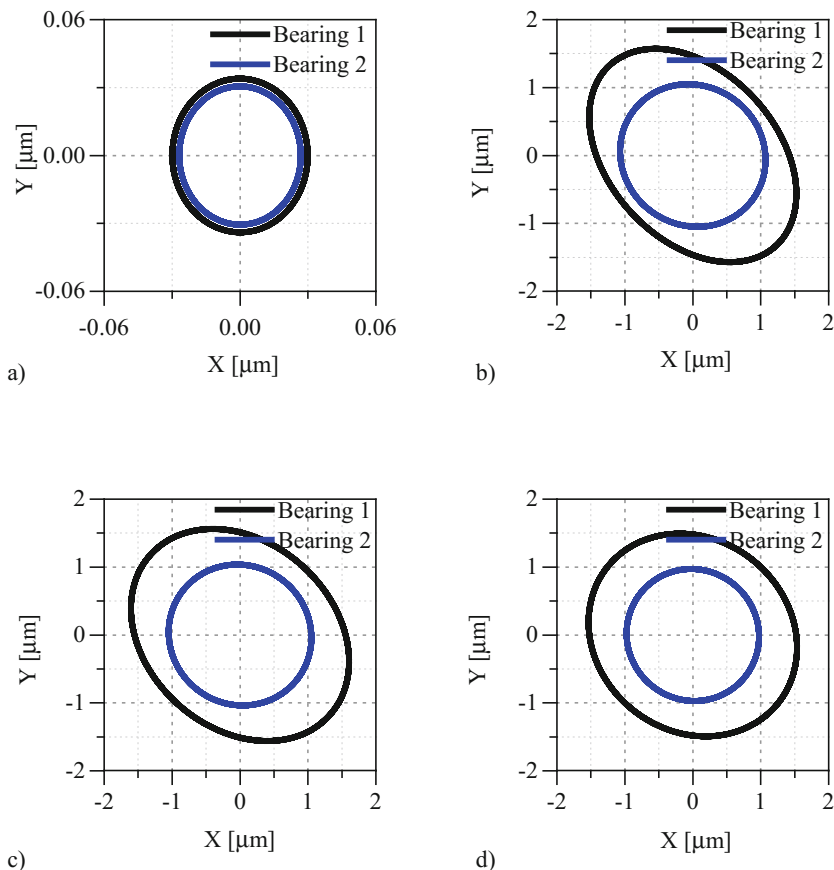


**Fig. 5.** Vibration trajectories of the aerodynamic bearings' journals of the 1 kW ORC microturbine at four rotational speeds: (a) 10,000 rpm, (b) 70,000 rpm, (c) 85,000 rpm, (d) 120,000 rpm.

## 4 Rolling Bearings

Rolling bearings are the second variant of bearings that perhaps will be used as components of the turbogenerator with an electric power of 1 kW. This chapter discusses the features of the selected super-precise rolling bearings and the dynamic performance of the rotor supported by such bearings.

### 4.1 Analysis of the Rotor with Rolling Bearings

Bearings marked with the 719/8 CE/HCP4A symbol [15], produced by the SKF company, were chosen based on the given operating parameters. A three-dimensional model of such a bearing is presented in Fig. 6. Selected bearings do not have seals. The '719' digits in the bearing symbol inform about the compliance of its dimensions with

the relevant ISO standard. The symbol ‘/8’ means that the bearing is designed for supporting shafts with a diameter of 8 mm. The letters “CE” indicate that it is an angular bearing with a contact angle of 15°, in ‘high-speed’ version. The ‘HC’ designation informs that the bearing balls are made of silicon nitride ( $\text{Si}_3\text{N}_4$ ), hence it is a hybrid bearing. The symbol ‘P4A’ means that the bearing dimensions are in accordance with the ISO standard with tolerance class 4. Moreover, the running accuracy is better than ISO tolerance class 4.

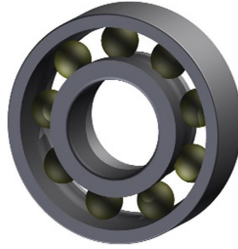


**Fig. 6.** Bearing marked with the 719/8 CE/HCP4A symbol.

The stiffness of the microturbine’s rolling bearings was determined based on the relationships given in paper [16]. These are dependencies determined on the basis of the Hertz theory, and they were verified experimentally. Based on the results of the numerical analyzes carried out, the axial stiffness of both bearings was assumed as 0 N/m, the damping was assumed as 0 Ns/m and the lateral stiffness coefficients are listed in Table 2.

**Table 2.** Stiffness and damping coefficients of ball bearings.

Parameter	Stiffness [N/m]	Damping [Ns/m]
Bearing 1 xx	$3.3 \cdot 10^6$	0
Bearing 1 yy	$3.3 \cdot 10^6$	0
Bearing 2 xx	$3.3 \cdot 10^6$	0
Bearing 2 yy	$3.3 \cdot 10^6$	0

## 4.2 Operating Characteristics of the Rotor with Rolling Bearings

The change of aerodynamic bearings to rolling bearings causes changes in the geometry of the turbogenerator’s rotor (Fig. 7). The parts related to the generator and rotor disk remained unchanged. The changes related to the bearings’ placement include reducing the diameter of the journals from 20 mm to 8 mm. In the case of aerodynamic bearings, it is necessary to use additional keep plates, while the use of rolling bearings requires considering additional elements of their fixing.

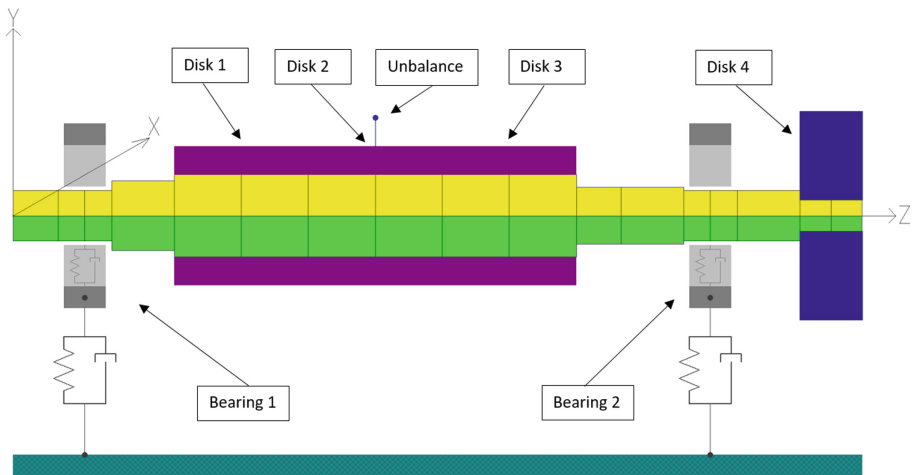
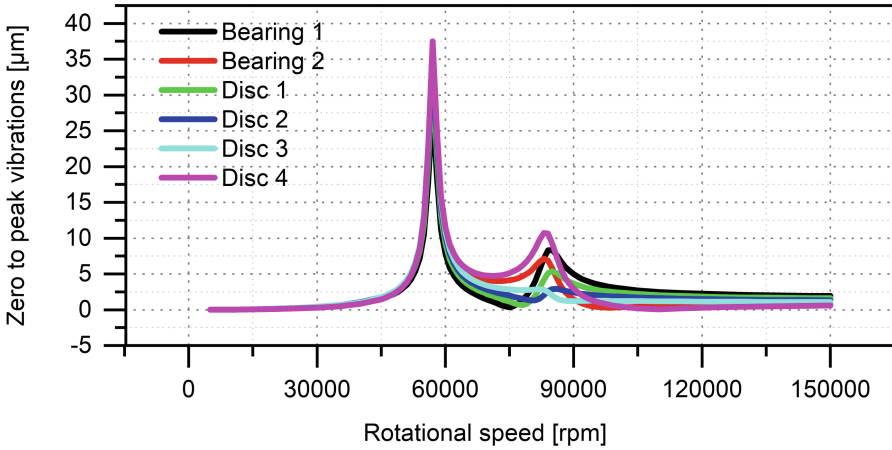


**Fig. 7.** FEM model of the 1 kW turbogenerator's rotor with rolling bearings.

The FEM model of the turbogenerator's rotor supported by rolling bearings is shown in Fig. 7. It differs slightly from the above-described model with aerodynamic bearings. The differences result from the necessity of changing the journal diameters. The model does not include elements needed for fixing the bearings. The unbalance value has been changed because the mass of the turbogenerator's shaft is now different.

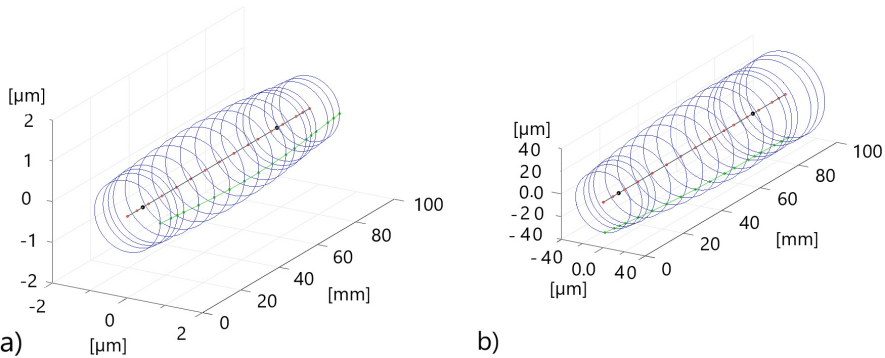
The model of the rotor shaft consists of 17 Timoshenko-type beam elements, with six degrees of freedom in each node. The generator was modeled using three disks located in the sixth, eighth and tenth shaft node. It was assumed that these discs—as well as the entire shaft—are made of steel with a density of  $7,860 \text{ kg/m}^3$ . The rotor disk was made of steel. Given the listed values, the shaft mass is  $0.069 \text{ kg}$  and the weight of the discs is  $0.103 \text{ kg}$ , which gives a total of  $0.172 \text{ kg}$ . The value of the residual unbalance is  $0.172 \text{ g}\cdot\text{mm}$  and was set in accordance with the ISO 1940-1 standard. The shaft is supported by two bearings, placed at nodes with numbers 3 and 14. Both bearings have a diameter of  $8 \text{ mm}$  and a width of  $6 \text{ mm}$ .

Figure 8 presents vibration amplitudes of six shaft nodes as a function of the rotational speed. Two resonant speeds, namely  $57,000 \text{ rpm}$  and  $85,000 \text{ rpm}$ , can be observed in this figure. The maximum vibration amplitudes of the first and second journal are approx.  $37 \text{ }\mu\text{m}$  and were registered at the first resonant speed. What is more, they were the largest vibration amplitudes of the entire rotating system. The maximum displacements of the first and second bearing journal were less than  $10 \text{ }\mu\text{m}$  at the second resonant speed. The figure also shows displacements of all disks. The maximum values of these displacements are almost identical to the maximum displacement values of the bearing journals.



**Fig. 8.** Vibration amplitudes of the rolling bearings’ journals vs. rotational speed.

Figures 9 and 10 depict vibration trajectories of the bearing nodes for the following speeds: 40,000 rpm, 57,000 rpm, 75,000 rpm and 85,000 rpm. These are the speeds corresponding respectively to:



**Fig. 9.** Vibration trajectories of the rotor shaft’s nodes at two rotational speeds: (a) 40,000 rpm, (b) 57,000 rpm.

- operation at a low rotational speed,
- first resonant speed,
- anti-resonant speed,
- second resonant speed.

At a speed of 40,000 rpm, small spherical vibrations, the amplitudes of which do not exceed a value of 2  $\mu\text{m}$ , can be observed. The largest vibration amplitudes occurred in the central part of the rotor. The right-hand side of Fig. 9 presents vibration trajectories obtained at a speed of 57,000 rpm, namely, at the first resonant speed. When

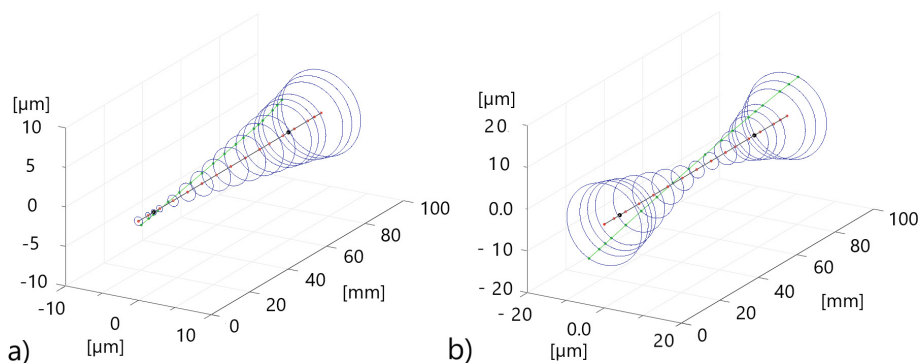


**Fig. 10.** Vibration trajectories of the individual rotor shaft's nodes at two rotational speeds: (a) 75,000 rpm, (b) 85,000 rpm.

the rotor rotates at this speed, the highest vibrations out of all performed analyzes occur. The highest registered peak to peak vibration amplitude is 74  $\mu\text{m}$ . The operation of the rotor under such conditions could be very dangerous and fast crossing through the resonant speed is required.

The left-hand side of Fig. 10 presents vibration trajectories obtained at the anti-resonant speed. This is the speed that occurred between two resonant speeds. The maximum vibration amplitude (approx. 10  $\mu\text{m}$ ) is the highest in the place where the rotor disk is. The right side of Fig. 10 depicts vibration trajectories of individual shaft nodes obtained at a speed of 85,000 rpm. The vibrations of the shaft are of the same shape as classic vibrations of a rigid body. Two ends of the shaft oscillate most (up to 20  $\mu\text{m}$ ), while its center oscillates least.

## 5 Summary and Conclusions

The article presents the results of works related to the selection of the bearing system for the rotor of a 1 kW turbogenerator. Two bearing systems—based on two different types of bearings, namely, on aerodynamic and rolling bearings—has been selected. Due to very demanding operating conditions, among other things, the nominal speed of the rotor is 100,000 rpm (moreover, a failure-free operation up to a speed as high as 120,000 rpm had been assumed) and temperatures can be as high as 130  $^{\circ}\text{C}$ , the bearing system has to be analyzed very thoroughly.

As part of works to select a bearing system, CAD models have been created that take into account different types of bearings used. Created numerical models were used to perform computations (based on the FEM) using in-house developed computer programs from the MESWIR series. These models consist of beam elements with appropriately modeled disks. The unbalance was placed between the bearings with a value adequate to the various analyzed cases. In each analyzed case, the rotor was supported by two bearings with carefully selected geometrical parameters and stiffness

and damping values. The bearings were placed within the turbogenerator's casing, which was modeled as a rigid support.

Due to the non-uniform load of the aerodynamic bearings, the operational performance of the rotor supported on bearings with a diameter of 20 mm, radial clearance of 15  $\mu\text{m}$  and different widths was investigated. In the ultimate variant of the bearing system, a width of 16 mm was assumed for the first bearing (located further away from the rotor disk), and the second bearing had a width of 18 mm. For this system, a lubrication wedge has formed itself already at a speed of 7,000 rpm. It turned out that the maximum values of vibration amplitudes, occurring at speeds in the range of 85,000 rpm–95,000 rpm, did not exceed 2  $\mu\text{m}$ . The results of the conducted analysis bear evidence of a stable operation of the bearings in the whole range of rotational speeds.

The second analyzed variant of the bearing system uses rolling bearings. Based on the design requirements, bearings with the "719/8 CE/HCP4" symbol were selected. These are super-precise angular ceramic bearings, the balls of which are made of silicon nitride, hence hybrid bearings. The stiffness of the bearings was computed and the dynamic properties of the generator's rotor supported by such bearings were analyzed. In the range of the investigated rotational speeds, there are two resonant speeds. The first and second resonant speed is 57,000 rpm and 85,000 rpm, respectively. The maximum vibration amplitude for one of the bearing journals was 74  $\mu\text{m}$  (at a speed of 87,000 rpm). The operation of the rotor supported by rolling bearings seems to be stable and the vibration trajectories of the journals are small. For the time being, it can be said that the nominal speed does not coincide with the resonant speed.

The conducted analyzes show that both aerodynamic gas bearings and rolling bearings are viable solutions for a bearing system. Each of these bearing systems has its advantages and disadvantages. Typically, gas bearings have a longer service life and generate less noise compared to rolling bearings, but they require higher manufacturing accuracy and an additional supply system. In addition to different design features, they have different dynamic properties. Changing the bearing system for a rotor entails a change in its geometry. Different bearings have different stiffness and damping coefficients, which results in a completely different dynamic response of the rotor – bearings system. The investigated rotor with rolling bearings is supercritical (as many rotors found in the literature), which means that the nominal speed is higher than the critical speed and during the run-up of the rotor it is necessary to pass through resonant speeds. The rotor supported by gas bearings is subcritical, which means that resonant speed is higher than the nominal speed. Gas bearings have much better damping properties than rolling bearings. The results of dynamic calculations of the 1 kW ORC turbine show that both investigated bearing systems could be used. Within the framework of the project, two turbines will be manufactured – one with a rotor supported by rolling bearings and the other with a rotor supported by aerodynamic gas bearings.

**Acknowledgments.** This work has been funded by the Polish Agency for Enterprise Development and Smart Growth Operational Programme (European funds) within the project No. POIR.02.03.02-22-0009/15 carried out in cooperation with the SARK company.

## References

1. Kaczmarczyk, T.Z., Żywica, G., Ihnatowicz, E.: The impact of changes in the geometry of a radial microturbine stage on the efficiency of the micro CHP plant based on ORC. *Energy* **137**, 530–543 (2017)
2. Klonowicz, P., Witanowski, Ł., Suchocki, T., Lampart, P.: A turbine based domestic micro ORC system. *Energy Procedia* **129**, 930–993 (2017)
3. Frigo, S., Gabbriellini, R., Puccini, M., Seggiani, M., Vitolo, S.: Small-scale wood-fuelled CHP plants: a comparative evaluation of the available technologies. *Chem. Eng. Trans.* **37**, 847–852 (2014)
4. Peirs, J., Reynaerts, D., Verplaetsen, F.: A microturbine for electric power generation. *Sens. Actuators Phys.* **113**, 86–93 (2004)
5. Hernandez-Carrillo, I., Wood, C.J., Liu, H.: Advanced materials for the impeller in an ORC radial microturbine. *Energy Procedia* **129**, 1047–1054 (2017)
6. Maia, T.A.C., Faria, O.A., Barros, J.E.M., Porto, M.P., Filho, B.J.C., Research, E.P.S.: Test and simulation of an electric generator driven by a micro-turbine. *Electr. Power Syst. Res.* **147**, 224–232 (2017)
7. De Paepe, W., Carrero, M.M., Bram, S., Parente, A., Contino, F.: Experimental characterization of a T100 micro gas turbine converted to full humid air operation. *Energy Procedia* **61**, 2083–2088 (2014)
8. Kaczmarczyk, T.Z., Ihnatowicz, E.: The experimental investigation of scroll expanders operating in the ORC system with HFE7100 as a working medium. *Appl. Mech. Mater.* **831**, 245–255 (2016)
9. Breńkacz, Ł., Żywica, G., Bogulicz, M.: Analysis of dynamical properties of a 700 kW turbine rotor designed to operate in an ORC installation. *Diagnostyka* **17**, 17–23 (2016)
10. Breńkacz, Ł., Żywica, G.: Comparison of experimentally and numerically determined dynamic coefficients of the hydrodynamic slide bearings operating in the nonlinear rotating system. In: *Proceedings of the ASME Turbo Expo2017: Turbomachinery Technical Conference and Exposition*, Charlotte, NC, USA, pp. 1–12 (2017)
11. Breńkacz, Ł., Żywica, G., Drosińska-Komor, M.: The experimental identification of the dynamic coefficients of two hydrodynamic journal bearings operating at constant rotational speed and under nonlinear conditions. *Pol. Marit. Res.* **24**, 108–115 (2017)
12. Kiciński, J.: *Dynamics of rotors and slide bearings* (in Polish). IMP PAN, Maszyny Przepływowe, Gdańsk (2005)
13. Hamrock, B.J., Schmid, S.R., Jacobson, B.O.: *Fundamentals of Fluid Film Lubrication*, 2nd edn. Marcel Dekker, New York (2004)
14. ISO 1940-1 Mechanical vibration - balance quality requirements for rotors in a constant (rigid) state. Part 1: Specification and verification of balance tolerances (2003)
15. SKF Catalogue: *Rolling bearings* (2014)
16. Krzemiński-Freda, H.: *Łożyska toczne*. Państwowe Wydawnictwo Naukowe, Warsaw (1989)





# Experimental and Theoretical Comparison Between the Ball and Pinned Bearing Working as Backup Bearing for Magnetically Levitated Rotors

Cesar Augusto Fonseca<sup>1(✉)</sup>, Hans Ingo Weber<sup>2(✉)</sup>,  
and Ilmar Ferreira Santos<sup>1(✉)</sup>

<sup>1</sup> Department of Mechanical Engineering, Nils Koppel Allé, 404,  
Konges Lyngby, Denmark  
{cefonse, ifs}@mek.dtu.dk  
<sup>2</sup> Pontifical Catholic University,  
Rua Marquês de São Vicente, 225, Rio de Janeiro, RJ, Brazil  
hans@puc-rio.br

**Abstract.** The papers focuses on the modelling and experimental validation the vibro-impact dynamic behaviour of rotors interacting with two types of backup bearings, i.e. one pinned backup bearing with polymeric pins (original contribution to the problem) and another common ball bearing (conventional). The impact forces are modelled using Hunt and Crossley approach. The parameters of the constitutive equation responsible for describing the contact forces are a priori identified in auxiliary tests. The vibro-impact model is built by coupling the nonlinear contact forces with the rotor-bearing system dynamics and the theoretical results are obtained by integrating the coupled equations in time. A fully-instrumented test bench is designed, built and used to validate the experimental results. The effectiveness of the pinned bearing is evaluated in terms of orbits and maximum vibration.

**Keywords:** Backup bearings · Nonlinear dynamics · Impacts

## 1 Introduction

The backup bearings have been a relevant topic of research because they are an essential element in the rotating machines with magnetic bearings, which have been in use for many industrial applications. Nowadays these machines are used mainly as turbines, compressors, pumps, and flywheels. The purpose of the backup bearings is to protect the integrity of the machine, on the occasion of a power loss or any kind of failure, which could lead to harmful impacts on the structure.

The design and study of magnetic bearings can be found in the book of Schweitzer and Maslen [1]. The rotor is levitated either by passive or active

magnets and the shaft is set to spin within a gap in vacuum or low-pressurized air. Before active magnetic bearings became a novelty, earlier investigations in the 1950s already explored the relationship between a rotor and bearing with a clearance. Black [2] was one of the first to deal with the subject of rotors with a clearance. In his modelling the friction force was neglected and it would be treated later in the work of Choy and Padovan [3]. In the work of Jin and Ulbrich [4] the dry friction whip movement of the unbalanced rotor was observed when it collided on the stator and was explained through the multiple-scale method.

The worst-case scenario for a magnetic bearing is a power loss, which makes the rotor to loose the support completely and falls. Therefore rotor drop tests are of immense value. One of the most cited works is from Pradetto [5], in which a one-ton rotor was left to fall and the orbit and forces were sampled. In the work of Ishii and Kirk [6] the transient response of a rotor drop was assessed. Fumagalli [7] replaced the circular clearance wall by a ball bearing and tested for several rotor drops, where the rotor interacts with the inner ring so the rotor slides and tumbles.

The inner shape of the backup bearing plays also an important role on its efficiency and in the dynamics after each impact. Polygonal shapes have been tested by Simon [8] in his doctoral thesis. He compared the geometries with a theoretical approach and mounted a test rig to observe their dynamical responses. Later, a more complex geometry for the backup bearing was considered which contained pins inside the circular wall. One of the first to deal with this problem was Lahriri et al. [9]. They described the mathematical model impacting on a housing in order to extract the forces and validated the model with a test rig. The goal was to set the rotor to perform the backward whirl on a common circular wall and compared with the pinned solution. From the work of Fonseca [18], the bearing with pins has been tested when the rotor is crossing its critical speed. Later in [19], chaotic behaviours of the impacts were analysed observing the impact forces on the pins the different orbit that emerge. Other examples of backup bearings can be found in the work of Ginzinger and Ulbrich [10] with linear actuators and Zülw and Liebich [11], who added small ball bearings to the stator. Its design can be found in the patent [12]. Ma et al. [13] also investigated theoretically the dynamical response of a pinned backup bearing using the finite-element method to characterize the impact phenomenon. The authors also showed the difference between three to four pins in the orbit patterns and performed a frequency analysis, where multiple frequencies were excited.

In this work one is interest in the validation the vibro-impact dynamical model with the observed behaviour performed by a rotor on the test bench at the Technical University of Denmark (DTU), [14]. The tests consist of a slow acceleration of the angular velocity in a sequence of steps until it reaches the rotor's resonance developing high magnitude orbits thus leading to impacts to the backup bearings. Then rotor accelerates until the lateral rotor-stator impacts stop after resonance passage. Two types of backup bearings are proposed to be tested: one with polymeric pins and the other a common ball bearing. A mathematical model is proposed to describe the dynamic interaction between

(a) the rigid rotor and the compliant surface of POM pin and (b) the rigid rotor and the compliant surface of the ball bearing inner ring. Some key parameter of the contact force model are extracted with help of auxiliary tests, as pin on disc friction tests. The contact force model is coupled to the dynamic equations of motion of the rigid rotor and then the equations are integrated numerically in time and compared with the experimental data. Finally, the effectiveness of the pinned bearing is approached regarding the orbits, maximum vibration and the contact forces.

## 2 Modeling the Rotor-Housing Kinematics

Figure 1 exhibits the test rig, where the rotor and its whole structure is assembled. It is a horizontal rotor with a steel disc (b) coupled to a motor (e), which is controlled externally by an embedded control hardware in order to ensure a constant driven velocity. The value of the desired angular velocity is provided either by a remote control (g) or by an acquisition board (h). A passive magnetic bearing (a) is positioned at end of the rotor and provides levitation forces. Close to the coupling, there is a spherical bearing (d) that supports the rotor but lets it to pivot in this position. Then between the disc and the spherical bearing, one finds the casing (f) where the backup bearing is (c). Depending on how loose the gap at this backup bearing is, impacts between the bodies occur at a specific angular velocity as it approaches the resonance frequency. Thanks to the design

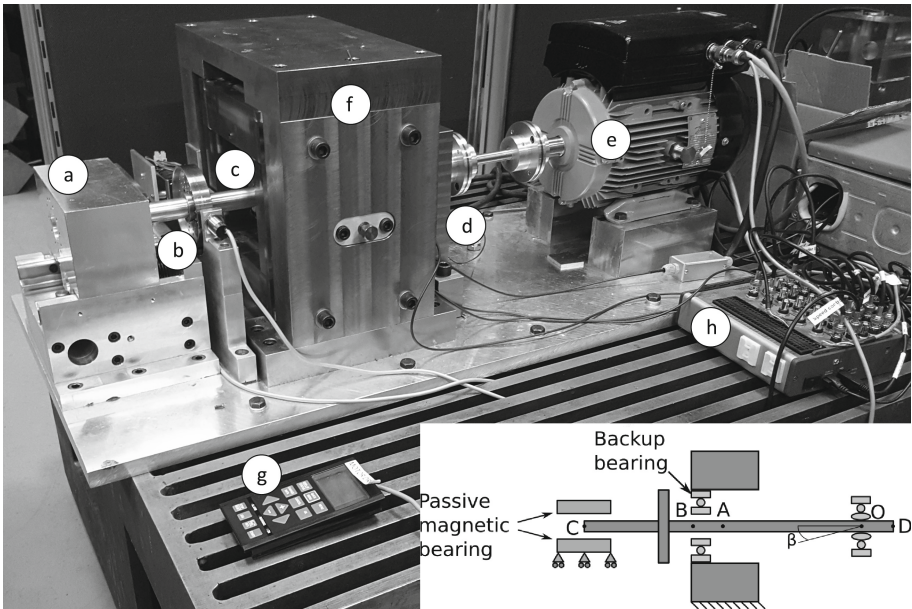


**Fig. 1.** The test rig containing the rotor and the backup bearing.

of the magnetic bearing, it works as a linear spring, creating a single resonance frequency around 10 Hz.

Figures 2a and b show the two types of bearings that are analyzed in the present work. The ball bearing is a SKF 62/28 and the pinned bearing is custom made for the test rig. Each one is tested individually and mounted in the same position.

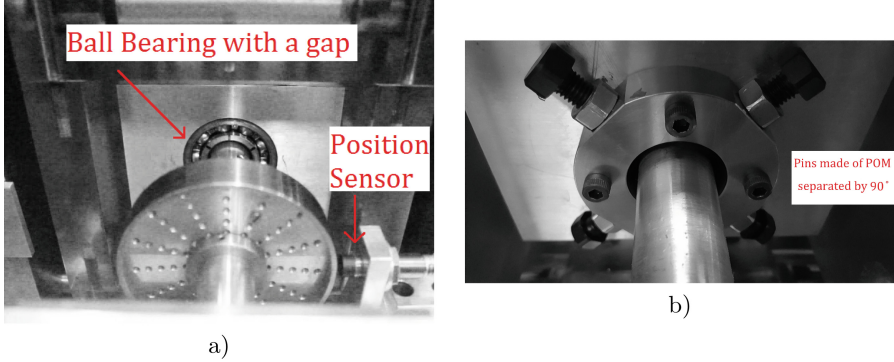


**Fig. 2.** (a) From the point-of-view of the magnetic bearing to the backup bearings. (a) Ball bearing; (b) Pinned bearing.

## 2.1 The Shaft

In Fig. 3, a schematic description of the rotor is presented to reproduce the dynamics of the assembled test rig shown in Fig. 1. The fixed reference frame is positioned where the rotor is supported by one spherical bearing at point  $O$ . The moving reference frames  $B_1$  and  $B_2$  are also positioned at the supporting point of the rotor and correspond to a rotation at the  $x_I$  and  $y_1$ -axes, respectively. Then the rotor turns around the  $z$ -axis which forms the last reference frame  $B_3$ . However, to develop the dynamics of the rotor, it is enough to describe the system from the reference frame  $B_2$ . Thus, the rotor is only allowed to rotate according to the following three angular degrees of freedom:  $\Gamma(t), \beta(t), \theta(t)$ , around the coordinate axes  $x_I, y_1, z_2$ , respectively, whose angular velocities are defined as

$${}_I\dot{\Gamma} = [\dot{\Gamma}(t) \ 0 \ 0]^T, \quad {}_{B_1}\dot{\beta} = [0 \ \dot{\beta}(t) \ 0]^T \text{ and } {}_{B_2}\dot{\theta} = [0 \ 0 \ \dot{\theta}(t)]^T. \quad (1)$$

The backup bearing is mounted at point B and the passive magnetic bearing is at point C. The rotor is modelled as a rigid body and external forces from the magnets, gravity, imbalance and coupling are applied at points C, A, E and D respectively.

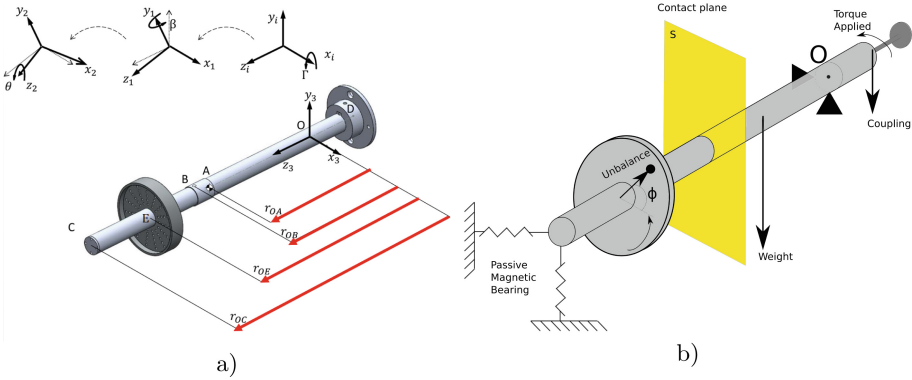


**Fig. 3.** Representation of the reference systems of the shaft in (a) and a schematic of the forces acting on the rotor in (b).

Then the rotational matrices  ${}^I T_\Gamma$ ,  ${}_{B1} T_\beta$  and  ${}_{B2} T_\theta$  are defined as

$$\begin{aligned}
 {}^I \mathbf{T}_\Gamma &= \begin{bmatrix} 1 & 0 & 0 \\ 0 & \cos \Gamma(t) & \sin \Gamma(t) \\ 0 & -\sin \Gamma(t) & \cos \Gamma(t) \end{bmatrix}, & {}_{B1} \mathbf{T}_\beta &= \begin{bmatrix} \cos \beta(t) & 0 & -\sin \beta(t) \\ 0 & 1 & 0 \\ \sin \beta(t) & 0 & \cos \beta(t) \end{bmatrix}, \\
 {}_{B2} \mathbf{T}_\theta &= \begin{bmatrix} \cos \theta(t) & \sin \theta(t) & 0 \\ -\sin \theta(t) & \cos \theta(t) & 0 \\ 0 & 0 & 1 \end{bmatrix}. & & (2)
 \end{aligned}$$

The inertia tensor referred to the supporting point is

$${}_{B2} \mathbf{I}_O = \begin{bmatrix} I_{xx} & 0 & 0 \\ 0 & I_{yy} & 0 \\ 0 & 0 & I_{zz} \end{bmatrix}. \quad (3)$$

The absolute angular velocity represented in the coordinates of the moving reference frame B2 is given by

$${}_{B2} \boldsymbol{\Omega} = {}_{B2} \dot{\Gamma} + {}_{B2} \dot{\beta} = \begin{bmatrix} \dot{\Gamma} \cos \beta \\ \dot{\beta} \\ \dot{\Gamma} \sin \beta \end{bmatrix}, \quad (4)$$

whereas the absolute reference frame velocity is

$${}_{B2} \boldsymbol{\omega} = {}_{B2} \boldsymbol{\Omega} + {}_{B2} \dot{\theta} = \begin{bmatrix} \dot{\Gamma} \cos \beta \\ \dot{\beta} \\ \dot{\Gamma} \sin \beta + \dot{\theta} \end{bmatrix}. \quad (5)$$

The absolute acceleration in ref. frame B2 is written as:

$${}_{B2} \dot{\boldsymbol{\omega}} = \begin{bmatrix} \ddot{\Gamma} \cos \beta - \dot{\Gamma} \dot{\beta} \sin \beta \\ \ddot{\beta} \\ \ddot{\Gamma} \sin \beta + \dot{\Gamma} \dot{\beta} \cos \beta + \ddot{\theta} \end{bmatrix}. \quad (6)$$

In the present case, the angular acceleration with respect to the  $z$ -axis,  $\ddot{\theta}$  is zero. Any change in velocity is considered instantaneous.

The determination of the equations of motion comes from the Euler formulation.

$$\sum B_2 \mathbf{M} \text{Moments}_0 = B_2 \mathbf{I}_O \cdot B_2 \dot{\boldsymbol{\omega}} + B_2 \boldsymbol{\Omega} \times (B_2 \mathbf{I}_O \cdot B_2 \dot{\boldsymbol{\omega}}). \quad (7)$$

The equations are:

$$\sum B_2 \mathbf{M}_0 = \begin{bmatrix} I_{xx} \left( \ddot{I} \cos \beta - \dot{\beta} \dot{I} \sin \beta \right) + (I_{zz} - I_{yy}) \dot{I} \dot{\beta} \sin \beta + I_{zz} \dot{\beta} \dot{\theta} \\ I_{yy} \ddot{\beta} + (I_{xx} - I_{zz}) \dot{I}^2 \sin \beta \cos \beta - I_{zz} \dot{I} \dot{\theta} \cos \beta \\ I_{zz} \left( \dot{\beta} \dot{I} \cos \beta + \ddot{I} \sin \beta \right) + (I_{yy} - I_{xx}) \dot{I} \dot{\beta} \cos \beta \end{bmatrix}. \quad (8)$$

The forces applied to the rotor are the magnetic  $\mathbf{F}_{Mag}$ , the damping force  $\mathbf{F}_D$ , the unbalance force  $\mathbf{F}_u$  and the contact forces  $\mathbf{F}_N$ ,  $\mathbf{F}_{fric}$ , the shaft's weight  $\mathbf{P}$ , and finally a vertical coupling force,  $\mathbf{F}_{coupl}$ , which necessary for the equilibrium position and written as:

$$B_2 \mathbf{F}_u = \begin{bmatrix} m_u \varepsilon \dot{\theta}^2 \cos(\dot{\theta}t + \phi) \\ m_u \varepsilon \dot{\theta}^2 \sin(\dot{\theta}t + \phi) \\ 0 \end{bmatrix}, \quad {}_I \mathbf{P} = \begin{bmatrix} 0 \\ -mg \\ 0 \end{bmatrix}, \quad {}_I \mathbf{F}_N = \begin{bmatrix} N \cos \alpha \\ N \sin \alpha \\ 0 \end{bmatrix}, \quad (9)$$

$${}_I \mathbf{F}_{fric} = \begin{bmatrix} \mu N \sin \alpha \\ -\mu N \cos \alpha \\ 0 \end{bmatrix}, \quad {}_I \mathbf{F}_{Mag} = \begin{bmatrix} K \cos \xi \\ K \sin \xi \\ 0 \end{bmatrix}, \quad {}_I \mathbf{F}_D = \begin{bmatrix} c \cos \rho \\ c \sin \rho \\ 0 \end{bmatrix}, \quad {}_I \mathbf{F}_{coupl} = \begin{bmatrix} 0 \\ -F_{coupl} \\ 0 \end{bmatrix}, \quad (10)$$

where the two angles  $\xi$  and  $\rho$  are defined as such;  $\xi$  is the angle of the displacement of the rotor to the origin in the fixed reference frame and  $\rho$  is the angle of the velocity of the rotor to the origin in the fixed reference frame. At the contact on the backup bearing the angle of contact is designated as  $\alpha$ . A diagram in Fig. 4 illustrates the role of each mentioned angles. Each force is applied at the points, whose vectors are as follows:

$$B_2 \mathbf{r}_{OA} = \begin{bmatrix} 0 \\ 0 \\ l_A \end{bmatrix}, \quad B_2 \mathbf{r}_{OB} = \begin{bmatrix} 0 \\ 0 \\ l_Q \end{bmatrix}, \quad B_2 \mathbf{r}_{OC} = \begin{bmatrix} x_B \\ y_B \\ l_S \end{bmatrix}, \quad B_2 \mathbf{r}_{OD} = \begin{bmatrix} 0 \\ 0 \\ -l_D \end{bmatrix}, \quad B_2 \mathbf{r}_{OE} = \begin{bmatrix} 0 \\ 0 \\ l_E \end{bmatrix}. \quad (11)$$

Finally, a torque from the motor is given as  $\mathbf{T} = [0 \ 0 \ T]^T$ . But the value of  $T$  is unimportant in the present analysis, because it is supposed that the torque is ideally supplied by the motor to keep the angular velocity  $\dot{\theta}$  constant. Therefore the expression of the sum of the moments is

$$\sum B_2 \mathbf{M}_0 = B_2 \left( \mathbf{r}_{OA} \times \mathbf{P} + \mathbf{r}_{OC} \times \mathbf{F}_{Mag} + \mathbf{r}_{OC} \times \mathbf{F}_D + \mathbf{r}_{OB} \times \mathbf{F}_N + \mathbf{r}_{OB} \times \mathbf{F}_{fric} + \mathbf{r}_{OE} \times \mathbf{F}_u + \mathbf{r}_{OD} \times \mathbf{F}_{coupl} + \mathbf{T} \right). \quad (12)$$

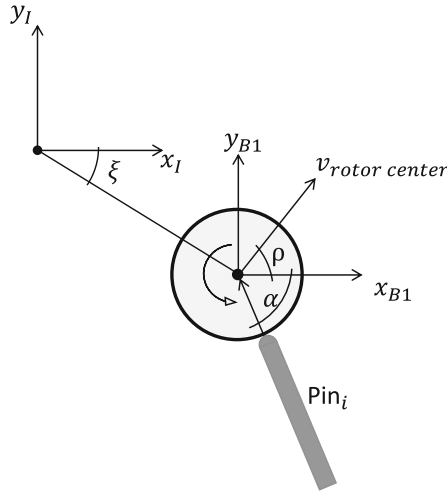


Fig. 4. Diagram of the rotor displaced from the origin and impacting on a pin.

### 2.2 Contact Criteria and Housing Dynamics

The contact on the backup bearing is responsible for a so strong interaction between the bodies in a way that it is not possible to be represented by linear models. Moreover, the impact force influences the dynamics of the structure that holds the backup bearing. This means its equations of motion have to be included in the mechanical system. Two housings holding the backup bearing are built in a manner that each one moves in a different direction, *i.e.* the inner house moves vertically and the outer house horizontally. Between them there are force transducers that are modelled as spring elements. A sketch of the inner and outer houses and the four force transducers is shown in Fig. 5. Sliding beams provide the damping effect and the restriction of coupled movements. The equations of motion are written as:

$$m_{ih}\ddot{y}_{ih} = -2k_{ft}y_{ih} - 2c_v y_{ih} - m_{ih}g + N \sin \alpha + \mu N \cos \alpha \quad (13)$$

$$(M_{oh} + m_{ih})\ddot{x}_{oh} = -2k_{ft}x_{oh} - 2c_h x_{oh} + N \cos \alpha - \mu N \sin \alpha. \quad (14)$$

For the impact to happen, the shaft centre has to cross a boundary surface, otherwise the normal force is nonexistent,  $N = 0$ . The two types of backup bearings have different geometries implying two rules for the threshold surface. The ball bearing is the easiest to define since it is a round surface too and yet it is a moving wall. So, whenever the shaft centre,  $r$ , at the plane  $S$  of backup bearing is at a distance greater than the nominal gap,  $r_0$ , an impact state is in place.

$$r_{ir} - r_s = r_0, \text{ or the gap} \quad (15)$$

$$r > r_0, \rightarrow \text{in contact,} \quad (16)$$

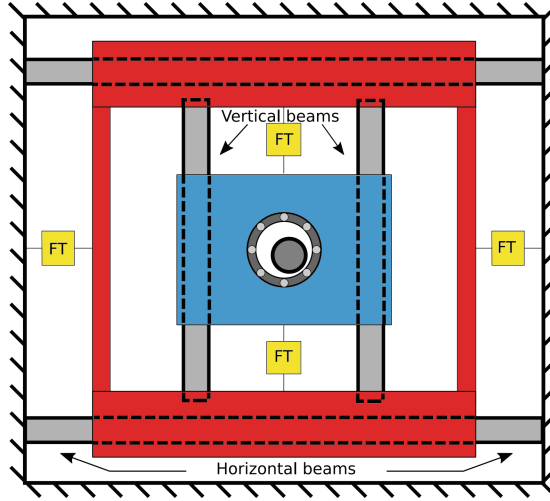


**Fig. 5.** Inner housings (blue), the outer housing (red) and the four force transducers (yellow).

where  $r_{ir}$  is the inner radius of the inner ring and  $r_s$  the radius of the shaft. The tangential velocity at the contact point is also relevant, because the friction force is exerted against the relative velocity between the edge of the shaft and the inner ring of the ball bearing.

Therefore we should include another degree of freedom to the mechanical system, namely, the acceleration of the bearing's inner ring:

$$I_{eq}\ddot{\theta}_{ir} = |_{B2}\mathbf{r}_s \times_{B2} \mathbf{F}_{\text{fric}}| - c_{ir}\dot{\theta}_{ir}, \quad (17)$$

where  $c_{ir}$  is a damping coefficient exclusive for the bearing that comes from the friction with the spheres. The other elements of the ball bearing, namely the spheres and the outer ring, and their interactions have not been included in the model, since the bearing mounted in the current test rig is thought to have few influence of them upon the overall dynamics of the test rig. Besides, by including the dynamics of each sphere and its interactions would consume too much computational time for the desired numerical result. However, the polar inertia parameter of Eq. 17 includes the inertia from the ring and the equivalent of the spheres.

The model of the contact is the one proposed by Hunt and Crossley [15]. This expression has been applied to model the impact between rotors and the inner ring in the works of references [16, 17]:

$$N = k_{\text{imp}}\delta^n \left(1 + 1.5\eta\dot{\delta}\right). \quad (18)$$

The term  $\eta$  represents the damping contribution of the impact. This damping depends not only on the velocity of the deformation but also on the deformation



itself, so with it one avoids the hysteresis effects or numerical errors. The value of this parameter was determined experimentally and will be commented later in this work. The term  $\eta$  is also correlated to the coefficient of restitution  $c_e$  and the initial velocity of contact as follows:

$$c_e = 1 - \eta \dot{\delta}^- \tag{19}$$

The pinned backup bearing simplifies the mechanical system, because the walls are not rotating, yet it makes the geometry of contact more complicated.

The formulae for the aperture  $\delta$  necessary for Eq. (18) are written as:

$$\delta = \sqrt{(X - x_{oh})^2 + (Y - y_{ih})^2} - r_0, \tag{20}$$

for the ball bearing and for the pinned one, from the center of shaft to the tip of the Pin  $i$

$$\delta \cong |(X - x_{oh}, Y - y_{ih}) - \text{Pin}_i|. \tag{21}$$

Figure 6 demonstrates geometrically the meaning of the penetration for the pinned case, where  $\mathbf{r}_{\text{pin}}$  is the position of the tip of a pin in relation to the moving housing.

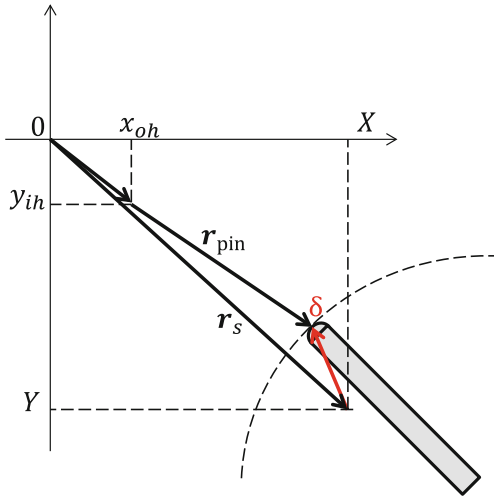


**Fig. 6.** Deformation  $\delta$  shown for the pinned case. The  $\text{Pin}_i$  is represented by the shaded area.

Here  $X$  and  $Y$  are the displacement of the centre of the shaft at the contact plane  $S$ , given by

$$\begin{bmatrix} X \\ Y \\ Z \end{bmatrix} = {}_I\mathbf{T}_\Gamma^T {}_B\mathbf{l}_\beta^T \begin{bmatrix} 0 \\ 0 \\ l_s \end{bmatrix}. \tag{22}$$

### 3 Parameters of the Test Rig

The parameters of the test rig are detailed in the Table 1 and having them correctly measured will ensure that the numerical integration gives appropriate results when compared to the experiments. Another important point is to find an adequate length of the pin so the gaps can be comparable with the ball bearing. This length has been determined to match the point that the rotor will not touch the structure between two consecutive pins, observe the dashed line creating the astroid function in Fig. 8, see [18]. However, some key parameters require have to be determined in a separate manner. It is necessary to estimate the coefficients from the compliance model in Eq. 18 as precise as possible, because this is the main source of nonlinearity of the current problem. Most important are the elastic coefficient  $k_{imp}$  and the coefficient of restitution  $c_e$ . Those parameters could be determined by letting the rotor drop on the surface of the inner ring of the ball bearing. The sampled data during the fall of the rotor is used by a Nonlinear Least Squares algorithm to find the averaged values of these parameters as well as their uncertainty levels.

For the pinned bearing, the elastic coefficient was considered as a cylinder-on-sphere contact type. Moreover, in Fonseca et. al [20] the value of the friction coefficient between the polymer and the aluminium has been estimated by a series of test runs where a sample of POM was positioned on a gyratory platform. The relationship between the applied force and the counter torque given by the platform defines the value of the friction.

With the correct estimation of the geometric and material parameters of the test rig and the ones belonging to the compliance model of the impact one can integrate numerically the equations of motion in time. The complete model is integrated using the function *ode45* supplied by the Matlab programming environment with an event function to ensure that the nonlinearity of impacts is correctly reproduced.

**Table 1.** Specifications of the parts of the test rig.

Shaft		Inner and outer house	
Mass without unbalance	1.28 kg	Mass from inner house	1.70 kg
Length to magnetic bearing	384 mm	Mass from outer housing	8.87 kg
Length to rolling bearing	211 mm	Force sensor	
Shaft diameter	25 mm	Force transducer stiffness	83 MPa
Rolling bearing		Pins	
Inner diameter	28 mm	Total length of the pins	1.0 mm
Inner race outer diameter	32 mm	Radius of the pins	4.0 mm
Sphere radius	5.0 mm	Radius of the circular wall	38 mm

### 4 Crossing the Natural Frequency. Experiments and Theoretical Results

As mentioned before a dedicated control guarantees the desired angular speed and gives sufficient power to the motor in order to maintain a constant speed regardless of any disturbance or impacts. Nevertheless, an encoder behind the motor gives the true angular velocity and its signal is captured and so the steadiness of the angular velocity is observed on time. The angular velocity increased step-wise from 0–20 Hz. Every step lasts 10 seconds and added 0.5 Hz to the previous one. The simulation program had the same velocity profile, but now it is given as an input function.

In Fig. 7, the maximal radial displacement of the centre of the shaft is plotted after the transient phase for both types of backup bearings. After the resonance is crossed around 10.0 Hz the shaft remains in contact with the backup bearing. In a linear model without impacts, the orbits' magnitude should decrease and the shaft should be away from the contact area. The mechanical barrier of the safety bearing creates a stiffening effect and the rotor is able to return to a safer orbit only at a much higher angular velocity than predicted by the simple linear case. Both types of backup bearing presented a similar behaviour, when the radial position drops sharply after 16.0 Hz for the ball bearing and 14.0 Hz for the pinned case. The results from the numerical integration reproduced the same experimental pattern qualitatively.

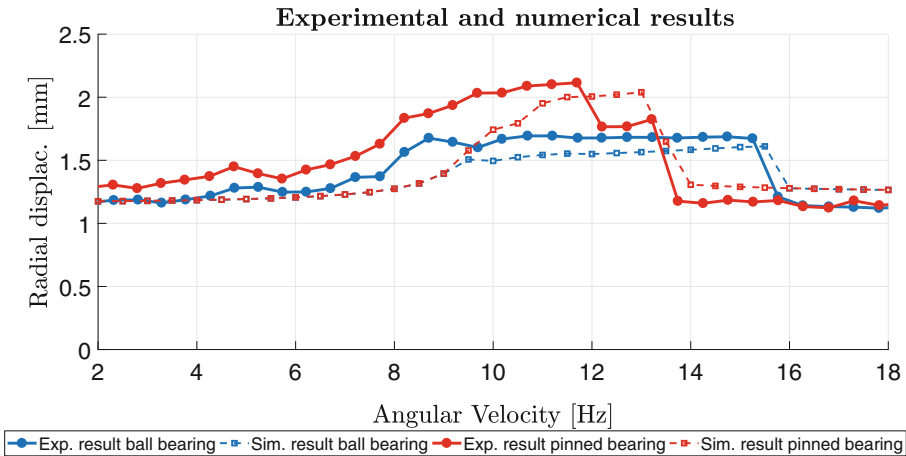


**Fig. 7.** Maximum displacement of the center of the shaft for ball bearing and the pinned one.

To reinforce the validity of the model, some orbits were selected for comparison. They are shown in Fig. 8. All velocities are above the resonance. On the top one sees the experimental data and numerical results for the ball bearing. One

observes that the patterns are similar. The rotor hits the lower half of the inner ring of the bearing in one point and changes for a clear two point orbit. Later, at 14.5 Hz, the orbit changes again and assumes an almost vertical trajectory. These results are equally reproduced by the simulation.

In the same Fig. 8, but below, the same comparison is done for the pinned bearing. Now, instead of a circular gap, the region defined by the pins is plotted as an astroid function. Initially the rotor does an erratic trajectory impacting on multiple pins, but later it performs a diagonal movement hitting on a single pin. This change explains the sudden fall in Fig. 7 at 12 Hz before the definitive one at 14.5 Hz. The diagonal orbit appears only at one case at 14 Hz. The last value velocity to show impacts remains the same, yet.

It is important to highlight that there are some discrepancies between the numerical solution with the observed data. The nonlinear parameters of the compliance model were determined by the signals of force transducers mounted between the housings and the proximity sensors close to the shaft, but slightly away of the backup bearing. Besides, the rotor should bend and vibrate during and after the impact, but it is modelled as a rigid body and these phenomena are not reproduced by the simulation. Therefore some deviations of the overall dynamical behaviour are expected to occur and, for both types of backup bearing, the magnitude of the orbits are lower than the ones observed experimentally.

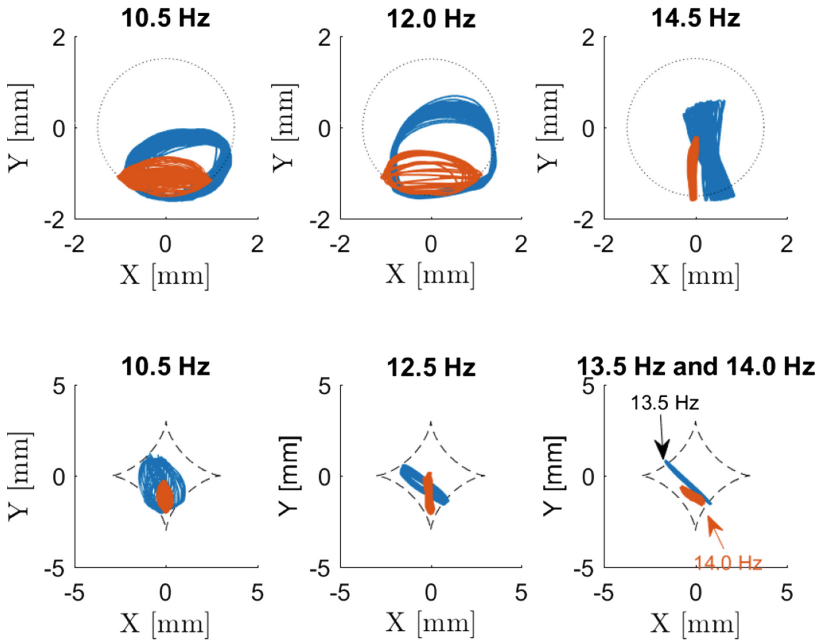


**Fig. 8.** Comparison between orbits, experimental in blue and theoretical in red. On the top for the ball bearing and below for the pinned bearing case.

### 4.1 Unbalance Influence on the Ball Bearing Case

When the unbalance becomes high it starts to influence not only on the magnitude of the orbit, but also on the nature of the nonlinear dynamics created by the impact on the backup bearing. The change can be so intense that the rotor no longer removes itself from the impacting orbit, at least between 0–20 Hz. Therefore, in order to address this issue, another set of experiments is executed. The rotor is kept spinning at a constant speed of 10 Hz and the magnetic forces are removed, so a full failure of a magnetic bearing is replicated by the test rig. Consequently, the rotor is initially in contact with its backup bearing. Now, there is only one type of backup bearing, namely the ball bearing and only the unbalance changes in this set-up.

Doing so, the dynamical analysis to be conducted is different than before. When the rotor crosses the vertical axis of round gap, the state space of the variables are sampled and saved. This is done for different levels of unbalance. The result can be seen in Fig. 9, where the blue dots represent the numerical outcome for several values of unbalance and the red ones represent the observed experimental results. The unbalance was included to the rotor by adding an extra piece to the disk of the rotor.

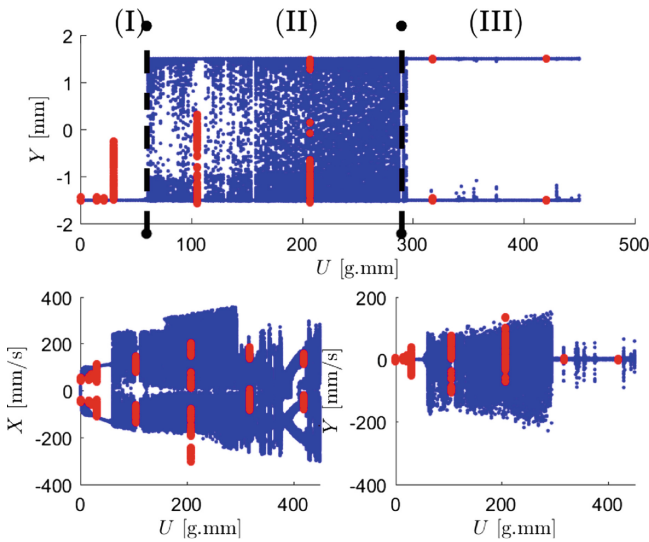


**Fig. 9.** Bifurcation diagrams where the unbalance is the control parameter. Top: Y position; below left: velocity horizontal component; below right; velocity vertical component.

The bifurcation diagrams show that there are three distinct dynamical behaviours. The first one (I) means that the rotor is always in contact at the bottom of the backup bearing and is executing an oscillatory movement. It remains

doing so until a certain threshold, around (60 gmm), from now on the rotor crosses the vertical axis through a different point each time. This second stage (II) is a clear representation of chaotic characteristics performed by the rotor. The reason is that the unbalance is strong enough to remove the rotor from the contact with the inner ring of the backup bearing and the shaft making colliding forces again on the other side. It means that the rotor will experience high impact forces. Experimentally, the rotor has achieved the second dynamical stage earlier than the numerical model and this can be explained due to the imprecision on determining the correct values of the nonlinear contact parameters. However, by given an even further increasing on the value of the unbalance, the rotor reaches a third behaviour (III). Now the rotor executes a full forward whirl throughout the surface of the bearing. It is seen on the bifurcation diagram on the top that the shaft is crossing the vertical axis in two points only, below and above. Since the rotor is always in contact the magnitude of the forces of interaction between the two bodies is relatively low. To better illustrate these three patterns, Fig. 10 exhibits the different trajectories for the three levels of unbalance performed by the rotor.

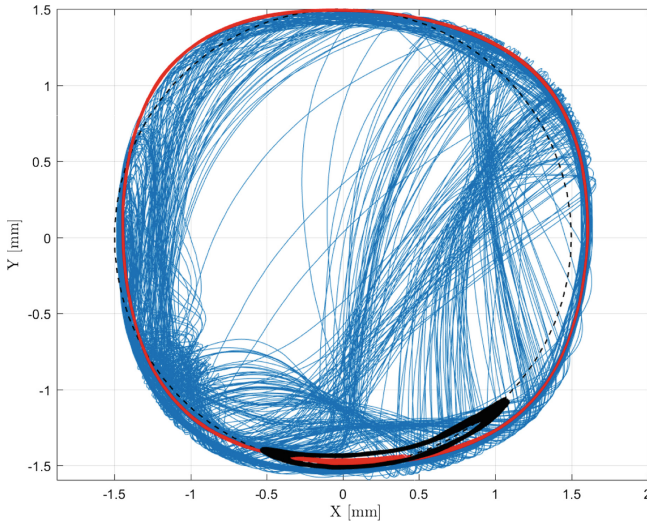


**Fig. 10.** Experimental orbits for the different dynamics. In black oscillatory behaviour (I), in blue the chaotic one (II), and the forward whirl one (III) with high unbalance in red.

## 5 Conclusion

This paper brings results for the behaviour of a rotor system supported by a magnetic bearing when a safety bearing is present to avoid critical behaviour.

Experiments validate the numerical model that now can be used for other conditions and parameters. Two particular situations that can become critical are chosen: in the first, the rotor spins up crossing the critical speed and due to some reason amplitudes exceed the limit, making the backup system to work. This situation was used to compare two types of backup bearings, namely the ball bearing and the pinned bearing. In the second, the influence of the increase in the unbalance on the dynamic behaviour of the rotor system when a backup bearing consists in a ball bearing is investigated.

Results for the first case: The ball bearing and the pinned bearing showed that although the critical speed was surpassed, the rotor remained impacting on the inner surface of the backup bearings. The pinned bearing had a better performance since it could return to a safer orbit about 2 Hz before.

Results for the second case show that the unbalance can change how the rotor interacts with the ball bearing as backup bearing if a full failure of the magnetic bearing happens. Three different dynamical patterns were identified: an oscillatory one for low unbalance, a chaotic one for intermediary unbalance, and a forward whirl always in contact for higher unbalances.

To attest even more the efficiency of the presence of pins for backup bearings one can further investigate different materials to manufacture them and later compare. Also, a better test rig to observe the deformation of the pin when in contact may improve the reliability of the parameters that constitute the compliance models.

A bearing that contains pins instead of a common ball bearing has an easier maintenance, because any damage on them can be solved by a simple replacement procedure. Thus the rotating machine does not have to be unmounted to perform a replacement of the whole backup bearing and the idle time of the machine is reduced.

## References

1. Schweitzer, G., Maslen, E.H.: *Magnetic Bearings Theory, Design, and Application to Rotating Machinery*, 1st edn. Springer, Heidelberg (2009)
2. Black, H.F.: Interaction of a whirling rotor with a vibrating stator across a clearance annulus. *Arch. J. Mech. Eng. Sci.* 1959–1982 (vols 1–23) **10**(1), 1–12 (1968)
3. Choy, F.K., Padovan, J.: Non-linear transient analysis of rotor-casing rub events. *J. Sound Vib.* **113**, 529–545 (1987)
4. Jiang, J., Ulbrich, H.: The physical reason and the analytical condition for the onset of dry whip in rotor-to-stator contact systems. *J. Vib. Acoust.* **6**(127), 594 (2005)
5. Pradetto, J.C., Schmied, J.: Behaviour of a one ton rotor being dropped into auxiliary bearings. In: *Proceedings of the 3rd International Symposium on Magnetic Bearings*, pp. 145–156 (1992)
6. Ishii, T., Kirk, R.G.: Transient response technique applied to active magnetic bearing machinery during rotor drop. *J. Vib. Acoust.* **118**, 154–163 (1996)
7. Fumagalli, M.A.: Modelling and measurement analysis of the contact interaction between a high speed rotor and its stator. Ph.D. thesis number 12509. ETH - Swiss Institute Of Technology Zurich (1997)

8. Simon, U.: Rotor-Stator-Kontakt in polygonförmigen Fanglagern, Von der Gemeinsamen Fakultät für Maschinenbau und Elektrotechnik der Technischen Universität Carolo Wilhelmina zu Braunschweig (2001)
9. Lahiri, S., Santos, I.F., Weber, H.I., Hartmann, H.: On the nonlinear dynamics of two types of backup bearings theoretical and experimental aspects. *J. Eng. Gas Turbines Power* **134**(11), 805–818 (2012)
10. Ginzing, L., Heckmann, B., Ulbrich, H.: Feedback control to prevent damage by rotor rubbing after an impact load, Proceedings of the ASME Turbo Expo, vol. 6, pp. 1003-1012 (2009)
11. Zülöw, D., Liebich, R.: Ein Aussenrollenlager als Fanglagerkonzept für magnetgelagerte Rotoren, SIRM 8. Internationale Tagung Schwingungen in rotierenden Maschinen, Wien, Austria, paper-ID 11 (2009)
12. Schubert, G., Walter, H., Zülöw, D.: Safety bearing for retaining a rotor shaft of a machine. US Patent 8786152 B2, 22 July 2014
13. Ma, H., Zhao, Q., Zhao, X., Han, Q., Wen, B.: Dynamic characteristics analysis of a rotor-stator system under different rubbing forms. *Appl. Math. Model.* **39**(8), 2392–2408 (2015)
14. Augusto, C., da Fonseca, L.L.: A theoretical-experimental study of backup bearings. The pinned vs ball bearing. Ph.D. thesis No. S228. Technical University of Denmark (2017)
15. Hunt, K.H., Crossley, F.R.E.: Coefficient Of restitution interpreted as damping in vibroimpact. *J. Appl. Mech. Trans. ASME* **42**(2), 440–445 (1975)
16. Halminen, O., Kärkkäinen, A., Sopanen, J., Mikkola, A.: Active magnetic bearing-supported rotor with misaligned cageless backup bearings: a dropdown event simulation model. *Mech. Syst. Signal Process.* **50–51**, 692–705 (2015)
17. Kärkkäinen, A., Sopanen, J., Mikkola, A.: Dynamic simulation of a flexible rotor during drop on retainer bearings. *J. Sound Vib.* **306**(3–5), 601–617 (2007)
18. Fonseca, C.A., Weber, H.I., Fleischer, P., Santos, I.F.: Analyzing the use of pins in safety bearings. *J. Braz. Soc. Mech. Sci. Eng.* **37**(4), 1425–1434 (2014)
19. Fonseca, C.A., Aguiar, R., Weber, H.I.: On the non-linear behaviour and orbit patterns of rotor/stator contact with a non-conventional containment bearing. *Int. J. Mech. Sci.* **105**, 117–125 (2015)
20. Fonseca, C.A., Santos, I.F., Weber, H.I.: Experimental comparison of the nonlinear dynamic behavior of a rigid rotor interacting with two types of different radial backup bearings: ball & pinned. *Tribol. Int.* **119**, 250–261 (2017)





# Stochastic Analysis of Asymmetric Tilting-Pad Journal Bearings

Heitor Antonio Pereira da Silva<sup>(✉)</sup> and Rodrigo Nicoletti<sup>(✉)</sup>

Sao Carlos School of Engineering, University of Sao Paulo,  
Trabalhador Sao-Carlense 400, Sao Carlos, SP 13566-590, Brazil  
heitorantonio@usp.br, rnicolet@sc.usp.br  
<http://www2.eesc.usp.br/labdin/rodrigo.en>

**Abstract.** Tilting-pad journal bearings (TPJBs) are symmetric from design. However, the machining and assembling tolerances of a TPJB can result in asymmetries of the pad position that strongly affect the final dynamic characteristics of the system. In this work, a numerical study is devised to analyze the stiffness and damping coefficients of an asymmetric TPJB with load-on-pad (LOP), evaluated by a thermo-hydrodynamic (THD) model for a wide range of Sommerfeld numbers. The uncertainty in the TPJB geometry is included in the model by varying the nominal bearing gap (assembled clearance) according to a distribution ruled by the Monte Carlo Method. The results show that, in most of the cases, the asymmetry represents a detrimental effect on the bearing characteristics. However, there are some cases where the asymmetry of the TPJB is beneficial, resulting in higher stiffness and damping than expected from designing a symmetric bearing.

**Keywords:** Lubricated bearing · Tilting-pad bearing · Uncertainty Thermo-hydrodynamic model · Monte Carlo simulation

## 1 Introduction

Tilting-pad journal bearings have been thoroughly investigated in the last 50 years and, consequently, their industrial application is established and mature [1]. Hence, much effort has been done to find the optimum geometry of such bearings aiming at achieving higher stiffness and damping levels for the rotating machine. However, it was only in the last few years that uncertainties called the attention of Engineers and Researchers. In this case, the tolerances adopted during bearing machining and those adopted during bearing assembling could result in a tilting-pad journal bearing with a geometry different from that originally designed. Consequently, the final bearing would present dynamic characteristics (stiffness and damping) significantly different from those nominally expected.

According to [2], the machining tolerances of the bearing pads can be of the same order of the clearance between the shaft and the bearing. In this case,

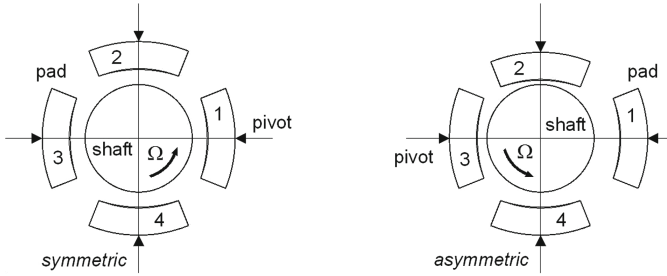


**Fig. 1.** Tilting-pad journal bearing with symmetric and asymmetric geometries (load-on-pad configuration).

important parameters of the bearing can be affected, such as the bearing clearance and the bearing pre-load, leading to an asymmetric configuration of the bearing (Fig. 1) where each pad is in a radial position different from that of the other pads. The observed consequences of such asymmetry of the bearing are: higher cross-coupling stiffness due to changes in the unloaded pads [3]; variation of direct stiffness and damping coefficients due to variations of the loaded pad geometry [3]; increase of standard deviation of the stiffness and damping coefficients, however keeping the average value near the nominal value [4].

This last observation explains why tilting-pad journal bearings have been applied successfully for such a long time without further investigation into their asymmetry (the production batch keeps the dynamic characteristics of the bearing at the average). However, individually, the variation can be high. For this reason, literature started to study the effects of such geometry asymmetry by stochastic analyses, focusing on the effects of dimensional variability. Despite the recent progress in such investigation, there are still design issues to be addressed, such as: what kind of asymmetry worsens the dynamic characteristics of a tilting-pad bearing? And, more importantly, are there asymmetric geometries that improve the dynamic characteristics of the tilting-pad bearings? Such questions motivate the present work. Here, we focus on the specific case of tilting-pad bearings with four pads under load-on-pad configuration (Fig. 1).

## 2 Mathematical Model

In this work, a numerical study is devised to analyze the stiffness and damping coefficients of an asymmetric tilting-pad journal bearing (TPJB) with load-on-pad (LOP) configuration, evaluated by a thermo-hydrodynamic (THD) model of the bearing. The uncertainty in the TPJB geometry is included in the model by varying the nominal bearing gap (assembled clearance) according to a distribution ruled by the Monte Carlo Method.

The THD model used to calculate the equivalent stiffness and damping coefficients of the rotor-bearing system is depicted schematically in the block

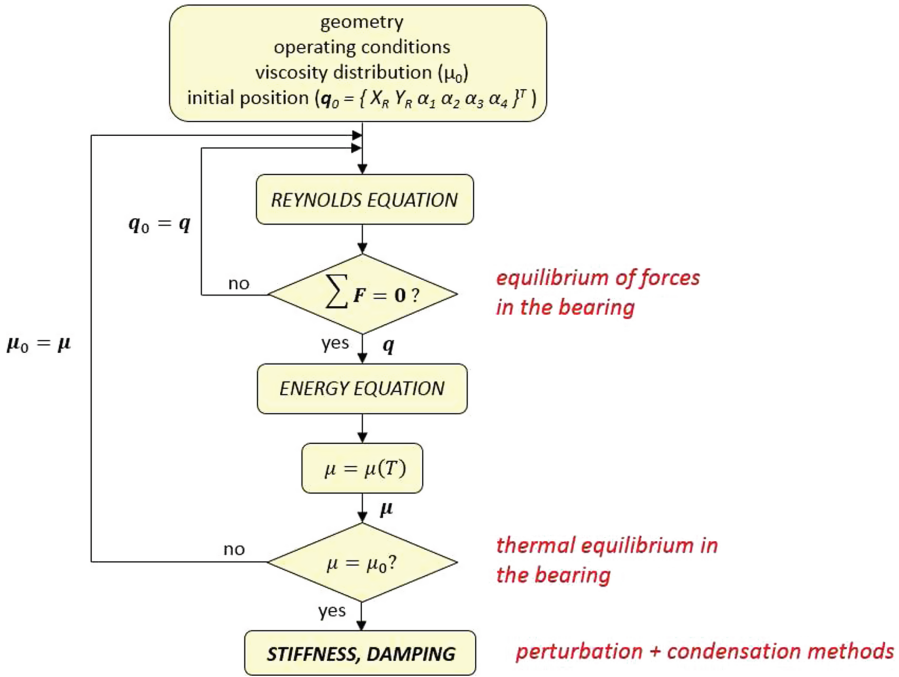


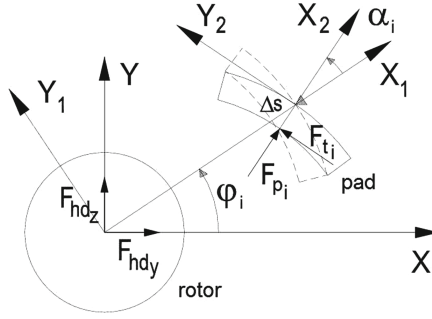
Fig. 2. Block diagram of the simulation algorithm of the TPJB.

diagram shown in Fig. 2. Initially, we set the geometric parameters of the bearing (rotor radius, pad inner radius, pad width, pad angle, pad thickness), the operating conditions (rotating speed, external loading, oil thermal conductivity, oil specific heat, oil density), the initial oil viscosity distribution over the pads ( $\mu_i$ ) and, the initial position of the rotor ( $X_R, Y_R$ ) and of the pads ( $\alpha_i$ ). After that, the Reynolds equation is solved numerically for each pad [5]:

$$\frac{\partial}{\partial y} \left( \frac{h_i^3}{\mu_i} \frac{\partial p_i}{\partial y} \right) + \frac{\partial}{\partial z} \left( \frac{h_i^3}{\mu_i} \frac{\partial p_i}{\partial z} \right) = 6U \frac{\partial h_i}{\partial y} + 12 \frac{\partial h_i}{\partial t} \tag{1}$$

where  $p_i = p_i(y, z)$  is the oil pressure distribution in the bearing clearance between the rotor and the  $i$ -th pad,  $h_i = h_i(y)$  is the clearance between the rotor and the  $i$ -th pad,  $\mu_i = \mu_i(y, z, T_i)$  is the oil dynamic viscosity over the  $i$ -th pad, and  $U$  is the linear velocity of the rotor surface. This equation is written for a coordinate system  $(y, z)$  fixed on the surface of the  $i$ -th pad, with  $y$  in tangential direction (direction of shaft rotation) and  $z$  in axial direction. The boundary condition adopted to solve the Reynolds (1) is ambient pressure at the edges of the pads (case of flooded bearing). The cavitation zones of the pads are treated by the Gumbel hypothesis (ambient pressure at cavitation zones).

By solving the Reynolds equation for each pad of the bearing, we find the oil pressure distribution over the pads. Such pressure distributions are numerically



**Fig. 3.** Hydrodynamic forces acting on the pads and on the shaft in the TPJB.

integrated over the surface area of the pads, thus resulting in the hydrodynamic forces acting perpendicularly ( $F_p$ ) and tangentially ( $F_t$ ) to the pads (Fig. 3). Such hydrodynamic forces are summed up to calculate the resultant hydrodynamic forces acting on the shaft ( $F_{hd_x}, F_{hd_y}$ ), in the form:

$$F_{hd_x} = - \sum_{i=1}^{np} F_{p_i} \cos(\varphi_i + \alpha_i) - F_{t_i} \sin(\varphi_i + \alpha_i) \tag{2}$$

$$F_{hd_y} = - \sum_{i=1}^{np} F_{p_i} \sin(\varphi_i + \alpha_i) + F_{t_i} \cos(\varphi_i + \alpha_i) \tag{3}$$

where  $np$  is the number of pads in the TPJB, and  $\varphi_i$  is the positioning angle of the  $i$ -th pad in the bearing casing in relation to the coordinate system (Fig. 3).

The equilibrium position of the shaft ( $X_R, Y_R$ ) and of the pads ( $\alpha_i$ ) is obtained by achieving the equilibrium of forces in the bearing: when the hydrodynamic forces on the shaft are equal to the external forces acting on the shaft. That is accomplished by using the Newton-Raphson algorithm, which will find the positions  $X_R, Y_R$ , and  $\alpha_i$  that zero the equilibrium equation:

$$\sum \mathbf{f}_{hd}(X_R, Y_R, \alpha_i) - \mathbf{f}_{ext} = 0 \tag{4}$$

where  $\mathbf{f}_{hd}$  is the vector of hydrodynamic forces (function of the rotor and pad positions), and  $\mathbf{f}_{ext}$  is the vector of external forces applied to the shaft.

After finding the equilibrium position of the TPJB, we solve numerically the Energy equation:

$$kh_i \left( \frac{\partial^2 T_i}{\partial y^2} + \frac{\partial^2 T_i}{\partial z^2} \right) + \left( \frac{\rho C h_i^3}{12 \mu_i} \frac{\partial p_i}{\partial y} - \frac{\rho C U h_i}{2} \right) \frac{\partial T_i}{\partial y} + \left( \frac{\rho C h_i^3}{12 \mu_i} \frac{\partial p_i}{\partial z} \right) \frac{\partial T_i}{\partial z} = -U^2 \frac{\mu_i}{h_i} - \frac{h_i^3}{12 \mu_i} \left[ \left( \frac{\partial p_i}{\partial y} \right)^2 + \left( \frac{\partial p_i}{\partial z} \right)^2 \right] \tag{5}$$

where  $T_i = T_i(y, z)$  is the oil temperature distribution over the  $i$ -th pad,  $k$  is the oil thermal conductivity,  $C$  is the oil specific heat, and  $\rho$  is the oil density (the variations of  $k$ ,  $C$ , and  $\rho$  as a function of the temperature are considered negligible). Again, these equations are written for a coordinate system  $(y, z)$  fixed on the surface of the  $i$ -th pad, with  $y$  in tangential direction (direction of shaft rotation) and  $z$  in axial direction. To solve the Energy Eq. (5), adiabatic temperature boundary condition is assumed in the pads, rotor, and in the bearing housing. The inlet temperature distribution at the leading edge of the pads is obtained from an energy balance applied to the mixing zone (area between pads), by considering the temperature distribution of the oil that exits the preceding pad.

By solving the Energy equation for each pad of the bearing, we find the oil temperature distributions over the pads. These temperature distributions are used to update the oil viscosity distributions over the pads ( $\mu_i$ ). In the present case, we adopt the following relationship between the oil viscosity and the oil temperature:

$$\mu = 0.0603 e^{(2.16 - 0.087T + 0.0005T^2)} \tag{6}$$

which is equivalent to the viscosity of an ISO VG 32 oil.

If the new oil viscosity distribution differs from the initial oil viscosity distribution by a certain tolerance value, this new oil viscosity distribution is used to recalculate the rotor-bearing equilibrium positions (Fig. 2). Such procedure is repeated until we achieve the convergence of the oil viscosity distributions (the difference between two successive iterations is smaller than the tolerance value).

### 2.1 Calculation of the Dynamic Coefficients

After achieving the convergence of the oil viscosity in the TPJB, we finally find the equilibrium position of the rotor in the bearing, and the equilibrium angular position of the pads, for the given operating and loading conditions. Hence, the equivalent dynamic coefficients of the rotor-bearing system can be estimated. For that, small perturbations are imposed to the degrees-of-freedom of the system (displacement/velocity of the rotor in horizontal and vertical directions, and angular displacement/velocity of the pads) [6]. The algorithm is run once again, and the resultant hydrodynamic forces and moments are calculated for the perturbed system. With these information (perturbations and resultant forces/moments), we find the stiffness and damping matrices of the system:

$$\Delta \mathbf{f} = \mathbf{K} \Delta \mathbf{x} + \mathbf{D} \Delta \dot{\mathbf{x}} \tag{7}$$

where  $\Delta \mathbf{f} = \{\Delta F_x \ \Delta F_y \ \Delta M_1 \ \Delta M_2 \ \Delta M_3 \ \Delta M_4\}^T$  is the vector of forces and moments variation,  $\mathbf{x} = \{\Delta x \ \Delta y \ \Delta \alpha_1 \ \Delta \alpha_2 \ \Delta \alpha_3 \ \Delta \alpha_4\}^T$  is the vector of displacement perturbations,  $\dot{\mathbf{x}} = \{\Delta \dot{x} \ \Delta \dot{y} \ \Delta \dot{\alpha}_1 \ \Delta \dot{\alpha}_2 \ \Delta \dot{\alpha}_3 \ \Delta \dot{\alpha}_4\}^T$  is the vector of velocity perturbations, and  $\mathbf{K}$  and  $\mathbf{D}$  are the stiffness and damping matrices of the system ( $6 \times 6$  matrices).

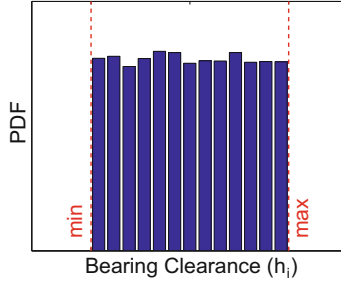


**Fig. 4.** Histogram of the random values adopted for the bearing assembled clearance of the  $i$ -th pad.

The global stiffness and damping matrices ( $4 \times 4$  matrices) are calculated using the condensation method described in [1], to eliminate the angular degrees-of-freedom of the pads and stay with the lateral displacements of the rotor only. That gives:

$$\Delta \mathbf{f}_R = \mathbf{K}_G \mathbf{x}_R + \mathbf{D}_G \Delta \dot{\mathbf{x}}_R \quad (8)$$

where  $\Delta \mathbf{f}_R = \{\Delta F_x \ \Delta F_y\}^T$ ,  $\mathbf{x}_R = \{\Delta x \ \Delta y\}^T$ ,  $\dot{\mathbf{x}}_R = \{\Delta \dot{x} \ \Delta \dot{y}\}^T$ , and the global stiffness and damping matrices are:

$$\mathbf{K}_G = \begin{bmatrix} k_{xx} & k_{xy} \\ k_{yx} & k_{yy} \end{bmatrix} \quad (9)$$

$$\mathbf{D}_G = \begin{bmatrix} d_{xx} & d_{xy} \\ d_{yx} & d_{yy} \end{bmatrix} \quad (10)$$

where subscripts  $xx$  and  $yy$  denote direct coefficients and subscripts  $xy$  and  $yx$  denote cross-coupling coefficients.

## 2.2 Assembled Clearance Variation

The asymmetry of the bearing is introduced in the model by adopting different bearing assembled clearances ( $h_i$ ) for each pad. The process of choosing the combination of values is based on the Monte Carlo method using uniform distribution [7]. Random values are created in the range of minimum and maximum bearing clearances, thus resulting in the histogram shown in Fig. 4. Such set of random values is created for each pad of the bearing, thus resulting in a set of four random variables  $\{h_1 \ h_2 \ h_3 \ h_4\}_{N \times 4}$ , where  $N$  is the number of random samples.

Given a combination of radial clearances for the bearing ( $h_1, h_2, h_3, h_4$ ), the dynamic characteristics of the bearing are recalculated and compared to those of the nominal case (symmetric bearing). This step is repeated extensively for all  $N$  random combinations of clearances.

### 3 Numerical Results

In the numerical results, a total of 5,000 sets ( $N = 5,000$ ) are randomly created by the MATLAB function `rand`, which gives uniformly distributed random numbers between 0 and 1. Such numbers are then proportionally shifted to the range of  $50 \times 10^{-6}$  (minimum) to  $90 \times 10^{-6}$  (maximum) to represent the possible clearance values in each pad (in meters). That represents an average clearance of  $70 \mu\text{m}$  (nominal clearance) with  $20 \mu\text{m}$  of random variation.

The mathematical model is used to calculate the thermal equilibrium, the equilibrium position, and the dynamic coefficients of the bearing under the operating conditions listed in Table 1. The case of nominal bearing clearance of  $70 \mu\text{m}$  represents the symmetric bearing with nominal geometry (all pads have the same clearance). All other 5,000 simulations, using the randomly created combinations of bearing-pad clearances, represent the cases of bearing asymmetry with equal probability of occurrence (uniform probability distribution - Fig. 4). The calculated dynamic coefficients are presented in dimensional form:

$$K_{ij} = \frac{C_p}{W} k_{ij} \quad (11)$$

$$D_{ij} = \frac{C_p \Omega}{W} d_{ij} \quad (12)$$

where  $C_p$  is the machined clearance (difference between the pad inner radius and the rotor radius),  $\Omega$  is the rotating speed (in rad/s), and  $W$  is the external load applied to the rotor. The obtained results are shown in Figs. 5 and 6, as a function of the Sommerfeld number ( $So = \mu \Omega L R (R/C_p)^2 / \pi W$ , where  $\mu$  is the average oil viscosity,  $L$  is the pad width, and  $R$  is the rotor radius). The external loading  $W$  is applied to the vertical direction ( $Y$  direction) towards pad #4. The total computational time of the 5,000 simulation was approximately 12 h in an Intel Core i7 computer with 8 cores, processing capacity of 2.2 MHz, and 6 GB of RAM memory.

The red lines in Figs. 5 and 6 refer to the nominal (symmetric) bearing case, whereas the shaded areas represent the scattering area of the results when the 5,000 random clearances are used (in the range of 50 to 90  $\mu\text{m}$ ). From the point of view of rotor stability, there are cases where the dynamic coefficients improve (i.e. higher direct coefficients or lower cross-coupling coefficients), and there are also cases where the dynamic coefficients worsen (i.e. lower direct coefficients and higher cross-coupling coefficients). Anyways, it is interesting to note that, for low Sommerfeld numbers ( $So < 0.1$ ), the scattering decreases and all the results for asymmetric bearings (shaded area) tend to the values of the symmetric bearing (red line), both for stiffness and damping. That is an indication that, for high external loading and/or low rotating speeds (low Sommerfeld numbers), the bearing behaves dynamically as a symmetric bearing, irrespective of its asymmetry.

Another important information obtained from Figs. 5 and 6 is that the cross-coupling coefficients do not increase significantly due to the random variations

**Table 1.** Bearing parameters.

<i>parameter</i>	<i>value</i>	<i>unit</i>
Rotor radius ( $R$ )	40.0	mm
Pad inner radius ( $R_p$ )	40.14	mm
Pad width ( $L$ )	80.0	mm
Pad angle	80.0	Degree
Pad thickness ( $\Delta s$ )	12.0	mm
Nominal radial clearance ( $h_N$ )	70.0	$\mu\text{m}$
Pivot position	Pad center	
Pad configuration	Load-on-pad	
Oil thermal conductivity ( $k$ )	0.14	$\text{W m}^{-1} \text{K}^{-1}$
Oil specific heat ( $C$ )	1800.0	$\text{J kg}^{-1} \text{K}^{-1}$
Oil density ( $\rho$ )	840.0	$\text{kg m}^{-3}$

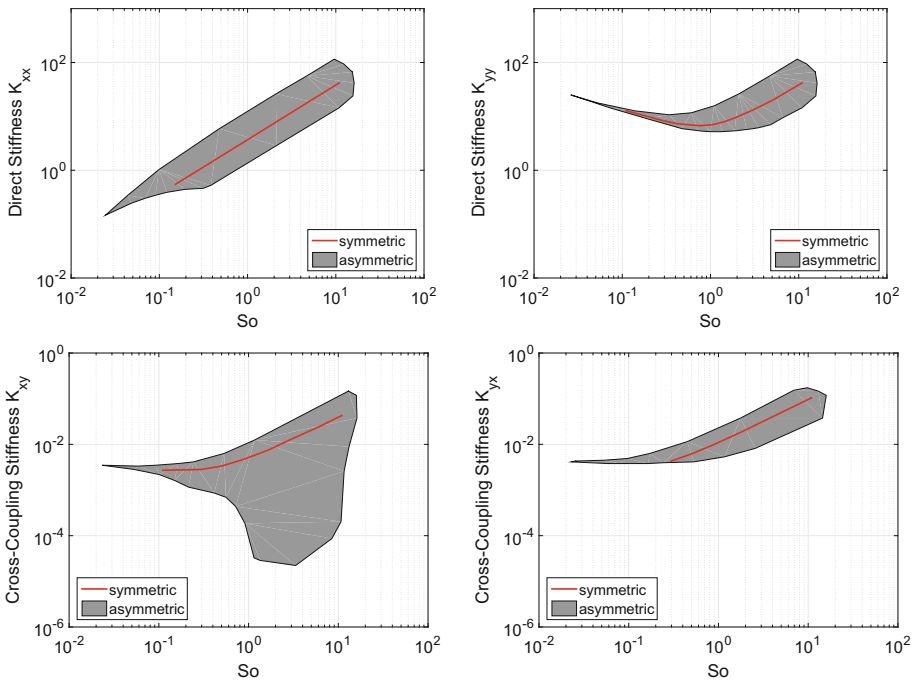


**Fig. 5.** Adimensional stiffness of the symmetric bearing with nominal clearance (red line) and asymmetric bearings (shaded area) as a function of the Sommerfeld number.

of the bearing clearances and asymmetry. The values of the cross-coupling coefficients still remain two orders of magnitude smaller than those of the direct coefficients, which is also good from the point of view of rotor stability. In fact,



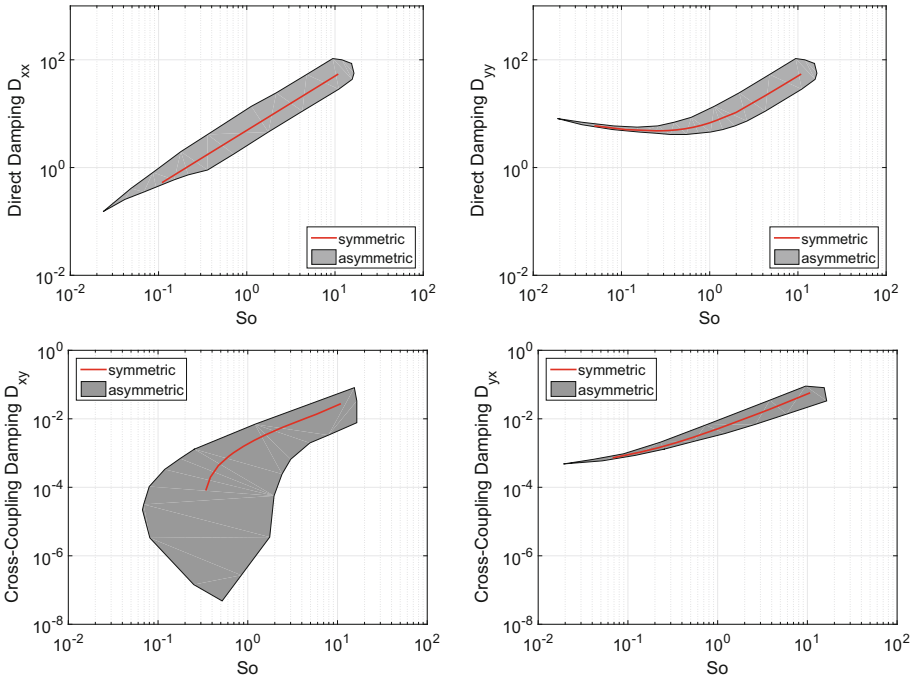


**Fig. 6.** Adimensional damping of the symmetric bearing with nominal clearance (red line) and asymmetric bearings (shaded area) as a function of the Sommerfeld number.

the biggest variation in the cross-coupling coefficients occur in the direction of lower values.

Among the 5,000 different asymmetric bearings tested, it would be interesting to find those that raised the direct coefficients and decreased the cross-coupling coefficients in comparison to the nominal (symmetric) case. That would represent an optimum case. On the other hand, the opposite situation would represent the worst scenario for an asymmetric bearing. Trying to answer the questions put in the end of the Introduction (which are the worst scenarios?, are there good design solutions?), we looked for asymmetric designs that presented bad or good compromise solutions among the obtained results. Some of the best and worst bearing designs found are listed in Table 2 and their respective direct dynamic coefficients are presented in Figs. 7 and 8 as a percentage variation to the dynamic coefficients of the symmetric bearing. As previously mentioned, the cross-coupling coefficients do not vary significantly towards higher values and, therefore, their variation is not presented here for brevity.

As one can see in Fig. 7 (best solutions), it is possible to find bearing geometries that significantly increase the stiffness in the unloaded direction X (bearing B), in the loaded direction Y (bearing A), and in both directions (bearings C and D). Regarding the damping, bearings A, C, and D presented the best results.

**Table 2.** Best and worst compromise solutions to the asymmetric design of the TPJB.

	Best					Worst			
	Bearing clearance ( $\mu\text{m}$ )					Bearing clearance ( $\mu\text{m}$ )			
	$h_1$	$h_2$	$h_3$	$h_4$		$h_1$	$h_2$	$h_3$	$h_4$
A	79.14	51.06	50.20	50.10	E	88.09	88.54	89.93	69.13
B	52.74	66.63	50.19	50.14	F	80.13	85.04	88.74	87.83
C	55.47	58.37	53.95	50.57	G	76.88	86.52	88.51	87.26
D	63.91	60.06	53.23	51.16	H	87.95	89.37	86.50	78.51

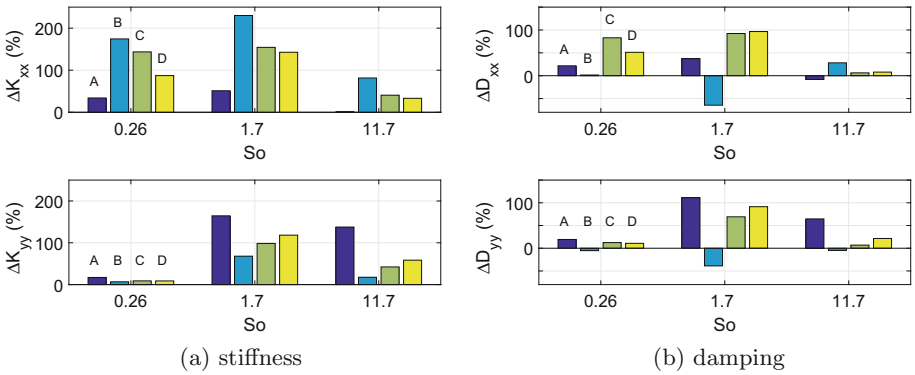


**Fig. 7.** Percentage variation of the direct dynamic coefficients for different asymmetric bearings and Sommerfeld numbers (best results).

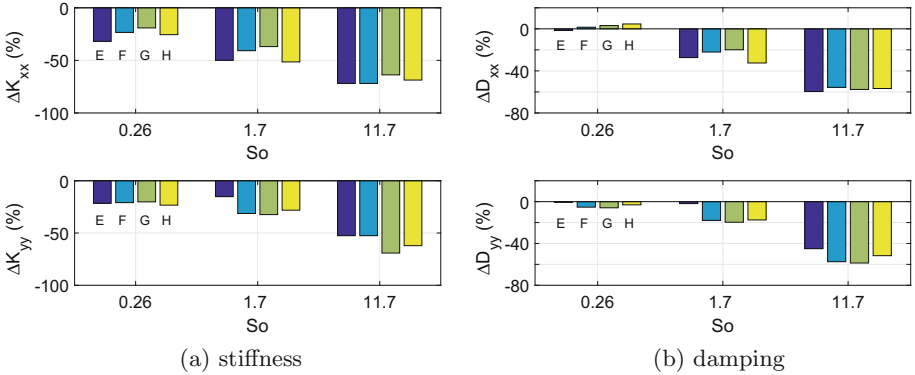


**Fig. 8.** Percentage variation of the direct dynamic coefficients for different asymmetric bearings and Sommerfeld numbers (worst results).

On the other hand (Fig. 8 - worst solutions), bearings E, F, G, and H presented significant decrease in both stiffness and damping, in both directions.

Looking at the geometry of these asymmetric bearings in Table 2, in general the best results are obtained with bearings with minimum clearance in the pad #3 ( $h_3$ ) and in the loaded pad #4 ( $h_4$ ) – see Fig. 1 for reference. The bearing clearance in the pads #1 and #2 ( $h_1$  and  $h_2$ ) remain in the range of  $\pm 15 \mu\text{m}$  from the nominal clearance of  $70 \mu\text{m}$ . In the case of the worst bearings, at least three of the pads have clearances near the maximum possible value (around  $90 \mu\text{m}$ ). Therefore, a combination of clearances that pushes the pads away from the rotor is detrimental to the dynamic performance of the tilting-pad bearing.

## 4 Conclusion

The THD analysis of load-on-pad TPJBs with asymmetric geometry showed that the resultant stiffness and damping coefficients scatter around the results of the symmetric bearing. In addition, for low Sommerfeld numbers ( $So < 0.1$ ), the scattering of the results decreases and converge to those of the symmetric bearing with nominal clearance. This is an indication that asymmetric bearings tend to behave dynamically as symmetric bearings with nominal clearance under high loading and/or low rotating speed conditions.

The results of the analysis also showed that there are specific asymmetric geometries that improve stiffness and damping, in both X and Y directions. There are also geometries that decreases stiffness and damping in both directions. Among the analyzed bearings, the best results were obtained with bearings with minimum clearance in the pad #3 and in the loaded pad #4. On the other hand, a combination of clearances that pushes the pads away from the rotor is detrimental to the dynamic performance of the tilting-pad bearing (worst results). It is important to point out that these results depend on the direction of the rotating speed of the rotor.

**Acknowledgement.** The authors acknowledge the support given to this project by FAPESP (Fundação de Amparo à Pesquisa do Estado de São Paulo), Grant no. 2017/14045-7, and by CNPq (Conselho Nacional de Desenvolvimento Científico e Tecnológico), Grant no. 304709/2015-8.

## References

1. Dimond, T., Younan, A., Allaire, P.E.: A review of tilting-pad bearing theory. *Int. J. Rotating Mach* (2011). Article no. 908469 (2011). <https://doi.org/10.1155/2011/908469>
2. Dang, P.V., Chatterton, S., Pennachi, P., Vania, A.: Effect of the load direction on non-nominal five-pad tilting-pad journal bearings. *Trib. Int.* **98**, 197–211 (2016). <https://doi.org/10.1016/j.triboint.2016.02.028>

3. Quintini, J.C.R., Pineda, S., Matube, J.A., Medina, L.U., Gomez, J.L., Diaz, S.E.: Determining the effect of bearing clearance and preload uncertainties on tilting-pad bearings rotordynamic coefficients. In: ASME Turbo Expo 2014 Turbine Technical Conference and Exposition, vol. 7B, GT2014-26773. ASME, New York (2014). <https://doi.org/10.1115/GT2014-26773>
4. Ruiz, R.O., Diaz, S.E.: Effect of uncertainties in the estimation of dynamic coefficients on tilting-pad journal bearings. In: ASME 2016 International Mechanical Engineering Congress and Expositions, vol. 4B, IMECE2016-67252. ASME, New York (2016). <https://doi.org/10.1115/IMECE2016-67252>
5. Santos, I.F., Nicoletti, R.: THD analysis in tilting-pad journal bearings using multiple orifice hybrid lubrication. *J. Trib.* **121**, 893–900 (1999). <https://doi.org/10.1115/1.2834152>
6. Allaire, P.E., Parsell, J.K., Barrett, L.E.: A pad perturbation method for the dynamic coefficients of tilting-pad journal bearings. *Wear* **72**, 29–44 (1981). [https://doi.org/10.1016/0043-1648\(81\)90281-7](https://doi.org/10.1016/0043-1648(81)90281-7)
7. Rubinstein, R.Y.: *Simulation and the Monte Carlo method*. Wiley, New York (1981)



# Experimental Structural Analysis of Gas Foil Bearings

Cédric Kayo<sup>(✉)</sup> and Robert Liebich

Technical University of Berlin, Strasse des 17. Juni 135, 10623 Berlin, Germany  
gervais.c.djokokayo@tu-berlin.de  
<http://www.kup.tu-berlin.de>

**Abstract.** Gas foil Bearing (GFB) are oil-free, high-speed and light bearings, which work according to the principle of fluid film lubrication. Thanks to their elastic structure, GFBs are able to compensate for minor pressure changes in the lubrication films. This paper presents the experimental structural analysis of first-generation gas foil bearings. The aim of the experimental investigation is to determine the behaviour of GFBs at static and dynamic loads. The tests are carried out with rotor speeds close to 0 rpm. In the course of the static investigation, the GFB was mounted on shafts with different diameters and loaded with a force of  $-150\text{ N}$  to  $150\text{ N}$ . Results from the static measurement show that not only the shaft diameter plays a role in determining the bearing clearance but also the number of activated bumps. It also shows that with a small bearing clearance ( $\leq 10\text{ }\mu\text{m}$ ), the GFB has an almost linear static stiffness. In the dynamic study, the GFB was mounted on a non rotating shaft and was excited by the shaker with a mono-frequency load. The goal of the dynamic investigation was to determine the dynamic stiffness behaviour and damping behaviour of GFBs at different amplitudes ( $2\text{ }\mu\text{m}$ ,  $6\text{ }\mu\text{m}$  and  $10\text{ }\mu\text{m}$ ) and over the frequency range of  $30\text{ Hz}$  to  $1000\text{ Hz}$ . In addition, this study aimed to find out whether the formation of subharmonic vibrations observed in the rotordynamic investigation can be attributed to the GFB structure. These subharmonic vibrations, as previous studies show, occur at speeds starting at about  $20\text{ }000\text{ rpm}$  ( $333\text{ Hz}$ ). For this reason, the dynamic measurement was performed up to  $1000\text{ Hz}$ . The results show that the damping decreases with increasing frequency up to  $490\text{ Hz}$  before rising again. This behaviour is amplitude independent. The stiffness of the bearings increases with increasing frequency. To verify the formation of subharmonic vibrations through the structure of GFBs, a Fourier transformation of the measurement signal was performed. However, no subharmonic vibration can be detected.

**Keywords:** Gas foil bearings · Bearing clearance · Stiffness  
Damping · Nonlinear vibrations

## 1 Introduction

Gas Foil Bearings (GFBs) are environmentally friendly, low-loss and cost-effective machine components used to support lighter and high-speed rotors.

© Springer Nature Switzerland AG 2019

K. L. Cavalca and H. I. Weber (Eds.): IFToMM 2018, MMS 60, pp. 264–280, 2019.

[https://doi.org/10.1007/978-3-319-99262-4\\_19](https://doi.org/10.1007/978-3-319-99262-4_19)

They were already employed in 1982 in the heart of the environmental control system called ACM (Air Cycle Machine) [1]. GFBs often consist of one or more top foils and bump foils fixed to a housing (Fig. 1). The top foil is considered as bearing surface for the rotor. The bump foil gives the bearing its elasticity and the frictional contacts between top foil and bump foil as well as bump foil and housing provide damping for the system. GFB generations can be differentiated by the number and design of their bump foil. Figure 1 shows a first generation GFB, which has been investigated in the course of this paper. The reason for the consideration of the first generation lies in the much larger amount of available experimental and numerical data in the literature that can be used for validation. Guidance on creating first and second generation bearings was published by DellaCorte in 2008 [2]. GFBs of all generations are based on a fluid dynamic lubrication principle and mostly use air as a lubricant but may also use other gases. The low viscosity of air gives GFBs a higher efficiency than roller bearings, but results in lower damping of the bearing. Due to this lower damping, subharmonic vibrations, which often occur in GFBs mounted systems, cannot be sufficiently damped. A classification of these nonlinear vibrations was done by Hoffmann et. al [3]. San Andrés et al. [4] identified this behaviour in their 2007 publication as Forced Nonlinearity Oscillations, which are influenced by unbalance. These nonlinear vibrations can cause the system to become unstable and so current efforts are necessary to predict and subdue their occurrence. The occurrence of nonlinear vibrations depends on several parameters such as the structural stiffness and damping of the GFBs.

In 1994, Heshmat and Ku [5] investigated the dynamic behaviour of GFBs. In their test stand, the bearing was mounted on a non rotating shaft and excited by two shakers with amplitudes of  $2.5\ \mu\text{m}$  and  $5.1\ \mu\text{m}$ . The aim of this study was to validate their analytical investigations. For this purpose, the bearing was excited at the frequencies of 142 Hz, 225 Hz und 350 Hz. The results show that stiffness and damping decrease with the increasing dynamic amplitude.

Salehi et al. [6] performed a dynamic study of GFBs in 2003 to determine the coefficient of friction. In this experiment, GFBs were excited over a frequency range of 50 Hz to 1400 Hz. The investigations show that the damping decreases exponentially with increasing frequency up to approximately 200 Hz.

Two years later, Kim et al. [7] presented experiments conducted to estimate the structural stiffness of a second generation bump-type gas bearing for increasing shaft temperatures. The test GFB was mounted on a shaft and excited over a frequency range of 40 Hz to 200 Hz. In the test, the shaft was heated to  $77\ ^\circ\text{C}$ ,  $123\ ^\circ\text{C}$  and  $188\ ^\circ\text{C}$ . The dynamic stiffness increases with increasing excitation frequency. However, the GFB's viscous damping decreases with the increasing excitation frequency.

The aim of this experimental investigation is to determine the behaviour of GFBs at static and dynamic loads. The goal of the dynamic investigation was to determine the dynamic stiffness behaviour and damping behaviour of GFB at different amplitudes ( $2\ \mu\text{m}$ ,  $6\ \mu\text{m}$  and  $10\ \mu\text{m}$ ) and over the frequency range of 30 Hz to 1000 Hz. In addition, this study aimed to find out whether the formation of subharmonic vibrations observed in the rotordynamic investigation can be attributed to the GFB structure.

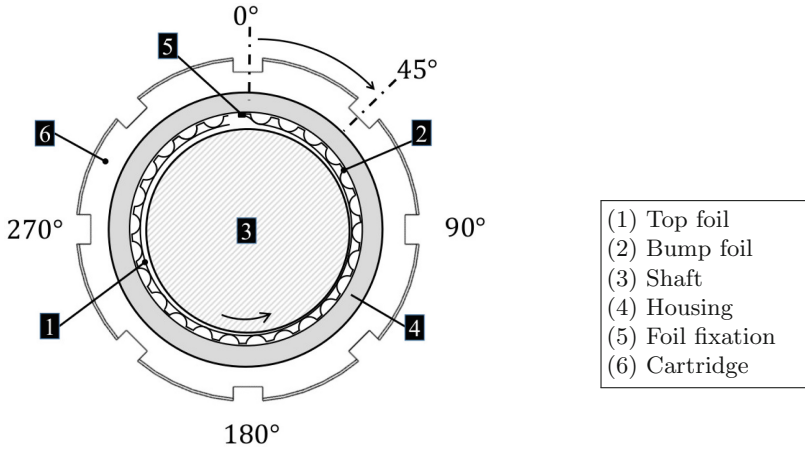


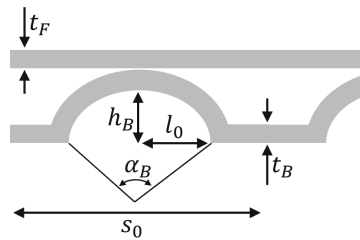
Fig. 1. Cross section of a test GFB

## 2 Static Load Investigation

The test GFBs were made from a 100  $\mu\text{m}$  Inconel X750 sheet. The bearings are heat treated at 640  $^{\circ}\text{C}$  for 4h after pressing. This increases the stiffness of the bump foil [2]. After the manufacture, it was checked if the GFB corresponded to the geometrical data from Table 1. In order to facilitate the mounting of the bearings in the test stand, the GFBs were mounted on a cartridge (Fig. 1). This allows the GFBs to be measured with an increment of 45 $^{\circ}$  in their circumference (Fig. 2).

Table 1. Geometrical data of test GFBs

Parameter		Value
Bearing radius	$R$	19.05 mm
Bearing length	$l$	38.1 mm
Bump height	$h_B$	0.51 mm
Bump thickness	$t_B$	0.102 mm
Bump pitch	$s_0$	3.17 mm
Bump arc angle	$\alpha_B$	87.52 $^{\circ}$
Bump number	$N_B$	38
Half bump length	$l_0$	1.27 mm
Foil thickness	$t_F$	0.102 mm
Young-modulus	$E$	$2.07 \times 10^{11} \text{ N/mm}^2$
Poisson's ratio	$\nu$	0.29



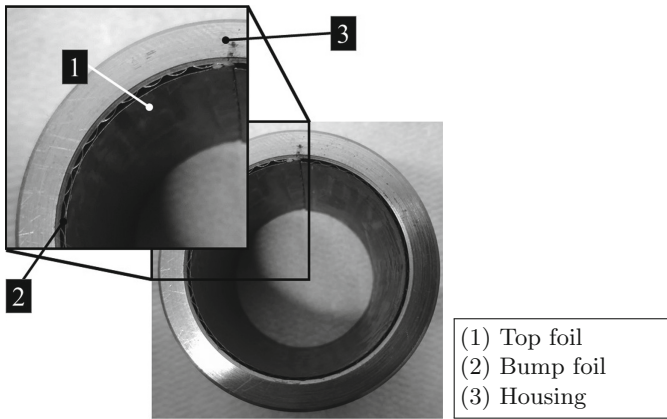


Fig. 2. GFB

### 2.1 Test Setup for Static Load

The experimental test rig for static load measurement is shown in Fig. 3 and consists of a load cell (3), a displacement sensor (4) and a shaft (2) clamped in a lathe chuck. The shaft consists of 42CrMo4 (1.7225) and has a ground surface. It was used in the investigation of three different rotors (see Table 3). After the load cell is mounted on the GFB, it is mounted on the shaft. Perpendicular to the bearing axis, the test GFB is loaded with a static force  $F_0$ . The resulting displacement is recorded on the opposite side with an eddy current sensor (4). The eddy current sensor has an accuracy of  $0.35 \mu\text{m}$  (see Table 2). The measurement

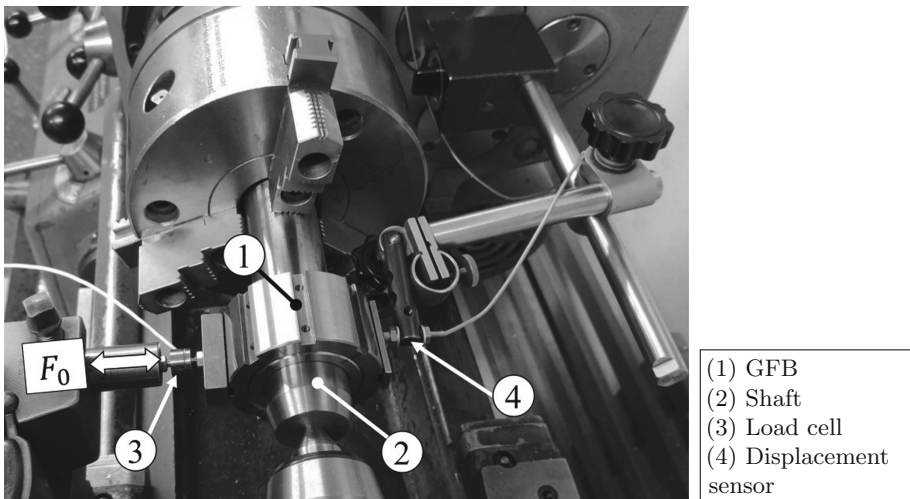


Fig. 3. Section view of the test setup for static load



**Table 2.** Test setup for static load

Sensor	Measurement range	Measurement accuracy	Manufacturer
Load cell	-500 . . . 500 N	2.5 N	Burster
Displacement sensor	0 . . . 0.5 mm	0.35 μm	Eddylab

**Table 3.** Test setup for static load

Shaft diameter	$D_1 = 37.95 \text{ mm}$
	$D_2 = 38.08 \text{ mm}$
	$D_3 = 38.10 \text{ mm}$
Angular position	$0^\circ - 180^\circ$
	$45^\circ - 225^\circ$
	$90^\circ - 270^\circ$
	$135^\circ - 315^\circ$
Load	-150 . . . 150 N
Sampling frequency	6000 Hz

data from the load cell and the displacement sensor are recorded with a frequency of 6000 Hz.

In order to investigate the influence of the radial clearances on the static stiffness of the bearing, the static measurements were carried out with different shaft diameters.

Settings and parameters for the measurement are recorded in Table 3. During one measurement process, two angles are measured. Figure 4 illustrates the measurement of the angles  $270^\circ$  and  $90^\circ$ . At a compressive force, the bearing is pushed at angle  $270^\circ$  on the shaft and the resulting displacement is recorded on the opposite side (at  $90^\circ$ ) and then the static load is measured. In the case of tensile force, it is pushed at angle  $90^\circ$  of the bearing and thus  $90^\circ$  is measured. The angular orientation is shown in Fig. 1.

## 2.2 Results of Static Load Test

Figure 5(a) shows the typical curve of a static load measurement. The lower half of the curve corresponds to the measurement of angle  $\alpha + 180^\circ$  and the upper half of angle  $\alpha$ . An explanation of the measuring principle was given in Sect. 2.1. The linear stiffness of the bearing at this angular position is defined as follows:

$$K_{linear} = \frac{\Delta F}{\Delta x} \tag{1}$$

$$\Delta F = F_{max} - F_{min} \qquad \Delta x = x_{max} - x_{min}. \tag{2}$$

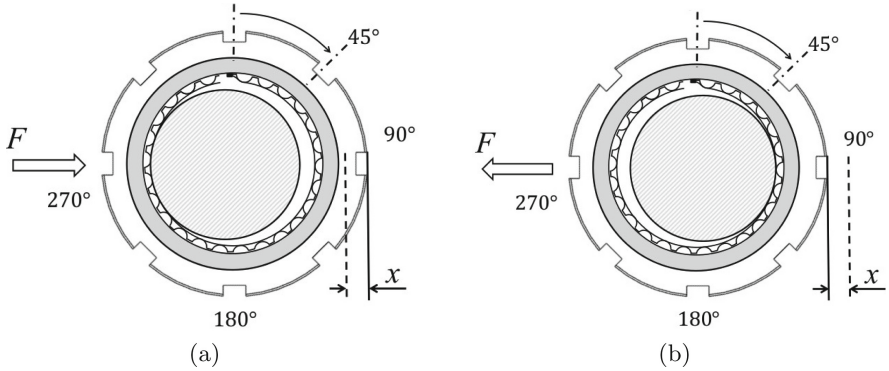


**Fig. 4.** Measuring principle for static load, 90°-270° bearing orientation, (a) measurement of the angles 270°, (b) measurement of the angles 90°

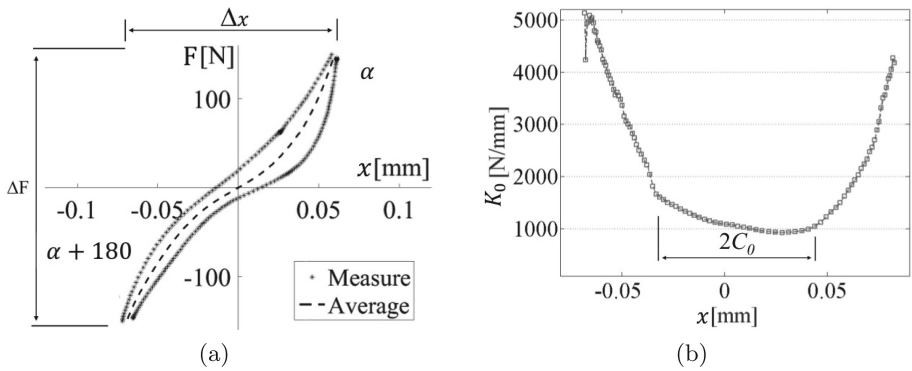


**Fig. 5.** Measured static loads at angular position 135°-315°, (a) hysteresis of static loading, (b) static stiffness vs. displacement

$\Delta F$  corresponds to the amplitude of the load applied to the bearing and  $\Delta x$  is the resulting displacement. By static measurement, the bearing clearance of the GFBS  $C_0$  can be determined (Fig. 5(b)). This length cannot be measured with a calliper. It corresponds to the deformation a bearing should experience until the bumps become active. A bump is active when the adhesive force at both its ends is so high that the bump cannot move. The activation of the bumps can be recognized on the hysteresis (Fig. 5(a)) by the sudden increase of the load. This effect is even more pronounced when looking at the stiffness curve (Fig. 5(b)). The following equation was used to plot this stiffness curve.

$$K_0 = \frac{\partial F}{\partial x} = \frac{F_{i+1} - F_i}{x_{i+1} - x_i} \tag{3}$$

where  $F_i$  and  $F_{i+1}$  are the loads measured at time  $t$  and  $t + dt$ , respectively.  $x_i$  and  $x_{i+1}$  are the displacement at each time. The algorithm for calculating the bearing clearance can be seen in Fig. 6. In the Calculating the bearing clearance,

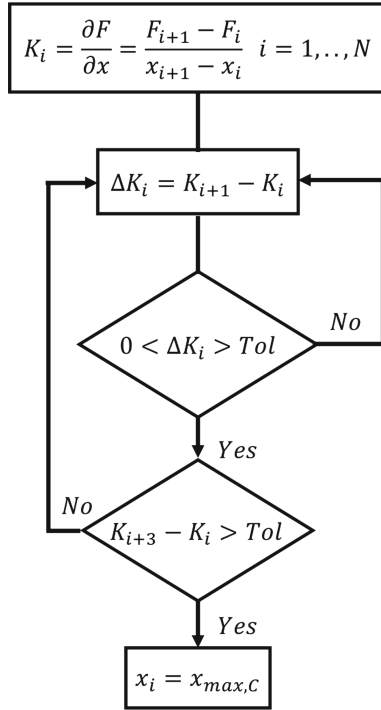


Fig. 6. Algorithm for calculating the bearing clearance

it is important to know where the bumps start and stop being active. These positions  $(x_{min,C}, x_{max,C})$  are detected by a sudden rise of stiffness  $(\Delta K_i)$ . The tolerance  $(Tol)$  for the increase in stiffness was set at 150 N/mm in the investigation. To calculate  $x_{min,C}$ ,  $\Delta K_i$  is calculated differently.

$$\Delta K_i = K_i - K_{i+1} \tag{4}$$

If  $x_{min,C_0}$  and  $x_{max,C_0}$  are identified, the clearance can be calculated

$$C_0 = \frac{x_{max,C} - x_{min,C}}{2}. \tag{5}$$

Table 4 lists the stiffness and the bearing clearance for each angular position and each shaft diameter with each shaft. It can be observed here that the bearing clearance decreases with the size of the shaft diameter. However, the decrease  $\partial C = C_{0,2} - C_{0,1}$  of the bearing clearance is not equal to the difference of the shaft diameter  $\partial D = \frac{D_2 - D_1}{2}$ . This is most likely due to the fact that the bearing clearance is unevenly distributed over the circumference. As a result, the bumps are activated unevenly. In addition, an active bump affects the adjacent bumps and increases the stiffness. Therefore the clearance of GFBS has less to

do with physical distance but much more with the bumps getting activated. Another influence is the measurement accuracy of the displacement sensor. For this reason, a dirt-resistant eddy current sensor was used for the measurement. The eddy current sensor has a resolution of  $0.35\ \mu\text{m}$  and was sampled at a frequency of 6000 Hz.

**Table 4.** GFB linear stiffness and radial clearances for different positions

Shaft diameter	Angular position	Clearances $C_0$ [ $\mu\text{m}$ ]	$K_{linear}$ [N/mm]
$D_1 = 37.95\ \text{mm}$	$0^\circ\text{--}180^\circ$	32.5	5919.5
	$45^\circ\text{--}225^\circ$	56.5	3760.6
	$90^\circ\text{--}270^\circ$	55	3844.9
	$135^\circ\text{--}315^\circ$	39.5	4553.9
$D_2 = 38.08\ \text{mm}$	$0^\circ\text{--}180^\circ$	11.5	11 314
	$45^\circ\text{--}225^\circ$	24.5	6367
	$90^\circ\text{--}270^\circ$	28.5	5749
	$135^\circ\text{--}315^\circ$	34.5	5896
$D_3 = 38.10\ \text{mm}$	$0^\circ\text{--}180^\circ$	0	27 728
	$45^\circ\text{--}225^\circ$	10	16 712
	$90^\circ\text{--}270^\circ$	5	20 919
	$135^\circ\text{--}315^\circ$	1	21 786

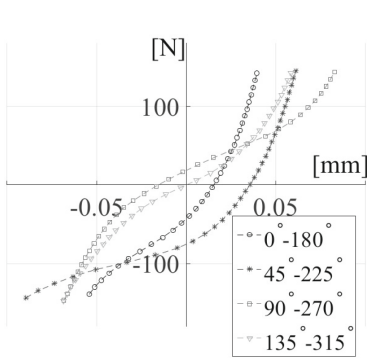
The figures in Fig. 7 show the measured static load and stiffness of a GFB. It can be seen that the stiffness of the GFB decreases with increasing angular position. This is due to the fact that bumps with a fixed end have a higher rigidity than those with a free end. In 1999, Iordanoff [8] presented the formula for calculating the rigidity of bumps with fixed ( $K_W$ ) and free end ( $K_F$ ). The investigation of Kim [7] confirmed that  $K_W$  is greater than  $K_F$ .

The measurement of the GFB with the lowest clearance (shaft  $D_3$ ) shows a nearly linear curve (Fig. 7e). This is likely because a large number of bumps are now active. In this case, the friction is low and the structure hardly shows nonlinearity.

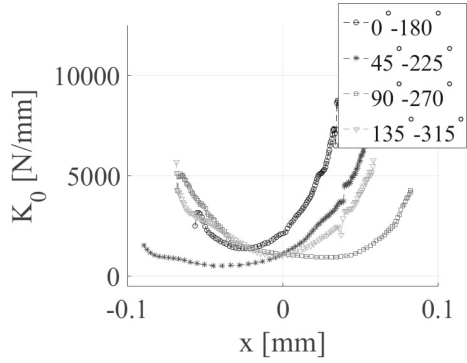
### 3 Dynamic Load Investigation

#### 3.1 Test Setup for Dynamic Load

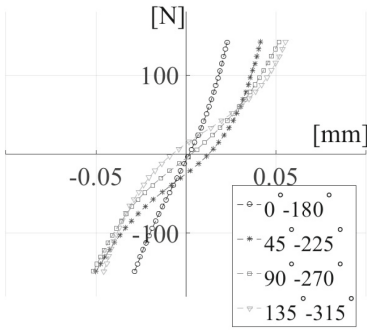
Figure 8 shows the test bench that was used for the dynamic measurement. It consists of a rigid shaft (2) mounted in two rigid bearing blocks. The test bench is fixed on a vibration-isolated machine bed. The test GFB (1) is mounted between the two bearing blocks on the shaft.



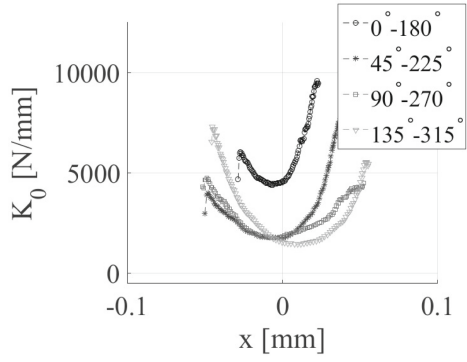
(a)  $D_1 = 37.95$  mm



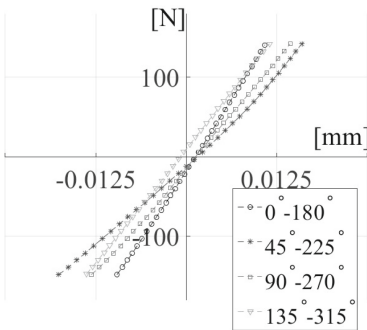
(b)  $D_1 = 37.95$  mm



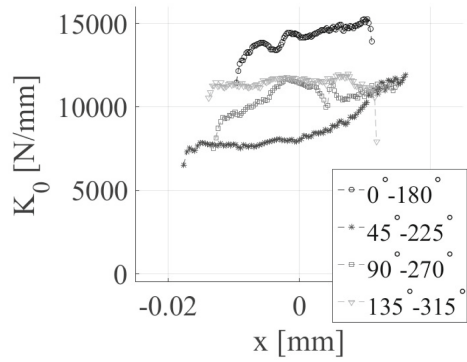
(c)  $D_2 = 38.08$  mm



(d)  $D_2 = 38.08$  mm



(e)  $D_3 = 38.10$  mm



(f)  $D_3 = 38.10$  mm

**Fig. 7.** Left side (a, c, e) GFB deflection versus static load, right side (b, d, f) GFB stiffness versus deflection

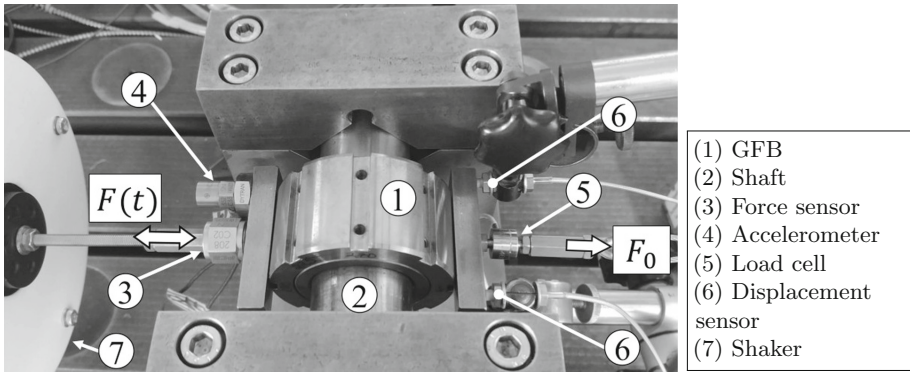


Fig. 8. Section view of experimental setup for dynamic Load

The measuring principle is illustrated in Fig. 9. To ensure constant contact between shaft and bearing, the GFB is loaded with a static force  $F_0$ . Its amplitude is detected by a load cell (5). By preloading the bearing, it is ensured that during the investigation only the elastic structure is excited and not the air film between bearing and shaft. Furthermore, the static force  $F_0$  should simulate the weight of the rotor. With the help of a shaker (7) the bearing is excited with a monofrequent harmonic force  $F(t)$ . To accommodate the deformation of the elastic structure, a metal block is screwed on the bearing housing, on which two eddy current sensors (6) are placed. The metal block increases the measuring accuracy thanks to its flat surface. Two eddy current sensors are used, to determine possible tilting of the GFB. Also fixed to the housing is an acceleration sensor (4). All sensors are connected to the corresponding card via a shielded cable. This should reduce the signal noise. Further information on the measuring instruments can be found in Table 5.

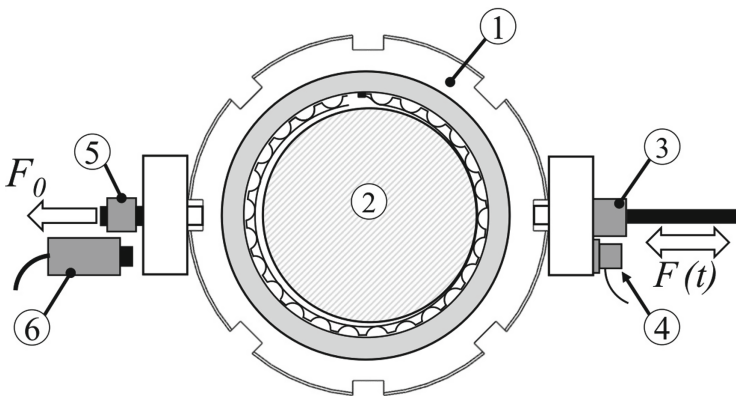


Fig. 9. Schematic view of the experimental setup for dynamic load

**Table 5.** Test setup for dynamic load

Sensor	Measurement range	Manufacturer
Force sensor	$\pm 444.8$ N	PCB Piezotronics
Accelerometer	$\pm 490$ m/s <sup>2</sup>	PCB Piezotronics
Load cell	$\pm 500$ N	Burster
Displacement sensor	0 . . . 0.5 mm	Eddylab

**Table 6.** Measurement configurations for dynamic load

Displacement amplitude	2 $\mu$ m	6 $\mu$ m	10 $\mu$ m
Frequency range	30 to 1000 Hz	30 to 600 Hz	30 to 570 Hz
Sensor position	90° to 270°	90° to 270°	90° to 270°
Static load	27; 37 N	27; 37 N	27; 37 N
Measurement time	8 s	8 s	8 s
Sampling frequency	12 000 Hz	12 000 Hz	12 000 Hz

The dynamic investigation consists of determining the frequency dependence of the elastic structure at different vibration amplitudes and static load. Therefore, a different measuring campaign was carried out (see Table 6). The goal at the beginning of the experiment was to measure the behaviour of the bearing at the oscillation amplitude of 2  $\mu$ m, 6  $\mu$ m and 10  $\mu$ m at the frequency of 30 Hz to 1000 Hz. However, at amplitudes of 6  $\mu$ m and 10  $\mu$ m, the exciting forces above 570 Hz were too high, so the measurements had to be interrupted to protect the bearing from destruction. But the measurement campaign with 2  $\mu$ m, 6  $\mu$ m and 10  $\mu$ m should give sufficient information about the nonlinear behaviour of the stiffness as well as about damping. In Table 6 the measuring instruments that were used in the context of this experiment are shown.

To evaluate the impact of the test rig on the measurement, a modal analysis was carried out on the test rig. This was used to find out if the resonance frequency of the test bench is in the measuring range. The system response shows a first resonance frequency at 8260 Hz and a second at 10 160 Hz which are outside of the measurement range (Table 6).

### 3.2 Results of Dynamic Load Test

In order to determine the stiffness and damping of the elastic structure, the measuring system from Fig. 9 is modeled using the following equation:

$$M\ddot{\tilde{x}}(t) + K\tilde{x}(t) + F_{dry} \cdot \text{sgn}(\dot{\tilde{x}}(t)) = -F_0 + F \cos(\omega t) \tag{6}$$

$M$  is the mass of the system.  $K$  represents the GFB stiffness. Frictional forces in the bearing are modeled with force  $F_{dry} \cdot \text{sgn}(\dot{\tilde{x}})$ . A weight is attached to the

bearing. This exerts a force  $F_0$  on the bearing. At the same time, the shaker excites the elastic structure with force  $F \cos(\omega t)$ . The consideration of Eq. (6) in the static case yields the following:

$$K\tilde{x}_0 = -F_0 \quad \Rightarrow \quad \tilde{x}_0 = \frac{-F_0}{K} \tag{7}$$

Let  $\tilde{x} = \tilde{x}_0 + x$ , it follows from Eq. (6).

$$M\ddot{x}(t) + Kx(t) + F_{dry} \cdot \text{sgn}(\dot{x}(t)) = F \cos(\omega t) \tag{8}$$

This model was developed by Kim et al. [7] and Salehi et al. [6] for calculating stiffness and damping of GFBs. The force  $F_{dry} \cdot \text{sgn}(\dot{x})$  is a dissipative force and can be modeled as damping force  $F_d$  with viscous damping  $C$ . The system was modeled with a single degree of freedom model consisting of a spring and a damper.

$$M\ddot{x}(t) + C\dot{x}(t) + Kx(t) = F \cos(\omega t) \tag{9}$$

By performing Fourier transformation of Eq. (9), the following equation is obtained:

$$-\omega^2 MX(\omega) - i\omega CX(\omega) + KX(\omega) = F(\omega) \tag{10}$$

$$(K - \omega^2 M) - i\omega C = \frac{F(\omega)}{X(\omega)} \tag{11}$$

$$K = \text{Re} \left( \frac{F(\omega)}{X(\omega)} \right) + \omega^2 M \tag{12}$$

$$C = -\frac{1}{\omega} \text{Im} \left( \frac{F(\omega)}{X(\omega)} \right). \tag{13}$$

Figure 10 shows the damping of the tested GFB in the frequency range from 30 Hz to 600 Hz and 30 Hz to 1000 Hz for different amplitudes. Figure 10 displays the 180° position as an example since the other angular positions provide similar damping behaviour. Between 30 Hz to 450 Hz the damping drops before it rises again between 450 Hz to 1000 Hz. This behaviour is qualitatively independent from the angular position. The same can be observed in the work of Kim et al. [7]. However, the measurement of Kim only goes up to 200 Hz and thus it is not possible to know if the damping would rise again. The sudden decrease of the attenuation between 190 Hz and 210 Hz as well as between 300 Hz and 400 Hz indicate resonance frequencies. Numerical investigations show that the housing and the cartridge have their first resonance frequencies at 6878 Hz and 5128 Hz. Therefore, we can assume that the observed sudden decreases are the resonance frequencies of the GFBs. To refute this assumption, a modal analysis of the GFB was carried out. Figure 12 shows the results of the modal analysis. The amplitude response as well as the phase response indicate a first resonance frequency between 190 Hz and 210 Hz and a second resonance frequency between 320 Hz and 350 Hz. The first resonance is clearly visible at each angular position.



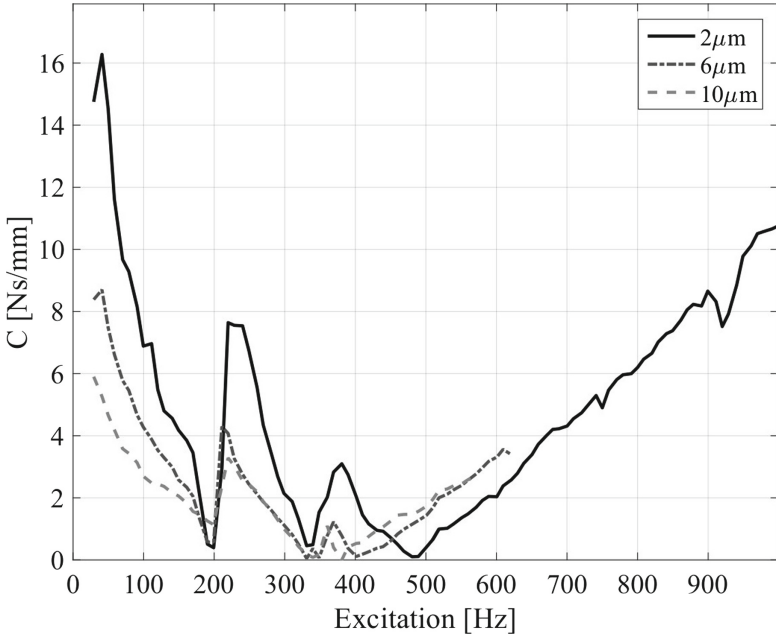


Fig. 10. GFB damping ( $C$ ) versus frequency at  $180^\circ$  position

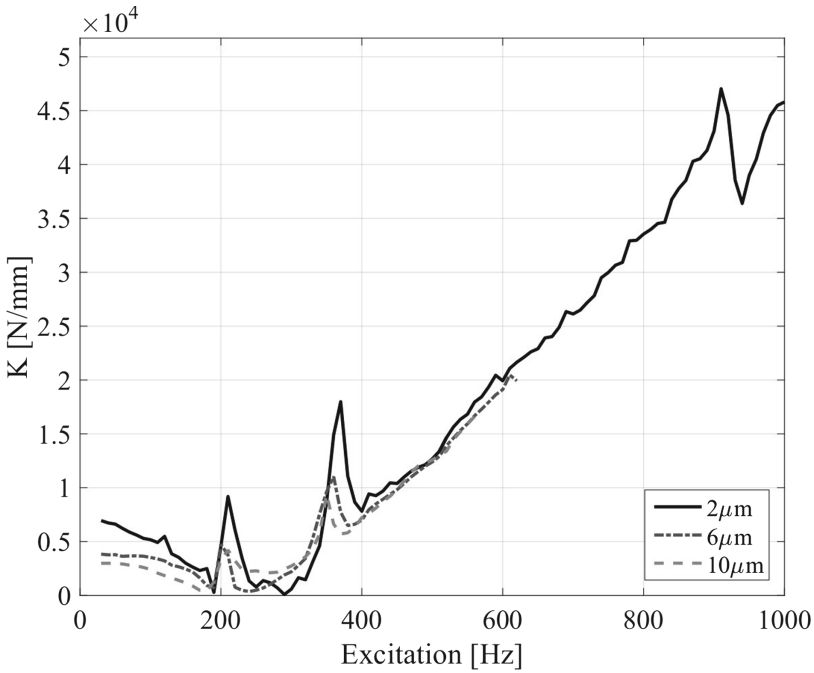
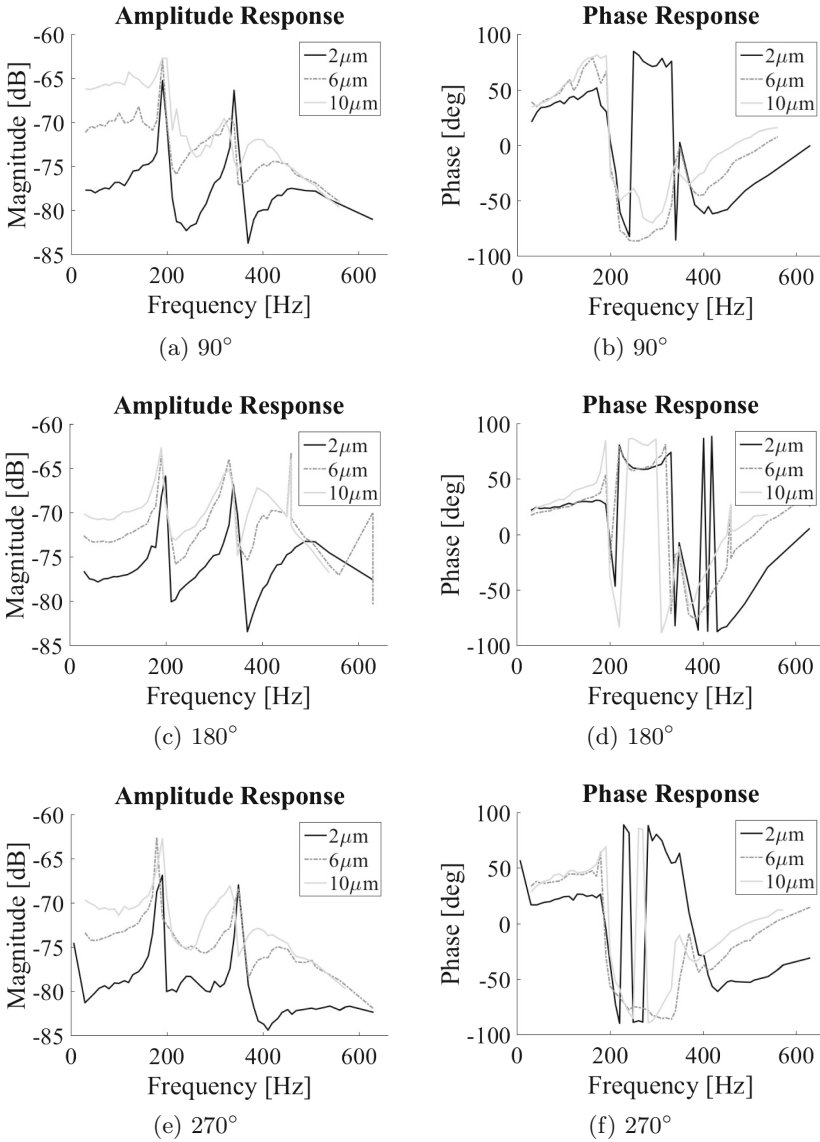


Fig. 11. GFB stiffness ( $K$ ) versus frequency at  $180^\circ$  position



**Fig. 12.** Frequency responses of GFB

So, it can be assumed that the drop-and-rise effect in the damping behaviour is independent from the angular position. It is probably due to the resonant frequency of the bump foil. The second resonance gradually disappears near the free end of the bump foil (see Fig. 12(f)). The second resonance can not be easily attributed to the drop-and-rise effect because, as can be seen in the phase plots of Fig. 12, it changes in frequency depending on the amplitude and the angular

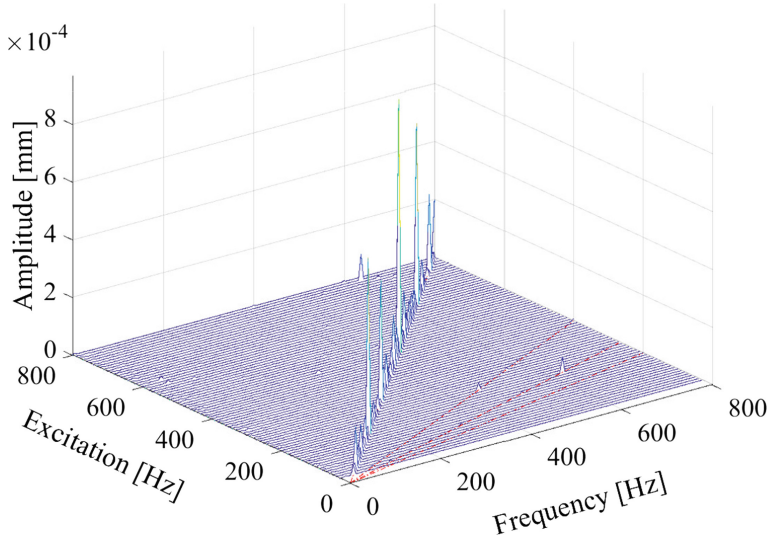


Fig. 13. Waterfall plot GFB at  $x = 2 \mu\text{m}$

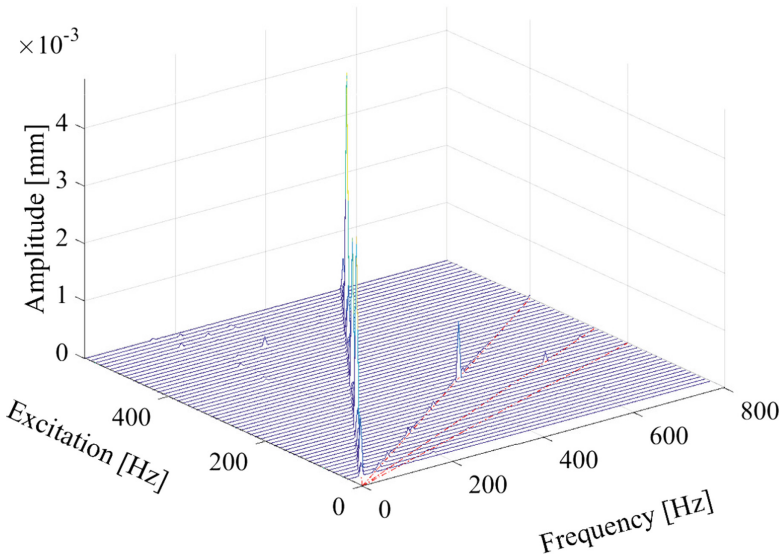


Fig. 14. Waterfall plot GFB at  $x = 10 \mu\text{m}$

position. But you can see in the amplitude curves that even in the area of the second drop-and-rise effect significant amplitude peaks exist that could explain the effect. Therefore, it is not possible to make a statement about the damping and the stiffness in the ranges from 190 Hz to 210 Hz and 320 Hz to 350 Hz,

because the influence of the resonance could not be determined. The dynamic damping shows a great similarity to the Stribeck effect [9].

The plot of the structural stiffness versus frequency is shown in Fig. 11. The stiffness of the GFB increases with increasing frequency. The first and second resonance frequencies can also be seen here at 190 Hz–210 Hz and 319 Hz–350 Hz. The increase in stiffness with frequency could have the following causes: For each measurement, the vibration displacements were always kept constant amplitude. This causes the excitation force to increase with the increasing frequency. This increases the contact forces and the number of active bumps.

Numerous studies [10–12] have shown that GFBs are often subject to subharmonic vibrations. Subharmonic vibrations are vibrations whose period is many times the period of the main vibration. These can lead to instability, because they often have a higher amplitude. To find out if their cause is directly attributable to the bearing structure, waterfall diagrams (see Figs. 13 and 14) were generated from the measurement signal. However, no subharmonic vibrations can be identified for displacement of  $2\ \mu\text{m}$ ,  $6\ \mu\text{m}$  and  $10\ \mu\text{m}$ . In previous investigations [3], subharmonic vibrations were seen already at 20 000 rpm. This speed corresponds to a frequency of 333 Hz. It can therefore be assumed that the subharmonic vibrations will be induced by the gas film.

## 4 Conclusions

This paper deals with the static and dynamic experimental structural investigation of first generation GFBs. In the course of the static investigation, the GFB was mounted on shafts with different diameters and loaded with a force of  $-150\ \text{N}$  to  $150\ \text{N}$ . Results from the static measurement show that not only the shaft diameter plays a role in determining the bearing clearance but also the number of activated bumps. It was found that the static stiffness of GFBs has a nearly linear behaviour at smaller bearing clearance ( $\leq 10\ \mu\text{m}$ ).

In the dynamic study, the GFB was excited by a shaker with the amplitude of  $2\ \mu\text{m}$ ,  $6\ \mu\text{m}$  and  $10\ \mu\text{m}$ . The investigation was carried out over a frequency range of 30 Hz to 1000 Hz. This investigation revealed that the test GFB has a first resonant frequency at approximately 200 Hz and a second at 350 Hz. The structural damping decreases with increasing frequency to 450 Hz before rising again. This behaviour is similar to the Stribeck effect. Due to the resonance, a sudden drop in the structure damping is observed at 200 Hz and 350 Hz. The stiffness of the GFB increases with increasing frequency as has been noted by Kim [7]. At the resonant frequencies, a sudden increase in stiffness can be detected. Further investigation was conducted to find out if the formation of subharmonic vibrations is caused by the structure. However, no subharmonic vibrations could be detected in the presented frequency analysis.

## References

1. Agrawal, G.L.: Foil air/gas bearing technology an overview. ASME paper no. 97 (1997)
2. DellaCorte, C., Radil, K.C., Bruckner, R.J., Howard, S.A.: Design, fabrication, and performance of open source generation I and II compliant hydrodynamic gas foil bearings. *Tribol. Trans.* **51**(3), 254–264 (2008)
3. Hoffmann, R., Kayo, C., Liebich, R.: Experimental analysis of the nonlinear vibrations of a rigid rotor in gas foil bearings. *Technische Mechanik* **37**, 226–238 (2017)
4. San Andrés, L., Kim, T.H.: Forced nonlinear response of gas foil bearing supported rotors. *Tribol. Int.* **41**(8), 704–715 (2008)
5. Heshmat, H., Ku, C.-P.R.: Structural damping of self-acting compliant foil journal bearings. *J. Tribol.* **116**(1), 76–82 (1994)
6. Salehi, M., Heshmat, H., Walton, J.F.: On the frictional damping characterization of compliant bump foils. *J. Tribol.* **125**(4), 804–813 (2003)
7. Kim, T.H., Breedlove, A.W., San Andrés, L.: Characterization of a foil bearing structure at increasing temperatures: static load and dynamic force performance. *J. Tribol.* **131**(4), 041703 (2009)
8. Iordanoff, I.: Analysis of an aerodynamic compliant foil thrust bearing: method for a rapid design. *J. Tribol.* **121**(4), 816–822 (1999)
9. Andersson, S., Sderberg, A., Björklund, S.: Friction models for sliding dry, boundary and mixed lubricated contacts. *Tribol. Int.* **40**(4), 580–587 (2007)
10. Heshmat, H.: Advancements in the performance of aerodynamic foil journal bearings: high speed and load capability. *J. Tribol.* **116**(2), 287–294 (1994)
11. Heshmat, H., Shapiro, W., Gray, S.: Development of foil journal bearings for high load capacity and high speed whirl stability. *J. Lubr. Technol.* **104**(2), 149–156 (1982)
12. Heshmat, H.: Operation of foil bearings beyond the bending critical mode. *J. Tribol.* **122**(1), 192–198 (1999)



# Influence of Manufacturing Errors on the Unbalance Response of Aerodynamic Foil Bearings

Aurelian Fatu<sup>(✉)</sup> and Mihai Arghir<sup>(✉)</sup>

Institut PPRIME, UPR CNRS 3346, Université de Poitiers,  
ISAE ENSMA, 11 bd. Pierre et Marie Curie, BP 30179,  
86962 Futuroscope Chasseneuil Cedex, France  
{aurelian.fatu,mihai.arghir}@univ-poitiers.fr

**Abstract.** The present work tackles the impact of manufacturing errors on the unbalance response of a Jeffcott rotor supported on aerodynamic foil bearings. The peculiarity of the model is the use of the Abaqus software for describing the dynamic response of the foil structure, for calculating the thin film pressures and for integrating the equations of motion of the rotor-bearing model. The numerical results show that the foil bearing without manufacturing errors and with a radial clearance of  $31.8 \mu\text{m}$  is unstable for the tested operating conditions (30 krpm rotation speed, 10 N static load and G1 unbalance class). However, taking into account manufacturing errors may lead to a different result. Bump height manufacturing errors were added to the model. Five cases with random manufacturing errors but all with  $10 \mu\text{m}$  standard deviation of the bump height were analyzed. In four cases, the unbalance response was a limit cycle dominated by the  $0.5 \Omega$  subsynchronous frequency. This result may explain the discrepancies between theoretical and experimental results reported up to now in the literature.

**Keywords:** Foil bearing · Unbalance response · Manufacturing errors

## 1 Introduction

Aerodynamic foil journal bearings are extensively tested since almost two decades because they represent an interesting design solution for small, high speed, “green” rotating machinery. In most cases, they operate with the working fluid of the compressor or of the turbine and therefore the design of the rotating machine is simpler, without lubrication systems and seals. Their drawback is a low static load capacity but in high speed rotating machines, this is of no importance because the dynamic load (usually due to imbalance) is much larger than the static one.

Experimental studies of rotors supported by foil bearings showed a multitude of rotordynamic responses. Most often, rotors supported on foil bearings operate with synchronous,  $1 \Omega$  and subsynchronous,  $0.5 \Omega$ , vibrations. The former vibration components are due to unbalance while the latter are known to be the signature of self-sustained vibrations. No other bearing could operate safely when self-sustained vibrations are present. However, the damping of the foil bearing comes from the

deformation of its foil structure: large deformations induce a large damping. Therefore, most often, a rotor on foil bearings operates with a limit cycle with two dominant frequencies, the  $1 \Omega$  and the  $0.5 \Omega$  [1]. The subsynchronous vibrations may even disappear with increasing rotation speed if the foil bearing can generate enough damping under the influence of the unbalance or if the foil bearing is provided with shims. In this latter case, the radial clearance is similar to the one in a lobed bearing.

This typical behavior of foil bearings is reproduced by calculations with the price of triggering parameters of the theoretical model. Depending on the model, this parameter can be the friction coefficient, the structural damping or the radial clearance. All these parameters have an impact on the stability of the foil bearing. The friction coefficient and the structural damping are most often obtained from experimental information. However, triggering the values of the radial clearance is more awkward to justify. A radial clearance is selected during the foil bearing design but its value is almost impossible to be measured. Foil bearings are obtained following a complex manufacturing process involving successive heat treatments and plastic deformations. Manufacturing errors are then expected. The designers of the rotating machinery that integrates the foil bearing often discards these manufacturing errors due to the objective impossibility of accurately measuring the radial clearance. The result is that during experiments, foil bearings of similar design may sometimes have quite different dynamic characteristics. The designer trying to reproduce theoretically the vibration signature of the rotor-bearing system might then trigger the radial clearance in order to obtain a result close to experiments. For example, the first generation foil bearing of 38 mm diameter and length and with 26 bumps was extensively used in the scientific literature a decade ago. It served for developing theoretical models and for experimental validations and its radial clearance was a parameter that was most often triggered. Values comprised between  $25 \mu\text{m}$  and  $38 \mu\text{m}$  can be found in the literature despite the fact that the manufacturer indicated a  $31.8 \mu\text{m}$  radial clearance.

The present work is a continuation of a previous paper dealing with the impact of manufacturing errors on the characteristics of foil bearings. Reference [2] presented the impact of bump height, bump length and bump foil outer radius manufacturing errors on the stiffness of the foil structure. In order to simulate static load-deflection tests, a displacement was incrementally applied to the rotor and the reaction force was calculated. The stiffness of the foil structure was subsequently calculated. The results showed that only the bump height had a significant impact. The manufacturing errors of the bump height lead systematically to a lower stiffness of the foil structure.

The foil structure was modeled by using the full capacities of the commercial code Abaqus [3]. Using a commercial code for modeling the foil structure of foil bearings was unusual but not completely new. Starting with 2009, Zywica [4, 5] used the same commercial code for investigating the static stiffness of the foil bearing structure. The analysis was carried out by imposing incremental rotor displacements against the foil structure. The work was continued in [6] with a dynamic analysis of the foil structure. The rotor was given a dynamic displacement with a 40 Hz frequency and the results underlined the energy dissipated by the structure. The air film was not considered and the work was focused on the foil structure. A review of the techniques employed by Zywica and co-workers can be found in [7].

A model combining Abaqus for the foil structure and a solver for the Reynolds equation governing the gas film was presented in [8] for static analysis of foil bearings. Temis and co-workers [9, 10] also used contact mechanics and finite-element codes for predicting the characteristics of the foil structure.

However, the use of contact mechanics models for bump foil bearings remain limited compared to the numerous simplifying approaches traditional employed. This can be appreciated from the review paper [11].

In the present work, the structure continues to be modeled with Abaqus but the rotor is considered to have a 30 krpm rotation speed. The pressures in the air film are obtained from the 2D unsteady Reynolds equation fully solved for a compressible fluid. Its numerical solution is obtained with the aid of a user-defined subroutine added to Abaqus.

A 2DOF Jeffcott model is used for describing the rotor-foil bearing system. Its equations of motion are added to the model that is integrated into Abaqus. The time transient calculations are performed with an explicit solver. For a given unbalance and rotation speed, the trajectory of the rotor is calculated over many cycles until obtaining a dynamic stable or a divergent (unstable) solution. Calculations are performed for the design values of the geometry of the foil bearing and by taking into account manufacturing errors. Net differences between the vibration signature of the ideal bearing and of the real one (i.e. with errors) are then enlightened.

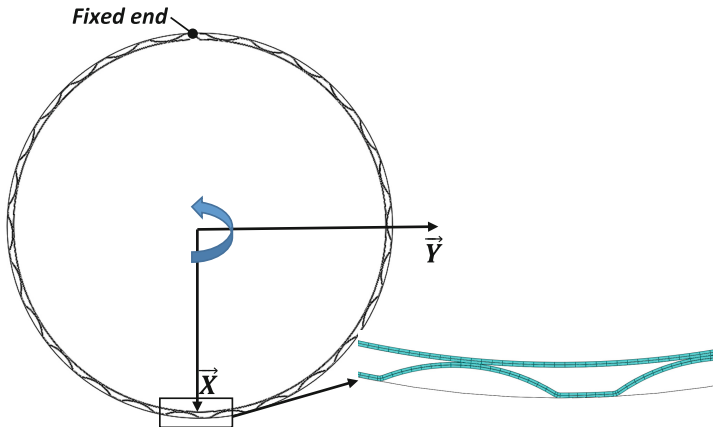


**Fig. 1.** Cut view of a generation 1 foil bearing modeled with Abaqus software

## 2 The Non-linear Model of the Foil Bearing

The analyzed bearing is depicted in Fig. 1 and belongs to the 1<sup>st</sup> generation of foil bearings. Its geometric and mechanical characteristics are given in Table 1 and detailed in Fig. 2.

Both top and bump foils are assumed to be flexible structures with inertia. They are discretized in Abaqus with conventional shell elements (S4R of the Abaqus library).



The sleeve is considered as an analytical rigid element. The interactions between the bumps and the sleeve and between the bumps and the top foil are taken into account by using a penalty contact algorithm. Friction is taken into account by using Coulomb's law.

New element formulations that are not available in the standard functionality of Abaqus can be defined via "User Subroutine" capabilities. Therefore, a new Reynolds User Element (RUE) is developed and implemented to model the fluid/structure interaction. The coupling between the RUE and the top foil is realized via a "tie contact" that gives the possibility of using non-conforming meshes for the two domains.

The pressure distribution in the air film is calculated with the compressible form of the Reynolds equation for perfect gas. The discretization of the Reynolds equation is made using four node linear elements and a finite elements Petrov-Galerkin procedure (the weighting functions are polynomial functions, which are upwind decentered).

A Newton-Raphson procedure is used for solving the resulting non-linear system of discretized equations. Ambient pressure boundary conditions were imposed at the bearing ends and in the vicinity of the welding line (the top of the bearing in Fig. 1).

**Table 1.** Geometric and mechanical characteristics of the foil bearing

Shaft radius (mm), $R$	19.05
Sleeve inner radius (mm), $R_s$	19.7938
Axial bearing length (mm), $L$	38.1
Radial clearance ( $\mu\text{m}$ ), $C_r$	31.8
Number of bumps, $N$	26
Bump pitch (mm), $p$	4.73
Bump length (mm), $2l_0$	3.556
Bump height (mm), $h$	0.508
Bump outer radius (mm), $R_{bo}$	19.7428
Bump inner radius (mm), $R_{bi}$	19.2348
Bump pitch circumferential length ( $^\circ$ ), $\theta_p = p/R_{bo}$	13.27
Inter-bumps circumferential length ( $^\circ$ ), $\theta_b = (p - 2l_0)/R_{bo}$	2.95
Top foil radius (mm), $R_r$	19.1328
Foil thickness (mm), $e_r$	0.102
Young modulus (GPa), $E$	214
Poisson's ratio, $\nu$	0.29
Density ( $\text{kg}/\text{m}^3$ ), $\rho$	7800
Friction coefficient, $\mu$	0.15

In order to reduce the computational time, it is considered that the foil bearing elastic behavior can be considered constant through the bearing width. This assumption gives the possibility to reduce considerably the structure mesh: only two elements are used to mesh the bearing axial direction for the top and bump foils, with appropriated symmetry boundary conditions. Consequently, the 2D pressure distribution obtained from Reynolds equation is averaged along the bearing width before being applied to the top foil.

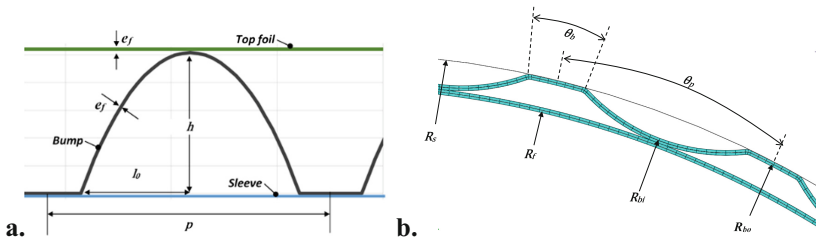


**Fig. 2.** Geometric characteristics of the bump (a - schematic, b - scaled representation)

At each time step Abaqus provides to the RUE the values of the nodal coordinates and of solution-dependent variables (displacements and velocities). The RUE contribution to the model must be provided in terms of nodal forces, depending on the known displacements and velocities. Therefore, a standard  $2 \times 2$  Gauss integration scheme is used to transform the hydrodynamic pressure in nodal forces.

### 3 Steady State Results

The coupling between the air film and the foil structure is first verified for a given static eccentricity: a positive  $15.9 \mu\text{m}$  displacement is applied to the rotor in  $X$  direction, which correspond to an eccentricity ratio value of 0.5.

Figure 3 shows the air film pressure and film thickness profiles obtained for the reference (without manufacturing errors) geometry and 30 krpm rotation speed. The pressure builds-up classically in the convergent zone with a maximum value just before the minimum film thickness. It is interesting to note the influence of the top foil radial deformation that is higher between two consecutive bumps and generates a circumferential variation of the pressure and film thickness fields. The sub-ambient pressure noted just before the fixed end generates an inwards deflection of the top foil.

Manufacturing errors of the bump height were added following the model used in reference [2]. As already explained in [2], the height of the bumps varies following a normal distribution with a controlled standard deviation. The average height of the bumps is the same to the theoretical value defined when the bearing was designed (see Table 1). As the top foil is tangent to the highest bump, the radial clearance is directly affected and, in the initial position, only one bump is in contact with the top foil. Thereafter, a standard deviation of  $10 \mu\text{m}$  will be used which represents 2% of its design value but 30% of the radial clearance.

Figure 4 shows the air film pressure and film thickness profiles obtained for the same operating conditions presented above but with a foil structure perturbed by bump height manufacturing errors. It can be noted that both pressure and film thickness variations are quite different from the results presented in Fig. 3. The predicted  $X$  rotor forces are very closed:  $-12.8 \text{ N}$  for the ideal case and  $-12.85 \text{ N}$  for the case presented in Fig. 4. However, the  $Y$  rotor forces are quite different:  $7.38 \text{ N}$  for the ideal case and only  $4.68 \text{ N}$  for the foil bearing affected by manufacturing errors.

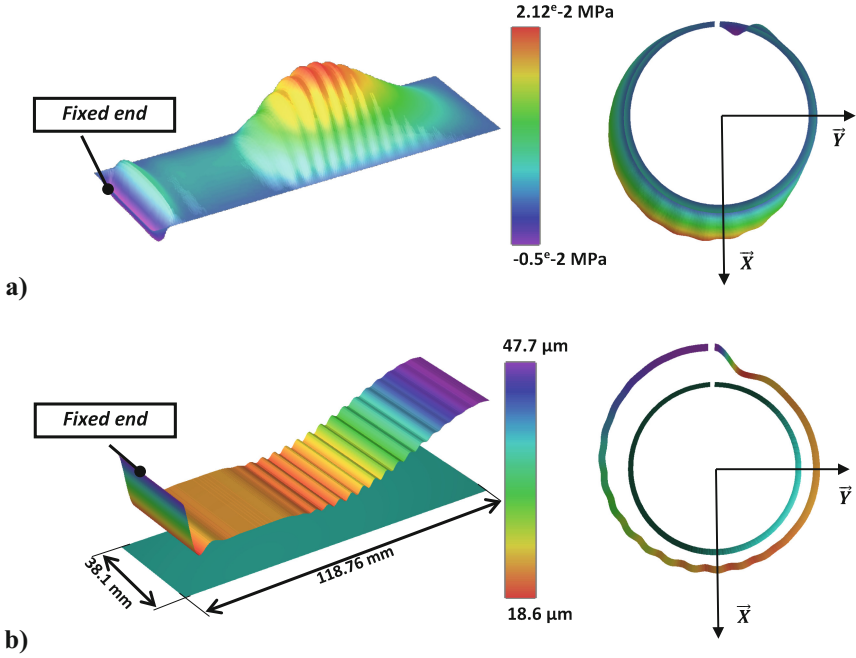


Fig. 3. Air film pressure (a) and film thickness (b) profiles for an imposed eccentricity without manufacturing errors

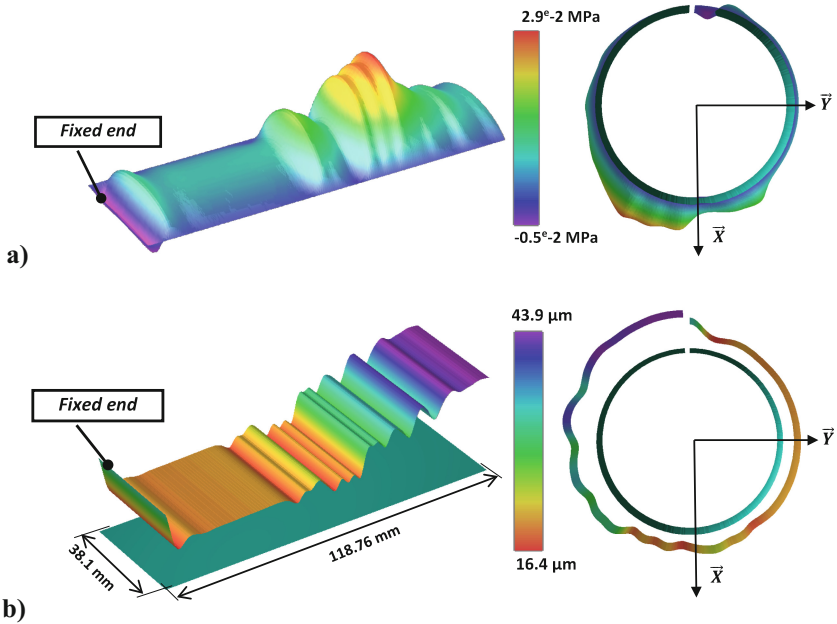


Fig. 4. Air film pressure (a) and film thickness (b) profiles for an imposed eccentricity and bump height manufacturing errors

In the reference case, the top foil is in contact with all the bumps and therefore the bump foil essentially generates the bearing stiffness. For the second geometry only a limited number of bumps are in contact with the top foil but, due to the positive displacement imposed on the rotor, these bumps are mainly located at  $180^\circ$  from the fixed end. Therefore, the bearing response in X direction is not very different from the reference case. However, in the Y direction, the loss of contact between the top foil and the bumps results in lower stiffness and, consequently, lower rotor force. This indicates that the hydrodynamic behavior of the foil bearing can be influenced by the investigated manufacturing errors, which anticipate the results presented in Sect. 4.2.

## 4 Unbalance Responses

### 4.1 The Original Foil Bearing

The dynamic response of a Jeffcott rotor supported by air foil bearings free of any manufacturing errors is depicted in Fig. 5.

The rotor mass imparted to one bearing was 1 kg and the static load was 10 N. An unbalance of 0.3183 g mm corresponding to the G1 ISO 1940-1 balancing class was considered. In Fig. 5, the dotted line represents the contour of the top foil before starting the computations. The trajectory is clearly unstable. Calculations were performed for approximately 40 rotation cycles (periods) and were stopped due to contact between the top foil and the rotor.

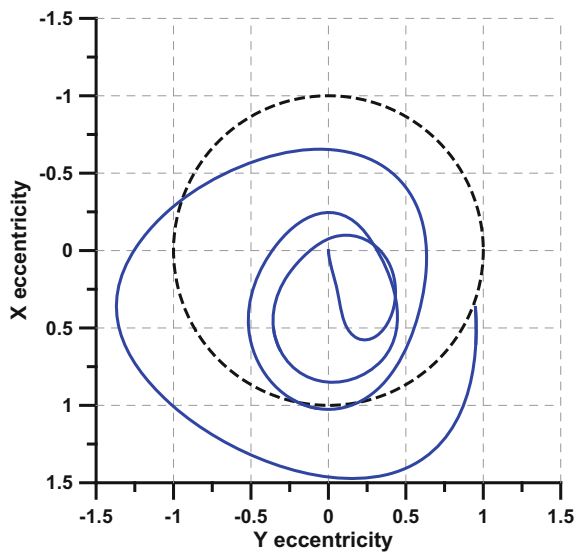


**Fig. 5.** Unbalance response of the rotor supported by the reference (without manufacturing errors) foil bearing

An explicit solver is used, so the unsteady problem is integrated by using small time increments. However, the explicit solver is not unconditionally stable and the size of the smallest foil finite element affects the maximum stable time increment. In addition, to correctly simulate the bumps/top foil contact, the foil mesh must contain relative small size finite elements: the maximum circumferential length of an element is about 0.5 mm that leads to a step time of  $5.6e-8$  s. As the same mesh size is used for all the results presented in this work, the step time is also keep constant.

### 4.2 The Foil Bearing with Bump Height Manufacturing Errors

Figure 6 depicts the unbalance response of five foil bearings affected by manufacturing errors of the bump height of  $10 \mu\text{m}$  standard deviation. X and Y are relative eccentricities computed by dividing the rotor displacements by the radial clearance of the ideal bearing ( $31.8 \mu\text{m}$ ). At  $t = 0$  the rotor was at center of the bearing. The computations are made for 80 rotational periods that correspond to approximately 0.16 s. Four of the five trajectories depicted in Fig. 6 converge to stable limit cycles. The fifth case shows an unstable trajectory with strong contacts between the rotor and the top foil as for the reference case depicted in Fig. 5.

The trajectories corresponding to the last 10 rotation periods of the stable cases  $h_1-h_4$  are depicted in Fig. 7. It is interesting to observe that, even if the manufacturing errors are identical from a statistical point of view, the limit cycles are different.

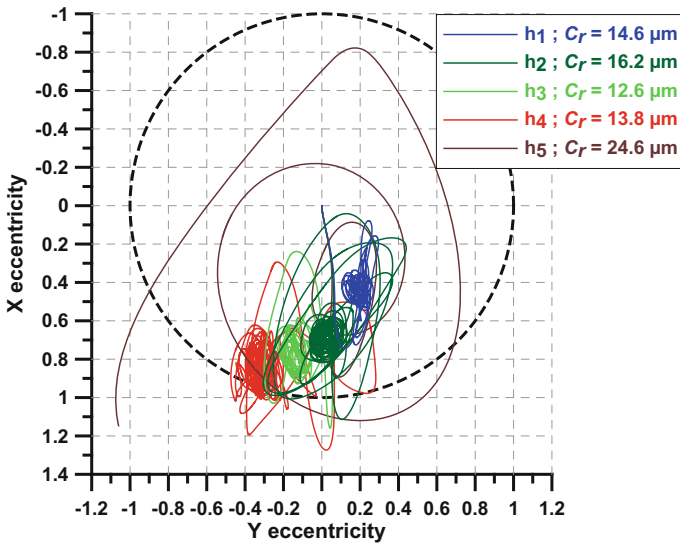
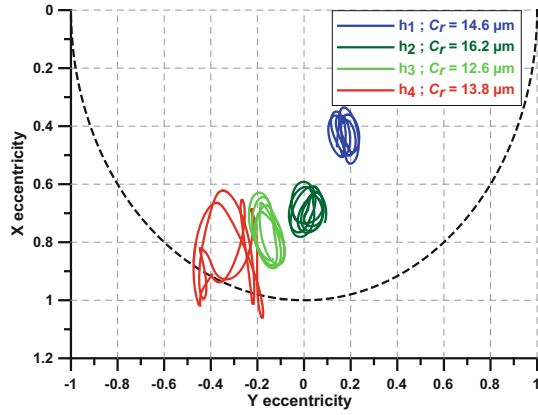
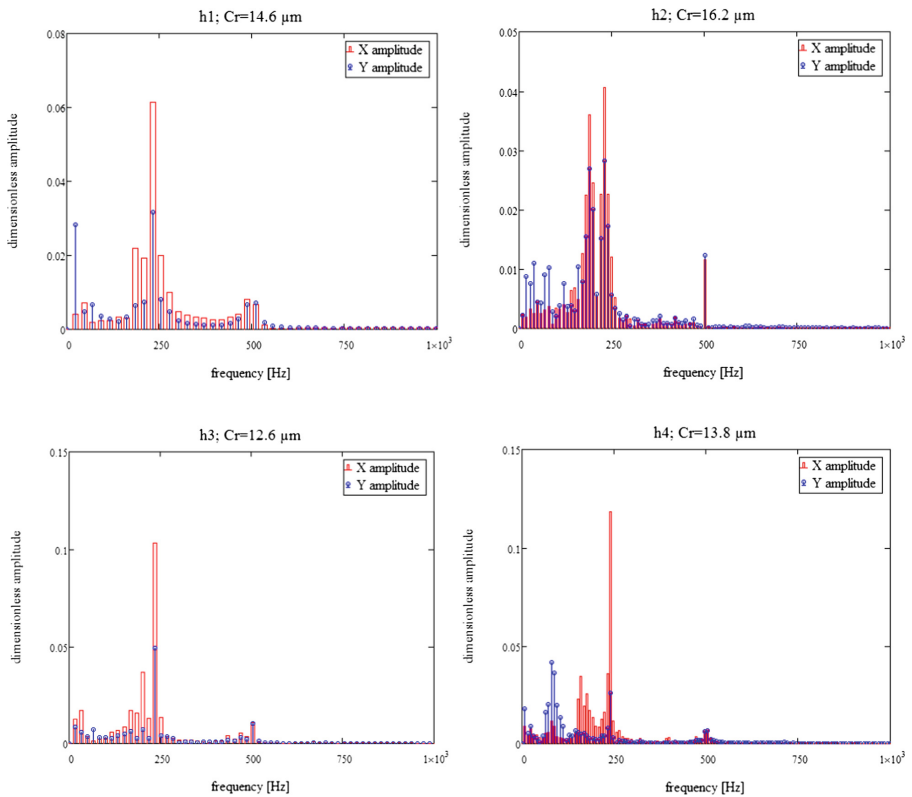


Fig. 6. Unbalance response of the rotor supported by the foil bearing with manufacturing errors

The frequency content depicted in Fig. 8 shows a dominant component, lower but close to  $0.5 \Omega$ . This is a common subsynchronous instability signature induced by



**Fig. 7.** The last 10 rotation periods of the unbalance response of the rotor supported by the foil bearing with manufacturing errors



**Fig. 8.** Frequency content of the stabilized trajectory of the rotor

aerodynamic bearings and generated by the fact that the overall circumferential velocity of the air inside the bearing is close to  $0.5 \Omega$  when the axial flow is greatly reduced by the thin film thickness. The amplitudes have also different values from case to case, thus reinforcing the observation made from Fig. 7 that the limit cycles are not identical. Figure 8 also shows that the frequency spectrum is continuous. However, it is difficult to appreciate if the limit cycle is a periodic, quasi-periodic or a chaotic trajectory because only a limited number of time steps was calculated. A much larger number of time steps would have been necessary for characterizing the limit cycle.

Subsynchronous  $0.5 \Omega$  vibrations have been also enlightened by the experimental investigations of aerodynamic foil bearings presented in reference [1]. It has been shown that  $0.5 \Omega$  instabilities were triggered by the unbalanced and then eliminated, at higher frequencies. The disappearance of the subsynchronous  $0.5 \Omega$  vibrations is explained by the Coulomb damping brought by large dynamic displacements. The current model is a step forward in understanding this behavior but the work must be continued by simulating different operating conditions in terms of rotational speeds and rotor unbalanced. More information is expected on the interactions between the manufacturing errors, the foil frictional behavior and the vibrational signature.

## 5 Conclusions

The presented model of foil journal bearings takes advantage of the standard functionality of Abaqus software to model the complex behavior of the elastic structure of the bearing and to couple it with a user-defined subroutine for the air film pressure. By exploiting the Abaqus capabilities, manufacturing geometrical errors can be integrated into the model and their effects on the static and dynamic response of the foil journal bearing can be investigated.

It has been shown that the bump height manufacturing errors can modify not only the steady state characteristics but, most important, the dynamic stability of the rotor-bearing system. The presented results show that theoretically identical foil journal bearings but affected by bump height manufacturing errors, can have different unbalance responses in terms of orbit and stability. This may explain the discrepancies between theoretical and experimental results reported up to now in the literature.

## References

1. Balducchi, F., Arghir, M., Gauthier, R.: Experimental analysis of the unbalance response of rigid rotors supported on aerodynamic foil bearings. *J. Vib. Acoust.* **137**(6), 061014 (2015)
2. Fatu, A., Arghir, M.: Numerical analysis of manufacturing errors on the structural stiffness of foil bearings. GT2017-63822 accepted for publication by the Journal of Gas Turbines and Power (2017). <https://doi.org/10.1115/1.4038042>
3. <http://www.3ds.com/fr/produits-et-services/simulia/Produits/abaqus/>. Accessed 18 Nov 2016
4. Miąskowski, W., Pietkiewicz, P., Żywica, G.: Modeling foil bearings. *Tech. Sci.* (2009). <https://doi.org/10.2478/v10022-009-0020-9>
5. Żywica, G.: The static performance analysis of the foil bearing structure. *Acta Mechanica et Automatica* **5**(4), 119–122 (2011)

6. Żywica, G.: The dynamic performance analysis of the foil bearing structure. *Acta Mechanica et Automatica* **7**(1), 58–62 (2013). <https://doi.org/10.2478/ama-2013-0011>
7. Żywica, G., Bogulicz, M., Baginski, P.: Modelling and Analysis of Rotating Systems with Gas Foil Bearings Under Transient Operating Conditions, pp. 167–173. *TRIBOLOGIA* 2/2017, ISSN 0208-7774 (2017)
8. Liu, J., Du, F.: Simulation of compliant bump foil journal bearing using coupled reynolds equation and finite element model method. *Adv. Mater. Res.* **479–481**, 2499–2503 (2012)
9. Temis, Y.M., Temis, M.Y., Meshcheryakov, A.B.: Gas-dynamics foil bearing model. *J. Frict. Wear* **32**(3), 212–220 (2011)
10. Temis, J., Temis, M., Egorov, A., Gavrilov, G.: Numerical and experimental investigation of rotor-simulator in foil gasdynamic bearings for compact gas turbine. In: Proceedings of the 9th IFToMM International Conference on Rotor Dynamics, pp. 1247–1258 (2014)
11. Branagan, M., Griffin, D., Goyne, C., Untaroiu, A.: Compliant gas foil bearings and analysis tools. *J. Eng. Gas Turbines Power* **138**(5), 054001 (2015)





# Parametric Sensitivity Analysis of Tilting Pad Bearings to Investigate the Dynamic Behavior of Rotating Machines

L. R. Ito<sup>1</sup>(✉), D. J. Ramos<sup>1</sup>, Z. de C. Silveira<sup>2</sup>, and G. B. Daniel<sup>1</sup>

<sup>1</sup> Faculty of Mechanical Engineering, State University of Campinas,  
Campinas, Brazil

leandroito@fem.unicamp.br

<sup>2</sup> Department of Mechanical Engineering,  
University of São Paulo, São Carlos, Brazil

**Abstract.** This paper presents a parametric sensitivity analysis based on Design of Experiments (DoE) applied to tilting pad bearings. The main objective is to explore a set of design parameters and its influence on the dynamic response of a rotor system. In this way, the computational analysis was based on the integration of the commercial design software HEEDS® and a numerical code that was implemented in MATLAB® to simulate the rotordynamics phenomena. The rotor system was modelled as Timoshenko beam and the computational model was implemented using Finite Element Method (FEM). The Finite Volume Method (FVM) was applied to the tilting pad bearings in order to determine the synchronously reduced equivalent stiffness and damping coefficients. The results indicate that the fluid film bearing has a strong effect on dynamic behavior of the rotating system and that a correct choice for its main geometric parameters can result in a safer operation condition by increasing the values of the second critical speed components. Since small variations in the design parameters can significantly change the rotating machine behavior is necessary to rigidly control their values during both processes of manufacturing and assembly.

**Keywords:** Tilting-pad · Rotordynamics · Design of experiments

## 1 Introduction

The use of rotary machines, such as pumps, turbines, and compressors, has become increasingly recurrent for the most diverse industrial applications. The search for rotors able to work with low vibration level and safely in severe operational conditions is recurrent in this area of engineering. For this, the optimization of machines' components, improvements in configurations and control have been objective of study for several researchers [1].

One of the components that have a great impact on the dynamic behavior of the rotary machine is the bearing, which supports the rotor and establishes the connection between the rotating elements and the supporting structure. Due to the high stability

condition, tilting pad journal bearings have presented large applicability in industrial machines.

As discussed in [2], studies related to the onset of instability are common in the literature, however, the prediction of critical bearing speeds, as well as the response to unbalance, are less common. Thus, this work focuses in the prediction of critical velocities in the rotor, aiming to evaluate the influence of tilting pad bearing geometry at these critical velocities and to understand how relevant these bearing's parameters are to the rotor's dynamic behavior.

In order to understand the influence of the geometry of the tilting pad bearing on the dynamic behavior of the rotary system, the use of a DoE methodology was proposed in which it is capable of evaluate the influence of each of the studied parameters and evidence possible couplings between them on a specific response of interest. In this study, the first and second critical speeds components of the rotating system are the responses of interest and the analyses allow to design the studied rotating system for a safer operating condition. The following sections describe the applied methods to execute this research work as well as the results found.

## 2 Methodology

In this section are explained the main topics concerning the research work: the modelling of both tilting pad journal bearings and the rotor system as well as the design of experiments methodology to explore the design space for the bearings.

### 2.1 Tilting Pad Journal Bearing

**Geometric Characteristics.** Figure 1 shows the component's main geometric characteristics. In Fig. 1(a) is shown a single pad with the respective pivot element where can be defined two Cartesian coordinates systems:  $xy$  as an inertial one and  $x'y'$  as a non-inertial one, which allows to measure the angle  $\alpha$  that corresponds to the pad's rotational degree of freedom relative to its pivot. In Fig. 1(b) are showed a single pad's width  $L_S$  and angle  $\beta_S$ .

In Fig. 1(c) a shaft-single pad subsystem is explored where  $O_E$ ,  $O_S$  and  $O_P$  are the origins of the coordinates systems located at the shaft, tilting pad journal bearing and pad's pivot, respectively,  $h_0$  is the radial clearance,  $h_S$  and  $R_S$  are the pad's thickness and curvature radius, respectively,  $R$  is the shaft radius. The angles  $\beta$  and  $\varphi$  are the angular positions inside the pad and the pivot's position in the pad. Thus, it's possible to define the pivot position relative to pad through the non-dimensional variable  $\gamma = \varphi/\beta_S$ , where the value 0.5 means that the pivot is positioned on the central portion of the respective pad.

As in elliptic and multi-lobe bearings, which have a fixed geometry, tilting pad journal bearings can have a pre-load represented by  $m = 1 - h_0/(R_S - R)$ , which enhances the load capacity and whose values are usually between 0.2 and 0.6. At last, can be defined two operating conditions for the tilting pad bearings namely LOP (load on pivot) and LBP (load between pivots) as schematically showed in Fig. 2.

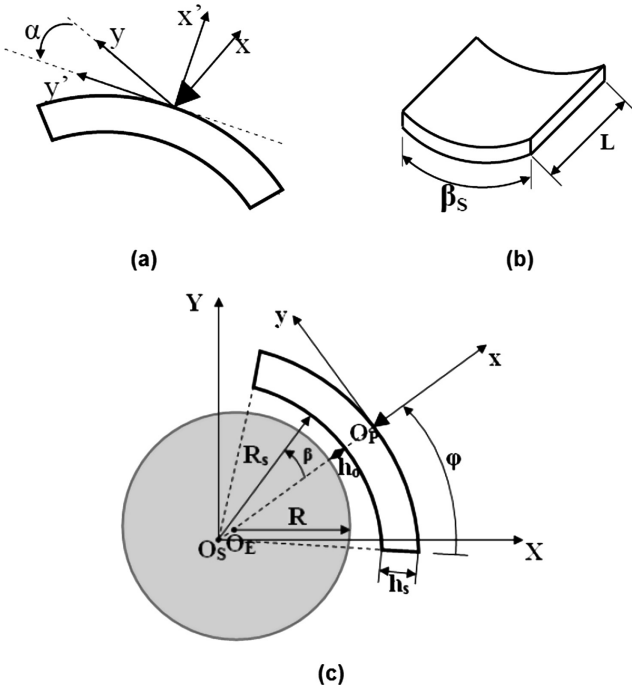


**Fig. 1.** Tilting pad journal bearing's main geometric characteristics. (a) Pad's frontal view; (b) pad's perspective view; (c) subsystem shaft-single pad. Source: adapted from [3].

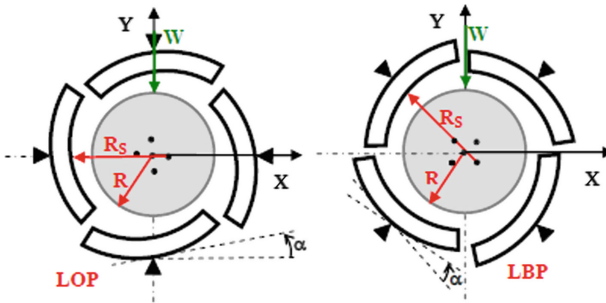


**Fig. 2.** Operating characteristics of a tilting pad journal bearing. Source: [3].

**Hydrodynamic Lubrication Modelling.** Tilting pad journal bearings are considered operating under hydrodynamic lubrication condition and, thus, it can be modelled by the Classical Reynolds equation as follows

$$\frac{\partial}{\partial x} \left( h^3 \frac{\partial p}{\partial x} \right) + \frac{\partial}{\partial z} \left( h^3 \frac{\partial p}{\partial z} \right) = 6\mu U \frac{\partial h}{\partial x} + 12\mu \frac{\partial h}{\partial t} \tag{1}$$

where  $p$  is the pressure field,  $h$  is the film thickness distribution,  $\mu$  is the dynamic viscosity and  $U$  is the relative velocity between the shaft and the bearing. The Finite Volume Method (FVM) is applied to numerically solve the Eq. (1), transforming the differential equation in a system of linear equations that is then solved through the Gauss-Seidel method. Finally, the shaft’s equilibrium position inside the bearing can be obtained coupling the algorithm that solves the pressure field with the Newton-Raphson algorithm, in which the shaft’s eccentricity and the pads angular position are obtained for each rotational speed and load.

**Dynamic Coefficients.** Once the shaft’s equilibrium position inside the tilting pad journal bearing is obtained the stiffness and damping equivalent coefficients can be determined in a linear form applying perturbations (displacement and velocity) around the respective equilibrium position. For each subsystem shaft-single pad, which are denoted by the sub index  $j = 1, 2, \dots, N$  with  $N$  being the number of pads, is possible to establish local stiffness and damping matrices according to a first order Taylor series approximation as follows [2]

$$\begin{Bmatrix} \Delta F_{x'} \\ \Delta F_{y'} \\ \Delta M \end{Bmatrix}_j = \underbrace{\begin{bmatrix} k_{x'x'} & k_{x'y'} & k_{x'\alpha} \\ k_{y'x'} & k_{y'y'} & k_{y'\alpha} \\ k_{\alpha x'} & k_{\alpha y'} & k_{\alpha\alpha} \end{bmatrix}_j}_{K'_j} \begin{Bmatrix} \Delta x' \\ \Delta y' \\ \Delta \alpha \end{Bmatrix}_j + \underbrace{\begin{bmatrix} c_{x'x'} & c_{x'y'} & c_{x'\alpha} \\ c_{y'x'} & c_{y'y'} & c_{y'\alpha} \\ c_{\alpha x'} & c_{\alpha y'} & c_{\alpha\alpha} \end{bmatrix}_j}_{C'_j} \begin{Bmatrix} \Delta \dot{x}' \\ \Delta \dot{y}' \\ \Delta \dot{\alpha} \end{Bmatrix}_j \quad (2)$$

where  $\Delta F_{x'}$ ,  $\Delta F_{y'}$  and  $\Delta M$  are the forces and moment that arise on the respective directions of the  $x'y'$  single pad local coordinate system due to the perturbations in displacement ( $\Delta x'$ ,  $\Delta y'$  and  $\Delta \alpha'$ ) and velocity ( $\Delta \dot{x}'$ ,  $\Delta \dot{y}'$  and  $\Delta \dot{\alpha}'$ ) imposed on the respective directions. As result can be calculated in the respective local coordinate system the stiffness  $K'_j$  and damping  $C'_j$  matrices for the studied subsystem shaft-single pad.

After an adequate coordinates transformation from the respective local coordinate system  $x'y'$  to the inertial coordinate system  $XY$ , the resulting  $K_j$  and  $C_j$  matrices relative to each pad can be composed in order to obtain the global stiffness  $K_{global}$  and damping  $C_{global}$  matrices of order  $N + 2$ .

However, according to [2] these tilting pad journal bearing’s global stiffness and damping matrices can have their order reduced to the number of shaft’s degrees of freedom  $e_x$  and  $e_y$  which refer to the shaft’s displacements in both  $X$  and  $Y$  directions, respectively, in order to obtain equivalent stiffness and damping matrices for the component. This reduction applied to the coefficients can be considered synchronous or non-synchronous, depending on the frequency assumed. In this work, the synchronous reduction is assumed and the following equation is obtained as described [2, 4]

$$[S(\gamma)]_{2 \times 2} = [(\gamma C_{uu} + K_{uu}) - G_{uu}] \quad (3)$$

with

$$G_{uu} = (\gamma C_{ux} + K_{ux})(\gamma^2 J_P + \gamma C_{xx} + K_{xx})^{-1}(\gamma C_{xu} + K_{xu}) \tag{4}$$

where  $S(\gamma)$  is an impedance matrix,  $\gamma$  is the natural damped frequency,  $J_P$  is the inertia moment matrix for the pads,  $C_{uu}$  and  $K_{uu}$  are damping and stiffness matrices, respectively, relative to the shaft's degrees of freedom,  $C_{xx}$  and  $K_{xx}$  are damping and stiffness matrices, respectively, relative to the pad's rotational degree of freedom and  $C_{ux}$ ,  $C_{xu}$ ,  $K_{ux}$  and  $K_{xu}$  are damping and stiffness matrices, respectively, relative to the cross-coupled terms. Finally, the stiffness and damping coefficients matrices for the tilting pad journal bearing are obtained from the impedance matrix  $S(\gamma)$  as follows

$$\begin{aligned} [K(\gamma)]_{2 \times 2} &= Re\{[S(\gamma)]_{2 \times 2}\} \\ [C(\gamma)]_{2 \times 2} &= Im\left\{\frac{1}{\gamma}[S(\gamma)]_{2 \times 2}\right\} \end{aligned} \tag{5}$$

### 2.2 Rotordynamics

A rotating system can be composed of different types of components, each one responsible for a function or effect in its operation. For this work, it was proposed the use of a rotor composed of shaft element, disc element and bearings in the simulations, since they are already consolidated modeling elements in the literature and can approach well the dynamic behavior of the rotor. Figure 3 presents a scheme of a rotational system used as example.

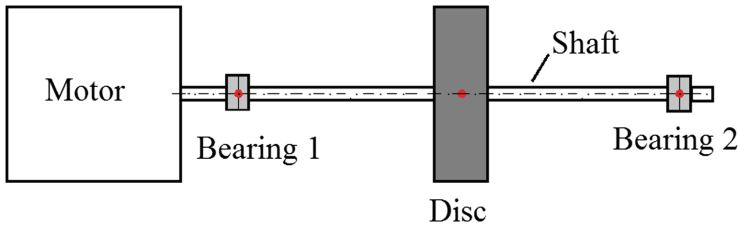


Fig. 3. Scheme of a general rotating system.

The main method used in the literature to model the components of a rotor is the Finite Element Method (FEM) which consists in the discretization of the global domain of the system in a finite number of elements with their respective characteristic matrices. The matrices used in this work to characterize the dynamic behavior of the rotor were the mass, stiffness, damping and gyroscopic matrices of each element. These matrices are responsible for indicating how the properties are distributed along the degrees of freedom of each element.

The degrees of freedom that characterize each node refers to the translation in the directions  $y$  and  $z$ , and bending rotation in the  $y$  and  $z$ -axes, as indicated in Eq. (6).

$$\{q\} = \{e_y, e_z, \theta_y, \theta_z\}^T \tag{6}$$

In the present work, the matrices proposed in [5] are used for the characterization of the shaft and disc elements. In [5], the authors show the methodology used for the deduction and construction of each of the matrices for these elements, and it has been used in the literature for discretization of the rotors by FEM.

The effects of the bearings are included in the system by both stiffness and damping matrices in the respective degrees of freedom in which they are located. The methodology used for the construction of these matrices was discussed in Sect. 2.1.

The assembly of the elements of shaft, disc and bearing for the construction of the model that represents the rotating system is done by associating the matrices of each element. This association is done by adding the matrices in their respective degrees of freedom, as shown in Fig. 4, allowing to obtain the global matrices of the system, being [M] the mass matrix, [K] the stiffness matrix, [C] the damping matrix and [G] the gyroscopic matrix.

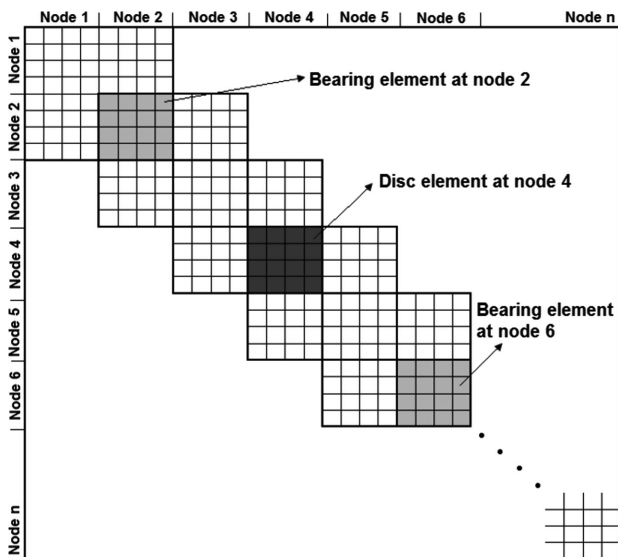


Fig. 4. Scheme indicating the construction of the global matrix. Source: adapted from [3].

The determination of the global matrices is fundamental for the analysis of the dynamic behavior of the rotor, since its characterization allows to obtain the system’s equation of motion, as showed in Eq. (7)

$$[M]\{\ddot{q}\} + ([C] + \Omega[G])\{\dot{q}\} + [K]\{q\} = \{F\} \tag{7}$$

where {F} indicates the vector of forces acting on the system. Writing this equation into state space, the dynamic matrix [A] of the system given by Eq. (8) can be obtained,

and this matrix leads to the determination of the Campbell’s diagram from its eigenvalues and the vibration modes from its eigenvectors.

$$[A] = \begin{bmatrix} [0] & \\ -[M]^{-1}[K] & -[M]^{-1}([C] + \Omega[G]) \end{bmatrix} \tag{8}$$

In this work was chosen to analyze the Campbell’s diagram, since it allows to determine the backward and forward modes of the system and the respective critical velocities. The gyroscopic effects of the rotating system and effects due to hydrodynamic lubrication are dependent on the rotational speed of the system, so for each speed of rotation, the dynamic matrix of the system takes a different form, and with that, it has different eigenvalues for each case. By analyzing the variation of each of these eigenvalues with the speed of rotation, it is possible to obtain the Campbell’s diagram, as schematized in Fig. 5.

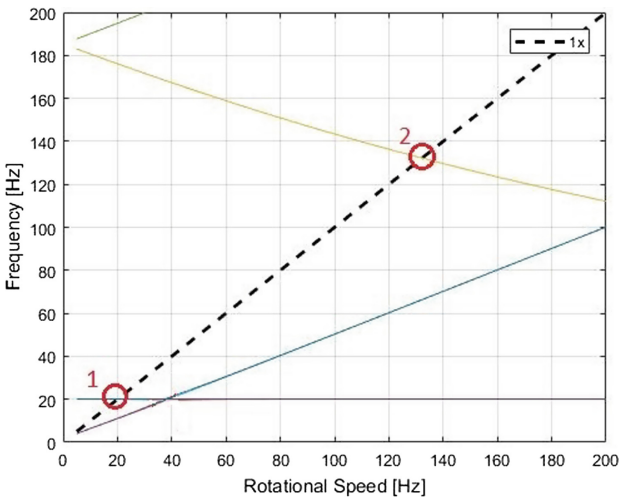


**Fig. 5.** Scheme of a Campbell’s diagram indicating some of the points of interest.

The detail shown in 1 in Fig. 5 shows the first crossing, which indicates the first critical speed of the rotor, backward and forward components. The detail indicated by 2 shows the second critical speed, in backward component. A computational code was implemented in MATLAB® in order to simulate the dynamic behavior of the rotating system.

### 2.3 Design of Experiments (DoE)

Any system, regardless the main physical principles that drive its behavior, may be studied through the statistical methodology named Design of Experiments in which more information is gathered during the experiment (or simulations), i.e., factors being

studied have their values changed not only separately but also simultaneously allowing the analysis for factors' interactions [6].

In the case of a full factorial design where three factors (A, B and C) each one varying between two levels or values (low (-) and high (+)) are studied, the possible combinations of the factors' levels also known as treatments may be written in a design matrix as shown in Fig. 6. In this case, the number of tested combinations is  $2^3 = 8$ .

Run	Factor		
	A	B	C
1	-	-	-
2	+	-	-
3	-	+	-
4	+	+	-
5	-	-	+
6	+	-	+
7	-	+	+
8	+	+	+

**Fig. 6.** Design matrix for the  $2^3$  factorial design.

The main effects, interaction effects and Pareto plots can be obtained from the collected values of the system's responses of interest for each run. The following analysis of the main effects and interaction plots allow to determine whether the factors' interactions are relevant instead of the respective main effects for the analyzed response. The Pareto plot analysis indicates the contribution of each studied factor on the observed variability of the respective response.

The software HEEDS® was used in order to obtain an automated execution of the DoE runs and also for post-processing of the results. Thus, the computational codes that emulate the rotordynamics behavior and tilting pad journal bearings dynamic coefficients characterization were integrated to the mentioned proprietary software.

### 3 Results and Discussions

Computational simulations are performed in order to verify the influence of the bearing's parameters on the dynamic behavior of the rotor through the DoE methodology. For this, the model of a steam turbine is built by FEM, as presented in Fig. 7. Table 1 shows the discretization details adopted in this steam turbine model, while the Table 2 shows the tilting pad bearing's parameters. Finally, it is important to mention that the steam turbine represented in the model has a nominal operating speed of 7500 rpm.



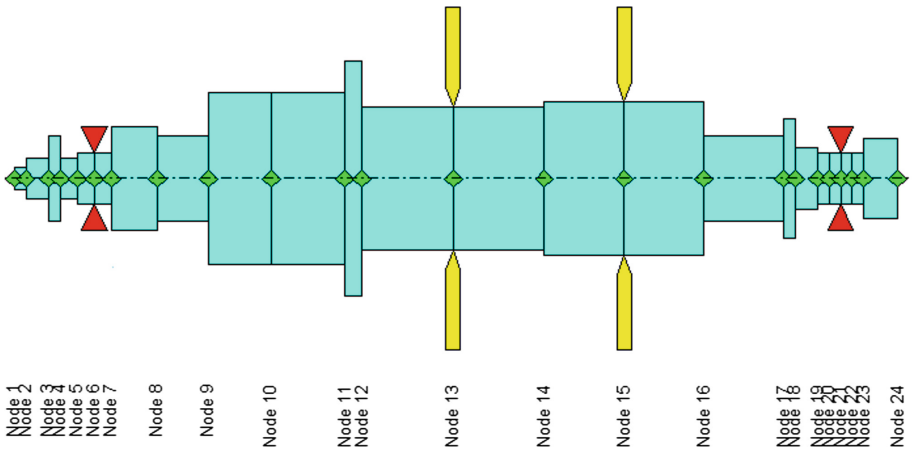


Fig. 7. Rotating system finite element model.

Table 1. Finite element model from the rotating system given in Fig. 6.

Element	Diameter [mm]	Length [mm]	Element	Diameter [mm]	Length [mm]
1	62	31	13	389	249
2	109	62	14	420	218
3	233	31	15	420	218
4	109	47	16	233	218
5	140	47	17	327	31
6	140	47	18	171	62
7	280	124	19	140	31
8	233	140	20	140	31
9	467	171	21	140	31
10	467	202	22	140	31
11	638	47	23	218	93
12	389	249			

Table 2. Tilting pad journal bearing parameters.

Parameter	Value
Viscosity SAE 10 20 °C [mPa s]	94.22
Diameter [mm]	140
Length [mm]	79.94
Radial Clearance [μm]	210

It is possible to notice that the bearings are located at the nodes numbered as 6 and 21 and each one of them possess 4 pads operating under LBP. A mesh with number of volumes equal to  $N_x = N_z = 47$  was established for each pad, after a grid density and

convergence study. The discs positioned at the nodes numbered as 13 and 15 have equal dimensions with outer diameter  $D_o = 933$  mm and length  $L = 40$  mm and unbalance momentum  $\eta\zeta = 178.5 \cdot 10^{-6}$  kg m.

The dynamic behavior of the rotating system, i.e. its critical speeds, is studied through the DoE methodology in order to evaluate the tilting pad bearing's geometric parameters sensitivity regarding the aforementioned dynamic responses from the rotor system. The chosen factors for the study are pad's width  $L_S$ , bearing's radial clearance  $h_0$  and pivot offset  $\gamma$ . The bearings' pre-load  $m$  was not considered as a DoE factor due to its dependence relative to the radial clearance  $h_0$ . The analyzed responses are the critical speeds on the range of rotational velocities varying from 3000 rpm to 15720 rpm, which was chosen according to the maximum value of the second critical speed encountered in the study. Once the evaluated problem is related to the rotor resonance condition, only the critical speeds evaluation was performed, i.e. stability analysis taking into account the damping factor was not performed. Moreover, the approach used in the present study considers the reduced coefficients for tilting pad bearings according to proposed in API, although some research studies indicate that critical speed analysis could be made more precisely through a full coefficients approach [7, 8].

In Table 3 is given the simulated design matrix which shows the adopted levels' values for each factor and their simulated treatments as well as the respective results.

**Table 3.** Design matrix and respective simulation results.

Run	$L_S$ [mm]	$C_r$ [ $\mu\text{m}$ ]	$\gamma$ [°]	1 <sup>st</sup> Mode		2 <sup>nd</sup> Mode	
				Backward	Forward	Backward	Forward
1	79.92	210	0.55	55.8393	55.9921	124.7157	167.2218
2	87.91	210	0.55	57.3105	57.4922	137.8574	190.6576
3	79.92	221	0.55	54.0170	54.1580	115.2117	151.3305
4	87.91	221	0.55	54.9010	55.0631	124.9907	169.6614
5	79.92	210	0.60	58.7217	58.8767	146.5648	200.2400
6	87.91	210	0.60	61.5322	61.7270	166.8474	231.9998
7	79.92	221	0.60	56.1782	56.3148	132.5656	178.4441
8	87.91	221	0.60	58.1498	58.3135	148.8890	205.1168

A Campbell's diagram of the rotating system is showed in Fig. 8 for the Run 1 in which the first and second critical speeds can be achieved. The critical speeds showed as responses for the respective DoE treatments are obtained from the intersection points between the natural frequencies curves and the 1x line in Campbell's diagram.

The aim is to explore which are the best and worst combinations of factors' levels in order to allow the rotating machine's operational condition to stay safely far from both the second backward and forward modes.

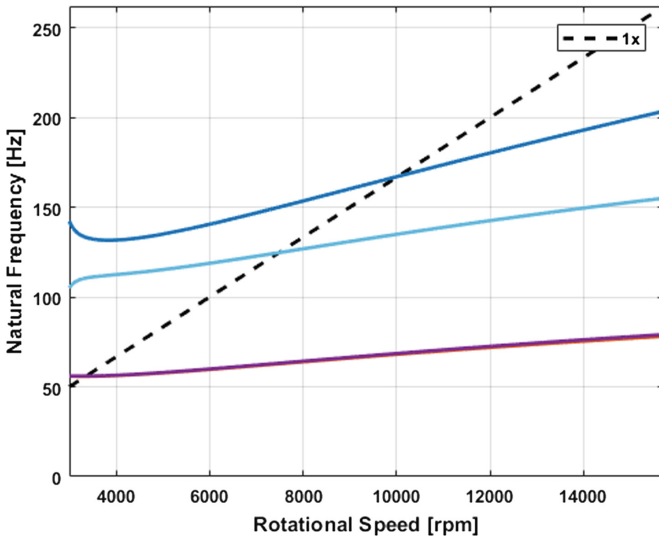


Fig. 8. Campbell's diagram for Run 1.

Figure 9 shows the resulting Pareto plot in order to verify the percent contribution of each factor on the observed full variability of the respective responses.

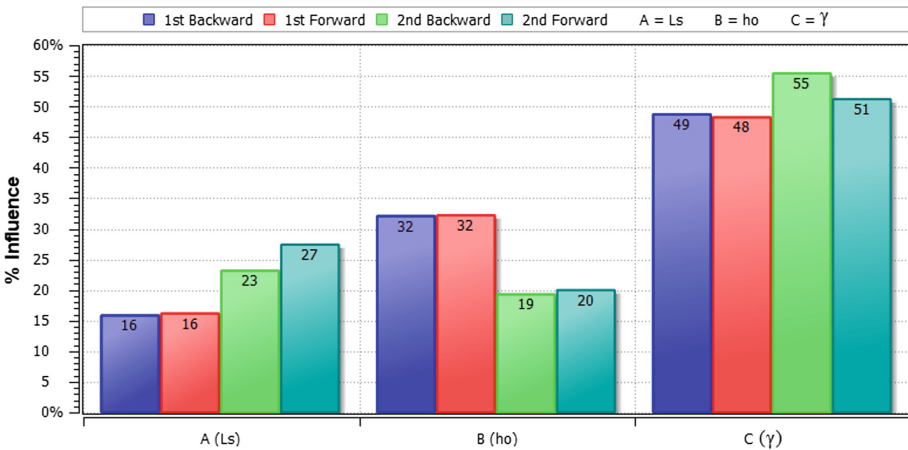


Fig. 9. Pareto plot.

According to the analyzed response, the factors' contributions are different and the pivot position  $\gamma$  (pivot offset) has the greater contributions on system's response variability in all cases. As can be seen in Fig. 9 the first backward and forward modes are more influenced by the radial clearance  $h_o$  and pivot on pad  $\gamma$  with approximately 32% and 48% of the total contribution, respectively. However, the pad's width  $L_S$

becomes an expressive contributor to the observed variability on the second backward and forward modes with 23% and 27%, respectively. Thus, all the three studied factors have great influence on the values of the second critical speed.

Table 3 shows that the first backward and forward modes have their values varying in a low range, but the opposite occurs with the variation seen in the second backward and forward modes. Figures 10(a) and (b) show the main effects graphs for both second backward and forward modes, respectively. It's noteworthy that radial clearance  $h_o$  tends to reduce the respective response value when varying from its low to high levels. However, pad's width  $L_S$  and pivot offset  $\gamma$  have the opposite behavior when varying from their respective low to high levels.

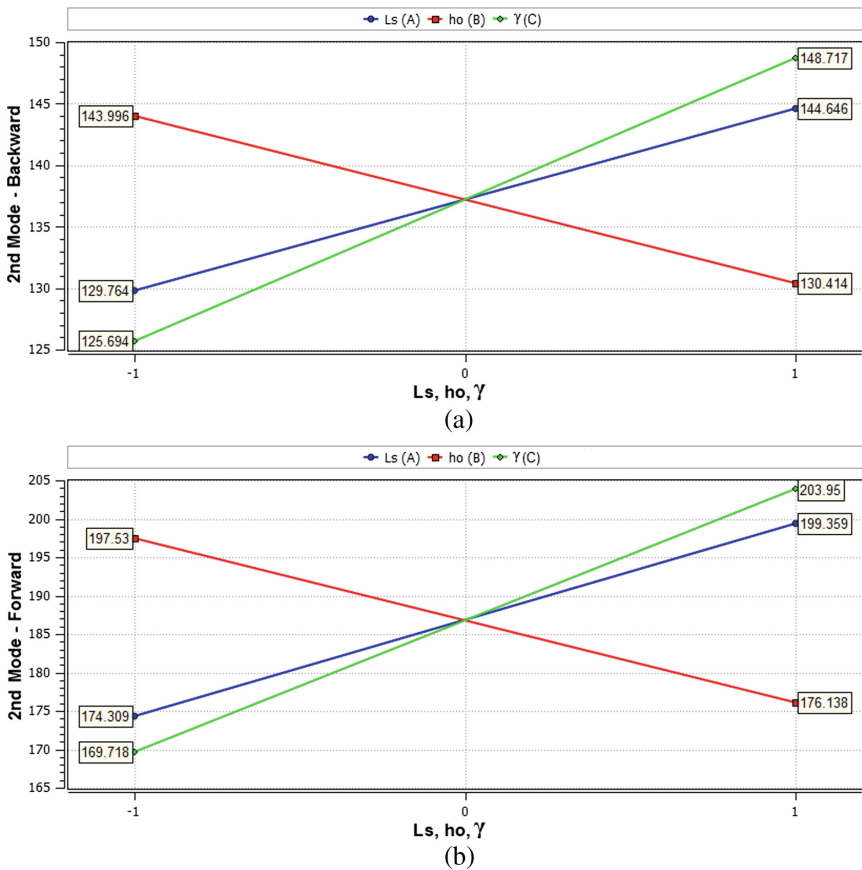
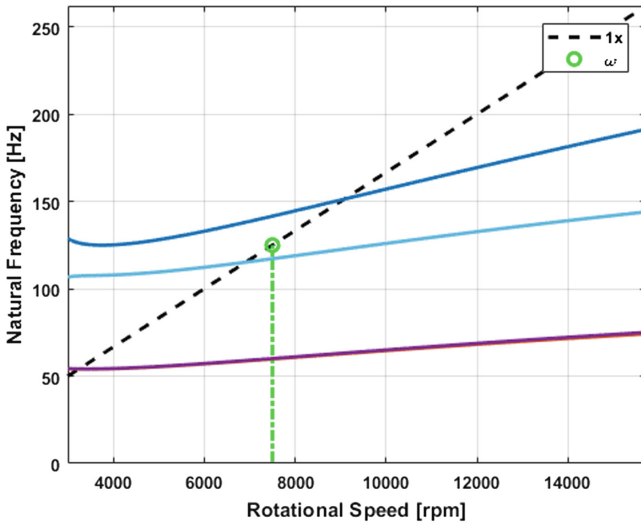
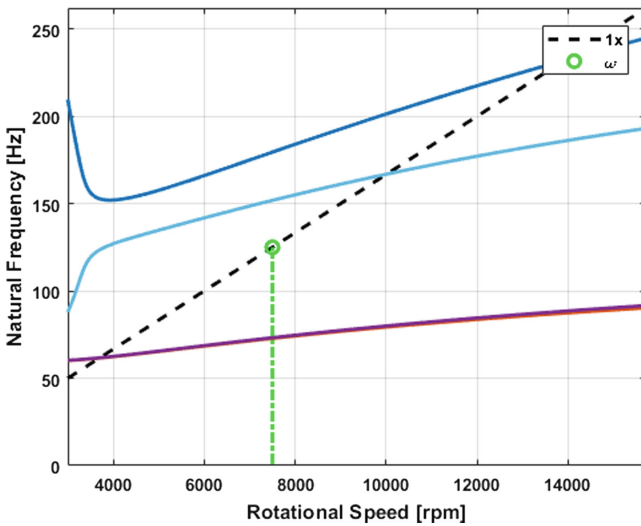


Fig. 10. Main effects graphs for the second: (a) backward mode; (b) forward mode.

Once increasing the radial clearance turns the gap between shaft and bearing surfaces greater, thus the load capacity is reduced and the stiffness equivalent coefficients for the tilting pad bearings become lower. In this sense, both backward and forward



(a)



(b)

**Fig. 11.** Campbell's diagram for (a) Run 3; (b) Run 6.

modes have their respective values reduced. The pad's width increases the bearings surfaces generating greater values of load capacity as well for the stiffness equivalent coefficients and thus elevates both backward and forward modes.

Therefore, becomes clear in which way each studied factor can influence on the critical speeds, especially for the second one. Once the rotating system operates at the speed  $\omega = 7500$  rpm is necessary to design the equipment to not achieve the second backward and forward modes and an adequate choice for the tilting pad geometric

parameters should be sufficient for that, since their respective influences on that response are well known through the DoE methodology and for the proposed factors' levels ranges.

Figures 11(a) and (b) show Campbell's diagram for both Runs 3 and 6 whose results are shown in Table 3. It can be seen that an inadequate choice for the tilting pad bearings geometric parameters, as occurred for the Run 3 where radial clearance assumes its highest value, makes the machine to operate close to the second critical speed. In this case, the percentage differences between the steam turbine's operating speed  $\omega = 125$  Hz and the second backward and forward modes are  $-7.83\%$  and  $+21.06\%$ , respectively, considering  $\omega$  as the reference value for percentage deviations calculation.

On the other hand the choice for high values of pad's width  $L_S = 87.91$  mm and pivot offset  $\gamma = 0.60$  results in both second backward and forward modes sufficiently greater than the operational speed. So, the rotating machine doesn't pass through those vibration modes and can achieve more safely the steady state condition. In this case, the percentage differences between the steam turbine's operating speed  $\omega = 125$  Hz and the second backward and forward modes are  $+33.47\%$  and  $+85.60\%$ , respectively, considering  $\omega$  as the reference value for percentage deviations calculation.

Therefore, it's highly recommended that the chosen tilting pad bearings geometric parameters values are  $L_S = 87.91$  mm,  $C_r = 210$   $\mu$ m and  $\gamma = 0.60$  whose values were obtained by a DoE analysis in order to achieve a safer operation of the rotating system. Notice that the manufacturing and assembly of tilting pad bearings should have special attention on the values of the studied factors since that low deviations from the baseline design values for those parameters can compromise the rotary system's performance.

## 4 Conclusions

The parametric sensitivity analysis can be an important design tool to explore the design space, in sense, first to identify design parameters with direct effect on the response studied, and its interaction in the set of parameters.

In this work, the results indicated that geometric parameters or factors contributions are different and that the pivot offset given by the ratio  $\gamma$  has the greater contributions on system's response variability in all cases. The results for first backward and forward modes are more influenced by the radial clearance  $h_o$  and pivot offset on pad  $\gamma$  with approximately  $32\%$  and  $48\%$  of contribution, respectively. However, for the second backward and forward modes the pad's width  $L_S$  becomes an expressive contributor to the observed variability on such responses with  $23\%$  and  $27\%$  of contribution, respectively. Thus, all the three studied factors have great influence on the second critical speed.

In this way, through a correct choice of the tilting pad journal bearings geometric parameters is possible to change the rotating system's critical speeds values in order to ensure a safer operating condition. Moreover, it's possible to establish manufacturing limits and assembly tolerances for the component's geometric parameters that have greater parametric sensitivities regarding the response of interest.

**Acknowledgements.** The authors would like to acknowledge the grants 2015/20036-5, 2015/20363-6 and 2016/20975-4, São Paulo Research Foundation (FAPESP).

## References

1. Urbiola-Soto, L., et al.: Rotordynamic optimization of fixed pad journal bearings using response surface design of experiments. *ASME. J. Eng. Gas Turbines Power* **138**(12) (2016). 10p
2. Dimond, T., Younan, A., Allaire, P.: A review of tilting pad bearing theory. *Int. J. Rotating Mach.* **2011**, 23 (2011)
3. Daniel, G. B.: Development of a thermohydrodynamic model for analysis in tilting pad journal bearings. Doctoral Thesis – State University of Campinas (2012)
4. Allaire, P.E., Parsell, J.A., Barret, L.E.: A pad perturbation method for the dynamic coefficients of tilting pad journal bearing. *Wear* **72**, 29–44 (1981)
5. Nelson, H., McVaugh, J.: The dynamics of rotor-bearing systems using finite elements. *J. Eng. Ind.* **98**(2), 593–600 (1976)
6. Montgomery, D.C.: *Design and Analysis of Experiments*, 5th edn. Wiley, New York (2001)
7. Dimond, T.W., Younan, A.A., Allaire, P.: Comparison of tilting-pad journal bearing dynamic full coefficient and reduced order models using modal analysis (GT2009-60269). *J. Vib. Acoust.* **132**(5), 051009 (2010)
8. Wilkes, J.C., Childs, D.W.: Tilting pad journal bearings—a discussion on stability calculation, frequency dependence, and pad and pivot. *J. Eng. Gas Turbines Power* **134**(12), 122508 (2012)



# Analysis of Analytical Hydrodynamic Bearing Models on a Reciprocating Compressor

Eduardo Paiva Okabe<sup>1</sup>(✉), Jaime Hideo Izuka<sup>1</sup>, and Reinhard Resch<sup>2</sup>

<sup>1</sup> School of Applied Sciences, University of Campinas - UNICAMP,  
PO Box 1068, Limeira, Brazil

{eduardo.okabe,jaime.izuka}@fca.unicamp.br

<sup>2</sup> Nidec Global Appliance Austria GmbH, Jahnstraße 30, 8280 Fürstenfeld, Austria  
reinhard.resch@mail.nidec.com

**Abstract.** Reciprocating compressors are one of the most common machines, as they are usually found in household refrigerators and air conditioners. The reciprocating compressor is a rotor-crankshaft-piston machine supported by lubricated bearings. They are sealed to retain and store the refrigerating gas, therefore, the maintenance of the compressor is difficult and expensive. Thus reciprocating compressors should be designed to last the life span of the appliance. Most models of reciprocating compressors considers rigid bearings, which completely neglects the influence of the hydrodynamic bearings on the dynamic behavior of the compressor. This work shows the modeling and analysis of a reciprocating compressor with flexible bearings. The rotor which is part of the motor is supported by a pair of hydrodynamic bearings that are modeled using three different analytical models: Capone, Vance and Butenschön. Analytical models of bearing are much faster than numerical ones, such as the ones that use the finite difference (FDM) or finite element method (FEM). The three models have different approaches to solve the Reynolds equation and, therefore, distinct results were found using each one of them. The model was developed in the OpenModelica software using the elements of the Mechanics.Multibody library. The Butenschön model was implemented in C and Fortran 95 and integrated to OpenModelica as an external library.

**Keywords:** Hydrodynamic bearing · Analytical models  
Reciprocating compressor

## 1 Introduction

Reciprocating compressors are one of the most common machines, and they are usually found in household refrigerators and air-conditioners. They are usually rotor-crankshaft-piston machines supported by lubricated bearings. They are sealed to retain and store the refrigerating gas, therefore, their maintenance is



difficult and expensive. Thus reciprocating compressors must be designed to last the life span of the appliance.

Most models of the reciprocating compressor consider rigid bearings, which completely neglects the influence of the hydrodynamic bearings on the dynamic behavior of the compressor.

This work shows the modeling and analysis of a reciprocating compressor with flexible bearings. The rotor which is part of the motor is supported by a pair of hydrodynamic bearings that are modeled using three different analytical models: Capone, Vance and Butenschön.

Hydrodynamic bearings are modeled using the Reynolds equation for a thin film lubrication. There are several approaches to solve this equation. For instance, Kim [10] used the Reynolds equation along with the finite bearing approach to model the lubrication between piston and cylinder of a reciprocating mechanism. This formulation was also applied to the journal bearings. The author concluded that smaller piston clearances yield a stable trajectory, and the increase of the viscosity or inertia of the crankshaft improved its stability. Kim and Han [11] compared finite and short bearing models. Although the dimensions of the main (primary) bearing were not in the range of a short bearing model, the results were similar and they concluded that the finite model yielded a lower pressure with greater power consumption.

Campbell et al. [3] reviewed the research on lubricated bearings of reciprocating machinery. They compared analytical and numerical bearing models to experimental data acquired from the eccentric bearing; this bearing links the connecting rod to the crank. The finite bearing models presented a better approximation, but the orbits obtained by the short and finite bearing were quite similar to each other.

Bukovnik et al. [1] compared several bearing models in the simulation of crankshaft and connecting rod bearings of a combustion engine. The result showed that Butenschön model can be applied when a medium accuracy and short simulation times are needed. It also provided a good approximation for the oil flow in the crankshaft bearings.

Estupiñan and Santos [7] presented a detailed model of a hermetic compressor using multibody dynamics and hydrodynamic bearings. They analyzed the dynamic behavior of the compressor using short and long bearing models, and the maximum pressure estimated by the long bearing was significant lower than the short one, which can be explained by the fact that the simulated bearing dimensions were closer to the short model, which they further adopted. In another work [6], they compared both models (short and long) to the finite bearing solved with finite differences. Their results show that the orbits and maximum pressure calculated using the short bearing model were pretty similar to the finite bearing.

Kurka et al. [12] modeled a reciprocating compressor with viscoelastic bearings and analyzed their influence on the dynamic behavior of the compressor. The authors compared the loads using rigid and flexible bearings; the RMS load values were pretty close to each other although the forces were very different

values during the cycle. They concluded that a hydrodynamic bearing model could provide a more realistic result.

Yang et al. [17] used a modified Reynolds equation to model the friction loss at the interface piston-cylinder of reciprocating compressor. They employed a regression method to determine the friction loss in the crankshaft bearings. They concluded that the friction loss in these bearings decreases as the stroke-to-bore ratio increases, due to the smaller diameter of the cylinder which results in a smaller force exerted on the piston.

Analytical bearing formulations are still used in the modeling of rotating machinery. Although these models are less accurate, they are much faster to calculate. Okabe and Masarati [14] employed the formulation developed by Capone et al. [4] in the model of wind turbine gearbox. Cavalini et al. [5] used the same model to determine dynamic response of a rotor with stochastic parameters. Okabe [13] include the fluid film inertia on an analytical model of a tilting pad bearing and simulated it under several conditions. The results were similar to a numerical finite bearing model.

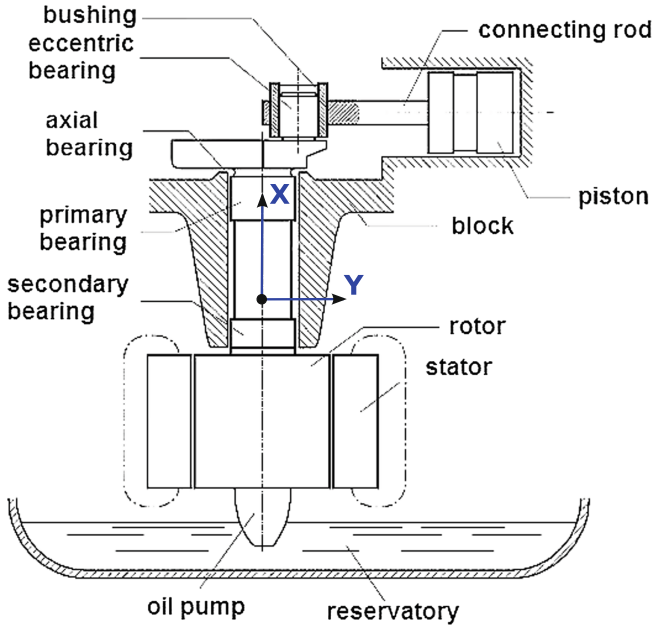


Fig. 1. Side view of the reciprocating compressor (adapted from [12]).

## 2 Methodology

A reciprocating compressor can be modeled as a mechanism composed by three parts: piston, connecting rod and rotor. These parts can be represented as rigid

bodies in a multibody system. The OpenModelica [8] is an open source software based on the Modelica language, and it has the Mechanics.Multibody library [15], which is capable of modeling of multibody systems with basic components such as rigid bodies, joints and forces.

Due to the the open source nature of OpenModelica it is possible to create new elements and libraries, that can be written in C++, Fortran or Modelica. This feature allows the use of a model that is fully functional and tested, to be introduced into the framework of OpenModelica and integrate it to multiphysics systems.

OpenModelica is based on the solution of Differential Algebraic Equation (DAE) systems. These systems can be overdetermined, which means that they have more equations than variables.

They can be described as [15]:

$$\mathbf{f}(\dot{\mathbf{x}}, \mathbf{x}, \mathbf{y}, t) = \mathbf{0} \quad (1)$$

where  $\mathbf{x}$  is the vector of the variables that are differentiated,  $\mathbf{y}$  is the vector of the algebraic variables,  $t$  is the time and the dot ( $\dot{\cdot}$ ) represents the time derivative. The connection between elements in the multibody library are performed by an entity denominated *Frame*.

The *Frame* defines a reference system attached to a component, that can be either a body or a joint. Inside of its structure it has the relative position from the world/absolute reference, the orientation matrix, the angular velocity, and forces and moments applied to the *Frame*. It is the connection of the two or more *Frames* that creates the overdetermined system of equations.

The equations associated to the rigid body (*Part*) are:

$$\begin{aligned} m_{body}(\mathbf{a} + \dot{\boldsymbol{\omega}}^a \times \mathbf{r}^{CM} + \boldsymbol{\omega}^a \times (\boldsymbol{\omega}^a \times \mathbf{r}^{CM})) &= \mathbf{f}^a \\ \mathbf{I}_{body} \dot{\boldsymbol{\omega}}^a + \boldsymbol{\omega}^a \times \mathbf{I}_{body} \boldsymbol{\omega}^a + \mathbf{r}^{CM} \times \mathbf{f}^a &= \boldsymbol{\tau}^a \end{aligned} \quad (2)$$

where  $m_{body}$  is the body mass,  $\mathbf{a}$  is the body acceleration,  $\boldsymbol{\omega}^a$  is the angular velocity of the *Frame a*,  $\mathbf{r}^{CM}$  is the the offset from *Frame a* to center of mass of the body,  $\mathbf{f}^a$  is the force applied to *Frame a*,  $\mathbf{I}_{body}$  is the moment of inertia matrix, and  $\boldsymbol{\tau}^a$  is the moment applied to *Frame a*.

Joints are defined by a set of algebraic equations that constrains the motion between two *Frames*. For instance, the revolute joint is defined by the following equations:

$$\begin{aligned} \mathbf{r}^b &= \mathbf{r}^a \\ \mathbf{R}^{rel} &= \mathbf{n} \otimes \mathbf{n} + (\mathbf{I} - \mathbf{n} \otimes \mathbf{n}) \cos \phi - [\mathbf{n} \times] \sin \phi \\ \mathbf{R}^b &= \mathbf{R}^{rel} \mathbf{R}^a \end{aligned} \quad (3)$$

where  $\mathbf{r}^a$  and  $\mathbf{r}^b$  are respectively the positions of *Frame a* and *Frame b*,  $\mathbf{R}^{rel}$  is the relative rotation matrix between the *Frames*, which is defined by unit direction vector  $\mathbf{n}$  and the angle  $\phi$ ,  $\mathbf{R}^a$  and  $\mathbf{R}^b$  are respectively the orientation matrices of *Frame a* and *Frame b*, and  $\mathbf{I}$  is the identity matrix.

In order to implement the hydrodynamic bearing into the reciprocating compressor model, it is necessary to get the relative motion between the bearing and the journal, calculate the hydrodynamic forces using the analytical expressions, and apply the forces to the bearing elements. The relative motion is calculated in the element *Sensor*, which encloses the following equations:

$$\begin{aligned}\mathbf{r}_{rel} &= \mathbf{R}_a^T(\mathbf{r}_b - \mathbf{r}_a) \\ \boldsymbol{\omega}_{rel} &= \mathbf{R}_a^T(\boldsymbol{\omega}_b - \boldsymbol{\omega}_a)\end{aligned}\quad (4)$$

where  $r_{rel}$  is the relative displacement between *Frame a* and *Frame b*, and  $\boldsymbol{\omega}_{rel}$  is the relative angular velocity. The linear velocity  $\dot{\mathbf{r}}_{rel}$  is calculated through the time derivative of  $\mathbf{r}_{rel}$ . The hydrodynamics forces are calculated in the local coordinates (bearing frame) and applied to both frames:

$$\begin{aligned}\mathbf{f}_a &= \mathbf{f}(\mathbf{r}_{rel}, \dot{\mathbf{r}}_{rel}, \boldsymbol{\omega}_{rel}) \\ \mathbf{f}_b &= -\mathbf{R}_b^T \mathbf{R}_a \mathbf{f}(\mathbf{r}_{rel}, \dot{\mathbf{r}}_{rel}, \boldsymbol{\omega}_{rel})\end{aligned}\quad (5)$$

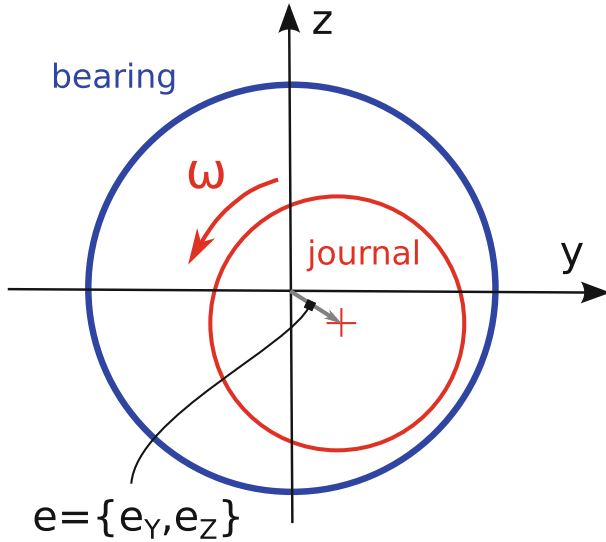


Fig. 2. Local coordinate system of the rotor bearings.

## 2.1 Bearing Models

Three analytical hydrodynamic models were tested in the compressor model: Capone, Vance and Butenschön. They have been adapted to consider the system of local coordinates shown on Fig. 2. The system is fixed at the center of the bearing, and the relative motion of the journal is used in the calculation of the hydrodynamic forces:

$$\begin{aligned} e_Y &= \mathbf{r}_{rel2} \\ e_Z &= \mathbf{r}_{rel3} \\ \omega &= \boldsymbol{\omega}_{rel1} \end{aligned}$$

The first model to be analyzed, the Capone model [4], is a development of the Ocvirk model (short bearing), and it includes the effect of the journal radial velocity (eccentricity speed) on the hydrodynamic forces:

$$\begin{aligned} \begin{Bmatrix} F_y \\ F_z \end{Bmatrix} &= -\text{So } r L \frac{\sqrt{(y - 2v_z)^2 + (z + 2v_y)^2}}{1 - y^2 - z^2} \cdot \\ &\begin{Bmatrix} 3y v_h - g_h \sin \theta - 2f_h \cos \theta \\ 3z v_h + g_h \cos \theta - 2f_h \sin \theta \end{Bmatrix} \end{aligned} \tag{6}$$

$$\begin{aligned} f_h &= \frac{y \cos \theta - z \sin \theta}{1 - (y \cos \theta - z \sin \theta)^2} \\ v_h &= \frac{2 + (z \cos \theta - y \sin \theta)g_h(\theta, y, z)}{1 - y^2 - z^2} \\ g_h &= \frac{2}{\sqrt{1 - y^2 - z^2}} \left( \frac{\pi}{2} + \tan^{-1} \frac{z \cos \theta - y \sin \theta}{\sqrt{1 - y^2 - z^2}} \right) \end{aligned}$$

where  $\text{So} = \frac{\eta \omega L^2}{4c^2}$  is the Sommerfeld number,  $\eta$  is the lubricant absolute (dynamic) viscosity,  $\omega$  is the angular speed of shaft,  $L$  is the bearing length,  $c = \frac{D-d}{2}$  is the bearing radial clearance,  $D$  and  $d$  are respectively the bearing and the journal diameter,  $r$  is the bearing radius,  $y = \frac{e_Y}{c}$  and  $z = \frac{e_Z}{c}$  are the dimensionless displacements of the journal on the  $y$  and  $z$ -axis,  $v_y = \frac{\dot{e}_Y}{c\omega}$  and  $v_z = \frac{\dot{e}_Z}{c\omega}$  are the dimensionless velocities of the journal,  $\theta = \text{atan2}(-z - 2v_y, -y + 2v_z)$  is the attitude angle.

The hydrodynamic forces of Capone bearing can be included in the compressor model using the following equation:

$$\mathbf{f}(\mathbf{r}_{rel}, \dot{\mathbf{r}}_{rel}, \boldsymbol{\omega}_{rel}) = \{ 0 \ F_y \ F_z \}^T \tag{7}$$

where  $\mathbf{f}$  is the vector of the forces in the bearing reference, and  $\mathbf{c}$  is the vector of the couples in the bearing reference.

The model proposed by Vance [16] is the cavitated ( $\pi$ -film) short bearing, which the radial and tangential forces can be calculated by:

$$\begin{aligned} F_r &= -\eta r L \left( \frac{L}{c} \right)^2 \left[ (\omega - 2\dot{\phi}) \frac{\varepsilon^2}{(1 - \varepsilon^2)^2} + \frac{\pi(1 + 2\varepsilon^2)\dot{\varepsilon}}{2(1 - \varepsilon^2)^{\frac{5}{2}}} \right] \\ F_t &= \eta r L \left( \frac{L}{c} \right)^2 \left[ (\omega - 2\dot{\phi}) \frac{\pi\varepsilon}{4(1 - \varepsilon^2)^{\frac{3}{2}}} + \frac{2\varepsilon\dot{\varepsilon}}{(1 - \varepsilon^2)^2} \right] \end{aligned} \tag{8}$$

where the attitude angle  $\phi$  and its velocity  $\dot{\phi}$  are calculated by:

$$\phi = \tan^{-1} \left( \frac{e_Z}{e_Y} \right) \quad (9)$$

$$\dot{\phi} = \frac{-\dot{e}_Y \sin \phi + \dot{e}_Z \cos \phi}{\sqrt{e_Y^2 + e_Z^2}}$$

and the dimensionless journal eccentricity  $\varepsilon$  and its velocity  $\dot{\varepsilon}$ :

$$\varepsilon = \frac{\sqrt{e_Y^2 + e_Z^2}}{c}$$

$$\dot{\varepsilon} = \frac{\dot{e}_Y \cos \phi + \dot{e}_Z \sin \phi}{c}$$

The forces of the Vance model can be calculated in the bearing local coordinates by:

$$\mathbf{f}(\mathbf{r}_{rel}, \dot{\mathbf{r}}_{rel}, \boldsymbol{\omega}_{rel}) = \begin{Bmatrix} 0 \\ F_r \cos \phi - F_t \sin \phi \\ F_r \sin \phi + F_t \cos \phi \end{Bmatrix} \quad (10)$$

Butenschön [2] based his solution of the Reynolds equation on a correction factor to account the finite width. Two Sommerfeld numbers are calculated relative to hydraulic wedge (So<sub>W</sub>) and fluid squeeze (So<sub>S</sub>):

$$\text{So}_W = a_1 \left( \frac{L}{D} \right)^2 \frac{|\varepsilon| - 1}{a_2 + |\varepsilon|} \cdot \frac{|\varepsilon| \sqrt{\pi^2 (1 - \varepsilon^2) + 16\varepsilon^2}}{2(1 - \varepsilon^2)^2} \quad (11)$$

$$\begin{aligned} \text{So}_S = 4a_8 (1 - \varepsilon^2)^{-\frac{5}{2}} \left( \frac{L}{D} \right)^2 \frac{\varepsilon - 1}{a_9 + \varepsilon} \left[ \left( \frac{\pi}{2} - \frac{1}{2} \arccos \varepsilon \right) (1 + 2\varepsilon^2) \right. \\ \left. + \frac{3}{2} \varepsilon \sqrt{1 - \varepsilon^2} \right] \quad (12) \end{aligned}$$

$$\beta = \arctan \frac{\pi \sqrt{1 - \varepsilon^2}}{2|\varepsilon|} \left( a_3 + a_4 |\varepsilon| + a_5 \varepsilon^2 + a_6 |\varepsilon|^3 + a_7 \varepsilon^4 \right) \quad (13)$$

where  $D$  is the bearing diameter,  $\varepsilon$  is the dimensionless journal eccentricity,  $\beta$  is the angle of the fluid squeeze. The sign of  $\varepsilon$  in Eqs. 11 and 12 is defined positive if  $\dot{\varepsilon}$  is positive and negative otherwise.

The coefficients  $a_i$  are:

$$\begin{aligned} a_1 &= 1.1642 - 1.9456\lambda + 7.1161\lambda^2 - 10.1073\lambda^3 + 5.0141\lambda^4 \\ a_2 &= -1.000026 - 0.023634\lambda - 0.4215\lambda^2 - 0.038817\lambda^3 - 0.090551\lambda^4 \\ a_3 &= 1.152624 - 0.104565\lambda \\ a_4 &= -2.5905 + 0.798745\lambda \\ a_5 &= 8.73393 - 2.3291\lambda \\ a_6 &= -13.3414 + 3.424337\lambda \\ a_7 &= 6.6294 - 1.591732\lambda \\ a_8 &= 0.70038 + 3.2415\lambda - 12.2486\lambda^2 + 18.895\lambda^3 - 9.3561\lambda^4 \\ a_9 &= -0.999935 + 0.0157434\lambda - 0.74224\lambda^2 + 0.42278\lambda^3 - 0.368928\lambda^4 \end{aligned} \quad (14)$$

where  $\lambda = \frac{L}{D}$ . The amplitude of the forces due to fluid squeeze and the hydraulic wedge are:

$$F_W = S_{oW} \frac{Ld\eta |\omega_r|}{\Psi^2} \tag{15}$$

$$F_S = S_{oS} \frac{Ld\eta \dot{\epsilon}}{\Psi^2} \tag{16}$$

where  $\eta$  is the dynamic viscosity,  $\Psi = 2\frac{c}{D}$  is the relative bearing clearance and the relative rotation speed  $\omega_r = \omega - 2\dot{\phi}$ .

The forces of the bearing can be calculated through:

$$\mathbf{f}(\mathbf{r}_{rel}, \dot{\mathbf{r}}_{rel}, \omega_{rel}) = \begin{Bmatrix} 0 \\ F_W \cos \alpha + F_S \cos \phi \\ F_W \sin \alpha + F_S \sin \phi \end{Bmatrix} \tag{17}$$

The angle  $\alpha$  determines the direction of the supporting force and it is the result of the rotational movement:

$$\alpha = \phi - \text{sign}(\omega_r)\beta \tag{18}$$

where  $\phi$  is attitude angle (Eq. 9) and  $\beta$  is the angle of the fluid squeeze (Eq. 13).

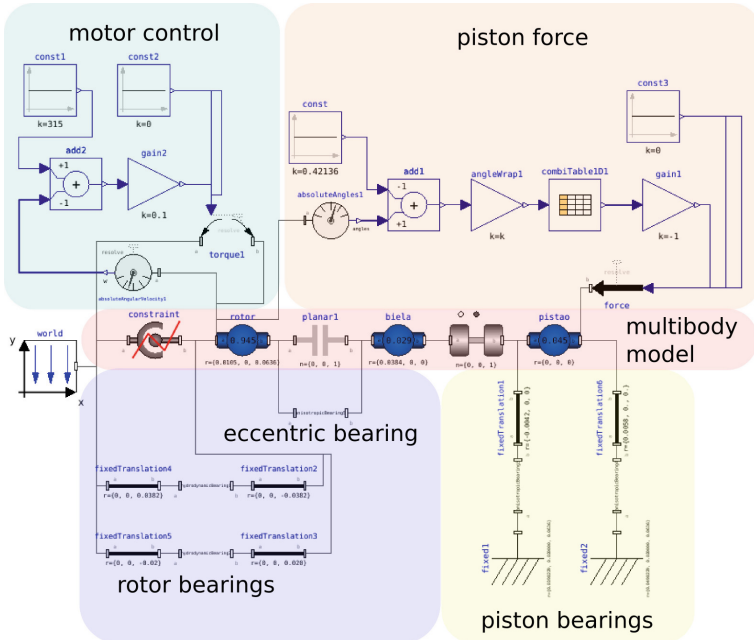


Fig. 3. Model of the compressor in the OpenModelica editor.

### 3 Compressor Modeling

The reciprocating compressor was modeled using the Mechanics.Multibody library of OpenModelica, which can be seen on Fig. 3. Its dimensions are based on the model presented by Kurka and Izuka [12].

The main parts of the model are:

- The piston, the connecting rod and the rotor (which includes the crank) were modeled as rigid bodies. There are several options to model rigid bodies in the multibody library, but the option that was most fitted to model these parts was the *BodyShape*, which has two frames;
- The rotor is supported by a pair of hydrodynamic bearings that were represented by the three analytical models presented in the previous section.
- Eccentric and piston bearing were represented by elements created in this work that were denominated *AnisotropicBearing*. This element gets the relative position, velocity, and angular velocity between two frames and applies a force calculated with stiffness and damping matrices. This force is applied in both frames.
- The electric motor was modeled as a torque, that is applied between the World frame and the rotor. The torque is calculated with a proportional control based on the rotor angular velocity.
- The piston force is interpolated from experimental data [12] through a *CombiTable1D*, which loads the data from a Matlab file into the compressor model.
- The bearing that connects the connecting rod to the piston is rigid and modeled as a revolute joint.

There are other two joints that complete the model: a joint that restricts the displacement of the rotor in the Z direction, and a planar joint that connects the rotor to the connecting rod. The parameters of the compressor model are presented in Table 1, and they follow the orientation presented on Fig. 1.

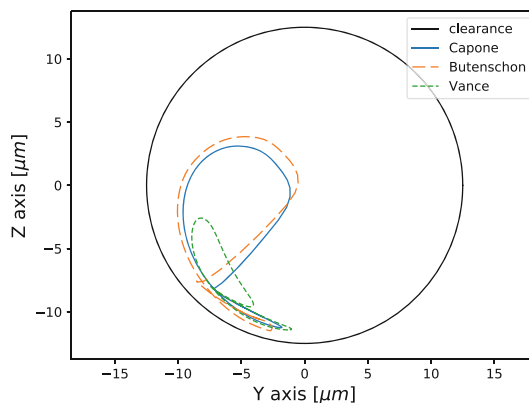


**Fig. 4.** Trajectory of the journal inside of the rotor primary bearing.



**Table 1.** Compressor model parameters.

Part	Parameter	Value
Rotor bearing	Radial clearance	12.5 $\mu\text{m}$
	Length	7.5 mm
	Diameter	15 mm
	Oil viscosity	28.5 $\text{mPa} \cdot \text{s}$
Eccentric bearing	$K_{yy}, K_{yz}, K_{zy}, K_{zz}$	$\{0.8, 4.8, -3.1, 1.6\} \cdot 10^8 \text{ N/m}$
	$C_{yy}, C_{yz}, C_{zy}, C_{zz}$	$\{4.0, 0.4, 0.4, 3.0\} \cdot 10^6 \text{ Ns/m}$
Piston bearing	$K_{xx}, K_{xy}, K_{yx}, K_{yy}$	$\{1.0, 0.0, 0.0, 1.0\} \cdot 10^7 \text{ N/m}$
	$C_{xx}, C_{xy}, C_{yx}, C_{yy}$	$\{6.0, 0.0, 0.0, 6.0\} \cdot 10^3 \text{ Ns/m}$
Rotor	mass	0.945 kg
	$I_{xx}, I_{xy}/I_{yx}, I_{yy}, I_{zz}$	$\{0.39, -0.01, 0.99, 0.99\} \cdot 10^{-3} \text{ kg m}^2$
Connecting rod	Mass	0.029 kg
	$I_{xx}, I_{yy}, I_{zz}$	$\{0.8, 0.85, 0.1\} \cdot 10^{-5} \text{ kg m}^2$
Piston	Mass	0.045 kg
	$I_{xx}, I_{yy}, I_{zz}$	$\{0.39, 0.33, 0.46\} \cdot 10^{-5} \text{ kg m}^2$

## 4 Results

The simulation is performed by accelerating the rotor to 315 rad/s (approximately 3000 rpm), and a proportional controller keeps the motor at this speed. The simulated time is two seconds with a time step of  $1 \times 10^{-4}$  s using the integration method DASSL. The rotor takes few tenths of a second to accelerate to its nominal speed, therefore, it does not take long to reach a regular motion. The computational time to simulate the compressor was pretty similar for all models. It was around 30 s on computer with a Core i7-2670 from which approximately 10 s were used to build and compile the model.

Figure 4 shows the trajectory of the journal inside of the primary bearing of the rotor, which is the one next to the connecting rod. The part of the trajectory which is close to the bearing clearance is related to the compression stroke, when the suction stroke starts the journal goes toward the center of the bearing, which is clearly demonstrated by Capone and Butenschön models and, in a lower scale, by the Vance model.

Another point to observe is the position of the orbits that are in the negative direction of both axes, due to the Z positive offset of the cylinder in relation to the center of the rotor. In the secondary bearing the journal's trajectories are in the opposite direction to the primary bearing's trajectories, which can be seen on Fig. 5. The position of the orbits can be associated to the rotor inclination, which was also found by Kurka et al. [12]. The primary bearing serve as a pivot to the rotor. The connecting rod is closer (25.4 mm) to the primary bearing than the secondary one (58.2 mm), and this means less force applied to the secondary bearing. This yields a motion of the journal further from the bearing

wall, however, the same patterns of the primary bearing during compression and suction strokes can be observed in the secondary bearing, where the tip of the orbit happens during the transition from compression to the suction.

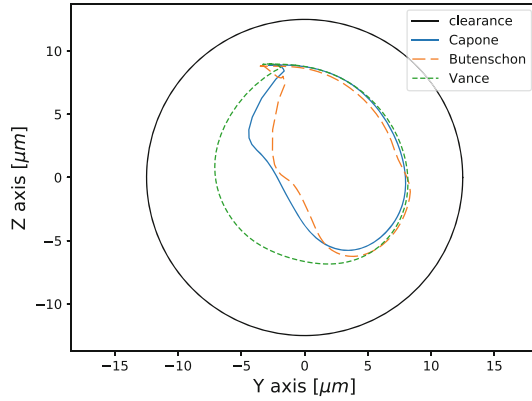


**Fig. 5.** Trajectory of the journal inside of the rotor secondary bearing.

The results presented in Figs. 4 and 5 are quite similar to the ones presented by Kim et al. [10,11], in which the primary bearing has a small orbit closer to the bearing wall and the secondary bearing has larger orbits closer to the center of the bearing.

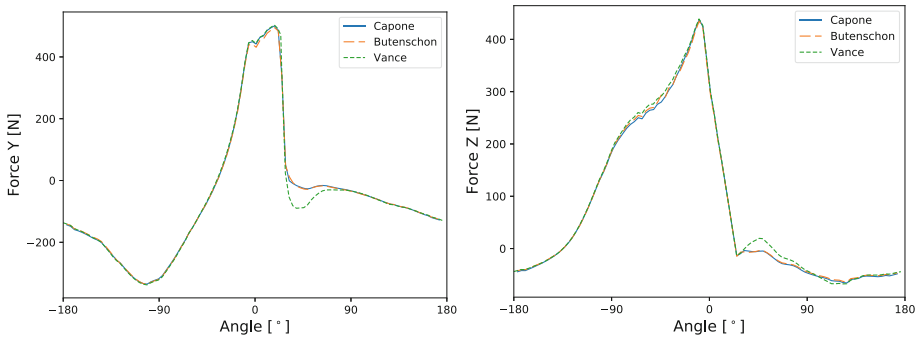


**Fig. 6.** Forces applied to the journal of the primary bearing (Y axis - left, Z axis - right).

Although the trajectories are quite different between Vance and other models, the hydrodynamic forces presented in Fig. 6 of the primary bearing are similar to each other, with the exception of one small segment approximately at  $45^\circ$ . The forces generated by the bearings counteract the pressure exerted on the piston,

and that is the main reason the force in the Y direction becomes negative during suction and positive during compression.

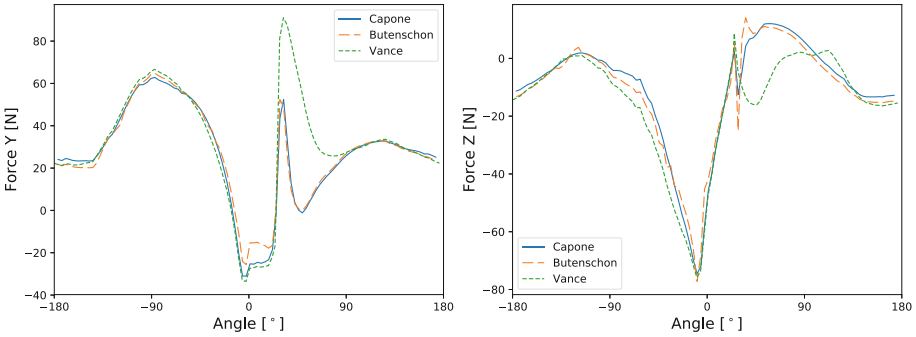


**Fig. 7.** Forces applied to the journal of the secondary bearing (Y axis - left, Z axis - right).

Figure 7 shows the hydrodynamic forces applied in the secondary bearing. The magnitude is lower than the primary bearing, which was previously observed in Fig. 5. Nevertheless, the differences between Vance and the other model are much bigger in the same region of the discrepancy in the primary bearing (Fig. 6).

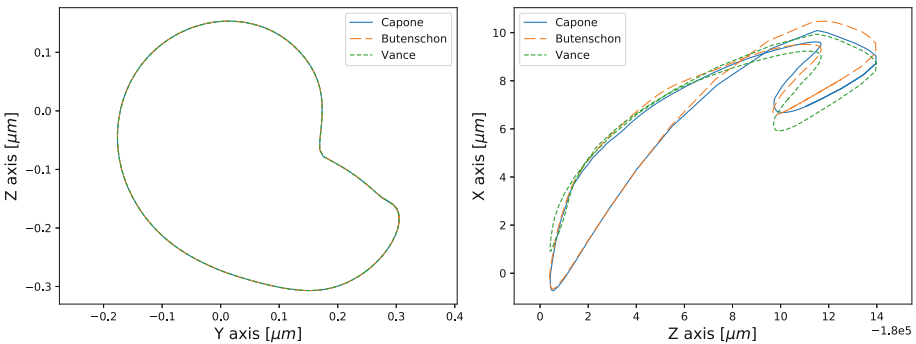


**Fig. 8.** Trajectory of the journal inside the eccentric bearing (left) and trajectory of the piston in relation to the cylinder (right).

The trajectory of the journal in the eccentric bearing is not influenced by the bearing model of the rotor which can be observed on Fig. 8. The eccentric bearing joins the rotor and the connecting rod. This bearing was modeled with linear anisotropic stiffness and damping coefficients that were quite high compared to the rotor bearings, which yielded a much smaller orbit of the journal inside of the

bearing. Figure 8 (right) presents the trajectory of the piston inside the cylinder and the Z motion is much smaller than the X motion. Both piston bearings were modeled with linear anisotropic coefficients and presented similar results, therefore, only the lower bearing trajectory is presented. The influence of the different rotor bearing models is almost negligible (less than  $1\ \mu\text{m}$ ).

## 5 Conclusions

A reciprocating compressor model was built in the open source software OpenModelica to compare different analytical bearing models. The OpenModelica has a basic library of multibody elements that can be integrated with components of other domains (eg. thermal, fluid, electrical). Nevertheless the compressor modeling demanded the developing of new elements such as the hydrodynamic and the anisotropic bearings. The integration of libraries that were developed in other languages is not straightforward, because of the way of variables are exchanged between the library and OpenModelica; arrays are especially difficult to configure. But it is possible to perform the integration and there is no perceptible loss of performance in the simulation.

Analyzing the results of the three different bearing models, Capone and Butenschön models presented very similar results in the simulation of the reciprocating compressor although the Capone model is much simpler. This is not completely unexpected since Kim et al. [11] obtained close results between a short bearing and finite element model.

Vance model presented the most distinct behavior, even though the forces in the primary bearing were close to the ones reported by the other models. The lower damping of the Vance model compared to the Butenschön model, as reported by Hannukainen [9], could indicate that under a fast variation of the eccentricity the Butenschön would present a higher damping and, therefore, smaller orbits.

Further developments of the reciprocating compressor should include numerical models (finite elements and finite volumes) to determine the influence of simplifying Reynolds equation. Other area that can be studied is the flexibility of the support system of the compressor which is a set of spring that connects the compressor mechanism to the gas reservoir.

## References

1. Bukovnik, S., Dörr, N., Čaika, V., Bartz, W.J., Loibnegger, B.: Analysis of diverse simulation models for combustion engine journal bearings and the influence of oil condition. *Tribol. Int.* **39**(8), 820–826 (2006). <https://doi.org/10.1016/j.triboint.2005.07.023>
2. Butenschön, H.J.: Das hydrodynamische, zylindrische gleitlager endlicher breite unter instationärer belastung. Ph.D. thesis, Technische Universitaet Karlsruhe (1976)

3. Campbell, J., Love, P., Martin, F., Rafique, S.: Paper 4: bearings for reciprocating machinery: a review of the present state of theoretical, experimental and service knowledge. In: Proceedings of the Institution of Mechanical Engineers, Conference Proceedings, vol. 182, pp. 51–74. SAGE Publications, London (1967)
4. Capone, G.: Descrizione analitica del campo di forze fluidodinamico nei cuscinetti cilindrici lubrificati. *Energ. Elettr.* **68**(3), 105–110 (1991)
5. Cavallini Jr., A.A., Lara-Molina, F.A., Sales, T.D.P., Koroishi, E.H., Steffen Jr., V.: Uncertainty analysis of a flexible rotor supported by fluid film bearings. *Lat. Am. J. Solids Struct.* **12**(8), 1487–1504 (2015)
6. Estupinan, E.A., Santos, I.F.: Linking rigid multibody systems via controllable thin fluid films. *Tribol. Int.* **42**(10), 1478–1486 (2009)
7. Estupiñan, E.A., Santos, I.F.: Modelling hermetic compressors using different constraint equations to accommodate multibody dynamics and hydrodynamic lubrication. *J. Braz. Soc. Mech. Sci. Eng.* **31**(1), 35–46 (2009)
8. Fritzon, P.: Principles of Object-Oriented Modeling and Simulation with Modelica 2.1. Wiley, Hoboken (2010)
9. Hannukainen, P., et al.: Non-linear journal bearing model for analysis of superharmonic vibrations of rotor systems. Ph.D. thesis, Lappeenranta University of Technology (2008)
10. Kim, T.J.: Dynamic analysis of a reciprocating compression mechanism considering hydrodynamic forces. *KSME Int. J.* **17**(6), 844–853 (2003)
11. Kim, T.J., Han, J.S.: Comparison of the dynamic behavior and lubrication characteristics of a reciprocating compressor crankshaft in both finite and short bearing models. *Tribol. Trans.* **47**(1), 61–69 (2004)
12. Kurka, P., Izuka, J., Paulino, K.: Dynamic loads of reciprocating compressors with flexible bearings. *Mech. Mach. Theory* **52**, 130–143 (2012)
13. Okabe, E.: Analytical model of a tilting pad bearing including turbulence and fluid inertia effects. *Tribol. Int.* **114**, 245–256 (2017)
14. Okabe, E.P., Masarati, P.: Detailed modeling of wind turbine gear set by general-purpose multibody dynamics. In: ASME 2014 International Design Engineering Technical Conferences and Computers and Information in Engineering Conference, pp. V006T10A074. American Society of Mechanical Engineers (2014)
15. Otter, M., Elmqvist, H., Mattsson, S.E.: The new modelica multibody library. In: 3rd International Modelica Conference, pp. 311–330 (2003)
16. Vance, J.M.: Rotordynamics of Turbomachinery. Wiley, Hoboken (1988)
17. Yang, B., Bradshaw, C.R., Groll, E.A.: Modeling of a semi-hermetic CO<sub>2</sub> reciprocating compressor including lubrication submodels for piston rings and bearings. *Int. J. Refrig.* **36**(7), 1925–1937 (2013)



# Radial Active Magnetic Bearing Design Optimization

Javier Betancor<sup>(✉)</sup>, M. Necip Sahinkaya<sup>(✉)</sup>, and Yahya H. Zweiri<sup>(✉)</sup>

Kingston University London, Roehampton Vale Campus Friars Avenue,  
Kingston upon Thames SW15 3DW, UK  
{k1436462,m.sahinkaya,y.zweiri}@kingston.ac.uk  
<https://sec.kingston.ac.uk>

**Abstract.** This paper presents a design optimization approach to minimize the volume of a radial Active Magnetic Bearing (AMB) by comparing Genetic Algorithm (GA) and Pattern Search (PS) methods. The flexible rotor dynamic analysis is performed to determine AMBs dynamic load under different unbalance cases. Preliminary design parameters are generated and results are compared with optimization results, showing around 35% reduction in volume. The PS method resulted a bigger diameter but shorter bearing length compared with GA. Nevertheless, GA generated a thicker AMB with reduced external diameter. All designs (PD, PS and GA) satisfied design constraints as determined by rotor bearing dynamics while keeping the same bearing load capacity, also validating the PD methodology as a prototyping alternative to optimization strategies.

**Keywords:** Radial active magnetic bearing · Flexible rotor Optimization · Genetic Algorithm · Pattern Search

## 1 Introduction

An Active Magnetic Bearing is a mechatronic device, where magnetic forces are used to levitate a rotor without any contact [1]. Magnetic Bearings (MB) can be classified as Active Magnetic Bearings (AMBs), Passive Magnetic Bearings (PMBs) and permanent-magnet-biased Hybrid Bearings (HMBs). Rotor levitation is achieved passively when using PMBs and HMBs. However, unlike AMBs, magnetic forces are always present. AMBs are widely used on flexible rotor systems due to their controllability and high stiffness compared to PMBs and HMBs [8]. The main advantages of MBs are that they are oil-free and frictionless, so higher rotational speeds can be achieved with minimum maintenance requirements, and they can be used in harsh environments.

In AMBs, the rotor displacement is measured from its reference position with a position sensor. Measurements are processed by a micro-controller to generate a control signal before being sent to the amplifiers. The control signal is turned into a control current that generates a magnetic field in the actuating magnets.

Resulting magnetic forces will produce the rotor levitation [13] and dynamic forces to suppress the rotor vibration.

AMBs can also be classified as [1] (i) radial bearings, which offer a magnetic stabilization in 2 Degrees of Freedom [DOF] and (ii) axial/thrust bearing with 1 DOF. Classical configuration comprehends two radial bearings and one thrust bearing separately. [12] suggested a combined radial-thrust bearing solution, also known as hybrid magnetic bearing. In this case, only two bearing components are required to fully stabilize the rotor position. Compact design and the reduced number of components are the main advantages of the system.

Based on structural configurations, radial MB can be homopolar (HOMB) and heteropolar (HEMB). In HOMB all poles have the same polarity in the same rotation plane whilst in HEMB magnetic poles change polarity perpendicular to the rotor axis. Heteropolar configuration for radial bearings is more common due to its simplicity and cost-effectiveness [12, 17]. In addition, [14] concluded that by increasing the number of poles on a radial AMB, power losses can be reduced.

Design steps implicated in the process can be very specific depending on the application, involving iterative and time-consuming processes, where the outcomes cannot normally be extrapolated to other applications. Therefore, computational tools are needed to optimize the design for a specific application. In general, optimization algorithms require the specification of a cost function, design variables, constraints associated with the design variables, and an optimization strategy.

## 1.1 Cost Function

Based on the literature, a widely used optimization objective is to minimize the bearing volume, mass or to maximize the load capacity [3, 5, 8–11, 16, 21, 22]. [3, 8] also optimized the AMB dynamics for heteropolar configurations and [21] for a homopolar radial AMB. [8] stated that the AMB's volume is determined by the rotor dynamics when flexible rotor is used. Thus, rotor dynamics should be included in the optimization as a constraint rather than a cost function.

## 1.2 Constraints

A vast majority of the literature uses the AMB current as a key factor when choosing the amplifiers and this depends on the material current density; geometry constraints involving space available for coils, contact in between windings, wire diameter, inner and outer bearing diameter and AMB pole area. Magnetic flux saturation of the material, air gap and the number of coil turns are also considered.

Power losses comprehend a key design factor as cost functions or constraints. Optimizations including losses due to current flowing through coils (copper losses) were carried out by [5, 9, 11, 14, 21]. Additionally, power losses due to hysteresis and Eddy currents effect (iron losses) were included as optimization

parameters by [7, 9, 21]. However, only [9, 20] included power dissipation capability of the AMB in the form of heat due to convection and heat due to conduction. This will assure that the AMB is able to dissipate more heat than it generates.

AMB load capacity is also considered as a constraint by [5, 7]. It is possible to determine the maximum load required under different unbalance cases on the rotor design stage by using simulation.

The air-gap clearance between the rotor and the stator is also a relevant design parameter. Smaller air-gap requires a lower control current and therefore power losses are reduced. However, it requires a robust control strategy and a higher manufacturing accuracy. [5, 7] selected an air-gap clearance of 0.4 mm for their designs whilst [1, 3, 8–11, 15, 22] chose 0.5 mm. [14] used an air-gap of 1 mm and [21] set this parameter as a design variable obtaining final values of 0.3 mm and 0.33 mm.

### 1.3 Design Variables

In most cases an initial design is needed to begin the optimization process. Upper and lower bounds for parameters are also required depending on the algorithm used. However, [3] defined a self-normalizing method that removes the requirement of an initial design.

Usual design variables found in the literature are: number of turns per pole, bearing width, pole leg width and design current [3, 7–9, 16, 22]. Other authors [3, 21, 22] also included proportional and derivative gain ranges, amplifier parameters [8], coil thickness [7] and the static load of the bearing [22].

### 1.4 Optimization Strategies

There are many possible satisfactory solutions when optimizing the radial AMB design. Some algorithms are suitable to find optimum parameters in the whole design space by generating a set of points at each iteration, like Genetic Algorithms (GA). On the other hand, some methodologies are more convenient to find solutions in the local design space, like Sequential Quadratic Programming (SQP), Interior-point, Trust-region and Pattern Search (PS) strategies.

GAs are adaptive heuristic search algorithms based on the evolutionary ideas of natural selection and genetics. GAs can be divided into Single Objective Genetic Algorithms (SOGAs) and Multi-Objective Genetic Algorithms (MOGAs). These two variations of GAs have been widely applied in the literature. SOGAs have been used by [2, 3] to minimize stack volume, weight, load capacity and power consumption as single objectives. MOGAs have been compared to SOGAs [10, 11, 14, 15, 21, 22]. Some examples of MOGAs include Non-dominated Sorting Genetic Algorithm-II (NSGA-II) and Neighborhood Cultivation Genetic Algorithms (NCGA).

[19] remarked on the efficiency of GA and SQP. These two methods were tested individually and as a combined strategy to optimize a rotor sub-assembly of a magnetically suspended motor. Other alternatives include Differential Evolution Algorithms (DEA) [16] and artificial immune system [4].



In this paper, a preliminary design of a radial MB is presented. Generated design parameters are optimized by selecting the MB stack volume as the cost function, where the aim is to keep the MB dynamic capacity while reducing its size. PS and GA optimization strategies are selected and compared due to multiple local minima solutions of the cost function. Optimization nonlinear constraints applied involve geometrical constraints and maximum bearing dynamic load capacity. Optimisation parameters are the number of coil turns, maximum coil current, pole length and pole width. PS outcome showed an increased diameter but thinner MB compared with PD. GA global solution revealed a reduced but thicker stack MB volume compared to PS, making it as a suitable optimization method for the proposed design.

## 2 Methodology

A preliminary design of the radial AMB is first developed to have a general idea of the system. Subsequently, the design is optimized by using MATLAB optimization tools.

### 2.1 Preliminary Design

The AMB should provide the necessary static and dynamic force to lift the rotor and counteract vibrations caused by unbalance forces and external loads. Each AMB has two orthogonal force axes, which are set at  $45^\circ$  to the vertical axis. Flexible rotor dynamics is simulated using FEA techniques in order to determine a reasonable maximum load capacity. The rotor data is shown in Table 1.

**Table 1.** Rotor data

Description	Value	Unit
Length	0.8	<i>m</i>
Uniform shaft diameter	15	<i>mm</i>
Density	7850	<i>kg/m<sup>3</sup></i>
Young's modulus	210	<i>GPa</i>
Poisson's ratio	0.283	
Total weight	5.3	<i>kg</i>
Polar MOI	2.24e-3	<i>kg · m<sup>2</sup></i>
Maximum speed	10,000	<i>rpm</i>

There are 11 discs in total as shown in Fig. 1. No sensor discs are needed since the position will be measured directly from the shaft. Only two MBs are required to control the system, hence a third one has been added to introduce disturbance forces. One of the thrust bearings can be used to introduce axial loads.

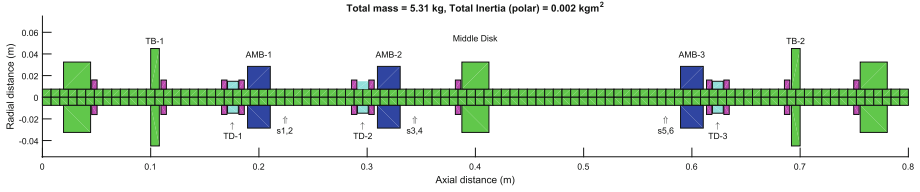


**Fig. 1.** Finite element modelling of the shaft and discs. Active magnetic bearing discs are denoted as AMB-i; touchdown bearing discs are denoted as TD-i; thrust discs are denoted as TB-i; sensor location points are denoted as  $s_{i,j}$ .

The designed rotor will ensure that the first two free-free bending modes are within 10,000 rpm. Approximate bearing stiffness coefficient of ( $K_b = 1 \cdot 10^5 N/m$ ) is chosen after evaluating eigen frequencies as a function of the bearing stiffness for zero rotational speed as shown in Fig. 2. The same bearing stiffness is assumed for both AMBs in two orthogonal directions.

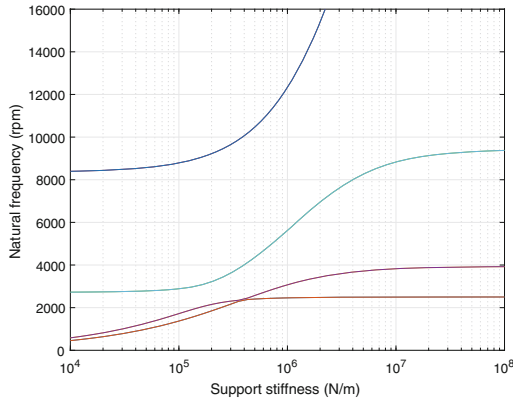


**Fig. 2.** Stiffness map at zero rotor speed showing the change of eigen frequencies as a function of bearing stiffness.

Using the aforementioned coefficients, it is possible to get the mode shapes at zero speed (Fig. 3). The first and second modes (Modes 1 and 2) refers to rigid body modes, while the other two (Modes 3 and 4) are the flexural modes. The effect of sensor non-collocation on the stability is also examined and established that the sensors should be positioned inboard of each MB.

The maximum load capacity ( $F_{max}$ ) per axis of the radial bearings is calculated by multiplying the static load (rotor weight) by a dynamic factor ( $D_f$ ).

$$F_{max} = D_f \frac{mg}{2\sqrt{2}} \tag{1}$$

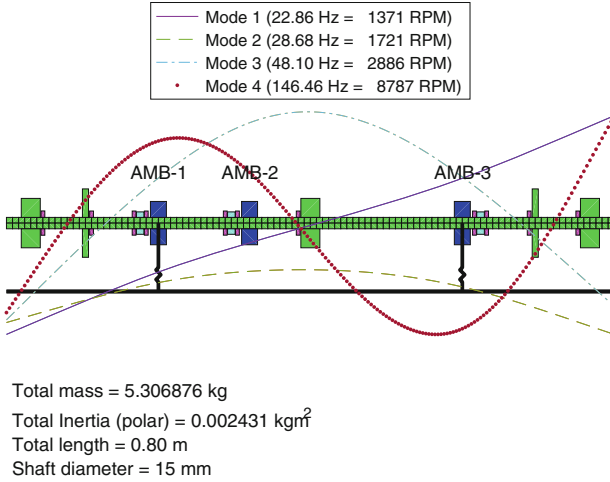


**Fig. 3.** Mode shapes for  $K_b = 1 \times 10^5 N/m$  at  $\Omega = 0$ .

A TD bearing clearance of 0.25 mm has been selected as a design requirement. Therefore, rotor static sag and unbalance cases need to be studied to ensure that there is no contact when the shaft is levitated and the designed MB is capable of providing the required force.

Three unbalance cases were considered. Figure 4 shows the most demanding case in terms of vibration levels and AMB force requirements. The unbalance mass considered is 4 times the unbalance recommended in the API 617 standard.

Results are displayed in two different graphs. The first one represents the orbit size, which relates the major axis of the elliptic rotor orbit. The second graph shows the amplitude of the dynamic forces exerted by AMB1 and AMB3. The largest of the forces in the two orthogonal planes is plotted. As it can be seen, AMB-3 load is around 9.5 N at 9,476 rpm with an orbit size less than 0.1 mm.

After verifying the AMB air gap and force capacity through rotor dynamics simulations, the sizing of the AMBs can now commence. The cross-sectional pole area ( $A_a$ ), shown in Fig. 5, can be calculated from the maximum force:

$$A_a = \frac{F_{max}\mu_0}{B_{max}^2 \epsilon \cos(\alpha)} \tag{2}$$

where the maximum flux density, the fringing and leakage reduction factor, pole angle and permeability of free space are denoted by  $B_{max}$ ,  $\epsilon$ ,  $\alpha$ , and  $\mu_0$ , respectively. A value of 0.8 is selected for the fringing and leakage factor [18].

Heteropolar design is chosen with eight poles which are equally spaced. The inner diameter of the stator ( $D_i$ ) should be greater than the outer diameter of rotor laminations. The pole width ( $c$ ) is calculated assuming that a 50% of the circumference is used:

$$D_i = \frac{8(D_{sh} + 2c_g)}{8 - \pi} \tag{3}$$

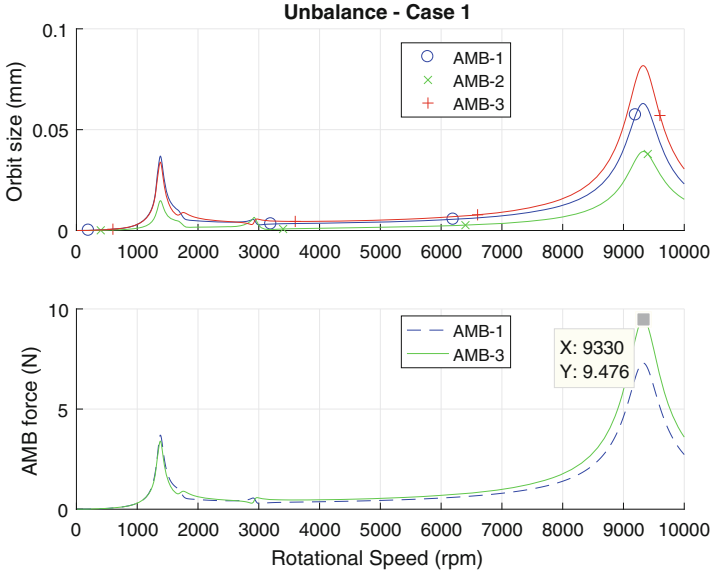


**Fig. 4.** Unbalance response and control forces for case 1.

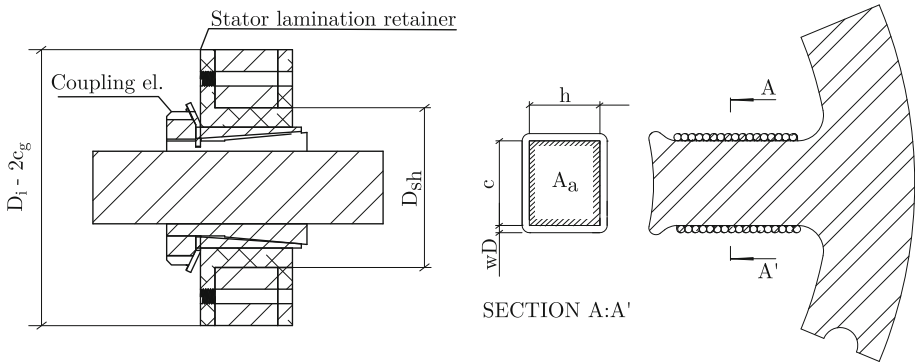


**Fig. 5.** Rotor and stator partial views.

where the shaft diameter and the radial clearance are denoted as  $D_{sh}$  and  $c_g$ , respectively. Figure 5 shows a partial view of the considered shaft diameter and a section of one pole leg with one layer of turns.  $D_{sh}$  is comprehended by the shaft diameter, the coupling element diameter and also the stator lamination retainer inner diameter considering thickness.  $(D_i)$  takes into account  $D_{sh}$ ,  $c_g$  and  $c$ . Based on above calculations, the bearing width ( $b$ ) is calculated as it follows:

$$b = \frac{A_a}{c} \quad (4)$$

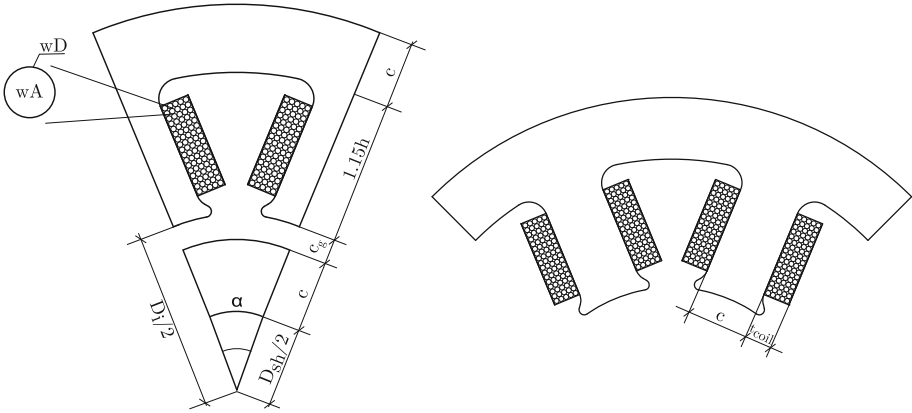


**Fig. 6.** Radial bearing design sketch. Wire area and wire diameter are denoted by  $wA$  and  $wD$ , respectively.

By using flux density and magnetomotive force [MMF] expressions, it is possible to calculate the number of turns needed ( $N$ ) per pole pair. The number of turns will also determine the maximum current ( $I_{max}$ ) required per magnetic pole:

$$N = \frac{2B_{max}c_g}{\mu_0 I_{max}} \tag{5}$$

The inductance per AMB pole pair ( $L$ ), the maximum voltage needed ( $V_{max}$ ) and the maximum power requirement ( $P_{max}$ ) are as follows:

$$L = \frac{\mu_0 N^2 A_a}{2c_g} \tag{6}$$

$$V_{max} \approx \left[ \frac{dI}{dt} \right]_{max} \approx L \frac{I_{max}}{2} \Omega_{max} \tag{7}$$

$$P_{max} = V_{max} I_{max} \tag{8}$$

The minimum wire diameter ( $\phi_{min}^{wire}$ ) that could be selected is calculated based on the current density for Cu ( $J_{Cu}$ ) and is adapted according to the AWG standardized diameter:

$$\phi_{min}^{wire} = \sqrt{\frac{4I_{max}}{\pi J_{Cu}}} \tag{9}$$

The stator diameter ( $D_{st}$ ) is calculated as (Fig. 6):

$$D_{st} = D_i + 2(c + 1.15h_w) \tag{10}$$

where the winding length is denoted by  $h_w$ ; 15% has been added to the winding length as a safety consideration. The total pole length ( $h$ ) is

$$h = h_w + 0.15h_w \tag{11}$$

The total pole leg thickness ( $w$ ) including the pole width is assumed to be constant. Coil thickness ( $t$ ) is constrained to be less than half of the pole leg width and is calculated as a function of the number of layers ( $n_L$ ). More details are given in Figs. 5 and 6. Initial design parameters are given in Table 2.

$$w = n_L \phi_{min}^{wire} \quad (12)$$

$$t = 2w + c \quad (13)$$

**Table 2.** AMB preliminary design parameters

Description	Symbol	Value	Unit
Dynamic factor	$D_f$	6.1	
Stator inner diameter	$D_i$	56	mm
Rotor mass	$m_r$	5.54	kg
Gravity constant	$g$	9.81	$m/s^2$
Permeability of free space	$\mu_0$	$4\pi \cdot 10^{-7}$	$N/A^2$
Max. flux density	$B_{max}$	1.3	Tesla
Fringing and leakage factor	$\epsilon$	0.8	
Pole angle	$\alpha$	22.5	deg
Shaft diameter	$D_{sh}$	33	mm
Radial air gap	$c_g$	0.5	mm
Current density (Cu)	$J_{Cu}$	$6 \cdot 10^6$	$A/m^2$
Max. rotational speed	$\Omega_{max}$	10,000	rpm
Amplifier current limit	$I_{max}^{amp}$	18	A
Amplifier voltage limit	$V_{max}^{amp}$	90	V
Amplifier output resistance	$R_{out}^{amp}$	0.075	$\Omega$

## 2.2 Design Optimization

As a part of the design process, SOGA and PS optimization strategies are applied by using MATLAB to find the optimum bearing dimensions for the required application. GA optimization method requires at least two input arguments, a fitness function and the number of parameters to be optimized. The PS function requires an objective function and a starting point. Lower and upper bounds are defined to provide a constrained range to the optimization. Both methods require the use of constraints which are depicted as follows:

**First Constraint** takes into account the maximum current intensity ( $I_{max}$ ) as a function of the maximum current density ( $J_{Cu}$ ) and therefore, the minimum wire diameter ( $\phi_{min}^{wire}$ ).

$$I_{max} \leq \frac{1}{4} J_{Cu} \pi (\phi_{min}^{wire})^2 \quad (14)$$

**Second Constraint** restrains the maximum MMF as a function of the maximum flux density ( $B_{max}$ ), radial air gap ( $c_g$ ) and permeability of free space ( $\mu_0$ ). It is also worth mentioning that the magnetic reluctance considered involves the iron path, rotor iron path and air gap [18].

$$NI_{max} \leq \frac{2B_{max}c_g}{\mu_0} \quad (15)$$

**Third Constraint** will restrict the maximum winding space available for coils (Fig. 5) assuming a bulking factor of 80% [6]:

$$N \frac{\pi (\phi_{min}^{wire})^2}{8} \leq 0.8 \left( \frac{\alpha}{2} \left( \frac{D_i}{2} + h \right)^2 - \frac{\alpha}{2} \left( \frac{D_i}{2} \right)^2 - \frac{ch}{2} - \frac{\alpha}{2} (h_w)^2 \right) \quad (16)$$

**Fourth Constraint** will avoid contact between windings assuming that the coil width ( $w$ ) is less than the equivalent arc chord with radius  $D_i + 0.15h_w$  (Fig. 5):

$$N \frac{\pi (\phi_{min}^{wire})^2}{8h_w} \leq \left( 2 \left( \frac{D_i}{2} + 0.15h_w \right) \sin \left( \frac{\alpha}{2} \right) - \frac{c}{2} \right) \quad (17)$$

**Fifth Constraint** takes into account the maximum force ( $F_{max}$ ) generated by the AMB pole pair:

$$F_{max} \leq \frac{\epsilon \mu_0 N^2 I_{max}^2 A_a \cos \alpha}{4c_g^2} \quad (18)$$

where the cross-sectional pole area and the fringing and leakage reduction factor are denoted by  $A_a$  and  $\epsilon$ , respectively.

**Cost Function** to be minimized is the total stack volume ( $V$ ) of the AMB considering it as a cylinder [3].

$$\min(V) = \min \left( \frac{\pi D_{st}^2 A_a}{4c} \right) \quad (19)$$

Design variables for GA and PS, and their upper and lower boundaries are based on the initial design values and given in Table 3.

**Table 3.** Design variables and boundaries used during the optimization

Description	Symbol	Lower bound	Upper bound
Turns per pole pair	$N$ [turns]	$0.1N$	$2N$
Max. current req	$I_{max}$ [A]	$0.1I_{max}$	$2I_{max}$
Pole width	$c$ [m]	$0.1c$	$2c$
Coil length	$h_w$ [m]	$0.1h_w$	$2h_w$

### 3 Results and Discussion

Optimizations were carried out by using the MATLAB optimization toolbox. The GA was set to a maximum population size of 50 and a maximum stall generations of 50. Initial Population range was set from  $-1$  to  $100$ , as the algorithm was giving different results with the values set by default. PS was executed using a constraint tolerance, function tolerance and a step tolerance of  $10^{-6}$ .

Optimization variables are shown in Table 5. Boundaries were set at 10% and 200% of the preliminary design parameters, as optimized results out of the defined boundaries are not suitable for the system design. It is theoretically possible to design a very thick MB but reduced external diameter by setting boundaries to 10%. The same principle can be applied to a solution close to 200% of the upper limit boundary. However, constraints take into consideration the design variables, showing satisfactory solutions within the predefined limit range. The selected optimization variables were selected due to their key role on the dynamics and geometry of the resulting AMB.

Both methods were computationally fast with average computation times of 1.02 and 1.63 s for PS and GA, respectively. Table 4 shows design parameters obtained by the preliminary design, GA and PS optimizations.

As it can be seen, the volume reduction is **35.48%** for GA method and **34.35%** when applying PS optimization method compared with the preliminary design. PS solution gives a greater external diameter, a smaller bearing width and around a 6% difference on the bearing stiffness constant, compared with GA results. This proves that there are many possible local solutions with slight variations on the design parameters, therefore the usage of GA compared to PS for this specific purpose is recommended.

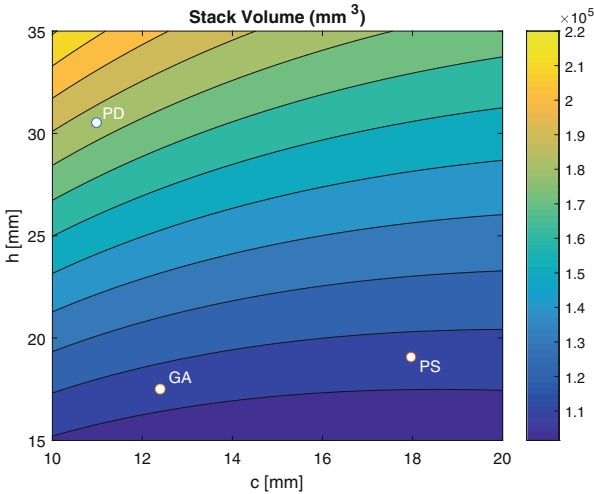
Optimization parameter boundaries and the optimized parameters are compared in Table 5.

Figure 7 offers a visual representation of the optimization, where pole leg length ( $h$ ) and pole width ( $c$ ) are displayed for PD, GA and PS. The background is the resulting stack volume for all possible values of ( $h$ ) and ( $c$ ) within a predefined range. A point located close to the yellow area would result in a great stack volume, whilst a point situated around the dark blue area would result in a reduced stack volume.



**Table 4.** Optimization results. Note that term ‘par.’ stands for ‘parameters’

Description	Symbol	Design par.	GA	PS
Inner diameter	$D_i$ [mm]	55.99	58.82	69.96
Pole width	$c$ [mm]	10.99	12.41	17.98
Pole length	$h$ [mm]	30.5	17.48	19.04
AMB width	$b$ [mm]	10.73	9.5	6.56
Wire diameter	$\Phi_{min}^{wire}$ [mm]	1.024	1.024	1.024
No. of turns	$N$ [turns]	259	210	209
Max. current	$I_{max}$ [A]	4	4.93	4.94
Stator diameter	$D_{st}$ [mm]	138.97	118.59	144.01
Max. force	$F_{max}$ [N/pole]	117.21	117.21	117.21
Bearing stiffness	$K_x$ [N/m]	3.0155e5	2.9582e5	3.1187e5
<b>Volume</b>	$V$ [mm <sup>3</sup> ]	<b>1.63e5</b>	<b>1.05e5</b>	<b>1.07e5</b>



**Fig. 7.** Optimization parameters. PD, GA and SP stands for preliminary design, Genetic Algorithms and Pattern Search, respectively

**Table 5.** Optimum parameter values and corresponding boundaries

Design variable	LB	UB	GA	PS
$N_{turns}$	25.9	518	308.1	308.64
$I_{max}$ [A]	0.49	9.88	4.95	4.94
$c$ [mm]	1.10	21.99	9.6	4.01
$h_w$ [mm]	2.65	53.04	37.8	36.48

## 4 Conclusion and Future Work

In this paper, a rotor dynamics informed optimization of AMB preliminary design is described. An optimization is carried out with design constraints based on the coil current, MMF, number of coil turns, winding interference and the bearing force capacity. Optimization strategies applied are Genetic Algorithms (GA) and Pattern Search (PS). Although the optimized designs are different, both optimization methods show about 35% volume reduction compared with the preliminary design with negligible computational cost. However, it is also shown that GA is more adequate for this specific application because of its global solutions.

Future work will involve an accurate representation of power losses and heat dissipation, integration of the rotor and bearing dynamics in the optimization process. Experimental validation will be performed in order to validate PD and optimized designs.

## References

1. Amrhein, W., Gruber, W., Bauer, W., Reisinger, M.: Magnetic levitation systems for cost-sensitive applications-some design aspects. *IEEE Trans. Ind. Appl.* **52**(5), 3739–3752 (2016). <https://doi.org/10.1109/TIA.2016.2561905>
2. Carlson-Skalak, S., Maslen, E., Teng, Y.: Magnetic bearing actuator design using genetic algorithms. *J. Eng. Des.* **10**(2), 142–162 (1999)
3. Chang, H., Chung, S.C.: Integrated design of radial active magnetic bearing systems using genetic algorithms. *Mechatronics* **12**(1), 19–36 (2002). [https://doi.org/10.1016/S0957-4158\(00\)00068-4](https://doi.org/10.1016/S0957-4158(00)00068-4)
4. Chou, Y.C., Nakajima, M., Fan, Y.H., Liao, Y.L.: Constrained design optimization of active magnetic bearings through an artificial immune system. *Eng. Comput.* **33**(8), 2395–2420 (2016). <https://doi.org/10.1108/EC-05-2015-0137>. (Swansea, Wales)
5. Fang, J., Wang, C., Wen, T.: Design and optimization of a radial hybrid magnetic bearing with separate poles for magnetically suspended inertially stabilized platform. *IEEE Trans. Magn.* **50**(5), 1 (2014)
6. Hsiao, F.Z., Chue-Fan, C., Chieng, W.H., Lee, A.C.: Optimum magnetic bearing design considering performance limitations. *JSME Int. J. Ser. C: Dyn. Control Robot. Des. Manuf.* **39**(3), 586–596 (1996)
7. Le, Y., Wang, K.: Design and optimization method of magnetic bearing for high-speed motor considering eddy current effects. *IEEE/ASME Trans. Mechatron.* **21**(4), 2061–2072 (2016). <https://doi.org/10.1109/TMECH.2016.2569822>
8. Le, Y., Fang, J., Wang, K.: Design and optimization of a radial magnetic bearing for high-speed motor with flexible rotor. *IEEE Trans. Magn.* **51**(6), 1–3 (2015)
9. Lijesh, K.P., Hirani, H.: Optimization of eight pole radial active magnetic bearing. *J. Tribol.* **137**(2), 024502 (2015)
10. Pilat, A.: AMB construction optimization tool. *Solid State Phenom.* **147–149**, 393–398 (2009)
11. Rao, J.S., Tiwari, R.: Design optimization of double-acting hybrid magnetic thrust bearings with control integration using multi-objective evolutionary algorithms. *Mechatronics* **19**(6), 945–964 (2009)

12. Reisinger, M., Grabner, H., Silber, S., Amrhein, W., Redemann, C., Jenckel, P.: A novel design of a five axes active magnetic bearing system (2010)
13. Schweitzer, G.: Introduction and survey. In: *Magnetic Bearings: Theory, Design, and Application to Rotating Machinery*, pp. 1–26 (2009). [https://doi.org/10.1007/978-3-642-00497-1\\_1](https://doi.org/10.1007/978-3-642-00497-1_1)
14. Shelke, S.N., Chalam, R.V.: Optimum power loss in eight pole radial magnetic bearing: multi objective genetic algorithm. In: *Communications in Computer and Information Science, CCIS*, vol. 250 (2011)
15. Smirnov, A., Uzhegov, N., Sillanpaa, T., Pyrhonen, J., Pyrhonen, O.: High-speed electrical machine with active magnetic bearing system optimization. *IEEE Trans. Ind. Electron.* **64**(12), 9876–9885 (2017)
16. Stumberger, G., Dolinar, D., Pahner, U., Hameyer, K.: Optimization of radial active magnetic bearings using the finite element technique and the differential evolution algorithm. *IEEE Trans. Magn.* **36**(4 PART 1), 1004–1008 (2000)
17. Traxler, A., Maslen, E.: Hardware components. In: *Magnetic Bearings: Theory, Design, and Application to Rotating Machinery*, pp. 69–109 (2009). [https://doi.org/10.1007/978-3-642-00497-1\\_3](https://doi.org/10.1007/978-3-642-00497-1_3)
18. Yoon, S.Y., Lin, Z., Allaire, P.E.: Fundamentals of magnetic bearings. No. 9781447142393 in *Advances in Industrial Control* (2013). [https://doi.org/10.1007/978-1-4471-4240-9\\_3](https://doi.org/10.1007/978-1-4471-4240-9_3)
19. Yuan, Q., Han, B., Dong, B.: The multiple objective optimization of high-speed rotor supported by magnetic bearing in BLDCM. *Int. J. Appl. Electromagn. Mech.* **46**(3), 663–673 (2014)
20. Zhang, L., Yu, M., Luo, Y., Liu, J., Ren, Y.: An overview of the thermal calculation and the cooling technology for active magnetic bearing. In: *IOP Conference Series: Materials Science and Engineering*, vol. 241 (2017). <https://doi.org/10.1088/1757-899X/241/1/012026>
21. Zhong, W., Palazzolo, A.: Magnetic bearing rotordynamic system optimization using multi-objective genetic algorithms. *J. Dyn. Syst. Meas. Control Trans. ASME* **137**(2), 021012 (2015)
22. Zhong, W., Palazzolo, A., Kang, X.: Multi-objective optimization design of nonlinear magnetic bearing rotordynamic system. *J. Vib. Acoust. Trans. ASME* **139**(1) (2017)



# Measurements of Rotordynamic Force Coefficients of Metallic Type Brush Seals

Pascal Jolly<sup>1</sup>(✉), Olivier Bonneau<sup>1</sup>, Mihai Arghir<sup>1</sup>, Florent Cochain<sup>2</sup>,  
and Jérôme Dehouve<sup>3</sup>

<sup>1</sup> Institut Pprime, CNRS - Université de Poitiers - ISAE ENSMA,  
Chasseneuil du Poitou, France

[pascal.jolly@univ-poitiers.fr](mailto:pascal.jolly@univ-poitiers.fr)

<sup>2</sup> Ariane Group, Vernon, France

<sup>3</sup> CNES, DLA, Paris, France

**Abstract.** The present paper presents experimental measurements of rotordynamic force coefficients for a multistage arrangement of four identical brush seals. The bristles are metallic, with a lay angle of  $50^\circ$  from radial centerline and have an initial radial interference with the shaft of 0.12 mm. According to a radial feeding groove, two pairs of two seals are tested face to face. The supply pressures are 0.54, 0.82, 1.1, 1.75 and 2.4 MPa, with a discharge pressure of 0.4 MPa. The working fluid is water. The rotor is centered and the operating spinning speeds are 50, 3000 and 6000 rpm. For given working conditions (supply pressure and rotor speed), a set of dynamic excitations (two directions and 8 frequencies), imposed to the rotor, provide complex impedances that are used for identifying rotordynamic force coefficients. Results are discussed in order to highlight the respective impact of rotor speed and supply pressure on brush seals performances.

**Keywords:** Brush seals · Rotordynamic force coefficients · Water

## 1 Introduction

Designing rotating shaft sealing device for turbomachinery purpose requires to optimize leakage control but also rotordynamic performances. In many cases, the straightforward solution is the use of a labyrinth seal, according to the vast amount of data and successful applications associated to this kind of seals. Considering permanent increase of rotational speeds, working pressures and temperatures, brush seals have arisen as an alternative solution for gas turbine engines, turbopumps, gas compressors and steam generators [1–3]. As indicated in [4], brush seals provide, compared to labyrinth seals, several advantages: leakage can be lowered up to 50% (in addition to stable leakage characteristics over long operating periods), permanent clearance is smaller or even zero (through bristles flexibility that accommodate transient shaft excursions) and less axial space is required. This space-saving property allows designers to arrange brush seals in a

row to obtain a multistage configuration [1,5,6]. Aslan-zada et al. [7] emphasis, through a literature review, the obvious rotordynamic benefits from implementing brush seals instead of conventional labyrinth seals in turbomachinery. In [9], the authors state that the operating conditions to be considered in brush seal design are: differential pressure, radial seal interference, inlet flow temperature, type of fluid. They add that in the case of rotor excursions, cant angle (around  $45^\circ$ ) helps reduce the contact loads, allowing bristles to bend rather than buckle. A coating on the rotor is also required in case of large radial excursions or initial preload of the bristles (negative clearance). For turbomachines of split-case design, the segmentation of the seals is needed. This segmentation can affect sealing performances but direct damping coefficients are increased [10]. Finally, as indicated in [8], two methods are common to manufacture brush seals, consisting in clamping vs welding the bristle pack. In this experimental work, the rotordynamic force coefficients are identified for a multistage arrangement of four identical brush seals. The results are presented for various inlet pressures and shaft rotational speeds.

## 2 Test Facility

The test rig BALAFRE (BAnc LAmes Fluides à haut nombre de REynolds) is dedicated to the identification of dynamic force coefficients of thin fluid film components of high speed rotating machines. These components often use a low viscosity process fluid as lubricant (in cryogenic applications for example). Therefore, the flow in the thin fluid film exhibits high Reynolds numbers. In order to reproduce experimentally these high Reynolds numbers regimes, the test rig uses hot water as lubricant (temperatures limited to  $50^\circ\text{C}$ ), inlet pressure as high as 4.5 MPa and tested components can have a nominal diameters up to 350 mm. These conditions lead to axial and circumferential Reynolds numbers up to  $10^5$ . The test rig is mainly composed of a test cell, an electric motor, a hydraulic system (with pumps, tanks, filters and valves) and a Programmable Logic Controller associated with DAQ device. A cross section view of the test cell is shown in Fig. 1, where the tested component (an annular seal in the present configuration) is overhung mounted at the left end of a rotating shaft [7]. The rotor and the stator of the annular seal are respectively indicated as [1] and [2]. This design gives a great modularity to the test cell, where various kinds of components have been mounted : seals, hydrostatic bearings and impellers.

The whole test rig is pressurized at 0.5 MPa. This means that an annular seal can have a maximum pressure difference of 4 MPa between the upstream and the downstream (discharge) chambers. The necessary flow rate (up to  $120\text{ m}^3/\text{h}$ ) is delivered by two centrifugal pumps driven by electrical motors whose total power is 330 kW. The maximum shaft speed (6000 rpm) is obtained with a three-phase asynchronous motor of 180 kW. A double conical hydrostatic thrust bearing is located close to the test component. It has many roles: first it must guide the rotation of the shaft and support the static axial load (which can reach as much as 200 kN) generated by the 4 MPa pressure difference between the two faces of

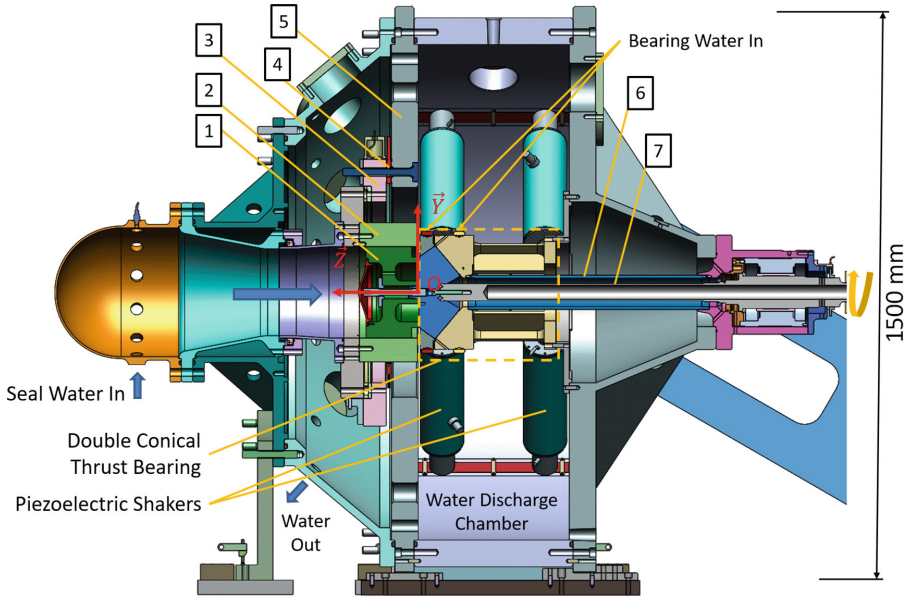


**Fig. 1.** Cross sectional view of the test cell - annular seal configuration

the annular seal. Its second role is to transmit the excitations imposed by the 8 piezoelectric actuators mounted four by four along two planes. The housing of the bearing is linked to the frame via a hollow tube [6] designed to be very stiff axially and flexible in the radial direction. The first natural frequency of the bending mode of the shaft is 460 Hz; the two first natural frequencies of the torsional modes are 14 Hz and 269 Hz. The double conical hydrostatic thrust bearing is provided with  $2 \times 6$  recesses and orifice restrictors [11] and is fed with water at 15 MPa. The average fluid film thickness in the two parts of the bearing is about  $40 \mu\text{m}$  and the axial and radial stiffnesses<sup>1</sup> are larger than  $10^9 \text{ N/m}$ . The outlet flow from both the tested component and the double conical hydrostatic thrust bearing is discharged in the test rig and then returns to a water tank of  $5 \text{ m}^3$  via several hoses and pipes. Dynamic displacements are applied to the rotor by 8 piezoelectric shakers, mounted 4 by 4 in the forward and in the rear plane of the double conical hybrid bearing. The maximum dynamic displacements are  $\pm 100 \mu\text{m}$  with a frequency range from 20 to 200 Hz, corresponding to dynamic loads of 20 kN per axis<sup>2</sup>. The housing [2] of the tested component is fixed on a rigid part [3] which is mounted on the test rig's frame [5] via three piezoelectric

<sup>1</sup> The stiffnesses of the double conical hydrostatic thrust bearing are high contrary to those of the tested component in order to lower the power of the shakers.

<sup>2</sup> The power of the shakers is set to a percentage of their total power. Therefore, the obtained amplitudes of displacements of the rotor depend on the direct stiffnesses of the tested component.

force transducers (Kistler 9167)  $\boxed{4}$  each one being able to measure three components, in a range  $[-20 \text{ kN}; 20 \text{ kN}]$ . Their stiffnesses are respectively  $4.6 \times 10^9 \text{ N/m}$  and  $1.67 \times 10^9 \text{ N/m}$  in directions  $\mathbf{Z}$  and  $\mathbf{X}, \mathbf{Y}$ . For each axis, the proportional error is  $\leq \pm 1\%$  and the hysteresis is  $\leq 2\%$ , both for the full scale output. The three sensors constitute a force balance. The first natural frequency of the axial mode of the stator assembly (housing and force sensors) is 280 Hz. The two first natural frequencies of the bending mode are 370 Hz and 520 Hz. The housing is equipped with 6 eddy current proximity probes (Bently Nevada 3300 XL 8 mm), positioned three by three in the front and rear plane (for an annular seal or a hydrostatic bearing). Their linearity error is  $\leq 5\%$ . These sensors measure the relative displacements between the rotor and the housing. Therefore, the position of the rotor center in the two planes as well as the radial clearance can be deduced. Before each test, a dedicated part, having an outside diameter that fits exactly the housing's inside diameter, is used to calibrate simultaneously the response (gain and offset) of the 6 displacement sensors. Misalignment of the rotor can also be obtained knowing that the two measuring planes are equidistant from the housing midplane. Three accelerometers are mounted on the housing enabling the measurement of its absolute movements.

### 3 Dynamic Coefficients Identification

The dynamic displacements of the rotor imposed by the shakers generate fluid forces that the housing transmits to the piezoelectric force transducers (acting like high stiffness springs). For lateral displacements of the rotor along  $\mathbf{X}$  and  $\mathbf{Y}$  axes of the coordinate system defined in Fig. 1, the equations of the fundamental principle of dynamics applied to the housing with respect to the center of the component  $O$  are:

$$\begin{cases} m\ddot{x} = -f_x + \sum_{k=1}^3 fb_x^k \\ m\ddot{y} = -f_y + \sum_{k=1}^3 fb_y^k \end{cases} \quad (1)$$

where  $f$  and  $fb^k$  are respectively the fluid film forces and the forces measured by the  $k^{\text{th}}$  sensor of the force balance while the subscript  $x$  and  $y$  denote their directions. In order to evaluate the contribution of inertial forces in Eq. 1, the assembly stator/force balance can be likened to a single degree of freedom spring (of stiffness  $K$ ) - mass ( $M$ ) system subjected to a harmonic force  $f(t) = f_0 \sin(\omega t)$ . The equation of motion of this system is  $M\ddot{x} + Kx = f(t)$  and the solution is  $x(t) = \frac{f_0}{K} \frac{\omega_0^2}{\omega_0^2 - \omega^2} \sin(\omega t)$ , where  $\omega_0 = \sqrt{\frac{K}{M}}$  is the natural frequency of the system. According to the ratio  $\frac{M\ddot{x}}{Kx} = \frac{M\omega^2}{K}$ , with  $M = 250 \text{ kg}$  and  $K = 3 * 1.67 \times 10^9 \text{ N/m}$ , the contribution of inertial forces can be calculated in respect of excitation frequency  $\omega$ . As shown in Fig. 2, inertial forces represent 1.7% of the total measured forces at  $\omega = 90 \text{ Hz}$  and 3% at  $\omega = 120 \text{ Hz}$ .

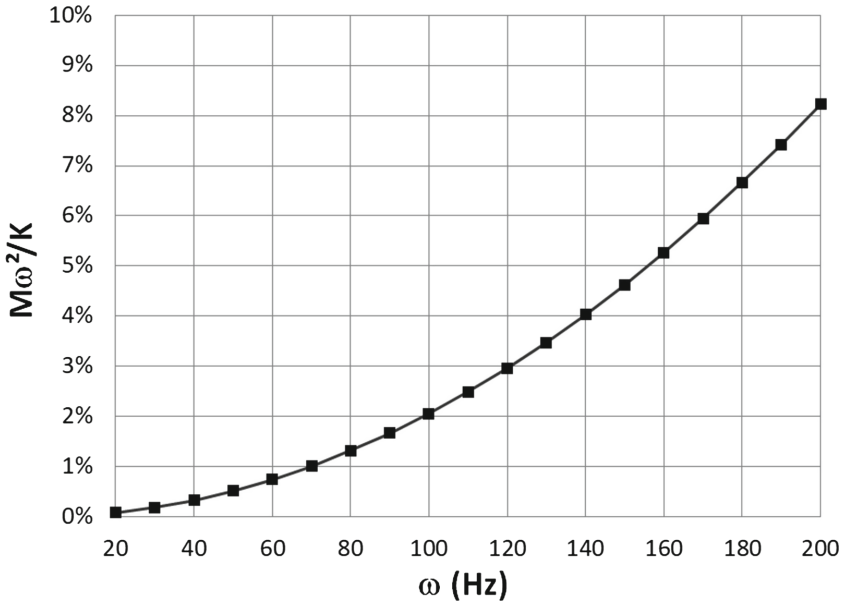


**Fig. 2.** Inertial forces contribution in the total measured forces in respect of excitation frequency at  $\omega$

For an excitation frequency in the range 20 to 120 Hz, the accelerations of the housing can be neglected [12], and Eq. 1 can be simplified as:

$$\begin{cases} f_x = \sum_{k=1}^3 f b_x^k \\ f_y = \sum_{k=1}^3 f b_y^k \end{cases} \quad (2)$$

Introducing the small perturbation hypothesis, fluid film forces can be described by linear dynamic coefficients (stiffness  $K$ , damping  $C$  and added mass  $M$ ) or impedances  $Z$ . In the frequency domain (after applying the Fourier transform), the fluid film forces and the displacements of the rotor are written as follows:

$$\begin{cases} F_x = Z_{xx}X + Z_{xy}Y \\ F_y = Z_{yx}X + Z_{yy}Y \end{cases} \quad (3)$$

The unknown impedances  $Z_{xx}$ ,  $Z_{xy}$ ,  $Z_{yx}$  and  $Z_{yy}$  are found by using two linearly independent excitations (denoted by the superscripts 1 and 2) consisting in lateral vibrations obtained by successively exciting the piezoelectric shakers in two orthogonal directions and with the same phase for the front and rear planes. The impedances are computed by inverting the displacement matrix as follows:



$$\begin{bmatrix} Z_{xx} & Z_{xy} \\ Z_{yx} & Z_{yy} \end{bmatrix} = \begin{bmatrix} F_x^1 & F_x^2 \\ F_y^1 & F_y^2 \end{bmatrix} \begin{bmatrix} X^1 & X^2 \\ Y^1 & Y^2 \end{bmatrix}^{-1} \tag{4}$$

The stiffness, damping and added mass matrices of coefficients are calculated from the real and imaginary part of the corresponding impedances as follows:

$$\begin{cases} K_{ij} - M_{ij}\omega^2 = \Re [Z_{ij}(\omega)] \\ j\omega C_{ij} = \Im [Z_{ij}(\omega)] \end{cases} \tag{5}$$

with  $[ij] = [xx; xy; yx; yy]$ . Equation 5 shows that in order to enable the identification of constant dynamic coefficients<sup>3</sup>, the real part of the impedance must describe a parabola and its imaginary part must describe a straight line. In order to perform a curve fitting by the least square procedure, the impedances are calculated for a significant number of excitation frequencies  $\omega$ . Examples of real and imaginary parts of the impedances used during the identification are respectively shown in Figs. 3 and 4.

The uncertainties in  $K_{ij}$  and  $C_{ij}$  are respectively estimated to  $\pm 15\%$  and  $\pm 30\%$ .

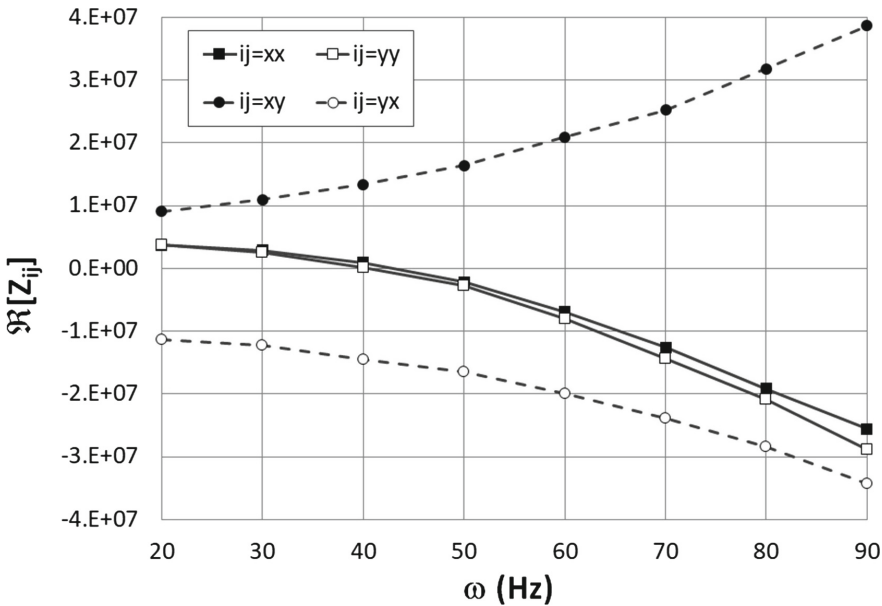


**Fig. 3.** Curve fitting of impedance’s real parts for identification as a function of  $\omega$ (Hz) in abscissa -  $P_s = 1.1$  MPa ;  $\Omega = 50$  Hz

<sup>3</sup> As the fluid is considered as incompressible, rotordynamic coefficients are independent from the exciting frequency.

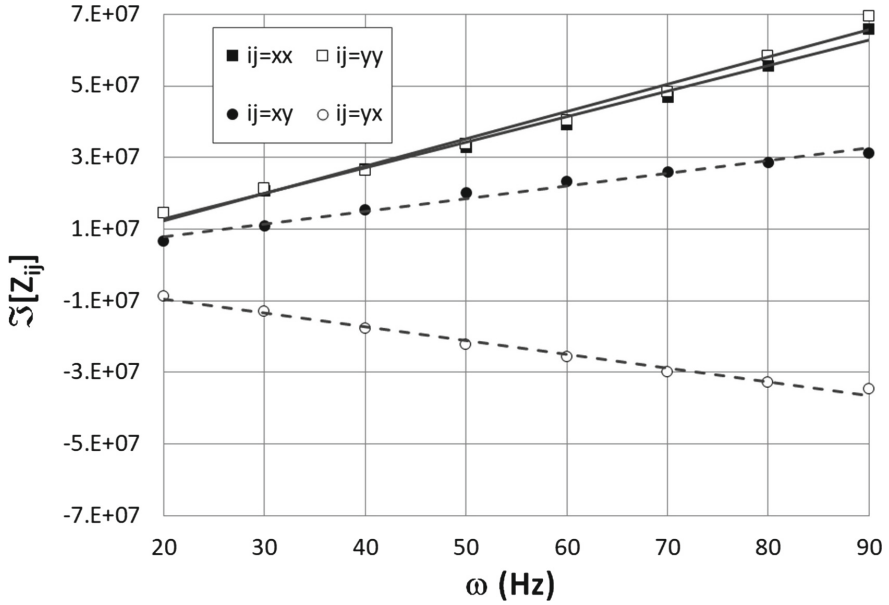


**Fig. 4.** Curve fitting of impedance's imaginary parts for identification as a function of  $\omega$ (Hz) in abscissa -  $P_s = 1.1$  MPa ;  $\Omega = 50$  Hz

## 4 Tested Brush Seals

Figure 5 shows the stator assembly equipped with the four brush seals (two arrangements of two identical brush seals). The fluid is introduced radially (no preswirl [5,13]), in the middle of the four seals. The process fluid is water, having an inlet temperature in the range 35 to 40.5°C and an inlet pressure up to 2.4 MPa. The seals are in one part (not segmented) with a welded design. The rotor is coated with a layer of chromium carbide. The main seals properties are listed above<sup>4</sup>:

- Manufacturing design: Welded
- Plates material: 304 L Stainless Steel
- Clearance at back plate: 0.53 mm
- Front plate diameter = Back plate diameter
- Bristle diameter: 0.07 mm
- Bristle material: *HAYNES* 25
- Radial shaft interference:  $c_0 = 0.12$  mm
- Bristle angle:  $50^\circ \lg 5^\circ$
- Bristle contact width: 2 mm
- Back plate width: 2.4 mm

<sup>4</sup> For confidentiality purposes, the authors are not allowed to communicate the diameter of the shaft.

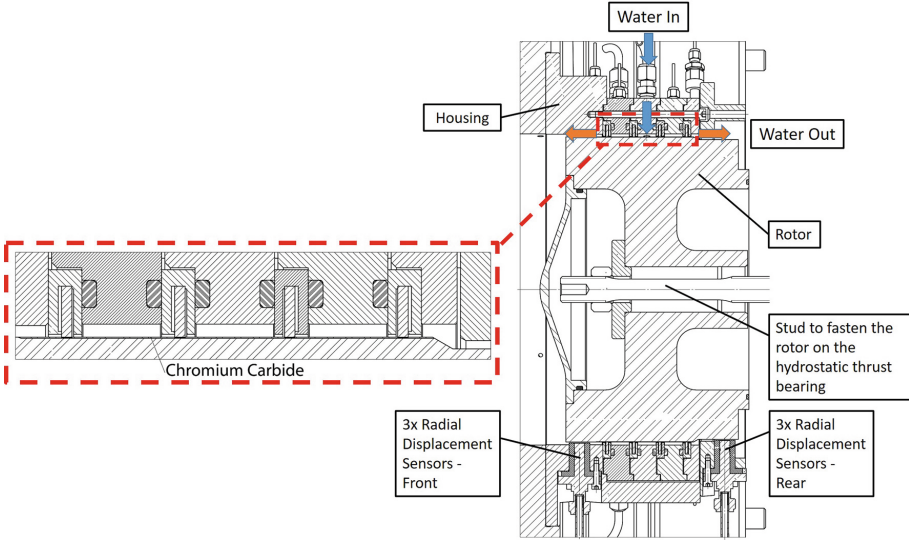


Fig. 5. Cross sectional view of the brush seals arrangement

## 5 Tests Conditions

All the tests have been operated with a centered position of the rotor. For each rotor speed  $\Omega$ , experimental data (displacements, forces, pressures, flowrates, temperatures, torque) are recorded for steady-state static case and dynamic excitations. The tests have been performed according to the following conditions:

- Rotor speed  $\Omega$ : 50, 3000 and 6000 rpm,
- Excitations frequencies  $\omega$ : 20, 30, 40, 50, 60, 70, 80 and 90 Hz,
- Water supply pressure  $P_S$ : 0.54, 0.82, 1.1, 1.75 and 2.4 MPa,
- No fluid preswirl.

Figure 6 shows the unwrapped form of the inlet diameter of the stator<sup>5</sup>, along with the four seals and the instrumentation distribution:

- 6 displacement sensors ( $C_{11}$  to  $C_{23}$ ),
- 15 pressure taps ( $P_{stat1}$  to  $P_{stat15}$ ),
- 5 PT100 sensors ( $T_1$  to  $T_5$ )<sup>6</sup>,
- 3 in situ pressure sensors ( $P_{dyn1}$  to  $P_{dyn3}$ ).

<sup>5</sup>  $\Omega$  is the rotating direction and  $\Theta$  is the circumferential coordinate according to  $\mathbf{X}$ .

<sup>6</sup>  $T_B$  corresponds to plugged PT100 positions.

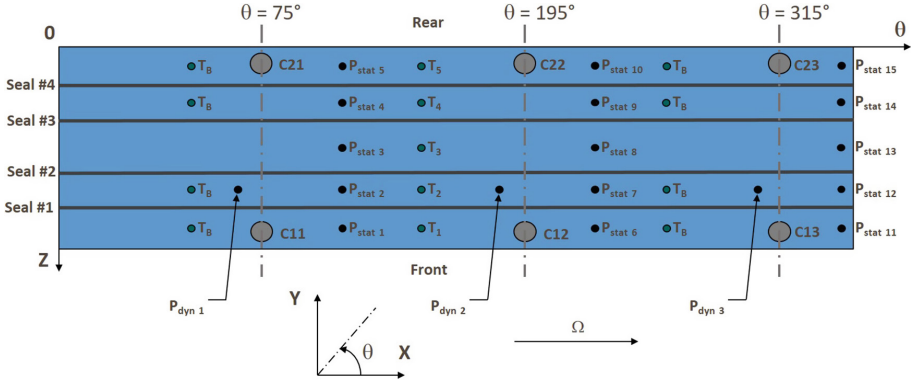


Fig. 6. Unwrapped form of the instrumented stator

## 6 Results and Discussion

The present experimental dynamic coefficients are made nondimensional as follows [10]:

$$\begin{cases} \text{Dimensionless stiffness coefficients} & K_{ij}^* = \frac{K_{ij}c_0}{\Delta P_{max}L_sD} \\ \text{Dimensionless damping coefficients} & C_{ij}^* = \frac{C_{ij}c_0\Omega_{max}}{\Delta P_{max}L_sD} \end{cases} \quad (6)$$

where  $\Delta P_{max} = 2.4$  MPa is the maximum pressure differential between the supply pressure and the discharge pressure,  $L_s$  is the sealing axial length,  $D$  is the shaft diameter,  $\Omega_{max} = 100$  Hz is the maximum shaft speed.

Figure 7 illustrates the evolution of the direct (top) and cross-coupled (bottom) stiffness coefficients versus  $\Delta P$ , for various running speed. Direct stiffness coefficients are always positive except for one case i.e. at maximum running speed and minimum pressure differential, as for an annular seals [12]. Furthermore, direct stiffness coefficients are not sensitive to  $\Omega$  but increase with  $\delta P$ , due to the phenomenon of pressure-stiffness coupling [9]. Cross-coupled stiffness coefficients are theoretically higher at maximum shaft speed but, contrary to conventional annular seals, their values decrease with increasing  $\Delta P$ , indicating the bristle packs can contribute to reduce the tangential velocity. Figure 8 illustrates the evolution of the direct (top) and cross-coupled (bottom) damping coefficients versus  $\Delta P$ , for various running speed. It is interesting to note that direct damping coefficients are always positive. As for annular seals, the direct-damping coefficients are higher than the cross-coupled damping coefficient. Furthermore, damping coefficients are generally not sensitive to rotor speed, except cross-coupled damping coefficients for low differential pressure. As a final observation, present experimental stiffness and damping coefficients often satisfy

theory: for small motion about a centered position, the matrices  $\mathbf{K}$ ,  $\mathbf{C}$  and  $\mathbf{M}$  are skew-symmetric with equal entries on the main diagonal, i.e.  $K_{xx} = K_{yy}$  and  $K_{xy} = -K_{yx}$ , etc.)

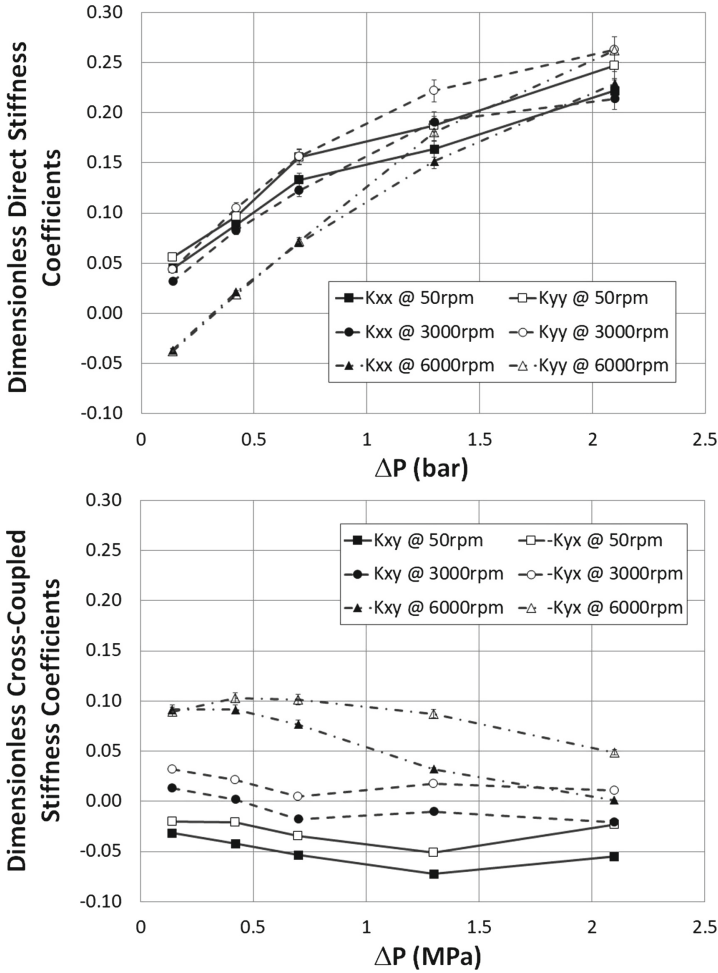


Fig. 7. Identified stiffness coefficients

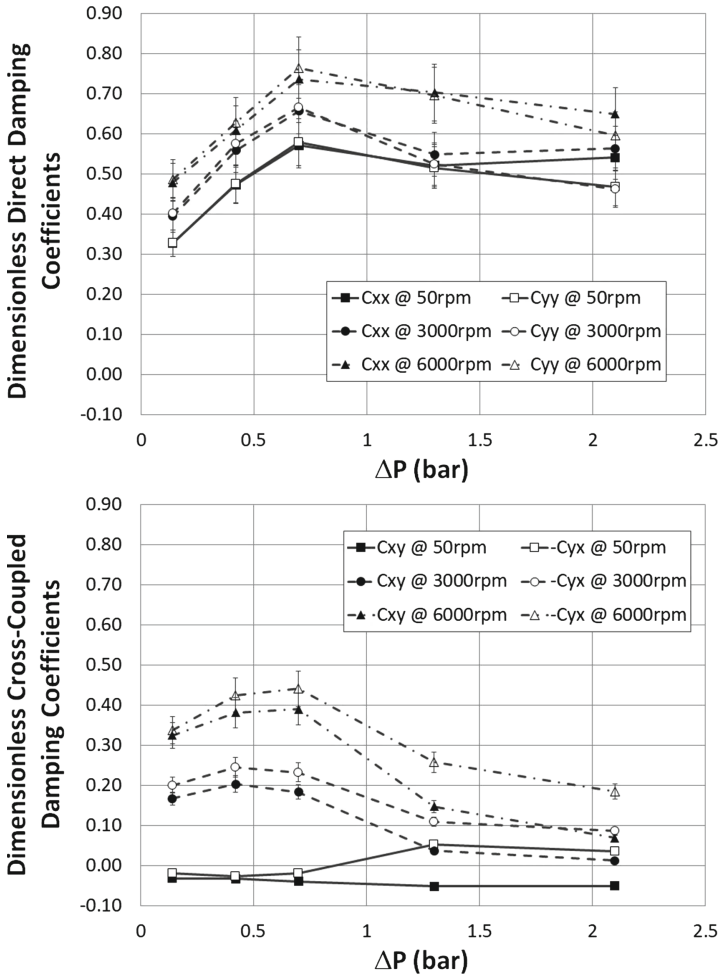


Fig. 8. Identified damping coefficients

## 7 Conclusion

Experimental results are presented for the direct and cross-coupled stiffness and damping coefficients for a multistage arrangement of four identical brush seals. Variable test parameters include pressure differential and shaft speed. Direct stiffness is shown to have positive value, to increase with pressure differential and to be almost the same at 3000 and 6000 rpm. Cross-coupled stiffness is generally lower than direct stiffness and is quasi-unchanged by increasing the pressure differential. Direct damping coefficients are always positive, softly dependent on shaft speed and begin to decrease after a pressure differential of 0.7 MPa.


**Acknowledgements.** The authors are grateful to Centre National d'Etudes Spatiales (CNES) and to ARIANE GROUP for using the test rig BALAFRE and for their agreement to present this experimental work. This work was partially funded by the French Government program "Investissements d'Avenir" (EQUIPEX GAP, reference ANR-11-EQPX-0018).

## References

1. Conner, K.J., Childs, D.W.: Rotordynamic and leakage characteristics of a four-stage brush seal. Final report for period October 1988–30 August 1992. Technical report, Turbomachinery Laboratories, Texas A&M University, College Station, Texas (1992)
2. Carlile, J.A., Hendricks, R.C., Yoder, D.A.: Brush seal leakage performance with gaseous working fluids at static and low rotor speed conditions. *ASME J. Eng. Gas Turbines Power* **115**(2), 397–403 (1993)
3. Chupp, R.E., Holle, G.F.: Generalizing circular brush seal leakage through a randomly distributed bristle bed. *ASME J. Turbomach.* **118**(1), 153–161 (1996)
4. Chupp, R.E., Hendricks, R.C., Lattime, S.B., Steinetz, B.M.: Sealing in turbomachinery. *J. Propul. Power* **22**(2), 313–349 (2006)
5. Pugachev, A.O., Deckner, M.: Experimental and theoretical rotordynamic stiffness coefficients for a three-stage brush seal. *Mech. Syst. Signal Process.* **31**, 143–154 (2012)
6. Raben, M., Friedrichs, J., Flegler, J.: Brush seal frictional heat generation—test rig design and validation under steam environment. *ASME J. Eng. Gas Turbines Power* **139**(3), 032,502–032,502-9 (2016)
7. Aslan-zada, F.E., Mammadov, V.A., Dohnal, F.: Brush seals and labyrinth seals in gas turbine applications. *Proc. IMechE Part A J. Power Energy* **227**(2), 216–230 (2012)
8. Hildebrandt, M., Schwitzke, C., Bauer, H.: Experimental investigation on the influence of geometrical parameters on the frictional heat input and leakage performance of brush seals. *ASME J. Eng. Gas Turbines Power* (2017). <https://doi.org/10.1115/1.4038767>
9. Aksit, M.F.: Brush seals and common issues in brush seal applications (2012). <http://research.sabanciuniv.edu/26863/1/RTO-AVT-188-KN4.pdf>
10. Pugachev, A.O., Gaszner, M., Georgakis, C., Cooper, P.: Segmentation effects on brush seal leakage and rotordynamic coefficients. *ASME J. Eng. Gas Turbines Power* **138**(3), 032,501–032,501-9 (2015)
11. Charles, S., Bonneau, O., Frêne, J.: Determination of the discharge coefficient of a thin-walled orifice used in hydrostatic bearings. *ASME J. Tribol.* **127**(3), 679–684 (2005)
12. Jolly, P., Hassini, A., Arghir, M., Bonneau, O.: Experimental and theoretical rotordynamic coefficients of smooth and round-hole pattern water fed annular seals. In: Proceedings of ASME Turbo Expo 2014, Turbine Technical Conference and Exposition, 16–20 June, Düsseldorf, Germany (2014)
13. Childs, D.W., Mclean, J.E., Zhang, M., Arthur, S.P.: Rotordynamic performance of a negative-swirl brake for a tooth-on-stator labyrinth seal. *ASME J. Eng. Gas Turbines Power* **138**(6), 062,505–062,505-8 (2015)



# Kriging Surrogate Model Dedicated to a Tilting-Pad Journal Bearing

Arinan De P. Dourado, Jefferson S. Barbosa, Leonardo Sicchieri, Aldemir A. Cavalini Jr. , and Valder Steffen Jr.

LMEst – Structural Mechanics Laboratory, School of Mechanical Engineering, Federal University of Uberlândia, Av. João Naves de Ávila, 2121, Uberlândia, MG 38408-196, Brazil  
aacjunior@ufu.com

**Abstract.** In this contribution, a kriging surrogate model was used to represent a tilting-pad hydrodynamic bearing of a Francis hydropower unit. The rotating machine is composed by a vertical shaft and three hydrodynamic bearings, namely (i) a combined tilting-pad radial/thrust bearing, which is located close to the generator; (ii) an intermediate radial tilting-pad bearing; (iii) and a cylindrical bearing located close to the Francis turbine. During the solution of the equations of motion, it was verified that the bearings are critical regarding the associated computational cost. Thus, the bearings were represented in the hydropower unit model by using surrogate models. The kriging model dedicated to the intermediate radial bearing is presented in this paper, in which the equilibrium position of the shaft and the inlet oil temperature were used as input values. The bearing supporting forces, maximum oil film pressure, and maximum oil film temperature were considered as output values. A thermohydrodynamic model of the bearing was used to determine the output variables from the input ones. Consequently, the kriging surrogate model was determined. The obtained results demonstrate the effectiveness of the proposed approach.

**Keywords:** Kriging surrogate models · Rotordynamics  
Hydrodynamic bearings · Francis hydropower unit

## 1 Introduction

Bearings are mechanical elements responsible for supporting rotating shafts, which can be classified as axial or radial (thrust or guide bearings, respectively), depending on the applied load direction. Regarding its geometry, they can have fixed or variable geometries (cylindrical or tilting-pad bearings, respectively). According to the origin of the supporting forces, they can be further classified as roller bearings, hydrodynamic, or magnetic bearings. In hydropower units, hydrodynamic bearings are widely used due to their load capabilities [1].

It is worth mentioning that the present work was developed under the R&D project *Robust Modeling for the Diagnosis of Defects in Generating Units* (02476-3108/2016) conducted by ANEEL (Brazilian Electric Energy Agency) with the financial support of the companies CERAN, BAESA, ENERCAN, and Foz do Chapecó. In this case, a



model-based approach was proposed aiming to detect incipient faults in a Francis hydropower unit.

Monitoring techniques are commonly used to increase efficiency in detecting hydraulic, electrical, and mechanical faults in hydropower units. Monitoring contributes to reducing maintenance costs and provides safety operating conditions to hydropower generation. However, widely used monitoring systems are not able to detect damages that are not included in their knowledge basis. Consequently, model-based approaches can be used to assist in fault detection for the cases in which conventional monitoring systems cannot work satisfactorily. The mathematical simulation of hydropower units is an indispensable resource for engineers, allowing a comprehensive understanding of the dynamic behavior of the system and the prediction of undesired operating conditions. Thus, faults can be detected by solving a typical inverse problem associated with the hydropower unit representative model. The numerical results are compared with experimental vibration measurements. Faults are detected when the model responses are similar to the experimental ones.

The considered Francis hydropower unit is composed by a vertical shaft, a generator unit, a Francis turbine, and three bearings, namely (i) a combined tilting-pad radial/thrust bearing, which is located close to the generator; (ii) an intermediate radial tilting-pad bearing; (iii) and a cylindrical bearing located close to the Francis turbine. In this case, the shaft is modeled by using the finite element method. The generator is represented by considering simplified mechanic and electric theories. Similarly, the Francis turbine is mechanically modeled by a rigid disc and the applied hydraulic forces were obtained from a CFD analysis. The bearings supporting forces are determined by using associated thermohydrodynamic models (THD models), in which the Reynolds and energy equations are solved simultaneously by using the finite volume approach.

The bearings THD models [2] combine the Reynolds and energy equations to obtain the oil film pressure and temperature fields. Coupled differential equations must be solved simultaneously, in which numerical procedures are required. An initial temperature distribution is estimated, leading to a corresponding pressure field. The obtained pressure is used to calculate a new temperature distribution, which is used to update the oil viscosity and pressure. This procedure must be repeated until convergence.

The proposed model-based fault detection methodology monitors the vibration responses of the Francis hydropower unit in the time domain, by comparing numerical and experimental data. Consequently, the bearings THD models should be solved at each integration time step of the system finite element model. Additionally, possible faults are detected through an optimization procedure. The resulting numerical procedure presents high computational cost, in which, approximately, 90% is associated with the THD models. Thus, it is interesting to replace the bearing models by a faster estimation procedure.

In this contribution, the response surface approach based on the kriging formalism [3] was used to obtain a surrogate model dedicated to the intermediate tilting-pad bearing of the Francis hydropower unit. The equilibrium position of the shaft and the inlet oil temperature were used as input values. The bearing supporting forces, maximum oil film pressure, and maximum oil film temperature were considered as output

values. Thus, the present work aims to demonstrate the efficiency of the obtained kriging surrogate model to predict the behavior of a complex bearing.

Besides the focus of the present work is dedicated to the intermediate radial tilting-pad bearing of a large-scale machinery, the proposed methodology can be applied in other class of bearings and rotor sizes.

## 2 THD Bearing Model

In this section, the THD model of the intermediate tilting-pad bearing of the Francis hydropower unit will be presented.

Mathematical models of hydrodynamic bearings are used to determine the pressure distribution generated in the oil film, according to their geometric characteristics and operational conditions. This is obtained by solving the so-called Reynolds equation, derived from simplifications on the Navier-Stokes equation. Commonly, the oil film temperature is considered constant. However, fractions of kinetic energy are dissipated as heat due to the motion between the bearing parts. The oil temperature increases and, consequently, the oil viscosity decreases. Aiming to develop more accurate hydrodynamic bearing models [2], THD models were proposed. The thermal effects are considered by associating the energy equation to the Reynolds equation.

Figure 1 presents the schematic representation of a radial tilting-pad bearing, in which  $\Omega$  is the shaft rotational speed,  $R$  is the shaft radius,  $R_s$  is pad radius,  $O_P$ ,  $O_E$ , and  $O_S$  are the pivot rotational center, the shaft center, and the pad center, respectively,  $h_S$ ,  $\beta_S$ , and  $L$  is the thickness, the coverage angle, and the length of the pad, respectively,  $h_0$  is the bearing radial clearance,  $\varphi$  is the angular position of the pivot,  $\beta$  is the pad angular position, and  $\alpha$  is the pad rotational angle relative to the pivot.

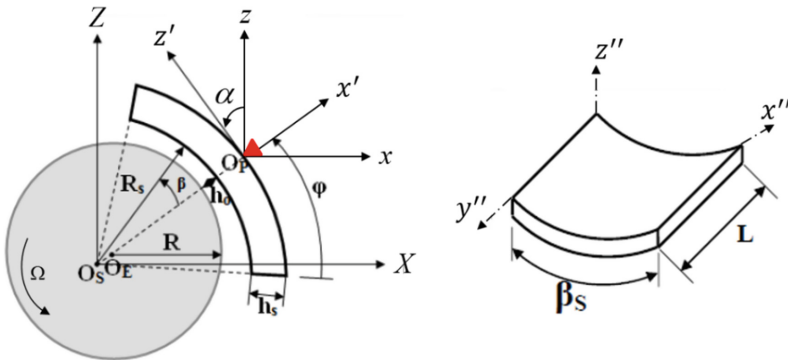


Fig. 1. Radial tilting-pad bearing physical model. (Adapted from [4])

The THD model is formulated based on four reference frames (see Fig. 1). The first one is placed at the center of the bearing;  $I (X, Y, Z)$  – the inertial system. The second

frame indicates the position of the  $j$ -th pad in the bearing;  $B(x, y, z)$  – auxiliary system. Each pad has its own auxiliary mobile system;  $B'(x', y', z')$  – mobile system. The last system follows the inner surface of the pad;  $B''(x'', y'', z'')$  – curvilinear mobile system.

For tilting-pad bearings, the Reynolds equation is applied to each pad following the procedure presented by [5]. Equation 1 presents the oil thickness as presented by [6].

$$h_h(\beta) = R_S - R - \{ \sin(\beta)[z_r + \alpha(R_S + h_S)] + \cos(\beta)(x_r + R_S - R - h_0) \} \quad (1)$$

in which  $x_r$  and  $z_r$  are the center position in the inertial system frame  $I(X, Y, Z)$  at  $X$  and  $Z$  directions, respectively.

Considering  $\mu_0$  as the reference oil viscosity at the oil inlet temperature  $T_0$ , the Reynolds equation for each pad of the tilting-pad bearing in its dimensionless form is given by Eq. (2). This is a partial differential equation with no analytical solution, that is numerically solved by using the finite volume approach [7–9]. Equation 3 illustrates the dimensionless parameters of the Reynolds equation.

$$\begin{aligned} & \left(\frac{1}{\beta_S}\right)^2 \frac{\partial}{\partial \bar{x}} \left( \bar{F}_2 \bar{h}_h^3 \frac{\partial \bar{p}_h}{\partial \bar{x}} \right) + \left(\frac{R_S}{L}\right)^2 \frac{\partial}{\partial \bar{y}} \left( \bar{F}_2 \bar{h}_h^3 \frac{\partial \bar{p}_h}{\partial \bar{y}} \right) \\ & = \left(\frac{R}{\beta_S R_S}\right) \frac{\partial}{\partial \bar{x}} \left[ \bar{h}_h \left( 1 - \frac{\bar{F}_1}{\bar{F}_0} \right) \right] + \left( \frac{\partial \bar{h}_h}{\partial \bar{t}} \right) \end{aligned} \quad (2)$$

$$\bar{x} = \frac{x}{\beta_S R_S} \quad \bar{y} = \frac{y}{L} \quad \bar{z} = \frac{z}{h_h} \quad t = \frac{\bar{t}}{\omega} \quad \bar{\mu} = \frac{\mu}{\mu_0} \quad \bar{\mu} = \frac{\mu}{\mu_0} \quad \bar{h}_h = \frac{h_h}{h_0} \quad \bar{p}_h = \frac{p_h h_0^2}{\mu_0 \omega R_S^2}$$

$$F_0 = \frac{h_0 \cdot \bar{h}_h}{\mu_0} \int_0^1 \frac{1}{\bar{\mu}} d\bar{z} = \frac{h_0 \cdot \bar{h}_h}{\mu_0} \bar{F}_0 \quad F_1 = \frac{h_0^2 \cdot \bar{h}_h^2}{\mu_0} \int_0^1 \frac{\bar{z}}{\bar{\mu}} d\bar{z} = \frac{h_0^2 \cdot \bar{h}_h^2}{\mu_0} \bar{F}_1$$

$$F_2 = \frac{h_0^3 \cdot \bar{h}_h^3}{\mu_0} \int_0^1 \frac{\bar{z}}{\bar{\mu}} \left( \bar{z} - \frac{\bar{F}_1}{\bar{F}_0} \right) d\bar{z} = \frac{h_0^3 \cdot \bar{h}_h^3}{\mu_0} \bar{F}_2$$

(3)

where  $p_h$  is the hydrodynamic pressure.

In order to determine the oil film temperature, the energy equation is applied by considering that variations of the oil specific mass ( $\rho$ ), thermal conductivity ( $k_r$ ), and specific heat ( $c_p$ ) with respect to the temperature can be disregarded. It is assumed that only the oil viscosity ( $\mu$ ) is treated as a function of the temperature. Additionally, the variation of the oil temperature along the  $y$  direction can be disregarded. Equation (4) presents the energy equation and how the oil viscosity is expressed as a function of the temperature.

$$\begin{aligned}
\rho c_p \left( u \frac{\partial T}{\partial x} + w \frac{\partial T}{\partial z} \right) &= k_t \left( \frac{\partial^2 T}{\partial x^2} + \frac{\partial^2 T}{\partial z^2} \right) + \\
2\mu \left[ \left( \frac{\partial u}{\partial x} \right)^2 + \left( \frac{\partial w}{\partial z} \right)^2 \right] &- \frac{2}{3} \left( \frac{\partial u}{\partial x} + \frac{\partial w}{\partial z} \right)^2 + \left( \frac{\partial u}{\partial z} + \frac{\partial w}{\partial x} \right)^2 + \left( \frac{\partial v}{\partial z} \right)^2 + \left( \frac{\partial v}{\partial x} \right)^2 \\
\mu &= a \exp \left( \frac{b}{T + 273, 15 + c} \right)
\end{aligned} \tag{4}$$

where  $u$ ,  $v$  and  $w$  are the fluid velocities along the bearing  $x$ ,  $y$  e  $z$  directions, respectively,  $T$  is the oil film temperature and  $a$ ,  $b$ , and  $c$  are constant coefficients related to the oil type (considering for instance oil ISO VG 68,  $a = 7.582 \times 10^{-8}$ ,  $b = 3991$ , and  $c = 0.09499$ ).

From the temperature field, the oil viscosity can be determined and, subsequently, the pressure field is obtained. The temperature is recalculated and this iterative procedure continues until convergence. Finally, the supporting hydrodynamic forces generated in each pad can be determined as shown in Eq. (5) (reference frame  $B''$ ). In tilting-pad bearings, the resulting moment in each pad must be null to achieve the equilibrium position of the shaft. Equation (6) shows how the moment in each pad is calculated.

$$F_{xm_j} = \int_0^{\beta_s} \int_0^L p_{h_j}(x, y) \cdot \cos(\beta_j) \cdot dy \cdot dx \tag{5}$$

$$F_{zm_j} = \int_0^{\beta_s} \int_0^L p_{h_j}(x, y) \cdot \sin(\beta_j) \cdot dy \cdot dx$$

$$M_{R_j} = F_{xm_j} \cdot (R_S + h_S) \tag{6}$$

whereas  $F_{xm_j}$  and  $F_{zm_j}$  are the resulting supporting forces along the  $x''$  e  $z''$  directions of the  $j$ -th pad, respectively.

After determining the supporting forces in each pad that satisfy the equilibrium condition, the resulting bearing supporting forces,  $F_X$  and  $F_Z$ , along with the  $X$  and  $Z$  directions, respectively, are calculated. These resulting supporting hydrodynamic forces are calculated as shown in Eq. (7). Figure 2 brings a simplified flowchart of the tilting-pad supporting forces estimation procedure. In this case, the Newton-Raphson approach was used to determine the equilibrium position of the shaft.

$$F_X = \sum_{j=1}^N [F_{xm_j} \cdot \cos(\varphi_j + \alpha_j)]$$

$$F_Z = \sum_{j=1}^N [F_{zm_j} \cdot \sin(\varphi_j + \alpha_j)]$$
(7)

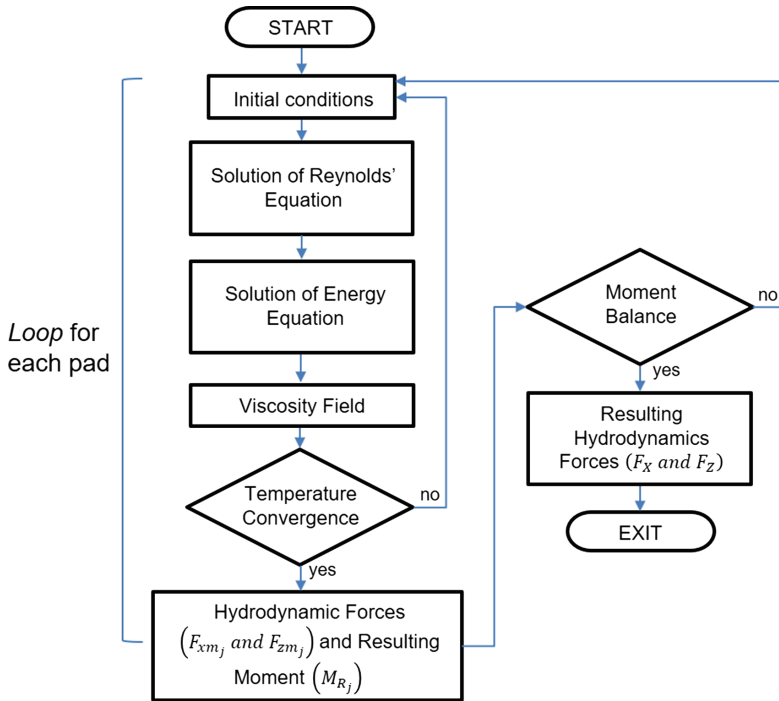


Fig. 2. Tilting-pad THD model flowchart

### 3 Kriging Meta-Modeling

In this section the mathematical concepts of the kriging formalism are presented following the procedures presented in [10, 11]. The general idea of meta-modeling is to construct simple functions capable of estimating required values by means of sets of input/output data previously generated in an experimental design. The main difference between kriging formalism and other meta-modeling approaches relies on the exploitation of spatial correlations between the function values to correct the average behavior of the regression model. Next, the key aspects related to kriging formalism are addressed focusing on the developed bearing meta-model.

The computer analysis codes are deterministic and, consequently, not subject to measurement error since they get the same output for the same input. Hence, the usual

measures of uncertainty derived from least-squares residuals have no obvious meaning and some statisticians [12, 13] have argued to use it for a deterministic analysis [10]. Thus, [13] suggested modeling the deterministic computer response as given by Eq. (8).

$$y(\mathbf{x}) = f(\mathbf{x}) + Z(\mathbf{x}) \quad (8)$$

where  $y(\mathbf{x})$  is the unknown function of interest,  $f(\mathbf{x})$  is a known polynomial function of  $\mathbf{x}$ ,  $Z(\mathbf{x})$  is the realization of a normally distributed Gaussian random process with mean zero, variance  $\sigma^2$ , and non-zero covariance [11].

The  $f(\mathbf{x})$  term in Eq. (8) is similar to the polynomial model in a response surface and provides a global model of the design space, while,  $Z(\mathbf{x})$  creates localized deviations so that the kriging model interpolates the sampled data points. The covariance matrix of  $Z(\mathbf{x})$  is given as in Eq. (9).

$$\text{Cov}[Z(\mathbf{x}^i), Z(\mathbf{x}^j)] = \sigma^2 \mathbf{R}([R(\mathbf{x}^i, \mathbf{x}^j)]) \quad (9)$$

in which  $\mathbf{R}$  is the correlation matrix, and  $R(\mathbf{x}^i, \mathbf{x}^j)$  is the correlation function between any two of the  $n_s$  sampled data points  $\mathbf{x}^i$  and  $\mathbf{x}^j$ .  $\mathbf{R}$  is a symmetric matrix with ones along the diagonal.

The correlation function  $R(\mathbf{x}^i, \mathbf{x}^j)$  is specified by the user. Table 1 illustrates some commonly used correlation functions, whereas  $\theta_k$  is the unknown correlation parameters used to fit the model, and the  $x_k^i$  and  $x_k^j$  are the  $k$ -th components of sample points  $\mathbf{x}^i$  and  $\mathbf{x}^j$ . In the present contribution, the linear correlation function was used in the construction of the THD kriging meta-models. Predicted estimates,  $\hat{y}(\mathbf{x})$ , at untried values of  $\mathbf{x}$  can be obtained as shown in Eq. (10).

$$\hat{y} = \hat{\beta} + \mathbf{r}^T(\mathbf{x})\mathbf{R}^{-1}(\mathbf{y} - \mathbf{f}\hat{\beta}) \quad (10)$$

$$\mathbf{r}^T(\mathbf{x}) = [R(\mathbf{x}, \mathbf{x}^1), R(\mathbf{x}, \mathbf{x}^2), \dots, R(\mathbf{x}, \mathbf{x}^{n_s})]^T \quad (11)$$

$$\hat{\beta} = (\mathbf{f}^T\mathbf{R}^{-1}\mathbf{f})^{-1}\mathbf{f}^T\mathbf{R}^{-1}\mathbf{y} \quad (12)$$

in which  $\mathbf{y}$  is the column vector of length  $n_s$  containing the values of the response at each sample point,  $\mathbf{f}$  is a column vector of length  $n_s$ ,  $\mathbf{r}^T(\mathbf{x})$  is the correlation vector of length  $n_s$  between an untried  $\mathbf{x}$  and the sampled data points  $\{\mathbf{x}^1, \mathbf{x}^2, \dots, \mathbf{x}^{n_s}\}$  (given by Eq. (11)), and  $\hat{\beta}$  is estimated by using Eq. (12).

It is worth mentioning that depending on the choice of the correlation function, kriging meta-models can either provide an exact or inexact interpolation of the data. Also, the second part of Eq. (8) (i.e.  $Z(\mathbf{x})$ ) is used to model the deviation from  $f(\mathbf{x})$  so that the whole model interpolates the experimental points of the design.

In order to validate the generated kriging meta-models, precision metrics were used in this contribution, mainly a metric known as RMSE (Root Mean Square Error), and the maximum absolute error (MAX) metric. RMSE is a metric of general precision of the meta-model, while MAX provides a local precision metric. The lower the values of

**Table 1.** Commonly used correlation models.

Correlation Model	$R(\mathbf{x}^i, \mathbf{x}^j)$
Linear	$\max\{0, 1 - \theta_k  x_k^i - x_k^j \}$
Gaussian	$\exp\left(-\sum_{k=1}^{n_s} \theta_k  x_k^i - x_k^j ^2\right)$
Exponential	$\exp\left(-\sum_{k=1}^{n_s} \theta_k  x_k^i - x_k^j \right)$
Cubic	$1 - 3\xi_k^2 + 2\xi_k^3; \xi_k = \min\{1, \theta_k  x_k^i - x_k^j \}$

RMSE and MAX, the more accurate and representative the meta-models are. Equations (13) and (14) define the RMSE and MAX metrics, respectively.

$$RMSE = \sqrt{\frac{\sum_{k=1}^{n_s} (y_k - \hat{y}_k)^2}{n_s}} \tag{13}$$

$$MAX = \max |y_k - \hat{y}_k| \quad k = 1, \dots, n_s \tag{14}$$

## 4 Numerical Results

In this section, the numerical results associated with the meta-model of the intermediate tilting-pad bearing of the Francis hydropower unit will be discussed. All models used in the present contribution were developed in *Matlab*<sup>®</sup> platform.

The construction of a kriging predictor (i.e. kriging meta-model) requires preliminary choices of the regression order, the spatial correlation function, and the size and type the experiment design. As mentioned, in the present contribution the linear correlation model was adopted along with a rectangular grid design considering 313 samples. Additional 312 samples were also generated following a rectangular grid design for the validation of the generated meta-models. Polynomials regressions of order zero (i.e.  $f(\mathbf{x}) = [1, \dots, 1]$ ), first order (i.e.  $f(\mathbf{x}) = [1, x_1, \dots, x_{n_s}]$ ), and second order (i.e.  $f(\mathbf{x}) = [1, x_1, \dots, x_{n_s}, x_1^2, \dots, x_1 x_{n_s}, \dots, x_{n_s} x_1, \dots, x_{n_s}^2]$ ) were evaluated.

The output variables of the bearing meta-model were the supporting forces ( $F_X$ , see Eq. (9)), the maximum temperature and maximum pressure in the oil film (Max. T and Max. P in Tables 3 and 4, respectively), and the minimum oil film thickness (Min. h in Tables 3 and 4). The considered input variables were the shaft position  $x_r$  and  $y_r$  (see Fig. 1), the bearing radial clearance ( $h_0$ ), and the oil film restitution temperature ( $T_R$ ). Table 2 presents the lower and upper bounds considered for rectangular grid design. It is important to mention that the validation samples were also generated within the bounds presented in Table 2.

It is worth mentioning that the intermediate tilting-pad bearing of the Francis hydropower unit presents 6 pads, in which  $\Omega = 300$  RPM,  $R = 0.465$  m,  $R_S = 0.467$  m,  $h_S = 0.070$  m,  $\beta_S = 25^\circ$ ,  $L = 0.197$  m,  $h_0 = 200$   $\mu$ m, and  $\varphi = 15^\circ$ . Due to the

**Table 2.** Considered intervals for the input variables.

Parameter	Interval
$x_r$	(-270,218) [ $\mu\text{m}$ ]
$y_r$	(-257,257) [ $\mu\text{m}$ ]
$h_0$	(200,300) [ $\mu\text{m}$ ]
$T_R$	(30,45) [ $^{\circ}\text{C}$ ]

associated computational cost of the THD model, only one pad of the bearing was simulated ( $\beta = 0$ ). However, this simulation was performed at the reference frame  $B(x, y, z)$ . Consequently, the obtained results can be addressed to the remaining pads by applying a simple geometric transformation (the shaft position was imposed) and the supporting forces represented in the inertial reference frame were obtained. This is possible since the distance between the pads of the considered bearing is large enough to guarantee the inlet oil in each pad presents the same temperature of the reservoir.

Tables 3 and 4 presents the *RMSE* and *MAX* metrics for the fitting procedure samples, and for the validation analysis (i.e. considering the 312 additional samples), respectively. Figure 3, 4, 5 and 6 illustrate the validation analysis results for each output variable. It can be noticed that the generated meta-model obtained an exact interpolation of the numerical data (i.e. *RMSE* and *MAX* practically null) in all considered regression orders. The best results were found for the second order regression model, indicating that the most accurate kriging predictor in the scenarios considered in this contribution is the second order with linear correlation kriging meta-model (maximum *RMSE* value of 0.605 and a maximum error of 2.8, see Table 4).

**Table 3.** Metric values for the fitting procedure.

Output	<i>RMSE</i>	<i>MAX</i>
Zero-order		
$F_X$ [kN]	$3.4 \times 10^{-13}$	$1.6 \times 10^{-13}$
Max. T [ $^{\circ}\text{C}$ ]	$3.6 \times 10^{-13}$	$1.6 \times 10^{-13}$
Max. P [MPa]	$3.5 \times 10^{-14}$	$1.6 \times 10^{-14}$
Min. h [ $\mu\text{m}$ ]	$4.6 \times 10^{-12}$	$2 \times 10^{-12}$
First order		
$F_X$ [kN]	$2.4 \times 10^{-13}$	$1.1 \times 10^{-12}$
Max. T [ $^{\circ}\text{C}$ ]	$1.7 \times 10^{-13}$	$8.5 \times 10^{-13}$
Max. P [MPa]	$2.4 \times 10^{-14}$	$1.1 \times 10^{-13}$
Min. h [ $\mu\text{m}$ ]	$5.8 \times 10^{-14}$	$2.7 \times 10^{-13}$
Second order		
$F_X$ [kN]	$1.4 \times 10^{-13}$	$5.6 \times 10^{-13}$
Max. T [ $^{\circ}\text{C}$ ]	$9.7 \times 10^{-14}$	$4.8 \times 10^{-13}$
Max. P [MPa]	$1.4 \times 10^{-14}$	$5.7 \times 10^{-14}$
Min. h [ $\mu\text{m}$ ]	$5.3 \times 10^{-14}$	$2.2 \times 10^{-14}$



**Table 4.** Metric values for the validation analysis (considering the additional samples).

Output	RMSE	MAX
Zero-order		
$F_X$ [kN]	1.44	7.83
Max. T [°C]	1.44	6.82
Max. P [MPa]	0.14	0.76
Min. h [ $\mu\text{m}$ ]	15.7	67.2
First order		
$F_X$ [kN]	1.00	5.16
Max. T [°C]	0.77	3.74
Max. P [MPa]	0.10	0.50
Min. h [ $\mu\text{m}$ ]	0.21	0.77
Second order		
$F_X$ [kN]	0.60	2.63
Max. T [°C]	0.50	2.80
Max. P [MPa]	0.06	0.26
Min. h [ $\mu\text{m}$ ]	0.20	0.73

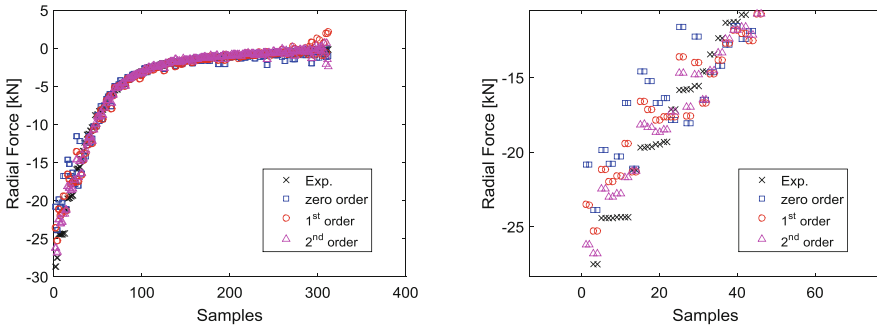


**Fig. 3.** Radial supporting force validation response.

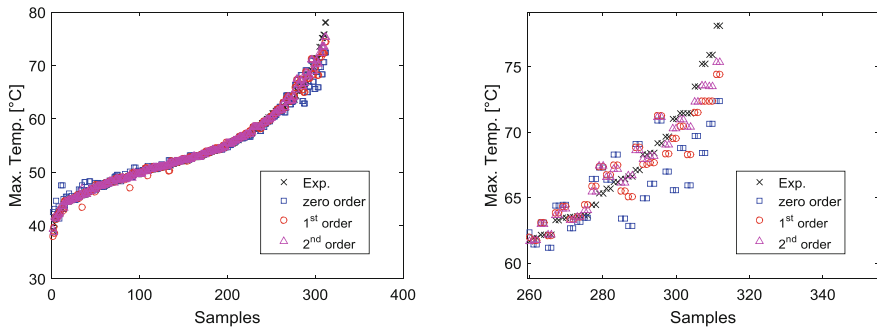


**Fig. 4.** Maximum oil film temperature validation response.

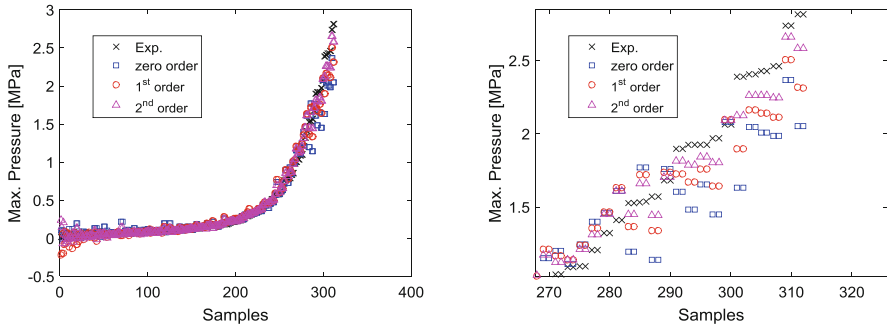


**Fig. 5.** Maximum oil film pressure validation response.

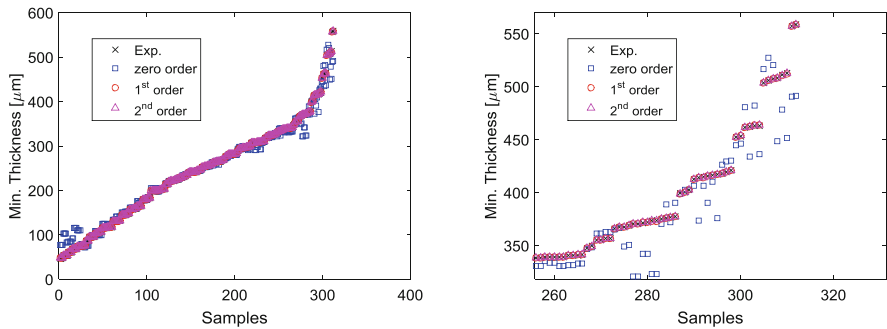


**Fig. 6.** Minimum oil film thickness validation response.

It is worth mentioning that despite been possible to observe relative high values of maximum error in the validation analysis (7.83 kN and 6.82 °C; see Figs. 3, 4, and Table 4) these errors are majorly observed for extreme values of force, temperature, and pressure, whereas along the nominal operating condition of the hydropower unit (i.e. around the median samples) no significant errors can be noticed, illustrating the accuracy of the generated kriging meta-model.

## 5 Final Remarks

In this contribution, a surrogate model approach was evaluated for reducing computational cost associated with a mathematical model of a Francis hydropower unit. The rotor is composed of a vertical rotor and three hydrodynamic bearings. However, only the kriging meta-model of the intermediate tilting-pad bearing was presented in the present contribution.

The intermediate guide bearing meta-model was capable of estimating the bearing radial supporting forces and the oil film properties (i.e. maximum temperature and pressure, and minimum thickness) by means of direct matrix operations without any convergence procedure.

This is an important feature since the goal of the proposed approach was to reduce the associated computational effort of the bearing model. It is worth mentioning that the THD model of the mentioned bearing takes around 10 s to estimate the supporting forces and corresponding pressure and temperature fields of the oil film. The same results were obtained in 0.1 s by using the formulated kriging model. This demonstrates the capability and significance of kriging meta-modeling for dynamic analysis of generating units. Further contributions will encompass the effects of the correlation models on the kriging estimator accuracy.

**Acknowledgements.** The authors are thankful to the Brazilian Research Agencies CAPES, FAPEMIG and CNPq (INCTEIE) for the financial support provided for this research effort. The authors are also thankful to the companies CERAN, BAESA, ENERCAN, and Foz do Chapecó for the financial support through the R&D project *Robust Modeling for the Diagnosis of Defects in Generating Units* (02476-3108/2016).

## References

1. Vance, J., Zeidan, F., Murphy, B.: *Machinery Vibration and Rotordynamics*. Wiley, New Jersey (2010)
2. Dowson, D.: A generalized reynolds equation for fluid film lubrication. *Int. J. Mech. Sci.* **4**, 159–170 (1962)
3. Kleijnen, J.: Kriging metamodeling in simulation: a review. *Eur. J. Oper. Res.* **192**(3), 707–716 (2009)
4. Daniel, G.: *Desenvolvimento de um Modelo Termodinâmico para Análise em Mancais Segmentados*. Ph.D. thesis (Portuguese), Universidade Estadual de Campinas (2012)
5. Childs, D.: *Turbomachinery Rotordynamics—Phenomena, Modeling, & Analysis*. Wiley, New York (1993)
6. Russo, F.H.: *Identification of the characteristics of hybrid tilting-pad bearings: theory and experimentation*. Ph.D. thesis (Portuguese), Universidade Estadual de Campinas (1995)
7. Maliska, C.: *Transferência de Calor e Mecânica dos Fluidos Computacional* (Portuguese). Livros Técnicos e Científicos Editora (2004)
8. Mazumder, S.: *Numerical Methods for Partial Differential Equations: Finite Difference and Finite*. Elsevier, New York (2015)
9. Moukalled, F., Mangani, L., Darwish, M.: *The Finite Volume Method in Computational Fluid Dynamics: An Advanced Introduction with OpenFOAM® and Matlab*. Springer, Berlin (2015)
10. Wang, H., Enying, L., Li, G., Zhong, Z.H.: Development of metamodeling based optimization system for high nonlinear engineering problems. *Adv. Eng. Softw.* **39**, 629–645 (2008)
11. Simpson, T., Peplinski, J., Koch, P., Allen, J.: Metamodels for computer-based engineering design: survey and recommendations. *Eng. Comput.* **17**, 129–150 (2001)
12. Welch, W., Buck, R., Sacks, J.W.H., Mitchell, T., Moriss, M.: Screening, predicting, and computer experiments. *Technometrics* **34**(1), 15–25 (1992)
13. Sacks, J., Welch, W., Mitchell, T., Wynn, H.: Design and Analysis of Computer Experiments. *Statistical Science* **4**(4), 409–435 (1989)



# Effect of Lubricant Supply Pressure on SFD Performance: Ends Sealed with O-rings and Piston Rings

Luis San Andrés<sup>(✉)</sup> and Bonjin Koo

Mechanical Engineering Department, Texas A&M University,  
College Station, TX 77840, USA  
lsanandres@tamu.edu

**Abstract.** A well-designed SFD must deliver enough damping to aid in decreasing rotor amplitudes of motion. Piston rings (PRs) and O-rings (ORs) are commonly used as end seals in dampers for commercial and military gas turbine engines, respectively. The paper details dynamic load tests conducted on a short length SFD ( $L/D = 0.2$ ) sealed with either (a) PRs or (b) ORs and the experimentally estimated damping and inertia force coefficients. Lubricant (ISO VG2) flows thru one feedhole at the land middle plane with supply pressure increasing from 0.7 bar(g) to 6.2 bar(g). In the PR-SFD, oil leaves the film land through the rings' abutted ends making a slit. The OR-SFD effectively seals any leakage; hence, lubricant flows out through a discharge hole at a location halfway of the film (upper) land length. Multiple sets of single frequency (10 Hz–100 Hz) dynamic loads produced circular centered orbits with amplitude ( $r$ ) equal to 30% of the radial clearance. For both PR-SFD and OR-SFD, the viscous damping coefficient diminishes quickly as the lubricant supply pressure drops below 3 bar(g). The added mass coefficient, on the other hand, remains nearly constant for the PR-SFD and slightly increases for the OR-SFD. The OR-SFD delivers  $\sim 10\%$  more viscous damping than the PR-SFD albeit it demands of a larger flow rate. Analysis of the recorded film dynamic pressures shows their *peak-peak* magnitude increases with whirl frequency. However, operation at the lowest oil supply pressure, 0.7 bar(g), generates film peak pressures not increasing as the excitation frequency rises, thus evidencing the presence of air ingestion and entrapment, as vividly shown by recorded film dynamic pressure waves, in particular for the PR-SFD.

**Keywords:** Squeeze film damper · Dynamic performance

## Nomenclature

$a_{\alpha(t)}$ , ( $\alpha=X,Y$ )	Acceleration of bearing cartridge [ $\text{m/s}^2$ ]
$c$	Nominal radial clearance [ $\mu\text{m}$ ]
$C_{\alpha\beta}$ , ( $\alpha,\beta=X,Y$ )	SFD damping coefficients [ $\text{N}\cdot\text{s/m}$ ]
$D$	Journal diameter [ $\text{m}$ ]
$F_{\alpha(t)}$ , ( $\alpha=X,Y$ )	External applied dynamic load [ $\text{N}$ ]
$H_{\alpha\beta}$ , ( $\alpha,\beta=X,Y$ )	System complex dynamic stiffness [ $\text{MN/m}$ ]
$i$	$\sqrt{-1}$ . Imaginary unit
$K_{\alpha\beta}$ , ( $\alpha,\beta=X,Y$ )	SFD stiffness coefficients [ $\text{N/m}$ ]

$K_S$	Structural support stiffness [N/m]
$L$	Film land length [m]
$M_{\alpha\beta, (\alpha,\beta=X,Y)}$	SFD added mass coefficients [kg]
$M_{BC}$	Bearing cartridge mass [kg]
$P$	Dynamic pressure in film land [Pa]
$P_s$	Static oil pressure at supply orifice [Pa(g)]
$Re_s$	$=(\rho/\mu)\omega c^2$ . Squeeze film Reynolds number [-]
$r$	Orbit amplitude [m]
$t$	Time [s]
$v_s$	$= r\omega$ . Squeeze film velocity [m/s]
$X, Y$	Coordinate system
$x(t), y(t)$	Displacement of BC respect to journal along $X$ and $Y$ axes [m]
$\rho, \mu$	Oil density [ $\text{kg/m}^3$ ] and viscosity [Pa·s]
$\theta$	Circumferential coordinate [rad]
$\omega$	Excitation frequency [rad/s]

### Vectors and Matrices

$\mathbf{a}_{(\omega)}$	Vector of accelerations $\{a_{X(\omega)}, a_{Y(\omega)}\}^T$ in frequency domain [ $\text{m/s}^2$ ]
$\mathbf{K}, \mathbf{C}, \mathbf{M}$	Matrices of stiffness, damping and added mass coefficients
$\mathbf{F}_{(\omega)}$	Vector of dynamic loads $\{F_{X(\omega)}, F_{Y(\omega)}\}^T$ in frequency domain [N]
$\mathbf{H}_{(\omega)}$	$\mathbf{K} - \omega^2\mathbf{M} + i\omega\mathbf{C}$ . Matrix of complex stiffnesss [N/m]
$\mathbf{Z}_{(\omega)}$	Vector of bearing displacements $\{x_{(\omega)}, y_{(\omega)}\}^T$ relative to a journal [m]

### Subscripts

BC	Bearing cartridge
L	Lubricated system
SFD	Squeeze film damper
S	Structure

### Acronyms

OR	O-ring
PR	Piston ring
SFD	Squeeze film damper

## 1 Introduction

Modern high performance turbomachinery demands high power density with proven efficiency. Squeeze film dampers (SFDs) aid to reduce excessive rotor synchronous vibration, to suppress non-synchronous instabilities, and to isolate a rotor from the stator or housing. Thus, rotating machinery often implements SFDs to traverse safely thru critical speeds and to reduce transmitted forces to the casing [1].

Figure 1 depicts a schematic view of a sealed ends SFD in series with a ball bearing supported rotor. The annular gap between the bearing cartridge and the outer race of a

ball bearing makes the lubricant film. An anti-rotation pin (dowel pin) or a centering spring (squirrel cage) prevents rotation of the outer race. Rotor displacements squeeze the lubricant film to generate a hydrodynamic pressure that produces a reaction dynamic force [1].

The damping effect depends on the damper geometry, lubricant physical properties, and operating conditions. Zeidan et al. [2] identify SFD operation with two distinct types of fluid cavitation and a regime due to air ingestion and entrapment. Vapor cavitation appears in tightly sealed ends SFDs when the film pressure reaches vapor pressure. Air ingestion occurs in vented or not tightly sealed ends SFDs operating with a high squeeze velocity and not supplied with sufficient lubricant to fill the clearance.

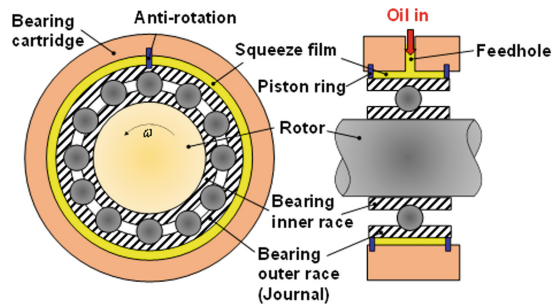


Fig. 1. Photograph and top view of SFD test rig with electromagnetic shakers and static loader.

## 2 An Appraisal of Prior Work

Della Pietra and Adiletta [3] critically review the major findings in SFD research and applications over a 40 year period, from 1960 to 2000. The paper, though offering comprehensive information, applies mainly to academic research.

San Andrés [1] notes that dampers with end seals are preferred in aircraft engine applications and centrifugal compressors as they provide substantial more damping than with an open ends damper while requiring of little through flow. Thus dampers with ends seals save both space and weight and reduce lubricant storage requirements, for example. End seals differ in type, some being more effective than others are. Piston rings and end plate seals apply to high temperature commercial aircraft engines, whereas O-rings (with segmented beams) are more adequate for lightweight compressors [4] and military air breathing engines. A piston ring is prone to distort the squeeze film pressure field due to profuse leakage through its abutted ends (slit) and also can cock and even lock preventing the damper to work effectively. O-rings produce very tight end seals but age quickly, are limited in their temperature capability, often creep and eventually harden after long periods of operation.

Prior experiments producing a vis-à-vis comparison of performance for either a SFD sealed with piston rings (PRs) or one with O-rings (ORs) is rather limited. Miyachi et al. [5] find that as the oil supply pressure increases, the damping capability for a PR-SFD nearly doubles when compared to that of an OR-SFD. The difference is

ascribed to additional (dry) frictional dissipation effects from the PR sidewalls. Levesley and Holmes [6] report a PR-SFD has larger damping than a damper with thigh end plate seals, likely due to the difference in flow conductance from the two sealing arrangements.

Other work, summarized in Ref. [7] at the authors' laboratory, produces a vast amount of experimental data for a number of SFD configurations applicable to aircraft engines, and aiming to verify predictive models and to optimize SFD design and performance with stringent performance requirements. The test damper elements vary in slenderness ratio ( $L/D$ ), with distinct clearances (from small to large,  $c/D = 0.001$  to  $0.002$ ), constructed with either a deep groove for oil delivery or with (one to three) orifices for direct supply of oil into the film land. Other configurations include PR seals, whose proper installation is crucial to ensure little leakage and large damping [8]. For example, Jeung and San Andrés [9] find that a short length PR-SFD ( $L/D = 0.2$ ) produces damping ( $C$ ) and inertia ( $M$ ) coefficients that are one order of magnitude larger than an open ends SFD of the same dimensions. The ratio of force coefficients, sealed over open ends, is approximately  $\sim \frac{1}{2} (D/L)^2$ , 50% of a theoretical prediction.

More recently, San Andrés et al. [10] report comprehensive experimental results, namely force coefficients and film dynamic pressure measurements, comparing the performance of a PR-SFD to that of an OR-SFD, and advance a predictive SFD flow model that departs from customary practice. This paper complements the early work and presents more experimental results towards assessing the effect of lubricant supply pressure (and flowrate) on the forced response of a SFD with two types of end seals, piston rings and O-rings.

### 3 Description of Test Rig Facility, SFD Damper and Seals

Figure 2 depicts a photograph and a schematic top view of the SFD test rig consisting of a bearing test stand, two orthogonally placed electromagnetic shakers (max. 2,450 N), and a hydraulic static loader located  $45^\circ$  away from the shakers. The shakers connect to the bearing cartridge via slender stingers. The static loader pulls the bearing cartridge to various static eccentric positions with respect to the journal fixed center. Note the disposition of the coordinates ( $X, Y$ ) and the angular coordinate ( $\theta$ ) with origin along the  $X$  axis.

The SFD test bearing consists of a rigid pedestal, journal base, support rods, journal, and bearing cartridge (BC). The journal base bolts onto the pedestal that is mounted to the table. Four elastic steel rods provide a structural stiffness  $K_S = 1.6$  MN/m and the BC has effective mass  $M_{BC} = 15$  kg.

The short length SFD ( $L/D = 0.2$ ) has a film land length  $L = 25.4$  mm, diameter  $D = 127$  mm, and a radial clearance  $c = 0.373$  mm. Note the damper has a large clearance ( $\frac{1}{2}D/c$ )  $\sim 170$  as requested by the sponsor. Two end grooves, each with width 2.5 mm and depth 3.8 mm, host either piston rings (PRs) or O-rings. The journal end lips have a width equal to 3.3 mm. The journal has one feedhole ( $\theta = 45^\circ$ ) at the film mid-plane ( $z = 0$ ) with diameter  $\phi_{in}$  of 2.5 mm. A hydraulic pump supplies a

mineral oil to the journal film land thru the feedhole. The lubricant ISO VG2 has density  $\rho = 820 \text{ kg/m}^3$  and kinematic viscosity  $\mu = 2.57 \text{ cPoise}$  at  $23 \text{ }^\circ\text{C}$ . Both physical properties are similar to those of a lubricant used in aircraft engines operating at a high temperature ( $T \sim 200 \text{ }^\circ\text{C}$ ).

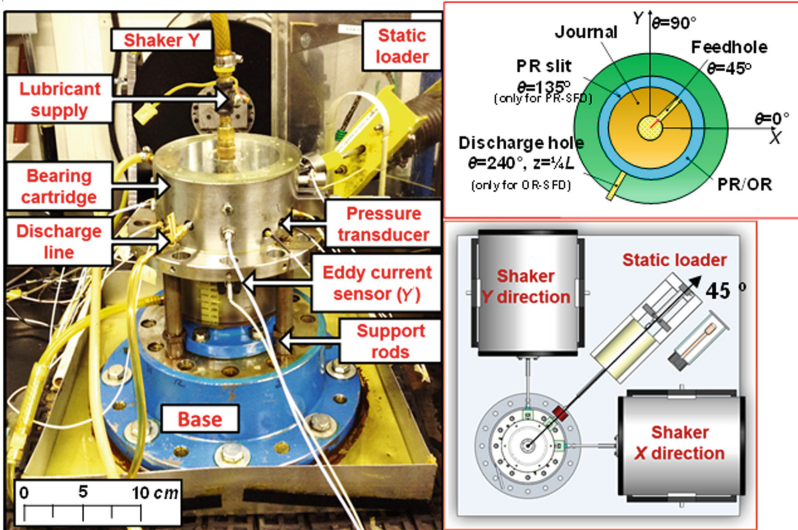
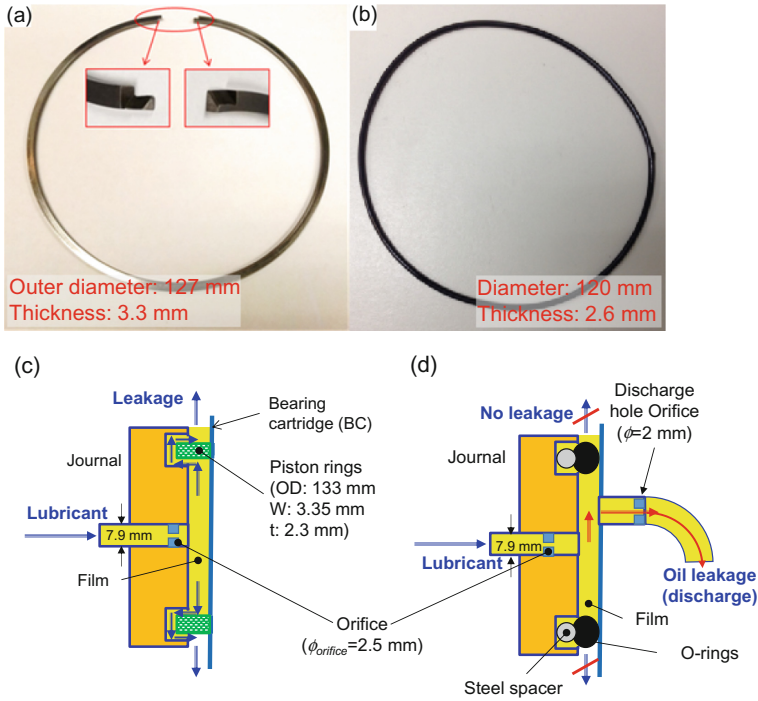


Fig. 2. Photograph and top view of SFD test rig with electromagnetic shakers and static loader.

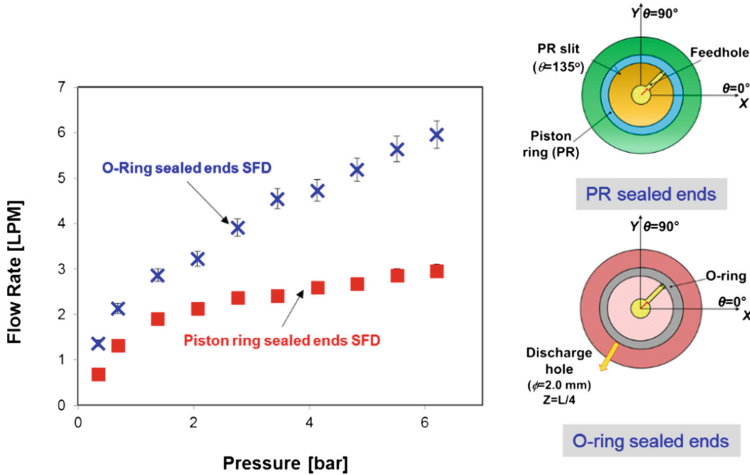
Figure 3 shows photographs of (a) a PR and (b) an O-ring as well as schematic views of the SFD with (c) PR sealed ends, and with (d) O-ring sealed ends. When closed, the PR outer diameter contacts the ID of the BC. For the tests with PRs, each piston ring slit (abutted ends) locates at  $\theta = 135^\circ$ . Upon installation, the lubricant fluid flows through the piston ring slit. The other sealed SFD uses multipurpose Buna-N O-ring with an outer diameter of 120 mm and a thickness of 2.6 mm. Note that the lubricant in the O-ring sealed ends SFD does not leak thru the axial sealed ends, but discharges through an orifice hole of diameter 2.0 mm at  $\theta = 240^\circ$  and  $z = \frac{1}{4} L$ .

Figure 4 shows the recorded flow rate through the dampers versus supply pressure. For an inlet pressure,  $\sim 689 \text{ kPa}$ , the flowrate thru the OR-SFD ( $19 \text{ cm}^3/\text{s}$ ) is larger than that for the PR-SFD ( $13 \text{ cm}^3/\text{s}$ ). Note the OR-SFD demands more flow as the lubricant is routed to a discharge orifice and return line. On the other hand, the PR-SFD leaks mainly thru the PR-slit ends. See the insets for a depiction of both dampers.





**Fig. 3.** Photographs of end seals and schematic views of their installation: (a, c) piston rings, and (b, d) O-rings.



**Fig. 4.** Lubricant flowrate ( $Q_s$ ) vs. oil supply pressure ( $P_s$ ) for damper sealed with piston rings or with O-ring seals. Lubricant supplies through a feedhole at  $\theta = 45^\circ$  at mid-plane ( $z = 0$ ). For PR-SFD, PR slits locate at  $\theta = 135^\circ$ . For the OR-SFD, lubricant discharges through a hole with diameter 2.0 mm at  $\theta = 225^\circ$  and  $z = \frac{1}{4}L$ .

## 4 Description of Tests with Periodic Loads and Identification of Force Coefficients

For whirl circular orbit motions, the experiments include single-frequency dynamic load excitations with amplitude  $F$  and frequency  $\omega$  over the frequency range 10–120 Hz, in steps of 10 Hz. The test rig is modeled as a two degree of freedom mechanical system and governed by the following equation of motion in the frequency domain

$$[\mathbf{K}_L - \omega^2\mathbf{M}_L + i\omega\mathbf{C}_L]\mathbf{Z}_{(\omega)} = \mathbf{H}_{L(\omega)}\mathbf{Z}_{(\omega)} = \mathbf{F}_{(\omega)} - M_{BC}\mathbf{a}_{(\omega)} \tag{1}$$

where  $\mathbf{F}_{(\omega)}$ ,  $\mathbf{Z}_{(\omega)} = \{x, y\}^T$ , are  $\mathbf{a}_{(\omega)}$  are vectors, with components along the  $X$  and  $Y$  directions, of the discrete Fourier transforms of the recorded dynamic load, bearing cartridge (BC) displacement relative to the journal, and BC acceleration, respectively. Above  $\mathbf{H}$  is the system complex dynamic stiffness; its real part,  $\text{Re}(\mathbf{H}_L) \rightarrow (\mathbf{K}_L - \omega^2\mathbf{M}_L)$ , yields the lubricated system stiffness ( $\mathbf{K}_L$ ) and added mass ( $\mathbf{M}_L$ ) coefficients, whereas the imaginary part  $\text{Im}(\mathbf{H}_L) \rightarrow (\omega\mathbf{C}_L)$  yields the lubricated system damping coefficients ( $\mathbf{C}_L$ ).

Separate tests (without lubricant) produce the *dry* system structural force coefficients  $K_S = 1.6$  MN/m,  $M_S = 1.9$  kg, and  $C_S = 0.65$  kN.s/m. The *dry* system natural frequency is  $\omega_n = 51$  Hz and the damping ratio ( $\zeta$ ) equals 0.06 and 0.08 along the  $X$  and  $Y$  directions, respectively.

The SFD complex stiffness matrix  $\mathbf{H}_{\text{SFD}}$  follows by subtracting the dry system complex stiffness ( $\mathbf{H}_S = \mathbf{K}_S - \omega^2\mathbf{M}_S + i\omega\mathbf{C}_S$ ) from the lubricated system complex stiffness. That is  $\mathbf{H}_{\text{SFD}} = \mathbf{H}_L - \mathbf{H}_S$ .

Note that test SFD cross-coupled complex stiffness coefficients ( $H_{XY}, H_{YX}$ ) are at least one order of magnitude smaller than the direct coefficients ( $H_{XX}, H_{YY}$ ). Due to their smallness cross-coupled coefficients are not reported.

## 5 Experimental Results

### 5.1 Comparison of Identified Force Coefficients for PR-SFD and OR-SFD

This section presents the experimental results obtained from circular centered whirl motions conducted with the sealed ends SFDs. The shakers exert single frequency dynamic forces to produce circular orbit motions with amplitude  $r = 0.1c$  and  $0.3c$ . During the tests, the lubricant supply pressure  $P_s$  ranges from 0.7 bar(g) to 6.2 bar(g). A decrease in supply pressure corresponds to a decrease in lubricant flow rate, see Fig. 4. At the highest whirl frequency, the squeeze film Reynolds number  $Re_s = (\rho/\mu)\omega c^2 \sim 26$ .

For both dampers, with PRs or with OR, Fig. 5 shows the real and imaginary parts of the lubricated system complex stiffnesses ( $H_{XX}, H_{YY}$ ) for whirl orbits with  $r/c = 0.3$  and operation at increasing oil supply pressure, 1.4 bar to 6.2 bar. The graphs include the curve fit models with an excellent correlation to the test data. That is  $\text{Re}(H) \rightarrow K - \omega^2M$  and  $\text{Ima}(H) \rightarrow C\omega$  are physically accurate. Test data for  $r = 0.1c$  are not shown for brevity.

For the PR sealed ends SFD, the intersection of  $Re(H)_L$  at  $\omega = 0$  delivers the structure stiffness  $K_S$ , whereas the OR-SFD produces a larger static stiffness, as noted in the graph, due to the compliance of the O-rings. Both test SFDs produce a significant added mass coefficient  $(M)_{SFD}$  which lowers the lubricated system natural frequency to 24 Hz and 35 Hz for the PR-SFD and OR-SFD, respectively. Note that the oil supply pressure ( $P_s$ ) has little effect on both the lubricated system stiffness ( $K_L$ ) and inertia coefficients ( $M_L$ ). Not so for the  $Ima(H_L)$  which shows an increasing slope as  $P_s$  increases.

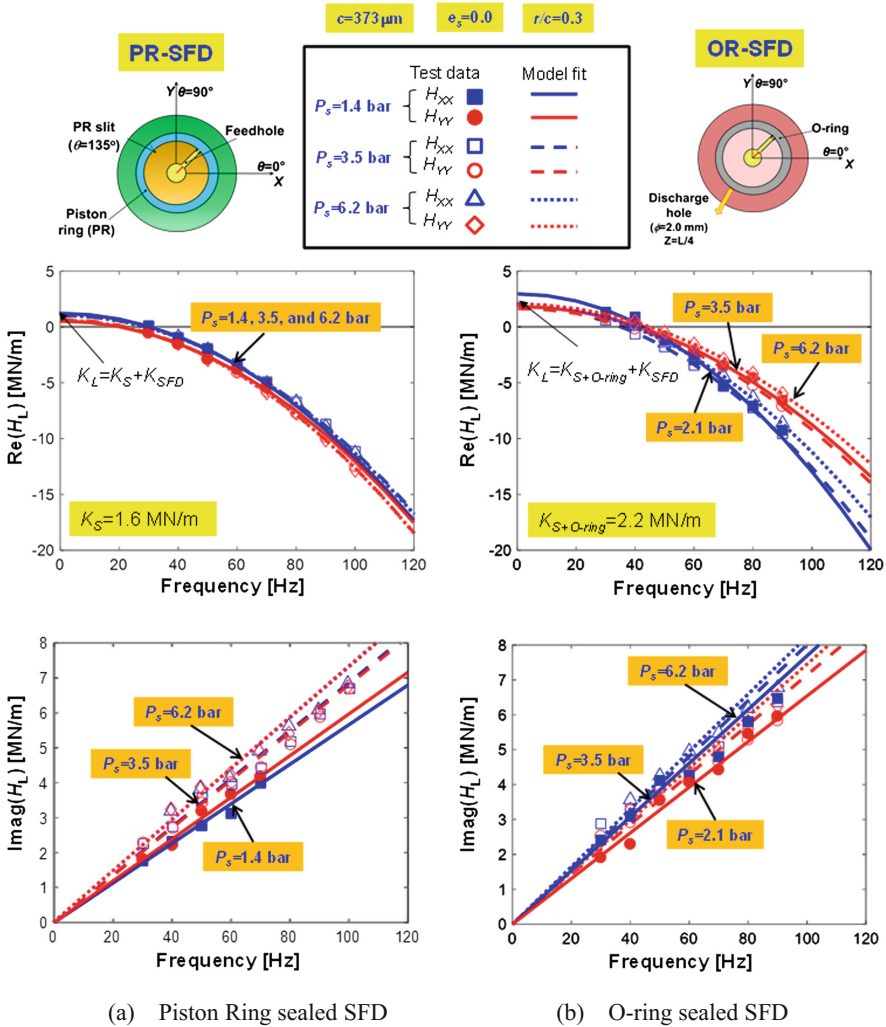


**Fig. 5.** Lubricated PR-SFD and OR-SFD: System real and imaginary parts of complex stiffnesses  $(H_{XX}, H_{YY})_L$  vs. excitation frequency. Circular centered orbits with radius  $r/c = 0.3$ . Lubricant supplies thru a feedhole at  $\theta = 45^\circ$  with supply pressure  $P_s = 1.4, 3.5, \text{ and } 6.2 \text{ bar(g)}$ . PR slits locate at  $\theta = 135^\circ$ .

For centered whirl orbits with amplitude  $r/c = -0.3$ , Fig. 6 presents the identified SFD direct damping ( $C$ ) and added mass ( $M$ ) coefficients for both test dampers as the oil supply pressure ( $P_s$ ) increases. The parameters shown are simple arithmetic averages of those coefficients along the  $X$  and  $Y$  directions. In the graphs, the bars denote the experimental uncertainty.

For the PR-SFD,  $C$  increases 30% as  $P_s$  grows from 2.1 bar to 6.2 bar whereas  $M$  remains nearly constant at  $\sim 30$  kg. For the OR-SFD,  $C$  increases  $\sim 11\%$  as  $P_s$  increases whereas  $M$  decreases  $\sim 13\%$ . The added mass ( $M$ ) for the OR-SFD is 16% higher than that of the PR-SFD. In short, for  $P_s > 2$  bar the OR-SFD produces slightly more damping (11% more) than the PR-SFD since the O-rings provide a perfect seal (no leakage). The PRs allow for leakage through its slits (abutted ends). Incidentally (not shown), note the OR-SFD shows dissimilar damping coefficients,  $C_{XX} \neq C_{YY}$ , likely due to the oil discharge hole locating at  $\theta = 240^\circ$  ( $30^\circ$  away from the  $Y$ -axis) which produce a local pressure sink.

Note that the damping discussed above is only viscous; the OR-SFD would actually produce  $\sim 10\%$  more damping with the addition of the damping coming from the viscoelasticity of the O-rings; see [10] for more details.

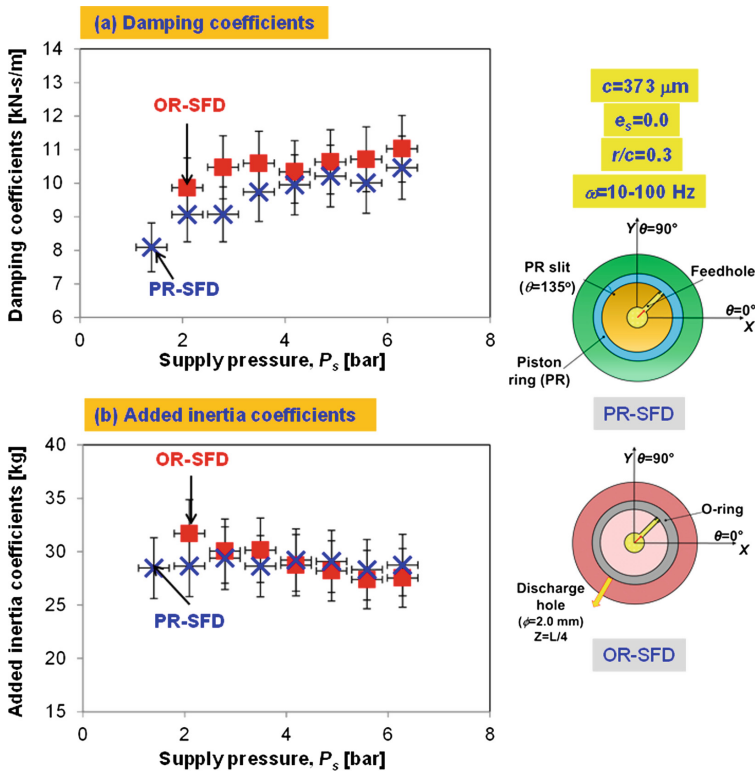


**Fig. 6.** PR-SFD and OR-SFD: Direct damping ( $C$ ) and added mass ( $M$ ) coefficients vs. lubricant supply pressure (gauge). Circular centered orbits with radius  $r/c = 0.3$  and whirl frequency to 100 Hz. Lubricant supplies thru a feedhole at  $\theta = 45^\circ$ . PR slits locate at  $\theta = 135^\circ$ .

### 5.2 Comparison of Recorded Film Pressures for PR-SFD and OR-SFD

In the experiments, two sets of three piezoelectric pressure sensors spaced apart by 90°, record the dynamic pressure at the top, bottom, and mid sections of the damper film land. Note that the pressure sensor tips are flushed with the inner surface of the bearing.

For operation with orbit radius  $r/c = 0.3$ , Fig. 7 displays the *peak-to-peak* dynamic film pressure recorded at the land mid-plane ( $z = 0$ ) and  $\theta = 225^\circ$  versus whirl frequency. In each graph, the data shows conditions with oil supply pressure increasing. The measurements reveal that operation with a low supply pressure (0.7 bar) does not produce a film peak pressure that increases with whirl frequency, as theory would otherwise indicate. The results likely evidence air ingestion in the fluid film land for the PR-SFD. Most notably, the OR-SFD does not produce as large peak pressures as the PR-SFD does because its oil flow is routed through a discharge orifice close to the location of pressure measurement. Nonetheless, recall the OR-SFD generates slightly more damping than the PR-SFD. For both dampers, operation with  $P_s > 2.1$  bar produces no changes in the film peak pressure as the excitation frequency increases.

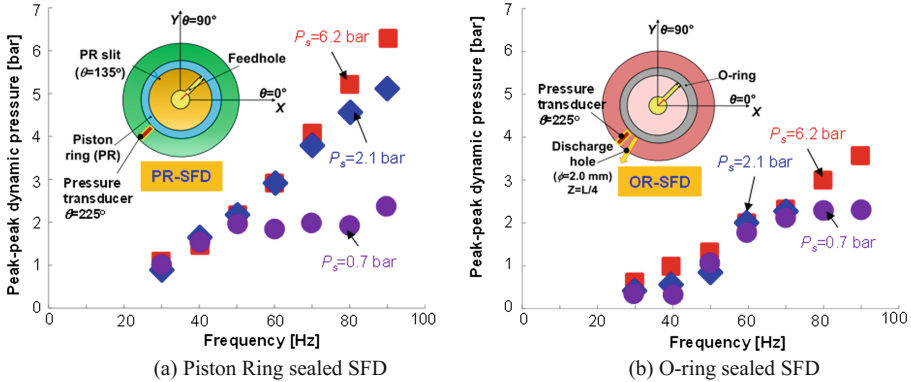


**Fig. 7.** Recorded *peak-to-peak* film dynamic pressures vs. whirl frequency for (a) PR-SFD and (b) OR-SFD. Circular centered orbits with radius  $r = 0.3c$ . Operation with lubricant supplied at pressure  $P_s = 0.7, 2.1,$  and  $6.2$  bar(g) thru one feed hole.

For both dampers supplied with pressure  $P_s$  increasing from 0.7 bar to 6.2 bar, Fig. 8 shows the dynamic pressure waves and film thickness for operation with a whirl orbit of radius  $r/c = 0.3$  and frequency  $\omega = 90$  Hz. The squeeze film velocity  $v_s = r\omega = 63$  mm/s. Each graph display three periods of whirl motion ( $T = 11$  ms) recorded at the land mid-plane and  $\theta = 225^\circ$ . In the graphs, a horizontal dash line represents a zero absolute pressure. Note that the position of the zero pressure is different for each graph since the position of the zero pressure scale on the right side represents the dynamic pressure,  $P_{dynamic} = P - P_{static}$ .

For both dampers, the film pressure waves recorded for oil delivered at a large supply pressure,  $P_s = 3.5$  bar and 6.2 bar, are almost the same, whereas the pressure

profiles with a small supply pressure ( $P_s = 0.7$  bar and 2.1 bar) generate a lesser *peak-to-peak* pressure magnitude.

For operation with a low supply pressure ( $P_s = 2.5$  bar), the PR-SFD shows the generation of pressure waves with high frequency content throughout a whole period of motion, the profiles are typical of air ingestion with bubble entrapment and collapsing. Note that for  $P_s = 3.5$  bar and 6.2 bar, the PR-SFD pressure profiles show a distinct spike when the film thickness is decreasing. This sudden spike may be due to the large leakage flowing as a jet thru the PR slits. Incidentally, this sudden spike in pressure explains the overly large *peak-peak* film pressures recorded for the PR-SFD, see Fig. 7 (a). On the other hand, the OR-SFD pressures do not show evidence of either air ingestion; the pressures recorded are cleaner than those measured in the PR-SFD.

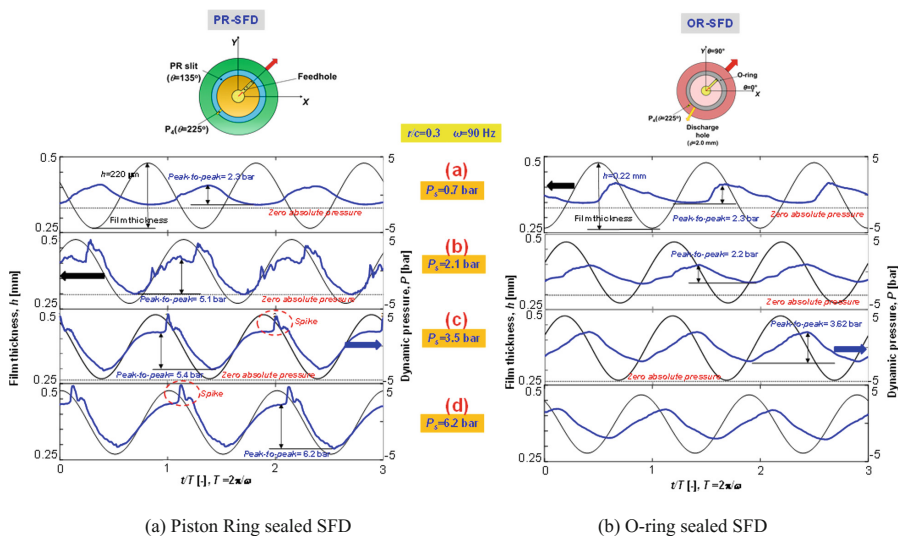


**Fig. 8.** Dynamic film pressures and film thickness recorded at mid-plane ( $z = 0$  and  $\theta = 225^\circ$ ) vs. time/ $T$ . PR and OR sealed ends dampers supplied with oil at  $P_s =$  (a) 0.7 (b) 2.1 (c) 3.5 and (d) 6.2 bar. Circular orbit with frequency  $\omega = 90$  Hz and  $r = 0.3c$  ( $v_s = r\omega = 63$  mm/s).

Please refer to San Andrés et al. [10] for a comprehensive assessment of the measurements conducted with both dampers, including a physically sound model for the leakage flow thru the PR slits and comparisons to predictions which reproduce with confidence the identified force coefficients. The work also correlates force coefficients determined directly from force/displacement frequency domain functions (as in the current paper) and estimations assuming the dynamic pressure field is invariant in a rotating coordinate system. This last approach, long held as a typical behavior for idealized SFDs, proves to be largely incorrect.

## 6 Conclusions

The paper consolidates measurements of the dynamic forced response of a short length SFD ( $L/D = 0.2$ ) sealed with either piston rings (PRs) or with O-rings (ORs). In the tests with ISO VG 2 lubricant, the supply pressure through one feed hole varies from  $P_s = 0.7$  bar(g) to 6.2 bar(g). Exerted single frequency loads produce circular centered orbits with radius  $r = 0.3c$ . The parameter identification delivers force coefficients valid over a frequency range (10–100 Hz). The maximum squeeze film velocity equals  $v_s = r = 90$  mm/s. The major conclusions drawn are:

- The damping coefficient  $C$  increases as the oil supply ( $P_s$ ) increases from 2.1 bar(g) to 6.2 bar(g). The added mass coefficient ( $M$ ) is nearly constant at  $\sim 30$  kg.
- For a large supply pressure ( $P_s > 2$  bar(g)), the OR-SFD produces 11% more viscous damping than the PR-SFD since the O-rings seal lubricant better than the PR seals. Furthermore, the OR-SFD actually produces  $\sim 10\%$  more damping with the addition of the elastomeric damping from the ORs.
- For low oil supply pressure  $P_s \sim 0.7$  bar(g) and operation with orbit radius  $r = 0.3c$ , the film *peak-to-peak* pressure does not increase with whirl frequency. The PR-SFD shows strong air ingestion thru the slit made by the piston rings abutted ends. Analysis of the dynamic pressure profiles reveals the PR-SFD shows unique features that include air ingestion and entrapment, and including sudden bursts of pressure at particular instances of the whirl motion.

San Andrés et al. [10] present more detailed measurements and predictions for comparison of SFDs operating with two distinctive end seal types, PRs and ORs.

## References

- San Andrés, L.: Squeeze Film Dampers (SFDs). Modern Lubrication Theory, Notes 13. Texas A&M University Digital Libraries (2002). <http://oaktrust.library.tamu.edu/handle/1969.1/93197>. Accessed 29 Jan 2018
- Vance, J., San Andrés, L., Zeidan, F.: Design and application of SFDs in rotating machinery. In: The 25th Turbomachinery Symposium 1996, pp. 169–188. Turbomachinery Lab., Houston (1996)
- Della Pietra, L., Adiletta, G.: Part I: characteristics and operating features. Shock Vib. Dig. **34**(1), 3–26 (2002)
- Kuzdzal, M.J., Hustak, J.F.: SFD bearing experimental vs analytical results for various damper configurations. In: The 25th Turbomachinery Symposium, pp. 57–70. Turbomachinery Lab., Houston (1996)
- Miyachi, T., Hoshiya, S., Sofue, Y., Matsuki, M., Torisaki, T.: Oil squeeze film dampers for reducing vibration of aircraft gas turbine engines. In: ASME 1979 International Gas Turbine Conference and Exhibit and Solar Energy Conference, p. V01bT02A032. ASME (1979)
- Leversley, M.C., Holmes, R.: The effect of oil supply and sealing arrangements on the performance of SFDs: an experimental study. J. Eng. Tribol. **210**, 221–232 (1996)
- San Andrés, L., Jeung, S.-H., Den, S., Savela, G.: Squeeze film dampers: a further experimental appraisal of their dynamic forced performance. In: The 45th Turbomachinery Symposium 2016. Turbomachinery Lab., Houston (2016)

8. San Andrés, L., Seshagiri, S.: Damping and inertia coefficients for two end sealed SFDs with a central groove: measurements and predictions. *ASME J. Gas Turbines Power* **135**(11), 112503 (2013)
9. Jeung, S.-H.: Experimental performance of an open ends SFD and a sealed ends SFD. Ph.D. dissertation, Texas A&M University, College Station (2017)
10. San Andrés, L., Koo, B., Jeung, S.-H.: Experimental force coefficients for two sealed ends SFDs (piston rings and O-rings): an assessment of their similarities and differences. In: *ASME Turbo Expo 2018: Turbine Technical Conference and Exposition*, GT-2018-76224, Oslo, Norway (2018)





# SEMAJIB: A Versatile High Performance Smart Bearing

Aly El-Shafei<sup>(✉)</sup>

RITEC, Cairo, Egypt  
elshafei@ritec-eg.com

**Abstract.** The experimental development of the Smart Electro-Magnetic Actuator Journal Integrated Bearing (SEMAJIB) is presented in this paper. The SEMAJIB is a smart high performance integrated bearing that combines a fluid film bearing (FFB) with an electro-magnetic actuator (EMA) in one integrated device. In all cases, the fluid film bearing shall carry the load, whereas the electro-magnetic actuator can be used as a pure controller or both as a controller and a load carrying element. In the latter case the electro-magnetic actuator can be considered as an active magnetic bearing (AMB). This paper summarizes the development of the SEMAJIB as a compact integrated bearing. It is shown that the SEMAJIB can easily transgress the multiple critical speeds of the 2-inch laboratory rotor, as well as suppress not only the first mode oil whip, but also the second mode oil whip, and additionally can control the rotor unbalance. The use of PD, H $\infty$  and Fuzzy Logic control to control the SEMAJIB is presented and compared. It is shown that the SEMAJIB is a high performance bearing that is versatile and can replace tilting-pad bearings in high performance rotating machinery.

## 1 Introduction

Fluid Film Bearings (FFBs) and Active Magnetic Bearings (AMBs) are competing devices in the marketplace. FFBs, in particular Journal Bearings (JBs), are superior load carrying elements due to their larger load carrying capacity and their ability to introduce passive damping to the rotor system. However, JBs exhibit an unstable vibration at high speed, called oil whip, which is excited when the rotor speed reaches about twice the first critical speed. This instability limits the possibility of increasing the rotor speed of rotation.

AMBs, on the other hand, provide contactless rotor support, at high speeds and are free from whip instabilities. They have an added feature which is their capabilities as controlling elements. AMBs can provide variable and controllable stiffness and damping and additionally can provide unbalance control and many other control features. However, AMBs suffer from certain shortcomings. In particular reliability issues are always a concern for AMB designers. In fact, AMBs are always designed with a redundant bearing system, called a “backup bearing”, such that the backup bearing carries the rotor in case of AMB failure.

This paper presents the SEMAJIB [1, 2], a smart high performance integrated bearing that combines a fluid film bearing (FFB) with an electro-magnetic actuator (EMA) in one integrated device. In all cases, the fluid film bearing shall carry the load,

whereas the electro-magnetic actuator can be used as a pure controller or both as a controller and a load carrying element. In the latter case the electro-magnetic actuator can be considered as an active magnetic bearing (AMB).

The integration of AMBs and JB's in one device has clear advantages. The SEMAJIB has all of the advantages of JB's and AMBs, and avoids all of the shortcomings of AMBs and JB's. The SEMAJIB is a superior load carrying element due to its larger load carrying capacity and its ability to introduce passive damping to the rotor system. Moreover, it is free from whip instabilities and has capabilities as a controller. A SEMAJIB can provide variable and controllable stiffness and damping and additionally can provide unbalance control and many other control features. Most importantly, there is no need for a backup bearing as the rotor is carried on the JB in all cases.

The author and his students have developed and published many papers describing the development of the SEMAJIB. In [3] controlling oil whip using the SEMAJIB through multiple algorithms is discussed. It is shown that damping control is an effective method for controlling the SEMAJIB [3]. Instability control and unbalance control using the SEMAJIB are introduced in [4]. An important contribution which shows that oil does not adversely affect the performance of AMBs is presented in [5]. In fact it is shown that oil in an AMB actually provides some minor improvements in AMB performance. The testing of a rotor on one SEMAJIB and one rolling element bearing using PID control is introduced in [6], while fuzzy logic control to the SEMAJIB is introduced in [7], and  $H^\infty$  control to the SEMAJIB is introduced in [8] and includes discussion of load sharing between the AMB and the JB. Testing of a rotor on two SEMAJIB bearings and the ability to transgress the oil whip instability for the first mode and the second mode by applying PD control is discussed in [9]. In fact this work [9] is a clear indication of the success of the SEMAJIB. It shows that the SEMAJIB can carry a high load rotor at high speeds and with ability to control multiple instabilities.

In all of the above experiments an off-the-shelf programmable controller is used. The control algorithms discussed in the previous paragraph were all implemented experimentally, and were quite successful. The choice of the control algorithm is a matter of choice for each application. In many cases, it is important to instruct the magnetic bearing not to interfere with the load carrying by the JB. In fact the  $H^\infty$  controller [8] actually tends to carry some of the load on the AMB, while the PD controller tends to act as a controller only. The problem is that the AMB likes to center the rotor, while the JB tends to move the rotor center downwards and sideways. These two competing devices need a controller designed to carry the load on the JB and keep all the AMB power for control. Only in special circumstances (like relocating resonances) should the AMB be allowed to carry the load.

In this paper, the author summarizes the development of the SEMAJIB, and presents new data on unbalance control. In the design of the SEMAJIB, the AMB is designed to be able to carry the static load. However, the load is carried by the JB, so actually the AMB is quite a sizable controller. It thus can sustain large unbalance forces (even at resonance). Moreover, the concept of a smart bearing is emphasized, where the bearing can correct malfunctions in a machine, thus increasing availability and reliability of machines.

## 2 Effect of Oil on Magnetic Bearing

The first issue that the author had to address while developing the SEMAJIB is the effect of oil on the AMB. The SEMAJIB is designed to have oil flood the AMB, contrary to current technology of oil free AMBs. The author and his students [5] developed a Finite Element Method (FEM) program that describes the AMB within the SEMAJIB and have replaced air in the gap by oil. The basic FEM model is shown in Fig. 1.

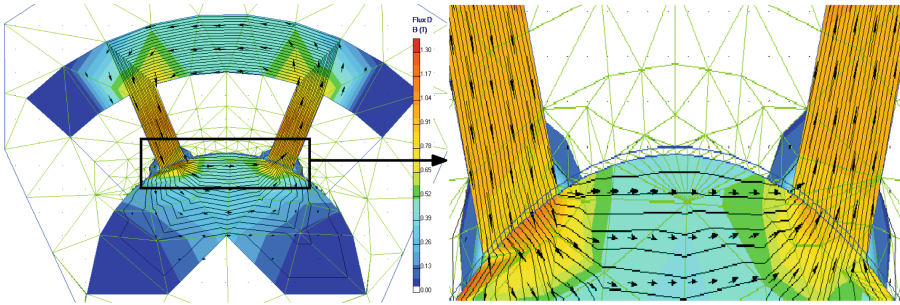


Fig. 1. FEM model of the AMB within the SEMAJIB [5]

A test rig was devised to examine the effect of oil on the AMB. The details of the test rig can be found in [5]; however the most important result is shown in Fig. 2. The magnetic forces generated by an input current are plotted for various gaps. Figure 2 shows that for a gap of 0.6 mm there is an excellent match between the performance of the AMB with an air gap and an oil gap, both experimentally and by the FEM model. There is a minor deviation at high currents that was seen experimentally (probably due

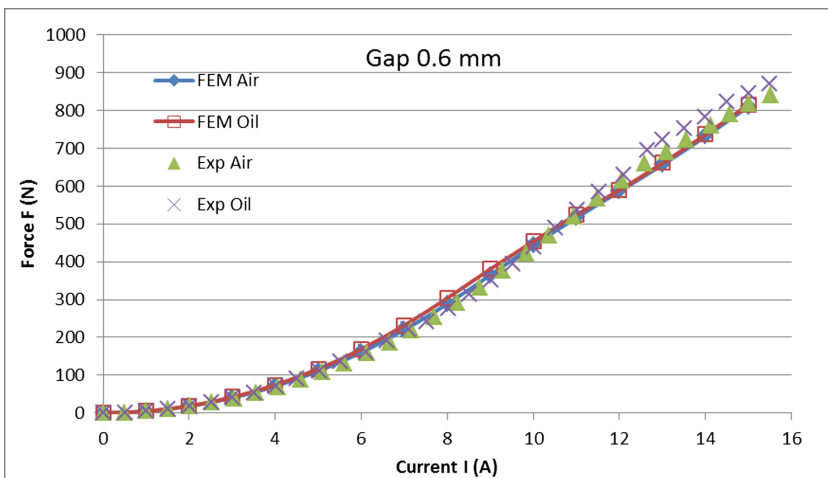
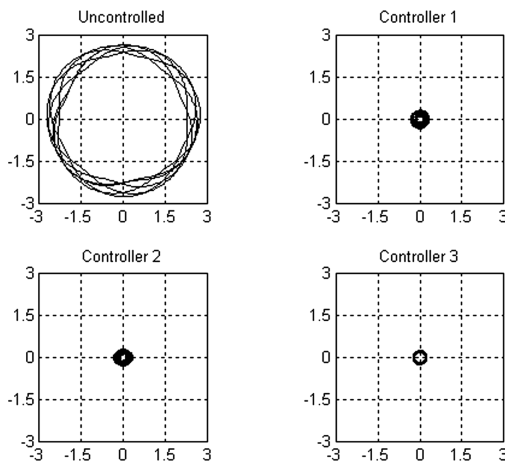


Fig. 2. Magnetic forces at 0.6 mm gap [5]

to thermal effects), however this is a positive deviation, meaning with oil; the AMB produces more force for a given current.

### 3 Initial Simulations

The initial simulations of applying the SEMAJIB on a Jeffcott rotor were developed in [3]. The results illustrated using three different controllers to control the oil whip instability generated by the JB. Three controllers were developed: Cross displacement, force and damping control [3]. The results are shown in Fig. 3 and summarized in Table 1.



**Fig. 3.** Orbits at center of jeffcott rotor [3]

**Table 1.** Reduction in orbit sizes [3]

Feedback	Journal amplitude	% reduction	Center disc amplitude	% reduction
Uncontrolled	0.62	-	2.67	-
Cross-displacement	0.11	82	0.33	88
Force	0.05	92	0.29	89
Damping	0.002	99	0.26	90

The results clearly indicate the success of the AMB in controlling the oil whip instability. Moreover, it was concluded the introducing damping by the AMB is quite effective, thus a PD controller would be appropriate for this application.

## 4 Experimental Results: Instability Control

A test rig was developed at Cairo University to test the SEMAJIB. It consisted of 50 mm diameter, 1.7 m long shaft, with 4 discs and mounted on a SEMAJIB [6] (see Figs. 4 and 5).

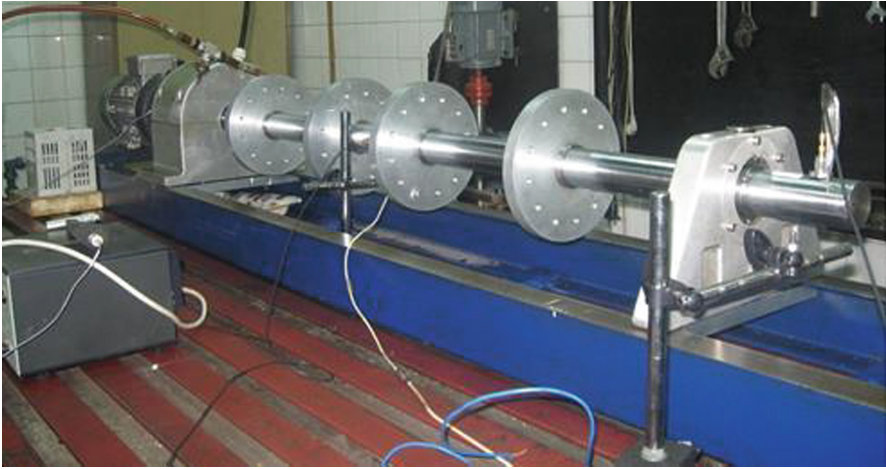


**Fig. 4.** Test rig used in testing the SEMAJIB [6]



**Fig. 5.** SEMAJIB used in testing [6]

An elaborate testing scheme is described in [6] for the test rig and for the SEMAJIB. The main purpose of the testing was to determine the capability of the AMB to control the JB instability. Figure 6 shows the waterfall diagram showing the run-up of the test rig. The 1x component increases at the critical speed and decreases thereafter, while the oil whip component appears when the oil whirl component reaches the critical speed and locks at the whip frequency. A PD controller was then used with the AMB within the SEMAJIB, and the results are shown in the waterfall of Fig. 7, where the oil whip instability was eliminated. Figure 8 shows the spectrum at the

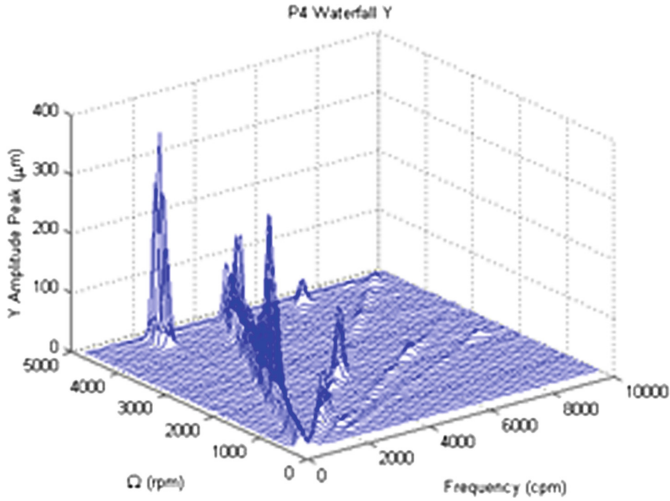


**Fig. 6.** Waterfall diagram showing oil whip instability [6]

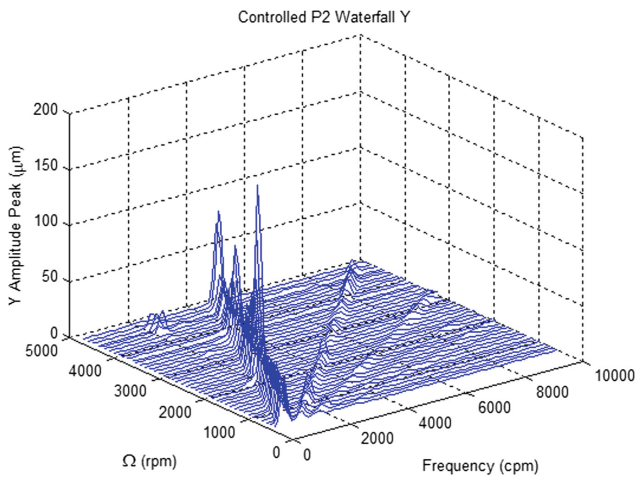


**Fig. 7.** Waterfall diagram with SEMAJIB showing the elimination of the oil whip instability [6]

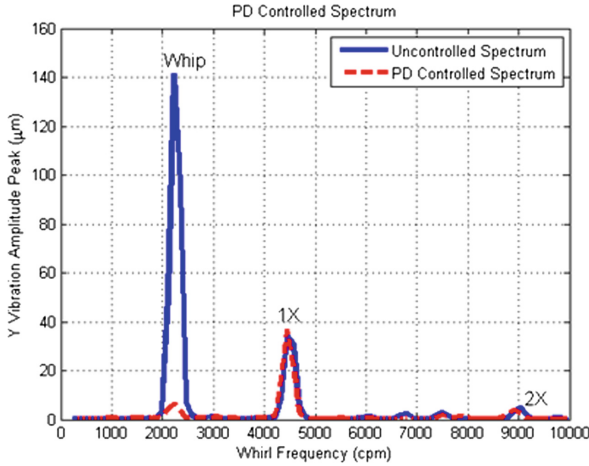


Fig. 8. Spectrum showing the elimination of oil whip instability [6]

operating speed with and without control. It is clear that the PD controller was able to control the oil whip instability and provide a stable bearing.

It is thus concluded that the SEMAJIB is a stable bearing that can transgress critical speeds and is an instability free bearing, due to the controller capabilities of the AMB.

It was suggested that actually high speed rotating machinery may actually encounter higher mode instabilities. Three controllers were developed PD control, Fuzzy Logic (FL) control and  $H^\infty$  control. All three controllers were applied experimentally [7–9] and were quite successful. Figure 9 shows the application of the 3 controllers on the test rig in eliminating the first mode instability, while Fig. 10 shows the application of the 3 controllers to eliminate second mode instability [9].

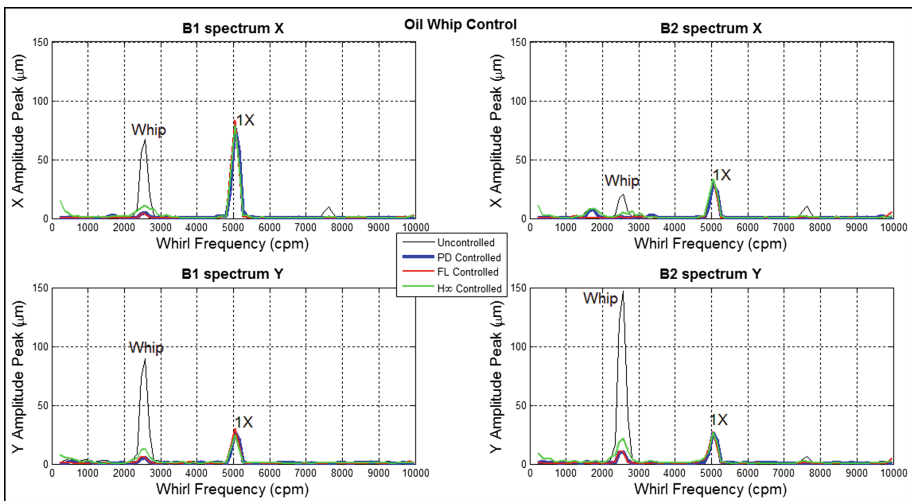
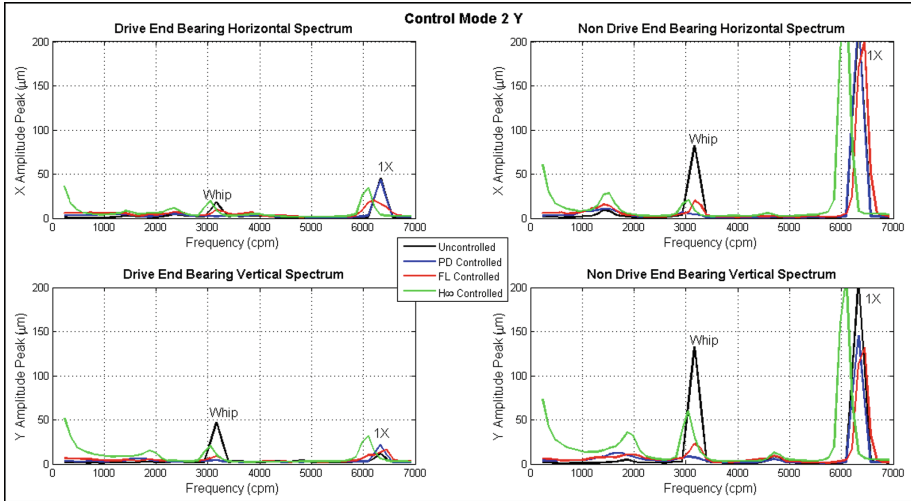


Fig. 9. Comparison of controllers for first mode oil whip control [9]



**Fig. 10.** Comparison of controllers for second mode oil whip control [9]

Table 2 shows the average reduction by the 3 controllers. It is clear that the  $H_{\infty}$  controller [8] is the lesser of the three in controlling the instability, since it tends to provide stiffness. This is evident in Fig. 10 where the  $H_{\infty}$  controller was able to move the critical speed by about 600 rpm.

**Table 2.** Average reduction by SEMAJIB controller

% reduction	PD	FL	$H_{\infty}$
First mode instability	94	93	82
Second mode instability	90	86	56

## 5 Unbalance Control

In order to realize the full potential of the SEMAJIB, as a smart bearing that can actually fix the machine, further experiments on the application of unbalance control on the test rig. Both single-plane and two-plane balancing were performed. The results were quite impressive, see Fig. 11.

Even though this test rig was severely unbalanced yet the unbalance control was quite impressive reaching between 70% to 95% 1x amplitude reduction. This is attainable because the AMB has extra capacity and is not carrying any static load, thus freeing the AMB to provide the necessary control actions.

Similar results were obtained for 2-plane unbalance control.



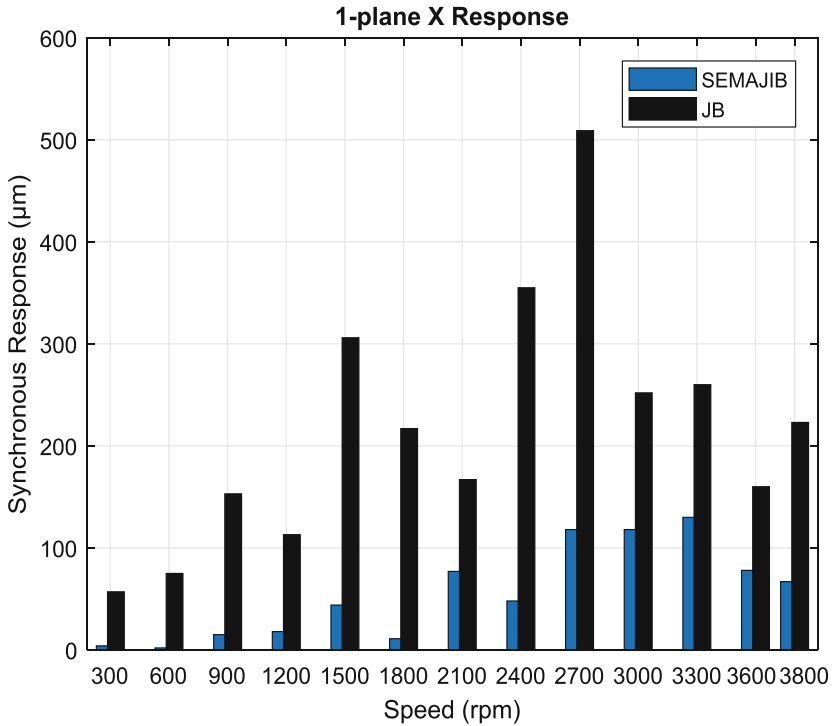


Fig. 11. Unbalance control with a SEMAJIB

## 6 Application to an Industrial Compressor

The SEMAJIB is implemented to an industrial compressor in order to investigate its effectiveness in eliminating the JB instability and considerably increasing the speed range of operation. The industrial compressor illustrated in Fig. 11 is modeled using finite element as shown in Fig. 12. The rotor which is operating at a speed of 3500 rpm has an axial length is 1.7 m and a total mass of 471 kg. The rotor finite element model

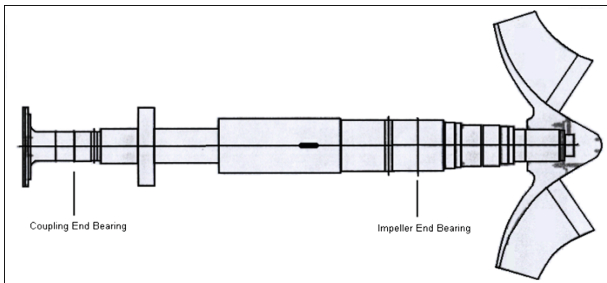
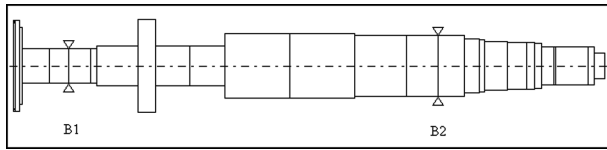


Fig. 12. Industrial compressor configuration

consists of 28 key points, where the bearings are located at key points 6, and 16. The impeller mass and inertia are added to the shaft at key point 26 (see Fig. 13).



**Fig. 13.** Finite element model

The industrial rotor stability is investigated when supported on JB only. Two JBs are designed depending on the bearing load and shaft diameter. The designed JB parameters having a coefficient of viscosity ‘ $\mu$ ’ of 0.014 Ns/m<sup>2</sup> are listed in Tables 3 [4].

**Table 3.** Rotor JB parameters [4]

Parameters	B1	B2
Shaft diameter D (mm)	50	89
Bearing load W (N)	340	4280
Bearing clearance c ( $\mu\text{m}$ )	100	175
Bearing axial length L (mm)	30	53

By solving the rotor eigen value problem and observing Figs. 14 and 15, the rotor critical speeds are found to be 3538, 21714, 46400 rpm. While, the rotor stability limit is 6300 rpm [4].

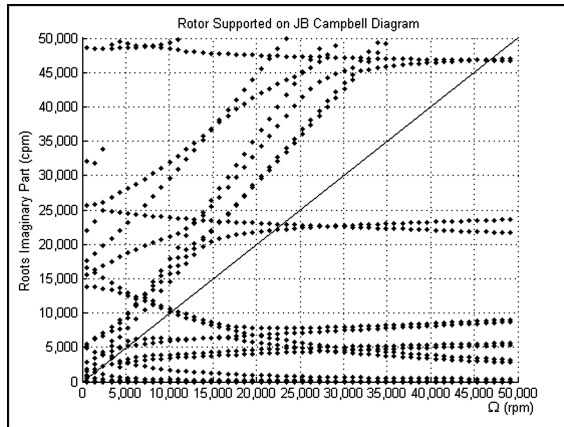


**Fig. 14.** Rotor supported on JB campbell diagram

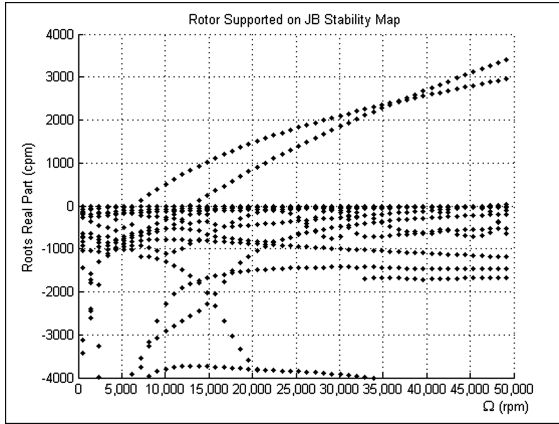


**Fig. 15.** Rotor supported on JB stability map

It is required to investigate whether a SEMAJIB can increase the stability limit to operate the compressor at 10,000 rpm. In order to stabilize the rotor over the desired speed range two SEMAJIB have been designed [4].

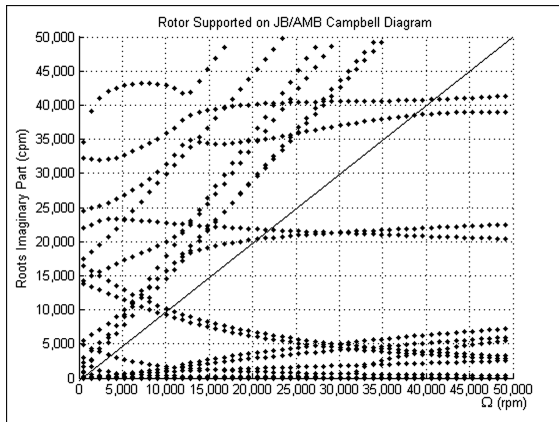


**Fig. 16.** Campbell diagram with SEMAJIB

By the solving the rotor eigen value problem and observing Figs. 16 and 17, it is clear that the SEMAJIB is capable of increasing the range of stable operation above the plotted range of 50,000 rpm. The rotor critical speeds are 3350, 20255, and 40700 rpm.

Clearly the SEMAJIB is successful in stabilizing this compressor in the 10,000 rpm speed range.

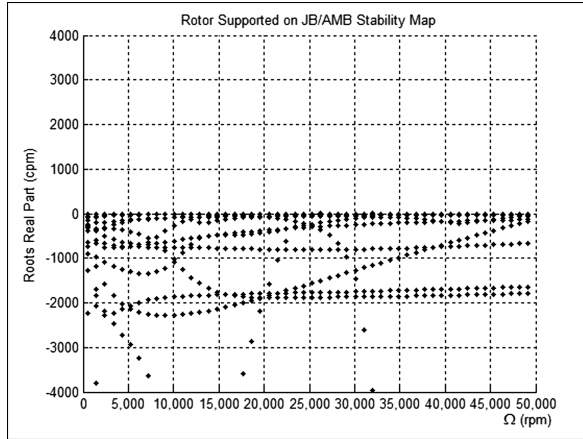


Fig. 17. Stability map with SEMAJIB

## 7 Smart Bearing Concept

Figure 18 shows a block diagram of the SEMAJIB system. The rotor is subjected to external forces  $F_{ext}$ , however the rotor states  $x$  and  $x'$  affect the JB which in turn provide a bearing force  $F_b$  that is added to the magnetic bearing force  $F_m$ . The feedback states  $x$  and  $x'$  are electronically directed to a programmable controller that provides a current through a power amplifier to the AMB thus producing the magnetic force  $F_m$ .

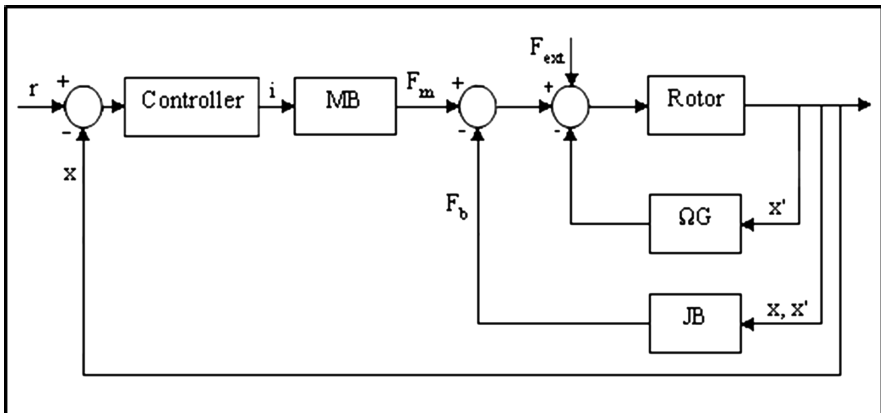


Fig. 18. SEMAJIB feedback system

This is inherent in an AMB system, however in an AMB there is limited control action, since most of the AMB work is to carry the static load. For a SEMAJIB, the static load is carried by the JB, leaving the AMB to act as an EMA. This allows the SEMAJIB to really act as a smart bearing.

In fact, if  $F_{\text{ext}}$  in Fig. 18 is considered as an unbalance, then the SEMAJIB acts to control the unbalance, which has been shown earlier in this paper. If however  $F_{\text{ext}}$  is a misalignment then the SEMAJIB acts to control misalignment, if it is looseness then the SEMAJIB acts to control looseness. This is possible because of the unique spectral maps of each of these faults, and the AMB within the SEMAJIB that acts as an EMA with abundant capacity. In fact, it is envisioned that the smart bearing concept can be used to extend the current condition-based maintenance (CBM) strategy to include smart condition based corrective maintenance (SCBCM).

## 8 Conclusions

The SEMAJIB is introduced as a high performance versatile smart bearing. Clearly the experimentation presented herein illustrate the following points:

- The SEMAJIB is free from instabilities
- The SEMAJIB has a high unbalance control capacity

It is also shown here that the SEMAJIB is capable to aid machines that have a stability limit, to perform beyond the stability limit. The industrial compressor that had a stability limit of 6300 rpm was shown to be stable to 50,000 rpm on SEMAJIB bearings.

Conceptually the SEMAJIB can provide much more, since with the use of feedback control, it is possible to act as a smart bearing identifying the problems, and providing control actions. This means that if an anomaly is identified in a machine supported by the SEMAJIB, it is possible to provide a control action through feedback that would fix the machine. This is possible because the AMB is free from load carrying, and acts only as an EMA. Thus it is possible to correct not only unbalance, but also misalignment and looseness which are common machine faults.

The net result is the improved availability and reliability of machines.

## References

1. El-Shafei, A.: Methods of controlling the instability in fluid film bearings. US Patent 7,836,601 (2010)
2. El-Shafei, A.: Integrated journal bearing. U.S. Patent Application 15/597,628 (2017)
3. El-Shafei, A., Dimitri, A.S.: Controlling journal bearing instability using active magnetic bearing. *ASME Trans. J. Eng. Gas Turbine Power* **132**(1), 012502-1–012502-9 (2010)
4. Dimitri, A.S., El-Shafei, A.: Instability control and unbalance compensation of flexible rotors supported on journal bearings using magnetic bearings. In: Proceedings of the 8th IFToMM International Conference on Rotordynamics, September 12–15. KIST, Seoul (2010)
5. El-Hakim, M., Dimitri, A.S, Saqr, T., Mahfoud, J., Adly, A.A., El-Shafei, A.: Numerical and experimental identification of a combined journal-magnetic bearing: smart integrated bearing. In: Proceedings of the 10th International Conference on Vibrations in Rotating Machinery, IMechE, London, UK, pp. 399–407, 11–13 September 2012

6. El-Shafei, A., Dimitri, A.S., Saqr, T., El-Hakim, M.: Test rig characterization and dynamic testing of a smart electro-magnetic actuator journal integrated bearing. In: Proceedings of 9th IFToMM International Conference on Rotordynamics, Milan, Italy, September 22–25 2014. Mechanisms and Machine Science, vol. 21. Springer, Cham (2012)
7. Dimitri, A.S., Mahfoud, J., El-Shafei, A.: Oil whip elimination using fuzzy controller. *J. Eng. Gas Turbines Power* **138**(6), 062502-1–062502-8 (2015)
8. Dimitri, A.S., El-Shafei, A., Adly, A.A., Mahfoud, J.: Magnetic actuator control of oil whip instability in bearings. *IEEE Trans. Magn.* **51**(11) (2015)
9. El-Shafei, A., Dimitri, A.S., Mahfoud, J.: PD control of a smart electro-magnetic actuator journal integrated bearing (SEMAJIB). In: Proceedings the 11th IMechE International Conference on Vibrations in Rotating Machinery, Manchester, UK, September 2016, paper C1030, pp. 239–250 (2016)



# Measurement Corrections for Active Magnetic Bearing Control

L. C. A. Almeida<sup>(✉)</sup>, J. M. A. Barbosa<sup>(✉)</sup>, F. C. G. Santos,  
and P. M. G. del Foyo<sup>(✉)</sup>

Universidade Federal de Pernambuco, Av. Prof. Moraes Rego, 1235 - Cidade  
Universitária, Recife, PE 50670-901, Brazil

lucas.coelhoa@outlook.com, flxcgs@yahoo.com.br, {jmab,pedro.foyo}@ufpe.br

**Abstract.** Rotor shaft position measurement is an important part of the algorithm performance in the active magnetic bearing control. The shaft centerline is estimated based on the measurement of the shaft surface distance to the sensor position. When the shaft surface has a large curvature, the measurement needs to be corrected in order to eliminate geometric correlations between measurements in the two axes. Such correlations have an impact on the control algorithm performance. The objective of this work is to propose a geometric model to estimate a more accurate position of the shaft centerline, considering also possible deviations of the sensor alignment. Corrections were applied to a control algorithm in an experimental active magnetic bearing workbench, showing an improvement of the control performance based on average distance to operation center criterion.

**Keywords:** Active magnetic bearing · Measurement correction  
Inductive sensor

## 1 Introduction

Control algorithms used in Active Magnetic Bearings (AMB) are often implemented based on the shaft position behavior regarding its center of mass and centerline. The information needed to execute the control loop is acquired through displacement sensors. Since the performance of AMB systems are directly affected by the quality of sensor signals, some setups may require additional algorithms to compensate for unwanted signal contents, such as roundness, unbalance or misalignment [1].

Distance measurements of round spinning objects are also a problem since the angular velocity may impact in radial and axial error motion of the spindle as stated in [2]. The angular position is also a problem as showed in [3]. Several methods has been proposed to deal with those problem like the Reversal Method introduced in [3] and an approach proposed in [4] resulting in the so called Improved Reversal Method.

Since the sensors readings are used in AMB control algorithms to determine the rotor shaft position and the shaft is a round object, they have a large impact on those control algorithms.

In addition, the shaft curvature may induce a correlation between both shaft position coordinates. Note that a pure vertical movement in the shaft will produce a variation in the horizontal distance to the sensor due to the shaft curvature and vice-versa.

Corrections for cylindrical objects have already been successfully implemented using capacitive displacement sensors [5]. Such approach require the choice of a proper calibration factor based on the problem requirements, but non-linearity become an issue when the cylindrical artifact is eccentric with respect to an axis of rotation.

Inductive linear displacement sensors are commonly used as the default choice for AMB systems [6, 7]. Due to its flexibility, robustness, and compact construction, the inductive linear displacement sensors are ideal for numerous industrial applications [8].

The purpose of this work intends to propose an algorithm that is able to correct the distorted sensors readings inside the control loop. Our main concern is the impact of the correlation between the systems coordinates in the system performance. Other corrections based on the shaft angular velocity and angular position will be addressed in future works.

Since the AMB control algorithm will run in a simple computational platform there are complexities constraints to be addressed. In addition, one more correction will be added to account for setups with non-centered sensors. Such characteristic will allow to modify the desired rotor shaft center position without changing the sensor position.

The paper is organized as follow. In Sect. 2 a geometric model to deal which measures corrections is presented. The impact in the AMB control performance is studied using an experimental active magnetic bearing workbench described in Sect. 3. The proposed method was implemented on that workbench and comparative results are presented in Sect. 4. In Sect. 5 the computational performance of the proposed algorithm is discussed and Sect. 6 summarized the conclusions.

## 2 The Proposed Geometric Model

The geometric model here proposed is based on the following assumptions:

- The rotor shaft is a cylindrical object with ratio  $R$ ;
- The sensors measures the distance from the axis surface in relation to the center of its measurement area;
- The center position of the rotor shaft coincides with the center of the stator;
- The sensors misalignment distances are known since there are part of the system design.

Figure 1 graphically represents a transversal cut of the rotor shaft in the position in which the sensors were installed. The dash circle represent the rotor



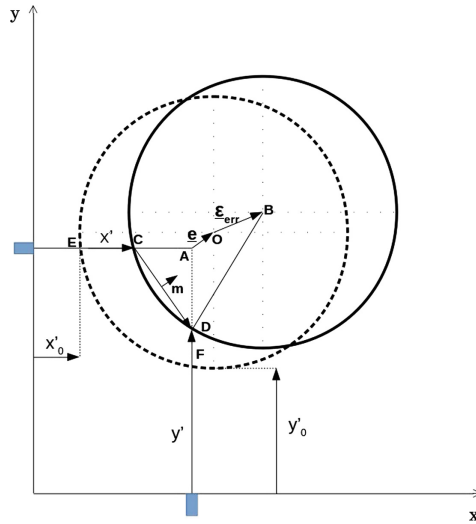


Fig. 1. Geometric model for coordinate corrections.

shaft in its desired position (center of the AMB) while the normal circle represent an arbitrary rotor shaft position while functioning.

Variables  $X'_0$  and  $Y'_0$  represent the respective sensor readings when rotor shaft is at the desired position, while variables  $X'$  and  $Y'$  represent sensor's readings for an arbitrary rotor shaft position. Variable  $e$  describes the sensor's location with respect to the desired rotor shaft position  $O$  which is identified through sensor's readings  $X_0$  and  $Y_0$ .

Let  $\mathbf{P}_{(i)}$  represent the two-dimensional position vector of point  $i$ . Thus define

$$\mathbf{P}_0 = \begin{pmatrix} X_0 \\ Y_0 \end{pmatrix} = \mathbf{P}_A + \mathbf{e};$$

$$\mathbf{e} = \begin{pmatrix} e_x \\ e_y \end{pmatrix};$$

$$\boldsymbol{\varepsilon}_{err} = \begin{pmatrix} X_{err} \\ Y_{err} \end{pmatrix};$$

$$\mathbf{P}_C = \begin{pmatrix} X' \\ Y_0 - e_y \end{pmatrix}$$

$$\mathbf{P}_D = \begin{pmatrix} X_0 - e_x \\ Y' \end{pmatrix}$$

As it can be seen,  $\mathbf{P}_B = \mathbf{P}_0 + \boldsymbol{\varepsilon}_{err}$  and  $X'$  and  $Y'$  are sensor distance measurements for the actual cylinder (centered at  $\mathbf{P}_B$ ). Next, we would like to write an expression for  $\boldsymbol{\varepsilon}_{err}$  in terms of known data. For that, define the point  $\mathbf{P}_m$

as the mid-point between  $\mathbf{P}_C$  and  $\mathbf{P}_D$ , and  $\mathbf{n}$  as the counter-clockwise normal to the segment  $CD$ . Therefore, there exists a real number  $s_B$  such that

$$\mathbf{P}_B = \mathbf{P}_m + s_B \mathbf{n},$$

and

$$\|\mathbf{P}_B - \mathbf{P}_C\|^2 = R^2.$$

After some algebraic manipulation it is possible to obtain

$$s_B = \pm \frac{1}{2} \sqrt{4R^2 - (\mu^2 + \nu^2)}$$

where

$$\nu = X' - X_0 + e_x$$

and

$$\mu = Y' - Y_0 + e_y;$$

The sign of  $s_B$  can be taken as positive provided the sum  $\boldsymbol{\varepsilon}_{err} + \mathbf{e}$  is sufficiently small. For instance, it is enough to require

$$\|\boldsymbol{\varepsilon}_{err} + \mathbf{e}\| < R.$$

Recalling that  $\boldsymbol{\varepsilon}_{err} = \mathbf{P}_B - \mathbf{P}_0$ , one can get

$$\boldsymbol{\varepsilon}_{err} = \frac{1}{2} \begin{pmatrix} X' - X_0 - e_x - \nu \sqrt{\frac{4R^2 - (\nu^2 + \mu^2)}{\nu^2 + \mu^2}} \\ Y' - Y_0 - e_y - \mu \sqrt{\frac{4R^2 - (\nu^2 + \mu^2)}{\nu^2 + \mu^2}} \end{pmatrix} \quad (1)$$

Equation 1 allow us to determine a correction in the real coordinates from the respective sensor readings in any moment. When the rotor shaft is perfectly aligned at the desired center position no other corrections will be necessary since the sensors alignment errors are already considered at that position.

If such alignment can not be achieved the corrections will vary based on the shaft angular position. Since the algorithm setup is determined for a specific fixed shaft angular position the corrections impact could not be as good as expected.

The desired shaft position is set to  $(X_0, Y_0)$  coordinates, which are the respective setpoints of each control loop.

### 3 Workbench Description

The impact of the correction algorithm in the system performance was evaluated experimentally. A workbench was constructed in the LAboratory of Robotics and Control (**LARC**) in order to teach tuning technics for PID controller devices. The workbench schematic is shown in Fig. 2.

A three-phase motor with nominal speed of 1800 rpm controlled by a frequency inverter provides the rotational torque to the shaft. The shaft is made of

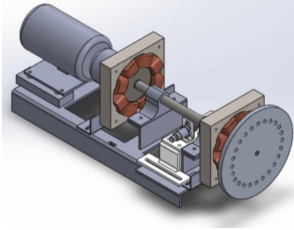


**Fig. 2.** Workbench schematic consisting in two Active Magnetic Bearings

steel with a 18 mm diameter. It is sustained for safety reasons by a touch-down bearing with a 0.5 mm gap. Two AMBs with a 1 mm air gap will balance the rotor shaft once the system is energized.

The inductive displacement sensors with a sensing range of 0 mm to 4 mm were placed 145 mm from the second AMB. A configurable mass disk was placed at the shaft end.

Hardware controller consists of a Printed Circuit Board (PCB) designed to interface the control system inputs and outputs and an *Arduino UNO* platform. The PCB was designed as an expansion shield for the *Arduino UNO* board. The electric schematic of that PCB is shown in Fig. 3.

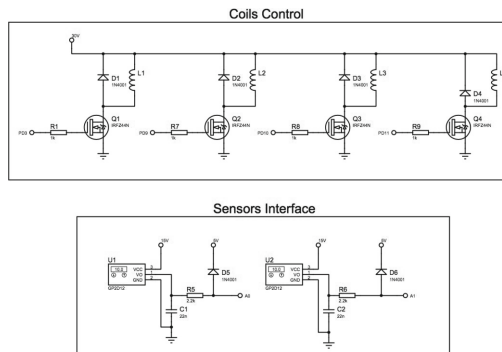


**Fig. 3.** Electric schematic of the custom PCB.

The coils control part is driven by a PWM signal produced by the *Arduino UNO* and feeds each of the 4 coils, 2 for each magnetic bearing. The inductive sensors output signal ranges proportionally from 0 V to 10 V and, since the *Arduino UNO* inputs maximum voltage is about 5 V, only the first half of the scale was actually used. Then the sensor interface protects the *Arduino UNO* pins from any voltage greater than 5 V.

The inductive sensors were placed mechanically for a useful range from 0 mm to 2 mm which is enough to cover the shaft displacement in every direction. Note that the AMB gap is 0.5 mm.

As an educational workbench for tuning PID controllers a serial interface was designed based on *Simulink* from *MATLAB*. Even when the control algorithm is running entirely in the *Arduino UNO*, data exchange is necessary to implement the desired functionality. Using the *MATLAB* Real-Time Windows Target kernel to interface with the operating system allows a “simulated real-time” execution. The *Simulink* Desktop Real-Time kernel assigns the highest priority of execution to our real-time executable, which allows it to run without interference at the selected sample rate [9].

Setpoints and PID controller parameters are sent to the *Arduino UNO* while sensors readings are received from it. The sample rate for the sensors readings was 500 Hz, which corresponds to the control loop execution time in the *Arduino UNO*. Setpoints and PID parameters were sent every 10 s since there is no need to change those parameters at higher rates. It also contributes to satisfy control algorithm execution time, which must be less than the selected sample time. A flow chart of the control algorithm is shown in Fig. 4.

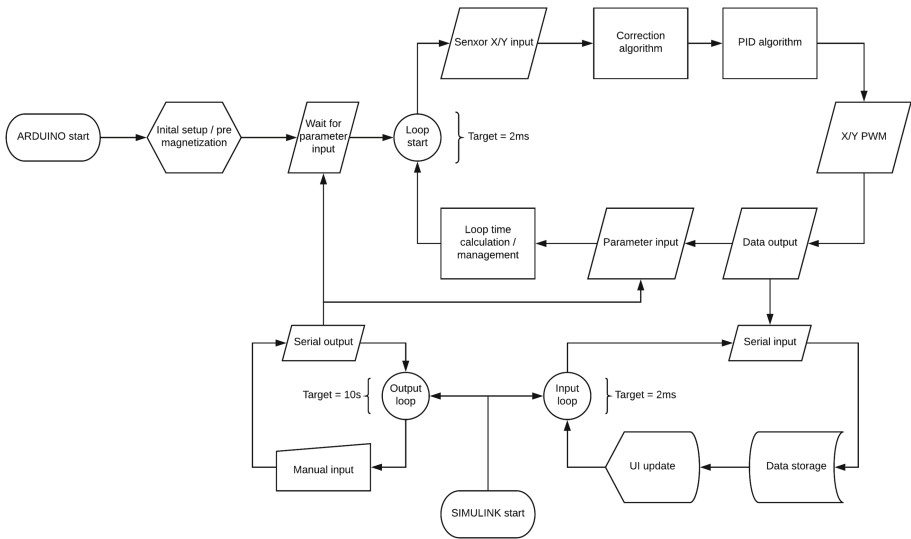
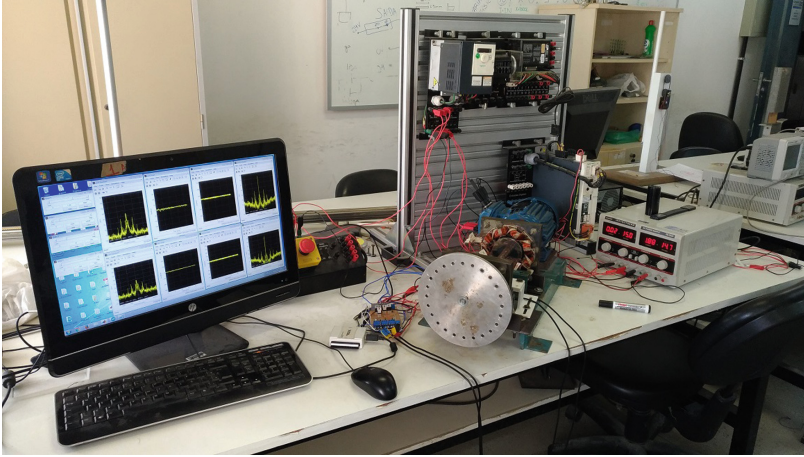


Fig. 4. Flow chart of the control algorithm.

A NI DAQ USB-6009 connected to the sensors interface in the PCB was also used for data validation purposes. The entire workbench is shown in Fig. 5.

## 4 Experimental Results

The control algorithm was implemented on the *Arduino UNO* platform. The chosen sample rate was 500 Hz which correspond to a sample period of 2 ms. The PWM base frequency was set at 3900 Hz. A bias was also established in order



**Fig. 5.** Picture of the workbench used for testing the correction algorithm.

to pre-magnetize the AMBs. The value initially chosen for that bias was 50 % of the voltage scale and there is a 5 ms of delay for the pre-magnet stabilization. All other constants like shaft misalignment with respect to sensors installation (vector  $\mathbf{e}$ ).

Following the initialization of all those parameters, the algorithm will wait for a message containing setpoints and PIDs parameters. Once it received all information, it will start running at the specified sample rate.

The sensors readings are filtered and then used to estimate the center position of the rotor shaft. With those coordinates, the setpoints errors for both axis are determined. A PID with derivative filter was implemented for both axis. For simplicity, and since we have only one measuring point, the same control actions were applied to the AMBs.

In order to establish a comparison, two experiments were conducted: one without any correction, which means that the rotor shaft center position was directly estimated for the filtered sensors readings (experiment 1), and the other applying the corrections defined by Eq. 1 (experiment 2).

Both experiments were conducted for a rotor angular velocity of 169 rpm and data were collected once the steady state regime was achieved. Figure 6 shows the diagram representing the coordinates  $X_{error}$  and  $Y_{error}$  for both experiments.

The black circle in Fig. 6 represents the mechanical limit imposed by the mechanical bearing. Blue trajectories represent the rotor shaft center position in the first experiment, where no correction were applied. The yellow trajectory represents the rotor shaft center position from the second experiment with PID control actions computed after corrections according to Eq. 1.

Red trajectories (calculated center) were obtained by applying corrections due to the curvature on blue trajectories (experiment 1) showing the actual shaft center position.

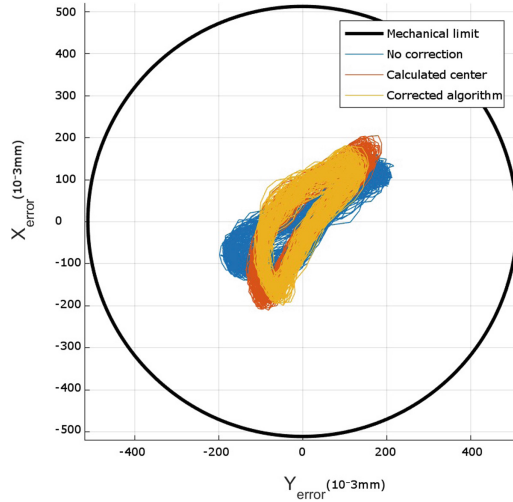


**Fig. 6.** Path diagram of  $X_{error}$  and  $Y_{error}$  for experiment 1 and 2.

Three parameters were used to evaluate the impact of the application of the correction on the control performance: The standard deviations of  $X_{error}$  and  $Y_{error}$ , represented by  $\sigma_x$  and  $\sigma_y$ , and the average distance to the operation center,  $\bar{r}$ . The results of the performance criteria can be seen in Table 1. In the correction algorithm, the following values were used:  $R = 9$  mm,  $e_x = 0.52$  mm and  $e_y = 0.40$  mm and setpoints  $X_0 = 1.09$  mm,  $Y_0 = 0.94$  mm.

**Table 1.** Performance evaluation criteria in experiments 1 and 2, in  $\mu m$ .

Criterion	Experiment 1		Experiment 2
	No correction	Calculated position	Corrected algorithm
$\sigma_x$	111.82	110.23	102.87
$\sigma_y$	55.87	53.59	45.47
$\bar{r}$	108.11	106.69	91.99

The diagram in Fig. 6 shows that the positions read by the sensors do not describe a circular trajectory. This distortion may happen due to several reasons, ranging from imperfections in construction to sub-optimal choices for correction parameters, as well as control behavior.

The experiment were repeated three times each at different rotor angular velocities. Table 2 shows the average distance to the operation center ( $\bar{r}$ ) and the corresponding improvement due to the corrections.

Experimental results show that at lower angular velocity the improvements were consistent and considerable, achieving a reduction in the mean distance

**Table 2.** Experimental results with setup  $e_x = 0.52$  mm,  $e_y = 0.40$  mm,  $X_0 = 1.09$  mm and  $Y_0 = 0.94$  mm

Experiment	Angular velocity ( <i>rpm</i> )	Correction	$\bar{r}$ ( $\mu\text{m}$ )	Improvement (%)
1	169	No	108.11	-
2	169	Yes	91.99	14.9
3	169	No	91.48	-
4	169	Yes	91.19	0.3
5	169	No	85.70	-
6	169	Yes	93.57	-9.2
7	84.5	No	63.98	-
8	84.5	Yes	34.32	46.3
9	84.5	No	57.70	-
10	84.5	Yes	37.30	35.3
11	84.5	No	81.93	-
12	84.5	Yes	36.37	55.6

from the desired center position. Such improvements achieved at least 35%. At higher angular velocity the results show no consistency due to misalignment problems.

Then other experiments were conducted with a different setup. A new setup was implemented for an arbitrary (different) rotor angular position. The algorithm setup was implemented while the motor is off and the rotor shaft was secured at its desired position by a mechanical support. Table 3 shows experimental results with the new algorithm setup.

**Table 3.** Experimental results with setup  $e_x = 0.51$  mm,  $e_y = 0.41$  mm,  $X_0 = 1.10$  mm and  $Y_0 = 0.93$  mm

Experiment	Angular velocity ( <i>rpm</i> )	Correction	$\bar{r}$ ( $\mu\text{m}$ )	Improvement (%)
13	169	No	116.95	-
14	169	Yes	105.00	10.2
15	169	No	117.97	-
16	169	Yes	101.12	14.3
17	169	No	117.37	-
18	169	Yes	100.89	14.1

Experimental results shows a consistent improvement at 169 rpm only due to the new setup since the PID parameters remains the same. Figure 7 shows the

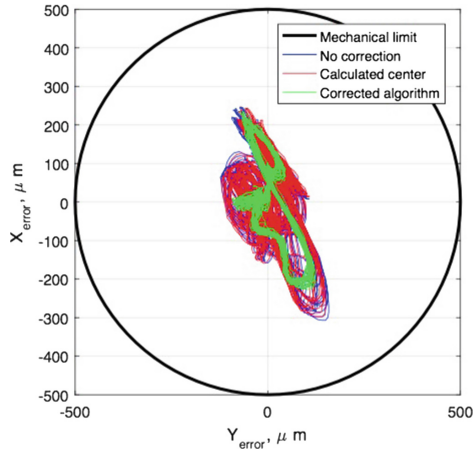


**Fig. 7.** Path diagram of  $X_{error}$  and  $Y_{error}$  for experiment 13 and 14.

trajectories of the rotor shaft center of mass for experiment 13 (No correction) and 14 (Corrected algorithm).

Even when the rotor shaft center of mass trajectory became more irregular due to the new setup, there was an improvement in the control behavior of the AMB.

## 5 Computational Performance

The implementation of the correction algorithm has a low impact in the control loop execution time. The *Arduino UNO* program was modified to communicate its overall control loop execution time and no significant execution time increasing was detected due to the correction algorithm. The control loop execution time was affected only by the function which obtain the parameters sent by the computer through the serial device. Even in those cases the 2 ms deadline was not missed.

## 6 Conclusion

The geometric model proposed here allowed us to improve AMB's control performance applying a simple correction algorithm without relevant impact in the control algorithm computational performance. Such achievement was possible by reducing the impact of rotor shaft curvature in the determination of the center of mass based on inductive linear sensors readings.

Even when the control performance improvement was not confirmed at higher speeds, it was still possible to obtain improvements by choosing an adequate setup for the algorithm. Such setup depend on the inductive sensor positioning and the type of system misalignment.



The workbench developed to test the algorithm was based on an old equipment that presented all kind of mechanic imperfections. Despite of that, the PID control algorithm was able to ensure the AMB correct behavior. Figures 6 and 7 shows that the rotor shaft center of mass stayed away of the mechanical limit imposed by the mechanical bearing.

We could not show conclusive improvements for higher angular velocities. Nevertheless, it was possible to observe that by using different setups some improvements were obtained. This opens up the perspective of obtaining optimal setup parameters in order to optimize the control performance and increase the high speed limit allowed for the AMB secure operation. Another approach could be to use more adequate tuning for the PID controller, for example, using a specific PID tuning according to angular velocity ranges.

As future work we planed to put an encoder attached to the rotor shaft to read the angular velocity and angular position in order to develop a more sophisticated algorithm that take into account the roundness issue and an adequate setup depended on angular position.

It's clear that the impact of the correction algorithm here proposed depends on parameters like shaft ratio and bearing gap. We also planed to conduct sensibility analysis in order to determine when correction measurements may have impact in system performance. In order to do that some improvements in our workbench are already be executed.

## References

1. Maslen, E.H., Schweitzer, G. (eds.): *Magnetic Bearings*. Springer, Heidelberg (2009). <https://doi.org/10.1007/978-3-642-00497-1>
2. Marsh, E., Grejda, R.: Experiences with the master axis method for measuring spindle error motion. *Precis. Eng.* **24**(1), 50–57 (2000)
3. Chetwynd, D.G., Siddall, G.J.: Improving the accuracy of roundness measurement. *J. Phys. E: Sci. Instrum.* **9**, 537 (1976)
4. Horikawa, O., Sato, K., Osada, H., Shimokohbe, A.: Roundness and absolute radial motion accuracy measured by an improved reversal method. *J. Jpn. Soc. Precis. Eng. JSPE* **57**(12), 151 (1991)
5. Smith, P.T., Vallance, R.R., Marsh, E.R.: Correcting capacitive displacement measurements in metrology applications with cylindrical artifacts. *Precis. Eng.* **29**(3), 324–335 (2005)
6. Guiráo, P.H.F.: *Controle Ativo de Vibrações de Rotores com Mancais Magnéticos - Influência dos Parâmetros do Controlador PID*. Ph.D. thesis, Universidade Estadual Paulista, São Paulo, Brasil (2006)
7. Siqueira, R.: *Projeto e Implementação de um Mancal magnético ativo com controle por modos deslizantes*. Master's degree, Universidade Federal do Rio de Janeiro, Rio de Janeiro, Brasil (2013)
8. Fericean, S., Droxler, R.: New noncontacting inductive analog proximity and inductive linear displacement sensors for industrial automation. *IEEE Sens. J.* **7**(11), 1538–1545 (2007)
9. MathWorks Documentation: Getting started with simulink desktop real-time. <https://www.mathworks.com/help/sldrt/ug/real-time-windows-target-kernel.html>



# Calculating Rotordynamic Coefficients of Liquid Annular Seals by CFD for Vibration Analysis and Validation at the Test Rig

Christian Wagner<sup>(✉)</sup>, Stephan Sinzig, Thomas Thümmel, and Daniel Rixen

Chair of Applied Mechanics, Technical University of Munich,  
85748 Garching, Germany  
c.wagner@tum.de  
<http://www.amm.mw.tum.de>

**Abstract.** This article presents a simulation methodology for calculating rotordynamic coefficients of liquid annular seals using the open source software OpenFOAM. Therefore, stationary fluid solutions for several boundary conditions are generated to represent the rotational shaft speed, the eccentricity and the whirling motion. Analyzing the acting forces in a whirling coordinate frame leads to a simple curve fit to determine the rotordynamic seal coefficients. The CFD approach is validated with an analytical solution and the coefficients of characteristic states are compared to literature results. Finally, the methodology is applied to our test rig's geometry to calculate its dynamic behavior. The comparison between the simulated and measured behavior shows good agreement.

**Keywords:** Rotordynamic · Seal coefficient · Dynamic analysis

## 1 Introduction

Seals in compressors or pumps mostly separate different fluids or gases and pressure levels. In high rotational speed turbomachinery, contactless seals in various layouts like labyrinth, brush, floating ring, or simply gap seals are used. However, the presence of a leakage flow through the clearance in the contactless seal causes forces on the rotor system. They are generated by an unsymmetrical fluid velocity distribution in the seal gap for the vibrating or eccentric rotor.

Usually, the vibrational behavior of the rotating machinery is strongly affected by the seals. In unfavorable design configurations, they can excite the rotor to large vibrations and lead to an instability, like the 'oil-whip' phenomenon in journal bearings, see [1].

The forces in the seals are described using linearized rotordynamic seal coefficients like stiffness, damping, and inertia for specific operating points as pressure drop, preswirl, and rotational speeds. A lot of work has been done over recent

years in order to determine these coefficients by means of simulation or experiments.

This article presents a simulation methodology for calculating rotordynamic coefficients of liquid annular seals using the open source software OpenFOAM. Then, the calculated coefficients are used to simulate our seals test rig dynamic behavior by means of a secondary structural simulation. The comparison to measured data confirms the approach of the methodology.

Since rotational speeds and pressures are increased in technical applications, investigations in industry and academia are applied to model and identify the dynamics of rotor seal systems. Among the first in modeling the rotordynamic seal behavior using linearized coefficients were Black [2] and Childs [3], who developed and solved the bulk-flow equations to create analytical solutions for short seals. Muszynska [1,4] improves these seal models by adding eccentricity effects.

Dietzen [5] and Nordmann [6] solved the fluid equations by means of finite difference techniques. Using a rotating coordinate system leads to a stationary formulation of the whirling seal rotor.

Others, such as Kwanka [7,8] and Deckner [9,10], use CFD calculations to determine the rotordynamic seal coefficients. They also include experimental investigations using Active Magnetic Bearings (AMB) in flexible rotor-seal systems/test rigs similar to [11–14], or [15]. Examples of the use of levitating rotor test rigs to analyze seals are given by [16,17].

The fundamentals of rotordynamics, modeling, and simulation are well described in [18–20].

## 2 Dynamics of Rotor Seal Systems

For the sake of clarity, we write the formulation and the analysis of the rotor seal system here again, which is already presented in [21]. In the following, the JEFFCOTT/LAVAL rotor model is used to describe the dynamic behavior of the system. Like the investigations of Black [2], Childs [20], and Muszynska [19], the seals are modeled using rotordynamic seal coefficients.

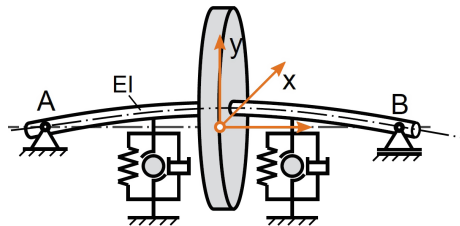


Fig. 1. Rotor seal model

### 2.1 Rotor Seal Model

The simplified rotor seal model, see Fig. 1, consists of a linear elastic, massless shaft with a mass disk supported by two rigid bearings. The seals, represented by their rotordynamic coefficients (mass, stiffness, and damping) are directly connected to the shaft. Using the rotor displacement  $[x \ y]^T$  and projecting all forces on the disk, the equation of motion is as follows:

$$\begin{bmatrix} m_r + m_{xx} & 0 \\ 0 & m_r + m_{yy} \end{bmatrix} \begin{bmatrix} \ddot{x} \\ \ddot{y} \end{bmatrix} + \begin{bmatrix} c_{xx} & c_{xy} \\ c_{yx} & c_{yy} \end{bmatrix} \begin{bmatrix} \dot{x} \\ \dot{y} \end{bmatrix} + \begin{bmatrix} k_r + k_{xx} & k_{xy} \\ k_{yx} & k_r + k_{yy} \end{bmatrix} \begin{bmatrix} x \\ y \end{bmatrix} = \mathbf{h} \tag{1}$$

where  $m_{xx}$ ,  $c_{xx}$ , and  $k_{xx}$  are the seal coefficients of direct mass, damping, and stiffness of the seals.  $c_{xy}$  and  $k_{xy}$  are the cross coupled damping and stiffness, same for the  $y$  direction, respectively.  $m_r = 9.5$  kg is the rotor’s mass and  $k_r = 0.436$  MN/m is the shaft stiffness. The equivalent forces  $\mathbf{h} = \mathbf{h}_u + \mathbf{h}_e$ , representing the unbalance force, external forces, and so forth, are used to couple different models (bearings etc.) and excitations. Therefore the rotor’s first (sealless) natural frequency is denoted by  $\omega_1 = \sqrt{\frac{k_r}{m_r}}$ .

The seal coefficients can be determined using measurements, numeric simulations, or simplified analytical solutions. In this research, the coefficients are numerically calculated using CFD simulations carried out by OpenFOAM.

### 2.2 Dynamic Behavior

The dynamic behavior of the rotor seal system is analyzed by its eigenvalues. Therefore, for the coupled symmetric ( $*_{xx} = *_{yy}$ ,  $*_{xy} = -*_{yx}$ ) system (rotor + seals), according to [18, 21], we write:

$$\begin{bmatrix} M & 0 \\ 0 & M \end{bmatrix} \begin{bmatrix} \ddot{x} \\ \ddot{y} \end{bmatrix} + \begin{bmatrix} C & c \\ -c & C \end{bmatrix} \begin{bmatrix} \dot{x} \\ \dot{y} \end{bmatrix} + \begin{bmatrix} K & k \\ -k & K \end{bmatrix} \begin{bmatrix} x \\ y \end{bmatrix} = \mathbf{h} \tag{2}$$

For improved readability, the summarized coefficients are:

$$\begin{aligned} M &= m_r + m_{xx} \\ C &= c_{xx} = c_{yy}; \quad c = c_{xy} = -c_{yx} \\ K &= k_r + k_{xx}; \quad k = k_{xy} = -k_{yx} \end{aligned}$$

The cross-coupled terms  $k$  and  $c$  lead to tangential forces, which are destabilizing the system by transmitting energy from the rotor’s rotation to the bending motion. Assuming a symmetrical rotor system, we substitute  $x$  and  $y$  with complex coordinates  $z = x + jy$  and  $F_z = h_x + jh_y$ , where  $j^2 = -1$ . To determine the system’s stability and its natural frequencies, the eigenvalues are calculated by  $F_z = 0$  and  $z = \hat{z}e^{\lambda t}$ :

$$M\lambda^2 + C\lambda + K - j(c\lambda + k) = 0 \tag{3}$$

with  $\lambda = -\delta + j\omega$ . When the decay constant  $\delta$  becomes negative, driven by the tangential forces above the system's stability limit, instability occurs. Note in particular that the coefficients are nonlinear functions of the rotational speed, the fluid properties, and the eccentricity (almost linear for  $\epsilon < 0.5$ ).

### 3 Seal Simulation

In this research, the seals are analyzed by CFD. The objective is to calculate the forces acting on the rotor and to deduct rotordynamic coefficients of the seal. Knowledge of the rotordynamic coefficients allows us to investigate the behavior of the entire rotor system in an additional simulation. In order to calculate the rotordynamic coefficients, the time-dependent problem of a vibrating rotor inside a seal gap is transformed into a stationary formulation. The fluid flow and pressure distribution are calculated from the geometry and boundary conditions. Integrating the pressure distribution on the surface leads to the seal forces and, therefore, to the rotordynamic coefficients.

#### 3.1 CFD Approach

The fluid flow inside the seal gap is a pressure and shear-driven problem. The fluid flow's motion is described exactly by the Navier-Stokes equations. For the assumed incompressible fluid (temperature and density are constant and Mach-number is less than 0.3) the momentum equation reads, according to [22]:

$$\rho \left( \frac{\partial \mathbf{v}}{\partial t} + (\mathbf{v} \cdot \nabla) \mathbf{v} \right) = -\nabla p + \mu \Delta \mathbf{v} + \mathbf{f} \quad (4)$$

The conservation of mass leads to the continuity equation:

$$\nabla \cdot \mathbf{v} = 0 \quad (5)$$

If the expected Reynolds number exceeds 2,300 within the simulation, turbulent flows need to be considered. There are multiple opportunities to solve the equations for turbulent flows. In this research, we applied the Reynolds-Averaged Navier-Stokes equations (RANS). The RANS equations are obtained by replacing every term of the Navier-Stokes equation with a constant and a fluctuation expression. Finally, the equations are averaged by time. The governing equation can be treated as laminar flow, with exception of the Reynolds stress tensor:

$$-\frac{\overline{\partial u_i^* u_j^*}}{\partial x_j}$$

The Reynolds stress tensor must be modeled using averaged quantities only. In this research, we used the model of eddy viscosity, which states that the influence of turbulence is analogue to molecular viscosity. The basic  $k - \epsilon$ -model is applied to specify the eddy viscosity as a functional expression of the turbulent energy and the turbulent dissipation.

In case of the eccentric shaft, no geometric symmetries can be found. Hence, the simulation is bound to be three dimensional. The smooth seal is described by its diameter, clearance, and length. A structured mesh of hexahedral elements was designed, because of the seal's simple geometry, see Fig. 2. For sure, more complex geometries can be investigated as well. The spatial discretization scheme is the finite-volume-method.

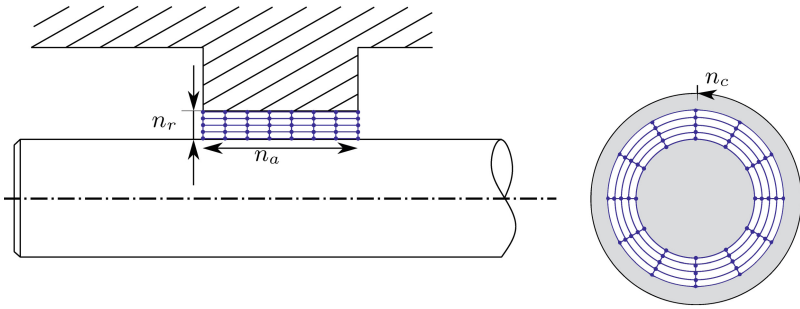


**Fig. 2.** Discretization of the seal: number of cells in axial direction  $n_a$ , in radial direction  $n_r$  and in circumferential direction  $n_c$

### 3.2 Coordinate Transformation: Calculate Rotordynamic Coefficients

The rotordynamic coefficients link the acting forces on a rotor to the shaft's displacement, velocity, and acceleration, respectively. The quantities that describe the shaft's movement are defined within the initial coordinate frame  $I$  at the bearing center line  $A - B$ , as stated before. In the seal CFD analysis, a moving coordinate system with origin  $C$  in the geometric center of the rotor is used to describe the forces and movement. The movement is assumed to be a circle with radius  $\epsilon = |\mathbf{r}_C|$  around center  $O$ . The coordinate system rotates with the angular whirl frequency  $\omega = \dot{\psi}_C = const.$ , see Fig. 3. This leads to expressions for displacements, velocities, and accelerations, respectively:

$$\begin{pmatrix} x \\ y \end{pmatrix} = \begin{pmatrix} \epsilon \cos(\omega t) \\ \epsilon \sin(\omega t) \end{pmatrix}$$

This results in different quantities of the wall velocities  $v$  (rotor and stator surface in the rotating coordinate frame) with the shaft speed  $\Omega = \dot{\psi}_R = const.$ :

$$\begin{aligned} v_{rotor} &= (\Omega - \omega) \frac{D}{2} \\ v_{stator} &= -\omega \left( \frac{D}{2} + c_r \right) \end{aligned}$$

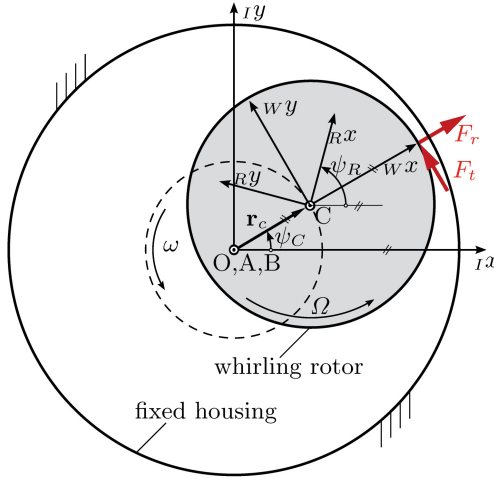


**Fig. 3.** Coordinate transformation and forces

with the rotor diameter  $D$  and the radial seal clearance  $c_r$ . The forces are represented in the rotating coordinate frame as well:

$$\begin{pmatrix} F_x \\ F_y \end{pmatrix} = \begin{pmatrix} F_r \cos(\omega t) - F_t \sin(\omega t) \\ F_r \sin(\omega t) + F_t \cos(\omega t) \end{pmatrix}$$

with the acting tangential and radial force,  $F_t$  and  $F_r$ . Thus, equation (1), which defines the rotordynamic coefficients, is no longer time dependent, but dependent on the whirl frequency  $\omega$  and the eccentricity  $\epsilon = |\mathbf{r}_C|$ :

$$\begin{pmatrix} -\frac{F_r}{\epsilon} \\ -\frac{F_t}{\epsilon} \end{pmatrix} = \begin{pmatrix} -m_{xx}\omega^2 + c_{xy}\omega + k_{xx} \\ c_{xx}\omega - k_{xy} \end{pmatrix} \quad (6)$$

The spatial movement of the shaft within the CFD simulation is described with boundary conditions only.

Now, it is possible to calculate the rotordynamic coefficients if there are simulated forces on hand for several whirl frequencies. There have to be at least three different simulations at different whirl frequencies, since the radial part of the force is a polynomial of second order with respect to the whirl frequency. The velocity at inlet and outlet surfaces has a zero gradient. Besides the boundary condition describing the velocity, there are boundary conditions for the pressure: At the inlet, the presetting of the total pressure ( $p_0 = p + \frac{1}{2}\rho u^2$ ) is given. At the outlet, the dynamic pressure is set to zero. In this work, we employed the algorithm SIMPLE (Semi-Implicit Method for Pressure Linked Equations) to solve the RANS-equations. This algorithm iteratively calculates the pressure distribution and the velocity distribution alternately. The solution from one field serves as the initial value for the other. Finally, Eq. (6) was fitted to the simulated values of the forces to calculate the rotordynamic coefficients.

## 4 Experimental Setup

This section describes the experimental setup for analyzing rotor seal systems at the Chair of Applied Mechanics at the Technical University of Munich, as in [21]. First, the seals test rig is presented, then the dynamic behavior is analyzed and compared to the simulation results.

The experimental analysis is examined on the seals test rig (see Fig. 4). The main components are a flexible shaft and a mass disk (1) with two symmetrically-arranged liquid annular seals (2) in the middle (see details in Fig. 5). Eddy current sensors for measuring the displacement (6) and a piezo force platform (7) are arranged in the seals stator housing (8). The fluid is injected between the two seals with a maximum pressure of 100 bar. The rotor runs at over-critical speed above the first (sealless) natural frequency  $\omega_1$  up to 12,000 rpm. An active magnetic bearing (3) is used as an exciter (2D shaker) at the shaft. The rotor shaft is supported by two ball bearings (4) and driven by a servo motor (5). The typical test procedure is the stationary rotor run-up (discrete rotational speeds) with or without AMB excitation. Therefore, the test rig is controlled and the signals are measured using a dSPACE 1103 system (10 kHz sampling rate), see [12, 21].

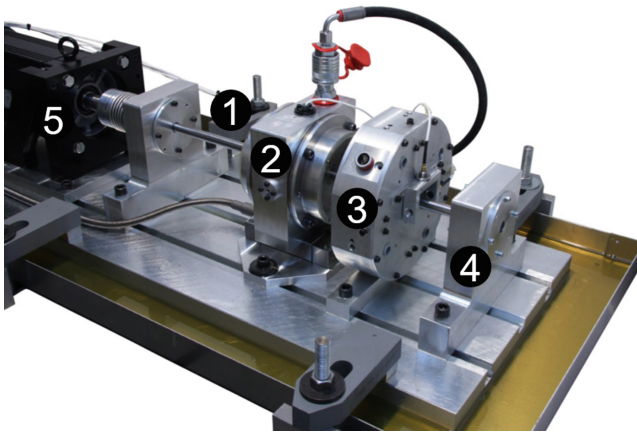


Fig. 4. Seals test rig

## 5 Validation and Dynamic Analysis

In this section, the CFD simulation methodology is validated. Therefore, an analytical solution is derived from the Navier-Stokes equations to define the numerical errors with respect to simple geometries. Additionally, the calculated rotordynamic coefficients are compared with those published by Dietzen and



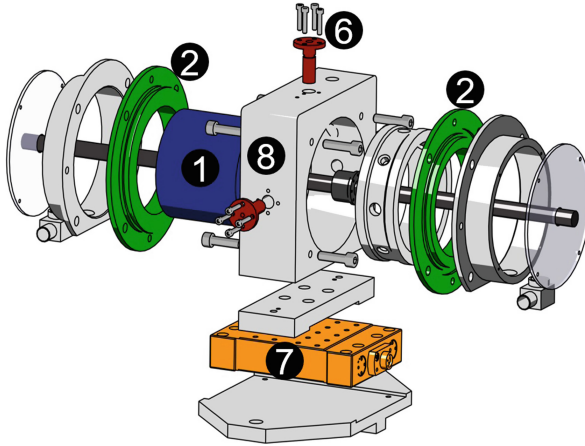


Fig. 5. Seals housing detail

Nordmann [5]. Afterwards, the geometry of the presented seals test rig configuration is simulated so that its vibrational behavior can be compared to experimental results.

### 5.1 Validation by an Analytical Solution

The numerical convergence of both the discretization scheme and the solving process has to be proved by applying the boundary conditions and the fluid properties for different grid resolutions. Thus, an analytical expression of the pressure and velocity distribution is generated. The analytical solution is only available if the Navier-Stokes equations are simplified by some assumptions. Hence, the configuration is stated to be time independent, to be a plain annular seal, to assume a centric rotor, to have no circumferential velocity, and to be laminar flow. These assumptions lead to a linear equation of the pressure distribution in axial direction:

$$p(z) = \frac{p_o - p_i}{l} z + p_i$$

with the pressure at inlet and outlet,  $p_i$  and  $p_o$ . A quadratic equation of the velocity distribution in radial direction follows as:

$$u_z(r) = \frac{p_o - p_i}{4\mu l} \left( (r^2 - r_i^2) + (r_o^2 - r_i^2) \frac{\ln\left(\frac{r_i}{r}\right)}{\ln\left(\frac{r_o}{r_i}\right)} \right)$$

where  $r_i$  and  $r_o$  denote the inner (i.e. the rotor) and outer radial wall coordinate. The axial velocity  $u_z$  is integrated over the cross section of the gap to gain an expression of the volume flow through the seal. A second-order Taylor-series approximation of the integrated expression yields a term for the leakage  $\dot{V}$ , also found in [18]:

$$\dot{V} = \frac{\Delta p d_m \pi h_0^3}{12\nu l} \quad (7)$$

The difference between a simulated value of the volume flow and Eq. (7) represents a quantity of the numerical error. The criteria for proving convergence of a scheme is that the numerical error decreases for an increasing number of cells. This was demonstrated (length: 20 mm, diameter: 1,000 mm, clearance: 0.17 mm):

- **3D case 1:** 4,000 cells (in axial direction  $n_a = 10$ , in radial direction  $n_r = 4$ , and in circumferential direction  $n_c = 100$ ), deviation of 20%
- **3D case 2:** 63,000 cells ( $n_a = 25$ ,  $n_r = 10$ ,  $n_c = 252$ ), deviation of 8%

In this special case, the rotor is assumed to be placed centrally as mentioned before. This symmetry can be exploited to handle the configuration as a two-dimensional one. Thus, a sector of the circumference is simulated only. Namely,  $\frac{1}{1,000}$  of the geometry is discretized using one cell in circumferential direction, so  $n_c = 1$ . The volume flow calculated is subsequently multiplied by 1,000. Again, two different cases are analyzed to prove the convergence:

- **2D case 1:** 2,000 cells ( $n_r = 20$ ,  $n_a = 100$ ), deviation of 0.5%
- **2D case 2:** 8,000 cells ( $n_r = 40$ ,  $n_a = 200$ ), deviation of 0.03%

## 5.2 Validation by Published Rotordynamic Coefficients

An example of validating the CFD approach with published rotordynamic seal coefficients is given in [5]. Water flows through a plain annular seal. The resulting flow is going to be turbulent, since the pressure boundary conditions lead to a Reynolds number of more than 2,300. Hence, the RANS equations are solved numerically. The eddy viscosity is modelled using the  $k-\epsilon$  model. The simulation is characterized by the following parameters:

- **Dimensions:** length: 23.5 mm, diameter: 57 mm, and clearance: 0.2 mm
- **Fluid:** density: 996 kg/m<sup>3</sup>, dynamic viscosity:  $7 \cdot 10^{-4}$  kg/ms
- **Boundary conditions:** total pressure drop: 4.5 bar, inlet loss ratio: 0.5, preswirl ratio: 0.5
- **Simulation case:** 27,264 cells ( $n_a = 12$ ,  $n_r = 8$ , and  $n_c = 284$ ), expected numerical deviation is 8–20%

Unfortunately, in [5] there is no boundary condition for the turbulence intensity given at the inlet. The assumption for the turbulence intensity within this study is 5%. It was brought to light that the scale of turbulence intensity at the inlet influences the results to a not-insignificant degree. The results show a mean difference of about 20% between the simulation and the published values, see Fig. 6.

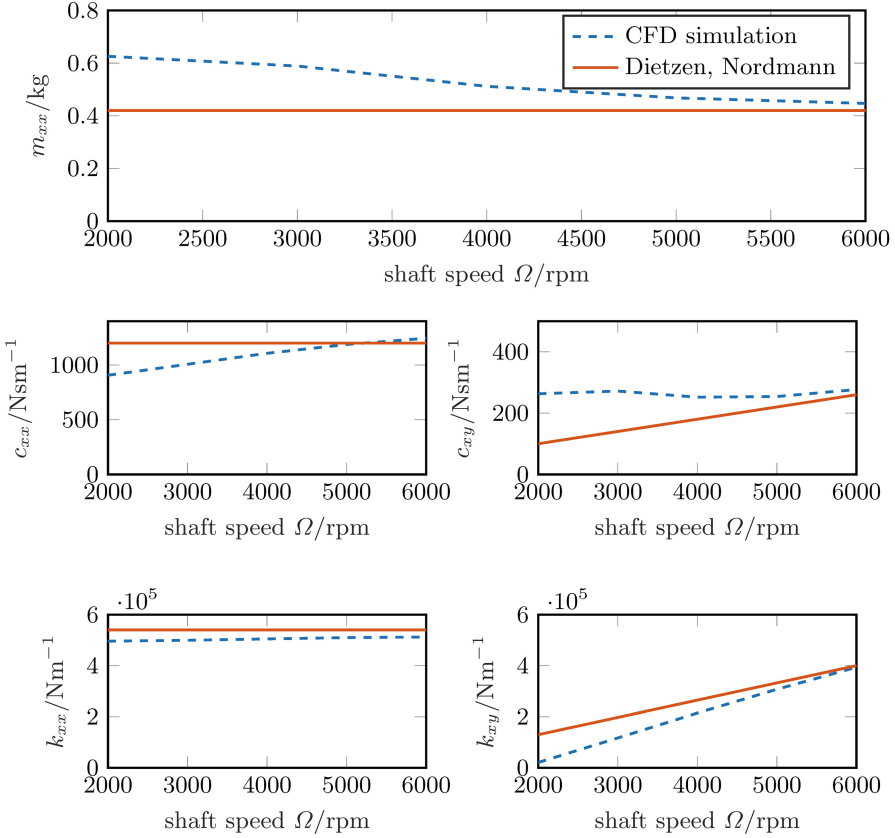


**Fig. 6.** Coefficients calculated by [5], comparison with CFD analysis approach

**Table 1.** Test rig and fluid parameters

	Name	Value
Rotor	Shaft	15 × 600 mm
	Mass	9.5 kg
	1 <sup>st</sup> seal-less natural freq.	34.1 Hz
Seal	Diameter	100 mm
	Length	20 mm
	Clearance	0.17 mm
	Pressure	200 kPa
	Dyn. viscosity	$40.48 \cdot 10^{-3} \text{ N}\cdot\text{s}/\text{m}^2$
	Density	$880 \text{ kg}/\text{m}^3$

### 5.3 Dynamic Analysis of the Test Rig

At the presented test rig, a run-up is performed with the parameters in Table 1.

The waterfall plot in Fig. 7 shows the two side spectra of the rotor's displacement signal at several rotational speeds. The 'dry' (without seal) 1st natural frequency is at 34.1 Hz and cannot be seen anymore. At this time, for safety reasons, the measurements were only up to 7,000 rpm, due to the large vibration amplitudes of the rotor at its natural frequency  $\omega_{1f}$  (the forward whirl'), which is significantly higher than the unbalance response  $\Omega$ .

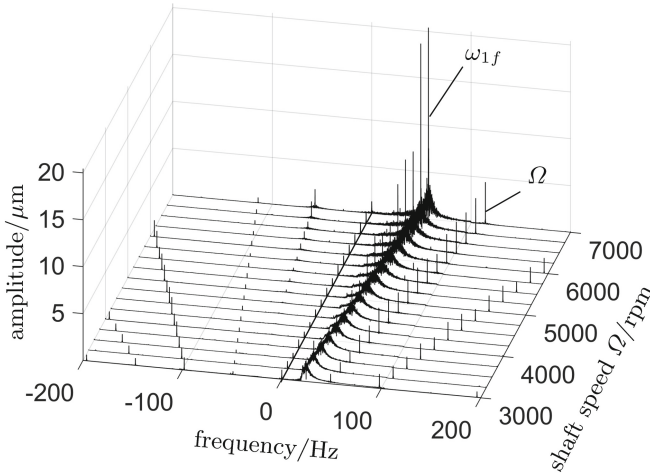


**Fig. 7.** Full spectrum waterfall plot of the measured test rig run-up

The whirl-frequency ratio is almost  $\omega_{1f}/\Omega \approx 0.4888$  for higher rotational speeds. The backward whirl natural frequency  $\omega_{1b}$  cannot be seen here because of its low excitation and the high damping.

The CFD analysis procedure described is applied to the seals geometry of the test rig to calculate its rotational speed-dependent rotordynamic coefficients. Therefore, one seal is discretized with 4,000 cells ( $n_a = 10$ ,  $n_r = 4$ , and  $n_c = 100$ ), the expected numerical deviation is 20%. The seal coefficients are then coupled to the 'dry' rotor parameters to analyze the system's rotational speed-dependent eigenvalues. The Campbell diagram in Fig. 8 shows the simulated 1st natural frequency in forward whirl direction  $\omega_{1f}$  compared to the frequency measured. The whirl frequency ratio of the simulated system is  $\omega_1/\Omega \approx 0.4909$ , which yields a difference of 0.42%.

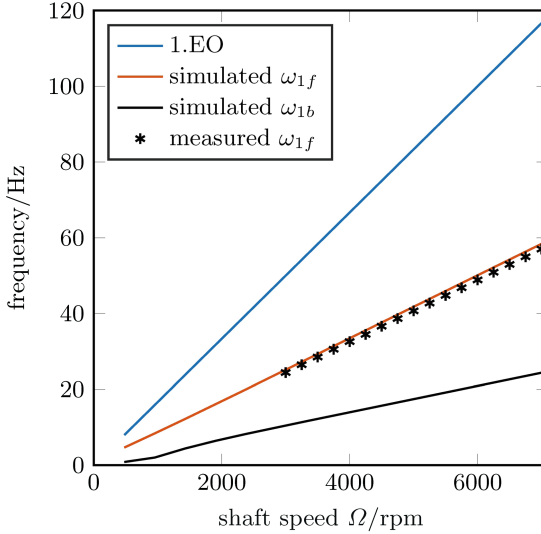


Fig. 8. Campbell diagram of the simulated and measured test rig

#### 5.4 Comparison and Analysis of the Results

The outlined CFD approach was confirmed by the validation. The analytical solution can be used for simple cases to determine the expected numerical simulation errors of the grid used. Thus, the rotordynamic seal coefficients calculated are within the numerical deviation compared to literature values. The calculation of the test rig's natural frequencies using the simulated coefficients shows a very good agreement with those of the experiment.

## 6 Conclusion: Summary and Outlook

In this research, a methodology for determining the rotordynamic coefficients of seals by CFD simulation is presented. To show the numerical errors of the discretization and the solving process, an analytical and, thus, exact solution is used for a simple case. The error rate of the 3D discretization is approximately 8% of the exact solution, the refined 2D case has a deviation of 0.003%. This confirms the discretization, the setup of the boundary conditions, and the solving process. The rotordynamic seal coefficients are calculated using stationary CFD simulations in a whirling coordinate frame. For various values of the rotational speed, different whirl frequencies are applied to simulate the forces acting on the rotor. A least squares fit of the tangential and the radial forces, depending on the whirl frequency, leads to the coefficients. The coordinate transformation, post processing, and finally the calculated rotordynamic coefficients, are validated by a literature example (DIETZEN and NORDMANN). Finally, the presented methodology is used to simulate the dynamic behavior of our seals test rig. The natural

frequency calculated (whirl frequency ratio) shows a good agreement with the measured test rig data. Future work will be made up of detailed experimental determination of coefficients and investigations in eccentricity/tilting effects.

**Acknowledgments.** This project is supported by the Ludwig Bölkow Campus and the Bavarian State. The friendly and effective cooperation between the partners of the research project is much appreciated.

## References

1. Muszynska, A.: Whirl and whiprotor/bearing stability problems. *J. Sound Vibr.* **110**(3), 443–462 (1986)
2. Black, H.F., Jenssen, D.N.: Black, Jenssen 1969-70 - Dynamic Hybrid Bearing Characteristics. In: Proceedings of the Institution of Mechanical Engineers, Conference Proceedings, vol. 184-14, pp. 92–100. SAGE Publications, Sage UK, London (1969)
3. Childs, D.W.: Dynamic analysis of turbulent annular seals based on hirs' lubrication equation. *ASME Lubr. Technol.* **105**, 429–436 (1983)
4. Muszynska, A.: Improvements in lightly loaded rotor/bearing and rotor/seal models. *J. Vibr. Acoust. Stress Reliab. Des.* **110**, 129–136 (1988)
5. Dietzen, F.J., Nordmann, R.: Calculating rotordynamic coefficients of seals by finite-difference techniques. *Trans. ASME J. Tribol.* **109**, 388–394 (1987)
6. Nordmann, R., Dietzen, F.J.: Finite difference analysis of rotordynamic seal coefficients for an eccentric shaft position. In: NASA, Lewis Research Center, Rotordynamic Instability Problems in High-Performance Turbomachinery, Kaiserslautern University, Department of Mechanical Engineering, no. N89-22906, pp. 269–284 (1989)
7. Kwanka, K.: Dynamic coefficients of stepped labyrinth gas seals. *J. Eng. Gas Turbines Power* **122**, 473–477 (1999)
8. Kwanka, K., Sobotzik, J., Nordmann, R.: Dynamic coefficients of labyrinth gas seals: a comparison of experimental results and numerical calculations. In: Proceedings of ASME Turbo Expo (2000)
9. Deckner, M.: Eigenschaften kombinierter Labyrinth - Bürstendichtungen für Turbomaschinen. Doktorarbeit, Technischen Universität München (2009)
10. Gaszner, M.: Rotordynamische Charakterisierung von Dichtungssystemen zur Anwendung in Kraftwerksdampfturbinen. Ph.D. thesis, Technical University of Munich (2015)
11. David, J.G.M., Thiago, G.R., Fernando, A.N.C.P.: Identification of rotordynamic seal coefficients by means of impedance matrix and an optimization strategy. In: Proceedings of the XVII International Symposium on Dynamic Problems of Mechanics, São Sebastião, SP, Brazil. ABCM (2017)
12. Wagner, C., Tsunoda, W., Matsushita, O., Berninger, T., Thümmel, T., Rixen, D.: Prediction of instability in rotor-seal systems using forward whirl magnetic bearing excitation. *J. Tech. Mech.* **37**(2–5), 358–366 (2017)
13. Wagner, C., Tsunoda, W., Berninger, T., Thümmel, T., Rixen, D.: Instability prediction and rotordynamic with seals: simulations based on the bulk-flow theory and experimental measurements. In: XVII International Symposium on Dynamic Problems of Mechanics DINAME, São Sebastião, SP, Brazil. ABCM (2017)

14. Ha, T.W., Choe, B.S.: Numerical simulation of rotordynamic coefficients for eccentric annular-type-plain-pump seal using CFD analysis. *J. Mech. Sci. Technol.* **26**(4), 1043–1048 (2012)
15. Kim, S.H., Ha, T.W.: Prediction of leakage and rotordynamic coefficients for the circumferential-groove-pump seal using CFD analysis. *J. Mech. Sci. Technol.* **30**(5), 2037–2043 (2016)
16. Zutavern, Z.S.: Identification of rotordynamic forces in a flexible rotor system using magnetic bearings identification of rotordynamic forces in a flexible rotor system using magnetic bearings. Ph.D. thesis, Texas AM (2006)
17. Santos, I.F., Svendsen, P.K.: Noninvasive parameter identification in rotordynamics via fluid film bearings—linking active lubrication and operational modal analysis. *J. Eng. Gas Turbines Power* **139**(6), 062507 (2017)
18. Gasch, R., Nordmann, R., Pfützner, H.: *Rotordynamik*. Springer, Heidelberg (2002)
19. Muszynska, A.: *Rotordynamics*. CRC Press, Boca Raton (2005)
20. Childs, D.W.: *Turbomachinery Rotordynamics*. Wiley-Interscience, Dallas (1993)
21. Wagner, C., Thümmel, T., Rixen, D.: Experimental prediction of instability in rotor seal systems using output only data. In: *International Symposium on Transport Phenomena and Dynamics of Rotating Machinery ISROMAC 2017*, Maui, Hawaii (2017)
22. Spurk, J.H., Nuri, A.: *Strömungslehre - Einführung in die Theorie der Strömungen* (2010)



# Coupled Simulation of Rotor Systems Supported by Journal Bearings

Nidish Narayanaa Balaji and I. R. Praveen Krishna<sup>(✉)</sup>

Department of Aerospace Engineering, Indian Institute of Space Science and Technology, Valiamala, Thiruvananthapuram 695547, India  
praveenkrishna@iist.ac.in

**Abstract.** Oil whirl and whip phenomena are fundamental to rotor systems supported by journal bearings. Published studies opt for a reduced formulation of the Reynolds equation of lubrication in order to aid the computations. In the current study, the complete Reynolds equation is solved using Pseudo Spectral Methods (PSM) and results compared with reduced solutions. The possibility of certain trends being missed in reduced model simulations is also brought out using a simple example. Rotor shaft and journal bearing systems are numerically modelled and coupled simulations have been carried out for test rotors inspired from literature. A semi analytical derivative estimation method is demonstrated to be superior to conventional finite difference methods in terms of processor load. This will be a useful addition for iterative solvers applied on rotors with more complicated geometry. Time transient analysis is carried out for two test rotors in order to bring out the oil whirl and whip phenomena, where the second one, with an added nonlinear node, shows a whirl along a branch which went undetected in the published reference. In the light of the above trends, the importance of full model numerical simulation is further emphasized.

**Keywords:** Pseudo Spectral Methods · Chebyshev polynomial Fluid film bearings

## Nomenclature

$\{F\}$	Forcing vector
$\{U\}$	Displacement Vector
$G$	Gyroscopic stiffness matrix
$K$	Element stiffness matrix
$M_R$	Rotational Inertia Matrix
$M_T$	Translational Inertia Matrix
$\epsilon$	Journal eccentricity magnitude
$\mu$	Kinematic viscosity
$\Omega$	Whirl frequency
$\omega$	Spin frequency



$\phi$	Journal eccentricity angle
$\theta$	Bearing angular coordinate
$c, h_0$	Nominal journal-bearing clearance
$e_x, e_y$	Orthogonal journal eccentricities
$F_X, F_Y$	Bearing forces
$h(\theta, t)$	Bearing clearance
$P$	Hydrostatic pressure
$R$	Mean bearing radius
$T_k(x)$	Chebyshev polynomial of first kind, degree $k$
$U = \omega R$	Wall speed
$z$	Bearing axial coordinate
FDM	Finite Difference Method
FEM	Finite Element Method
PSM	Pseudo-Spectral Method

## 1 Introduction

Journal bearings provide a cheap and effective support alternative for high speed rotor applications. They are preferred mainly due to the absence of surfaces in contact (leading to wear) and the high fluid film forces [1]. A practical issue that accompanies the use of journal bearings is what is known as oil whip instability [2,3] which occurs at rotor spin frequencies far above the linearized first critical. Being a classical problem, extensive literature is available in studying the bearing modelling [1,4,5], bifurcations [6,7], instability [2,3,8,9], etc.

Mathematically, the bearings are modelled using the Reynolds equation of lubrication [10]. The equation is arrived at as an integral form of the continuum and the momentum equation after making necessary assumptions. The same equation is used for modelling squeeze film dampers too (refer [1] for more details). The Reynolds equation of lubrication is a second order partial differential equation with a single unknown: the fluid static pressure. The fluid film forces are obtained as area integrals of the fluid pressure on the journal surface. Popular numerical techniques employed to solve the same include the Finite Element Method (FEM) [11], Pseudo Spectral Method (PSM) [5], etc. In [5] it has been demonstrated that PSM is computationally less intensive as compared to FEM. This is mainly due to the fact that a finite element formulation will involve matrix stitching, a process that constructs matrices of global support using locally supported matrices. Since PSM is formulated as a method with global support, this step is avoided, leading to a speed up in the calculations (element formulation/assembly time). However, matrix sparsity, which is one of the most appealing features of any FEM formulation, is absent in the case of PSM.

For a general rotor dynamic simulation, in addition to the bearings, it is also necessary to model the rotor shaft. Various transfer matrix and lumped matrix approaches are available in the literature apart from the Finite Element Method (see [1]). The rotor shaft is modelled using finite Euler Bernoulli beam elements in the current study, following the formulation in [12]. Timoshenko

beam models have been formulated [13] but the current study focuses on slender rotors for Euler Bernoulli beams are reasonably accurate.

In studying rotor-bearing problems involving fluid film bearings, few studies make use of complete formulations of both the rotor shaft as well as the bearing. Common practice is to reduce the rotor to a linear stiffness element and reduce the rotor dynamic system into a set of coupled ordinary differential equations. Another reduction that may be seen in the literature is in the Reynolds equation -short bearing and long bearing approximations reduce one of the two coordinate dependencies of the bearing fluid pressure. Classically, these were made in order to reduce computational load. In the current study, the validity of the reduction of the Reynolds equation is questioned, positing that the advent of modern computers have effectively removed the necessity for such reductions and fully coupled solvers reveal certain details which may not be perceptible with the reductions incorporated.

## 2 Theory

Euler Bernoulli beam model used for the FEM formulation for the rotor shaft model. The equations of motion for each element takes the form as in Eq. (1).

$$(\mathbf{M}_T + \mathbf{M}_R) \{\ddot{U}\} - \omega \mathbf{G} \{\dot{U}\} + \mathbf{K} \{U\} = \{F\} \quad (1)$$

with  $\mathbf{M}_T$  and  $\mathbf{M}_R$  denoting translational and rotational inertia matrices respectively, and the matrices  $\mathbf{G}$  and  $\mathbf{K}$  denoting the gyroscopic and the element stiffness matrices respectively. The gyroscopic effects, as expected, are modelled as being proportional to the spin frequency  $\omega$ . See [12] for further details on the formulation.

Figure 1 is a schematic illustration of a simple journal bearing. The central circle is the shaft-journal surrounded by the bearing. The Reynolds equation of lubrication written for the hydrodynamic journal bearing may be expressed as in Eq. (2).

$$\frac{1}{R^2} \frac{\partial}{\partial \theta} \left( \frac{h^3}{\mu} \frac{\partial P}{\partial \theta} \right) + \frac{\partial}{\partial z} \left( \frac{h^3}{\mu} \frac{\partial P}{\partial z} \right) = 6 \left( \frac{1}{R} \frac{\partial (hU)}{\partial \theta} + 2 \frac{dh}{dt} \right) \quad (2)$$

where  $R$  is the mean bearing radius,  $\theta$  &  $z$  are the angular and axial coordinates,  $\mu$  is the kinematic viscosity,  $U$  is the wall speed ( $\omega R$ ), and  $h(\theta, t)$  is the bearing clearance (assumed independent of the axial coordinate). The hydrostatic fluid pressure  $P$  is the only unknown in the equation. In terms of the orthogonal eccentricities  $e_x$  &  $e_y$ , the bearing clearance and its time derivative may be expressed as in Eq. (3).

$$\begin{aligned} h(\theta, t) &= c - e_x \cos \theta - e_y \sin \theta \\ \frac{dh(\theta, t)}{dt} &= -\dot{e}_x \cos \theta - \dot{e}_y \sin \theta \end{aligned} \quad (3)$$

with  $c$  being the nominal clearance between the journal and the bearing.

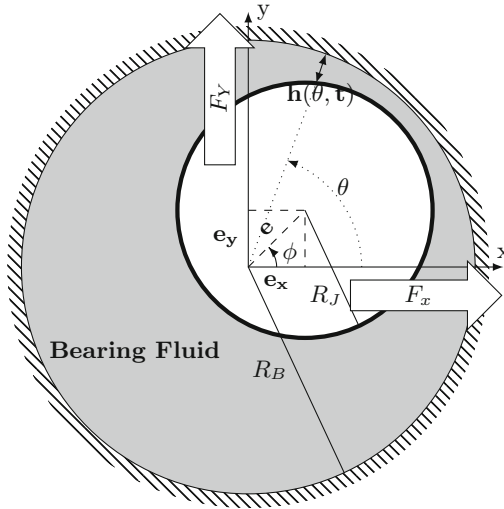


Fig. 1. Journal bearing (schematic)

Spectral methods work by expressing the solution in terms of a series of orthogonal basis functions. Each set of polynomials comes with a set of properties and advantages. For example, the Fourier basis functions naturally extend themselves for the solution over periodic domains. The *Chebyshev polynomials* [14] are found to be well suited to most problems in practice without any restrictions on the boundary conditions. The notation for spectral series representation is,

$$\hat{u}(x) = \sum_{k=0}^N u_k \phi_k(x)$$

where,

$\phi_k(x) = e^{\iota kx}$ , (Fourier spectral method)

$\phi_k(x) = T_k(x)$ , (Chebyshev spectral method)

with  $T_k(x) = \cos(k \cos^{-1} x)$  denoting the Chebyshev polynomial of first kind, degree  $k$  [5].

For modelling the journal bearing, the fluid is modelled as a 2D surface meshed uniformly in the circumferential direction and with Gauss-Lobatto grid points in the axial direction. Following collocation at the grid points, the equation becomes a matrix equation. The unknown pressure is obtained as a set of grid values  $P$ , which has to be further integrated (numerically) with  $\cos \theta$  and  $\sin \theta$  in order to obtain the bearing forces  $F_X$  and  $F_Y$  (see Eq. (4)).

$$\begin{Bmatrix} F_X \\ F_Y \end{Bmatrix} = -2 \int_0^{L/2} \int_{-\pi}^{\pi} P(\theta, z) \begin{Bmatrix} \cos \theta \\ \sin \theta \end{Bmatrix} R d\theta dz \tag{4}$$

A recurring problem while using semi analytical techniques (for eq, shooting methods, Harmonic Balancing, Time Variational Formulation, etc.) for rotor dynamics is the calculation of bearing force derivatives. Using a finite difference scheme for this would involve four additional sets of linear equations that have to be solved separately followed by the evaluations of the corresponding area integrals. A semi analytical approach may be derived by direct differentiation of the Reynolds equation, with respect to the independent variables  $e_x$  and  $e_y$  and integrating the pressure derivative fields for the force derivative calculation as given (Eq. 5).

$$\begin{aligned} \frac{1}{R^2} \frac{\partial}{\partial \theta} \left( \frac{h^3}{\mu} \frac{\partial}{\partial \theta} \left( \frac{\partial P}{\partial e_x} \right) \right) + \frac{\partial}{\partial z} \left( \frac{h^3}{\mu} \frac{\partial}{\partial z} \left( \frac{\partial P}{\partial e_x} \right) \right) = 6\omega \sin \theta + \\ 3 \left[ \frac{1}{R^2} \frac{\partial}{\partial \theta} \left( \frac{h^2}{\mu} \cos \theta \frac{\partial P}{\partial \theta} \right) + \frac{\partial}{\partial z} \left( \frac{h^2}{\mu} \cos \theta \frac{\partial P}{\partial z} \right) \right] \end{aligned} \quad (5a)$$

$$\begin{aligned} \frac{1}{R^2} \frac{\partial}{\partial \theta} \left( \frac{h^3}{\mu} \frac{\partial}{\partial \theta} \left( \frac{\partial P}{\partial e_y} \right) \right) + \frac{\partial}{\partial z} \left( \frac{h^3}{\mu} \frac{\partial}{\partial z} \left( \frac{\partial P}{\partial e_y} \right) \right) = -6\omega \cos \theta + \\ 3 \left[ \frac{1}{R^2} \frac{\partial}{\partial \theta} \left( \frac{h^2}{\mu} \sin \theta \frac{\partial P}{\partial \theta} \right) + \frac{\partial}{\partial z} \left( \frac{h^2}{\mu} \sin \theta \frac{\partial P}{\partial z} \right) \right] \end{aligned} \quad (5b)$$

$$\frac{1}{R^2} \frac{\partial}{\partial \theta} \left( \frac{h^3}{\mu} \frac{\partial}{\partial \theta} \left( \frac{\partial P}{\partial \dot{e}_x} \right) \right) + \frac{\partial}{\partial z} \left( \frac{h^3}{\mu} \frac{\partial}{\partial z} \left( \frac{\partial P}{\partial \dot{e}_x} \right) \right) = -12 \cos \theta \quad (5c)$$

$$\frac{1}{R^2} \frac{\partial}{\partial \theta} \left( \frac{h^3}{\mu} \frac{\partial}{\partial \theta} \left( \frac{\partial P}{\partial \dot{e}_y} \right) \right) + \frac{\partial}{\partial z} \left( \frac{h^3}{\mu} \frac{\partial}{\partial z} \left( \frac{\partial P}{\partial \dot{e}_y} \right) \right) = -12 \sin \theta \quad (5d)$$

An efficient formulation, on account of the left hand side operators being identical, enable one to solve the equations together. The force derivatives may be obtained by numerical integration.

Solution of the Reynolds equation will give rise to negative pressure values too. Since this does not represent the physical situation, cavitation conditions are applied. One of the simplest of these is the Gumbel or the Half-Sommerfeld condition which ‘‘chops off’’ the pressures to the cavitation pressure value and the derivatives to zero when the solved pressure value is below the cavitation pressure level at the operating temperature. Book by Szeri [4] and other such textbooks may be referred for more detailed models.

### 3 Test Case Results

#### 3.1 Fluid Force Derivative Calculation

In order to demonstrate the fluid film force derivative calculation developed above, a journal bearing with the following specifications (as in [5]) is considered. Table 1 summarizes the specifications of the bearing used for the calculations.

The fluid film forces themselves, when calculated on a  $24 \times 11$  grid, are verified with the published values for different journal eccentricities in Table 2.

**Table 1.** Bearing specifications as in [5]

Parameter	Value
Diameter	$50.8 \times 10^{-3}$ m
Length	$12.7 \times 10^{-3}$ m
Radial clearance	$50.8 \times 10^{-6}$ m
Oil viscosity	0.00689 Pa s
Journal speed	10,000 rpm

**Table 2.** Comparison of fluid film forces calculated using PSM with the published values in [5]

Journal position		Published values		Calculated values	
Eccentricity ( $\epsilon$ )	Attitude angle ( $\phi$ )	$F_X$ (N)	$F_Y$ (N)	$F_X$ (N)	$F_Y$ (N)
0.3	45°	-47	11	-46.58	11.04
0.5	45°	-136	0	-134.09	-0.34
0.7	45°	-469	-119	-462.77	-115.97
0.8	45°	-1139	-459	-1121.33	-445
0.9	45°	-4729	-2853	-4666.14	-2792.99

Since the  $L/D$  ratio for the current bearing is lesser than 0.5, the bearing is conventionally termed as a short bearing, for which [15] provides an analytical expression of the forces after making a  $\pi$ -field cavitation assumption in the rotating reference frame (as in Eq. (6)).

$$\begin{aligned}
 F_r &= -\mu RL \left(\frac{L}{c}\right)^2 \left[ (\omega - 2\dot{\phi}) \frac{\epsilon^2}{(1 - \epsilon^2)^2} + \frac{\pi}{2} \frac{(1 + 2\epsilon^2)\dot{\epsilon}}{(1 - \epsilon^2)^{5/2}} \right] \\
 F_t &= \mu RL \left(\frac{L}{c}\right)^2 \left[ (\omega - 2\dot{\phi}) \frac{\pi}{4} \frac{\epsilon}{(1 - \epsilon^2)^{3/2}} + \frac{2\epsilon\dot{\epsilon}}{(1 - \epsilon^2)^2} \right]
 \end{aligned} \tag{6}$$

Table 3 provides the comparison of fluid film force derivatives calculated through the above analytical expression, finite difference on the complete formulation, and the derivative estimation described in Sect. 2. The derivatives are computed for an operating condition corresponding to row 1 of Table 2. In terms of the actual values of the derivatives, the FDM results are taken as the most accurate. Looking at the results, it may readily be observed that the analytical calculations are completely off. A slight computational advantage was also observed for the pressure derivative formulation (time calculations conducted on a 4 GB RAM machine with a quad core i3 processor clocked at 2.63 GHz). For a coupled iterative solver, this will be a very significant advantage.

Since all linearizations of bearing forces over particular solution branches are done through mean derivative estimates over one cycle, the inaccuracy of

Vance's [15] solution must be kept in mind. These arise mainly due to the  $\pi$ -field cavitation assumption that is used in the derivation of the analytical equation.

**Table 3.** Comparison of derivative estimates (all quantities in SI units)

Derivative	Force component	Analytic estimate	FDM estimate	Current approach
$\partial/\partial e_x$	$F_X$	4.23e6	2.37e6	2.37e6
	$F_Y$	1.78e6	-2.18e6	2.18e6
$\partial/\partial e_y$	$F_X$	2.43e6	3.89e6	3.89e6
	$F_Y$	-2.41e6	1.56e6	1.56e6
$\partial/\partial \dot{e}_x$	$F_X$	734	7660	7660
	$F_Y$	3700	1030	1030
$\partial/\partial \dot{e}_y$	$F_X$	7663	1171	1171
	$F_Y$	734	3991	3991
Average computation time (s)			0.575	0.365

### 3.2 Coupled Rotor Bearing Systems

The rotor bearing model in Fig. 2a (Case 1 rotor), consists of a rotor shaft (with the depicted properties) with two unbalances supported by a rigid pin at one end and a fluid film bearing at another. A five element formulation as shown is used for the following analysis. The properties of the journal bearing and the mass offsets are given in Table 4.

**Table 4.** Specifications of nonlinear rotor model for Case 1 rotor

Journal bearings	
L	$28.5 \times 10^{-3}$ m
D	$57.2 \times 10^{-3}$ m
$\mu$	0.0069 Pa s
$h_0$	$51.0 \times 10^{-6}$ m
$F_s$	395 N
Mass offsets	
M	4.83 kg
e	$6.21 \times 10^{-6}$ m

Transient simulation of the above model involves solving the corresponding equations of motion with suitable initial conditions for a considerable number of time steps until transients are completely removed. The above is conducted

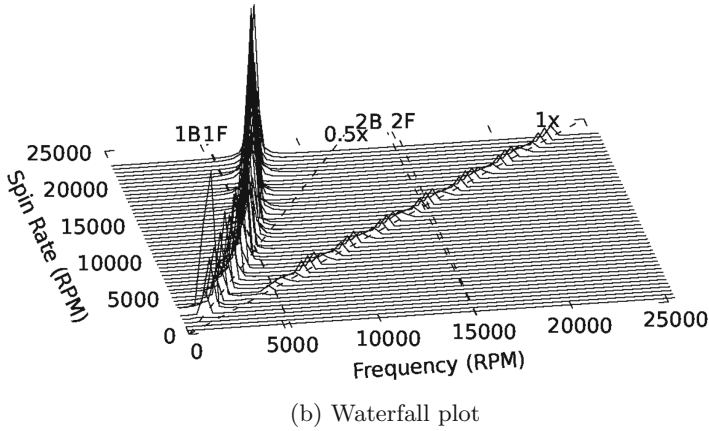
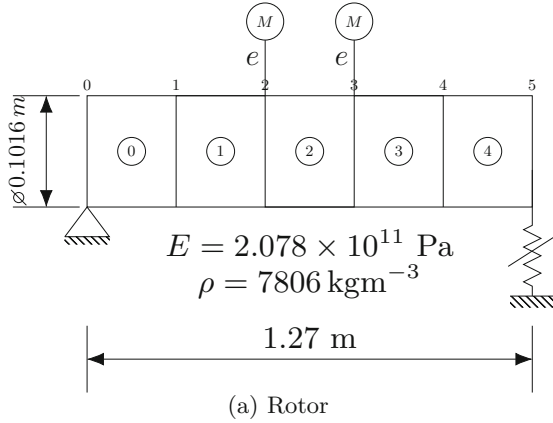
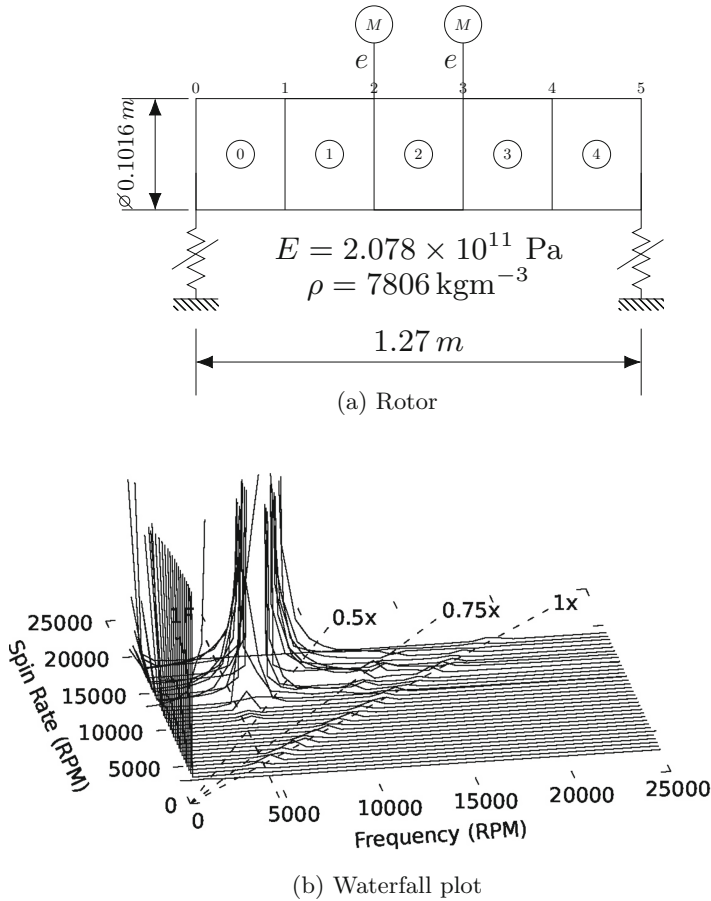


Fig. 2. Case 1 nonlinear rotor

for a range of spin frequencies  $\omega$  and a waterfall plot is generated. The waterfall plot consists of the frequency content of the time series of an expedient degree of freedom in the model (taken here as the x deflection of node 2) plotted against the spin frequency. Figure 2b depicts the time transient analysis result for this rotor.

Both the synchronous branch, occurring at  $\Omega = \omega$  and the sub-synchronous branch corresponding to oil whirl and oil whip can be observed in the Fig. 2b. Lines are drawn corresponding to the first and second backward and forward whirl modes of the linearized rotor model. Oil whirl happens until the spin frequency reaches approximately twice the first normal mode frequency wherein the oil film precession accounts for a distinct whirl at  $0.5\omega$ . For higher spin rates, the system gets “locked on” to the first normal, leading to the *oil whip* phenomenon. The oil whipping becomes unstable at larger spin speeds than a critical speed (not depicted in the figure).



**Fig. 3.** Case 2 nonlinear rotor (from [16])

Figure 3a depicts the Case 2 rotor [16]. Only difference with Case 1 rotor is that the pin in Case 1 is replaced with an identical fluid bearing. The properties are all as in Table 4. The formulation in [16] makes use of the short bearing approximation for the bearings in order to reduce the Reynolds equation. The authors use a shooting technique to obtain periodic solutions. Since solutions with an oil whip are quasi-periodic (and hence aperiodic), the whip phenomena may not be observed in the paper. The waterfall plot for this rotor is depicted in Fig. 3b. Due to the presence of two journal bearings, the instability is apparent at lower spin rates itself. The peak at zero frequency is due to the side force applied at each bearing which offsets the whole rotor by a finite distance. An interesting feature of the plot in Fig. 3 is that apart from the synchronous whirl and the oil whip, there is a distinct peak at  $0.75\omega$ . This is posited to be due to an effect of the coupling of the two journal bearings in the presence of mean



load. Further study must be conducted for the same, but the trend is brought out here to emphasize the importance of full model simulations.

## 4 Conclusion

Rotor shaft and journal bearing systems are numerically modelled and coupled simulations have been carried out for test rotors inspired from literature. A semi analytical derivative estimation method is demonstrated to be superior to conventional finite difference methods in terms of processor capability. This will be a useful addition for iterative solvers applied on rotors with more complicated geometry.

Time transient analysis is carried out for two test rotors in order to bring out the oil whirl and whip phenomena, where the second one, with an added bearing, shows another branch which went undetected in the published reference. In the light of the above trends, the importance of full model numerical simulation is further emphasized.


## References

1. Childs, D.: Turbomachinery Rotordynamics: Phenomena, Modeling, and Analysis. Wiley, Hoboken (1993)
2. Muszynska, A.: Whirl and whip-rotor/bearing stability problems. *J. Sound Vibr.* **110**(3), 443–462 (1986)
3. Jing, J., Meng, G., Sun, Y., Xia, S.: On the oil-whipping of a rotor-bearing system by a continuum model. *Appl. Math. Model.* **29**(5), 461–475 (2005). <https://doi.org/10.1016/j.apm.2004.09.003>
4. Szeri, A.: Fluid Film Lubrication: Theory and Design. Cambridge University Press, Cambridge (1998)
5. Gantasala, S., Krishna, I.R.P., Sekhar, A.S.: Dynamic analysis of rotors supported on journal bearings by solving reynolds equation using pseudospectral method. In: Pennacchi, P., (ed.) Proceedings of the 9th IFToMM International Conference on Rotor Dynamics, pp. 1009–1019. Springer, Cham (2015)
6. Miura, T., Inoue, T., Kano, H.: Nonlinear analysis of bifurcation phenomenon for a simple flexible rotor system supported by a full-circular journal bearing. *J. Vibr. Acoust.* **139**(3), 031,012 (2017). <https://doi.org/10.1115/1.4036098>
7. Wang, J.K., Khonsari, M.M.: Bifurcation analysis of a flexible rotor supported by two fluid-film journal bearings. *J. Tribol.* **128**(3), 594 (2006). <https://doi.org/10.1115/1.2197842>
8. Black, H.F.: The stabilizing capacity of bearings for flexible rotors with hysteresis. *J. Eng. Ind.* **98**(1), 87–91 (1976)
9. Lund, J.: Stability and damped critical speeds of a flexible rotor in fluid-film bearings. *J. Eng. Ind.* **96**(2), 509–517 (1974)
10. Dowson, D.: A generalized Reynolds equation for fluid-film lubrication. *Int. J. Mech. Sci.* **4**(2), 159–170 (1962)
11. Huebner, K.H.: Application of finite element methods to lubrication: an engineering approach. *J. Lubr. Technol.* **94**(4), 313–323 (1972)

12. Nelson, H.D., McVaugh, J.M.: The dynamics of rotor-bearing systems using finite elements. *J. Eng. Ind.* **98**(2), 593–600 (1976)
13. Nelson, H.D.: A finite rotating shaft element using timoshenko beam theory. *J. Mech. Des.* **102**(4), 793–803 (1980)
14. Boyd, J.P.: *Chebyshev and Fourier Spectral Methods*. Courier Corporation, North Chelmsford (2001)
15. Vance, J.: *Rotordynamics of Turbomachinery*. Wiley, Hoboken (1988)
16. Sundararajan, P., Noah, S.: An algorithm for response and stability of large order non-linear systems—application to rotor systems. *Journal of sound and vibration* **214**(4) (1998)



# Effect of Texture Region on the Static and Dynamic Characteristic of Partially Textured Journal Bearings

Hiroo Taura 

Nagaoka University of Technology, 1603-1, Kamitomioka,  
Nagaoka, Niigata 940-2188, Japan  
htauro@mech.nagaokaut.ac.jp

**Abstract.** The effect of the texturing region on the static and dynamic characteristics of partially textured bearings, of which the texturing area is limited on the bearing surface in the circumferential direction, were investigated theoretically. The load carrying capacity and stiffness and damping coefficients of some partially textured journal bearings with the different textured region were calculated by using a numerical model considering the effects of both fluid inertia and energy loss at the edges of the dimples. The results showed that when the surface texturing was formed in the unloaded region of the journal bearing surface, the load carrying capacity maintains as much as the smooth bearing for a wide range of Sommerfeld number. The linear stability threshold speeds of a symmetrical rigid rotor supported in two identical textured bearings was also calculated with the dynamic coefficients of the oil film. The results obtained showed that when the texture region starts from  $270^\circ$  from the top of the bearing in the rotating direction, the stability threshold speeds are higher than those of the fully textured bearing at relatively high Sommerfeld number. From these results, it was concluded that an appropriate partial texturing formed on the bearing surface can improve both the load carrying capacity and the stability characteristics simultaneously.

**Keywords:** Journal bearing · Surface texture · Load carrying capacity  
Stability

## Nomenclature

$C$	Mean radial clearance
$D$	Bearing diameter ( $=2R$ )
$L$	Bearing length
$N$	Journal rotational speed
$O_b, O_j$	Origin of bearing or journal
$R$	Bearing inner radius
$S$	Sommerfeld number
$W$	Static load
$X, Y$	Vertical and horizontal axes
$e$	Eccentricity
$f_x, f_y$	Oil-film-force components in the vertical and horizontal directions

$H$	Dimensionless oil-film-thickness
$h_t$	Depth of square dimple
$l_{tz}, l_{t\theta}$	Width of square dimples in the axial and circumferential directions
$l_{pz}, l_{p\theta}$	Pitch of square dimples in the axial and circumferential directions
$m$	Half of mass of a model rotor
$P$	Oil film pressure (above ambient)
$x, z$	Coordinates in the circumferential and axial directions
$\delta$	Ratio of dimple depth to mean radial clearance ( $=h_t/C_r$ )
$\varepsilon$	Eccentricity ratio ( $=e/C$ )
$\eta$	Viscosity of fluid
$\theta$	Angular coordinate ( $=x/R$ )
$\theta_t$	Start angle of texture region
$\theta_{ts}$	Circumferential angle of texture region
$\phi$	Attitude angle, deg
$\omega$	Journal angular velocity, rad/s

## 1 Introduction

Surface texturing has been applied to various mechanical elements with the mating surfaces for the improvement of lubrication performance. This technique has also attracted attention in a field of the journal bearings, and many researchers have investigated the effect of surface texturing on the static characteristics of journal bearings [1–10]. The present authors [11, 12] have also analyzed numerically and experimentally the load carrying capacity and dynamic coefficients of textured journal bearings with square dimples. They proposed a numerical model considering both effects of the fluid inertia and the energy loss at the edge of dimples, and the results agreed qualitatively and quantitatively with the experimental ones, confirming the validity of the numerical model. They also demonstrated that the fully textured bearings improve the stability of a rotor supported in the bearings, but decrease the load carrying capacity. As for the load carrying capacity, Tala-Ighil et al. [1] and Brizmer [5] also revealed that the load carrying capacity was increased by manufacturing an appropriate texturing area on the bearing surface, but they have not investigated the dynamic characteristic of the bearings.

In the study, we focus on the partially textured bearings, of which the texturing area is limited on the bearing surface in the circumferential direction, and numerically investigate the effect of the texturing region on the static and dynamic characteristics of the bearings.

## 2 Numerical Analysis

### 2.1 Analytical Model

Figure 1 shows a partially textured journal bearing used in this analysis. The journal rotates with a rotational speed  $\omega$  about its axis, which locates at the static equilibrium position with eccentricity  $e$  and attitude angle  $\phi$ . The static load  $W$  is applied to the journal vertically downward. A Cartesian coordinate system is also shown in Fig. 1. The  $x$ -axis is along the vertical direction, the  $z$ -axis is in the direction of the journal length, and the  $Y$  axis is perpendicular to the  $x$ - and  $z$ -axes. The circumferential coordinate  $\theta$  is measured from the positive  $X$  axis in the rotating direction. An axial oil groove is set on the top of the bearing and lubricating oil is supplied from it. The texture region is formed from  $\theta_{ts}$  to  $\theta_{ts} + \theta_s$  on the bearing surface in the circumferential direction, and to the whole in the axial direction.

Figure 2 shows a schematic of the dimples on the bearing surface. We chose the square dimples according to our previous study [11, 12]. As shown in Fig. 1, the square dimples are formed at an equal interval in the texture region. Three parameters characterize the square dimples; the depth  $h_d$ , the length and the pitch. Considering the direction, the length are represented  $l_{d\theta}$ ,  $l_{dz}$  in the circumferential and axial direction respectively, and the pitch  $l_{p\theta}$ ,  $l_{pz}$  in the circumferential and axial direction respectively.

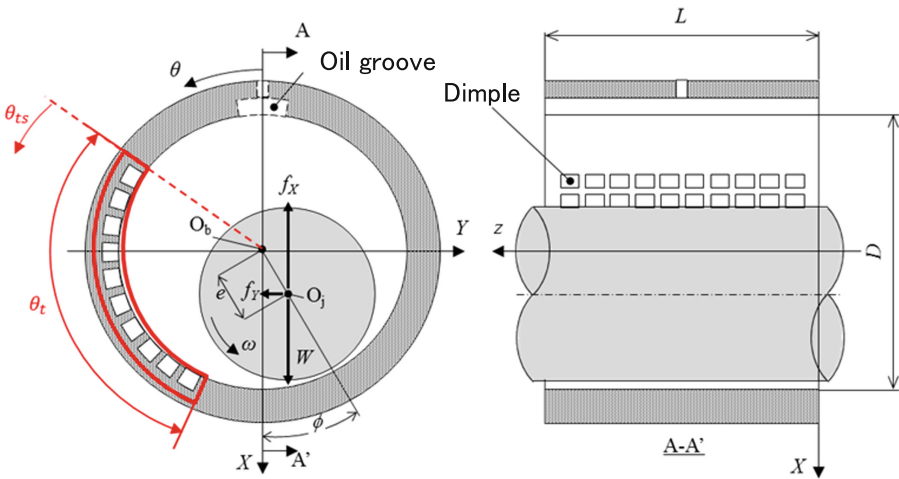


Fig. 1. Analytical model of the partially textured journal bearing with a coordinate system

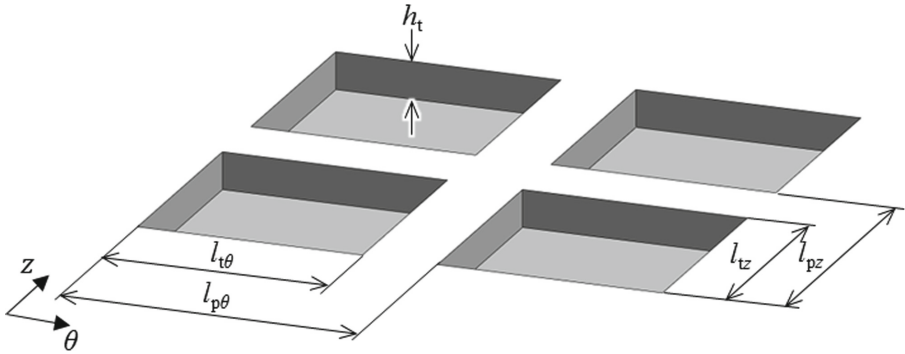


Fig. 2. Schematic view of the square dimples [11]

**2.2 Governing Equation for the Pressure Distribution**

As the calculation procedure used in the study were almost similar to the reference [11, 12], we described it briefly here.

In the study, the pressure distribution of the oil film is determined based on the Reynolds equation, considering the inertia effect and the energy loss due to the film discontinuity at the edge of dimples. In this study, the pressure jump due to the inertial effect is evaluated by using Bernoulli’s equation and the energy loss is calculated using expressions that depend upon film expansion or contraction.

As the governing equation for the pressure distribution, we used the incompressible and iso-viscous Reynolds equation written in dimensionless form as follows:

$$\frac{\partial}{\partial \theta} \left( H^3 \frac{\partial P}{\partial \theta} \right) + \frac{1}{4} \left( \frac{D}{L} \right)^2 \frac{\partial}{\partial Z} \left( H^3 \frac{\partial P}{\partial Z} \right) = 6 \frac{\partial H}{\partial \theta} + 12 \frac{\partial H}{\partial \tau} \tag{1}$$

The dimensionless forms of the variables in Eq. (1) are defined in Eq. (2):

$$\theta = \frac{x}{R}, Z = \frac{z}{L}, H = \frac{h}{C}, P = \frac{p}{\eta \omega} \left( \frac{C}{R} \right)^2, \tau = \omega t \tag{2}$$

The dimensionless film thickness in the land is given by

$$H = 1 + \varepsilon \cos(\theta - \phi) \tag{3}$$

and in the dimple

$$H = 1 + \varepsilon \cos(\theta - \phi) + \delta \tag{4}$$

where  $\varepsilon (=e/C)$  is the eccentricity ratio and  $\delta (=h_t/C)$  is the dimple-depth ratio.

The inertia effect and energy loss of the fluid in the discontinuous clearance at the edge of the dimples are evaluated by using a combination of Bernoulli’s equation and

some loss formula. At a film-expansion point, the loss formula of a sudden expansion pipe is applied to estimate the pressure variation:

$$p^- - p^+ = \frac{\rho}{2} \left( (u^{*+})^2 - (u^{*-})^2 \right) + \xi_{\text{loss}} \cdot \frac{\rho}{2} (u^{*-})^2 \tag{5}$$

Where,  $u^*$  denotes the average fluid velocity in the film-thickness direction, and the superscripts + and - indicate quantities in the dimple section just after flowing out of the smooth section and quantities in the smooth section just before entering a dimple, respectively. The coefficient of loss,  $\xi$ , is defined as

$$\xi_{\text{loss}} = \zeta \left( 1 - \frac{h^-}{h^+} \right)^2 \tag{6}$$

where  $\zeta$  is 1.0 in the study [11]. At an abrupt reduction point, the empirical formula [13] of step bearings is used.

$$p^- - p^+ = \beta \frac{\rho}{2} \left( (u^{*+})^2 - (u^{*-})^2 \right) + \zeta_1 \frac{\rho}{2} \left( (u^{*+})^2 - (u^{*-})^2 \right) - \zeta_2 \rho U^2 \ln \frac{h^-}{h^+} \tag{7}$$

In the laminar regime, coefficient  $\beta$  takes a value of 1.2 and coefficients  $\zeta_1$  and  $\zeta_2$  each take values of 0.133 [13].

As the boundary conditions for pressure, Reynolds boundary condition is applied. The pressures at both bearing ends and in the oil-feeding groove were set to zero (ambient pressure).

After the pressure distribution was obtained, the vertical and horizontal components of the oil-film reaction force can, respectively, be calculated by the following integrals:

$$f_X = -\eta\omega \left( \frac{R}{C} \right)^2 RL \int_0^1 \int_0^{2\pi} P \cos \theta d\theta dZ \tag{8}$$

$$f_Y = -\eta\omega \left( \frac{R}{C} \right)^2 RL \int_0^1 \int_0^{2\pi} P \sin \theta d\theta dZ \tag{9}$$

The above two force components under the steady state condition,  $f_{X0}$  and  $f_{Y0}$ , are as follows:

$$f_{X0} = W \tag{10}$$

$$f_{Y0} = 0 \tag{11}$$

where  $W$  is the static load applied vertically downward on the journal.

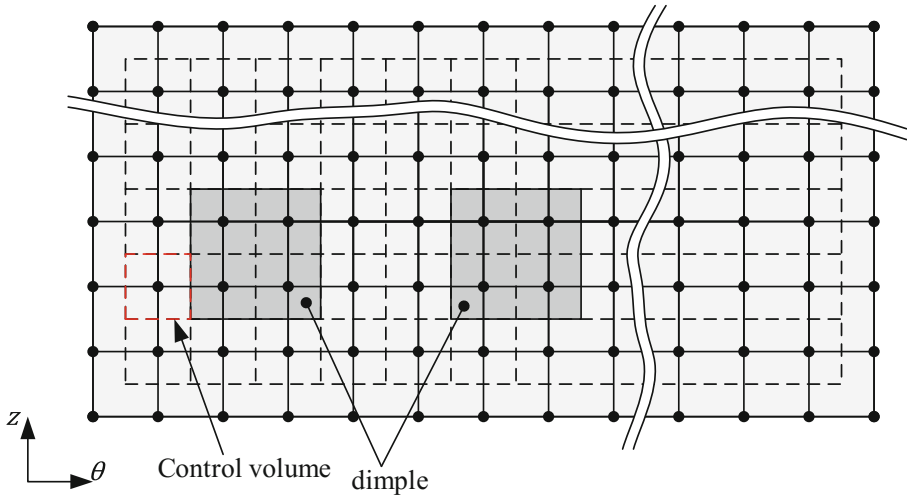


Fig. 3. Discretization of the bearing surface

### 2.3 Numerical Calculation of the Pressure Distribution

To obtain the pressure distribution numerically, the Reynolds Eq. (1) was discretized by using a cell method, which is proposed by Arghir [14]. The calculation region is divided into an orthogonal grid with 180 in the circumferential direction by 60 across the bearing width, and the edges of the square dimple are placed on the cell boundary as shown in Fig. 3. The pressures at the cell's centers are calculated with a difference equation derived from Eq. (1) using a successive over-relaxation scheme, whereas the pressures at the cell boundaries on the step between the dimple and the smooth region are also calculated considering the inertia effect and the energy loss. If any negative pressures obtained during the iteration, the pressure are set to zero to maintain the Reynolds boundary conditions.

### 2.4 Calculation of the Dynamic Coefficients of the Oil Film

When the rotor is applied small displacements,  $\Delta X$  and  $\Delta Y$ , and small velocities,  $\Delta \dot{X}$  and  $\Delta \dot{Y}$ , in vertical and horizontal directions around its equilibrium position, the dynamic reacting forces,  $f_X$  and  $f_Y$ , are described with eight dynamic coefficients based on the assumption of linearization as follows:

$$\begin{cases} f_X = f_{X0} + k_{XX}\Delta X + k_{XY}\Delta Y + c_{XX}\Delta \dot{X} + c_{XY}\Delta \dot{Y} \\ f_Y = f_{Y0} + k_{YX}\Delta X + k_{YY}\Delta Y + c_{YX}\Delta \dot{X} + c_{YY}\Delta \dot{Y} \end{cases} \quad (12)$$

where  $k_{ij}$  and  $c_{ij}$  ( $i, j = X, Y$ ) are the stiffness and damping coefficients, respectively. Stiffness and damping coefficients are defined as follows:



$$\begin{bmatrix} k_{XX} & k_{XY} \\ k_{YX} & k_{YY} \end{bmatrix} = \begin{bmatrix} \left. \frac{\partial f_x}{\partial X} \right|_0 & \left. \frac{\partial f_x}{\partial Y} \right|_0 \\ \left. \frac{\partial f_y}{\partial X} \right|_0 & \left. \frac{\partial f_y}{\partial Y} \right|_0 \end{bmatrix} \tag{13}$$

$$\begin{bmatrix} c_{XX} & c_{XY} \\ c_{YX} & c_{YY} \end{bmatrix} = \begin{bmatrix} \left. \frac{\partial f_x}{\partial \dot{X}} \right|_0 & \left. \frac{\partial f_x}{\partial \dot{Y}} \right|_0 \\ \left. \frac{\partial f_y}{\partial \dot{X}} \right|_0 & \left. \frac{\partial f_y}{\partial \dot{Y}} \right|_0 \end{bmatrix} \tag{14}$$

where the subscript “0” denotes the quantities in an equilibrium position.

In the present analysis, the dynamic coefficients were numerically calculated using a perturbation method. For a given small displacement or velocity of the journal at an equilibrium position, the dynamic pressure distribution was calculated and the film force components were obtained. The dynamic coefficients were determined from the difference between the force components just obtained,  $f_x$  and  $f_y$ , and the corresponding ones in the equilibrium position,  $f_{x0}$  and  $f_{y0}$ , divided by the relevant displacement or velocity. For example, in the case of  $k_{XX}$  and  $k_{YX}$ , a small displacement  $\Delta_X$  is only applied while the other infinitesimals are set to zero. With the resulting difference of the oil-film reaction forces due to  $\Delta_X$ ,  $k_{XX}$  and  $k_{YX}$  are calculated as follows:

$$k_{XX} = \frac{f_x - f_{x0}}{\Delta_X}, k_{YX} = \frac{f_y - f_{y0}}{\Delta_X} \tag{15}$$

In the study, we used 0.001 as the values of the small displacement or velocity.

### 2.5 Calculation of the Linear Stability Threshold Speed

Figure 4 illustrates a model rotor used for the stability analysis. The rotor is composed of a massless rigid shaft and a disk with a concentrated mass of  $2m$  located in the middle, and it is supported by two identical journal bearings at each end.

Considering small vibrations of the rotor at the equilibrium position, the equations of motion of the rotor in the  $X$  and  $Y$  directions can be written with the dynamic coefficients obtained above as follows:

$$\begin{cases} m\ddot{X} + c_{XX}\dot{X} + c_{XY}\dot{Y} + k_{XX}X + k_{XY}Y = 0 \\ m\ddot{Y} + c_{YX}\dot{X} + c_{YY}\dot{Y} + k_{YX}X + k_{YY}Y = 0 \end{cases} \tag{16}$$

Applying the Routh–Hurwitz stability criterion to the characteristic equation obtained from Eq. (12), the linear stability-threshold shaft speed  $\omega_c$  for the rigid rotor is obtained in dimensionless form  $v_c$  [15],

$$v_c = \frac{v_c}{\sqrt{g/C}} = \sqrt{\frac{a_1 a_3 a_5}{a_1^2 + a_2 a_5^2 - a_1 a_4 a_5}} \tag{17}$$

where  $g$  is the acceleration of gravity, and the coefficients  $a_1$  to  $a_5$  are expressed by the following dimensionless dynamic coefficients:

$$\left\{ \begin{array}{l} a_1 = K_{XX}C_{XX} - K_{XY}C_{YX} - K_{YX}C_{XY} + K_{YY} \\ a_3 = C_{XX}C_{YY} - C_{XY}C_{YX} \\ a_3 = C_{XX}C_{YY} - C_{XY}C_{YX} \\ a_4 = K_{XX} + K_{YY} \\ a_5 = C_{XX} + C_{YY} \end{array} \right. \quad (18)$$

In Eq. (14),  $K_{ij}$  and  $C_{ij}$  ( $i, j = x, y$ ) are the dimensionless stiffness and damping coefficients, respectively, and are defined as follows:

$$K_{ij} = \frac{C}{W} k_{ij}, C_{ij} = \frac{C\omega}{W} c_{ij} \quad (19)$$

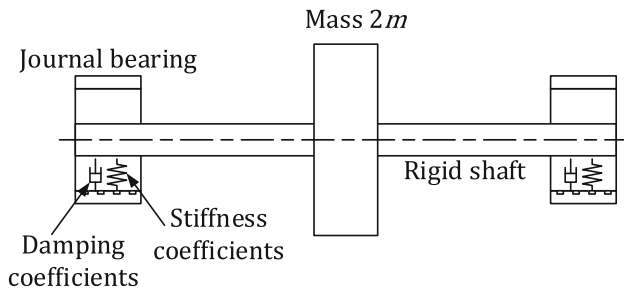


Fig. 4. A model rotor

### 2.6 Analytical Conditions

The analytical conditions are listed in Table 1. In the analysis, we changed the texture start angle  $\theta_{ts}$  from  $0^\circ$  to  $270^\circ$  to investigate the position of the textured area under the constant texture angle  $\theta_t = 90^\circ$ . A fully textured bearing and a smooth bearing were also calculated for comparison. Schematics of the bearing shape used in the study are shown in Fig. 5.

Table 1. Analytical conditions

$L/D$	1.0
$\theta_t$	$90^\circ$
$\theta_{ts}$	$0^\circ, 90^\circ, 180^\circ, 270^\circ$
$l_{p\theta}/(2\pi R)$	1/60
$l_{pz}/L$	1/10
$l_{t\theta}/l_{p\theta} = l_{tz}/l_{pz}$	0.5
$h_t/C$	1.0

The data obtained in the study was summarized by using the Sommerfeld number  $S$ , which is defined by

$$S = \frac{\eta NDL}{W} \left(\frac{R}{C}\right)^2 \tag{20}$$

where  $N$  is the rotational speed of shaft.

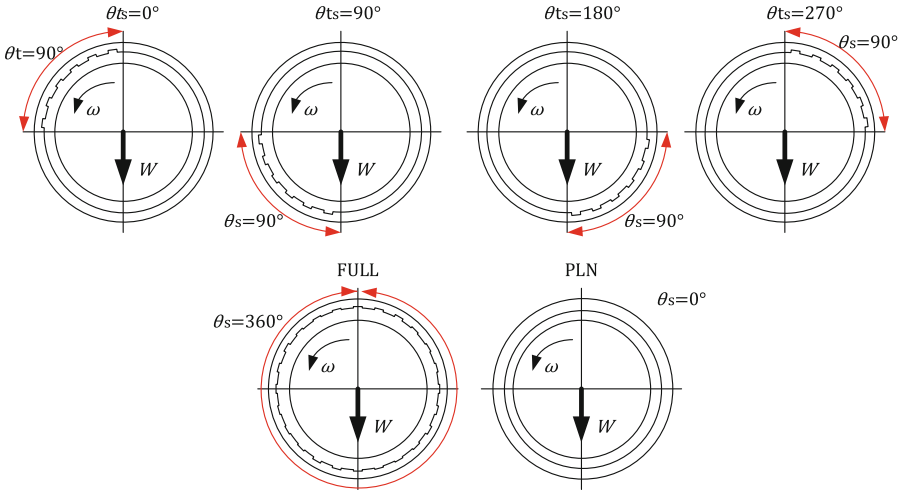


Fig. 5. Schematic diagram of bearing shape used in the analysis

### 3 Results and Discussion

Figure 6 illustrates the eccentricity ratio  $\epsilon$  for various Sommerfeld number  $S$ . In the figure, the blue and red lines denote the numerical results obtained for partially textured bearings, whereas the black lines for the smooth (PLN) or fully textured ones (FULL). The eccentricity of the partially textured bearings is smaller than that of fully textured one, but larger than that of smooth one for a wide range of  $S$ . This means that the reduction of the texture region is effective for improvement of the load carting capacity for the fully textured bearings. In addition, it is difficult to use the surface texturing for the increase of the load carrying capacity. As for the position of the texture region, the eccentricity of  $\theta_{ts} = 0^\circ$  and  $270^\circ$  are smaller than those of  $\theta_{ts} = 90^\circ$  and  $180^\circ$ . This trend becomes prominent when  $S$  is low. The dimples on the loaded region ( $90^\circ < \theta < 270^\circ$ ) on the bearing surface has substantial impact on the load carrying capacity than unloaded region ( $\theta < 90^\circ, \theta > 270^\circ$ ).

From the above results, in order to suppress the reduction of the load carrying capacity the texture region should be formed in the unloaded region. This results qualitatively agree with the results of Tala-Ighil et al. [1] and Brizmer [5].

Figure 7 shows the variations of the attitude angle  $\phi$ . When  $S$  is lower, the results of partially textured bearings except  $90^\circ$  are close to that of PLN. As  $S$  increases, the influence of  $\theta_{ts}$  increases. In particular, in the case of  $\theta_{ts} = 0^\circ$ ,  $\phi$  becomes larger than that of PLN.

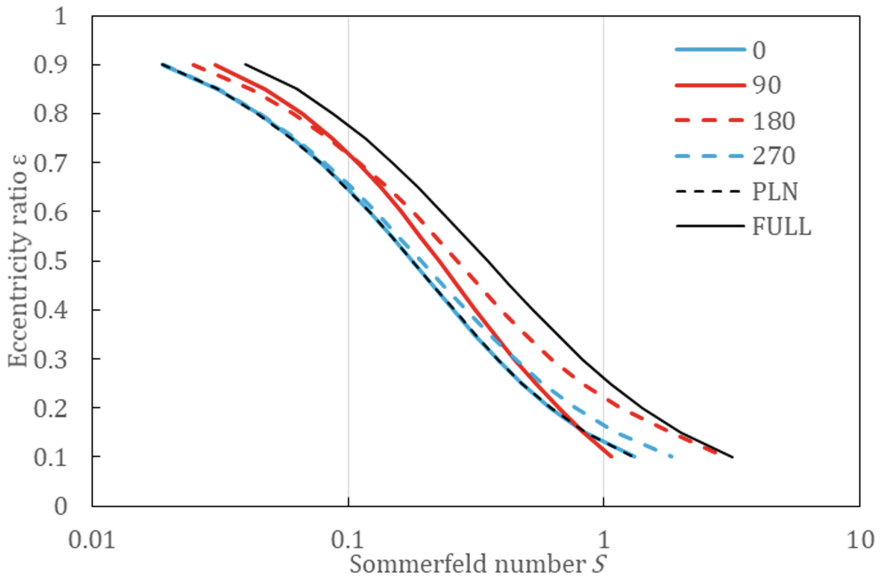


**Fig. 6.** Variations of eccentricity ratio with Sommerfeld number.

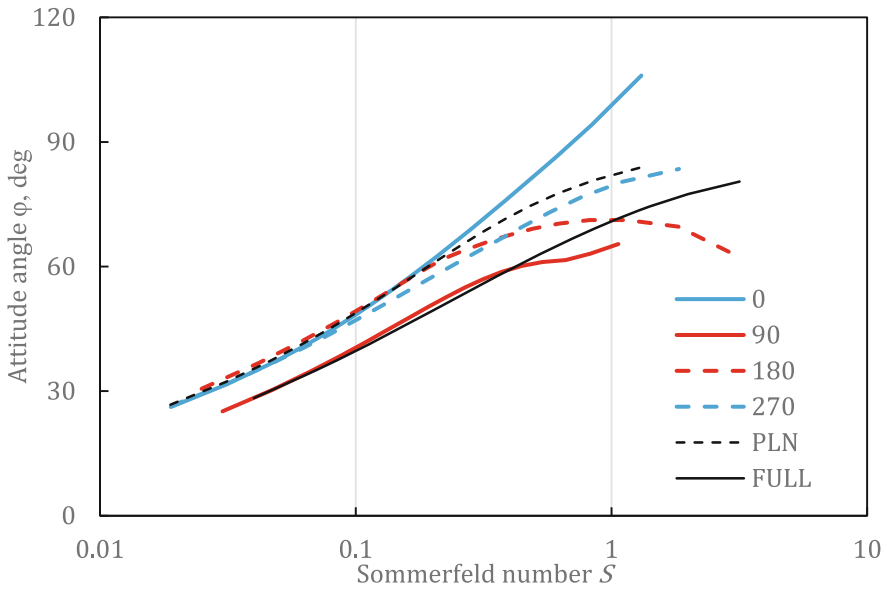


**Fig. 7.** Variations of attitude angle with Sommerfeld number.

Figure 8 shows a stability chart for the model rotor shown in Fig. 4. It is found that the stability shaft speed of  $\theta_{ts} = 270^\circ$  is significantly higher than those of others including FULL and PLN at high Sommerfeld numbers. As the load carrying capacity

of  $270^\circ$  is higher than that for FULL, an appropriate partial texturing can improve both the load carrying capacity and the stability simultaneously. However, the increase of the stability threshold speed in  $270^\circ$  is smaller than the improvement in two lobe bearings with preload factor 0.5, which was calculated on the basis of the stiffness and damping coefficients of the Journal-bearing Databook [16]. On the other hand, the stability shaft speeds for  $0^\circ$ ,  $90^\circ$ ,  $180^\circ$  do not exceed that of FULL. Even on the same unloaded region, stability characteristics of  $0^\circ$  and  $270^\circ$  are entirely different.

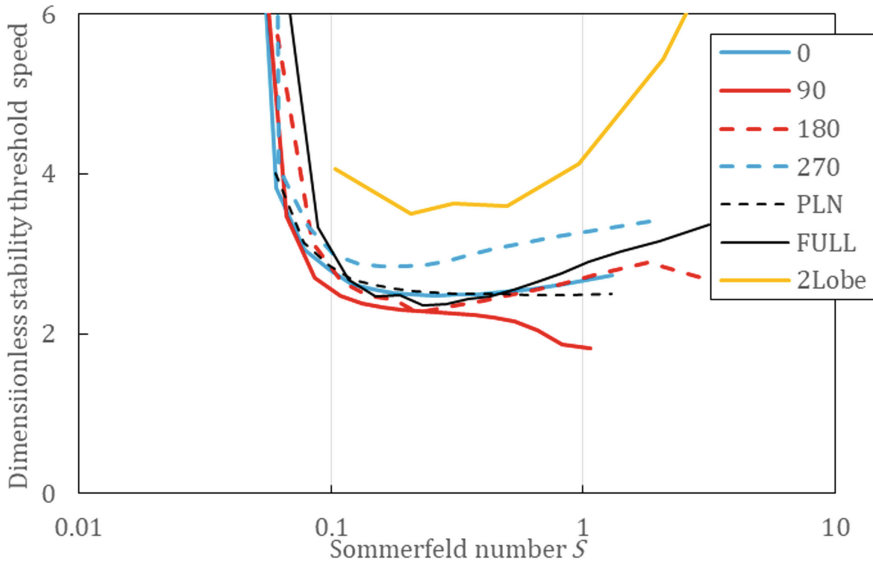


**Fig. 8.** Stability chart of a rigid rotor supported in the two identical partially textured bearings

Figures 9 and 10 show the stiffness and damping coefficients respectively. These values are used to create the stability chart shown in Fig. 8. Focusing on the results of  $270^\circ$  which have high stability threshold speeds, two specific features seem to exist at high Sommerfeld number. One is that the magnitude of the cross-coupling stiffness coefficient  $K_{YX}$  is relatively smaller than those of the other partially textured bearings at higher Sommerfeld numbers. The other is the direct damping coefficients  $C_{XX}$  and  $C_{YY}$  are larger than those of FULL at higher Sommerfeld numbers. The decrease of the cross-coupling stiffness coefficients and the increase of the direct damping coefficients is known to improve the stability characteristics of the rotor system. Hence the stability of  $270^\circ$  is relatively higher than the others.

In the case of  $180^\circ$ , some stiffness and the damping coefficients change discontinuously at high Sommerfeld number. This is due to the large step of the Sommerfeld number.

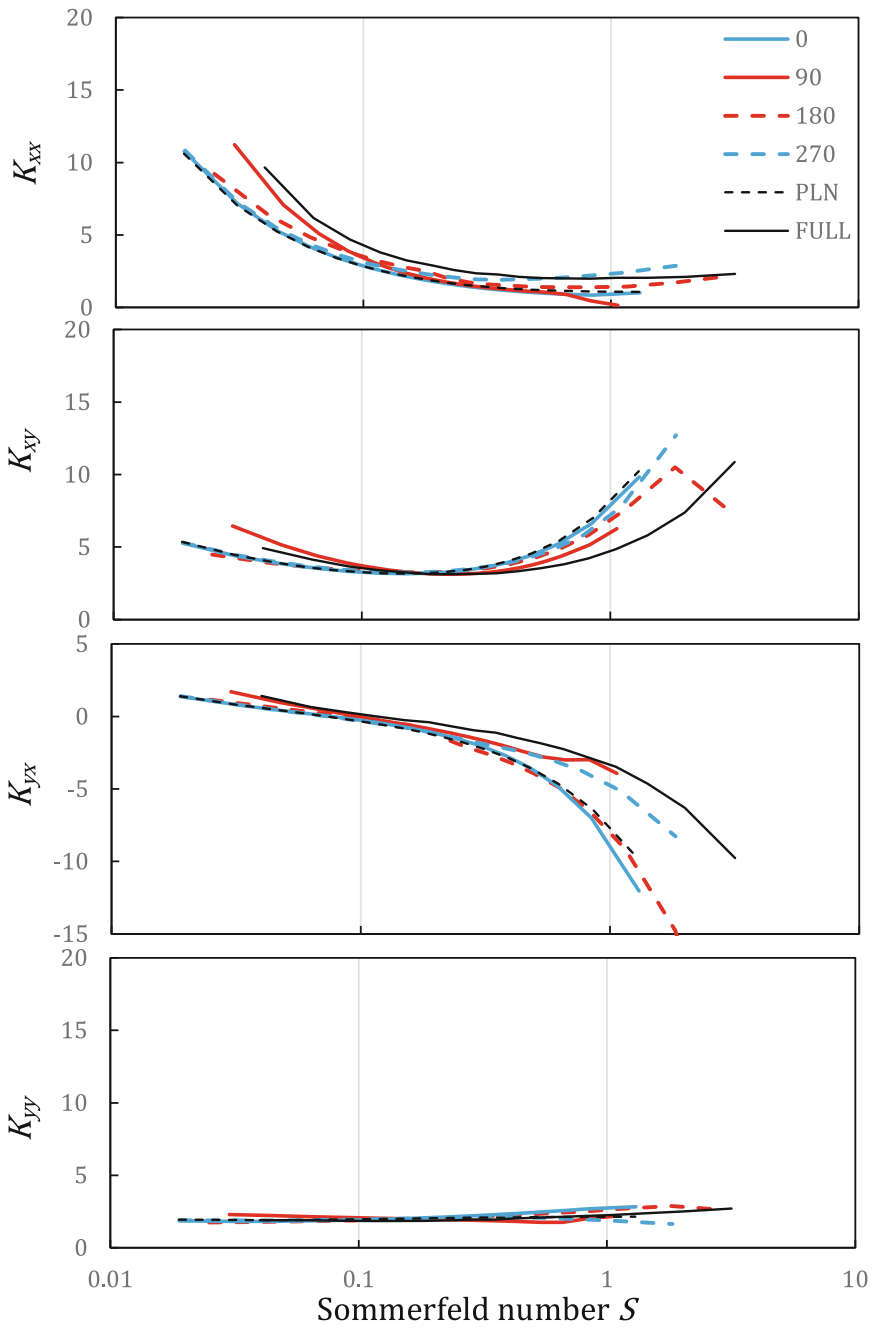


**Fig. 9.** Stiffness coefficients for partially textured bearings

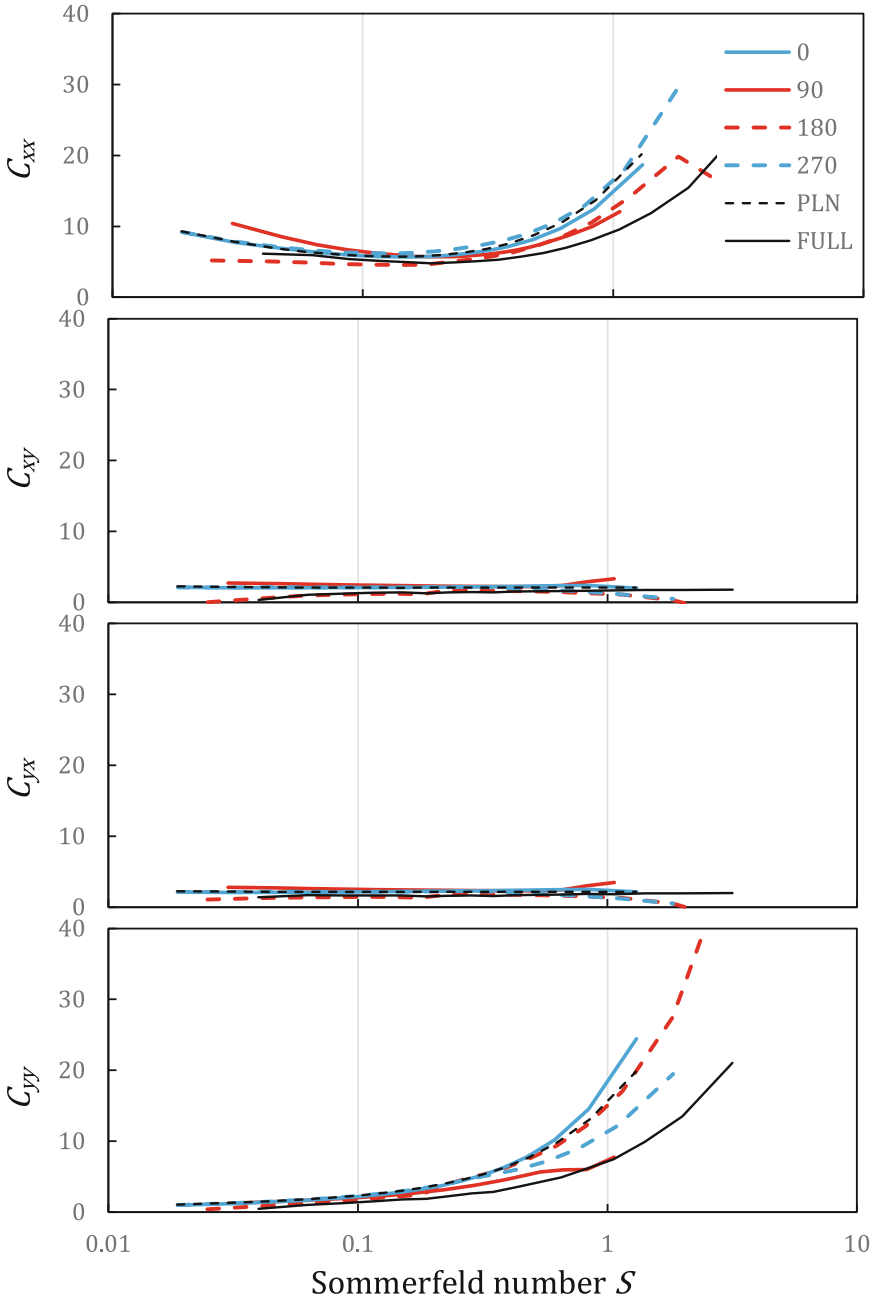


**Fig. 10.** Damping coefficients for partially textured bearings

## 4 Conclusions

In the study, we investigated the effect of the texturing region on the static and dynamic characteristics of partially textured bearings theoretically. We performed numerical calculations to obtain the load carrying capacity and the stiffness and damping coefficients of the oil film and the linear stability-threshold shaft speed of the rigid rotor supported by textured bearings by changing the start angle of the texture region.

1. An appropriate partial texturing formed on the bearing surface can improve both the load carrying capacity and the stability characteristics simultaneously.
2. The start angle of the texture region should be set at 270 from the top of the bearing in the rotating direction to improve the bearing characteristics.

## References




1. Tala-Ighil, N., Fillon, M., Maspeyrot, P.: Effect of textured area on the performances of a hydro-dynamic journal bearing. *Tribol. Int.* **44**, 211–219 (2011)
2. Ausas, R., Ragot, P., Leiva, J., Jai, M., Bayada, G., Buscaglia, G.C.: The impact of the cavitation model in the analysis of microtextured lubricated journal bearings. *Trans. ASME J. Tribol.* **129**(4), 868–875 (2007)
3. Cupillard, S., Cervantes, M., Glavatskih, S.: A CFD study of a finite textured journal bearing. In: IAHR 24th Symposium on Hydraulic Machinery and Systems, Brazil, October 27–31 (2008)
4. Tala-Ighil, N., Maspeyrot, P., Fillon, M., Bounif, A.: Hydrodynamic effects of texture geometries on journal bearing surfaces. *The annals of university “Dunareade Jos” of Galati, Fascicle VIII, ISSN1221-4590, Tribology, XIV2008*, pp. 47–52 (2008)
5. Brizmer, V., Kligerman, Y.: A laser surface textured journal bearing. *Trans. ASME J. Tribol.* **134**(3), 031702 (2012)
6. Kango, S., Singh, D., Sharma, R.K.: Numerical investigation on the influence of surface texture on the performance of hydrodynamic journal bearing. *Meccanica* **47**(2), 469–482 (2012)
7. Kango, S., Sharma, R.K., Pendey, R.K.: Comparative analysis of textured and grooved hydrodynamic journal bearing. *Proc. Inst. Mech. Eng. Part J: J. Eng. Tribol.* **228**(1), 82–95 (2014)
8. Mishra, S., Choudhury, A., Sahu, S.: CFD investigation of influence of reverse textures on bearing surface of a journal bearings. *J. Appl. Fluid Mech.* **7**(3), 395–399 (2014)
9. Tala-Ighil, N., Fillon, M.: A numerical investigation of both thermal and texturing surface effects on the journal bearings static characteristics. *Tribol. Int.* **90**, 228–239 (2015)
10. Meng, F.M., Zhang, L., Liu, Y., Li, T.T.: Effect of compound dimple on tribological performance of journal bearing. *Tribol. Int.* **91**, 99–110 (2015)
11. Yamada, H., Taura, H., Kaneko, S.: Static characteristics of journal bearings with square dimples. *Trans. ASME J. Tribol.* **139**(5), 051703-051703-11 (2017)
12. Yamada, H., Taura, H., Kaneko, S.: Numerical and experimental analyses of the dynamic characteristics of journal bearings with square dimples. *Trans. ASME J. Tribol.* **140**(1), 011703-011703-13 (2017)
13. Constantinescu, V.N., Galetuse, S.: Pressure drop due to inertia forces in step bearings. *Trans. ASME J. Tribol.* **98**, 167–174 (1976)



14. Arghir, M., Alsayed, A., Nicolas, D.: The finite volume solution of the reynolds equation of lubrication with film discontinuities. *Int. J. Mech. Sci.* **44**, 2119–2132 (2002)
15. Gasch, R., Pfützner, H.: *Rotordynamik Eine Einführung*. Springer, Berlin (1975)
16. Someya, T.: *Journal-Bearing Databook*. Springer, Berlin (1989)



# Optimized Tribo-Design of Lubricants for Power Loss Reduction in Journal Bearings Used in Process Industry

Steven Chatterton , Paolo Pennacchi , and Andrea Vania 

Department of Mechanical Engineering, Politecnico di Milano,  
Via G. La Masa 1, 20145 Milan, Italy  
{steven.chatterton, paolo.pennacchi,  
andrea.vania}@polimi.it

**Abstract.** The aim of the paper is to optimize the tribological characteristics of lubricating oils that are used in the process industry during machining. In several cases, the machines employed are organized in several “stands” forming “lines” and are equipped by several spindles supported by journal bearings, fed by the same oil. Typically, the spindles supported by the bearings rotate at increasing speeds from the feeding of the blank material to the outlet of the machined one. The power loss on the single spindle is different from the others, not only for the different rotational speed, but also because the oil with which the single bearing is fed has different temperature and, thus, different viscosity. At present, standard mineral oils for typical use are employed. Owing to the large power loss in these kinds of plants, an attractive idea for power saving is, therefore, to formulate a lubricating oil which, globally, along the entire line, has the best rheological characteristics depending on the actual rotational speed of all spindles. In this paper, the modelling of the line is presented, by using a TEHD (thermo-elasto-hydro-dynamic) model for the calculation of the power dissipated in each journal bearing and the lubricating oil characteristics are defined by means of a multivariate optimization on the parameters of viscosity, temperature and thickness of the oil film. Finally, the optimized dynamic viscosity curve is obtained and can be used for the formulation of an oil, not necessary of mineral origin, with suitable additives.

**Keywords:** Power loss · Power saving · Lubricants · Viscosity  
Journal bearings · Tribology

## 1 Introduction

Oil-film journal bearings in industrial field are still widely employed for their simplicity in high-load or high-speed applications [1–6]. Typical applications are represented by machines with medium/large diameter shafts, operating at low Sommerfeld numbers [7] and characterized by both low tangential speeds and high loads. Conversely other applications can be characterized by high speeds and low loads.

In the paper the case of a steel roll forming machine equipped with several bearings [8, 9] operating in different operating conditions has been considered.

The steel roll forming process is a multi-stage industrial process used to reduce the thickness of metal sheets or metal profile [9]. Typically, two counter-rotating rollers are used to generate the necessary force. The aim is to obtain the desired cross section shape. At each stage the cross-section surface decreases and so the length of the whole workpiece will change (see Fig. 1). The first stages have lower speeds, whereas the last ones have high rotational speeds. In this paper, the modelling of the line is presented, by using a TEHD model for the calculation of the power dissipated in each journal bearing [10–13]. Finally, the optimized dynamic viscosity curve that reduce the overall power loss, is obtained and can be used for the formulation of the oil.

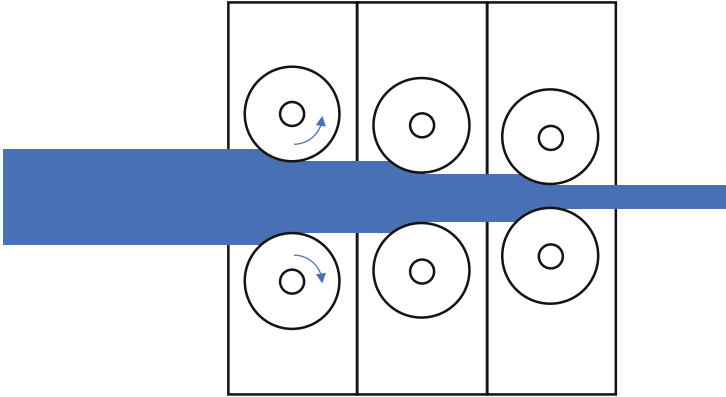


Fig. 1. Example of steel roll forming process.

## 2 Typical System Description

The steel roll forming machine considered in the paper is composed by 10 equal stands with increasing rolling speed. Each stand is composed by 2 spindles in parallel configuration, rotating at the same speed as shown in Fig. 2.

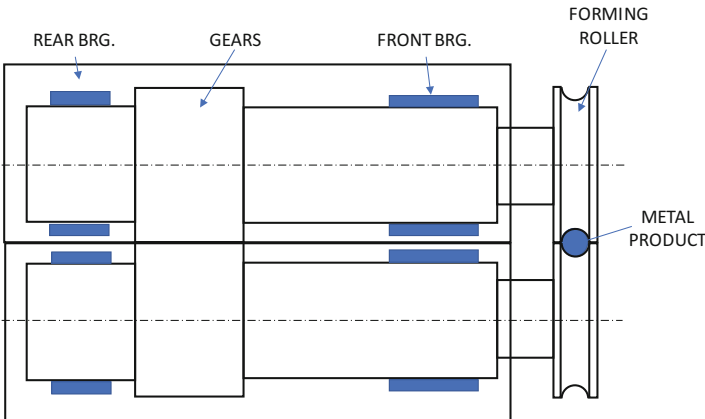


Fig. 2. Example of stand of steel roll forming machine.

Each spindle is supported by two oil-film plain journal bearings, namely the front and the rear ones. The front bearings of all the stands have the same geometry as well as the rear bearings but they have smaller dimensions with respect to the front ones.

For confidential reasons the rotational speed in each stand has been normalized with respect to the maximum rotational speed of the last stand and the estimated load on the bearings with respect to the maximum load obtained in the front bearing of the first stand. The normalized rotational speed and load are shown in Fig. 3. For instance, the speed in the last stand is about 7.5 times the speed in the first one and the load in the rear bearing of the last stand is about 26 times lower than the front bearing of the first stand.

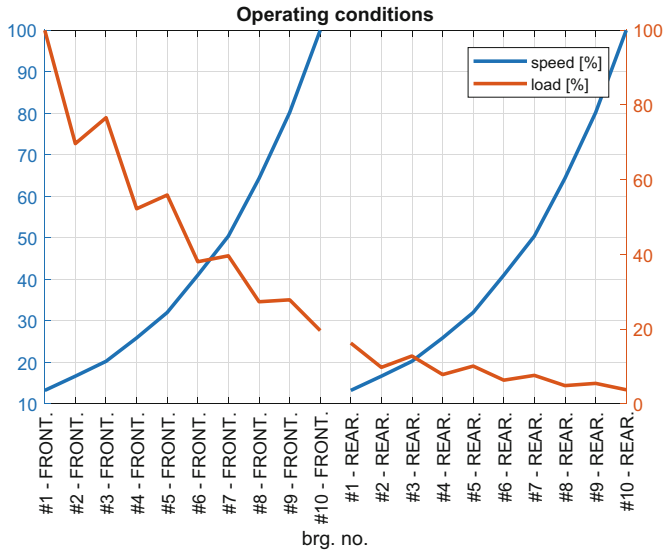


Fig. 3. Operating speed and load of the bearings.

### 3 Oil Properties

The investigation for the reduction of power loss in the oil-film bearing is based on the simulation of the behaviour of all the bearings installed in the machine for different oil characteristics. The dependence of kinematic viscosity  $k_v$  on temperature  $T$  is given by Walther’s viscosity equation [6]:

$$k_v(T) = \exp[\exp[A - B \ln(T)]] - 0.7 \tag{1}$$

Constants  $A$  and  $B$  can be evaluated by the kinematic viscosity of the oil at 40 °C ( $k_{v40^\circ\text{C}}$ ) and 100 °C ( $k_{v100^\circ\text{C}}$ ) as:

$$B = \frac{\ln\left(\frac{\ln(kv_{100^\circ\text{C}} + 0.7)}{\ln(kv_{40^\circ\text{C}} + 0.7)}\right)}{\ln\left(\frac{T_{100^\circ\text{C}}}{T_{40^\circ\text{C}}}\right)} \tag{2}$$

$$A = \ln(\ln(kv_{40^\circ\text{C}} + 0.7)) - B \cdot \ln(T_{40^\circ\text{C}})$$

Mass density  $\rho$  and specific heat capacity  $c_p$  are given as follow:

$$\begin{aligned} \rho(T) &= C - D \cdot T \\ c_p(T) &= E + F \cdot T \end{aligned} \tag{3}$$

where  $C, D, E, F$  are all positive constants.

Therefore, the temperature behaviour of the oil is wholly defined by the two values of the kinematic viscosity at 40 °C and 100 °C that are  $kv_{40^\circ\text{C}}$  and  $kv_{100^\circ\text{C}}$ . The reduction of power loss for the new oils will be evaluated in comparison to the actual oil used in the steel roll forming machine, named in the following as reference condition.

### 4 Bearing Model

The TEHD model of the bearing includes the laws of hydrodynamic lubrication, the thermal effect due to shear stresses in the oil-film and the deformation of the bearing due to mechanical and thermal stresses [14].

The hydrodynamic model is based on the well-known Reynolds equation, see for instance [3, 4, 6]:

$$\frac{\partial}{\partial x} \left( \frac{\rho h^3}{12\mu} \frac{\partial p}{\partial x} \right) + \frac{\partial}{\partial z} \left( \frac{\rho h^3}{12\mu} \frac{\partial p}{\partial z} \right) = \frac{\partial}{\partial x} \left( \frac{\rho h U}{2} \right) - \rho V \tag{4}$$

where  $x$  is the tangential direction,  $z$  the axial direction,  $h$  the oil-film thickness,  $p$  the pressure,  $\mu$  the dynamic viscosity and  $U, V$  represent the velocity terms in the tangential and radial directions of the shaft.

Cavitation and turbulence effects are not negligible for plain journal bearings operating at high speed as the last stage in the steel roll forming machine. The cavitation problem has been solved on the basis of the algorithm presented in [15], which is an extension of the Elrod’s algorithm [16], that uses the complementarity concept and also ensures the mass conservation. Turbulence has been considered by means of Constantinescu’s model [17].

Therefore, the following complementary problem must be solved:

$$\left\{ \begin{aligned} \frac{\partial}{\partial x} \left( \frac{h^3}{k_x \mu} \frac{\partial p}{\partial x} \right) + \frac{\partial}{\partial z} \left( \frac{h^3}{k_z \mu} \frac{\partial p}{\partial z} \right) &= -\frac{\partial}{\partial x} \left( \frac{rhU}{2} \right) + \frac{\partial}{\partial x} \left( \frac{hU}{2} \right) + V(r - 1) \\ r &= \frac{\rho_0 - \rho}{\rho_0} \geq 0 \\ p &\geq 0 \\ p \cdot r &= 0 \end{aligned} \right. \tag{5}$$

In the active (non cavitated) region the fluid density is constant and equal to  $\rho_0$ . In the cavitated (non-active) region the density becomes lower due to the presence of vapor and gas bubbles. The pressure, instead, has a complementary behaviour. It assumes zero as value in the cavitated region, whereas it has a greater value in the other part of oil bearing. The solution of Eq. (5) can be obtained through a linear complementarity problem (LCP) solver.

The turbulence has been considered using the Prandtl's mixing length hypothesis [17], by means of coefficients  $k_x$  and  $k_z$ :

$$\begin{aligned} k_x &= 12 + 0.53 \cdot (k^2 \cdot R_h)^{0.725} \\ k_z &= 12 + 0.296 \cdot (k^2 \cdot R_h)^{0.65} \\ k &= 0.125 \cdot \text{Re}_h^{0.07} \\ \text{Re}_h &= Uh/\nu \end{aligned} \quad (6)$$

where  $\text{Re}_h$  is the global Reynolds number,  $R_h$  the local Reynolds number,  $h$  the oil-film thickness and  $\nu$  the kinematic viscosity.

The distribution of the temperature in the bearing is obtained by means of a three-dimensional thermal model that include a portion of the shaft, the oil-film and the bearing. The energy equation for the oil-film is as follows:

$$\rho c_p \left( u \frac{\partial T}{\partial x} + v \frac{\partial T}{\partial y} + w \frac{\partial T}{\partial z} \right) = k_{OIL} \left( \frac{\partial^2 T}{\partial x^2} + \frac{\partial^2 T}{\partial y^2} + \frac{\partial^2 T}{\partial z^2} \right) + \mu \left[ \left( \frac{\partial u}{\partial y} \right)^2 + \left( \frac{\partial w}{\partial y} \right)^2 \right] \quad (7)$$

where  $c_p$  and  $k_{OIL}$  are the heat capacity of the thermal conductivity of the oil respectively. The use of a two-dimensional thermal model based on the assumption of adiabatic conditions at shaft and bearing surfaces and constant oil temperature in the oil-film thickness leads to the overestimation of the temperature in the oil-film especially in the case of bearings operating at high speeds where shear stresses can be very high. Therefore, a more accurate three-dimensional model must be adopted [13].

The temperature distributions in the bearing and shaft at the steady state are governed by the following equations:

$$\begin{aligned} -\nabla(k_{BRG} \nabla T) &= 0 \\ -\nabla(k_{SHAFT} \nabla T) &= 0 \end{aligned} \quad (8)$$

where  $k_{BRG}$  and  $k_{SHAFT}$  are the thermal conductivity of the bearing and shaft respectively.

Equations (7) and (8) have been solved by means of the finite element approach using a structured mesh for the oil-film and unstructured meshes for the bearing and shaft as shown in Fig. 4 for the lower front bearing in the first stand. In Fig. 4 the load acts in the upward direction.

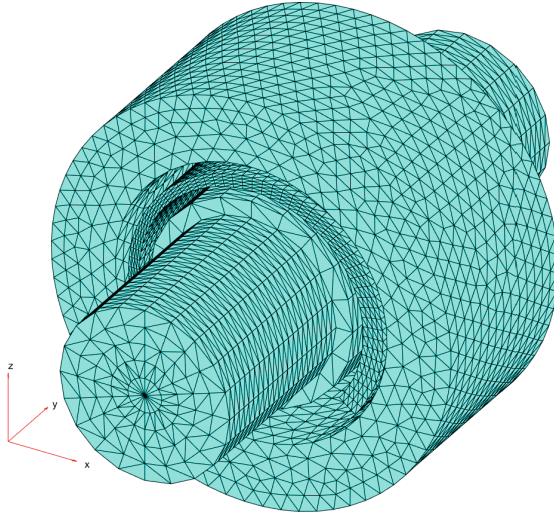


**Fig. 4.** Meshes used for the solution of the thermal problem.

Convective boundary conditions with convection coefficients  $q = 50 \text{ W/m}^2$  are applied on all the non-active surfaces of the bearing and shaft.

An example of temperature distribution in the system is shown in Fig. 5 for the lower front bearing in the first stage of the machine in reference condition. In Fig. 5, a fixed temperature of  $40 \text{ }^\circ\text{C}$  is assumed as boundary condition for the inlet surface of the oil.

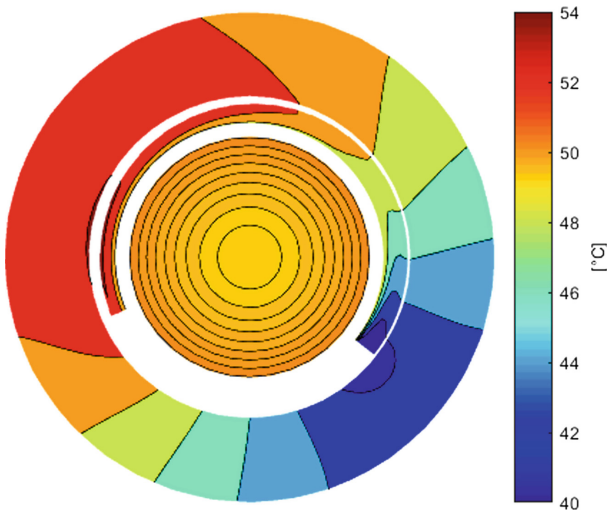


**Fig. 5.** Example of temperature distribution in the cross section (middle plane) of the bearing obtained with a three-dimensional thermal model.

The effect of the deformation of the bearing because of the pressure distribution and bearing thermal expansion has been considered and evaluated by means of a finite element analysis. The resultant deformation of the bearing surface has been transformed in the change in oil-film thickness.

By considering an isotropic material, the deformation of the bearing (displacement  $\mathbf{u}$ ) due to thermal and mechanical stresses is governed by the elasticity equation:

$$-\nabla(C \otimes \nabla \mathbf{u}) = \frac{E}{1 - 2\nu} \alpha_t \nabla T \tag{9}$$

where  $C$  is the tensor of mechanical properties,  $\alpha_t$  the thermal expansion coefficient,  $E$  the Young’s modulus, and  $\nu$  the Poisson’s ratio of the material.

Additional boundary conditions are applied on all surfaces of the pad to consider the traction stresses for the evaluation of the thermal deformation.

An example of bearing deformation is shown in Fig. 6 for the lower front bearing in the first stand of the machine in reference condition.

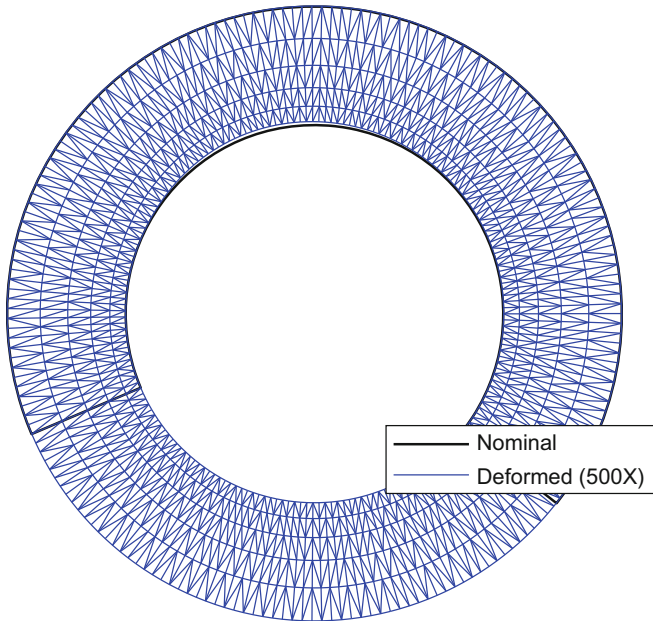


**Fig. 6.** Example of bearing deformation in the cross section (middle plane) of the bearing.

In conclusion, for a given static load, the following conditions must be satisfied:

- convergence of the pressure distribution in the oil-film;
- convergence of the temperature distribution in the system;
- convergence of bearing deformation;
- equilibrium of the forces on the shaft.



The results of the numerical simulations have been obtained by using the code developed by the authors and based on Matlab®. The optimization toolbox has been used for solving the equilibrium position of the system, the partial differential equation toolbox for solving the three-dimensional thermal model for the temperature distribution and the three-dimensional structural-mechanics model for the bearing deformation.

### 4.1 Results for the Reference Oil

The bearings of the machine operate in a wide range of conditions in terms of load and rotational speed. The bearings in the first stage run at low speed and high load whereas the bearing in the last stand operate at high speed and low load (see Fig. 3).

Considering the results of the simulations, the maximum power loss for the reference oil is obtained in the last stands that runs at high speed as shown in Fig. 7 where all the values have been normalized with respect to the maximum value. Conversely the minimum oil-film thickness is obtained in the first stage of the machine as shown in Fig. 8.

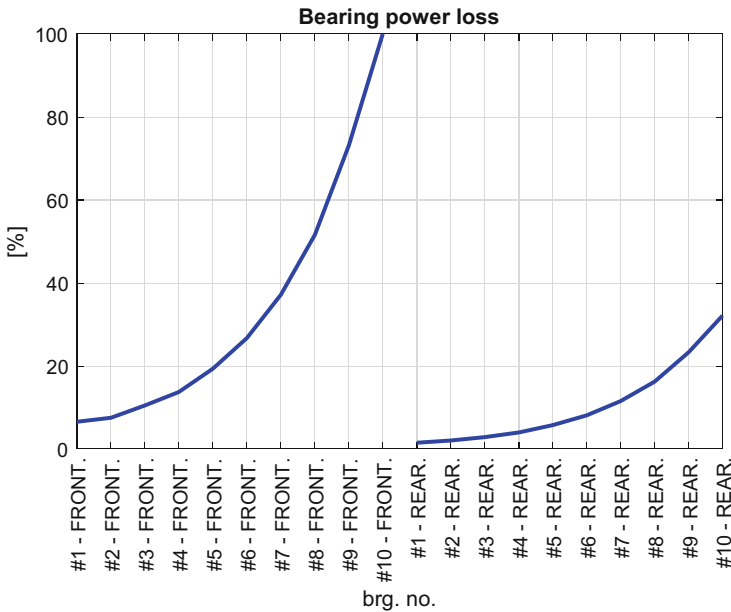
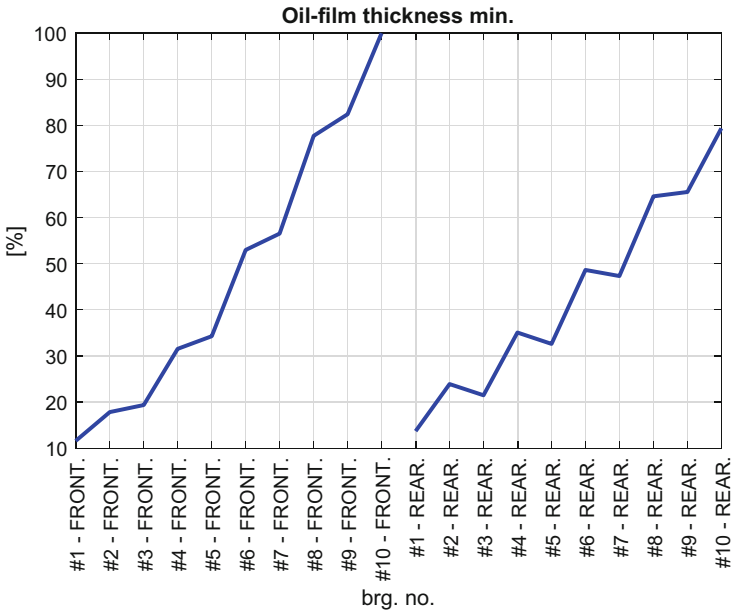


Fig. 7. Power losses in the bearings for the reference oil.

The minimum oil-film thickness has been normalized with respect to the maximum value obtained in the last stand in Fig. 8.



**Fig. 8.** Minimum oil-film thickness in the bearings for the reference oil.

Therefore, the design of the new oil will be a trade-off between the reduction of power loss that can be easily obtained by reducing the viscosity of the oil in the last stage and the limit of the minimum oil-film thickness reached in the first stages of the line.

## 5 Characteristics of the New Oil

The behaviour of all the 40 bearings in the steel roll forming machine has been simulated for different oil properties given by the two kinematic viscosities at 40 °C and 100 °C. The aim of the analysis is the reduction of the power loss. The percentage variation of the power loss with respect to the reference oil, that is the actual oil used in the system is shown in Fig. 9 where the black dot represents the reference condition. In Fig. 9 it is possible to note that the highest power loss reduction can be obtained by reducing the viscosity of the oil. However, the two viscosity parameters are not independent themselves. Real oils show a behaviour represented by a limited range of the viscosity index that relates the kinematic viscosities. The two black lines in Fig. 9 represent the boundaries of the new energy saving oil. Conversely, the reduction of the oil viscosity leads to a reduction of the minimum oil-film thickness as shown in Fig. 10.

The value of the minimum oil-film thickness is critical for the bearings in the first stand that operate at high load and low speed.

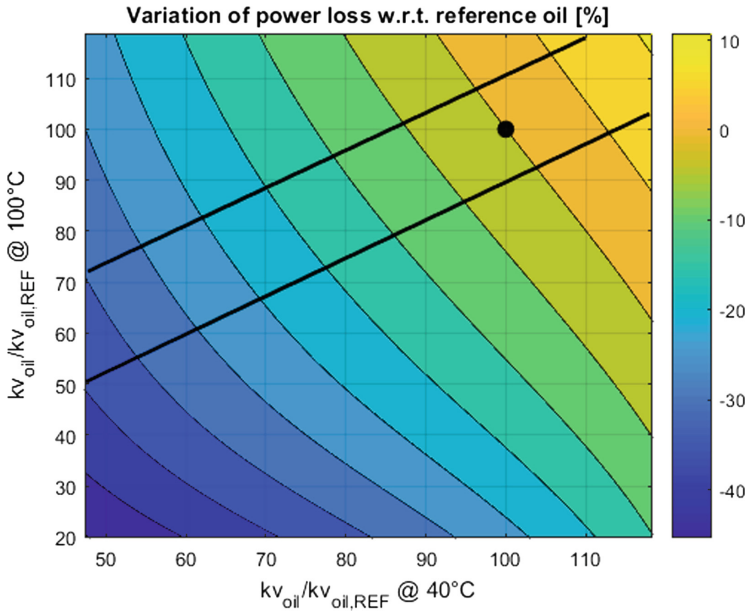


Fig. 9. Variation of power loss with respect to the reference oil.

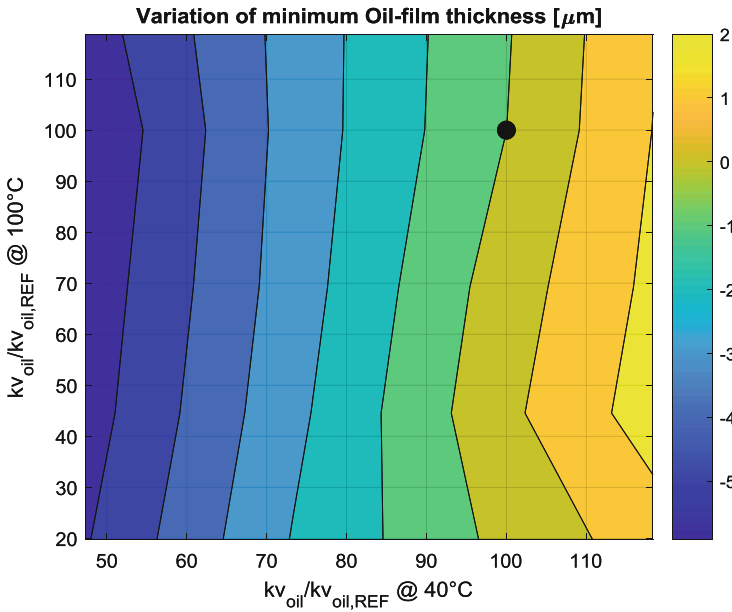


Fig. 10. Variation of minimum oil-film thickness with respect to the reference oil.

## 6 Conclusions

The reduction of the total power loss due to shear stresses in the oil of the bearings of a steel roll forming machine has been investigated in this paper.

The analysis has been performed by simulating the behavior of all the bearings by means of an accurate TEHD model. The reduction of the power loss can be obtained by the reduction of the oil viscosity. The following conclusions can be drawn:

- the maximum power loss is obtained in the bearings operating at high rotation speed;
- the bearings operating at low rotational speed are critical because they show the minimum oil-film thickness;
- the minimum oil-film thickness is mainly a function of the kinematic viscosity at 40 °C;
- the overall power loss of the machine can be reduced of 30% by using an oil with kinematic viscosities at 40 °C and 100 °C that are about half the values of the reference oil.





## References

1. Pennacchi, P.: Introduction of advanced technologies for steam turbine bearings. In: Tanuma, T. (ed.) *Advances in Steam Turbines for Modern Power Plants*, pp. 321–380. Elsevier, Amsterdam (2016)
2. Forsthoffer, W.E.: *Forsthoffer's Best Practice Handbook for Rotating Machinery*. Butterworth-Heinemann, Oxford (2011)
3. Frêne, J., Nicolas, D., Degueurce, B., Berthe, D., Godet, M.: *Hydrodynamic Lubrication—Bearing and Thrust Bearings*. Elsevier Science BV, Amsterdam (1997)
4. Hori, Y.: *Hydrodynamic Lubrication*. Springer-Verlag, Tokyo (2006)
5. Someya, T.: *Journal-Bearing Databook*. Springer-Verlag, Berlin (1989)
6. Stachowiak, G.W., Batchelor, A.W.: *Engineering Tribology*. Butterworth Heinemann, Burington (2005)
7. Chatterton, S., Dang, P.V., Pennacchi, P.: Experimental evidences of a cylindrical journal bearing operating at very low Sommerfeld numbers. In: *Vibrations in Rotating Machinery, VIRMA 11*, Manchester, UK, 13–15 September 2016, pp. 455–463 (2016)
8. Wojtkowski, T.C., Osgood, P.N.: Development of large, high capacity oil film bearings for steel rolling applications. In: *AISTech—Iron and Steel Technology Conference Proceedings*, Nashville, USA, vol. 2, pp. 535–544 (2004)
9. Xu, Z., Chen, D.: Analyses of the oil film compensation and critical rolling speed for hydrodynamic journal bearing in rolling mill. *Run Hua Yu Mi Feng/Lubr. Eng.* **4**, 41–42 + 45 (1998)
10. Kalpakjian, S., Schmid, S.R.: *Manufacturing Engineering and Technology*, 7th edn. Pearson College Division, London (2008)
11. Rohde, S.M., Oh, K.: A thermoelastohydrodynamic analysis of a finite slider bearing. *ASME J. Lubr. Technol.* **97**(3), 450–460 (1975)
12. Suh, J., Palazzolo, A.: Three-dimensional dynamic model of TEHD tilting-pad journal bearing—part I: theoretical modeling. *J. Tribol.* **137**(4), 1–11 (2015)

13. Chatterton, S., Dang, P.V., Pennacchi, P., De Luca, A., Flumian, F.: Experimental evidence of a two-axial groove hydrodynamic journal bearing under severe operation conditions. *Tribol. Int.* **109**, 416–427 (2017)
14. Dang, P.V., Chatterton, S., Pennacchi, P., Vania, A.: Effect of the load direction on non-nominal five-pad tilting-pad journal bearings. *Tribol. Int.* **98**, 197–211 (2016)
15. Giacomini, M., Foweel, M.T., Dini, D., Strozzi, A.: A mass-conserving complementarity formulation to study lubricant films in the presence of cavitation. *J. Tribol.* **132**(4), 12 p. (2010). Article no. 041702
16. Elrod, H.G.: A cavitation algorithm. *J. Lubr. Technol.* **103**(3), 350–354 (1981)
17. Prandtl, L.: The mechanics of viscous fluids. In: Durand, W.F. (ed.) *Aerodynamic Theory*, vol. 3, pp. 34–208. Dover, New York (1935)



# Numerical Modeling of Spiral Vibrations Caused by the Presence of Brush Seals

Paolo Pennacchi<sup>(✉)</sup> , Filippo Cangioli , Andrea Vania ,  
and Steven Chatterton 

Department of Mechanical Engineering, Politecnico di Milano,  
Via G. La Masa 1, 20145 Milan, Italy  
paolo.pennacchi@polimi.it

**Abstract.** Clearance is of paramount importance for turbomachinery manufacturers to meet today's aggressive power output, efficiency, and operational life goals. To minimize leakages, there are various seal types used, and new sealing concepts are in development. Because of their inherent flexibility and compliance, brush seals are capable of significantly reducing the leakage, and allow sufficient geometrical margins to accommodate design and operational variations of turbomachines. Brush seals can be assembled at very tight or zero radial clearance or even with interference on the rotor to minimize the leakage. This means that the risk of contact between the rotor and the seal bristles exists, especially in case of zero clearance or interference. If the contact occurs, a hot-spot develops on the rotor and this may cause the vibration to diverge, resulting in a synchronous instability, the so-called Newkirk effect. The objective of this paper is the development of a numerical model to analyze the dynamic behavior of real turbomachines subject to thermally-induced vibration caused by light-rub of the rotor against brush seals. The model developed in the paper is based on the work of Bachschmid et al. [1]: the dynamics is analyzed in the frequency domain using the standard rotordynamic model, whereas the heat transfer analysis, to calculate the temperature distribution and the associated thermal bow, is studied in the time domain. The contact analysis has been deeply revised, aiming at estimating suitable normal and tangential force and the friction heating generated by the contact.

**Keywords:** Rotordynamics · Brush seal · Spiral vibration

## Acronyms

1X	Synchronous vibration
KP	Key-Phasor
PCS	Point of the orbit Closest to the Stator
FD	Finite difference

## Nomenclature

$C_p$	Specific heat capacity of the rotor
$d(t)$	Distance of the centre of the rotor w.r.t. to centre of the seal as a function of time
$E$	Young modulus

$\bar{F}$	External force in the complex notation
$F(t)$	External forces applied in the rotordynamic model as a function of time
$f_{eq,p_i}$	Equivalent force per unit of circumferential length of the point $p_i$
$f_{n,p_i}$	Normal force per unit of circumferential length of the point $p_i$
$f_{t,p_i}$	Tangential force per unit of circumferential length of the point $p_i$
$F_{x_{KP},p_i}$	Contact force generated correspondent to the point $p_i$ along the $x_{KP}$ axes
$F_{y_{KP},p_i}$	Contact force generated correspondent to the point $p_i$ along the $y_{KP}$ axes
$F_{x_{KP}}$	Contact force along the $x_{KP}$ axes
$F_{y_{KP}}$	Contact force along the $y_{KP}$ axes
$F_{eq}$	Equivalent contact force
<b>G</b>	Gyroscopic matrix of the rotordynamic model
$H_{p_i}$	Interference between the point $p_i$ and the stator
$h_{tc}$	Heat transfer convection coefficient
$I$	Geometrical moment of inertia of the brush bristle
$j$	Imaginary unit
<b>K</b>	Stiffness matrix of the rotordynamic model
$k_{bristle}$	Stiffness of a single brush seal bristle
$k_T$	Thermal conductivity
$k_u$	Brush seal stiffness per unit of circumferential length
$L$	Characteristic length to define the heat transfer convection coefficient
$L_{bristle}$	Free length of the brush seal bristle
<b>M</b>	Mass matrix of the rotordynamic model
$M_x(z)M_y(z)$	Equivalent bending moments along the $x$ and $y$ direction as a function of the axial coordinate
$n_p$	Number of point $p_i$ on the rotor surface
<b>Nu</b>	Nusselt number
$Op_i$	Distance between the point O and the point $p_i$
<b>Pr</b>	Prandlt number
$q_{rub}$	Heat flux generated by the rotor/brush rub
$q_{p_i}$	Heat flux generated by the point $p_i$ in contact with the rotor surface
$r$	Radial coordinate of the reference system used in the heat transfer model
<b>R</b>	Damping matrix of the rotordynamic model
$R$	Rotor radius
<b>Re</b>	Reynolds number
$s$	Rotor/brush seal radial clearance
$t$	Time
$T$	Temperature
$T_{steady}$	Steady-state rotor temperature field
$T_{steam}$	Temperature of the steam at the boundary
$u_r$	Radial deformation
$w_{seal}$	Width of the brush seal
$\bar{x}$	Displacement of the rotor in the complex notation
$x(t), y(t)$	Displacements of the rotor as a function of time
$\dot{x}(t), \dot{y}(t)$	Velocities of the rotor as a function of time
$\ddot{x}(t), \ddot{y}(t)$	Accelerations of the rotor as a function of time

$X, Y$	Magnitude of the rotor displacements
$x_{pi}, y_{pi}$	Coordinates of the $p_i$ point of the rotor surface
$x_0, y_0$	Eccentricity of the rotor
$x_{KP}, y_{KP}$	Coordinates of the KP point
$x_{PCS}, y_{PCS}$	Coordinates of the PCS point
$z$	Axial coordinate of the reference system used in the heat transfer model
$\alpha$	Angle between the $x'$ axis and the KP point
$\alpha_T$	Linear thermal expansion coefficient
$\beta$	Angle between the KP and PCS
$\xi$	Angle between the $x'$ axis and the PCS point
$\varepsilon_r, \varepsilon_\vartheta, \varepsilon_z$	Mechanical strains along the radial, angular and axial direction
$\gamma_{pi}$	Angle between the KP point and the point $p_i$ on the rotor surface
$\gamma_i$	Angle between the KP point and the point $p_i$ on the rotor surface after discretization adjustment
$\gamma_{pi, min}$	Minimum angle of the $\gamma_{pi}$ angles
$\omega$	Whirling speed of the rotor
$\Omega$	Rotational speed of the rotor
$\phi$	Angle between $f_{eq, pi}$ and $f_{n, pi}$
$\phi_x, \phi_y$	Phase of the rotor displacements
$\lambda$	Angle between $F_{eq}$ and $F_{y_{KP}}$
$\lambda'$	Angle between $F_{eq}$ and $x_{KP}$ axes
$\rho$	Material density of the rotor
$\rho_{bristle}$	Density of the bristle along the circumferential direction
$\sigma_z$	Mechanical stress along the axial direction
$\vartheta$	Angular coordinate
$\vartheta_{bristle}$	Angle of inclination of the brush bristle
$\vartheta_{pi}$	Angle between the $x_R$ axis and the point $p_i$ on the rotor surface
$\vartheta_i$	Angle between the $x_R$ axis and the point $p_i$ on the rotor surface after discretization adjustment
$\nu$	Poisson modulus

## 1 Introduction

Similar to the oil and gas market, the technology trend in the power-generation field is to increase the power and efficiency of turbomachines. The need of high efficiency leads, among other things, to the introduction of new sealing technologies such as brush seals. Brush seals can be assembled at very tight or zero radial clearance or even with interference on the rotor. This means that the contact between the rotor and the seal bristles exists, especially in case of zero clearance or interference. If a contact occurs, a hot-spot develops on the rotor and this may cause the vibration to diverge, resulting in a synchronous instability (spiral vibration). The development of numerical models to analyze this phenomenon is therefore important to assess the rotordynamic stability during the design phase and avoid excessive vibrations, which may have severe impact on the operability and on the mechanical integrity of the turbomachinery.



This phenomenon is often caused by light-rubs, between rotating and stationary parts, that occurs at a constant rotational speed. The friction forces caused by the rotor-to-stator contacts give rise to a hot-spot and a consequent shaft thermal bow. The thermal effect derives from the generation of the heat due to the contact. This leads to a non-uniform temperature distribution of the shaft. Thermal stresses arise in the rotor, causing its deflection, which is well known in the literature as rotor thermal bow [1]. The overall heat introduced in the rotor is the difference between the friction heating generated by the rub and the dissipated heating thanks to the heat convection phenomena.

In case of rather light-rubs, the heat-removal capacity of the rotor can be sufficient to ensure that the shaft vibration reaches a limit cycle. In this case, amplitude and phase of the 1X vector are affected by cyclical changes and the maximum vibration level might not exceed a limit value. The evolution over time of the shaft thermal bow is commonly so slow that the cyclical nature of the oscillations of the vibration amplitude can range from a few minutes to some hours. Therefore, the machine dynamic behaviour can be assumed to be quasi static.

Many studies have been carried out on the response of rotating machines that are affected by rubbing phenomena and friction-induced thermal bow. The earliest investigation on the effects of the temperature difference between opposite diametrical sides of a shaft, caused by rotor-to-stator contacts, was by Newkirk [2], who observed and described qualitatively the physical phenomenon. From this reason, this phenomenon is well-known in the literature also as Newkirk effect [1].

In 1939, Kroon and Williams [3] investigated experimentally in which conditions this phenomenon is stable or unstable and they called this phenomenon spiral vibration.

Further important contributions to the analysis of this phenomenon have been provided by Kellenberger [4], who is the first that investigate this phenomenon from the thermal view point. He developed a thermo-elasto model of a simple rotor. The seal was considered isotropic and modeled with inertial, damping and stiffness properties. The model is described by two partial differential equations. The first one is a second-order partial derivative equation related to the dynamics. The other is a first-order equation that described the thermal bow caused by the friction heating. Kellenberger assumed that the bow was proportional to the difference of temperature between the hot-spot and the external temperature. The two equations were coupled: the thermal deflection depends on the stiffness of the stator, while, the heat depends on the dynamic deflection of the rotor. In case of constant angular velocity, these equations brought to the description of the spiral vibration phenomenon of Kroon and Williams [3]. Kellenberger's model defined the period of rotation of the spiral and the conditions that cause an increasing spiral (unstable) or a decreasing one (stable). These conditions mainly depended on the thermal parameters, rotor material and geometry.

In recent years, most of the studies about rubbing phenomena in rotating machines are based on the stability analysis of spiral vibrations, evaluating the eigenvalues of mathematical models that integrate computation of the machine dynamic response with that of the thermal response.

Schmied [5] coupled the standard rotordynamic beam model with the Kellenberger thermal model. The coupling between the equations derives from the fact that the friction heat depends on the shaft displacements. The eigenvalues associated to the

thermal part give information about the direction of the spiral vibrations (outward or inward) and about the amplification factor of the spiral. The limit cycle is not expected in this model. In [6], the authors investigated three different approaches: the heat dependent from the shaft displacements, from the shaft velocity and shaft acceleration. From the comparison with experimental data, the friction heat dependent from the shaft velocity has been confirmed as the most accurate.

The evolution over time of the friction-induced thermal bow and the consequent dynamic response of the rotating machine can be also studied with further methods that combine a thermal model of the shaft, whose response is evaluated in the time domain, with the motion equations of the rotor-system that are solved in the frequency domain, under the assumption that the vibration is dominated by the synchronous harmonic component.

Bachschnid et al. [1] proposed a rather complex model. Beam finite elements method is employed to solve the dynamics of a real machine while a heat transfer model, based on the finite difference method, is employed to calculate the rotor temperature distribution. The thermal bow was reproduced in the rotordynamic model by equivalent bending moments.

In this paper, the model proposed by Bachschnid et al. [1] has been revised to consider light-rub against brush seals. Dynamics of brush seal has been described in the literature by only few scholars, among which Deckner [7], Fay et al. [8], Kreuzner et al. [9] and Demiroglu et al. [10]. The contact analysis and the definition of the hot-spot points has been improved, as well as the heat transfer model, with respect to [1].

## 2 Model Architecture

The model is based on the one developed by Bachschnid et al. in [1]. They started from the consideration that often rotor-to-stator contacts are not severe impact, but large partial arc rubs or full annular rubs. In these cases, the contact forces gradually rise and decrease during the rub. When the rubs show this characteristic, the machine dynamic behavior is rarely affected by chaotic motion [11]. Conversely, the synchronous (1X) component often gives the most important contribution to the harmonic content of the shaft vibrations. When these conditions are satisfied, 1X spiral vibrations induced by the thermal effects due to friction forces can occur.

The evolution of the 1X vibration vector due to thermal-induced vibration takes place in a rather long time. The thermal time transient is much higher than the time transient of the system dynamics. Therefore, the dynamics response of the system, under this assumption, can be evaluated in the frequency domain, whereas, the heat transfer analysis in the time domain.

The rotordynamic finite beam element model of the fully-assembled machine is used to evaluate the synchronous vibrations in the frequency domain. Linear analysis can be employed when rub occurs in partial-annular or full-annular rub and no impacts occur. In accordance to the previous assumption, Fig. 1 shows the flowchart of the domain swap method proposed by Bachschnid et al. [1] and used in the model developed in this paper.

The model has been improved and modified to consider the occurrence of light-rub of the rotor against brush and labyrinth seals.

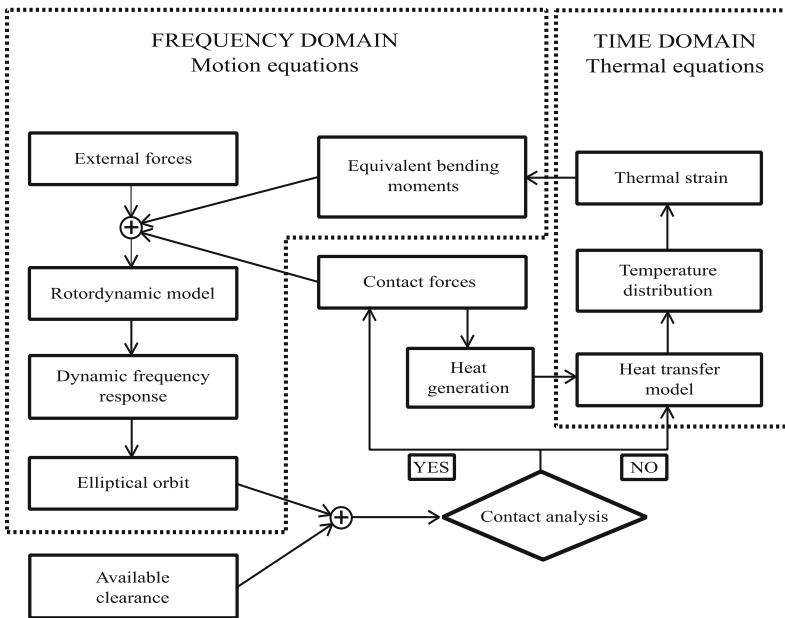


Fig. 1. Flowchart of the model.

The standard finite beam element model [12, 13], with gyroscopic, shear and secondary inertia effects, is used to evaluate the dynamic frequency response. The contact analysis is then performed. If the rotor interferes with the seals, the interaction causes contact forces on the rotor and, due to the friction, heat is introduced in a small arc of the rotor surface. This determines a temperature gradients in radial, axial and circumferential directions of the rotor region which is close to the rubbing section. To calculate the thermal strain distribution, the rotor region is discretized and the thermal analysis is computed. The thermal strain distribution can cause a thermal bow of the rotor, that can be reproduced by equivalent bending moments as shown in [14–17] in the rotordynamic beam model.

Consequently, considering the initial unbalance, equivalent bending moments due to the thermal bow and the forces generated by the contact, the dynamic response of the rotating machine is computed again and the contact analysis is one more time performed. The temperature distribution that causes the thermal bow is calculated by the heat transfer model and, after that, the equivalent bending moments that reproduce the thermal bow are considered in the dynamic model. The analysis continues to iterate till the vibration vector converges or the spiral vibration can be detected. If the rotor does not come in contact with the seals, contact forces are equal to zero and no heat is introduced.

The procedure is valid as long as the thermal transient time constant is much higher than the dynamic transient time constant, as is also observed in [15]. This condition is usually satisfied in large rotating machines that have considerable thermal inertia.

The model developed in [1] considered only a single point of contact with an average interference with the stationary part because the authors considered that the stator is not flexible. In the present work, instead, the calculation of punctual deflection has been performed.

Moreover, the calculation of the forces generated by the contact is more realistic. This is effective on both the mechanical and thermal parts of the study, because:

- the resultant equivalent force will not be the one relative to an average deflection, but rather the result of several points in contact; this is particularly effective when the rotor touches the stator in an arc of the brush seal;
- the heat will no longer enter (always) through only one point, but instead different points will be present, making the thermal gradient distribution rather different from the original model; therefore, the bow will not derive from only one heat point, but from the heating of one (or more) entire arc of points.

Furthermore, the heat transfer model has been revised to consider a domain more similar to rotor regions of real machines. In the original model [1], the rotor region where the contact occurs was simplified with a single cylinder, whereas in the mode proposed in this paper, the model can handle more complex geometries.

The following assumptions are used in the entire model proposed in this paper:

- the rotor is supposed to be in the position of the orbit with the minimum clearance, even with interference. This assumption derives from the observation that, because of the high rotational speed, the heat entering in this position is much higher than the one dissipated along the remaining orbit;
- light-rub does not affect the shape of the rotor orbit;
- the torque generated by the friction force due to the rub does not affect the lateral dynamics of the rotor. It is assumed that the lateral and the torsional dynamics are uncoupled;

the rotor and stator radial growth due to the steady-state temperature is supposed to be equal in the radial direction. Therefore, the nominal clearance does not change due to the steady-state temperature.

### 3 Dynamic Frequency Response

The equations of motion in the time domain can be stated as,

$$\mathbf{M}\ddot{x}(t) + (\mathbf{R} + \mathbf{G}(\Omega))\dot{x}(t) + \mathbf{K}x(t) = F(t) \quad (1)$$

where  $\mathbf{M}$  is the mass matrix,  $\mathbf{R}$  is the damping matrix,  $\mathbf{G}$  is the gyroscopic matrix as a function of the rotational speed and  $\mathbf{K}$  is the stiffness matrix of the machine model considering also the rotating equipment such as bearings, coupling, seals etc.

The solution of this second-order differential equation is determined summing the general integral of the associated homogeneous to the particular integral. Because of the damping of the system, the general integral is decreasing in time. After a long enough time, its contribution can be neglected and the steady state is reached: at that moment, the system motion only depends on the particular integral.

The vector  $F(t)$  of the external forces can be expressed in the complex form as:

$$F(t) = \bar{F} \cdot e^{j\omega t} \quad (2)$$

Because the system is linear, the solution of the particular integral is:

$$x(t) = \bar{x} \cdot e^{j\omega t} \quad (3)$$

By substituting Eq. (3), Eq. (2) and its derivatives into Eq. (1) and eliminating the term  $e^{j\Omega t}$  that is always different from zero, Eq. (1) results in:

$$[\Omega^2 \mathbf{M} + j\omega(\mathbf{R} + \mathbf{G}(\Omega)) + \mathbf{K}] \bar{x} = \bar{F} \quad (4)$$

The solution of the particular integral can be obtained by defining the inverse matrix of the mechanical impedance that depends on the whirling speed  $\Omega$  and rotational speed  $\omega$ .

$$\bar{x} = [\Omega^2 \mathbf{M} + j\omega(\mathbf{R} + \mathbf{G}(\Omega)) + \mathbf{K}]^{-1} \bar{F} \quad (5)$$

## 4 Dynamic Frequency Response

During the rotational and precessional motion of the shaft the available clearance between the rotating and stationary parts reaches a minimum value. Rubs happen when the radial clearance nullifies or a geometrical interference between rotor and obstacle occurs. The point on the external surface of the rotor that is located at the maximum interference with the stationary part is the so called high-spot.

Whereas, the diametrical plane in which the rotor thermal bow is generated by the friction-induced heat input is highly determined by the hot-spot position. In case of light-rubs, the friction-induced thermal bow causes a slow precession of the vibration phase because the shaft high-spot and hot-spot do not coincide, due to the way with which the contacts occur and the rotor thermal bow evolves.

The friction-induced thermal bow of the rotor depends on the intensity of the rubs and the way with which they occur. In many cases, the stationary part is circular-shaped, as for seals, brushes and oil-deflectors. The center of the 1X elliptical orbit is commonly affected by a not null eccentricity.

The shaft rotates about its longitudinal axis while its center is subjected to a precessional motion as a consequence of not null vibrations. In this study the shaft rotational speed has been assumed equal to the angular speed of the precessional motion (whirling speed). This is in good accordance with the assumption of very light-rubs, like those that commonly cause spiral vibrations.

For a given set of geometrical characteristics of rotating and stationary parts, as well as for given 1X vibrations of the rotor, the available radial clearance between the shaft and the circular obstacle can be evaluated for any position of the shaft center over the orbit, during a complete precessional motion. In this model, the rotor is supposed to be in the position of the orbit with the minimum clearance, even with interference. This assumption derives from the observation that, because of the high rotational speed, the heat entering in this position is much higher than the one dissipated along the remaining orbit.

At any time rubs may occur if the minimum radial clearance nullifies or it becomes negative. In case of light-rubs, a linear relationship can be assumed between the normal contact force and the interference between shaft and obstacle.

The length of the arc of the external surface of the shaft that is involved in the contacts with the stationary part depends on various factors like, such as the radial interference and the orbit shape along with the eccentricity of the orbit center.

Therefore, the curve of the interference is not symmetric with respect to its peak (high-spot). The asymmetry of this curve is commonly very small and even infinitesimal, but it is rarely null. Owing to this, the resultant vector of the normal contact forces may be shifted, backward or forward, with respect to the angular position of the peak of the curve of the cumulative normal contact forces. At a given time, the angular position of the hot-spot depends on the angular position of the resultant vector of the normal contact forces evaluated over the orbit as well as on the current thermal state of the rotor.

The contact analysis aims to identify the interference between the rotor and the seal and to evaluate the normal, tangential forces and the heat generated by the contact. Two reference systems have been defined.

The  $S(x, O, y)$  reference system is rigidly connected to the seal and its origin  $O$  corresponds to the center of the sealing ring. The  $S'(x', O', y')$  reference system has the axes parallel to those of  $S(x, O, y)$ , the center is located in the center of the orbit of the rotor:  $(O' - O)$  is the eccentricity between the center of the seal and of the rotor orbit.

The amplitude and phase of the vibrations, along the  $x$  and  $y$  directions, are calculated by the rotordynamic model in the frequency domain, therefore, the orbit can be defined.

Considering that the starting point of the orbit corresponds to the position of the rotor when the key-phaser is along the vertical direction and that the whirling speed is synchronous with the rotational one, the angle between the starting point of the orbit (KP) and the instant position of the rotor is the same between the vertical direction and the rotor key-phaser, as shown in Fig. 2.

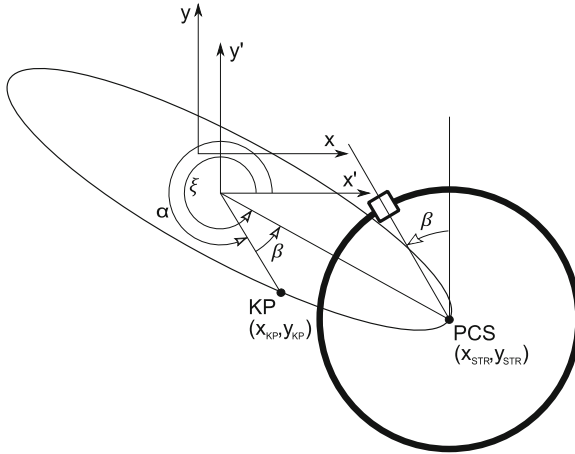


**Fig. 2.** Definition of angles used in the contact analysis and of the KP and PCS points.

The orbit can be expressed in the  $S'(x', O', y')$  reference system. The orbit can be eccentric with respect to the center of the seal, and  $x_0$  and  $y_0$  represent the Cartesian coordinates of the orbit center referred to the  $S(x, O, y)$  reference system. Therefore, the orbit in the  $S(x, O, y)$  reference system can be defined as:

$$\begin{cases} x(t) = x_0 + X e^{j(\omega t + \phi_x)} \\ y(t) = y_0 + Y e^{j(\omega t + \phi_y)} \end{cases} \tag{6}$$

The angle  $\alpha$  (see Fig. 2) between the point KP of the orbit and the horizontal axis of the  $S'(x', O', y')$  reference system can be defined as:

$$\alpha = \text{atan} \left( \frac{y_{KP} - y_0}{x_{KP} - x_0} \right) \tag{7}$$

It follows the determination of the point closer to the seal, where the rotor is supposed to be. To define the point with the maximum interference or the point closest to the stator named PCS point, the distances between the point  $O$  and the positions assumed by the rotor along the orbit are calculated as:

$$d(t) = \sqrt{x^2(t) + y^2(t)} \tag{8}$$

The PCS point corresponds to the position of the rotor in correspondence of the maximum value of  $d(t)$ . The position of the point PCS is defined by the angle  $\zeta$ , starting from the axis  $x'$ , as shown in Fig. 2. It is defined as:

$$\xi = \text{atan} \left( \frac{y_{PCS} - y_0}{x_{PCS} - x_0} \right) \quad (9)$$

The angle  $\beta$  between the KP point of the orbit and the point PCS is a function of the angles  $\alpha$  and  $\xi$ :

$$\beta = \begin{cases} \xi - \alpha & \text{if } \xi \geq \alpha \\ 2\pi - (\xi - \alpha) & \xi < \alpha \end{cases} \quad (10)$$

At the same time, because of the whirling speed is synchronous with the rotational speed,  $\beta$  is also the angle between the vertical axis and the key-phasor position of the rotor when this is in the point PCS.

Because the rotor is assumed to rotate in the counter-clockwise direction, if the orbit is clockwise, the actual value of  $\beta$  is calculated by subtracting  $\beta$  from  $2\pi$ . The clockwise  $\beta$  is the complementary angle of the counter-clockwise  $\beta$ .

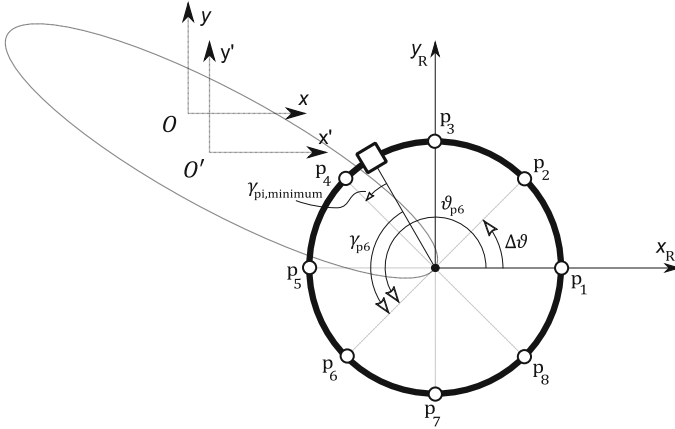


**Fig. 3.** Discretization of the rotor external surface.

To calculate the interference between the rotor and the seal, a new reference system  $(x^R, O^R, y^R)$  centered in the rotor and with the axes parallel to the ones of  $S(x, O, y)$  is defined. The rotor surface is discretized with  $n$  points  $p_i$ , starting from the horizontal axis  $x^R$ . The angle between two consecutive points is  $\Delta\theta$  (see Fig. 3). Consequently, each point will be at angle  $\theta_{pi}$  with respect to  $x^R$ . The angle between the key-phasor and the  $i$ -th point on the rotor surface can be calculated as:

$$\gamma_{pi} = \vartheta_{pi} - \beta + \frac{\pi}{2} \quad (11)$$

represented in Fig. 3. The points  $p_i$  are then aligned with the position of the key-phasor, as:





Once the interference values are calculated, it is possible to estimate the normal and tangential forces and the friction heating (see Fig. 5).

The brush seal stiffness per unit of circumferential length depends on the material properties, geometry and circumferential bristle density. The stiffness of the single bristle is given by [10]:

$$k_{bristle} = 3 \frac{EI}{L_{bristle}^3 \sin^2(\vartheta_{bristle})} \quad (17)$$

where  $\vartheta_{bristle}$  is the designed angle of the bristle and  $L_{bristle}$  is the free length of the bristle.

In working conditions, the bristles work together, therefore the brush seal stiffness per unit of circumferential length is:

$$k_u = k_{bristle} \cdot \rho_{bristle} \quad (18)$$

where  $\rho_{bristle}$  is the density of the bristle per unit of circumferential length that takes into account the axial width.

The machine manufacturers consider also the seal boundary pressure in the calculation of the stiffness by using empirical correlation.

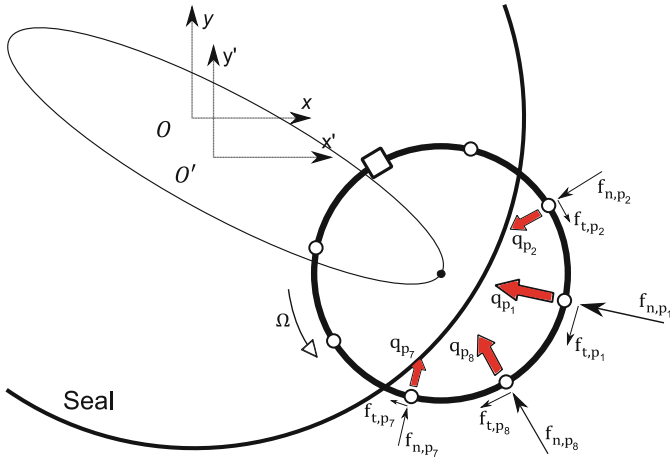


Fig. 5. Heat and contact forces.

The normal force per unit of circumferential length, for each point  $p_i$  of the rotor surface is:

$$f_{n,p_i} = k_u \cdot |H_{p_i}| \quad (19)$$

Once the normal force  $f_{n,p_i}$  is calculated, the tangential force per unit of circumferential length can be obtained by multiplying the normal force for the friction coefficient  $\mu$ , as follows:

$$f_{t,p_i} = \mu \cdot f_{n,p_i} \quad (20)$$

The heat flux, due to the friction, is the product between the tangential force and the rotor peripheral speed divided by the width of the seal, as:

$$q_{p_i} = \frac{f_{t,p_i} \cdot R \cdot \Omega}{w_{seal}} \quad (21)$$

Normal, tangential forces and the heat fluxes have been defined for each point of the rotor surface in contact with the seal (see Fig. 5).

The heat flux, due to the friction, generated a non-axisymmetric temperature distribution of the rotor and consequently a rotor thermal bow, changing the dynamic response of the machine by the equivalent bending moments. Additionally, also the normal and tangential forces due to the contact are considered as external forces in the rotordynamic model.

In order to correctly consider these forces in the rotordynamic model, it is necessary to calculate the equivalent resultant force and its direction.

The tangential forces of the points  $p_i$  produce a torque that is not considered in the dynamics of the machine. The torsional dynamics is assumed to be uncoupled from the lateral one, therefore the torque generated by the tangential force has been neglected.

The normal and tangential forces, in each point  $p_i$ , are summed to obtain the resultant force. The magnitude of the equivalent force for each point in contact can be calculated as,

$$f_{eq,p_i} = \sqrt{f_{n,p_i}^2 + f_{t,p_i}^2} \quad (22)$$

whereas, the angle with respect to the normal force  $f_{n,p_i}$  is:

$$\phi = \arctan\left(\frac{f_{t,p_i}}{f_{n,p_i}}\right) \quad (23)$$

In Fig. 6, the normal and tangential force per unit of circumferential length of the point  $p_1$  are shifted in the center of the rotor (the torque generated by the friction force is not considered). By summing the forces, the equivalent force per unit of circumferential length  $f_{eq,p_i}$  is obtained.

The equivalent forces per unit of circumferential length, of the points in contact with the seal, are summed to obtain the resultant equivalent force  $f_{eq,p_i}$ .

The equivalent force  $f_{eq,p_i}$  is divided into its components along the  $x_{KP}$  and  $y_{KP}$  axes (see Fig. 6). The reference system  $S_{KP}(x_{KP}, O_{KP}, y_{KP})$  is centered in the center of the rotor with the  $x_{KP}$  axis correspondent to the key-phasor position.

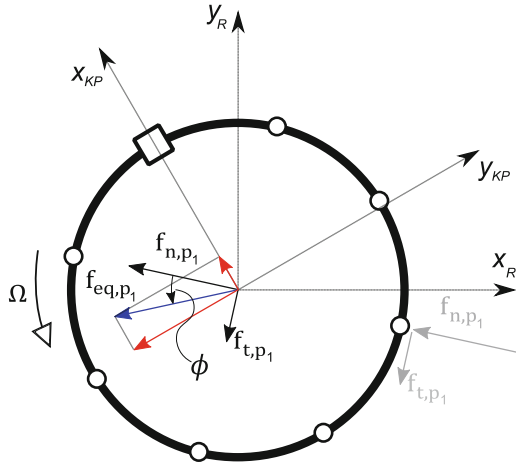


**Fig. 6.** Brush seal force projections.

The equivalent forces per unit of circumferential length are projected along the  $x_{KP}$  and  $y_{KP}$  axes and multiplied by the portion of the rotor surface correspondent to each point in contact. The resultant forces expressed in Newton, are:

$$F_{x_{KP},pi} = -f_{eq,pi} \cdot \sin(\gamma_i + \phi - \pi) \cdot \frac{2\pi R}{n_p} \quad (24)$$

$$F_{y_{KP},pi} = f_{eq,pi} \cdot \cos(\gamma_i + \phi - \pi) \cdot \frac{2\pi R}{n_p} \quad (25)$$

where  $n_p$  is the number of the nodes along the angular direction. The contact forces are summed:

$$F_{x_{KP}} = \sum_{i=1}^{n_p} F_{x_{KP},pi} \quad (26)$$

$$F_{y_{KP}} = \sum_{i=1}^{n_p} F_{y_{KP},pi} \quad (27)$$

Consequently, the resulting equivalent force is calculated as:

$$F_{eq} = \sqrt{F_{x_{KP}}^2 + F_{y_{KP}}^2} \quad (28)$$

The angle  $\lambda$  between the  $y_{KP}$  direction and the equivalent force  $F_{eq}$  (see Fig. 7) can be calculated as:

$$\lambda = \arctan\left(\frac{F_{y_{KP}}}{F_{x_{KP}}}\right) \tag{29}$$

Finally, the angle between  $F_{eq}$  and the  $x$  axes is calculated as:

$$\lambda' = \lambda + \beta + \frac{\pi}{2} \tag{30}$$

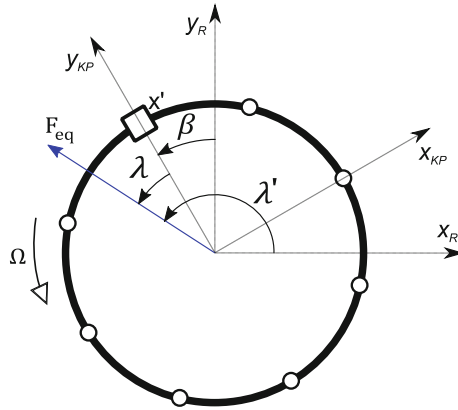


Fig. 7. Equivalent contact force.

### 5 Dynamic Frequency Response

The objective of this analysis is to determine the temperature distribution in a region of the rotor as a function of time ( $T = f(r, \theta, z, t)$ ). The heat equation is stated in a compact form as,

$$\rho C_p \frac{\partial T}{\partial t} = \nabla \cdot (k_T \nabla T) \tag{31}$$

The solutions must satisfy suitable initial and boundary conditions. Because of the axisymmetric geometry of the rotor, the cylindrical coordinates are more suitable with respect to the Cartesian ones. Equation (31) can be written as:

$$\rho C_p \frac{\partial T}{\partial t} = k_T \left( \frac{\partial^2 T}{\partial z^2} + \frac{1}{r^2} \frac{\partial^2 T}{\partial \theta^2} + \frac{\partial^2 T}{\partial r^2} + \frac{1}{r} \frac{\partial T}{\partial r} \right) \tag{32}$$

The Robin boundary condition [18] is used to impose the heat convection with the fluid at the boundaries:

$$k_T \frac{\partial T}{\partial n} + h_{tc} T = h_{tc} T_{steam} + q_{rub} \quad (33)$$

where  $h_{tc}$  is the heat transfer convection coefficient,  $T_{steam}$  is the temperature of the steam at the boundary,  $q_{rub}$  is the heat flux generated by the contact of the rotor against the seal. The heat transfer convection coefficients can be estimated using Eq. (34) The Nusselt number (Nu) is calculated using empirical correlations (see Eq. (35)). The values reported in [19, 20, 25–27] can be used to calculate the heat transfer convection coefficients.

$$h_{tc} = \frac{Nu \cdot k_T}{L} \quad (34)$$

$$Nu = 0.023 \cdot Re^{4/5} \cdot Pr^{0.3} \quad (35)$$

where  $L$  is the characteristics length, Re is the Reynolds number and Pr is the Prandtl number (Pr).

The heat transfer model analyzes a rotor region that must be reasonably long to reproduce the thermal bow caused by the rub between the rotor and brush seals.

Finite difference (FD) method is used to numerically solve the heat transfer problem. The treatment of the geometrical singularity in cylindrical coordinates has for many years been a difficulty in the development of accurate finite difference schemes. Generally, methods discussed in the literature use pole equations, which are akin to boundary conditions to be applied at the singular point. The treatment of the pole as a computational boundary can lead to numerical difficulties. These include the necessity of special boundary closures for FD schemes [21], undesirable clustering of grid points [22], and, in FD schemes, the generation of spurious waves which oscillate from grid point to grid point [23].

The method proposed by Mohseni and Colonius in [24] has been used in this paper. In their approach, the authors avoid the grid point directly at the pole. This eliminates the need of any pole equation. The approach is a very simple technique and it is an effective and systematic way to treat many scalar and vector equations in cylindrical coordinates. The mesh grid is re-arranged as shown in Fig. 8.

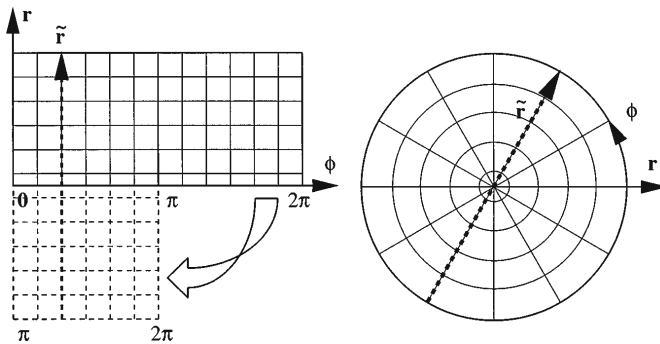


**Fig. 8.** FD grid scheme used in the heat transfer model.

## 6 Dynamic Frequency Response

The region close to the seal has been discretized with a number of longitudinal nodes equal to the ones of the axial section of the thermal mesh, consequently the bending moments simulating the bow are placed only in these nodes (see Fig. 9). In the nodes external to this zone no bending moments are applied because the bow is not present.

Once the temperature distribution is evaluated, thanks to the isotropy of the rotor, standard thermomechanical relations are used to get the thermal strains along the main directions as

$$\varepsilon_r = \varepsilon_\vartheta = \varepsilon_z = \alpha_T (T - T_{steady}) \quad (36)$$

where  $\alpha_T$  is the thermal expansion coefficient. The axial stress distribution is equal to

$$\sigma_z = \frac{E}{1 - 2\nu} \varepsilon_z \quad (37)$$

It allows calculation of equivalent bending moments, which should generate similar strains and a similar overall deformation.

The local radial deformation  $u_r$  due to rotor-to-stator rub is calculated starting with its finite difference derivative definition:

$$\frac{\partial u_r}{\partial r} = u_r(r - \Delta r, \vartheta, z, t) + \varepsilon_r dr \quad (38)$$

The local radial deformation  $u_r$  is much less than the overall thermal bow and could be neglected. It contributes however to the seal deflection and it is considered in the calculation.

The bow caused by the thermal stress can be reproduced by mechanical stress. Because of the linear relation between  $\sigma$  and  $\varepsilon$ , the distribution of the stresses is the same considering a proportionality factor.

To reproduce properly the thermal bow, the moments  $M_x$  and  $M_y$  are calculated using the stress distribution as:

$$M_x(z) = \int_0^R \int_0^{2\pi} \sigma_z(r, \vartheta) \cdot r^2 \sin(\vartheta) dr d\vartheta \quad (39)$$

$$M_y(z) = \int_0^R \int_0^{2\pi} \sigma_z(r, \vartheta) \cdot r^2 \cos(\vartheta) dr d\vartheta \quad (40)$$

The equivalent bending moments are applied in the nodes of the rotordynamic model correspondent to the rotor region where the heat transfer analysis has been conducted.

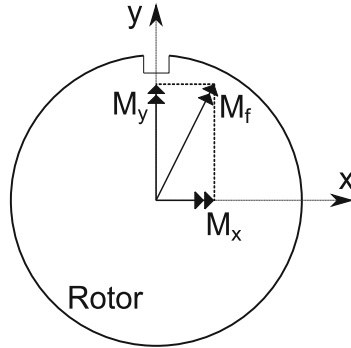


Fig. 9. Equivalent bending moments applied in the rotordynamic model.

### 7 Simulation Results

The proposed model has been used to simulate the behavior of several steam turbines. For confidential reasons, it is not possible to publish all the data of the following example, nor to show the machine layout and the brush seal position and characteristics. Anyhow, the turbine is equipped by five brush seals on the balancing drum.

Figures 10, 11 and 12 show some results which are obtained by using the proposed model. In particular, Fig. 10 shows the polar plot of the vibration vector in one of the bearings of the considered unit. It is possible to observe that the vibration vector tends to a limit cycle and the spiral vibration is not asymptotically diverging. This is also evident considering the corresponding time history of the vibration amplitude, shown in Fig. 11.

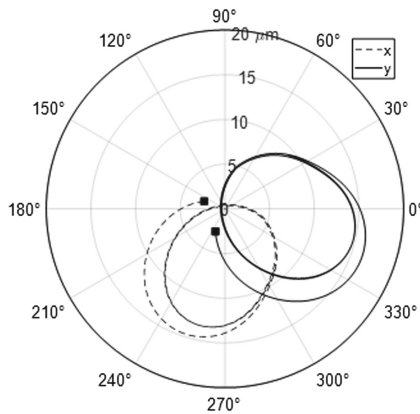
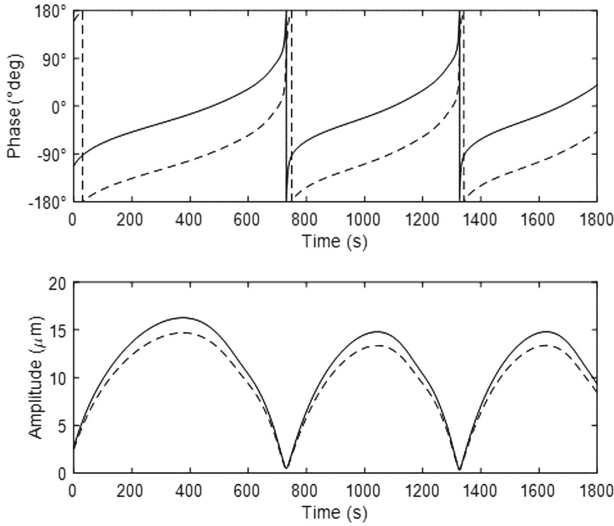
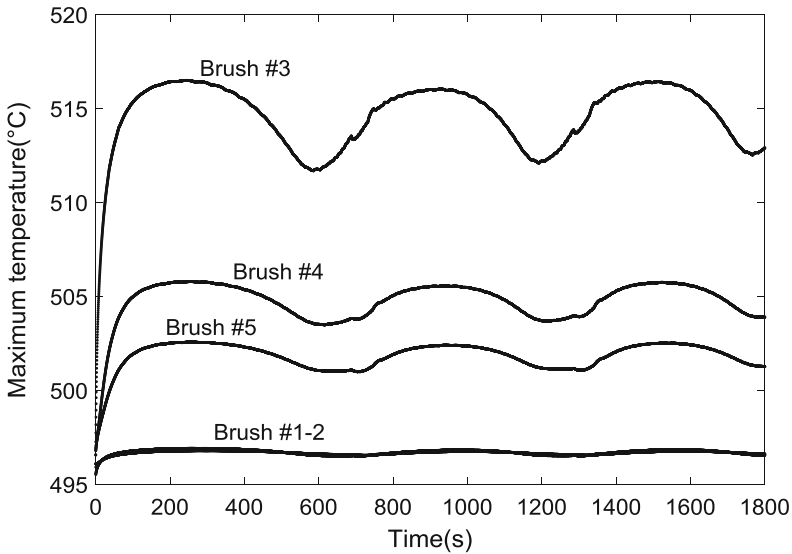


Fig. 10. Polar plot of the vibration vectors in a bearing of the turbine. The dot is the first simulation step.





**Fig. 11.** Amplitude and phase of the vibration vectors of Fig. 10.



**Fig. 12.** Time history of the maximum temperature of each cross-section in correspondence of the brush seals.

Finally, Fig. 12 shows the maximum temperature reached in the cross sections corresponding to the five brush seals, as the function of the simulation time. Note that the starting temperature is close to 500 °C, being the balancing drum the considered section of the steam turbine.

## 8 Conclusion

In this paper, a model for the analysis of thermally-induced vibrations caused by light-rub of the rotor against brush seals has been developed. The model is based on the one developed by Bachschmid et al. The model has been deeply improved, especially regarding the contact analysis and heat transfer model to extend its versatility to a wide class of rotor geometry and contact types.

The model developed by Bachschmid et al. has been validated experimentally, a further validation could be necessary to extend the validity of the model developed in this paper to the case of brush seals. In the near future, the model will investigate the dynamic behavior a real gas turbine equipped with brush seals that shows spiral vibrations in the polar diagram.

## References

1. Bachschmid, N., Pennacchi, P., Vania, A.: Thermally induced vibrations due to rub in real rotors. *J. Sound Vib.* **299**(4–5), 683–719 (2007)
2. Newkirk, B.: Shaft rubbing: relative freedom of rotor shafts from sensitiveness to rubbing contact when running above their critical speeds. *Mech. Eng.* **48**(8), 830–832 (1926)
3. Kroon, R., Williams, W.: Spiral vibrations in rotating machinery. In: 5th International Conference of Applied Mechanics. Wiley, NY (1937)
4. Kellenberger, W.: Spiral vibrations due to the seal rings in turbogenerators thermally induced interaction between rotor and stator. *J. Mech. Des.* **120**(1), 177–184 (1980)
5. Schmied, J.: Spiral vibrations of rotors. In: Proceedings of the ASME Design Technology Conference, Boston, USA (1987)
6. Eckert, L., Schmied, J.: Spiral vibration of a turbogenerator set: case history, stability analysis, measurements and operational experience. *J. Eng. Gas Turbines Power* **130**, 1–10 (2008)
7. Deckner, M.: Eigenschaften kombinierter Labyrinth-Bürstendichtungen für Turbomaschinen, Berlin (2009)
8. Fay, R., Kreuzer, D., Liebich, R.: The influences of thermal effects induced by the light-rub against the brush seal to the rotordynamics of turbo machines. In: ASME Turbo Expo 2014, Düsseldorf, Germany (2014)
9. Kreuzer, D., Fay, R., Liebich, R., Werner, S., Wiedemann, T.: Investigations on non-steady behaviour of rotors due to light rubbing to brush seals. In: Proceedings of the 9th IFToMM International Conference on Rotor Dynamics, Milan, Italy (2014)
10. Demiroglu, M., Tichy, J.A.: An investigation of heat generation characteristics of brush seals. In: ASME Turbo Expo 2007: Power for Land, Sea, and Air, Montreal, Canada (2007)
11. Cangioli, F., Pennacchi, P., Vania, A., Chatterton, S., Dang, P.V.: Analysis of the dynamic behavior of two high-pressure turbines for the detection of possible rub symptoms. In: Proceedings of ASME Turbo Expo 2016: Turbomachinery Technical Conference and Exposition, Seoul, South Korea (2016)
12. Adams, M.: Rotating Machinery Vibration. Marcel Dekker Inc., New York (2001)
13. Lalanne, M., Ferraris, G.: Rotordynamic Prediction in Engineering. Wiley, Chichester (1998)

14. Bachschmid, N., Pennacchi, P., Venini, P.: Spiral vibrations in rotors due to a rub. In: Proceedings of IMechE-7th International Conference on Vibrations in Rotating Machinery, University of Nottingham, UK (2000)
15. Goldman, P., Muszynska, A.: Rotor to stator, rub-related, thermal/mechanical effects in rotating machinery. *Chaos Solitons* **5**(9), 1579–1601 (1995)
16. Larsson, B.: Heat separation in frictional rotor-seal contact. *J. Tribol.* **125**, 600–607 (2003)
17. Bachschmid, N., Pennacchi, P., Vania, A.: Modelling of spiral vibrations due to rub in real rotors. In: ISROMAC-10 Conference, Honolulu, Hawaii, pp. 1–10 (2004)
18. Gustafson, K., Abe, T.: (Victor) Gustave Robin: 1855–1897. *Math. Intell.* **20**(2), 47–53 (1998)
19. Moran, M., Shapiro, H., Munson, B., DeWitt, D.: Introduction to Thermal Systems Engineering: Thermodynamics, Fluid Mechanics, and Heat Transfer. Wiley, New York (2003)
20. Cangioli, F., Chatterton, S., Pennacchi, P., Nettis, L., Ciuchicchi, L.: Thermo-elasto bulk-flow model for labyrinth seals in steam turbines. *Tribol. Int.* **119**, 359–371 (2018)
21. Griffin, M., Everett, J., Anderson, J.: A computational fluid dynamic technique valid at the centerline for non-axisymmetric problems in cylindrical coordinates. *J. Comput. Phys.* **30**(3), 352–360 (1979)
22. Huang, W., Sloan, D.: Pole condition for singular problems: the pseudospectral approximation. *J. Comput. Phys.* **107**(2), 254–261 (1993)
23. Colonius, T.: Numerically nonreflecting boundary and interface conditions for compressible flow and aeroacoustic computations. *AIAA J.* **35**(7), 1126–1133 (1997)
24. Mohseni, K., Colonius, T.: Numerical treatment of polar coordinate singularities. *J. Comput. Phys.* **157**(2), 787–795 (2000)
25. Cangioli, F., Pennacchi, P., Vannini, G., Ciuchicchi, L.: Effect of energy equation in one control-volume bulk-flow model for the prediction of labyrinth seal dynamic coefficients. *Mech. Syst. Signal Process.* **98**, 594–612 (2018)
26. Cangioli, F., Pennacchi, P., Vannini, G., Ciuchicchi, L., Vania, A., Chatterton, S., Dang, P. V.: On the thermodynamic process in the bulk-flow model for the estimation of the dynamic coefficients of labyrinth seals. *J. Eng. Gas Turbines Power* **140**(3), 1–9 (2018)
27. Cangioli, F., Pennacchi, P., Riboni, G., Vannini, G., Ciuchicchi, L., Vania, A., Chatterton, S.: Sensitivity analysis of the one-control volume bulk-flow model for a 14 teeth-on-stator straight-through labyrinth seal. In: Proceedings of ASME Turbo Expo 2017: Turbomachinery Technical Conference and Exposition, Charlotte, NC, USA (2017)



# Development and Validation of a Bulk-Flow Model for Staggered Labyrinth Seals

Filippo Cangioli<sup>1</sup> , Giuseppe Vannini<sup>2</sup>, Paolo Pennacchi<sup>1</sup> ,  
Lorenzo Ciuchicchi<sup>3</sup>, Leonardo Nettis<sup>2</sup>, Steven Chatterton<sup>1</sup> ,  
and Andrea Vania<sup>1</sup>

<sup>1</sup> Politecnico di Milano, Via La Masa 1, 20156 Milan, Italy  
paolo.pennacchi@polimi.it

<sup>2</sup> Baker Hughes, a GE Company, Via Felice Matteucci 2, 50127 Florence, Italy

<sup>3</sup> Baker Hughes, a GE Company, 480 Allée Gustave Eiffel, Le Creusot, France

**Abstract.** As well known, the stability assessment of turbomachines is strongly related to internal sealing components. For instance, labyrinth seals are widely used in compressors, steam and gas turbines and pumps to control the clearance leakage between rotating and stationary parts, owing to their simplicity, reliability and tolerance to large thermal and pressure variations. Labyrinth seals working principle consists in reducing the leakage by imposing tortuous passages to the fluid that are effective on dissipating the kinetic energy of the fluid from high-pressure regions to low-pressure regions. Conversely, labyrinth seals could lead to dynamics issues. Therefore, an accurate estimation of their dynamic behavior is very important. In this paper, the experimental results of a long-staggered labyrinth seal will be presented. The results in terms of rotor-dynamic coefficients and leakage will be discussed as well as the critical assessment of the experimental measurements.

Eventually, the experimental data are compared to numerical results obtained with the new bulk-flow model (BFM) introduced in this paper.

**Keywords:** Rotordynamics · Staggered labyrinth seal · Bulk-flow

## Nomenclature

$a_{ri}, a_{si}$	Length of the rotor and stator of the $i$ -th cavity
$A_i, A_{0i}$	Unsteady and steady cross-sectional area of the $i$ -th cavity
$B$	Step height
$C_{eff}$	Effective damping of the seal
$c_{xx}, c_{yy}$	Direct damping of the seal in the x and y-directions
$c_{xy}, c_{yx}$	Cross-coupled damping of the seal in the x and y-directions
$C$	Average direct damping of the seal
$Dh_i, Dh_{0i}$	Unsteady and steady hydraulic diameter of the $i$ -th cavity
$e$	Absolute roughness of the rotor and stator surface
$F_x(t), F_y(t)$	Lateral forces acting on the rotor
$h_i, h_{0i}$	Unsteady and steady enthalpy of the $i$ -th cavity
$H_i$	Perturbed clearance of the $i$ -th cavity
$k_{xx}, k_{yy}$	Direct stiffness of the seal in the x and y-directions
$k_{xy}, k_{yx}$	Cross-coupled stiffness of the seal in the x and y-directions

$k$	Average cross-coupled stiffness of the seal
$\dot{m}_i, \dot{m}_{0i}$	Unsteady and steady mass flow rate in the $i$ -th cavity
$NJ$	Number of teeth
$P_i, P_{0i}$	Unsteady and steady pressure in the $i$ -th cavity
$r_0$	Radius of the circular orbit of the rotor
$R$	Rotor radius
$R_i$	Rotor radius in the tooth location
$s_i$	Clearance of the $i$ -th cavity
$t$	time
$V_i, V_{0i}$	Unsteady and steady tangential velocity in the $i$ -th cavity
$W$	Tooth width at the tip of the $i$ -th cavity
$x(t), y(t)$	Rotor displacement in the lateral directions
$\dot{x}(t), \dot{y}(t)$	Velocity of the rotor displacement in the lateral directions
$\varepsilon$	Perturbation parameter
$\vartheta$	Angular coordinate
$\mu$	Kinematic viscosity of the fluid
$\rho_i, \rho_{0i}$	Unsteady and steady density in the $i$ -th cavity
$\zeta_i$	Speed of sound of the fluid in the $i$ -th cavity
$\tau_{si}, \tau_{s0i}$	Unsteady and steady stator shear stress in the $i$ -th cavity
$\omega$	Whirling speed of the orbit of the rotor
$\Omega$	Rotational speed of the rotor

### Abbreviations

BC	Boundary condition
BFM	Bulk-flow model
CFD	Computational fluid dynamics
HPSTR	High-pressure seal test-rig

## 1 Introduction

The current trend in the field of power generation is the reduction of rotor-to-seal clearances to match the requirements of power output, efficiency and operational life. Conversely, this design approach leads to stability issues [1]. Therefore, the prediction of labyrinth seals dynamics needs much more attention.

Labyrinth seal is a non-contact seal, composed of two or more teeth arranged in a manner able to impose a tortuous passage to the fluid. The working principle is based on reducing the fluid leakage by dissipating the kinetic energy of the fluid via sequential cavities that are defined by position of the teeth. The teeth can be located on the rotor, stator or both. Depending on the teeth location, various configurations can be defined: straight-through, staggered, slanted and stepped labyrinth seals. Straight-through configuration is the most common labyrinth seal used in real applications because it is the easiest to be manufactured. However, staggered seals are becoming popular because they can reduce the leakage on equal radial clearance with respect to the straight-through ones. Generally, staggered seals are widely used in steam turbines

whereas straight-through seals are used in high-pressure compressors that historically show instability issues and this is the reason why academic research are mainly focused on this configuration. For staggered seals, there are few analytical models and experimental data for the prediction of their stability or instability contribution [2, 3].

The fluid-dynamics within the cavities of labyrinth seals is definitively influenced by the teeth location. Furthermore, the angle at which the flow approaches each tooth is correlated to the coefficients of discharge and to the kinetic energy carry-over coefficient, which strongly influence the leakage.

The dynamic force, produced by the non-uniform pressure distribution within the seal, in the direction of the rotor displacement (direct force) can change the natural frequencies of the machine, whereas the force in the orthogonal direction of the rotor displacement (cross-coupled force) can influence the stability.

The influence of labyrinth seals on the machine stability is typically investigated by using the standard finite beam-element rotordynamic model [16]. The dynamic behavior of labyrinth seals is modeled by the linearized coefficients [4], the so-called rotordynamic coefficients, using stiffness and damping matrices as,

$$-\begin{pmatrix} F_x(t) \\ F_y(t) \end{pmatrix} = \begin{bmatrix} k_{xx}(\omega) & k_{xy}(\omega) \\ k_{yx}(\omega) & k_{yy}(\omega) \end{bmatrix} \begin{pmatrix} x(t) \\ y(t) \end{pmatrix} + \begin{bmatrix} c_{xx}(\omega) & c_{xy}(\omega) \\ c_{yx}(\omega) & c_{yy}(\omega) \end{bmatrix} \begin{pmatrix} \dot{x}(t) \\ \dot{y}(t) \end{pmatrix} \quad (1)$$

The inertia contribution in gas labyrinth seals is negligible; hence, the mass matrix is generally not considered. Due to the axisymmetric geometry of labyrinth seals, the eight linearized rotordynamics coefficients can be reduced to four. The stiffness and damping matrices are re-arranged as,

$$-\begin{pmatrix} F_x(t) \\ F_y(t) \end{pmatrix} = \begin{bmatrix} K(\omega) & k(\omega) \\ -k(\omega) & K(\omega) \end{bmatrix} \begin{pmatrix} x(t) \\ y(t) \end{pmatrix} + \begin{bmatrix} C(\omega) & c(\omega) \\ -c(\omega) & C(\omega) \end{bmatrix} \begin{pmatrix} \dot{x}(t) \\ \dot{y}(t) \end{pmatrix} \quad (2)$$

In the following, the dependence of stiffness and damping coefficients from the whirling speed  $\omega$  will be omitted for simplicity. The cross coupled stiffness coefficient  $k$  and direct damping coefficient  $C$  are responsible of destabilizing forces. The resulting cross-coupled force is given by,

$$F_t = (C\omega - k)r_0 \quad (3)$$

where  $r_0$  is the radius of the orbit. The effective damping can be defined as,

$$C_{eff} = C - \frac{k}{\omega} \quad (4)$$

Labyrinth seals contribute with destabilizing effects on the machine dynamics when the effective damping is negative. The effective stiffness is defined as:

$$K_{eff} = K + c\omega \quad (5)$$

and it is related to the machine natural frequency. Usually, the effective stiffness of labyrinth seals is not considered for the dynamic behavior for the machine because its value is one order of magnitude lower than that of journal bearings [5, 6].

The first analytical model of labyrinth seals, containing the fundamental physical elements for a dynamic characterization was given by Iwatsubo [7]. The model, well known as the bulk-flow model, is based on one-control volume (1CV) for each cavity of the labyrinth seal. Bulk-flow quantities can be defined in each CV. The continuity and circumferential momentum equations are solved for each cavity. The leakage mass-flow rate can be estimated via empirical correlations. The turbulence is considered by estimating the friction factor between the fluid and wall boundaries. The governing equations are solved using the perturbation method. Initially, the steady-state problem (rotor centered with the seal) must be solved. Then, the solution of the perturbed problem (by imposing an orbit to the rotor) that is also truncated at the first order, can be estimated by imposing an analytical form solution. Finally, the dynamic forces can be estimated by integrating the pressure along the circumferential direction. The rotordynamic coefficients are calculated by knowing the radius of the rotor orbit.

The bulk-flow model (BFM) represents the most used calculation method applied for industrial design to calculate the seal rotordynamic coefficients because it is time efficient compared to Computational Fluid Dynamics (CFD) approaches. Moreover, the accuracy of CFD predictions is comparable to BFM predictions [8].

A new BFM has been introduced starting from the considerations made from the authors in [9] and the results shown by Moore in [10]. New boundary conditions (BCs) can be defined in the BFM. The authors' assumption has been also validated by dedicated CFD analysis.

In this paper, the authors present the experimental results for a staggered labyrinth seal tested using the high-pressure seal test-rig (HPSTR) owned by the authors' company. The test rig allows the characterization of labyrinth seals in high-pressure conditions. The main capabilities and the identification procedures of the test-rig are described in a previous paper of the same authors [11]. The results of an experimental campaign on a 14 tooth-on-stator straight-through labyrinth seal have been reported in [9, 12]. The comparison with the experimental data shows improvement in the prediction of the rotordynamic coefficients.

## 2 Bulk-Flow Model

The baseline structure of the BFM developed by the authors for staggered labyrinth seals is here described. The model is based on the 1CV BFM developed by the same authors in [9, 13, 14]. The substantial differences with respect to the BFM for straight-through labyrinth seals are given by the geometry of the CVs, the leakage correlation used to estimate the axial velocity and by the impact of the inlet and outlet regions on the calculation of the rotordynamic coefficients.

The most innovative contribution, with respect to the models available in the literature, is the perturbation of the pressure and circumferential velocity in the inlet and outlet regions, where, usually, they are considered equal to zero in common BFMs [4, 9].

Moore observed in [10] that the contribution of the upstream and downstream sections on the calculation of the rotordynamic coefficients is not negligible. He proposed a 3D-CFD model to predict the flow conditions and rotordynamic coefficients. By considering the inlet and outlet regions for the estimation of the fluid forces on the rotor, the predictions become more accurate compared to experimental results. Because the seal force is generated by the perturbation of the pressure, the assumption of null perturbation of the pressure in the inlet and outlet regions is not correct.

In the model proposed in this paper, two additional CVs have been added at the inlet and outlet regions with a proper mathematical treatment of the governing equations.

### 2.1 Governing Equations

The governing equations are represented by the continuity, circumferential momentum and energy equations. The energy equation is evaluated only in the zeroth-order problem as described in [13]. 1CV for each cavity has been considered as shown in Fig. 1.

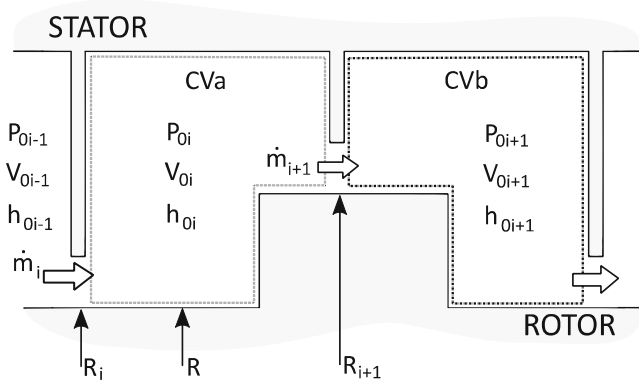


Fig. 1. CVs and bulk-flow quantities.

Because long teeth alternate with the rotor steps, two different CVs can be defined. The control volume labelled as CVa in Fig. 1, presents the long tooth on the upstream side and the short tooth combined with the rotor step on the downstream side. The control volume labelled as CVb in Fig. 1, presents the short tooth combined with the rotor step on the upstream side and the long tooth on the downstream side. Because the enthalpy is assumed to be independent on the orbit motion of the rotor as explained in [9], the derivatives of the enthalpy with respect to the time and to the angular coordinate are null. The governing equations can be stated as,



- Continuity equation:

$$\frac{\partial}{\partial t}(\rho_i A_i) + \frac{\partial}{\partial \vartheta} \left( \frac{\rho_i A_i V_i}{R} \right) + \dot{m}_{i+1} - \dot{m}_i = 0 \tag{6}$$

- Circumferential momentum equation:

$$\frac{\partial}{\partial t}(\rho_i A_i V_i) + \frac{\partial}{\partial \vartheta} \left( \frac{\rho_i A_i V_i^2}{R} \right) + \dot{m}_{i+1} V_i - \dot{m}_i V_{i-1} = -\frac{A_i}{R} \frac{\partial P_i}{\partial \vartheta} + \tau_{ri} a_{ri} - \tau_{si} a_{si} \tag{7}$$

- Energy equation:

$$\dot{m}_i \left( h_i + \frac{V_i^2}{2} \right) - \dot{m}_{i+1} \left( h_{i-1} + \frac{V_{i-1}^2}{2} \right) = \tau_{ri} a_{ri} R \Omega \tag{8}$$

where  $P_i$ ,  $V_i$ ,  $\rho_i$  and  $h_i$  are the bulk-flow pressure, the circumferential velocity, the density and the enthalpy in the  $i$ -th cavity of the seal respectively.

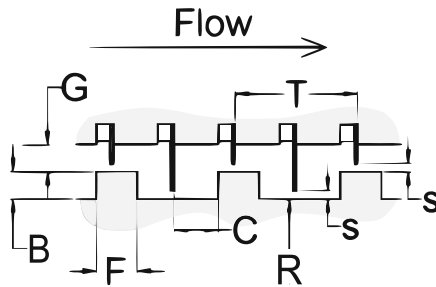


**Fig. 2.** Scheme and nomenclature used to describe staggered labyrinth seals.

The geometrical quantities  $A_i$ ,  $a_{ri}$  and  $a_{si}$  represent the tangential area and the dimensional lengths where the shear stresses are applied. The tangential area has different expressions depending on the type of CV considered.

Using the nomenclature given in Fig. 2, the tangential area for CVa and CVb, is defined, respectively, as

$$A_i = \left( \frac{T}{2} - W \right) (B + G) - \left( \frac{T}{2} - W - C \right) B \tag{9}$$

and

$$A_i = \left( \frac{T}{2} - W \right) (B + G) - \left( C + F - \frac{T}{2} \right) B \tag{10}$$

whereas,  $a_{ri}$  and  $a_{si}$  are defined for both the CVs as,

$$a_{ri} = \frac{T}{2} - W + B \quad (11)$$

$$a_{si} = \frac{T}{2} - W + 2(G - s) + B \quad (12)$$

The leakage correlation replaces the axial momentum equation in defining the axial velocity and pressure distributions along the seal cavities. The leakage correlation employed in the model is the generalized Neumann correlation for real gases [15]:

$$\dot{m}_i = \frac{R_i}{R} C_{fi} H_i \sqrt{P_{i-1} \rho_{i-1} - P_i \rho_i} \quad (13)$$

where  $C_{fi}$  is the discharge coefficients and  $H_i$  is the dynamic radial clearance. The leakage is per unit circumferential length because the governing equations are divided by  $2\pi R$ . The axial cross-sectional area for the leakage (annulus area) is equal, for the CVa, to  $\pi(R + H_i)^2 - \pi R^2$  that can be approximated to  $2\pi R H_i$ . Thus, dividing the leakage by  $2\pi R$ , only the term  $H_i$  remains in the leakage equation. Thus, for the CVa control volume,  $\frac{R_i}{R} = 1$  and  $\frac{R_i}{R} = 1 + \frac{H_i}{R}$  for the CVb control volume.

In staggered labyrinth seals, the kinetic energy carry-over coefficient is equal to the unity for all the teeth as suggested by Childs [5]. The discharge coefficient has been estimated by the Chaplygin correlation as,

$$C_{fi} = \frac{\pi}{\pi + 2 - 5s_{0i} + 2s_{0i}^2} \quad (14)$$

$$s_{0i} = \left( \frac{P_{i-1}}{P_i} \right)^{\frac{\gamma-1}{\gamma}} - 1$$

If the flow sonic condition is reached under the last tooth (choked flow), the leakage mass flow-rate becomes independent by the downstream pressure. To check if the flow is subsonic or choked, the axial velocity is compared with the speed of sound ( $\varsigma$ ) of the fluid. The speed of sound is evaluated using the fluid properties database and it is a function of the pressure and density of the previous cavity ( $\varsigma_i = f(P_{i-1}, \rho_{i-1})$ ).

The axial velocity is estimated using the definition of the leakage mass flow-rate, which is:

$$U_i = \frac{\dot{m}_i}{C_{fi} H_i \rho_{i-1}} \quad (15)$$

If the axial velocity is equal or larger than the speed of sound, the leakage mass-flow rate equation becomes:

$$\dot{m}_i = C_{fi} H_i \rho_{i-1} \varsigma_i \quad (16)$$

For the calculations of the circumferential shear stresses ( $\tau_{si}$  on the stator and  $\tau_{ri}$  on the rotor), it is necessary to use a correlation explicit formula to estimate the Darcy friction factor ( $f_{si}$  and  $f_{ri}$ ). The shear stresses are defined as:

$$\tau_{si} = \frac{\rho_i}{2} f_{si} V_i V_{Si} \tag{17}$$

$$\tau_{ri} = \frac{\rho_i}{2} f_{ri} (R\Omega - V_i) V_{Ri} \tag{18}$$

where  $V_{Si}$  and  $V_{Ri}$  are the modulus of the fluid velocity, on the stator and rotor surfaces respectively, considering the axial and circumferential components of the velocity. They can be defined as:

$$V_{Si} = \sqrt{U_i^2 + V_i^2} \tag{19}$$

$$V_{Ri} = \sqrt{U_i^2 + (R\Omega - V_i)^2} \tag{20}$$

For the calculation of the circumferential shear stresses, the Swamee-Jain correlation is used to estimate the friction factor between the fluid and the rotor/stator wall, as described in [13].

### 2.2 Perturbation Analysis

The perturbation analysis is used to solve the continuity and circumferential momentum equations. The rotor position is perturbed with respect to the centred position, and a circular orbit is assumed.

$$P_i = P_{0i} + \varepsilon P_{1i}(t, \vartheta) \tag{21}$$

$$\rho_i = \rho_{0i} + \varepsilon \rho_{1i}(t, \vartheta) \tag{22}$$

$$h_i = h_{0i} \tag{23}$$

$$V_i = V_{0i} + \varepsilon V_{1i}(t, \vartheta) \tag{24}$$

$$H_i = s_i + \varepsilon H_{1i}(t, \vartheta) \tag{25}$$

The perturbation theory comprises mathematical methods for finding an approximate solution of the problem, by starting from the steady-state solution (centred rotor within the seal). The solutions of the problem are expanded and truncated at the first-order, hence the thermodynamic and kinematic variables of the model (generally indicated with the symbol  $\square$ ) are separated in the steady-state terms  $\square_{0i}$  and in the perturbed terms  $\square_{1i}(t, \vartheta)$ .

### 2.3 Zeroth-Order Problem

The continuity, circumferential momentum and energy zeroth-order equations, for each CV in the seal cavities, are iteratively solved using the multi-variate Newton-Raphson algorithm to find the solution in terms of pressure, density, enthalpy and circumferential velocity in each cavity. The boundary conditions (BCs) used in the zeroth-order problem are the Dirichlet BCs in the inlet and outlet sides. The inlet pressure, circumferential velocity and enthalpy are imposed at the inlet, whereas the outlet pressure, circumferential velocity and enthalpy are imposed at the outlet side. These quantities are calculated by using the seal operating conditions: inlet/static pressure, inlet temperature, pre-swirl and rotor rotational speed. The solution of the zeroth-order problem must satisfy the following equations:

$$\dot{m}_{01} \equiv \dots \equiv \dot{m}_{0i} \equiv \dots \equiv \dot{m}_{0NT} \equiv \dot{m}_0 \quad (26)$$

$$\dot{m}_0 V_{0i} - \dot{m}_0 V_{0i-1} = \tau_{0ri} a_{ri} - \tau_{0si} a_{ri} \quad (27)$$

$$\dot{m}_0 \left( h_{0i} + \frac{V_{0i}^2}{2} \right) - \dot{m}_0 \left( h_{0i-1} + \frac{V_{0i-1}^2}{2} \right) = \tau_{0ri} a_{ri} R \Omega \quad (28)$$

The main contribution of the energy equation is the coupling of the continuity equation with the circumferential momentum equation in the zeroth-order problem. Considering an isenthalpic process, these equations are independent one from each other, and the estimation of the mass flow-rate and thermodynamic properties of the fluid (steady pressure and density) does not depend on the circumferential velocity. In the model developed in this paper, the equations are linked because the density depends on the enthalpy that is calculated (in the energy equation) based on the circumferential velocity and rotor shear stress.

### 2.4 First-Order Problem

The first-order problem is governed by the continuity and circumferential momentum equations. By imposing a circular orbit to the rotor and linearizing the governing equations, the only solutions admitted for the perturbed pressure and circumferential velocity have the same mathematical expression of the perturbed clearance.

By imposing them, the first-order equations result as,

- Continuity first-order equation:

$$\begin{aligned} & \frac{A_{0i} \frac{\partial \rho_i}{\partial P_{1i}} V_{0i}}{R} \frac{\partial P_{1i}}{\partial \vartheta} + A_{0i} \frac{\partial \rho_i}{\partial P_{1i}} \frac{\partial P_{1i}}{\partial t} + \frac{A_{0i} \rho_i}{R} \frac{\partial V_{1i}}{\partial \vartheta} \\ & + \left( \frac{\partial \dot{m}_{i+1}}{\partial P_{1i}} - \frac{\partial \dot{m}_i}{\partial P_{1i}} \right) P_{1i} - \frac{\partial \dot{m}_i}{\partial P_{1i-1}} P_{1i-1} \\ & + \frac{\partial \dot{m}_{i+1}}{\partial P_{1i+1}} P_{1i+1} = - \frac{(\frac{T}{2} - W)}{R} \rho_i V_{0i} \frac{\partial H_1}{\partial \vartheta} \\ & - \left( \frac{T}{2} - W \right) \rho_i \frac{\partial H_1}{\partial t} - \left( \frac{\partial \dot{m}_{i+1}}{\partial H_1} - \frac{\partial \dot{m}_i}{\partial H_1} \right) H_1 \end{aligned} \quad (29)$$

- Circumferential momentum first-order equation:

$$\begin{aligned}
 & \frac{(\frac{T}{2}-W)\rho_i V_{0i}^2}{R} \frac{\partial H_1}{\partial \theta} + \left( \frac{A_{0i}}{R} + \frac{A_{0i} V_{0i}^2}{R} \frac{\partial \rho_i}{\partial P_{1i}} \right) \frac{\partial P_{1i}}{\partial \theta} + \frac{2A_{0i} \rho_i V_{0i}}{R} \frac{\partial V_{1i}}{\partial \theta} \\
 & + A_{0i} \rho_i \frac{\partial V_{1i}}{\partial t} + \left( \frac{T}{2} - W \right) \rho_i V_{0i} \frac{\partial H_1}{\partial t} \\
 & + H_1 \left( -a_{ri} \frac{\partial \tau_{r1i}}{\partial H_1} + a_{si} \frac{\partial \tau_{s1i}}{\partial H_1} + \frac{\partial \dot{m}_i}{\partial H_1} (V_{0i} - V_{0i-1}) \right) \\
 & + V_{1i} \left( -a_{ri} \frac{\partial \tau_{r1i}}{\partial V_{1i}} + a_{si} \frac{\partial \tau_{s1i}}{\partial V_{1i}} + \dot{m}_0 \right) \\
 & + P_{1i-1} \left( \frac{\partial \tau_{r1i}}{\partial P_{1i-1}} (a_{si} - a_{ri}) + \frac{\partial \dot{m}_i}{\partial P_{1i-1}} (V_{0i} - V_{0i-1}) \right) \\
 & + P_{1i} \left( \frac{\partial \tau_{s1i}}{\partial P_{1i}} (a_{si} - a_{ri}) + \frac{\partial \dot{m}_i}{\partial P_{1i}} V_{0i-1} - \frac{\partial \dot{m}_{i-1}}{\partial P_{1i}} V_{0i} \right) + A_{0i} V_{0i} \frac{\partial \rho_i}{\partial P_{1i}} \frac{\partial P_{1i}}{\partial t} \\
 & + \frac{\partial \dot{m}_{i+1}}{\partial P_{1i+1}} V_{0i} P_{1i+1} - \dot{m}_0 V_{1i-1} - \dot{m}_0 V_{1i-1} + \frac{\partial \dot{m}_i}{\partial P_{1i-1}} (V_{0i} - V_{0i-1}) P_{1i-1} = 0
 \end{aligned} \tag{30}$$

Generally, the perturbation of the pressure and circumferential velocity at the inlet and outlet regions are assumed to be equal to zero.

As already said, a novelty has been introduced in the model proposed in this paper by considering the perturbation of the pressure and circumferential velocity in the inlet and outlet regions. Two additional CVs, one in the inlet and one in the outlet region, have been introduced in the seal model. Consequently, the first-order continuity and circumferential momentum equations are solved also in the additional CVs. Nevertheless, the zeroth-order solution for these CVs is required, as well as the BCs for the zeroth-order problem. It is reasonable to assume that the zeroth-order upstream pressure with respect to the inlet region ( $P_{0ui}$ ) is the same of the inlet ( $P_{0in}$ ).

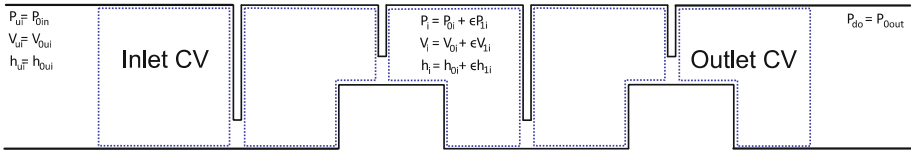


Fig. 3. Control volumes used in the BFM proposed by the authors.

The same assumption is made for the zeroth-order downstream pressure with respect to the outlet region ( $P_{0do}$ ) that is equal to the outlet pressure ( $P_{out}$ ). The zeroth-order circumferential velocities ( $V_{0ui}$ ,  $V_{0do}$ ) and enthalpies ( $h_{0ui}$ ,  $h_{0do}$ ) can be calculated using the zeroth-order circumferential momentum and energy equations.

Regarding the BCs for the first-order problem, it can be reasonably assumed that the perturbed pressures ( $P_{1ui}$ ,  $P_{1do}$ ) and circumferential velocities ( $V_{1ui}$ ,  $V_{1do}$ ) at the seal CVs boundaries can be considered null sufficiently far from the seal cavities. The scheme of the BCs is reported in Fig. 3. Because the perturbed pressure in the upstream inlet region is null and the steady-state pressure is equal to that of the inlet region ( $P_{ui} = P_{0in}$ ), the mass-flow rate between these two CVs cannot be expressed using the Neumann correlation (see Eq. (13)). However, a leakage exists, and it is assumed to be equal to the steady-state mass-flow ( $\dot{m}_0$ ) and independent on the perturbation of the

inlet region. Therefore, by considering the continuity and circumferential momentum equations for the Inlet CV, the derivatives of the incoming mass-flow with respect to the perturbed pressures  $P_{1in}$  and  $P_{1ui}$  are equal to zero. Consequently, the following terms are null in the first-order equations:

$$\frac{\partial \dot{m}_{in}}{\partial P_{1in}} = 0 \quad (31)$$

$$\frac{\partial \dot{m}_i}{\partial P_{1ui}} = 0 \quad (32)$$

For the same reasons, by considering the continuity and circumferential momentum equations in the Outlet CV, the derivatives of the outgoing mass-flow with respect to the perturbed pressure are equal to zero. Consequently, the following the terms are null in the first-order equations:

$$\frac{\partial \dot{m}_{out+1}}{\partial P_{1out}} = 0 \quad (33)$$

$$\frac{\partial \dot{m}_{out+1}}{\partial P_{1do}} = 0 \quad (34)$$

As previously stated, Moore in [10] demonstrated that the upstream and downstream sections contribute to the rotordynamic coefficients. By comparing the CFD results with experimental measurements, the introduction of inlet and outlet regions, improved the CFD predictions [17]. In this paper, the authors performed a CFD analysis based on the Integral Perturbation Method (IPM) aimed at estimating the perturbation of the pressure in the inlet region and to prove the assumptions made in the BFM. The IPM considers the full unsteady simulation with the mesh motion to directly consider rotor oscillatory movements. The CFD analysis clearly shows that the contribution of the inlet and outlet regions to the dynamic forces, generated by the surrounding fluid, is not negligible. This fact conflicts with the assumption in the original BFM in which the perturbation of the pressure is considered null at the inlet and outlet regions.

## 2.5 Calculation of the Rotordynamic Coefficients

The dynamic force acting on the rotor [9] surrounded by the labyrinth seal is given by:

$$F = F_x + jF_y = -\varepsilon R_s \sum_{i=1}^{N-1} L_i \left[ \int_0^{2\pi} (P_{1i} e^{j\vartheta} - j a_{ri} \tau_{r1i} P_{1i} e^{j\vartheta}) \right] \quad (35)$$

The solution of the two equations obtained by considering the real and imaginary parts of Eq. (35) allows the rotordynamic coefficients to be defined as:

$$K = \frac{1}{2} \text{Re}(Z^+ + Z^-) \quad k = -\frac{1}{2} \text{Im}(Z^+ + Z^-) \tag{36}$$

$$C = -\frac{1}{2\Omega} \text{Im}(Z^+ - Z^-) \quad c = -\frac{1}{2\Omega} \text{Re}(Z^+ - Z^-) \tag{37}$$

where,

$$Z^+ = \pi R_s \sum_{i=1}^{N-1} \left( \frac{T}{2} - W \right) \int_0^{2\pi} \left[ P_{li}^+ \left( 1 - ja_{ri} \frac{\partial \tau_{ri}}{\partial P_{li}} \right) - ja_{ri} \frac{\partial \tau_{ri}}{\partial V_{li}} V_{li}^+ + ja_{ri} \frac{\partial \tau_{ri}}{\partial H_1} \right] \tag{38}$$

$$Z^- = \pi R_s \sum_{i=1}^{N-1} \left( \frac{T}{2} - W \right) \int_0^{2\pi} \left[ P_{li}^- \left( 1 - ja_{ri} \frac{\partial \tau_{ri}}{\partial P_{li}} \right) - ja_{ri} \frac{\partial \tau_{ri}}{\partial V_{li}} V_{li}^- + ja_{ri} \frac{\partial \tau_{ri}}{\partial H_1} \right] \tag{39}$$

Each cavity contributes to the overall rotordynamic coefficients. The sum of the rotordynamic coefficient of each cavity allows the coefficients of the seal to be obtained.

### 3 Experimental Campaign

The main features of the HPSTR are [11]:

- inlet pressure up to 500 bar;
- pressure ratio up to 2.5;
- rotational speed up to 15000 rpm;
- control of the rotor orbit by active magnetic bearings (AMBs) with an excitation frequency up to 250 Hz;
- multiple excitation frequencies;
- interchangeable swirler device to set the desired pre-swirl ratio (also negative pre-swirl ratio by inverting the rotational speed);
- possibility to test off-center rotor position.

Figure 4 shows the external casing of the HPSTR that is very similar to an actual industrial plant because it is equipped with a high-pressure compressor, a gearbox and an electric motor connected to a complex high-pressure gas loop. All these details are not provided here because already illustrated in [11].

The HPSTR working principle consists of injecting the nitrogen into the casing at controlled pressure. The gas flows through the swirler device which sets the circumferential velocity of the fluid and the pre-swirl at the seal entrance. Then, the nitrogen flows into the two test seals that are the object of the test. Their back-to-back configuration is used to balance the axial load. The orbit motion of the rotor is controlled by AMBs, which apply the needed dynamic forces to shake the rotor. These forces are measured through current measurements and dedicated calibrations, see [11].

The rotordynamic coefficients associated to the labyrinth seals are finally computed applying an identification algorithm which is based on simple rotor equations of

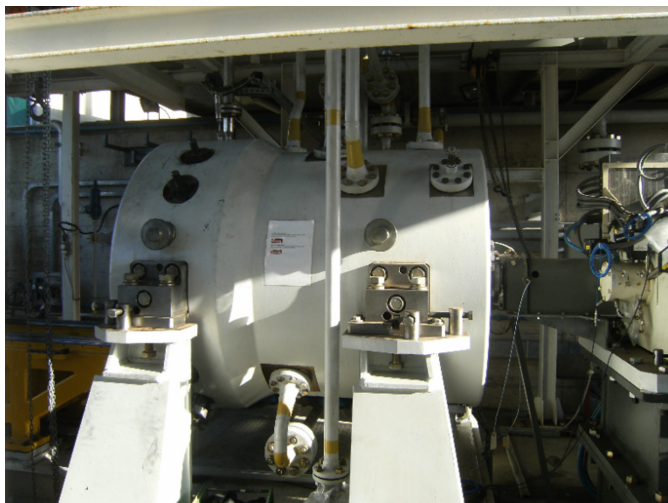


**Fig. 4.** High-pressure seal test-rig.

motion. All relevant forces and displacements are measured and equations are inverted solving for the unknown coefficients. With respect to the experimental activity described in [12], the instrumentation has been improved by introducing a specific probe to measure more precisely the pre-swirl at the seal entrance. An accurate measurement of process parameters is critical to compare the experimental tests data to predictions.

The staggered labyrinth seal tested in the HPSTR is representative of a balancing drum seal mounted in a medium steam turbine (see Fig. 5). The final layout of the staggered labyrinth seals is shown in Fig. 6. The geometrical parameters of the labyrinth seal and operating conditions are listed in Table 1.

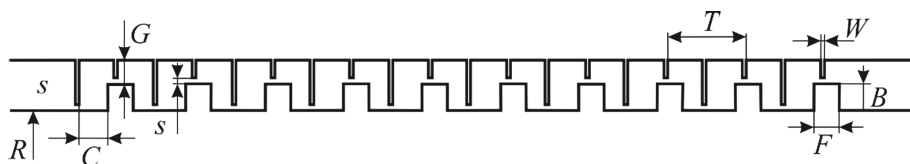


**Fig. 5.** Scheme of the staggered labyrinth seal used in the experimental tests.

The radial clearance listed in Table 1 is the nominal one, therefore it doesn't consider the radial growth caused by the centrifugal force. For confidential reasons, only two experiments are shown in the paper.



The experimental data in terms of rotordynamic coefficients and leakage mass-flow are shown, compared to the numerical predictions, in the body of the paper and in the Appendix A.

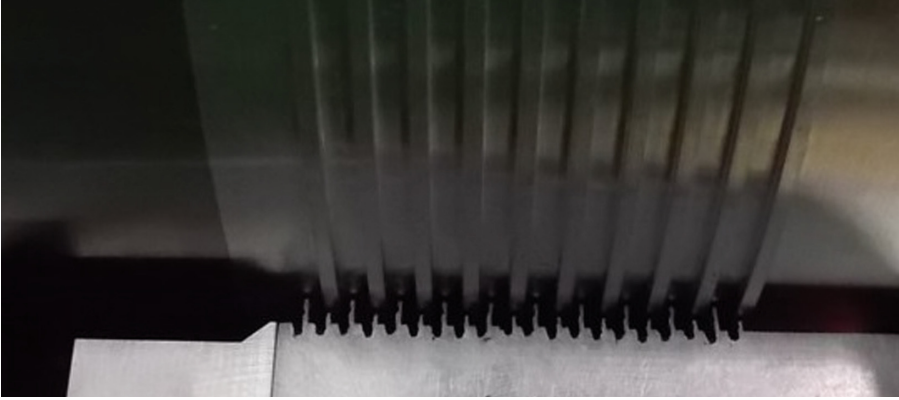


**Fig. 6.** Final layout of the staggered labyrinth seal installed in the HPSTR.

**Table 1.** Seal geometry and operating conditions.

Geometry		
Shaft radius ( $R$ )	110	mm
Nominal radial clearance ( $s$ )	0.50	mm
Steps-to-casing radial distance ( $G$ )	2.00	mm
Steps height ( $B$ )	2.00	mm
Steps width ( $F$ )	2.00	mm
J-strips width at tip ( $W$ )	0.30	mm
J-strips pitch ( $T$ )	3.00	mm
J-strip-to-step axial distance ( $C$ )	2.20	mm
J-strips number	20	
Rotor steps number	10	
Rotor/stator roughness	3.2	$\mu\text{m}$
Operating conditions		
Inlet pressure (bar) $P_{in}$	64.57	91.94
Outlet pressure (bar) $P_{out}$	46.38	70.41
Pressure ratio	1.39	1.30
Inlet temperature ( $^{\circ}\text{C}$ )	31.46	21.13
Pre-swirl ratio	0.36	0.34
Rotational speed (rpm) $\Omega$	12000	12000
Whirling speeds (rpm) $\omega$	4200, 5880, 7560, 9240, 10920	4200, 5880, 7560, 9240, 10920

## 4 Comparison with Experimental Data and Numerical Results

The numerical results, in terms of rotordynamic coefficients and leakage mass-flow, have been compared with the experimental measurements.

The direct damping and cross-coupled stiffness are shown in Figs. 7 and 8, where the numerical results of the original BFM and those considering also the inlet and outlet regions are also plotted. The BFM with the inlet and outlet regions takes into account for the rotordynamic coefficients generated in the two “new” CVs. By considering only the CVs in the cavities of the seal, and taking into account the perturbation of the pressure and circumferential velocity at the seal boundaries, a new BFM can be introduced. The new BFM considers different BCs with respect to the original one. Thus, three different models are shown in the following paper.

It can be noticed in Figs. 7 and 8 that both the BFM with the inlet and outlet regions and the BFM with new BCs are more accurate in the estimation of the rotordynamic coefficients than the original BFM. Slight differences can be observed between the two new BFMs. It can be deduced that the assumption of considering the perturbation of the pressure and circumferential velocity at the seal boundaries equal to zero is not correct if compared to CFD result as already noticed by Moore. Moreover, the predictions of the rotordynamic coefficients is strongly improved.

The uncertainty range for each measured point is also reported. The uncertainties are larger with the increase in the whirling speed. The trends of the two experiments are very similar. As expected, the coefficients are frequency dependent as already shown for a teeth-on-stator straight-through labyrinth seal in [12]. The experimental coefficients of the experiment B are higher than those of the experiment A because of the higher pressure drop condition.

Generally, the trend of the coefficients as a function of the whirling speed is well reproduced by the three BFMs. The direct damping is slightly underestimated with respect to the experimental one. Thus, BFMs result to be conservative in the rotordynamic design phase.

The comparison of the mass-flow measured during the experiments with those predicted by the bulk-flow model for both experiments is shown in Fig. 9. The uncertainty range is almost 10% of the average value. The predictions are very accurate compared to the experimental measurements. The mass-flow is the same for the BFMs considered in the paper.

The contribution of each cavity of the seal to the rotordynamic coefficients is shown in Fig. 10. The solid lines are the results of the original BFM, whereas the dotted lines are the results of the model by considering the perturbation in the inlet and outlet regions. Five lines for each model are represented in the Fig. 10, consistently with the five whirling frequencies.

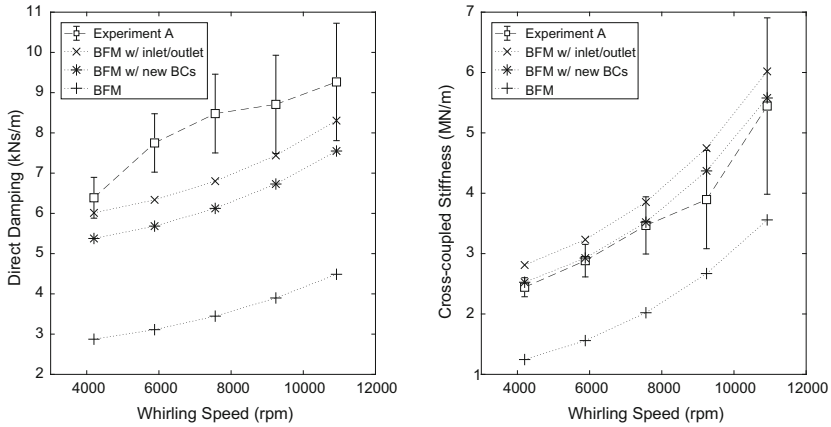


**Fig. 7.** Comparison of predictions and measurements of direct damping and cross-coupled stiffness coefficients as a function of the whirling speed for the experiment A.

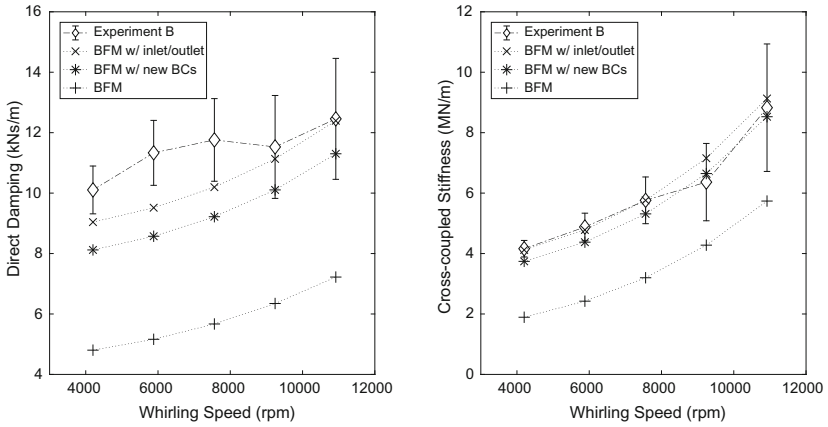


**Fig. 8.** Comparison of predictions and measurements of direct damping and cross-coupled stiffness coefficients as a function of the whirling speed for the experiment B.

It can be observed that the new BFM's show a different trend of the coefficients. In the original BFM seems that the coefficients in the first and last cavities are constrained to be close to zero by the fact that the perturbations are null at the boundaries.

Despite the perturbations are considered both in the inlet and outlet in the new BFM, the coefficients at the seal end are equal to the coefficients calculated with the original BFM. Trying to figure out a correlation between the coefficients and the zeroth-order quantities, the trend of the coefficients of the new BFM is similar to that of the zeroth-order pressure and density along the seal cavity. Whereas, the coefficients calculated with the original BFM are uncorrelated with all the zeroth-order quantities.

By considering the results in Figs. 7 and 8 for the experiment B, the BFM with the inlet and outlet regions consider the coefficients contribution of the inlet and outlet cavities as shown in Fig. 10.

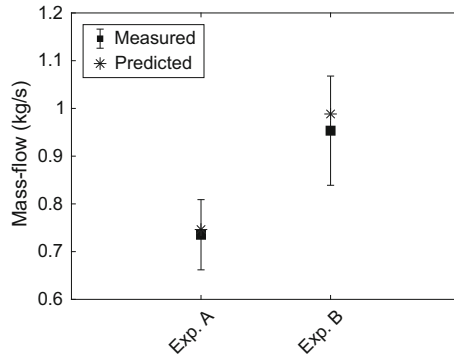


Fig. 9. Comparison of the mass-flow measured and predicted.

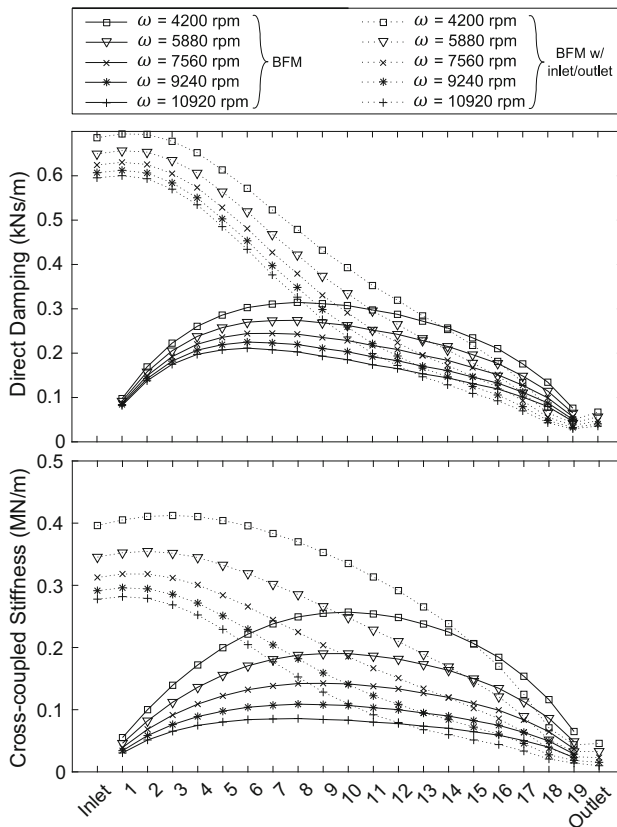


Fig. 10. Trend of the predicted direct damping and cross-coupled stiffness as a function of the seal's cavity for the experiment B.

The BFM with new BCs considers the coefficients of the model with the inlet and outlet regions but the overall seal coefficients do not take into account the coefficient contributions of the inlet and outlet regions, but only those corresponding to the cavities from 1 to 19 (see Fig. 10), such as for the original BFM.

This approach is finally making the BFM physically more consistent and improves the match with experimental data by an average factor 2 which is not negligible at all.

### 5 Conclusion

In the paper, the experimental results obtained from an experimental campaign on a staggered labyrinth seal have been presented and a new BFM has been introduced by considering the perturbation of the pressure and circumferential velocity in the inlet and outlet regions.

Actual BFMs consider the perturbations null despite perturbations are captured by Moore comparing CFD analysis with experimental measurements. The new BFMs improve the predictions of the rotordynamic coefficients compared to experiments by an average factor 2. The predicted mass-flow are very accurate for both the tests. The baseline structure of the BFM developed by the authors for staggered labyrinth seals is here described. The model is based on the 1CV BFM developed by the same authors in [9, 13, 14]. The substantial differences with respect to the BFM for straight-through labyrinth.

### Appendix A

The experimental measurements and numerical predictions of the direct stiffness and cross-coupled damping coefficients are reported here for both the experiments. Additionally, the effective stiffness coefficients is shown (Figs. 11, 12 and 13).

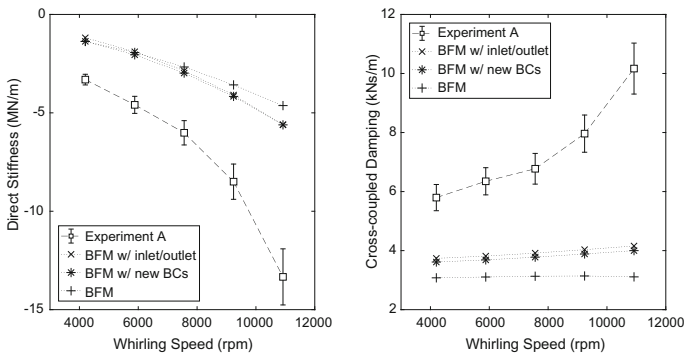
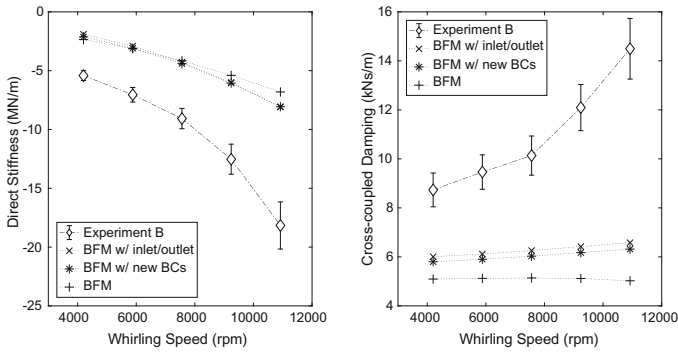
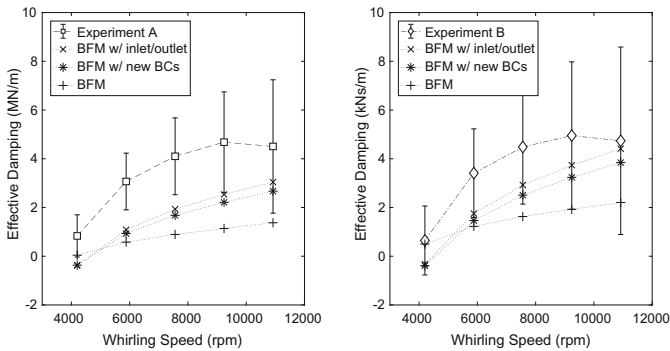


Fig. 11. Comparison of predictions and measurements of direct stiffness and cross-coupled damping coefficients as a function of the whirling speed for the experiment A.



**Fig. 12.** Comparison of predictions and measurements of direct stiffness and cross-coupled damping coefficients as a function of the whirling speed for the experiment B.



**Fig. 13.** Comparison of predictions and measurements of the effective damping coefficient as a function of the whirling speed for the experiment A and B.




## References

1. Cangioli, F., Pennacchi, P., Vania, A., Chatterton, S., Dang, P.V.: Analysis of the dynamic behavior of two high-pressure turbines for the detection of possible rub symptoms. In: Proceedings of ASME Turbo Expo 2016: Turbomachinery Technical Conference and Exposition, Seoul, South Korea (2016). <https://doi.org/10.1115/gt2016-56627>
2. Kirk, R.: Labyrinth seal analysis for centrifugal compressor design—theory and practice. In: Second IFToMM International Conference on Rotordynamics, Tokyo (1986)
3. Wagner, N.G.: Reliable rotor dynamic design of high-pressure compressors based on test rig data. *J. Eng. Gas Turbines Power* **123**(4), 849–856 (2000)
4. Childs, D.W., Scharrer, J.K.: An Iwatsubo-based solution for labyrinth seals: comparison to experimental results. *J. Eng. Gas Turbines Power* **108**, 325–331 (1986)
5. Dang, P., Chatterton, S., Pennacchi, P., Vania, A., Cangioli, F.: An experimental study of nonlinear oil-film forces in a tilting-pad journal bearing. In: ASME Conference, Boston, USA (2015)

6. Dang, P., Chatterton, S., Pennacchi, P., Vania, A., Cangioli, F.: Investigation of load direction on a five-pad tilting pad journal bearing with variable clearance. In: Proceedings of the 14th IFToMM World Congress, Taipei, Taiwan (2015)
7. Iwatsubo, T.: Evaluation of instability forces of labyrinth seals in turbines or compressors. In: NASA CP 2133, Proceedings of a Workshop at Texas A&M University, Rotordynamic Instability Problems in High Performance Turbomachinery, pp. 205–222 (1980)
8. Sreedharan, S., Vannini, G., Mistry, H.: CFD assessment of rotordynamic coefficients in labyrinth seals. In: ASME Turbo Expo 2014: Turbine Technical Conference and Exposition, Düsseldorf, Germany (2014)
9. Cangioli, F., Pennacchi, P., Vannini, G., Ciuchicchi, L.: Effect of energy equation in one control-volume bulk-flow model for the prediction of labyrinth seal dynamic coefficients. *Mech. Syst. Signal Process.* **98**, 594–612 (2018)
10. Moore, J.J.: Three-dimensional CFD rotordynamic analysis of gas labyrinth seals. *J. Vib. Acoust.* **125**(4), 427–433 (2003)
11. Vannini, G., Cioncolini, S., Calicchio, V., Tedone, F.: Development of a high pressure test rig for centrifugal compressors internal seals characterization. In: Proceedings of the Fortieth Turbomachinery Symposium, vol. %1 di %2 Houston, Texas, 12–15 September 2011
12. Vannini, G., Cioncolini, S., Del Vescovo, G., Rovini, M.: Labyrinth seal and pocket damper seal high pressure rotordynamic test data. *J. Eng. Gas Turbines Power* **136**(2), 022501 (2014)
13. Cangioli, F., Pennacchi, P., Vannini, G., Ciuchicchi, L., Vania, A., Chatterton, S., Dang, P. V.: On the thermodynamic process in the bulk-flow model for the estimation of the dynamic coefficients of labyrinth seals. *J. Eng. Gas Turbines Power* (2017). <https://doi.org/10.1115/1.4037919>
14. Cangioli, F., Chatterton, S., Pennacchi, P., Nettis, L., Ciuchicchi, L.: Thermo-elasto bulk-flow model for labyrinth seals in steam turbines. *Tribol. Int.* **119**, 359–371 (2018)
15. Cangioli, F., Pennacchi, P., Riboni, G., Vannini, G., Ciuchicchi, L., Vania, A., Chatterton, S.: Sensitivity analysis of the one-control volume bulk-flow model for a 14 teeth-on-stator straight-through labyrinth seal. In: Proceedings of ASME Turbo Expo 2017: Turbomachinery Technical Conference and Exposition, Charlotte, NC (2017). <https://doi.org/10.1115/gt2017-63014>
16. Lalanne, M., Ferraris, G.: *Rotordynamics Predictions in Engineering*. Wiley, Chichester (1998)
17. Cangioli, F., Pennacchi, P., Nettis, L., Ciuchicchi, L.: Design and analysis of CFD experiments for the development of bulk-flow model for staggered labyrinth seal. *Int. J. Rotating Mach.* **2018**, 1–16 (2018). Article no. 9357249



# Effects of Severe Operating Conditions (High Loads/Low Rotational Speeds) on Sleeve Journal Bearings

Paolo Pennacchi<sup>(✉)</sup> , Steven Chatterton , and Andrea Vania 

Department of Mechanical Engineering, Politecnico di Milano,  
Via G. La Masa 1, 20145 Milan, Italy  
{paolo.pennacchi, steven.chatterton,  
andrea.vania}@polimi.it

**Abstract.** Journal bearings are often employed in rotating machines and several papers deal with their modelling and design. On the contrary, experimental tests are seldom presented, in particular when the bearings are used in severe operating conditions, i.e. with very high values of specific pressure and very low rotational speeds. This paper presents an experimental investigation about the influence of the applied static load on the behavior of a cylindrical journal bearing with two axial grooves. The profiles of the pressure and the oil-film thickness during the shaft rotation have been measured by one pressure probe and one proximity probe installed in the rotating shaft. Measurements of the shaft center position, dynamic coefficients, hydrodynamic pressure, temperature distributions on the bearing, oil-film thickness, and bearing profile deformation under several operating conditions are presented and discussed.

**Keywords:** Sleeve bearings · Two-axial groove journal bearing  
Bearing experimental testing · Bearing profile deformation  
Severe operating conditions · Tribology

## 1 Introduction

The use of sleeve oil-film journal bearings is still suitable in industrial machines owing to the simpler design and the lower cost than rolling element bearings or oil-film tilting-pad journal bearings. However, some conditions may become critical, like in the case of machines equipped by shafts of medium/large diameter, which operate at very low Sommerfeld's number and have both high bearing loads (with the specific pressure higher than 10 MPa) and low peripheral speeds (less than 1 m/s). Typically, high-viscosity lubricants are used in these cases.

These critical conditions determine the occurrence of the so-called mixed or partial lubrication regime. The use of simple models, like the hydrodynamic (HD) or the thermo-hydrodynamic (THD) ones, in the design phase may cause bearing oversizing, principally owing to the over-estimation of the maximum pressure value in the oil-film. In these cases, the use of thermo-elasto-hydrodynamic models (TEHD) usually



improve the accuracy of the calculation of pressure distribution, because also bearing deformation, under the effect of large loads, is taken into account.

The thermal effects in a cylindrical sleeve bearing have been extensively studied in the literature. The results of both THD/TEHD models and experimental tests have been published by several scholars, aiming at fully understanding the comportment of oil-film journal bearings [1–10].

Lu et al. [11, 12] have investigated the mixed lubrication regime in a small bearing operating at very low rotational speed, ranging from 2 to 500 rpm, in different thermal and applied load conditions. Sommerfeld's number was less than 0.002 and large friction coefficient were corresponding to high oil temperatures.

The study of the differences caused by local temperature variations in journal bearings was presented by Allmaier et al. [13, 14], with a TEHD derived from previously developed EHD model. By imposing suitable boundary conditions, the TEHD model can forecast, with very high accuracy, the temperature distribution in the bearing. A quite wide range of operating conditions, including different oils (SAE10, SAE20, SAE30 and SAE40), operational speeds, hydrodynamic or mixed lubrication regime, with even dry friction, have been presented in [15, 16].

This paper introduces a wide experimental campaign, aimed at studying static and dynamic characteristics of a plain journal bearing, in different static load conditions. Some data have been concealed and some results have been normalized to the maximum value for confidential reasons.

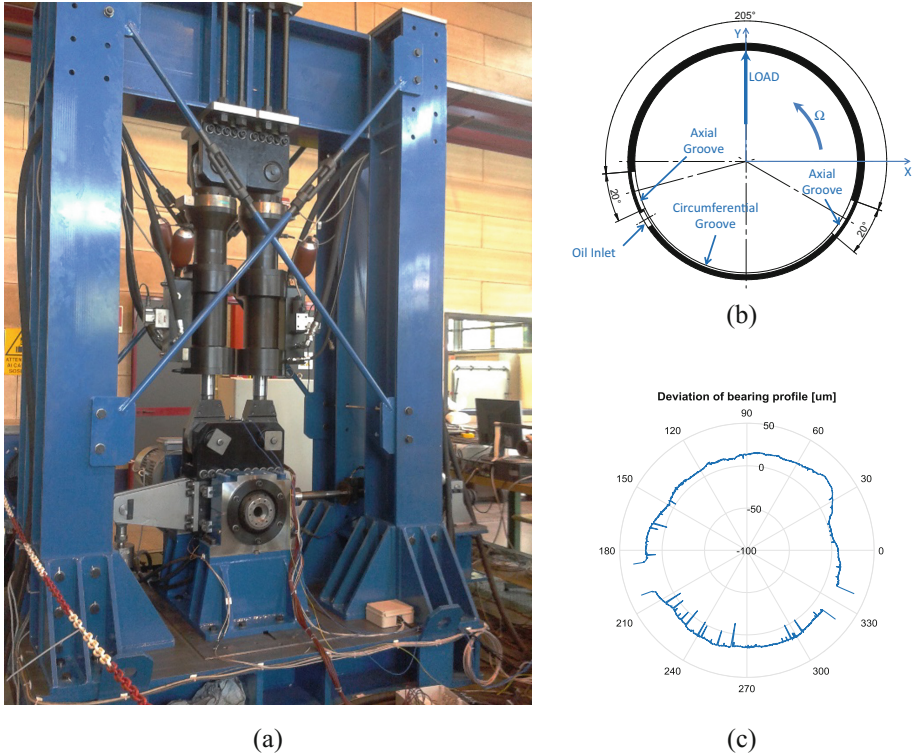
## 2 Test-Rig Description

Figure 1a shows the test-rig used during the tests. The 15.0 kW electric motor drives the rigid shaft by a flexible, double steel lamina coupling up to 1465 rpm. The lamina that are extremely rigid in sense of rotation enable a compensation for high radial displacements with low restoring forces, neglecting the influence of wrong alignment between the motor and the shaft.

An additional gearbox, with a gear ratio of 1:9, can also be installed to reduce the rotational speed.

Two hydraulic actuators, installed in the vertical direction and working in parallel, with the maximum force of 400 kN, apply the vertical static load on the top of the bearing case. Thanks to this load, the very high specific pressure of approximately 17 MPa can be reached, considering that the values of about 2–3 MPa are normally employed in the industrial field.

The vertical static load acts in the downward direction on the housing support. Thus, the load applied on the shaft is in the upward direction. The third hydraulic actuator (maximum force of 20 kN) is installed in the orthogonal direction to the two vertical actuators. During the static tests, described in the paper, the horizontal force has been set equal to zero. Conversely, dynamics load along general directions have been applied by means of all the actuators, to estimate the dynamic coefficients of the bearing. However, all the actuators can apply both static and dynamic loads simultaneously.



**Fig. 1.** View of the test-rig from the NDE side (a), bearing sketch from the NDE view (b) and bearing measured profile compared to nominal one in correspondence of the NDE edge (c).

Figure 1b shows a sketch of the bearing, which is centered on the rotating shaft and has the nominal diameter of 160 mm and the length of 145 mm. Bushing thickness is about 5 mm and is mainly made of steel. The average surface roughness  $R_a$  of the inner surface of the bearing is  $0.8 \mu\text{m}$ . Shaft rotation is counter-clockwise from non-driven end (NDE) view.

Two axial grooves are situated in the lower part (unloaded part) of the bearing. A further groove in the circumferential direction is located in the middle of the bearing and connects the two axial grooves. The oil is supplied by the inlet hole and flows in the grooves during the shaft rotation. The angular span of the loaded part (upper part) is about  $205^\circ$  (see Fig. 1b).

The bushing is fit by interference in the bearing ring as shown in Fig. 1b. Bearing bushing rotation is inhibited by an anti-rotation pin (see lower part of Fig. 2a). The differences of the actual bearing profile to the nominal one has been measured by using a ZEISS PRISMO bridge-type CMMs scanning machine, after the installation in the bearing ring. The profile shown in Fig. 1c is that on the NDE edge, in correspondence of which also the rotating proximity probe, shown in Fig. 4, is installed. Figure 1c shows a small deformation of the actual profile, which is generally wider than the nominal one.

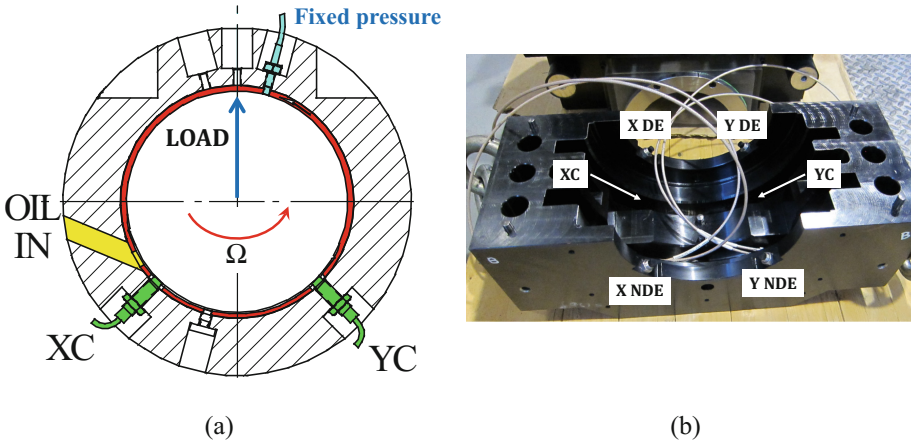


**Fig. 2.** Sensors on the bearing: (a) a couple of proximity probes and some pressure probes installed in the central diameter of the bearing and (b) four proximity probes placed in the bearing housing on both DE and NDE sides.

A housing support, horizontally split, directly connected to the actuators, hosts the bearing ring, see Fig. 2b. A fixed pressure probe, in the central diameter, at 15° from the vertical direction (see Fig. 2a) is placed in the bearing ring. The loaded part only of the sleeve is equipped by nine temperature probes (see Fig. 3), spaced by 22.5° and located at a distance of  $L/4$  from the center of the bearing on the NDE side (T1 and T9 probes correspond to the horizontal direction).

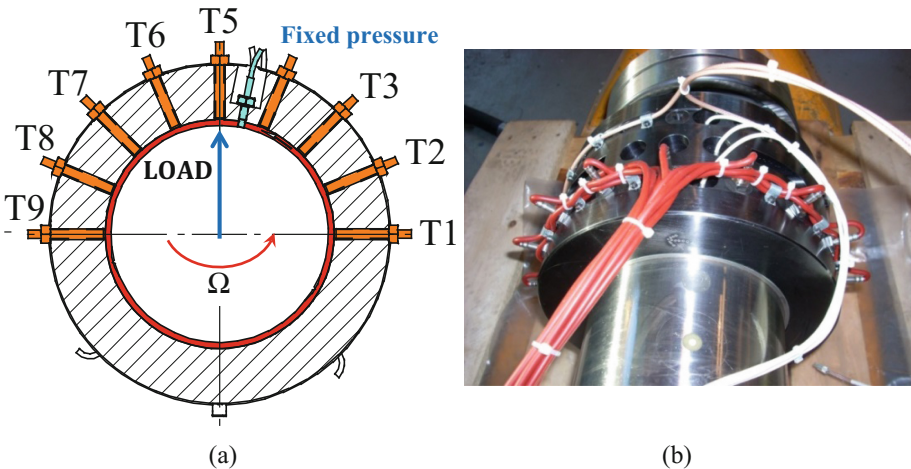


**Fig. 3.** Layout of the temperature probes installed on the bearing loaded part.

Two proximity probes,  $X_C$  and  $Y_C$  in Fig. 2a, are installed at  $45^\circ$  apart in the vertical direction, in correspondence of the bearing grooves. Four additional proximity probes are installed at  $45^\circ$  apart in the vertical direction on both the driven end (DE) and the NDE side (see Fig. 2b) of the housing.

These four probes measure the shaft center position and can detect the angular misalignment between the shaft and the housing. The same shaft center position should be measured by the three couples of proximity probes, in absence of angular misalignment and deformations.

A further proximity probe acts as key phasor. Finally, a couple of accelerometers (in horizontal and vertical directions) are mounted on the housing and are used to compensate inertial forces in the calculation of the dynamic coefficients.

Rotor shaft is made of 17NiCrMo6-4 steel, with surface roughness  $R_a = 0.2 \mu\text{m}$ . A pressure probe and a proximity probe are installed inside the shaft, to measure the pressure and the oil-film thickness during the rotation. The pressure probe is in the center of the bearing. The proximity probe is next to the bearing edge (see Fig. 4) on the NDE side. A slip-ring device is used to transmit the signal these two sensors. Main bearing dimensions, lubricant properties and operating parameters are listed in Table 1.

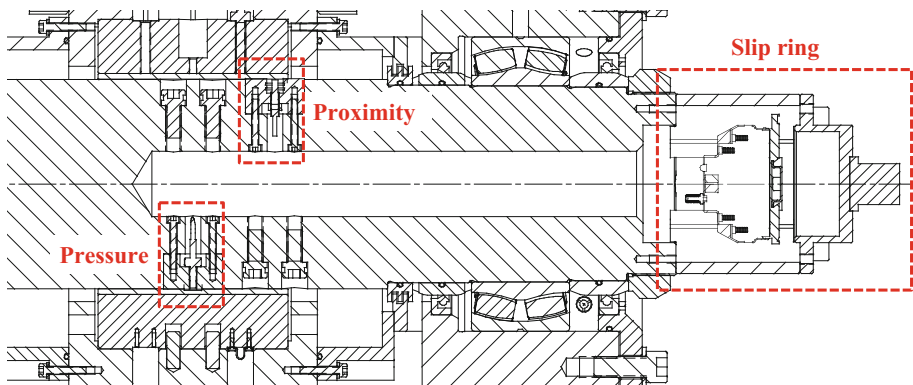


**Fig. 4.** Layout of proximity probe, pressure probe, and slip ring device on the instrumented hollow shaft.

### 3 Results of the Experimental Tests

During the test campaign, several tests have been performed to analyse the performance of the sleeve bearing corresponding to different rotational speeds and static loads. In this paper, only the results at 66 rpm are shown. A closed-loop PI temperature control allowed keeping the oil inlet temperature at  $40^\circ\text{C}$  during the tests. Results are normalized for confidential reasons.

**Table 1.** Technical specifications of the test-rig.

Parameter	Value
Bearing diameter, $D$	160 mm
Bearing length, $L$	145 mm
Applied load, $W$	0–350 kN
Journal speed, $\Omega$	1 Hz
Lubricant type	ISO VG150
<i>Pressure probe</i>	
Model	MEAS XPM6 – 1KBS
Range	1000 bars
Accuracy	$\pm 0.25\%$ F.S
<i>Temperature probe</i>	
Model	PT 100
Range	$-40-120$ °C
Accuracy	$\pm 1\%$ measured temperature
<i>Fixed proximity probe</i>	
Model	CEMB T-NC/8-API
Range	$\pm 1$ mm
Accuracy	$\pm 1\%$ measured value
<i>Rotating proximity system</i>	
Sensor	KAMAN 5U/KD-2446
Resolution	$<0.008\%$ of the measured range
Thermal drift	$<0.22\%$ per °C of full scale for the sensor

### 3.1 Estimation of the Dynamic Coefficients

To estimate the linearized dynamic coefficients, dynamic and static loads have been applied along several directions, as described in [17–19].

Considering the  $k$ -th direction of the loading and the frequency domain, the corresponding oil-film forces,  $\Delta F_x^{oil}(\omega) - \Delta F_y^{oil}(\omega)$  can be estimated by means of:

$$\begin{bmatrix} \Delta F_x^{oil}(\omega) \\ \Delta F_y^{oil}(\omega) \end{bmatrix}_k = \begin{bmatrix} h_{xx}(\omega) & h_{xy}(\omega) \\ h_{yx}(\omega) & h_{yy}(\omega) \end{bmatrix}_k \begin{bmatrix} \Delta X(\omega) \\ \Delta Y(\omega) \end{bmatrix}_k \tag{1}$$

in which  $\Delta X(\omega) - \Delta Y(\omega)$  are the displacements,  $h_{ij}(\omega) = k_{ij}(\omega) + i\omega c_{ij}(\omega)$  is the general dynamic coefficient, composed by the stiffness and damping coefficient, and  $\omega$  is the frequency of the dynamic force. Considering all the  $N$  directions of the excitation, Eq. (1) can be rewritten in the form:

$$\Delta \mathbf{F} = \begin{bmatrix} [\Delta F_1(\omega)] \\ [\Delta F_2(\omega)] \\ \vdots \\ [\Delta F_N(\omega)] \end{bmatrix} = \begin{bmatrix} [R_1(\omega)] \\ [R_2(\omega)] \\ \vdots \\ [R_N(\omega)] \end{bmatrix} \begin{bmatrix} h_{xx}(\omega) \\ h_{yy}(\omega) \\ h_{yx}(\omega) \\ h_{xy}(\omega) \end{bmatrix} = [\mathbf{R}]\mathbf{h} \quad (2)$$

in which

$$[R_k(\omega)] = \begin{bmatrix} \Delta X(\omega) & \Delta Y(\omega) & 0 & 0 \\ 0 & 0 & \Delta X(\omega) & \Delta Y(\omega) \end{bmatrix}_k \quad (3)$$

A robust M-estimator technique, described in [20–22] has been used to estimate the dynamic coefficients vector  $\mathbf{h}$  from Eq. (2). Finally, the stiffness and damping coefficients, ignoring the “virtual” mass in the stiffness terms, can be calculated as:

$$k_{ij} = \text{Re}[h_{ij}], c_{ij} = \frac{\text{Im}[h_{ij}]}{\omega} \quad (4)$$

in which  $i, j = x, y$ .

The results in the case of rotational speed equal to 66 rpm, excitation frequency to 1.5 Hz and dynamic load to 3 kN are shown in Fig. 5, after normalization. The experimental values correspond to the markers.

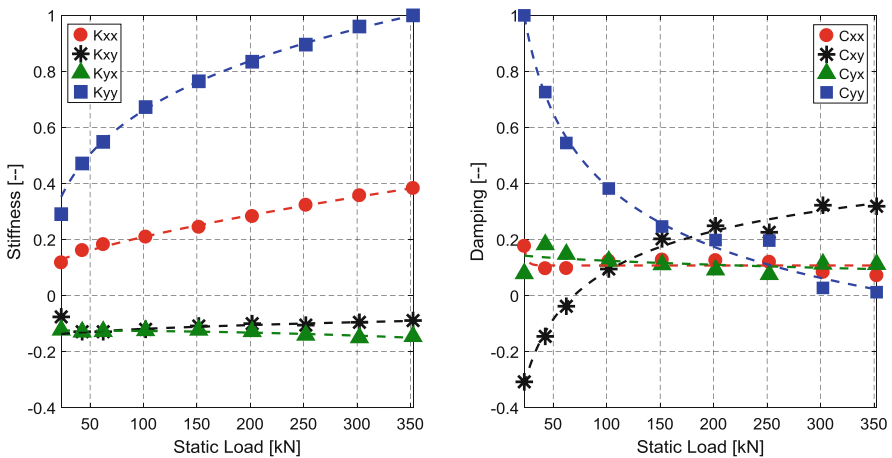


**Fig. 5.** Stiffness (left) and damping coefficients as a function of the applied static load, corresponding to the rotational speed of 66 rpm.

The direct stiffness coefficients are influenced by the static load, particularly in the loading direction (coefficient  $k_{yy}$ ). This last shows a remarkable monotonic trend in the static load range from 20 kN to 350 kN. Vertical stiffness coefficients  $k_{yy}$  are greater

than those in the unloaded, i.e. horizontal, direction ( $k_{xx}$ ). Cross coupling stiffness coefficients ( $k_{xy}$  and  $k_{yx}$ ) are practically insensitive to the static load and smaller than the direct ones.

The trend is opposite for the direct damping coefficients in vertical direction since they decrease with loading increase. One of the cross-coupling damping coefficient ( $c_{yx}$ ) is practically insensible to the static load, while the other one ( $c_{xy}$ ) is strongly dependent on the applied load, changing also its sign.

### 3.2 Shaft Centreline

Journal centreline has been evaluated by the average of the measurements of the four proximity probes of the bearing housing as  $X_{shaft} = (X_{NDE} + X_{DE})/2$  and  $Y_{shaft} = (Y_{NDE} + Y_{DE})/2$ . The comparison with the measurements of the two proximity probes in the central diameter of the bearing ring ( $X_C$  and  $Y_C$ ) is shown in Figs. 6 and 7, for two different loading conditions (respectively 50 kN and 350 kN). Besides, the average of six probes  $X_{avg} = (X_{shaft} + X_C)/2$  and  $Y_{avg} = (Y_{shaft} + Y_C)/2$  are plotted as well.

Under a theoretical point of view, the differences of the centreline curves should be determined only by bearing housing and shaft deformations, since the only the probes on NDE and DE housing sides can be affected by backlashes or deformations. Considering Fig. 6, the three centreline are practically coincident, while, when the load is high (see Fig. 7) some differences may be appreciated, likely owing to the shaft bending or the bearing housing deformation.

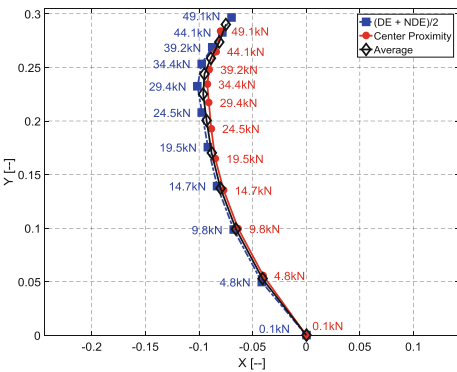


Fig. 6. Centreline as function of static load up to 50 kN at 66 rpm.

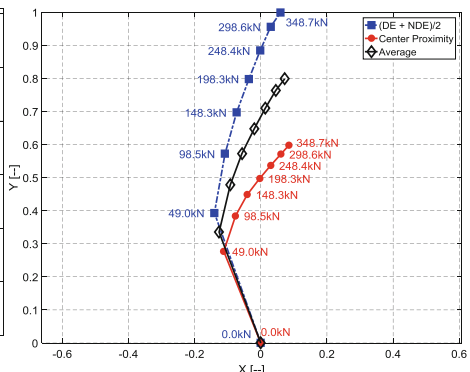


Fig. 7. Centreline as function of static load up to 350 kN at 66 rpm

### 3.3 Distribution of Bearing Surface Temperature

Figure 8 shows the distributions of the temperature, measured by the sensors shown in Fig. 3, for the rotational speed of 66 rpm and increasing loads, starting from 0 to 350 kN. In general, it is possible to observe that the temperature in the loaded part of

the bearing tends to increase with the increasing of the loads. This can be explained by the increment of shear stresses and the corresponding heat generation, in the bearing region where the oil-film thickness is reduced. Independently from the bearing load, considering a counter clockwise rotation, the minimum temperature is in correspondence of sensor T1 at  $0^\circ$ , then the temperatures reach their maxima in correspondence of sensor T6 at  $112.5^\circ$ .

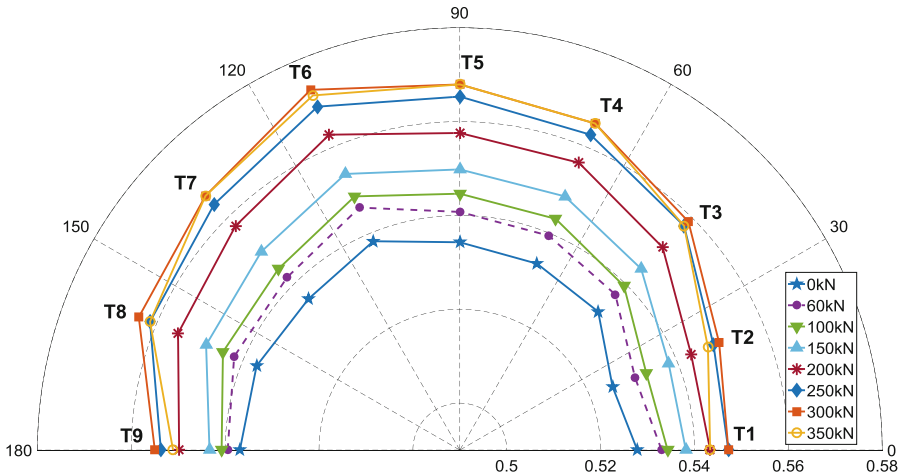


Fig. 8. Bearing surface temperature distribution as function of increasing loads, at 66 rpm.

### 3.4 Distribution of Oil-Film Pressure

The distribution of the oil-film pressure, measured by the sensor in the hollow shaft and after synchronous averaging, is shown in Fig. 9, for increasing loads from 0 kN to 350 kN and for the rotational speed equal to 66 rpm. As expected, the pressure in the lower part of the bearing is equal to the oil feeding pressure (equal to about 3–4 bar), owing to the circumferential groove. The maximum of the pressure is in correspondence of about  $105^\circ$ , while the pressure decreases suddenly from  $150^\circ$  to  $180^\circ$  for cavitation in the oil-film. The hole of the fixed pressure probe causes the deformation in the pressure distribution that can be easily observed in Fig. 9. The fixed probe has been used as a cross-check of the pressure measured by the rotating pressure probe.

The two tests performed at the highest loading (namely 300 kN and 350 kN), produces very similar pressure distributions, likely for the thermal drift of the pressure probe.



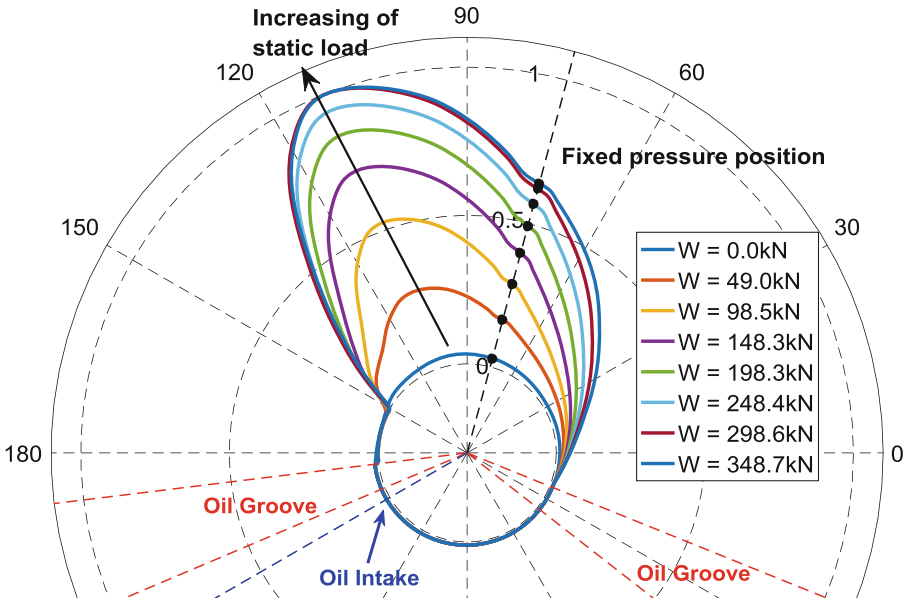


**Fig. 9.** Distribution of the pressure in the bearing for static load from 0 to about 350 kN, at 66 rpm.

### 3.5 Distribution of Oil-Film Thickness and Bearing Deformations

Figure 10 shows the distribution of the oil-film thickness as the function of the different applied loads, for the rotational speed of 66 rpm. The thickness has been measured by means of the proximity probe of Fig. 4, which points out clearly the presence of the axial grooves.

The increasing of the applied static load has a shifting effect towards down and left on the oil-film thickness distribution, as the consequence of the different centreline position. The profiles of the oil-film thickness distribution are deformed with respect to the circular one, likely because of the bushing deformation during its installation in the bearing ring (as shown in Fig. 1c), of the deformation caused by the static loads and of the uneven thermal distribution along the bearing radial profile.

The relative deformation of the bearing, as the function of the static load, can be calculated by considering the differences between the profile at 0 kN loading and the other loading cases. For brevity, only three cases are considered, namely those at 49.0 kN, 148.3 kN, and 248.4 kN. The results are shown, in normalized form, in Fig. 11.

To obtain the results of Fig. 11, it is necessary to consider that:

- shaft centreline position is different, depending on the static load;
- at high loading, the measurements of the fixed proximity probes (centre, NDE and DE sides) are different (see Fig. 7).

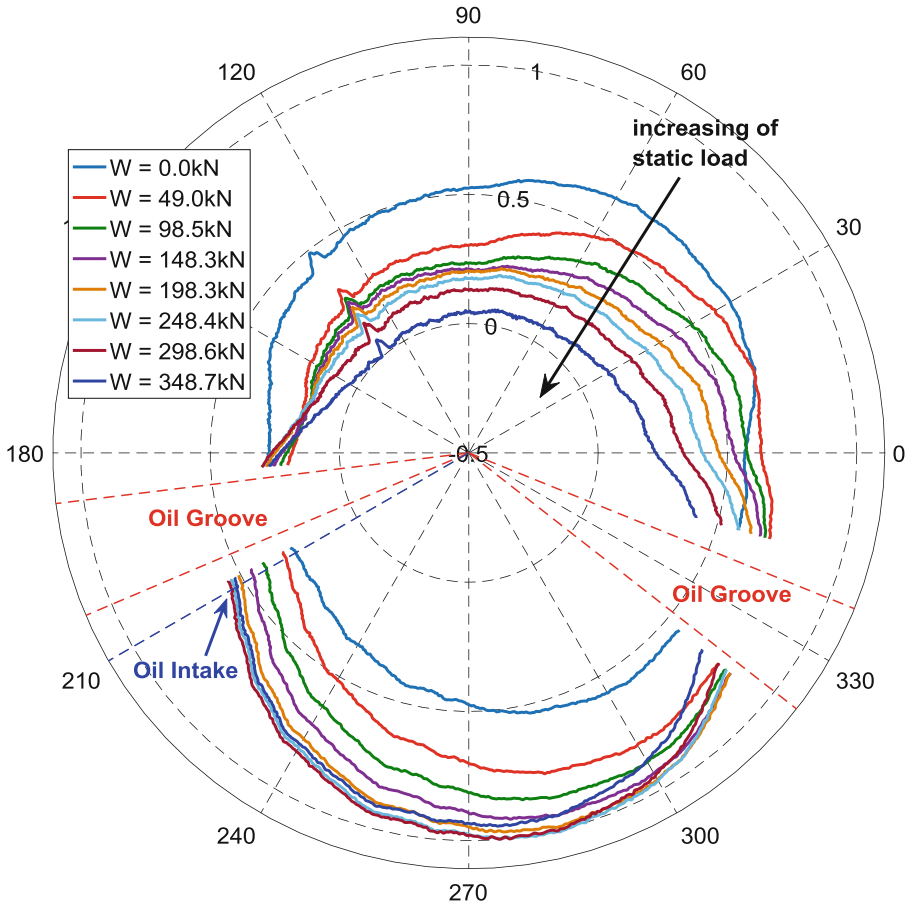


**Fig. 10.** Distribution of the oil-film thickness for static load from 0 to about 350 kN, at 66 rpm. Then, a fitting procedure has been applied only in the lower part of the bearing (from  $210^\circ$  to  $315^\circ$ ), where no deformations are probable due to the low-pressure values. The bearing profile can be expressed in the shaft reference system as:

$$\begin{cases} (R_s + h) \cos \theta = x_b + R_b \cos \beta \\ (R_s + h) \sin \theta = y_b + R_b \sin \beta \end{cases} \quad (5)$$

in which:

- $R_s$  is the journal radius;
- $R_b$  is the bearing radius;
- $\theta$  is the angular co-ordinate;
- $\beta$  is the angular position of the bearing profile;
- $x_b, y_b$  are the co-ordinates of the centre of the bearing profile;
- $h$  is the oil-film thickness.

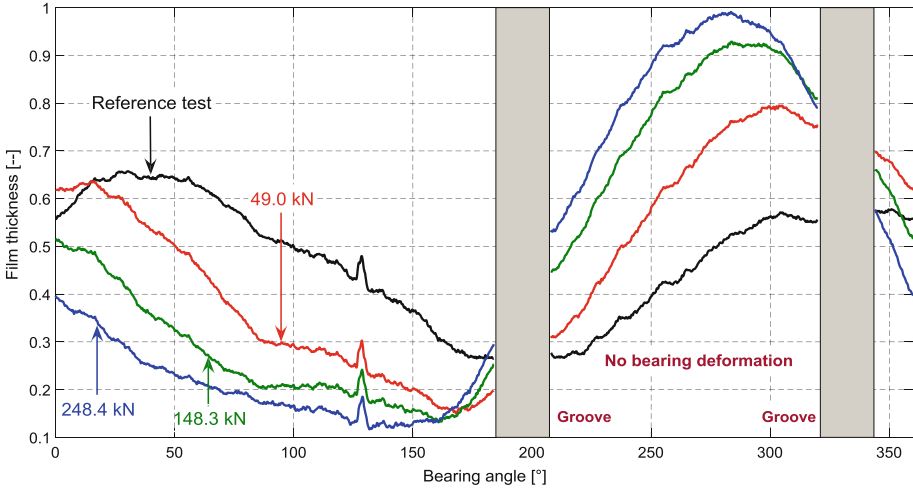


**Fig. 11.** Relative oil-film thickness as the function of the load, at 66 rpm.

The fitting procedure for bearing static load equal to 248.4 kN is shown in Fig. 12. The position of the bearing centre  $x_b, y_b$  is estimated by minimizing the objective function:

$$\vartheta = \sum (R_{b,profile} - R_{b,ref})^2 \tag{6}$$

in which  $R_{b,ref}$  is the co-ordinate of the reference bearing at 0 kN loading, and  $R_{b,profile}$  is the co-ordinate of the fitted bearing profile.

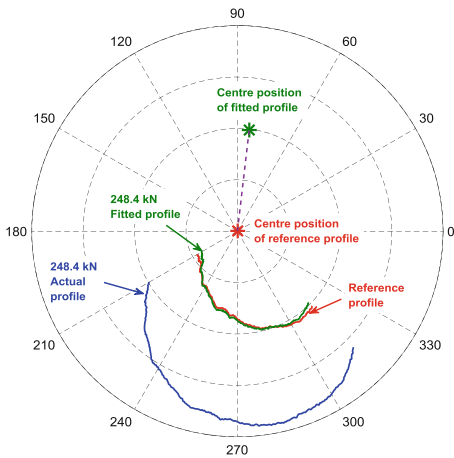


**Fig. 12.** Evaluation of the bearing deformation: actual, reference and fitted profile for 248.4 kN static load.

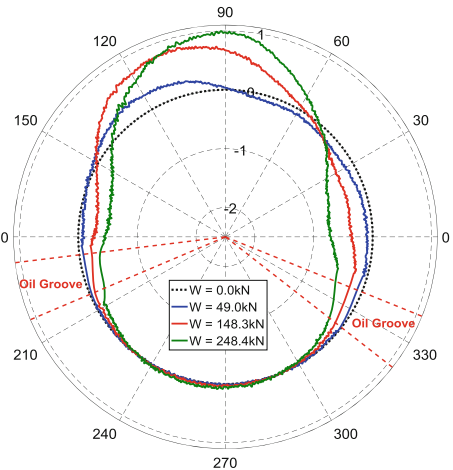


**Fig. 13.** Bearing estimated deformations at 66 rpm.

Once the co-ordinates  $x_b, y_b$  have been obtained, then the bearing profile can be plot in the same reference system, and the deformation can be calculated by the difference of this profile with that corresponding to 0 kN. The results are shown in Fig. 13, in which the original measurements have been acquired in short time to mitigate and to neglect unwanted thermal effects. Two effects can be observed: the first is the increasing bearing deformation with the increasing of the applied static load, mainly in vertical direction. The second is the “necking” in the horizontal direction.

## 4 Conclusions

The results of testing a two axial-groove journal bearing have, under severe operating conditions (i.e. high static loads and low rotational speed), have been presented in this paper.

Shaft centerline position was remarkably affected by the static loading and the effects of bearing housing deformation and shaft bending have been highlighted. Similarly, static loading influences the dynamic stiffness coefficients, but in different manners: direct stiffness in the load direction increases with load increment, while direct damping coefficients show an opposite trend.

Considering the temperature distribution in the bearing loaded part, static load increasing causes temperature increment. Similar effects happen for the pressure distribution. The maximum value of the temperature is reached close to the radial position of the maximum pressure.

Finally, a method to estimate the bearing deformation from the oil-film thickness measurements is also presented.

## References

1. Tala-Ighil, N., Fillon, M.: A numerical investigation of both thermal and texturing surface effects on the journal bearings static characteristics. *Tribol. Int.* **90**, 228–239 (2015)
2. Solghar, A.A.: Three-dimensional hydrodynamic analysis of journal bearings using lattice Boltzmann method. *Proc. IMechE Part J: J. Eng. Tribol.* **230**, 817–826 (2016)
3. Trachsel, M., Pittini, R., Dual, J.: Friction and 2D position measurements in small journal bearings. *Tribol. Int.* **102**, 555–560 (2016)
4. Cheng, F., Ji, W.: Velocity-slip model for analysis of the fluid film in the cavitation region of a journal bearing. *Tribol. Int.* **97**, 163–172 (2016)
5. Dousti, S., Allaire, P., Dimond, T., Cao, J.: An extended Reynolds equation applicable to high reduced Reynolds number operation of journal bearings. *Tribol. Int.* **102**, 182–197 (2016)
6. Kango, S., Sharma, R.K., Pandey, R.K.: Comparative analysis of textured and grooved hydrodynamic journal bearing. *Proc. IMechE Part J: J. Eng. Tribol.* **228**, 82–95 (2014)
7. Mehrjardi, M., Rahmatabadi, A.D., Meybodi, R.R.: A comparative study of the preload effects on the stability performance of noncircular journal bearings using linear and nonlinear dynamic approaches. *Proc. IMechE Part J: J. Eng. Tribol.* **230**, 797–816 (2016)
8. Illner, T., Bartel, D., Deters, L.: Determination of the transition speed in journal bearings under consideration of bearing deformation. *Tribol. Int.* **82**, 58–67 (2015)

9. Brito, F.P., Miranda, A.S., Bouyer, J., Fillon, M.: Experimental investigation of the influence of supply temperature and supply pressure on the performance of a two-axial groove hydrodynamic journal bearing. *J. Tribol.* **129**, 98–105 (2007)
10. Brito, F.P., Miranda, A.S., Clara, J.C.P., Teixeira, J.C., Costa, L., Fillon, M.: Thermohydrodynamic modelling of journal bearings under varying load angle and negative groove flow rate. *Proc. IMechE Part J: J. Eng. Tribol.* **228**, 955–973 (2014)
11. Lu, X., Khonsari, M.M., Gelinck, M.: The Stribeck curve: experimental results and theoretical prediction. *J. Tribol.* **128**, 789–794 (2006)
12. Lu, X., Khonsari, M.M.: On the lift-off speed in journal bearing. *Tribol. Lett.* **20**(3), 299–305 (2005)
13. Allmaier, H., Priestner, C., Reich, F.M., Priebisch, H.H., Novotny-Farkas, F.: Predicting friction reliably and accurately in journal bearings—extending the EHD simulation model to TEHD. *Tribol. Int.* **58**, 20–28 (2013)
14. Allmaier, H., Priestner, C., Sander, D.E., Reich, F.M.: Friction in automotive engines. In: *Tribology in Engineering*, pp. 149–184 (2013)
15. Allmaier, H., Priestner, C., Priebisch, H.H., Forstner, C., Novotny-Farkas, F.: Predicting friction reliably and accurately in journal bearings—a systematic validation of simulation results with experimental measurements. *Tribol. Int.* **44**(10), 1151–1160 (2011)
16. Sander, D.E., Allmaier, H., Priebisch, H.H., Reich, F.M., Witt, M., Füllenbach, T., Skiadas, A., Brouwer, L., Schwarze, H.: Impact of high pressure and shear thinning on journal bearing friction. *Tribol. Int.* **81**, 29–37 (2015)
17. Chatterton, S., Pennacchi, P., Dang, P.V., Vania, A.: Identification dynamic force coefficients of a five-pad tilting-pad journal bearing. In: *Proceedings of 9th International Conference on Rotor Dynamics (IFTOMM)*, Milan, Italy (2014)
18. Dang, P.V., Chatterton, S., Pennacchi, P., Vania, A.: Effect of the load direction on non-nominal five-pad tilting-pad journal bearings. *Tribol. Int.* **98**, 197–211 (2016)
19. Dang, P.V., Chatterton, S., Pennacchi, P., Vania, A.: Numerical investigation of the effect of manufacturing errors in pads on the behaviour of tilting-pad journal bearings. *Proc. IMechE Part J: J. Eng. Tribol.* **232**(4), 480–500 (2018)
20. Pennacchi, P.: Robust estimate of excitations in mechanical systems using M-estimators—theoretical background and numerical applications. *J. Sound Vib.* **310**(4–5), 923–946 (2008)
21. Chatterton, S., Ricci, R., Pennacchi, P.: Application and comparison of high breakdown-point and bounded-influence estimators to rotor balancing. *J. Vib. Acoust. Trans. ASME* **132**(6), 1–6 (2010). Article no. 064502
22. Ricci, R., Chatterton, S., Pennacchi, P.: Robust estimation of excitation in mechanical systems under model uncertainties. *J. Sound Vib.* **332**(2), 264–281 (2013)



# Investigation of Cooled Pads for Tilting-Pad Bearings

Steven Chatterton<sup>(✉)</sup> , Paolo Pennacchi , and Andrea Vania 

Department of Mechanical Engineering, Politecnico di Milano,  
Via G. La Masa 1, 20145 Milan, Italy  
{[steven.chatterton](mailto:steven.chatterton@polimi.it),[paolo.pennacchi](mailto:paolo.pennacchi@polimi.it),  
[andrea.vania](mailto:andrea.vania@polimi.it)}@polimi.it

**Abstract.** Several rotating machines are nowadays equipped with both thrust and journal tilting-pad bearings. The maximum temperature in the pads is critical for applications running at high speeds and loads, where significant temperatures can originate, due to shear stresses in the oil-film or by the surroundings. In these cases, the minimum oil-film thickness and the pad thermal crowning must be considered. Leading edge groove bearings can partially solve the problem by controlling the oil inlet temperature in the shoes. Other attempts to reduce the bearing temperature can be found in several industrial bearings and are mainly focused on the nozzles of the oil inlet. Another approach for the reduction of the heat generated in the lubricant fluid, is based on the use of suitable cooling circuits inside the pads, where the pads are cooled by an external cooling fluid. This method can be applied both to the pads of tilting-pad thrust bearings (axial load) and tilting-pad journal bearings (radial load). The cooling circuit among consecutive pads of the bearing can be also optimized considering for the temperature distribution in the bearing. Furthermore, the same oil used for the lubrication process can be used as cooling fluid. Because rotating machines are already equipped with an external cooling system for the lubricant fluid, negligible modifications in the machine layout can be required for the installation of this kind of pads, if the same lubricating oil is used as cooling fluid. Conversely, a more suitable and efficient cooling fluid can be adopted. The manufacturing issues of the cooling channels inside the pad, can be solved with the additive manufacturing technology. In the paper, the results of numerical simulations for a cooled pad bearing will be described. Several paths and cross sections of the cooling circuit will be investigated by means of computational fluid dynamics (CFD) simulation allowing the maximum temperature reduction to be obtained.

**Keywords:** Hydrodynamic lubrication · Cooled pads · CFD analysis  
Thermal deformation · Tribology

## Nomenclature

$\mu$  dynamic viscosity;  
 $\rho$  mass density;  
 $c$  specific heat capacity;  
 $k_L$  thermal conductivity;

$L_{TOT}$	total length of the path;
$p_{IN}$	inlet pressure of the fluid;
$\dot{Q}_{OUT}$	total heat exchange between the pad and the cooling fluid;
$T$	temperature;
$T_{MAX}$	maximum temperature on the active surface of the pad;
$T_{MEAN}$	mean temperature on the active surface of the pad.

## 1 Introduction

The behavior of hydrodynamic bearings used in heavy duty systems is strongly influenced by the temperature distribution in the bearing, i.e. given by the heat generated by shear stresses in the oil-film. The high dependence of the oil viscosity on the temperature affects the pressure distribution in the oil-film. Secondly the temperature distribution can produce large thermal deformation in the bearing leading to modification in the actual oil-film thicknesses. Eventually, the anti-friction materials, such as Babbit metals, that cover the active surface of the pads usually have a limited maximum operating temperature [1]. Therefore, prediction of temperature distribution in the bearing or at least of the maximum oil-film temperature is mandatory during the design phase of bearings in such applications.

Hydrodynamic bearings are mainly cooled by the inlet lubricating oil and large oil-inlet flow rates are usually adopted and carefully selected to overcome those temperature-related issues. Prediction of operating temperature have been widely investigated in the literature. Early studies of conventional thrust or journal bearings has been reported in [2] as well as the fundamental work on thermo-hydrodynamic lubricating (THD) with temperature-viscosity variation through the thickness of lubricating film was developed in [3], where both conduction and convection through lubricating film have been also provided. A more recent TEHD model for tilting-pad journal bearings (TPJB) that include the pad deformation due to the temperature, has been introduced in [4].

In THD models, the pressure distribution in the oil-film can be obtained by integrating the generalized Reynolds equation with common assumptions: laminar flow, invariant pressure in the film thickness direction, a negligible shaft curvature effect, negligible fluid inertia, constant fluid density, and temperature-affected viscosity [5]. The relationship between viscosity and temperature of the fluid can be expressed as:

$$\mu = \mu_0 \left( \frac{T}{T_0} \right)^n \quad (1)$$

The governing equation of the fluid film temperature is the three-dimensional energy equation, where fluid pressure distribution, fluid velocity profile, viscosity and thermal boundary conditions are required. The relationship between fluid film and viscosity couples the generalized Reynolds equation and the energy equation. If a laminar flow, incompressible and Newtonian fluid are assumed, the energy equation can be expressed as:

$$\rho c \left( \frac{\partial T}{\partial t} + u \frac{\partial T}{\partial x} + w \frac{\partial T}{\partial z} \right) = k_L \left( \frac{\partial^2 T}{\partial x^2} + \frac{\partial^2 T}{\partial y^2} + \frac{\partial^2 T}{\partial z^2} \right) + \mu \left[ \left( \frac{\partial u}{\partial y} \right)^2 + \left( \frac{\partial w}{\partial y} \right)^2 \right] \quad (2)$$

Heat exchange also occurs between the oil and the runner leading to a reduction of the oil-film temperature. The shaft, for journal bearings, or the runner, for thrust bearings, are generally assumed to be isothermal components, although the interactions between the local film and these components are very complex. It is of interest to note that for tilting-pad bearings, the lubricant film is colder than the rotor/runner at the leading edge of the pad, while reverse condition occurs at the trailing edge. Furthermore, the heat transfer in the grooves between pads occurs in turbulent regime and it is a 3D phenomenon [6].

## 2 Cooled Bearings

As already stated in the introduction, the reduction of the maximum temperature in the oil-film can be also obtained by suitable cooling circuits or devices inside the pads of the bearing. Cooled pads for thrust bearings have been investigated in [7, 8], where a simple numerical and thermal analysis has been performed for studying the effect of a water cooling circuit within the thrust pads of hydrogenator bearings. Different circuits that reduce the surface temperature and modifies the entire temperature profile of the bearing or pad are described in several patents (see some examples in Fig. 1).

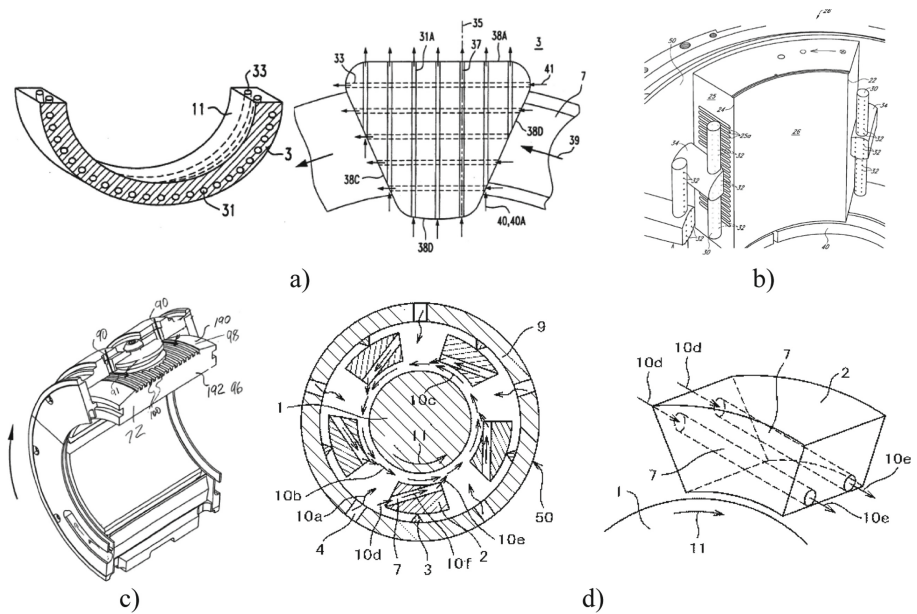


**Fig. 1.** Examples of cooling systems in patents no.: (a) EP1002965 [9]; (b) US 20140270607 [10]; (c) US 20020141670 [11]; (d) JP4930290 [12].



In these patents, the cold lubricating oil can naturally flow within channels, pipes or holes of the bearing or is externally feed using a suitable nozzle system.

In the paper, the results of the numerical simulations of a cooled pad of a tilting-pad bearing will be described. Several paths and cross-sections of the cooling circuit will be investigated by means of CFD simulation, allowing the temperature reduction to be obtained. All the results have been compared to the reference solid pad without internal cooling circuits.

### 3 Manufacturing and Application

Cooled pads can be installed both in tilting-pad thrust and journal bearings as shown in Fig. 2a. The overall serial-connection scheme of the cooling circuit of the bearing is shown in Fig. 2b, where the output of one pad is connected to the input of the following pad. Similar parallel-connection schemes can be also adopted.

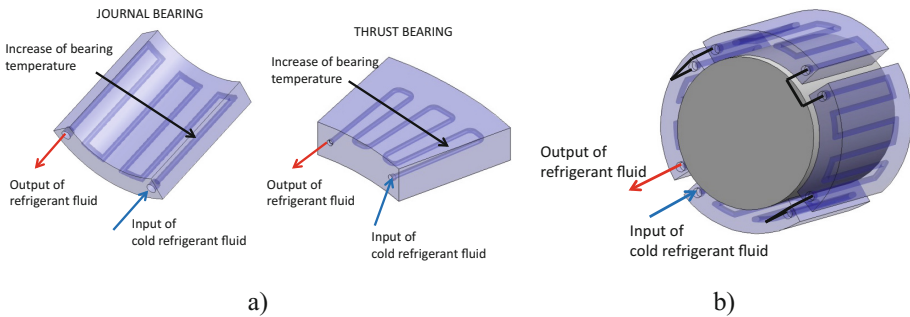


**Fig. 2.** (a) Application of cooled pads in tilting-pad journal and thrust bearings. (b) Serial-connection of the cooling circuit for tilting-pad journal bearings.

The cooling circuit among consecutive pads of the bearing can be further optimized by considering the temperature distribution along the tangential direction of the bearing. For instance, for TPJB, only the loaded pad, where high shear stresses arise, can be equipped with the internal circuit. Conversely, for high preloaded TPJB, the overall reduction of the bearing temperature can be obtained by equipping all the bearing with cooled pads. Due to the limited value of the pressure in the cooling circuit, flexible rubber hoses can be used, avoiding any restriction in the tilting motion of the pads.

The same oil used for the lubrication process can be adopted as cooling fluid. Rotating machines are usually equipped with an external cooling system for the lubricant fluid, able to reduce the outlet temperature of the oil from about 80 °C to the inlet temperature of about 40 °C. Negligible modifications in the machine layout can be required for the installation of this kind of bearings if the same oil is used. Conversely, a more suitable cooling fluid can be adopted.

The presence of holes and channels of the cooling circuit inside the pad can be critical from a mechanical point of view and difficult to be obtained by common machining processes. The manufacturing issues of such internal circuits can be overcome by means of the additive manufacturing (AM) technology and an authors' patent is pending [13].

In this way, it will be also possible to maximize the heat transfer from the hot pads to the cooling fluid and to reduce the mechanical strains-stresses by optimizing the shape of the cross-section, the path (snake path, spiral path, etc.) and the number of channels of the internal cooling circuit. The turbulent flow condition that maximize the heat exchange can be also reached. AM can be used only for obtaining the base part of the pad with the internal circuit, not for obtaining the final desired pad. For instance, the bonding of Babbitt metal on the sliding surface of the pad must be likely performed with standard technology, using heating and centrifugal machines. A typical superficial roughness of  $R_a = 12 \div 20 \mu\text{m}$  can be obtained by AM process. Therefore, additional processes will be necessary to improve the superficial finishing of the component.

#### 4 Pad Model

In this study, all the simulations have been performed using Ansys Fluent for CFD analysis. For simplicity and to highlight the effect of the proposed cooled pad, a simple square pad is considered in the analysis. Therefore, the analysis is representative of a tilting-pad thrust bearing with very large pitch diameter. The average specific load on the pad is equal to 2 MPa, whereas the tangential speed of the runner is equal to 26.1 m/s.

The simplified shape of the pad is shown in Fig. 3, where the net active area for the lubricating process is  $0.01 \text{ m}^2$ . The pressure and the oil-film thickness distributions are shown in Fig. 4.

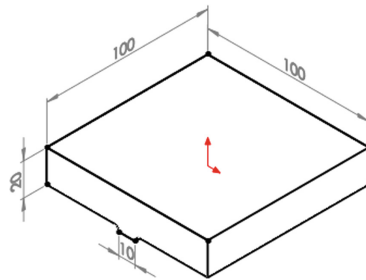


**Fig. 3.** Shape of simplified pad.

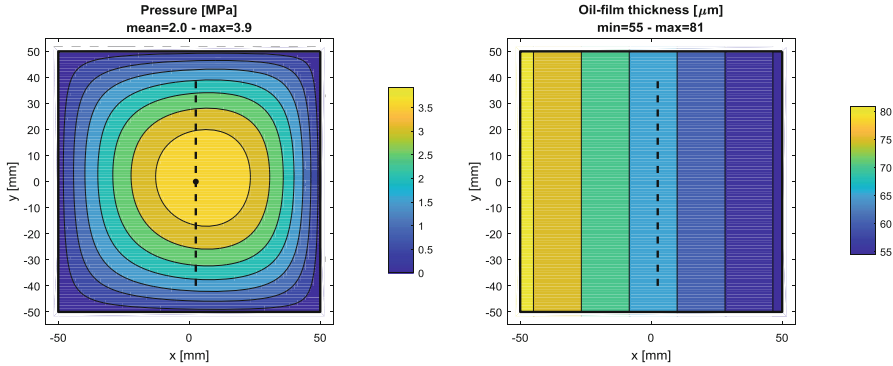


**Fig. 4.** Pressure and oil-film thickness distributions.

A structured orthogonal mesh and a free tetrahedral mesh have been used for the fluid and the pad respectively, as shown for example in Fig. 5 for a circular cross-section internal circuit with a M-path. In Fig. 5, the fluid had 15498 nodes and the pad 43617 nodes. About 3–4 elements can be detected from the wall to the center of the fluid.

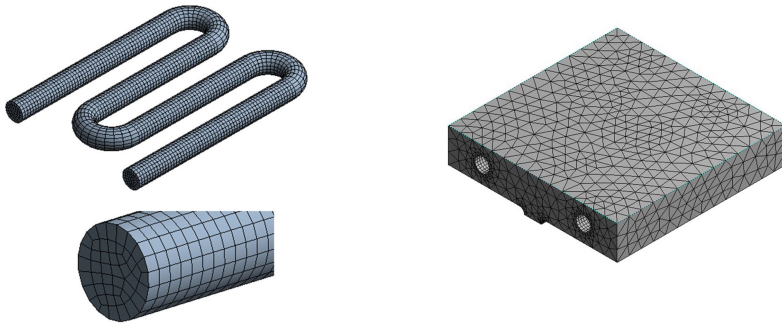


**Fig. 5.** Fluid and pad meshes for a circular cross-section internal circuit.

The shear stresses in the lubricant are responsible for the pad heating. This effect has been modelled by considering a fixed heat flux applied on the active (upper) surface of the pad for all the simulations. The total heat input is 100 W with a heat flux density given by the triangular distribution as shown in Fig. 6. This distribution represents the typical (simplified) heat flux density of a real application and has been assumed the same for all the analyses. With this simplification, the interaction between the cooled pad and the lubricating fluid in the active surface has been neglected. Besides, the reduction of the temperature in the pad does not affect the pressure or the oil-film thickness shown in Fig. 4.

Convection condition with ISO-VG46 oil at 40 °C has been assumed for all other surfaces of the pad.

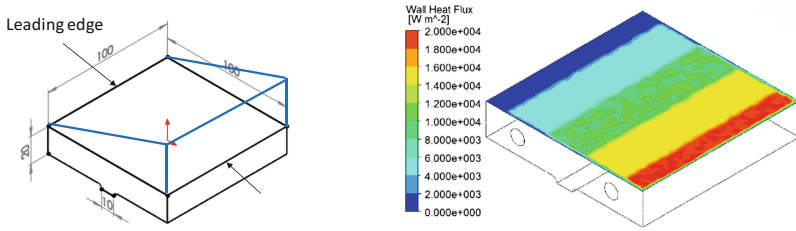


**Fig. 6.** Heat flux density distribution.

The effectiveness of the cooling system has been evaluated by analyzing the heat exchange between the pad and the cooling fluid. By considering the reference solid pad, without cooling circuit, and the previous heat flux density distribution, the maximum temperature of about 87.4 °C is reached on the active surface of the pad close to the trailing edge and a mean temperature of 72.1 °C on the same surface. These values correspond to the typical temperatures of high-loaded bearings in real applications. The temperature distribution for the reference solid pad can be find later in Fig. 12a.

## 5 Simulation Results

All the simulations have been performed by assuming the same following conditions:

- cross-sectional area of the cooling circuit: 60 mm<sup>2</sup>;
- inlet temperature of the cooling fluid: 40 °C;
- countercurrent exchange condition.

The following investigations have been performed:

- effect of cooling path;
- effect of inlet flow rates;
- effect of fluid type (oil ISO VG 46 or water);
- effect of cross-section.

For each investigation, the total heat exchange between the pad and the cooling fluid  $\dot{Q}_{OUT}$ , the inlet pressure of the fluid  $p_{IN}$  and the maximum  $T_{MAX}$  and mean  $T_{MEAN}$  temperature on the active surface of the pad will be reported.

For the optimal circuit geometry, the pad deformation due to the pressure load and the temperature distribution will be also analyzed.

### 5.1 Effect of Cooling Path

In this analysis, a circular cross section having a diameter of 8.7 mm has been assumed as well as an inlet flow rate of 3.5 L/min for a ISO-VG46 oil at 40 °C. The temperature distributions on a cutting plane in the middle of the pad thickness for “M”, “U” and “S” paths of the cooling circuit are shown Fig. 7 and the results summarized in Table 1, where the total length  $L_{TOT}$  of each path is also reported.

**Table 1.** Effect of cooling path on temperature distribution.

Circuit shape	$L_{TOT}$ [mm]	$\dot{Q}_{OUT}$ [W]	$p_{IN}$ [bar]	$T_{MAX}$ [°C]	$T_{MEAN}$ [°C]
M	267	46.0	1.11	71.0	58.1
U	194	32.0	1.07	72.8	61.1
S	247	46.4	1.10	69.7	57.6

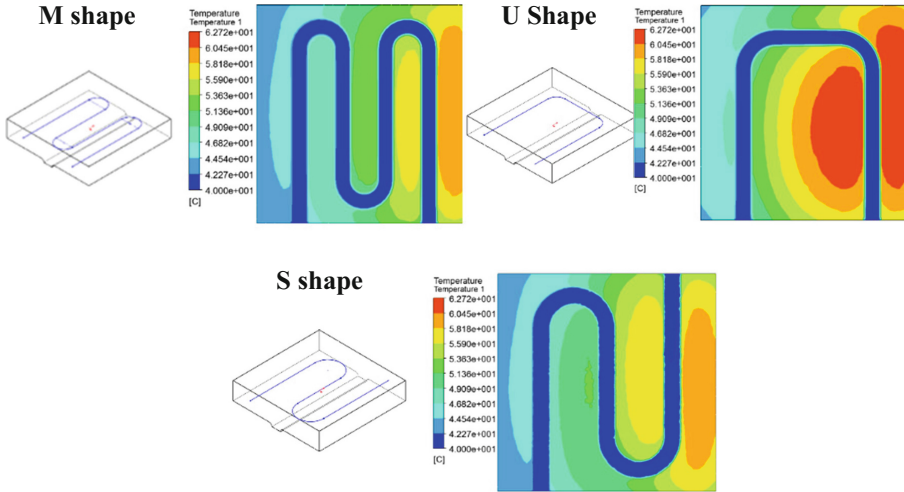


**Fig. 7.** Effect of path shape on temperature distribution.

The best result in terms of highest heat exchange and highest reduction of the maximum temperature in the pad, has been obtained by the S-shape path due to its highest path length.

Anyway, the M-shape profile will be considered in the following analyses because (i) it is very difficult to adopt a S-shape path in thrust bearings due to the presence of the rotating shaft and (ii) it allows a lower complexity for the connecting pipelines.

### 5.2 Effect of Inlet Flow Rate

Obviously, by increasing the inlet flow rate of the fluid, the maximum temperature in the pad decreases as reported in Table 2 for the ISO-VG46 oil at 40 °C.

**Table 2.** Effect of inlet flow rate on temperature distribution.

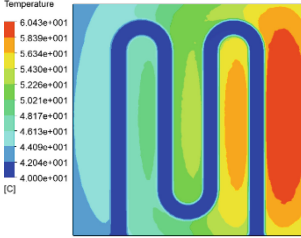
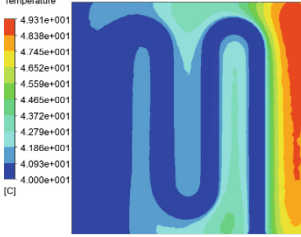
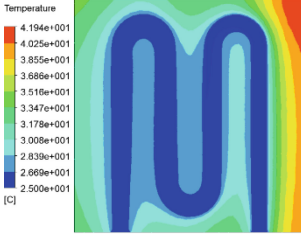
Inlet flow rate [L/min]	$\dot{Q}_{OUT}$ [W]	$p_{IN}$ [bar]	$T_{MAX}$ [°C]	$T_{MEAN}$ [°C]
3.5	46.0	1.11	71.0	58.1
7	54.5	1.23	68.3	55.9
10.5	59.1	1.37	66.9	54.7
14	62.3	1.52	65.8	53.8

### 5.3 Effect of Fluid Type

In this analysis the same flow rate of 3.5 L/min for oil ISO-VG46 and water has been considered. The temperature-viscosity Vogel's equation has been assumed for the case of oil as cooling fluid and a constant value of viscosity has been assumed for water. Oil ISO-VG 46 has been considered in the analysis, because it is the oil used in typical oil-film bearing applications for turbomachinery. Two different values of temperature have been investigated for water fluid, namely 25 °C and 40 °C. With the same inlet temperature condition of 40 °C for the oil, better results (lower pad temperature) are obtained if water is used as cooling fluid (see results in Table 3).

Conversely, more care must be taken for the connecting circuit to avoid the contamination of the lubricant.

**Table 3.** Effect of fluid type on temperature distribution.

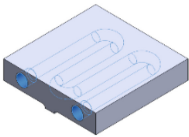


















Fluid type	Temperature distribution	$\dot{Q}_{OUT}$ [W]	$P_{IN}$ [bar]	$T_{MAX}$ [°C]	$T_{MEAN}$ [°C]
ISO-VG46 Oil @ 40°C		46.0	1.11	71.0	58.1
Water @ 40°C		83.9	1.03	58.6	47.7
Water @ 25°C		138.5	1.03	50.5	35.1

### 5.4 Effect of Cross Section

In this section, different cross-sections of the cooling circuit have been investigated, as listed in Table 4. Single and multi-channels profiles have been investigated. The circular section profile is the most commonly used in the design of various heat exchanger. However, non-circular profiles allow the increase of the heat exchange due to the turbulence and heat exchange surface area with respect to the circular one to be obtained. These kinds of profiles can be obtained by AM.

All the simulations have been performed with the same cross-sectional area ( $60 \text{ mm}^2$ ), path length, inlet temperature of the cooling fluid of  $40 \text{ }^\circ\text{C}$ , inlet flow rate of  $14.4 \text{ L/min}$  and only for ISO-VG46 oil.

**Table 4.** Cross-sections.

<b>A</b>	Circular		<b>B</b>	Rectangular	
<b>D</b>	Star		<b>C</b>	Square	
<b>E2</b>	6 Triangular Radial Features		<b>E1</b>	4 Triangular Radial Features	
<b>F</b>	4 Rectangular Radial Features		<b>E3</b>	8 Triangular Radial Features	
<b>F2</b>	B/A = 1:1.5		<b>F1</b>	B/A = 1:1	
<b>G1</b>	4 Multi Channels Square		<b>F3</b>	B/A = 1:2	
<b>G3</b>	8 Multi Channels Square		<b>G2</b>	6 Multi Channels Square	
<b>H1</b>	3 Multi Channels Rectangular		<b>G4</b>	5 Multi Channels Square	
<b>H3</b>	2 Multi Channels Rectangular		<b>H2</b>	2 Multi Channels Rectangular	
			<b>H4</b>	3 Multi Channels Rectangular	

The temperature distributions are shown for several single and multi-channels profiles in Figs. 8 and 9 respectively. All the results are then summarized in Table 5.

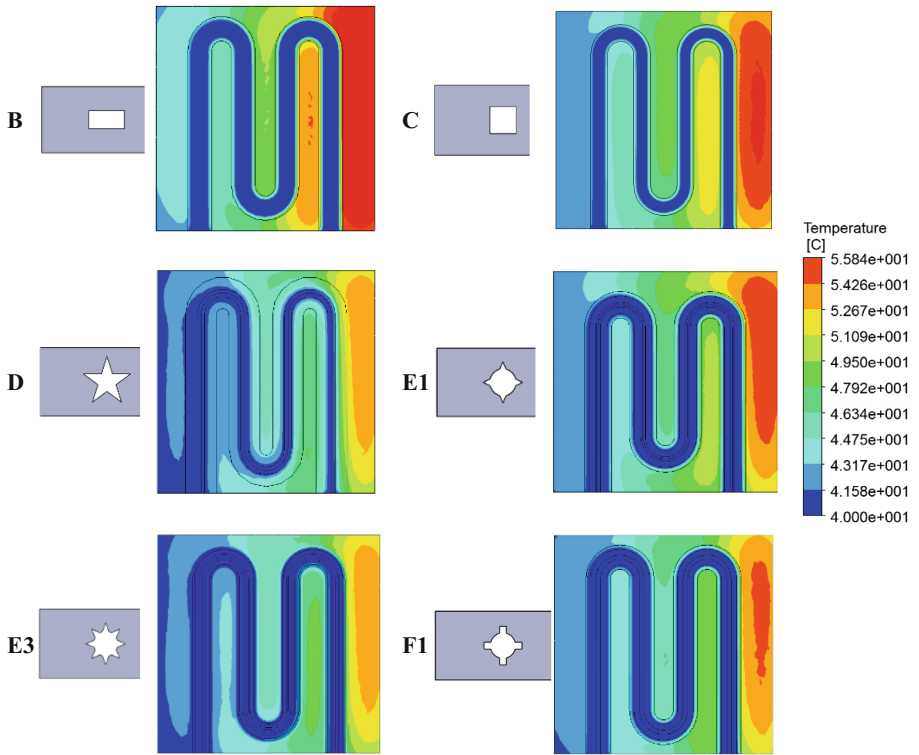


Fig. 8. Temperature distribution for different cross-sections (single channel).

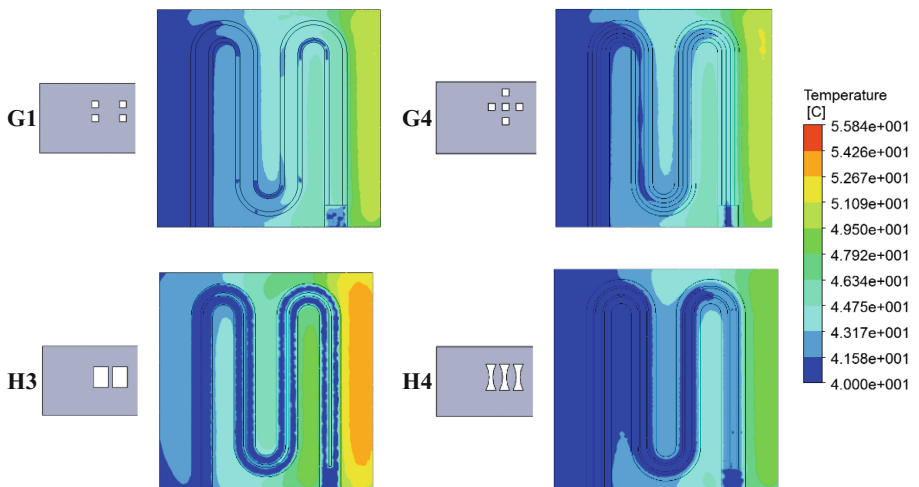



















Fig. 9. Temperature distribution for different cross-sections (multi-channels).



**Table 5.** Results of cross-section analysis.

Case	$\dot{Q}_{OUT}$ [W]	$p_{IN}$ [bar]	$T_{MAX}$ [°C]	$T_{MEAN}$ [°C]	Case	$\dot{Q}_{OUT}$ [W]	$p_{IN}$ [bar]	$T_{MAX}$ [°C]	$T_{MEAN}$ [°C]
<b>0</b> Solid	-	-	87.4	72.1	<b>A</b> Circular	62.3	1.52	65.8	53.8
<b>B</b> 	72.0	1.58	69.4	56.1	<b>C</b> 	59.3	1.46	66.7	54.6
<b>D</b> 	71.8	1.83	63.8	51.8	<b>E1</b> 	64.5	1.64	65.2	53.1
<b>E2</b> 	67.6	1.70	64.7	52.6	<b>E3</b> 	71.7	1.88	63.1	51.5
<b>F1</b> 	69.6	1.79	64.0	52.1	<b>F2</b> 	70.9	1.90	63.4	51.7
<b>F3</b> 	74.5	2.12	62.6	51.1	<b>G1</b> 	76.8	13.60	60.0	49.1
<b>G2</b> 	78.0	8.43	59.7	48.7	<b>G3</b> 	<b>79.1</b>	<b>6.21</b>	<b>59.5</b>	<b>48.7</b>
<b>G4</b> 	78.0	10.54	59.8	48.4	<b>H1</b> 	74.8	3.20	61.4	50.3
<b>H2</b> 	70.7	4.73	62.2	50.7	<b>H3</b> 	70.2	2.09	62.9	51.5
<b>H4</b> 	78.7	4.90	60.0	49.0					

In general, higher heat exchanges can be obtained by multi-channel cross-sections than single channel ones.

The maximum reduction of the temperature on the active surface of the pad can be obtained by the 8 square channels profile (G3 highlighted in Table 5). Conversely this profile requires higher inlet pressure than single channel profiles.

### 6 Static Deformation

In this last analysis, the static deformation of the pad, due to the pressure load and the thermal stresses given by the temperature distribution, has been investigated. The pressure distribution of the oil-film assumed in this analysis has a maximum value equal to about 4 MPa and is applied on the active surface of the pad as shown in Fig. 10a. A fixed constraint is also assumed as boundary condition of the pivot (Fig. 10b).

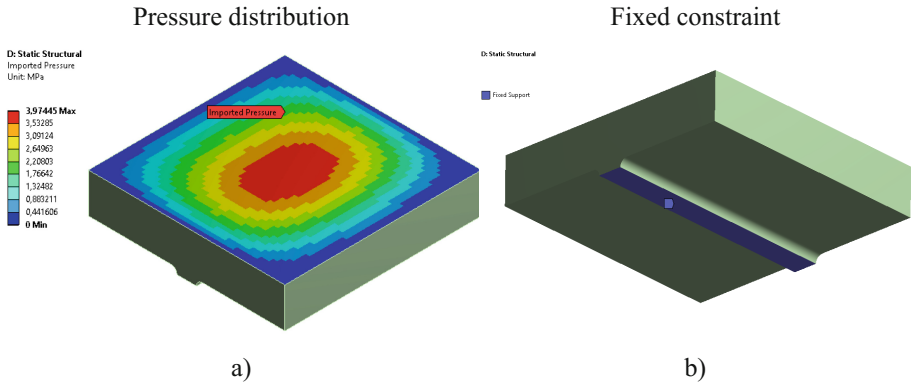


Fig. 10. (a) Pressure distribution, (b) Fixed constraint for the static deformation analysis.

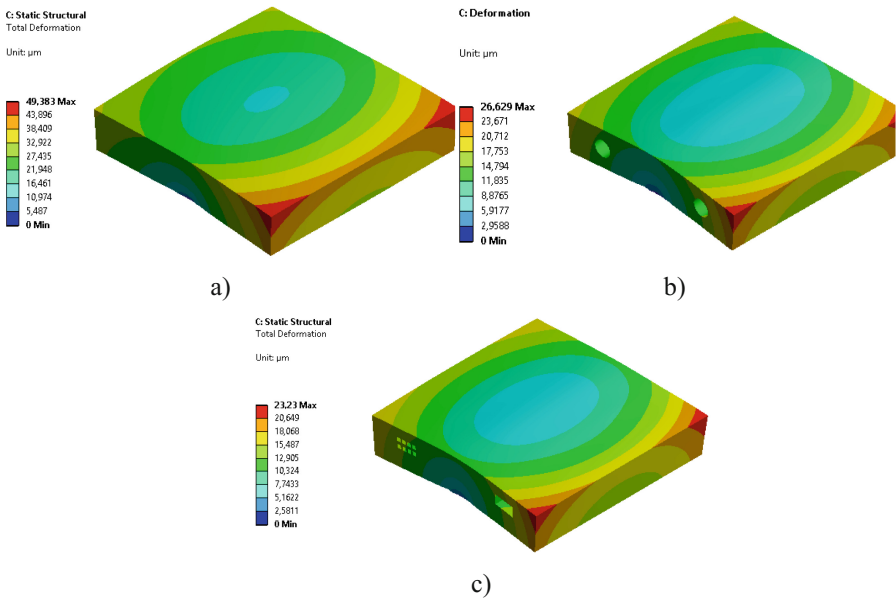
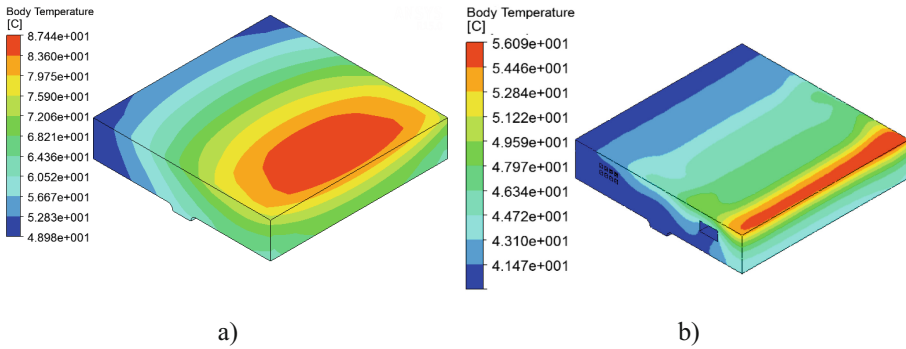


Fig. 11. Static deformation of the pad (a) solid pad (b) circular cooled pad and (c) 8-channels cooled pad.



**Fig. 12.** Temperature distribution from the thermal analysis: (a) solid pad, (b) 8-channels cooled pad.

In particular, the mechanical deformations for the circular cross-section and 8-channels cross-section have been compared to the solid pad configuration, as shown in Fig. 11; whereas the corresponding temperature distributions obtained by the thermal analysis are shown in Fig. 12 for the solid and 8-channels cross-section only. A maximum total deformation of about 23  $\mu\text{m}$  is obtained for the 8-channels cooled pad vs. the total deformation of 43  $\mu\text{m}$  for the solid pad. Conversely a total deformation of about 26  $\mu\text{m}$  has been obtained by the simple circular cross-section.

These results highlight that the deformation of the pad is mainly given by the thermal stresses. For the solid pad, high temperature can be detected on the active surface of the pad (about 87 °C in Fig. 12) with respect to the cooled pad (about 56 °C in Fig. 12). This corresponds to significant temperature gradients in the pad thickness resulting in a thermal bending of the pad due to thermal stresses. Conversely, the presence of the internal channels seems to not influence the deformation of the pad.

## 7 Conclusions

In the paper, the reduction of the temperature in the pads of tilting-pad bearings has been investigated, by means of cooled pads having suitable internal cooling circuits. Different geometries of the cooling circuit within the pad have been considered in the analysis.

The best results are represented by the highest heat exchange and reduction of the maximum temperature on the active surface of the pad. The reduction of the pad temperature allows the reduction of pad deformation due to thermal expansion to be obtained.

In general, the temperature reduction can be achieved by:

- using a S-shape path. However, the M-shape path can be preferred because it allows a better piping connection and installation;
- increasing the inlet flow rate of the fluid;

- using water as cooling fluid. However, water can contaminate the lubricant and requires a dedicated circuit;
- using a suitable cross-section that increases the turbulence of the cooling fluid;
- using a multi-channels cross-section. The main drawback of multi-channel profiles is given by the higher feeding pressure than single-channel profile.

These special cross-sections of the cooling circuit can be obtained by means of AM.

## References

1. Pennacchi, P.: Introduction of advanced technologies for steam turbine bearings. In: Tanuma, T. (ed.) *Advances in Steam Turbines for Modern Power Plants*. Elsevier Ltd., Duxford (2017)
2. Vohr, J.H.: Prediction of operating temperature of thrust bearings. *ASME J. Lubr. Technol.* **103**, 97–106 (1981)
3. Rohde, S.M., Oh, K.: A thermoelastohydrodynamic analysis of a finite slider bearing. *ASME J. Lubr. Technol.* **97**(3), 450–460 (1975)
4. Suh, J., Palazzolo, A.: Three-dimensional dynamic model of TEHD tilting-pad journal bearing—part I: theoretical modeling. *J. Tribol.* **137**(4), 1–11 (2015)
5. Dang, P.V., Chatterton, S., Pennacchi, P., Vania, A.: Effect of the load direction on non-nominal five-pad tilting-pad journal bearings. *Tribol. Int.* **98**, 197–211 (2016)
6. Ettles, C., Cameron, A.: Consideration of flow across a bearing groove. *ASME J. Lubr. Technol.* **90**(1), 312–319 (1968)
7. Najjar, F.A., Harmain, G.A.: Novel approach towards thrust bearing pad cooling. In: *Proceedings of the ASME 2014 Gas Turbine India Conference, GTINDIA2014*, New Delhi, India (2014)
8. Najjar, F.A., Harmain, G.A.: Performance characteristics in hydrodynamic water cooled thrust bearings. *J. Tribol.* **10**, 28–47 (2016)
9. Becker, B.: Coolable bearing. Patent no. EP 1002965 A1 (1998)
10. Livermore-Hardy, R., Blair, B.: Trailing edge cooling on hydrodynamic bearings. Patent no. US 20140270607 A1 (2014)
11. Nicholas, J.: Sleeve bearing with bypass cooling. Patent no. US 20020141670 A1 (2002)
12. Miya, T., Kuwano, T., Himemi, S., Hitoi, H.: Tilting pad type journal bearing, Patent no. JP4930290 (2007)
13. Pennacchi, P., Chatterton, S.: Cuscinetto lubrificato per macchine rotanti. Patent pending 102017000046660 (2017)



# Vibration Control of a Gas Turbine-Generator Rotor in a Combined Cycle System by Means of Active Magnetic Bearings

Rafael Pilotto<sup>(✉)</sup> and Rainer Nordmann

Fraunhofer LBF, Bartningstr. 47, 64289 Darmstadt, Germany  
rafael.pilotto@lbf.fraunhofer.de

**Abstract.** It is well known that many lateral vibration problems occur in rotating machinery systems, for which nowadays in most cases passive measures are used to mitigate these vibrations. With the requirements for more powerful, efficient and secure rotating machinery with high availability the demand for more efficient vibration reduction measures increases. Active magnetic bearings (AMB) can be used as a possible solution, since it generates magnetic fields and forces to control the rotor vibrations, without rotor-bearing contact. AMBs are often used in special applications, for example in high-speed/high-performance turbomachinery like turbo-compressors for the oil and gas industry or in machine tool applications. The main problems of implementing active vibration control by means of AMBs are the energy transfer towards the rotating system, best suited concepts to control the lateral vibrations and the design of reliable backup bearings for special applications. One of the most common causes of high vibration amplitudes is the unbalance of a rotor, which leads to  $1xN$  vibrations. In this work it will be shown, how these unbalance vibrations can be best controlled by an AMB. This paper consists of a purely numerical analysis for a combined cycle turbine, in which two separated cases are studied: 1. the complete analysis of the operational setup, where the turbine is supported with radial oil-film bearings (RFBs) only, and 2. The oil-film bearing in the gas turbine side, where the vibration amplitudes are higher due to the unbalance generated by the fluid flow, is replaced by one AMB.

**Keywords:** Turbines · Active magnetic bearings · Active vibration control

## 1 Introduction

Rotating machines have a prominent presence in several areas, like large turbines in hydroelectric and thermoelectric plants, propulsion engines in ships, automobiles and aircrafts, as well as compressor and pumps in the oil and gas industry. These applications are usually associated with high rotational speeds and long operational (sometimes continuous) cycles. Therefore, the dynamic behavior of these machines must be well known for a project to be robust since an accident can cause serious damage to the whole system and therefore long repairing periods with very high costs.

With the emergence of new, and more complex, engineering problems, the development of new technologies becomes mandatory [1]. The many knowledge fields

of engineering, once independent nowadays are interrelated in order to develop new solutions and suitable methods to new patterns of testing and analysis.

Mechanical systems are always subjected to vibrations and therefore exposed to the temporal effects of fatigue and wear which can, in a short period of time, cause sudden losses in the properties and efficiency of these systems. The most important operating condition for rotor machinery is the maintenance of the clearance gaps between rotating and non-rotating parts. This is necessary in order to allow a safe transition throughout the resonance stage, where the amplitudes of vibration are the highest, during run-up/run-down without damaging any components. In this scenario it is often necessary to employ auxiliary components (passive and/or active) to work in parallel to the main system, with the purpose of maintain the performance of the system as intended and extend its operational life.

On the passive side, there are the well-known radial oil-film bearings; the most used support in turbomachinery, as they allow the rotor system to sustain high loads at high speeds. The availability and the reliability of this type of bearing is very high, since there is only fluid contact between parts with relative motion, ensuring long operational lifetime, but they are far from perfect due to the occurrence of rotor-bearing hydrodynamic instabilities, such as sub synchronous vibrations with high amplitudes (oil-whip). Besides that, these instability problems due to self-excitation in fluid bearings can also be controlled and avoided if the operation conditions are taken into account during its project and design.

The use of active vibration control to reduce these clearances can contribute to the reduction of undesirably high lateral vibrations, mainly bending oscillations of the rotors, and therefore an increase of the efficiency of the machine will be possible due to a designed clearance reduction. Active magnetic bearings (AMBs) can be applied to these vibration control problems, usually used as contactless suspension for rotating machinery parts; it also enables the application of compensating magnetic forces in the system (usually to counter unbalance loads), which have no mechanical interaction with the structure in analysis [2]. It is also important to find the needed space for the positioning of the AMB, considering the low specific pressure that AMBs have compared to other bearings.

The combined cycle turbine consists of a system with a gas turbine and a steam turbine. The gas turbine compresses the air and mixes it with hot fuel, the air-fuel mixture moves through the turbine blades, making them spin and driving a generator that converts some of that energy into electricity. A HRSG (heat recovery steam generator) captures exhaust heat from the gas turbine, and creates steam, delivering to the Steam turbine, which generates additional energy for the system, thus resulting in the system having a higher efficiency than the standalone turbines.

This paper is a case study of an existing shaft train, where the complete combined cycle turbine is composed by 7 flexible shafts and supported by 9 oil-film bearings but this paper describes the numerical results of the gas turbine-generator system only. Two cases are studied: 1. The system with only oil-film bearings as supports (RFB). 2. The replacement of the bearing at the gas turbine side by an AMB. The comparison between these two cases is done using both harmonic (unbalance response) and transient analysis (run-up).

## 2 Methodology and Theory

### 2.1 Turbine Model and FEM

The complete model of the combined cycle turbine system is composed of seven different shafts which are all connected via rigid couplings, except from the connection between the generator and the right part of the dual turbine, which works as a separation between both gas and steam partitions (decoupling). In this work, only the gas turbine and the generator are considered for analysis. This part system has to be considered when the unit is started.

The model was built using FEM (finite elements method) using the software MADYN 2000 and all the geometrical data of the turbine and bearings coefficients were supplied by the manufacturer. The complete turbine system can be seen in Fig. 1. The turbine system has a length of 44 m and weight of 268 tons. The gas turbine-generator system has a length of 25.8 m and 183 tons of weight.

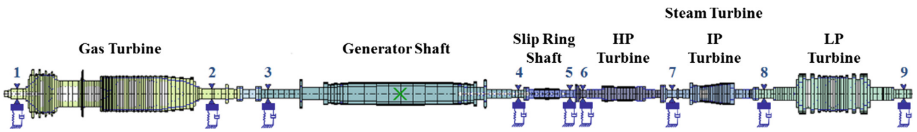


**Fig. 1.** Complete combined cycle turbine FEM model with the bearings and foundation locations numbered.

The system is supported using radial oil-film bearings and each bearing (numbered in Fig. 1) has an added lumped-mass system that simulates the foundation and suspension in which the turbine is assembled (Fig. 2). Since this work only corresponds to the gas turbine-generator system; only the first 4 marked locations are used in this work. The range of mass (foundation), stiffness and damping (suspension) coefficients [3] are shown in Table 1.

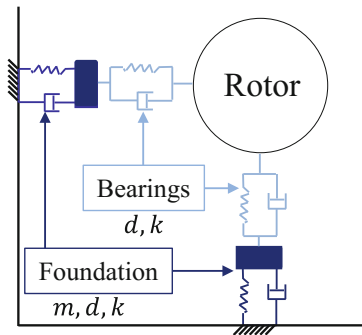


**Fig. 2.** Rotor-bearing-lumped-mass foundation scheme.

**Table 1.** Range of foundation and suspension coefficients.

Location	Mass (kg)	Stiffness (N/m)	Damping (Ns/m)
1	x: ~10e+4; y: ~10e+4	x: ~7e+9; y: ~5e+9	x: ~5e+5; y: ~7e+5
2	x: ~10e+4; y: ~10e+4	x: ~7e+9; y: ~5e+9	x: ~6e+5; y: ~8e+5
3	x: ~10e+4; y: ~10e+4	x: ~7e+9; y: ~5e+9	x: ~5e+5; y: ~8e+5
4	x: ~10e+4; y: ~10e+4	x: ~7e+9; y: ~5e+9	x: ~5e+5; y: ~7e+5

Using the assumption of a linear system behavior, the equation of the FEM model (without the foundations) can be described as it follows (Eq. 1).

$$[M]\{\ddot{q}\} + ([C] + \Omega[G])\{\dot{q}\} + [K]\{q\} = \{F\} = \Omega^2\{F_u\} + \{F_{amb}\} + \{Q_b\} \quad (1)$$

Where  $[M]$  corresponds to the global mass matrix,  $[G]$  to the gyroscopic effect matrix,  $[K]$  the stiffness matrix,  $[C]$  is the structural damping matrix and  $\Omega$  is the rotational speed of the shaft [4, 5]. The Damping matrix is assumed to be proportional to  $[K]$  by a factor of  $2 \times 10^{-4}$  [6]. The external forces vector is given by  $\{F\}$ , and contains the unbalance  $\{F_u\}$ , the AMB force  $\{F_{amb}\}$  and the interaction between the bearings and foundation  $\{Q_b\}$ .

The complete system, with the inclusion of foundation can be seen when the Eq. (1) is separated into submatrices, as it follows:

$$\begin{aligned} & \begin{bmatrix} [M_{aa}] & [M_{ba}] \\ [M_{ab}] & [M_{bb}] \end{bmatrix} \begin{Bmatrix} \{\dot{q}_a\} \\ \{\dot{q}_b\} \end{Bmatrix} + \left( \begin{bmatrix} [D_{aa}] & [D_{ba}] \\ [D_{ab}] & [D_{bb}] \end{bmatrix} + \Omega \begin{bmatrix} [G] & 0 \\ 0 & 0 \end{bmatrix} \right) \begin{Bmatrix} \{q_a\} \\ \{q_b\} \end{Bmatrix} \\ & + \begin{bmatrix} [K_{aa}] & [K_{ba}] \\ [K_{ab}] & [K_{bb}] \end{bmatrix} \begin{Bmatrix} \{q_a\} \\ \{q_b\} \end{Bmatrix} = \begin{Bmatrix} \{F_{amb} + \Omega^2 F_u\} \\ \{Q_b\} \end{Bmatrix} \end{aligned} \quad (2)$$

Where the subscript  $a$  refers to all interior and free-end d.o.f. (degrees of freedom) of the rotor-bearing system, while subscript  $b$  denotes the common d.o.f. of the bearing and foundation [3]. In this scenario, we can observe that the combined subscript  $aa$  correspond to the rotor-bearing system,  $ab$  and  $ba$  correspond to the coupling between the bearings and foundation and  $bb$  correspond solely to the foundation. Also,  $\{q_a\}$  is the generalized coordinate vector, and  $\{q_b\}$  is the associated generalized coordinate vector for the foundation of the system, each with two translations and two rotations for each node of the FEM model. This can be more easily visualized on Fig. 3.

In order to improve computational time and to help with the optimization of the controller, a Guyan reduction [7] was used on the 1212 d.o.f. model which was reduced to 100 d.o.f.

There are two unbalances on the system, both located on the gas turbine and with a difference of 180 degrees in phase angle, with magnitudes of  $7.15 \times 10^{-2}$  kg m ( $U_1$ ) and  $4.25 \times 10^{-2}$  kg m ( $U_2$ ). The locations can be seen on Fig. 4.



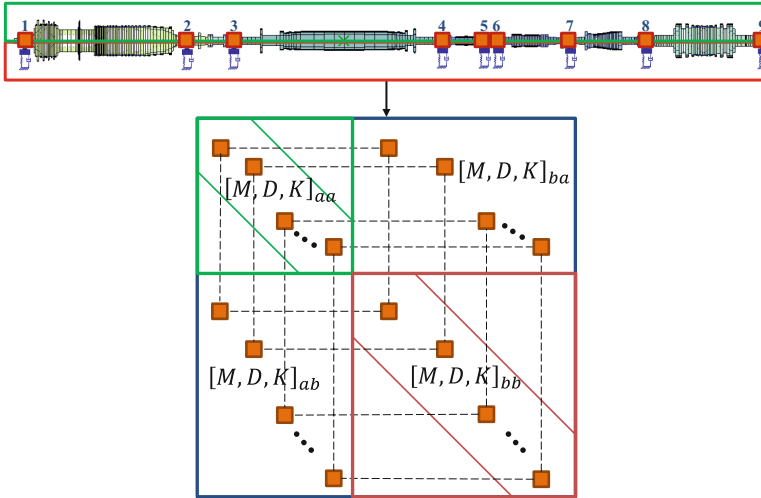


Fig. 3. Rotor-bearing-foundation matrix interaction.

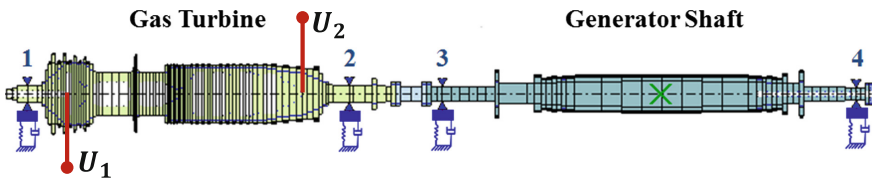


Fig. 4. Studied system model, with unbalance locations

2.2 Active Magnetic Bearings (AMBs)

Considering a typical 8-pole radial magnetic bearing, the eight poles are divided into four electromagnets (Fig. 4). Magnet 1 generates radial force in the x-axis direction whereas magnet 3 generates radial force in the opposite (-x-axis) direction. Therefore magnets 1 and 3 are working in differential mode; the same is true for magnets 2 and 4 (Fig. 5).

Considering only the x-axis for the mathematical deduction since the same assumptions are valid for the y-direction, first, we have the self-inductance of the magnets [2]:

$$L_0 = \frac{N^2 \mu_0 S}{2g} \tag{3}$$

Where  $N$  is the sum of the number of winding turns of two short-pitched coils,  $\mu_0$  is the permeability factor of the mean (i.e. environment) where the AMB is immersed (air),  $S$  is the area of one stator pole,  $g$  is the airgap between the pole and the turbine shaft.

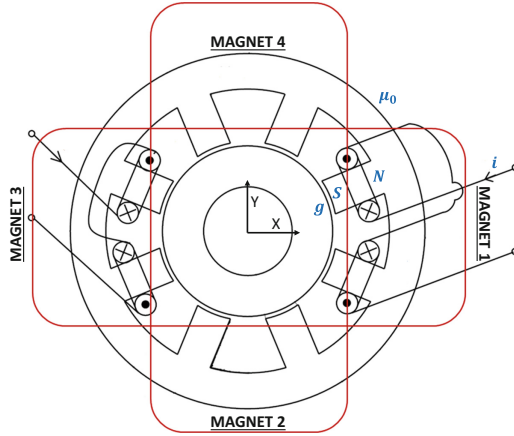


Fig. 5. Radial magnetic bearing model. (Adapted [2])

Using the Eq. (3), we have the forces in each magnet, since we are working with an 8-pole AMB, we have a geometrical factor of  $\cos(\pi/8)$  included in the factors:

$$F_1 = k_i i_1 + k_q x_1, \quad F_3 = k_i i_3 + k_q x_3 \quad (4)$$

$$k_i = \frac{2L_0 \cos(\frac{\pi}{8}) I_b}{g}, \quad k_q = \frac{2L_0 \cos(\frac{\pi}{8}) I_b^2}{g^2} \quad (5)$$

$$i_1 = I_b + i_x, \quad i_3 = I_b - i_x \quad (6)$$

$$x_1 = g - x, \quad x_3 = g + x \quad (7)$$

$I_b$  is the bias (permanent) current and  $i_x$  is the regulating current (control) current and  $x$  is the instant separation between rotor and the AMB at any given time as seen in [2]. It can be seen that  $k_q$  has a negative sign since the greater the distance  $x$  the smaller the resulting force on the bearing [8]. Since  $i_1 > i_3$ ,  $x_1 < x_3$ , as the greater the current, greater the attraction force and therefore smaller the distance between rotor and bearing is. Therefore, for the resulting force in the  $x$ -axis and similarly for the  $y$  axis, we have:

$$F_{AMB_x} = F_1 - F_3 = k_i i_x + k_q x \quad (8)$$

$$F_{AMB_y} = F_4 - F_2 = k_i i_y + k_q y \quad (9)$$

Where  $k_i$  is known as the force-current factor and  $k_x$  is the force-displacement factor. Equations (8) and (9) shows that the force of the magnetic bearings in the  $x$ -axis and  $y$ -axis are exclusively dependant of the regulating current  $i_x$  and the distance  $x$  between rotor and bearing: The data regarding the components of the AMB system can be found on Table 2.

**Table 2.** AMB system data.

Force-current factor ( $k_i$ )	$2.54 \times 10^6$ N/A
Force-displacement factor ( $k_q$ )	$8.71 \times 10^9$ N/m

The values of these two factors may seem a bit elevated, but the AMB has to exert a force of 595000 N just to counter the weight (levitate) of the shaft at the inlet location. Since  $k_q$  has a positive value for radial AMBs, the AMB-Rotor system is inherently unstable. Therefore, for an optimized controller, the collocation, alongside with the observability and controllability of the system must be carefully considered [2] and also there is a requirement to provide enough negative position feedback to cancel the effect of this coefficient [8].

**2.3 PID Controller**

As mentioned on the previous section, the rotor-AMB system is unstable in nature, so the controller must, first and foremost, stabilize the system. A PID controller was chosen for its simplicity and ease of tuning and optimization. The modelling of the controller was made using the Ziegler-Nichols Method [9] and manual tuning. The aforementioned method is not applicable to an system with an AMB, since the system is unstable due to the force-displacement factor ( $k_q$ ) of the AMB being negative in magnitude, so the method is applied on the system without the AMB as to use the obtained values of  $K_p$ ,  $K_i$  and  $K_d$  as a 1<sup>st</sup> iteration of the controller. The  $K_p$  (Stiffness) and  $K_d$  (damping) values are manually tuned based on this iteration. The derivative term has a drawback once it amplifies high frequency measurements, which compromise the controller performance. This limitation can be overcome by adding a filter coefficient ( $N_f$ ) that acts as a filter in order to remove high-frequency noise components from the measurements. The controller with the added filter is given by Eq. (10).

$$PID(s) = K_p + \frac{K_i}{s} + \frac{K_d N_f s}{s + N_f} = \frac{(K_p + K_d N_f) s^2 + (K_p N_f + K_i) s + K_i N_f}{s^2 + N_f s} \tag{10}$$

The Fig. 6 shows the PID model with the filter in the derivative part:

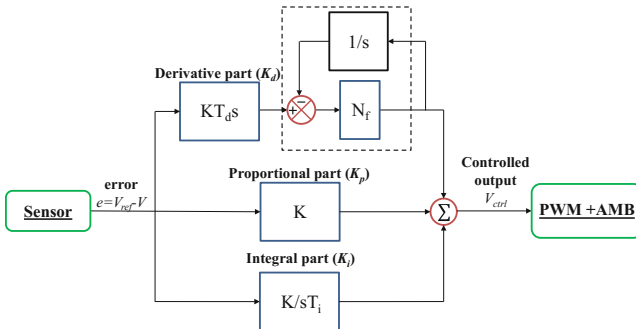


**Fig. 6.** PID with added derivative filter

Considering that for the Rotor-AMB system, the most important criteria for a controller is to minimize the amplitude of vibration during the passing of the critical speeds, it is important to take into consideration the use of other filters to reduce the control forces after the passing of the critical speed (low-pass), otherwise the controller can become another source of excitation to the system.

### 2.4 Complete System

The flowchart seen in Fig. 7 shows all the previously mentioned components working in tandem. The AMB is located at the bearing placement n°1. The displacements (in both directions x and y) resulting of the unbalances ( $U_1$  and  $U_2$ ) are measured by the displacement sensors whose signal is compared to the reference signal, the error signal is sent to the controller, the output voltage of the controller is transformed into electric current by a power amplifier and then sent to the coils of the magnetic bearing, generating the magnetic actuator force  $F_{AMB}$  that is applied to the mechanical system.

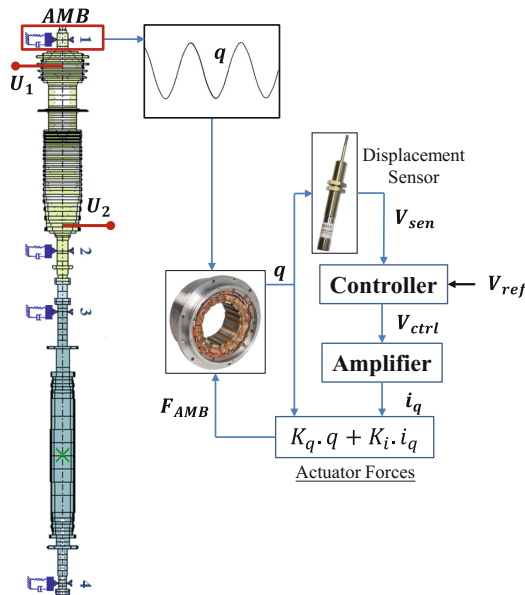


Fig. 7. Turbine-generator-system-AMB interactions.

## 3 Results

The replacement of the RFB for an AMB at the gas turbine side has the objective to minimize the vibration amplitudes as good as possible for the complete shaft line. The analysis of the system consists of two separate analyses, on the harmonic spectrum (unbalance response) and on the transient spectrum (run-up). For both cases, 4 (four) points of interests were considered, namely, the place where the four bearings are

located. This is done to verify that the vibration throughout the whole system is not increased after the AMB is placed, i.e. the AMB is not exciting some modes while controlling others.

### 3.1 Harmonic Analysis (Unbalance Response)

The unbalances  $U_1$  and  $U_2$  are located on the gas turbine, its locations are shown in Figs. 4 and 7. This harmonic analysis is made in order to check the peak amplitudes and differences in natural frequencies of the system with and without the AMB. Since the system is built upon a foundation in each bearing location, the results are shown as relative shaft displacements instead of absolute values. The results for each bearing location can be seen on the following figures, where the red curves represent the system on RFBs only, and de blue curves represent the system harmonic response with the AMB on the gas turbine side (Figs. 8, 9, 10, 11).

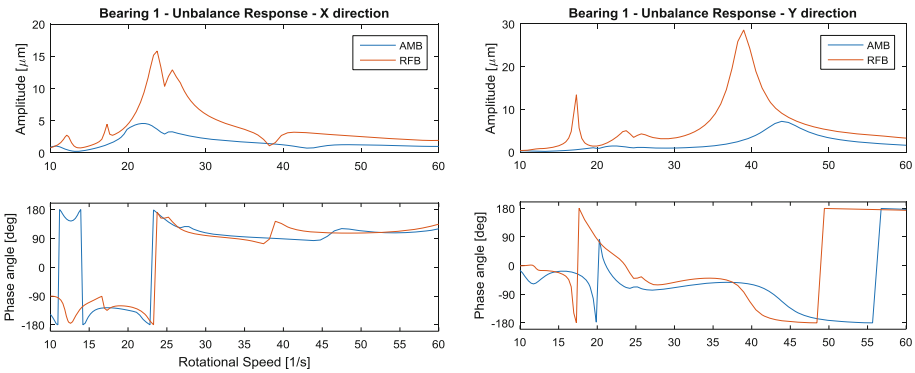


**Fig. 8.** Unbalance response (relative shaft displacement) on the 1<sup>st</sup> bearing location.

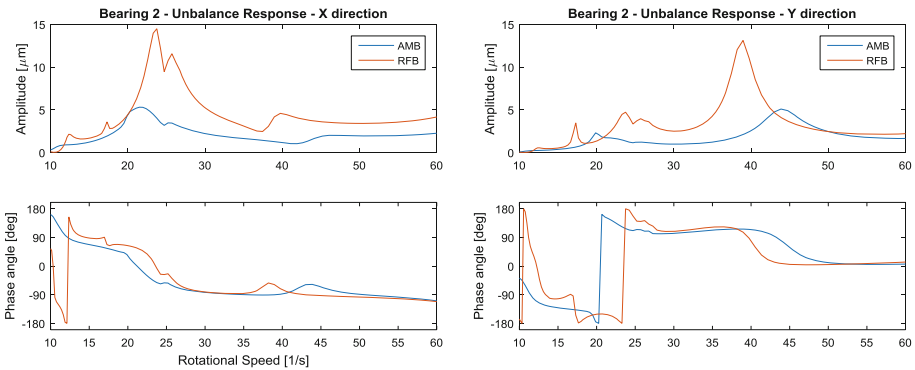


**Fig. 9.** Unbalance response (relative shaft displacement) on the 2<sup>nd</sup> bearing location.

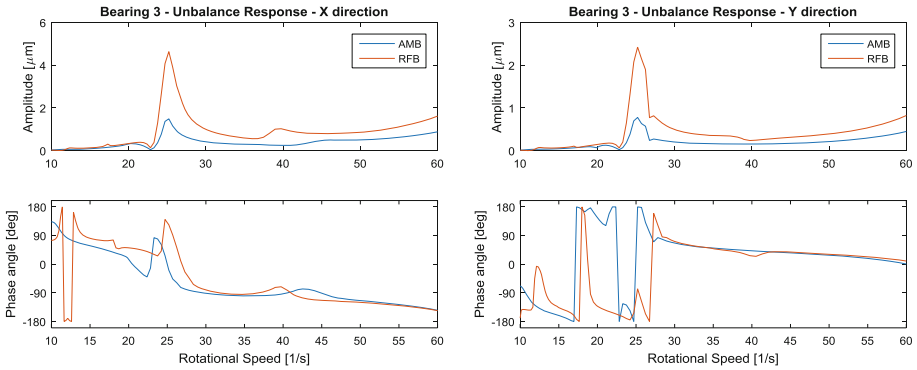


**Fig. 10.** Unbalance response (relative shaft displacement) on the 3<sup>rd</sup> bearing location

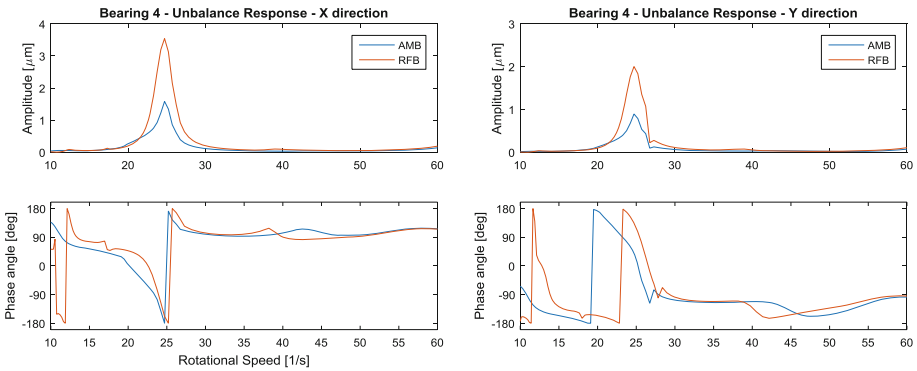


**Fig. 11.** Unbalance response (relative shaft displacement) on the 4<sup>th</sup> bearing location.

The amplitudes of the harmonic response are all reduced, when using an AMB at the gas turbine side instead of the RFB. This is particular the case at the 1<sup>st</sup> bearing, where the AMB can reduce the amplitude at the turbine side by upwards of 75% (in X direction) and 80% (in Y direction). The analysis of the other bearing locations shows, that the AMB doesn't excite the other locations of the turbine-generator system. Instead the amplitudes are also reduced, although in more discrete amounts in the range of 50%, the reduction effect is even remarkable at the outer generator bearings.

### 3.2 Transient Analysis (Run-Up)

For the Transient analysis, the simulated run-up covers from 10 Hz to 60 Hz in 7 s, and then there is a 3 s settling time, resulting in a 10 s analysis. This settling time is used to assure that the system is not near its instability threshold, since a mere straight run-up analysis can be deceiving, especially on systems that use fluid bearing support, on the account of fluid induced instabilities.

The amplitudes of vibration were particularly compared when crossing the critical speeds. The results of these simulations regarding the displacement of the node where the unbalances are located (highest vibration amplitudes) can be seen on Figs. 12, 13, 14 and 15.

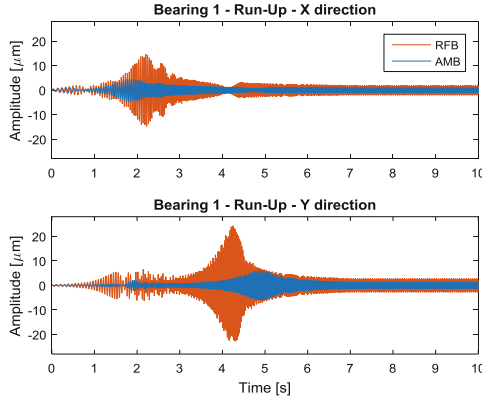


**Fig. 12.** Run-up analysis for the 1<sup>st</sup> bearing location

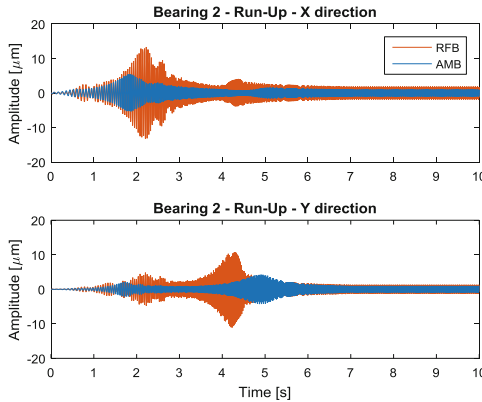


**Fig. 13.** Run-up analysis for the 2<sup>nd</sup> bearing location

All that was said in the previous section can be confirmed here, where we can see again a great reduction of the vibration amplitudes on the gas turbine bearings (Figs. 12 and 13). The displacement of the generator shaft bearings is several times smaller than that of the turbine since there are no unbalances in its neighborhood and therefore no extra sources of vibration.

Both analysis results – harmonic as well as transient - have shown, that the amplitudes of the relative shaft vibrations can remarkably be reduced (50% and more),

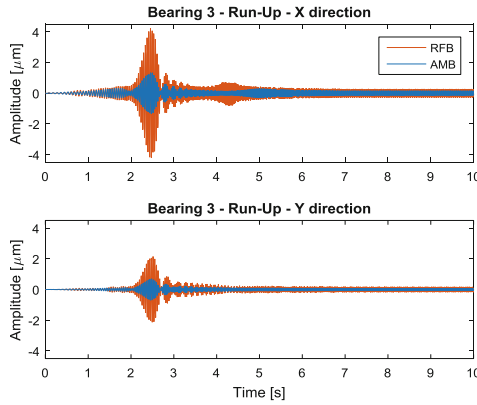


**Fig. 14.** Run-up analysis for the 3<sup>rd</sup> bearing location

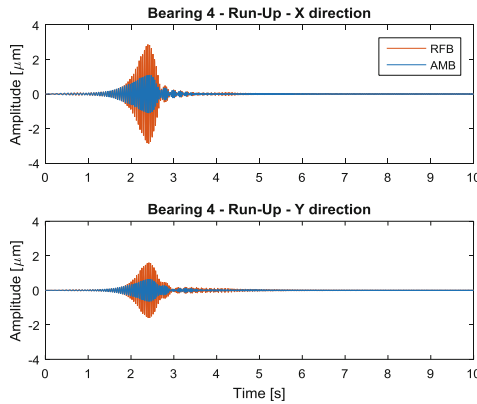


**Fig. 15.** Run-up analysis for the 4<sup>th</sup> bearing location

when using an AMB instead of a fluid film bearing at the gas turbine side. This offers from a practical point of view the possibility for the machine designer of reducing also the clearances in the gas turbine with an effect of reduced clearance losses and a higher thermodynamic efficiency.

### 4 Conclusion and Future Works

Theory and design of AMBs in rotating machinery has been presented in several publications in the past years. This paper is about a practical application and presents the possibility of the replacement of a regular Radial oil Film Bearing (RFB) by an Active Magnetic Bearing (AMB) on the turbine side of a gas turbine-generator system. The numerical results of harmonic and transient vibrations due to unbalance excitation



show, that the amplitudes of the relative shaft vibrations can remarkably be reduced (50% and more), when an AMB is used instead of the regular RFB. The vibration control is not only possible at the AMB location, but also across the whole rotor system, especially when crossing critical speeds, where the system is at its most unsafe state. As a practical consequence of the vibration reduction the machine design can be improved by decreasing the clearances in the gas turbine with the effect of a reduction of clearance losses and an increase of the machine efficiency. This is not only an advantage during normal operation, but also when at machine run ups thermal effects with thermal shaft bows may lead to higher unbalance vibrations. Due to the possibility of the vibration control self-excited vibrations due to fluid film bearings and seals can also be avoided by means of the AMB. Furthermore an AMB with its sensor and actuator characteristics can be used as a powerful tool to identify the dynamic behavior of a rotor system during operation. By measuring input and output-quantities (forces and displacements) it is possible to determine frequency response functions at normal operation with valuable information about the rotor dynamic behavior. This is an important step into the direction of practical Model Based Monitoring.

Despite that, there are still a lot of potential to this system that could not be included in this work; such as: the analysis of the other “half” of the combined cycle, since the inlet of the Steam turbine is also subjected to high vibration amplitudes, and extending the analysis to the complete system (including the Steam turbine), this would bring another level of complexity to the AMB-controller system, since the combined cycle turbine model has 31 critical speeds up to 90 Hz, and so the controller must be more robust to make it worthwhile, one such optimization option is the LPV (Linear Parameter varying) technique [10] to transform the AMB-Controller system into an adaptive controller with optimized parameters for several critical speeds of a complex system, such as this one.

**Acknowledgements.** The authors would like to acknowledge the European Commission for its support of the Marie Skłodowska-Curie program through the ITN ANTARES project (GA 606817), and GE-Power for the provided data that made this paper possible.

## References

1. Lee, C.-W.: Mechatronics in rotating machinery. In: 7th IFToMM-Conference on Rotor Dynamics. AUT, Vienna (2006)
2. Chiba, A., Fukao, T., Ishicawa, O., Oshima, M., Takemoto, M., Dorrell, D.G.: Magnetic Bearings and Bearingless Drives. Newnes, Oxford (2005)
3. Kang, Y., Chang, Y.-P., Tsai, J.-W., Mu, L.-H., Chang, Y.-F.: An investigation in stiffness effects on dynamics of rotor-bearing-foundation systems. *J. Sound Vib.* **231**(2), 343–374 (2000)
4. Nelson, H.D., McVaugh, J.M.: The dynamics of rotor-bearing systems using finite elements method. *J. Eng. Ind.* **98**, 593–600 (1976)
5. Greenhill, L.M., Bickford, W.B., Nelson, H.D.: A conical beam finite element for rotor dynamics analysis. *J. Vib. Acoust. Stress Reliab. Des.* **107**, 421–430 (1985)
6. Weiming, L., Novak, M.: Dynamic behavior of turbine-generator-foundation systems. *Earthq. Eng. Struct. Dyn.* **24**, 339–360 (1996)

7. Guyan, R.J.: Reduction of stiffness and mass matrices. *AIAA J.* **3**(2), 380 (1965)
8. Schweitzer, G., Maslen, E.H. (eds.): *Magnetic Bearings: Theory, Design and Application to Rotating Machinery*. Springer, Berlin (2009)
9. Aström, K.J., Hägglund, T.: *Advanced PID Control*. Instrument Society of America, Research Triangle Park (2006)
10. De Caigny, J., Camino, J.F., Oliveira, R.C.L.F., Peres, P.L.D., Swewers, J.: Gain-scheduled dynamic output feedback control for discrete-time LPV systems. *Int. Nonlinear Control* **22**, 339–360 (2012)